GRID FAULT RIDE THROUGH FOR WIND TURBINE DOUBLY-FED INDUCTION GENERATORS

Graham Pannell

A thesis submitted for the degree of
Engineering Doctorate

Newcastle University
School of Electrical, Electronic & Computer Engineering

ABSTRACT

Wind farms must contribute to the stability and reliability of the transmission grid, if they are to form a robust component of the electrical network. This includes providing grid support during grid faults, or voltage dips. Transmission system grid codes require wind farms to remain connected during specified voltage dips, and to supply active and reactive power into the network.

Doubly-fed induction generator (DFIG) technology is presently dominant in the growing global market for wind power generation, due to the combination of variable-speed operation and a cost-effective partially-rated power converter. However, the DFIG is sensitive to dips in supply voltage. Without specific protection to 'ride through' grid faults a DFIG risks damage to its power converter due to over-current and/or over-voltage. Conventional converter protection via a sustained period of rotor-crowbar closed-circuit leads to poor power output and sustained suppression of the stator voltages.

This thesis presents a detailed understanding of wind turbine DFIG grid fault response, including flux linkage behaviour and magnetic drag effects. A flexible 7.5kW test facility is used to validate the description of fault response and evaluate techniques for improving fault ride-through performance.

A minimum threshold rotor crowbar method is presented, successfully diverting transient over-currents and restoring good power control within 45ms of both fault initiation and clearance. Crowbar application periods were reduced to 11-16ms. A study of the maximum crowbar resistance suggests that this method can be used with high-power DFIG turbines.

Alternatively, a DC-link brake method is shown to protect the power converter and quench the transient rotor currents, allowing control to be resumed; albeit requiring 100ms to restore good control. A VAr-support control scheme reveals a 14% stator voltage increase in fault tests: reducing the step-voltage impact at fault clearance and potentially assisting the fault response of other local equipment.

TABLE OF CONTENTS

ACKNOWLEDGEMENTS

The author would like to thank the EPSRC for their financial support.

I would like to give special thanks to Econnect for the extended support given throughout this project; in particular to Ruth Kemsley for making things happen and for healthy doses of pragmatism.

Thanks go of course to my supervisor, Dave Atkinson, for his guidance and encouragement. I would like to thank Tusitha Abeyasekera for all his efforts in the building and commissioning of the test rig.

I am happy to acknowledge the support of Gamesa, who provided advice and information on their experience with DFIG wind turbines, and in particular Oscar Moja Ruiz for his diligence.

Thanks are due to Andrew Causebrook for the use of the grid fault emulator and for his willingness to talk over the hairier aspects of the physics of fault response.

I would like to thank the administrative and IT-support staff in the department, the whole technical support team; in particular Dave Branch for his 'magic' sound absorption pads. I would like to thank friends in the lab, for making life easier. Special thanks go to Jack Noble and Andrew Smith for sharing their knowledge of the beautiful game. I'd like to add a line for Phil Taylor, for getting the ball rolling! Finally, thanks to Laurie, for having patience.

GLOSSARY AND SYMBOLS

Glossary and commonly used acronyms

Crowbar	Rotor-windings temporary closed-circuit device.
DC-brake	DC-link power sink
DC-Link	DC connection of the back-back DFIG power converter arrangement
DFIG	Doubly Fed Induction Generator
DSP	Digital Signal Processor
emf	Electromagnetic Force
EMI	Electromagnetic Interference
Estop	Emergency stop.
FRT	(Grid) Fault Ride Through
GTO	Gate Turn-Off
GUI	Graphical User Interface
HRC	High Rupture Capacity (fuse)
HV	High-voltage (greater than 100kV)
IGBT	Insulated Gate Bipolar Transistor
I/O	Input and output interface
LC	Inductor-capacitor filter
LCL	Inductor-capacitor-inductor ('T'-shaped) filter
LSC	DFIG Line-side Converter
LV	Low-voltage (less than 1kV)
MMF	Magneto-Motive Force
MV	Medium-voltage (1kV – 100kV)
PI	Proportional-Integral (Controller)
PIC	Programmable Interrupt Controller
PLL	Phase Locked Loop
p.u.	per-unit(s)
PWM	Pulse Width Modulation
RFI	Radio Frequency Interference
rms	root-mean-square average value
RSC	DFIG Rotor-side Converter
SCR	Silicon-Controlled Rectifier
SFIG	Singly-Fed Induction Generator (shorted rotor)
SI	International System of measurement units
TSO	Transmission-System Operator
UPS	Uninterruptible Power Supply
Variac	Variable auto-transformer
VPLL	Space-Vector based PLL
VSC	Voltage-Source Converter
WT	Wind Turbine

Labelling of space vectors

Space vector $\underline{u}_b^a$ or $\overline{u}_b^a$ — *reference frame*; *circuit reference*

Space vector of Variable ***u*** on circuit ***b*** measured in the reference frame ***a***

Space vector component u_{bd}^a or u_{bda} — *Direct (or quadrature) axis component*

Direct-axis, ***d***, (or quadrature-axis, ***q***) component of space vector of variable ***u*** on circuit ***b*** measured in the reference frame ***a***

Superscripts (reference frames)

s	stationary reference frame with respect to the stator circuit
r	stationary reference frame with respect to the rotor circuit
e	excitation reference frame, aligned with stator voltage
g	general reference frame

Other Superscripts

⊗	controller reference quantity
*	complex conjugate

Subscripts

0	initial conditions, i.e. the state of the variable at time zero[1]
0	per-unit base value[1]
0	zero sequence component[1]
1	positive sequence component
2	negative sequence component
σ	leakage quantity
mag, μ	magnetising quantity
a, b, c	electrical phases in three-phase system
d	d-axis or 'direct-axis' quantity: aligned with the orthogonal ref. frame
q	q-axis quantity: aligned in quadrature with the direct axis of the same reference frame
s	DFIG stator circuit quantity
r	DFIG rotor circuit quantity
c	DFIG line-side converter circuit quantity
BC	DC-link brake-chopper quantity
cb	rotor crowbar-circuit quantity
ref	a controller reference value
ph	a phase quantity
ph-ph	a line-line quantity
L	mechanically the low-speed (hub) side of the turbine gearbox
m	mechanically the high-speed (generator) side of the turbine gearbox

[1] Context-specific!

Symbols

Electrical variables

$\bar{v}_s^e$	space vector of stator voltage viewed in the excitation reference frame
v_{sa}, v_{sb}, v_{sc}	phase *a, b* and *c* instantaneous stator voltages
v_{sd}^e, v_{sq}^e	d-q components of stator voltage viewed in the excitation frame
$\bar{v}_r^e$	space vector of rotor voltage viewed in the excitation frame
v_{ra}, v_{rb}, v_{rc}	phase *a, b* and *c* instantaneous rotor voltages
v_{rd}^e, v_{rq}^e	d-q components of rotor voltage viewed in the excitation frame
$\bar{i}_s^e$	space vector of stator current viewed in the excitation frame
i_{sa}, i_{sb}, i_{sc}	phase *a, b* and *c* instantaneous stator currents
i_{sd}^e, i_{sq}^e	d-q components of stator current viewed in the excitation frame
$\bar{i}_r^e$	space vector of stator current viewed in the excitation frame
i_{ra}, i_{rb}, i_{rc}	phase *a, b* and *c* instantaneous stator currents
i_{rd}^e, i_{rq}^e	d-q components of rotor current viewed in the excitation frame

Permutations of voltages, currents, flux linkages and other variables can be developed for any space vector or three-phase quantity, in any combination of reference frame or electrical circuit, using the examples given above. From here onwards only a single example of each parameter is generally given. Certain stator and rotor parameters are repeated, purely for the purposes of clarity.

$\bar{u}_s^e$	space vector of stator voltage viewed in excitation frame (alternative)
$\bar{\psi}_s^e$	space vector of stator flux linkage viewed in the excitation frame
$\bar{v}_{s0}^r, \bar{i}_{s0}^r, \bar{\psi}_{s0}^r$	initial conditions of stator voltage, current, flux linkage viewed in the rotor frame
$\bar{\Theta}_r^e$	space vector of rotor MMF viewed in the excitation frame
$\bar{B}_r^e$	space vector of rotor magnetic field strength in the excitation frame
V_{dc}	DC-link voltage

Frequency, speed and angle

f	frequency
f_0	frequency of electrical system, normally 50Hz
t	time elapsed
Ω_r	mechanical angular frequency of rotor in mechanical rad/s
ω	angular frequency
ω_r	angular frequency of rotor in electrical rad/s
ω_e	angular frequency of the excitation reference frame in elec. rad/s
ω_χ	relative rotor frequency from the excitation reference frame in elec. rad/s
θ	angle

θ_r	angle of the rotor frame with respect to the stationary
θ_e	angle of the excitation frame with respect to the stationary
θ_χ	angle of the rotor frame with respect to the excitation frame
θ_ς	slip angle, negative of θ_χ
θ_{r0}	initial angle of the rotor frame (at time zero).
θ_{e0}	initial angle of the excitation frame.
$\theta_{\chi 0}$	initial angle of the rotor frame with respect to the excitation frame.
$\theta_{\varsigma 0}$	initial slip angle.

Machine and circuit parameters

a	effective turns ratio of electrical machine, stator:rotor
N_s	effective number of stator winding coils per phase
N_r	effective number of rotor winding coils per phase
p'	magnetic pole pair number
s	slip
R	resistance
R_s , R_r	per-phase resistance of respective winding
Z	impedance
C	capacitance
X	reactance
L	inductance
L_s , L_r	per-phase inductance of respective winding
L_{es} , L_{er}	per-phase leakage inductance of respective winding
L_m	per-phase mutual inductance
L'_s , L'_r	operational inductance of respective winding
k_s	ratio of mutual / stator inductance p.u. values
k_r	ratio of mutual / rotor inductance p.u. values
σ	dimensionless machine leakage factor
τ_s , τ_r	transient time constant of respective circuit
τ'_s , τ'_r	effective transient time constant of respective circuit
τ_T	torque transient time constant
τ_{cb}	crowbar application period
ς_f	complex frequency adjustment factor
κ	timescale adjustment factor
δ	frequency adjustment factor
$\mathcal{R}$	magnetic reluctance
μ_0	permeability of free space

Space

A	area
h	average width of the rotating machine's airgap
l	length
r	radius

Power and torque

E	energy
F	force
T	torque
T_e	electromagnetic torque
T_L	load torque
P	power
P_m	mechanical power
P_s / P_r	active power of electrical machine stator / rotor
Q_s / Q_r	reactive power of electrical machine stator / rotor
S_s / S_r	apparent power of electrical machine stator / rotor

Mechanical

B	mechanical friction coefficient
D	mechanical damping coefficient
K	mechanical shaft stiffness
J	mechanical moment of inertia

Feedback control

$1/s$	integration operator
$PI(x)$	PI feedback control performed on the error feedback of 'x'
k_p , k_i	proportional & integral control constants
m	modulation signal for PWM generation

Mathematical artifices

A , B , C	general-use coefficients
$f(x)$	general function of 'x'
x	general variable
i , j	imaginary number operator, +90° phase shift in a complex plane
A_s^s	stator-circuit natural fault response coefficient in the stator frame
A_r^r	rotor-circuit natural fault response coefficient in the rotor frame
A_1^s , B_1^s	stator flux linkage fault response solution coefficients in the stator frame
A_2^r , B_2^r	rotor flux linkage fault response solution coefficients in the rotor frame
$k_x(u)$	a derived coefficient: a function of the voltage u
k_σ	derived leakage factor, a combination of σ, τ_s, τ_r
α , β	complex roots of the induction machine natural fault response (in stator frame unless otherwise notated)
ρ_s , ρ_r	complex factors of stator and rotor flux linkage equations
$\Gamma\{f(t)\}$	Laplace transform operation
$F(\nu)$	Laplace transform (denoted by capitalisation of the variable)
ν	Laplace variable
∂	time differential operator

Vectors

Vector definitions

Space vector: $\bar{u}_b^a = u_{bd}^a + j u_{bq}^a$

Complex conjugate: $\bar{u}_b^{a*} = u_{bd}^a - j u_{bq}^a$

Vector operations

The sections below define various vector operations as used in this work.

Direct product

A 2D direct product combines all components of both vectors

$$\bar{u}\bar{v} = u_d v_d - u_q v_q + j\left(u_d v_q + u_q v_d\right)$$

Dot product

The dot product is a non-dimensional scalar, projecting one vector onto another and forming a product of the resulting lengths. Definition:

$$\bar{u} \cdot \bar{v} = |\bar{u}||\bar{v}| \cos\left(\theta_v - \theta_u\right)$$

In two dimensions:

$$\bar{u} \cdot \bar{v} = u_d v_d + u_q v_q$$

Cross product

The vector cross product produces a vector perpendicular to both its dependants, with a magnitude proportional to the sine of the angle between them. The orientation can be found using the right-hand rule.

$$\bar{u} \times \bar{v} = |\bar{u}||\bar{v}| \sin\left(\theta_v - \theta_u\right)\hat{\bar{n}}, \qquad \left|\hat{\bar{n}}\right| = 1$$

In three dimensions:

$$\bar{u} \times \bar{v} = \begin{vmatrix} \hat{x} & \hat{y} & \hat{z} \\ u_x & u_y & u_z \\ v_x & v_y & v_z \end{vmatrix}$$

A note of caution: In many texts it is common to see the × sign used for the direct product, although the different use can normally be inferred by the context.

Cross product determinant

The determinant of the vector cross product is useful in expressing phase dependent products such as the definition of electric torque using stator and rotor current space vectors. To avoid any confusion with the direct- or cross-products, a ^ symbol is used for the cross product determinant:

$$\bar{u} \wedge \bar{v} = |\bar{u}||\bar{v}| \sin(\theta_v - \theta_u)$$

In two dimensions:

$$\bar{u} \wedge \bar{v} = u_d v_q - u_q v_d$$

Time differential shorthand

The operation of a partial differential with respect to time is sometimes shortened to:

$$\partial \bar{u} = \frac{\partial \bar{u}}{\partial t}$$

Reference frames example

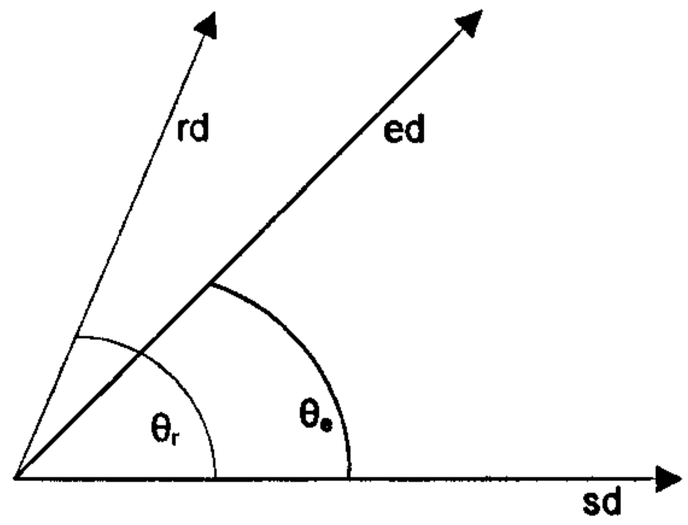

Figure i. Direct or "d" axes of commonly used reference frames.

Relationships between the direct-axes of three common reference frames are shown in Figure i. Quadrature ('q') axes for each frame are defined as π/2 radians ahead of the corresponding 'd' axis. Relative velocities for these frames can be defined as follows:

$\partial \theta_e = \omega_e$ Excitation frame angular velocity with respect to the stator frame.

$\partial \theta_r = \omega_r$ Rotor frame angular velocity with respect to the stator.

Note that the rotor circuit rotates at electrical rotor frequency, which completes 2π radians *per magnetic pole pair* for each mechanical rotation (Eq. i).

$$\omega_r = p' \Omega_r \quad \text{(i)}$$

The reference frame in which a particular parameter is measured is denoted by a superscript. A reference frame transformation is defined by an appropriate angle, using an appropriate rotational transformation; e.g. consider an arbitrary voltage vector measured in the stator (s), rotor (r) and excitation (e) frames:

$$\bar{v}^s = \bar{v}^e \exp(j\theta_e) \quad \text{(i)}$$

$$\bar{v}^r = \bar{v}^e \exp(j\{\theta_e - \theta_r\}) \quad \text{(ii)}$$

Vector quantities are indicated with an underline or an over-bar.

1 INTRODUCTION

1.1 Grid fault ride through for wind turbine doubly-fed induction generators

1.1.1 Background

Wind power is gradually becoming a more significant part of worldwide electrical generation. Planned and existing large offshore wind farms are a particular feature of Europe's growing wind energy supply, with significant engineering challenges for their assimilation and operation within mature transmission networks. Large wind farms in general need to contribute to the stability and reliability of the transmission grid, if they are to form a robust component of the generation network. This includes providing grid support during grid faults, or voltage dips. In the past, grid codes required wind farms to disconnect from the grid when a voltage dip was detected, because the typical response of the induction generators employed in wind turbines was not helpful in terms of fault recovery or network stability. However, revised grid codes now require wind farms to remain connected during a voltage dip, and to supply active and reactive power into the network.

This fault ride through behaviour could be achieved at wind turbine level, by engineering the individual wind turbines to provide the required response; or at wind farm level, for example, by employing additional auxiliary equipment at the wind farm substation. The former solution avoids adding potentially costly wind farm power level equipment, and forms the focus of this thesis.

Many wind turbines incorporate a doubly-fed induction generator (DFIG) to permit variable rotor speed operation and provide independent control of active and reactive power output. A DFIG has a power electronic converter which can vary the voltage applied to the rotor windings, providing significant control capability. Without specific protection for fault ride through a DFIG risks damage to its power converter in response to a grid fault due to over-current and/or over-voltage. Any proposed fault ride through protection scheme must take into account the requirements for active and reactive power delivery in order to support the faulted transmission grid.

Figure 1.1. DFIG Wind Farm near Pamplona, Spain; from a research visit.

1.1.2 Research project

The Engineering Doctorate research project behind this thesis was created between Newcastle University and the renewable electricity firm Econnect to investigate the grid fault ride through behaviour of DFIG wind turbines.

As an early part of the research project a number of wind turbine manufacturers were approached to gain further understanding of their development activities regarding DFIGs and their views regarding the most important areas on which to focus. The following manufacturers contributed to the consultation:

- Gamesa
- DeWind
- Vestas (incorporating NEG Micon)

Key academic contributors were also consulted, involving universities which were active in DFIG research such as Durham, Nottingham and Manchester (formerly UMIST). National Grid, the UK transmission system operator, and NaREC, the New and Renewable Energy Centre in Blyth were also involved in the survey.

The outcome of the consultation [1] concluded that fault ride through was a key area for potential innovation. Most manufacturers have developed in-house techniques to meet the minimum grid code requirements, although these remain largely confidential; neither the performance nor the cost-effectiveness of the solutions has to date been publicly scrutinised.

It was further concluded that a low-power DFIG test facility with the ability to apply flexible grid fault conditions in a safe, controllable and repeatable manner would be of great benefit. This kind of testing is difficult and expensive to achieve on a full-scale wind turbine, which may expose equipment to the risk of costly failures.

The fault response of DFIG systems has not to date been comprehensibly treated in contemporary literature. A complete description therefore forms a cornerstone of the contribution made by this thesis.

The focus of this thesis is on the grid fault ride through behaviour of the electrical generator system. Mechanical dynamics are considered only where they contribute to the electric response (e.g. the effect of rotor speed on slip frequency). The failure of wind turbine components is not considered. The nature of the grid fault conditions studied is assumed from transmission system grid code regulations.

1.1.3 Research objectives

The objectives of the research project were:

- To develop a comprehensive understanding of the grid fault response of wind turbine DFIGs.
- To establish the limitations of wind turbine DFIG fault response and summarise the challenges for fault ride through behaviour.
- To develop a test facility to permit the detailed investigation of DFIG fault response in a laboratory setting.
- To develop techniques to improve the fault ride through performance of wind turbine DFIGs.
- To validate the description of fault response and evaluate the performance of new DFIG control and configuration techniques through the use of the test facility.
- To provide recommendations for cost-effective solutions for wind turbine DFIG fault ride through.

1.2 Thesis overview

1.2.1 Thesis layout

The thesis moves on to detail the problem from the points of view of both the transmission system and the electrical machine. A low-power DFIG test facility is then presented, followed by a complete description of the fault response of a conventional wind turbine DFIG. Finally, proposed fault ride through solutions are reviewed; certain techniques are further developed and test results are presented.

Chapter 2 introduces the problem of fault ride through (FRT) from a transmission system point of view and relates it to the fault response of wind turbine generators, particularly DFIG wind turbines. Grid faults are defined and typical generator fault response is explored. Finally transmission operator grid codes for fault ride through behaviour are summarised.

Chapter 3 provides an overview of the theory and principles of DFIG operation and control. The aim is to cover the necessary background to analyse the fault response of a conventional wind turbine DFIG. Generalised machine theory is introduced and used to demonstrate vector control of the DFIG system.

Chapter 4 introduces the 7.5kW DFIG test facility which was built and commissioned at Newcastle University and referred to throughout this work as the 'test rig'. The test rig included a DFIG system, wind turbine simulator, grid fault emulation equipment and a flexible control hardware installation. A dynamic simulation of the complete DFIG system is also presented; its prime function was to develop techniques and control methods before implementation on the test rig.

Chapter 5 provides a comprehensive study of DFIG fault response, supported by results from the DFIG test rig. The physical behaviour is presented through a detailed description of the flux linkage response and later developed with analytical solutions of the generalised DFIG machine equations operating under fault conditions. Fault response is separated into the natural response and the forced response: the natural response describes zero rotor-voltage behaviour while the forced response superposes an applied rotor voltage via the power converter. The full DFIG system fault response is described with reference to test results and used to extract the key issues for fault ride through.

Chapter 6 presents possible solutions to the requirements of fault ride through. DFIG fault response is summarised with respect to its own protection and its transmission system contribution. Design aims for a fault ride through solution are deduced and explained. A range of proposed solutions are reviewed and a promising few taken on for further development. Three techniques are explored in depth and evaluated on the test rig; their comparative performances leading to recommendations for their potential application to high-power wind turbine DFIGs.

1.2.2 Parallel research project

The Engineering doctorate project behind this thesis was operated in parallel with a research project carried out as part of the DTI technology programme "New and Renewable Energy" which was managed by Future Energy Solutions. The work was carried out by the author, Econnect Ventures Ltd. and Newcastle University [2].

TRANSMISSION SYSTEMS & FAULT RIDE THROUGH 2

This chapter introduces the problem of Fault Ride Through (FRT) from a transmission system point of view and relates it to the fault response of wind turbine generators, particularly DFIG wind turbines.

Firstly, the relevance of wind power is highlighted followed by the three main topologies for wind power generation, underlining the importance of the DFIG. Secondly, transmission system operation and grid code regulations are introduced, with reference to the particular challenges facing the integration of wind power into large transmission systems, including most notably the need to ride through grid faults.

Grid faults are defined and an example containing a wind turbine and typical grid connection equipment explained. The different types of grid faults are discussed along with the rate at which they occur. Typical fault response for major generator topologies are summarised and the limiting capabilities of the conventional DFIG are highlighted.

Finally, transmission system regulations for fault ride through are presented and the general requirements for good fault response are discussed. The fault ride through regulations for two grid codes with contrasting focuses are detailed: The relatively small and isolated GB system, and the geographically larger and more widely connected German system. Fault voltage profiles for other countries are shown for comparison.

2.1 Wind power

2.1.1 Wind energy

Wind is a clean and sustainable fuel source and is the first renewable energy source to compete commercially both in terms of cost and quantity of generation [4], with significant future cost savings expected [5][6]. In 2007, wind energy comprised 3% of the EU's electrical generation and 30% of all new electricity-generating capacity installed in the EU in the last five years [7]. The UK government's "Renewable Obligation" lays a legally binding target for suppliers to achieve 10% of electricity supply from renewable sources by 2010 and 15% by 2015 [8]. Wind is expected to comprise 75% of this renewable energy target [9]. In short, wind energy will contribute increasingly significantly to European and global energy generation.

In networks where wind power and other distributed power sources represent a small percentage of total generation, as is the case historically, the technical management of the electricity system such as voltage and frequency control is performed entirely by the dominant conventional synchronous generation plant. In these networks the typical approach to large voltage disturbances was to disconnect the wind turbines at fault initiation and reconnect after the restoration of a healthy voltage conditions.

As wind power begins to represent a greater proportion of total generation, wind farms are having greater influence over power system behaviour. In this scenario wind farms are required to contribute to the stability of the system, including the key issue of fault ride through.

2.1.2 Wind turbine topologies

In the following sections, the main wind turbine generator topologies are introduced. This list comprises the three types which dominate grid connecting wind power installations, as shown in Figure 2.1 [10].

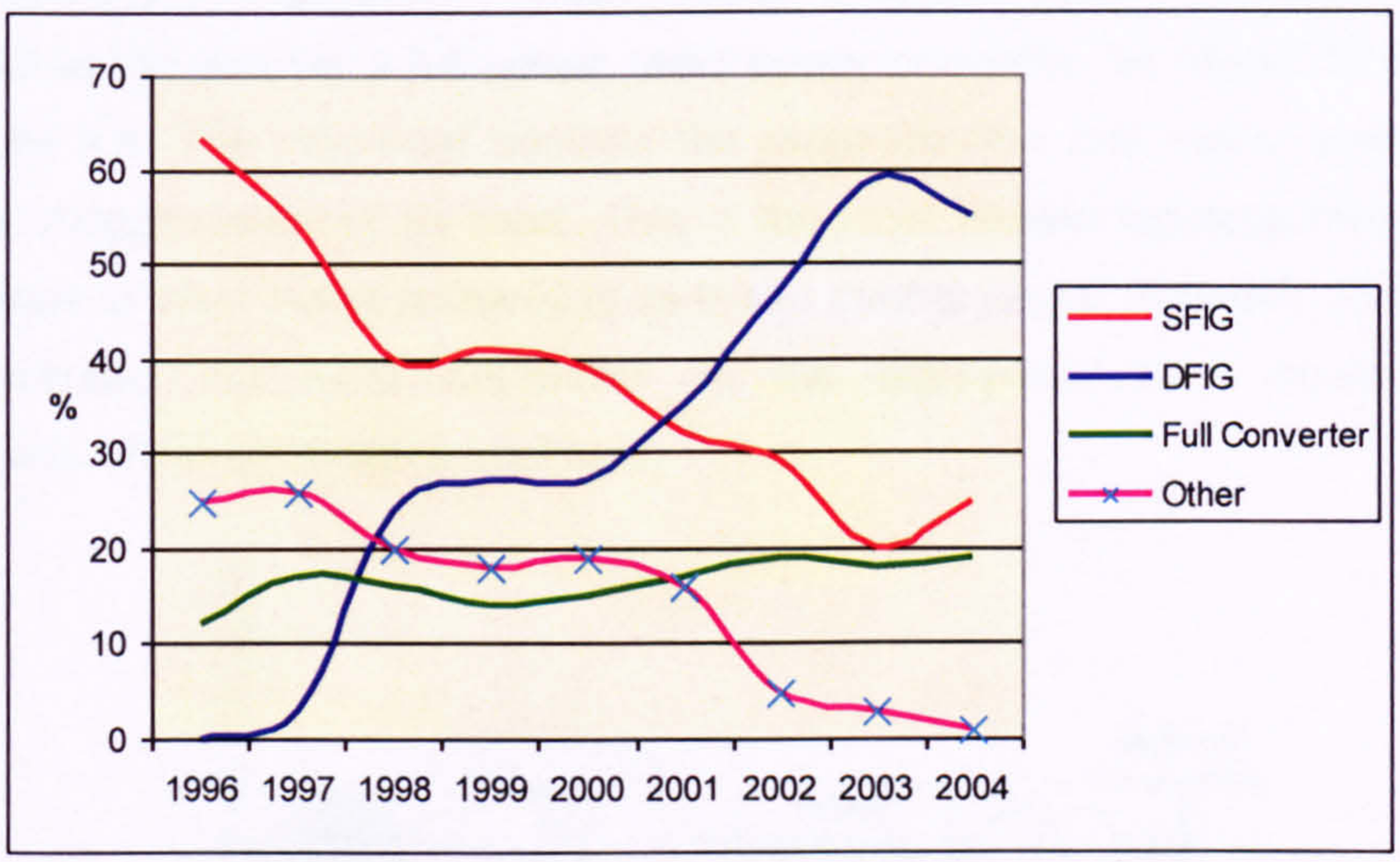

Figure 2.1. World market share of wind turbine topologies [10].

Singly-Fed Induction Generator wind turbine (SFIG)

The standard squirrel cage induction generator design is hereafter referred to as the Singly-Fed Induction Generator (SFIG) in order to readily distinguish it from the more versatile doubly-fed version. Well understood, robust and cheap; these turbines dominate in low-power installations (<1MW per turbine) [11].

The induction generator is directly coupled to the grid as shown in Figure 2.2. As such, SFIGs run at very close to synchronous speed over their whole torque range and are often referred to as 'fixed-speed' machines. The mechanical power input is directly coupled to the electrical power output and control of the generator is very limited.

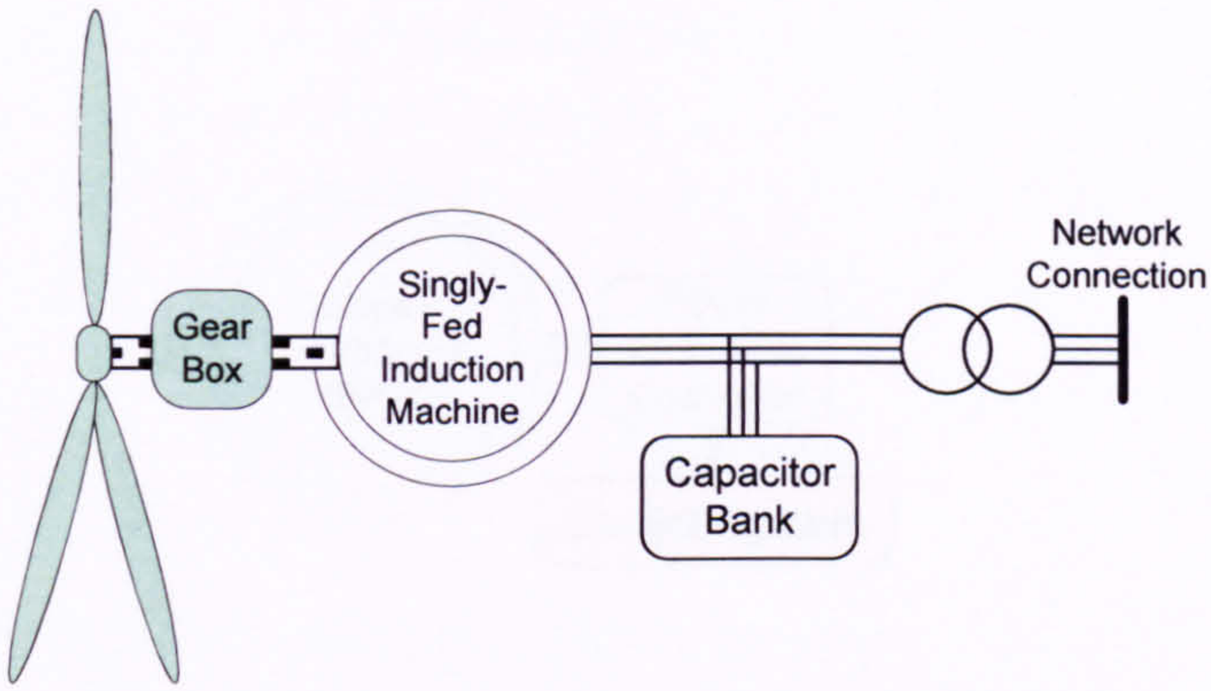

Figure 2.2. SFIG wind turbine topology.

As for all the wind turbine electrical topologies, the generator's LV terminals are stepped up to wind farm distribution voltage levels by a dedicated three-phase transformer. For local earthing, the transformer also offers the option of isolating the neutral point of the generator [12].

Fully-rated converter wind turbine

In this topology the generator, which maybe a synchronous or induction type, is connected to the grid via a full-power rated power converter, as shown in Figure 2.3 and Figure 2.4. The converter controls the magnetisation and output power of the generator independently of its input. This is the most flexible topology from a power system point of view owing primarily to its broad control range. However, this topology is considerably the most expensive as the high-power-rated converter adds considerably to the generator's total cost.

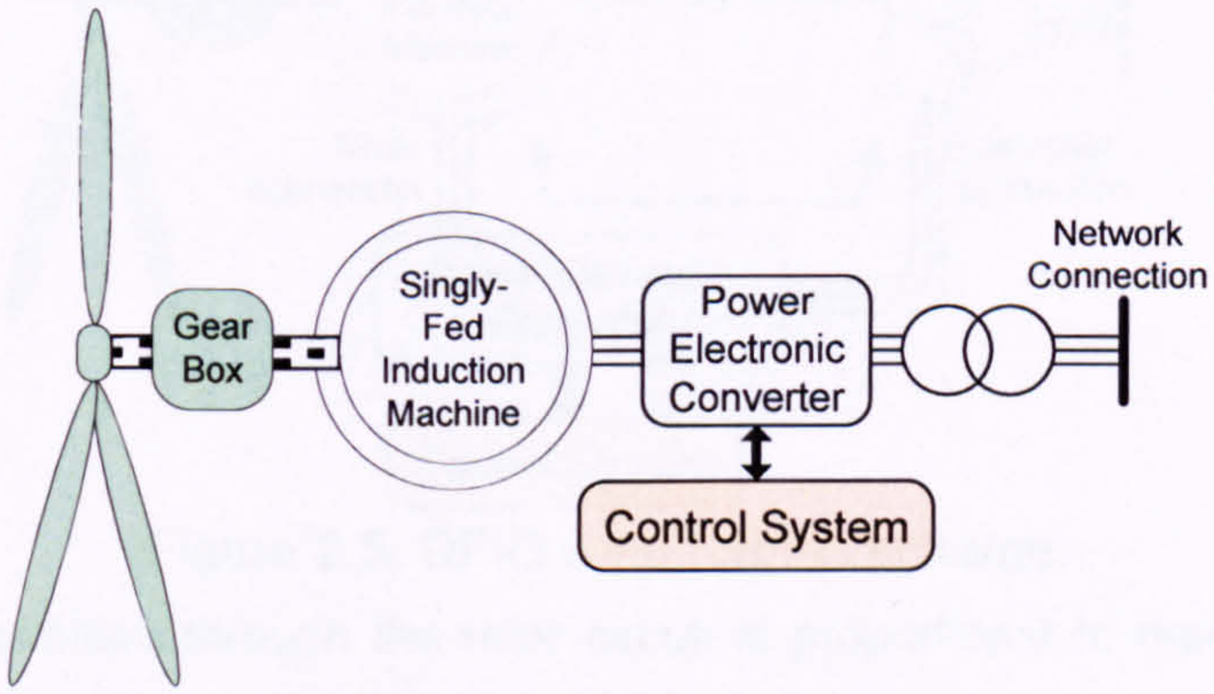

Figure 2.3. Fully-rated converter wind turbine scheme – with gearbox.

One version of the fully-rated converter type employing a gearbox is shown in Figure 2.3. This setup is mechanically similar to the DFIG. Another version of the fully-rated converter type omits the gearbox and uses a very large multi-pole generator, as shown in Figure 2.4. These two possess broadly similar capabilities from the point of view of the electrical network.

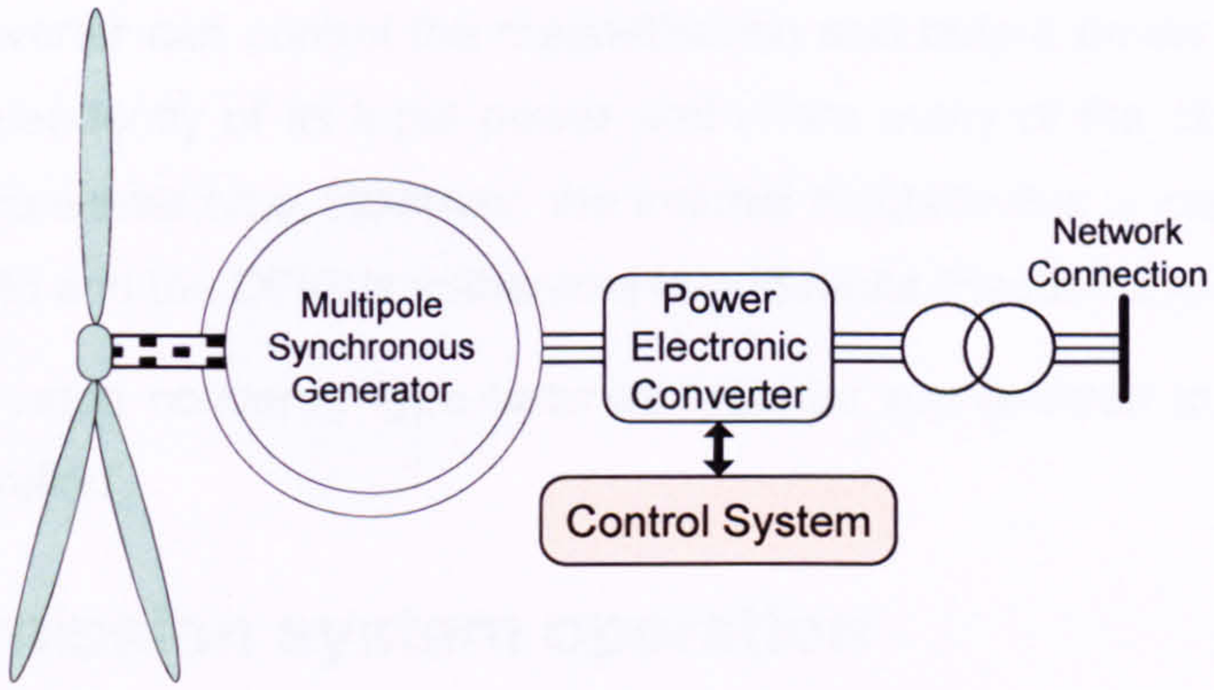

Figure 2.4. Fully-rated converter wind turbine scheme – without gearbox

Doubly-Fed Induction Generator wind turbine (DFIG)

As illustrated in Figure 2.5, a Doubly-Fed Induction Generator (DFIG) comprises a wound-rotor induction generator supplied on the stator-side by the grid connection and on the rotor-side by a power electronic converter. The converter supplies slip-frequency voltages to the rotor via slip-rings and brushes, and conveys power in either direction at grid frequency via an intermediary network connection point. The converter's grid connection is often (but not necessarily) via a tertiary transformer winding to administer appropriate voltage levels.

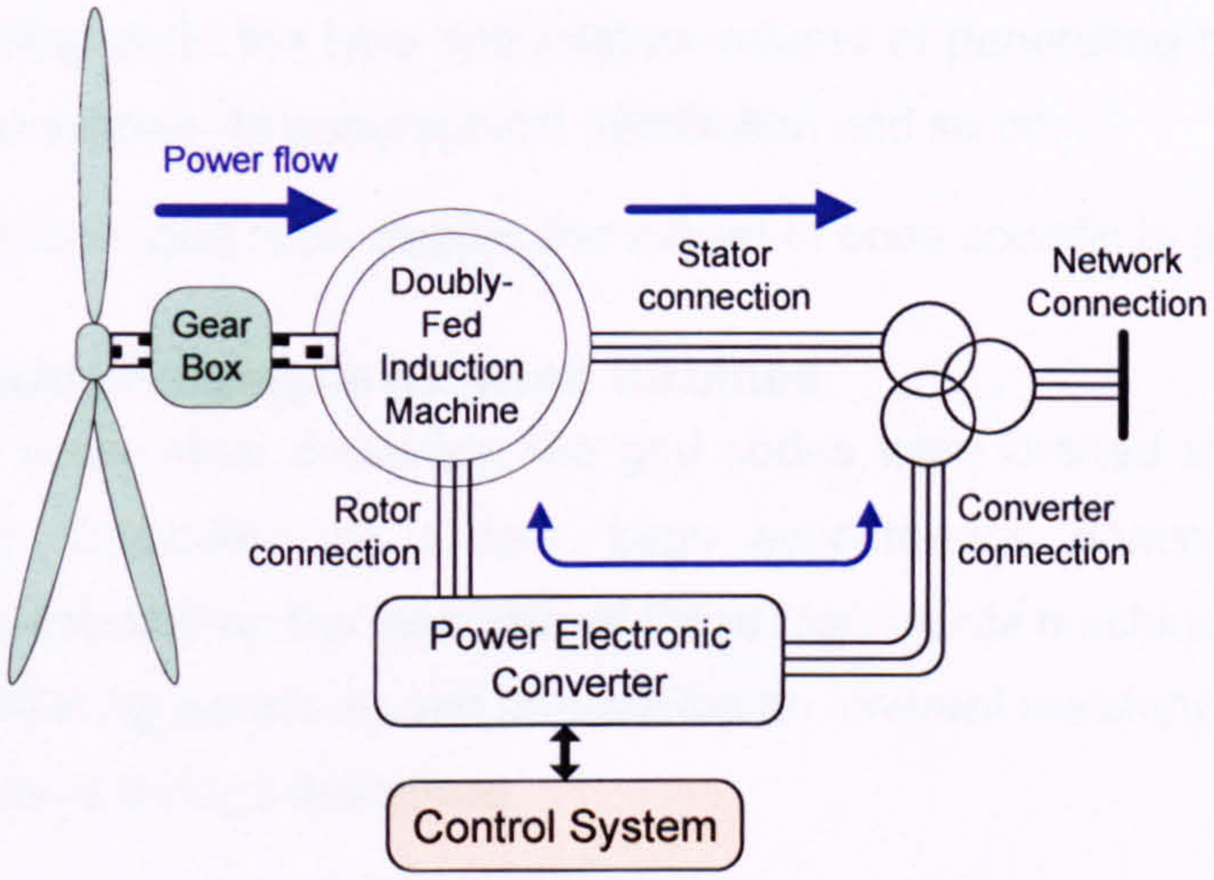

Figure 2.5. DFIG wind turbine scheme.

The power transmitted through the rotor circuit is proportional to machine slip. As a result the converter may be rated for a fraction of the generator's power capacity and still offer a considerable operating speed range; typically within ±25% of synchronous speed and therefore requiring a 25% rated-power converter. The lower converter rating also results in lower losses and hence higher overall electrical efficiency than a fully-rated converter topology.

The power converter rating compromise offers a considerable cost saving over the fully-rated converter type, which explains why DFIGs dominate global installations of medium and high power wind turbines (>1MW each) ([11], also Figure 2.1).

The power converter can control the magnetisation and output power of the induction generator independently of its input power and offers many of the control benefits of the fully-rated converter type. However, the internal machine flux is exposed directly to the electrical grid and the DFIG is vulnerable to grid faults (Section 2.4.4).

DFIG and fully-rated converter type turbines together are referred to in this work as 'converter-controlled'.

2.2 Transmission system operation

2.2.1 Grid codes

Transmission System Operators (TSOs) impose a body of regulations, so-called grid codes, which govern the connection, planning and operating procedures for all users of their transmission system. As described by GB's National Grid Electricity Transmission plc. (NGET), this code is intended to ensure an "efficient, coordinated and economical transmission system" [13].

Specific regulations exist within the code for the operation of generating plant on the transmission system. This subset of grid code is designed to ensure system stability, maximise transmission, and maintain voltage levels. The rules vary from country to country; depending upon the type and relative volume of generating plant, the size of the transmission system, its geographical distribution and so on.

In this work, the term 'grid code' implies the subset of code specific to generation plant.

2.2.2 Grid code challenges for wind turbines

In the UK and many other countries, the grid codes were drafted in a period when generation was dominated by a few, large synchronous generators. As such, regulations concentrated on the response of these high-inertia machines; typically fitted with voltage regulating governors and possessing an inherent resistance to the adverse effects of short-term voltage deviations.

As new technologies such as wind power and other renewable sources have grown in their share of total energy generation, grid codes have had to be revised to account for the contributions made by induction generators and directly-connected power electronic equipment [14][15][16][17].

Wind farms in particular pose additional challenges to grid operators. Large wind farms are typically connected far from load centres or strong grid transmission points (areas of tightly-controlled voltage). Wind turbines also provide a variable power source and as such offer an economic challenge in predicting and utilising the available wind energy resource.

Relevant technical issues for wind farms are summarised below.

Non-system frequencies

Power electronic equipment operated using PWM methods add frequency distortions to the system voltages. Older power electronics equipment, using for example thyristor switches, is more problematic in this aspect [18]. IGBT voltage source converters, such as is now almost exclusively used in DFIG and fully-rated converter wind turbines, operate well within transmission system limits for harmonic distortion [19] and can be controlled to aid transmission system stability during system faults.

Low-order electrical harmonics are typically restricted by the design of the generators. Sub-system frequency noise can be found in the current output of wind turbine generators, arising from tower shadow or flicker [20]. This is a significant problem for directly grid-coupled fixed speed generators. Converter-controlled wind turbines may set their output power independently from their input, offering a power smoothing effect which can minimise this problem. Turbine drive-shaft resonance is referred to in Chapter 5.

Frequency control

The system frequency is controlled by balancing power generation against load. A net power difference will cause synchronously rotating plant to accelerate or decelerate at a rate limited by the gross system inertia. Certain generator governors are controlled to respond to frequency deviations by adjusting their power output until the system frequency stabilises. Higher inertia power systems are desirable because they offer greater resistance to changes in system frequency.

A converter-controlled wind turbine's output power is set independent of the turbine's speed. Hence DFIG wind turbines would not naturally contribute to system inertia. In replacing synchronous plant, the total system inertia would be reduced. However, inertia effects may be synthesised by the DFIG controller. This controlled response may be used to compensate for the loss of synchronous plant inertia [21].

Power ramp rate

To assist frequency regulation, wind farms are obliged by grid codes to limit the rate of change of power they deliver to the network. Converter-controlled wind turbines can be controlled to meet such standards. However, this limit may unfortunately prevent the wind turbine from using all of the available wind power, as illustrated in Figure 2.6.

This effect is partially mitigated by the power aggregation of increasingly large wind farms. The utilisation of wind energy as a variable source is an economic question not further considered in this work.

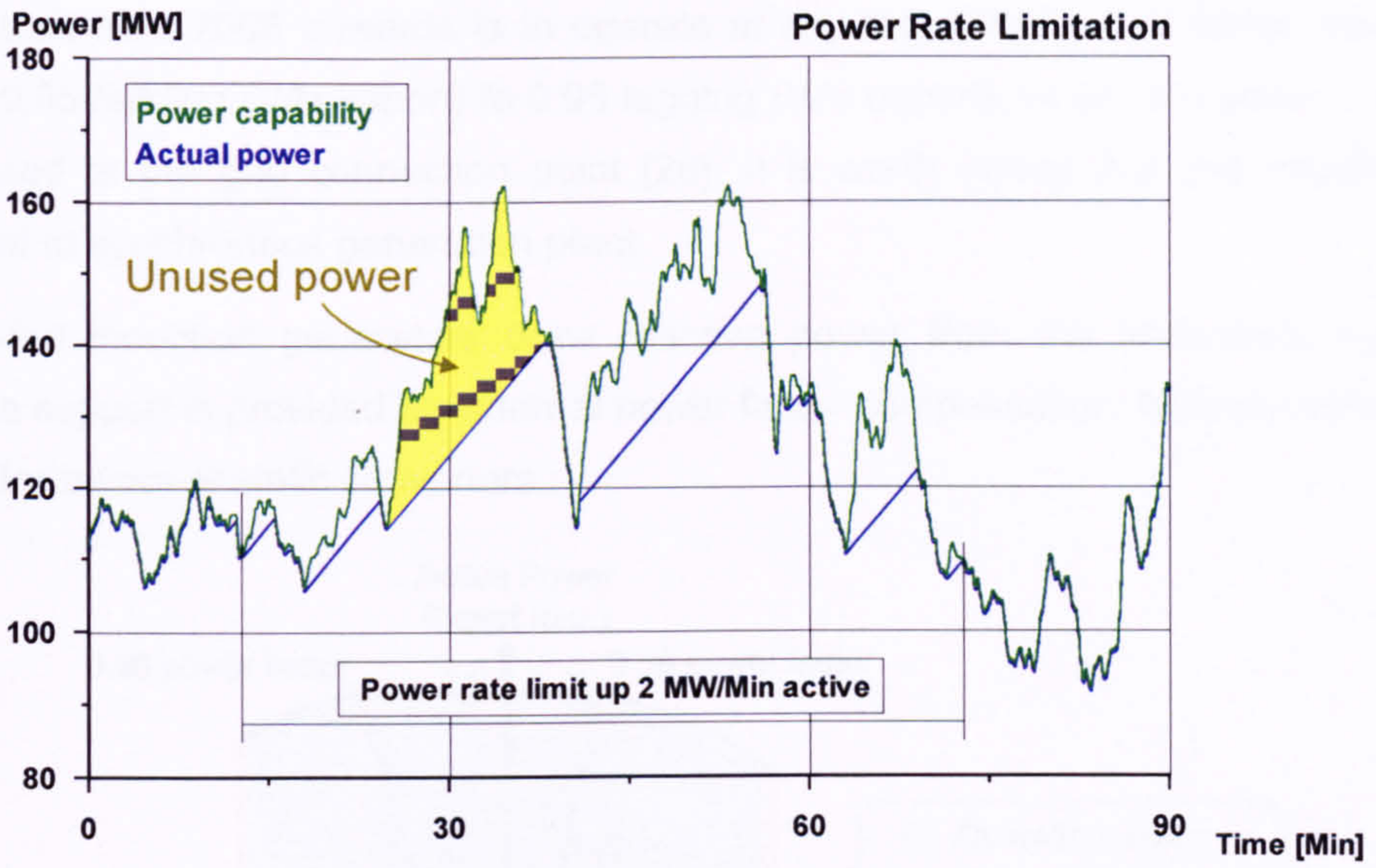

Figure 2.6. Example of a power ramp rate limit and the associated loss of available wind energy capture.

Frequency event response

In the event of the rapid loss of a large power source or load the system frequency may accelerate rapidly. For stability, this demands a rapid change of active power in proportion to the frequency deviation. Specific droop rates and frequency deadbands of power response are set locally, with necessary response times of 10's of seconds [22]; far shorter than the startup times necessary to engage backup generation units. Converter-controlled wind turbines may respond in milliseconds by adjusting their power output.

In the case of *over*-frequency events, a turbine may achieve stability through reducing its power input. This can be achieved in a fraction of a second through blade pitch control [23].

In the case of *under*-frequency events, although output power may be momentarily increased, additional input power may not be readily available and the turbine would be dynamically unstable. The duration of the turbine's frequency response capability is limited by the relatively low inertia of its rotor [24].

To provide a standby under-frequency capability from a wind farm would require a continuous under-use of the available wind resource, an economic question which lies beyond the scope of this work.

Voltage regulation

Transmission system voltages are controlled to ensure efficient power transmission and useful power distribution. Owing to the inductive nature of transmission lines, voltage control requires that reactive power demands are dispatched to selected generation plant [25]. For example, In England and Wales the requirement for wind

farms built from 2006 onwards is to operate at any requested power factor within the range 0.95 leading (VAr import) to 0.95 lagging (VAr export), where the power factor is measured at the grid connection point [26]. It is worth noting that this capability is inherent to synchronous generation plant.

Singly-fed induction generators draw reactive power from the immediate network. Voltage support is provided by external power factor compensation: typically switchable capacitor banks or static converters.

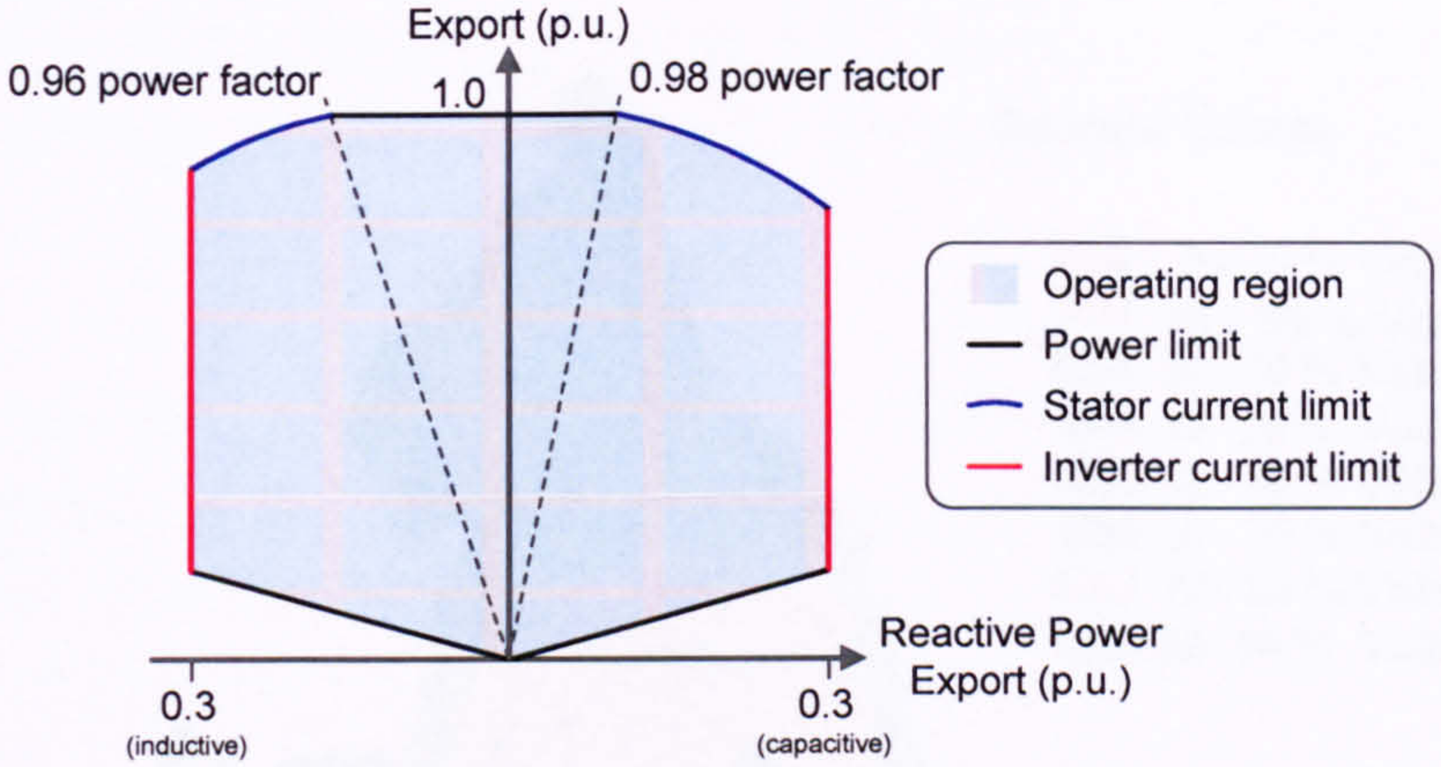

Figure 2.7. Typical operational power factor capability for a DFIG.

Converter-controlled wind turbines provide the requisite power factor control. DFIG systems provide controllable reactive power through the stator terminals, by over- or under-exciting the generator magnetisation via the rotor-side converter, and a limited amount from the line-side converter. The range of power factor operation for a typical DFIG is illustrated in Figure 2.7 [2] (adapted from [27]). A DFIG controller may be set to control either the power factor, reactive power output or connection voltage.

Fault ride through

Fault Ride Through (FRT) refers to the capability of generation plant to remain connected, dynamically stable and offer network support throughout a serious voltage disturbance on the transmission network. As stated in [28]: "fault ride through... is a critical aspect for Wind Farms which for a conventional synchronous plant is a natural capability".

Although the voltage dips associated with grid faults may last for only a few cycles, they can bring about certain undesirable characteristics of induction-machine based generators. These include: uncontrolled active and reactive power, continued voltage suppression, or, catastrophically, the cascade disconnection of generators leading to a

[2] Note that the induction machine characteristic of consuming reactive power is evident in the asymmetric stator limit locus, i.e. that the DFIG has a greater capacity for reactive power *import*.

system under-frequency event and widespread consumer disconnection. The problem of fault ride through forms the focus the rest of this chapter.

2.3 Grid faults

2.3.1 Fault event

A grid fault is a short-circuit or earthing event on one or more phases of the grid system. This may be caused for example by: momentary earthing of a single overhead line, a line-line clash or a three-phase short-circuit at a substation.

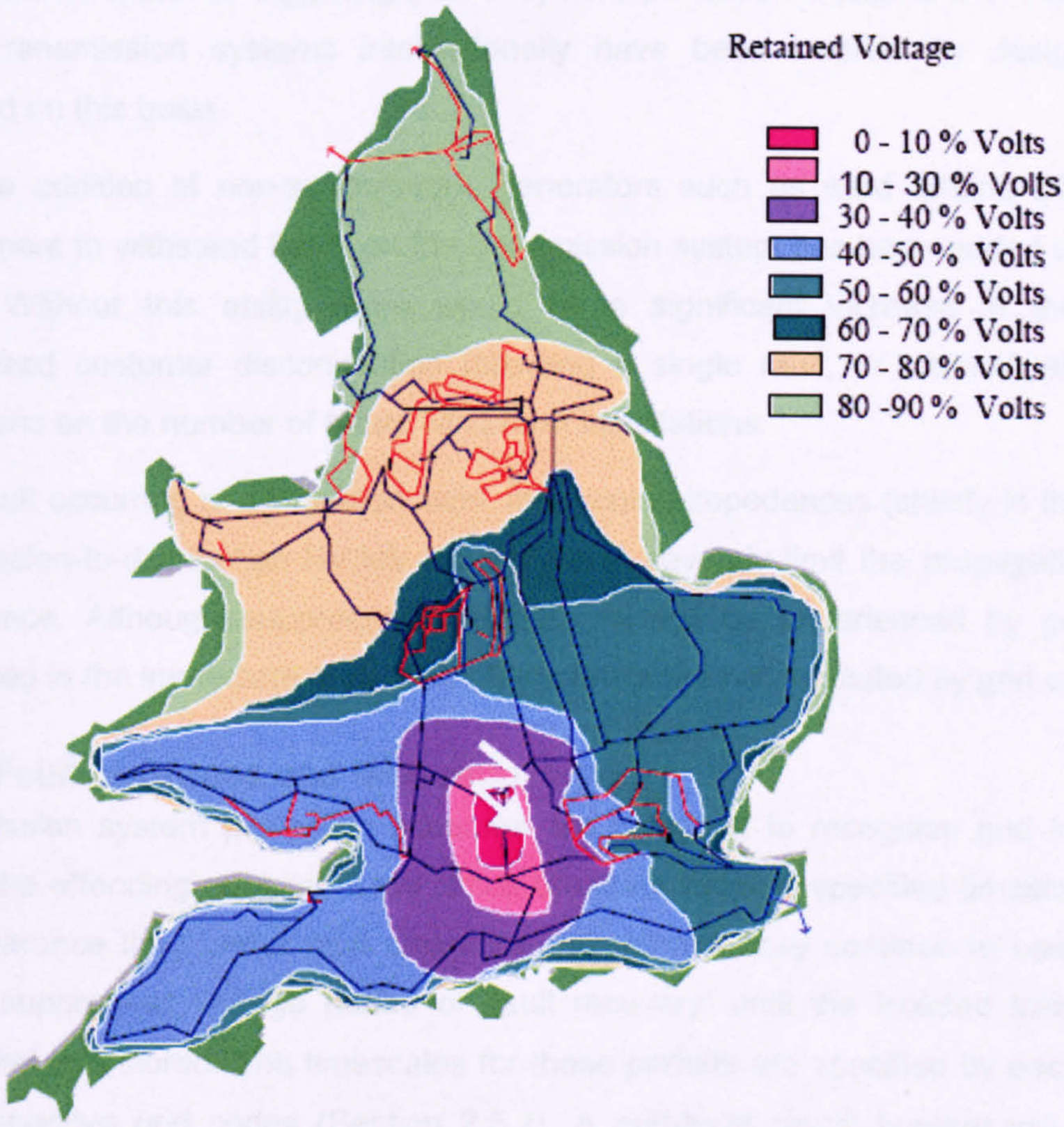

Figure 2.8. Grid fault voltage suppression in England and Wales due to a three-phase substation fault in Oxfordshire [16].

The direct consequence is zero voltage at the source of the fault. With increasing distance from the fault source, and depending upon power flows, voltages are depressed but non-zero across the whole network. Figure 2.8 illustrates an example of system voltage suppression in England and Wales due to a three-phase short circuit at a 400kV substation in Cowley, Oxfordshire. This shows that most of the county suffered less than 10% voltage and more than half the country suffered less than 60%.

In the event of a grid fault, equipment sensitive to low voltages will automatically disconnect (trip off) from the grid, causing a sudden imbalance in net power flow. The

system frequency may become unstable, rapidly falling if large numbers of generators are disconnected. The frequency fall may cause the cascade tripping off of further generation units, leading to forced widespread consumer disconnection or, in a catastrophic case, to widespread blackouts.

2.3.2 Fault withstand

Synchronous generators are inherently capable of operating continuously throughout credible transmission grid faults. A fault close to a synchronous unit will not typically cause it to disconnect; in fact the induced fault current from connected synchronous generators is critical in triggering power system protection equipment in the affected area. Transmission systems internationally have been traditionally designed and operated on this basis.

With the addition of non-synchronous generators such as wind turbine DFIGs, the requirement to withstand faults on the transmission system has been added to the grid codes. Without this ability there would be a significant increase in the risk of widespread customer disconnection following a single fault, or alternatively severe restrictions on the number of future wind farm installations.

For a fault occurring at distribution level, intervening impedances (chiefly in the form of transmission-to-distribution HV:MV transformers) severely limit the propagation of the disturbance. Although suppressed voltages will still be experienced by generators connected in the immediate area, distribution faults are not regulated by grid code.

2.3.3 Fault clearance and fault recovery

Transmission system protection schemes are designed to recognise grid faults and isolate the offending equipment via circuit breakers within a specified timescale – 'the fault clearance time'. After fault clearance the network may continue to operate in a slightly suppressed voltage period of 'fault recovery' until the isolated transmission equipment is restored. The timescales for these periods are specified by each TSO in their respective grid codes (Section 2.5.2). A grid-level circuit breaker will clear an overhead line fault well within one second and a close-up three-phase zero-voltage fault within a handful of cycles (80-200ms).

2.3.4 Grid fault example

Figure 2.9 shows the typical connections between a single DFIG wind turbine in a wind farm and the GB transmission grid. Other countries' networks have a similar structure but with different voltage levels and transformer arrangements.

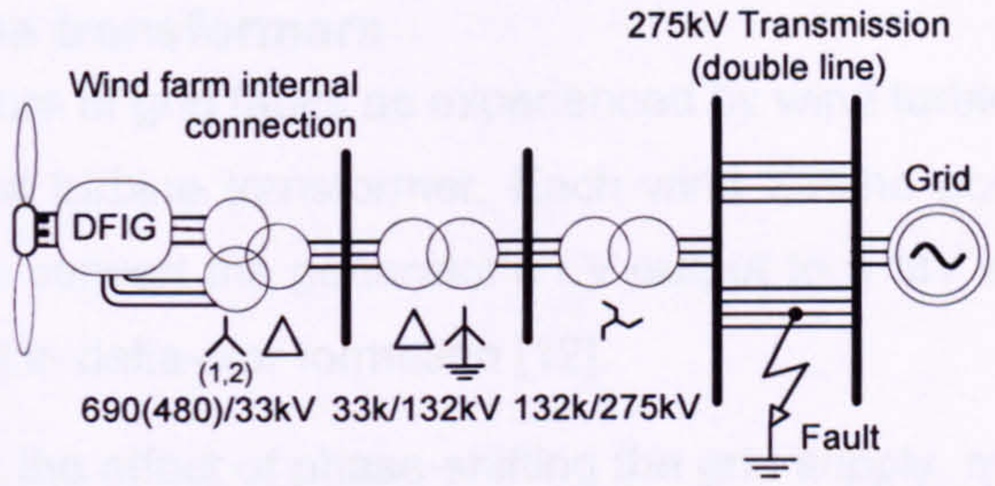

Figure 2.9. Network model and fault location.

The wind turbines within a farm are interconnected by a small MV network which is routed to a dedicated MV/HV substation. In the example of Figure 2.9, the windfarm collects power from the turbines at 33kV and connects to the transmission grid via a 132kV circuit and the nearest 132kV/275kV substation. Lengths of the interconnecting lines vary considerably [12].

As illustrated, a three-phase-to-ground fault is assumed to occur on one of the double-circuit transmission lines nearest the wind farm. The transmission system experiences zero voltage at the point of fault, and a near-zero voltage at the transmission substation until the line is cleared.

The voltages at the wind turbine are suppressed but non-zero due to the intervening MV connection impedance and the current carried. After clearance of the faulted line, the wind farm is connected to the grid by a single healthy transmission line; the local voltage will rise to a significant but sub-rated magnitude until the faulted section of transmission line can be re-instated. The resultant voltages seen at the wind turbine for such a fault are demonstrated in Figure 2.10.

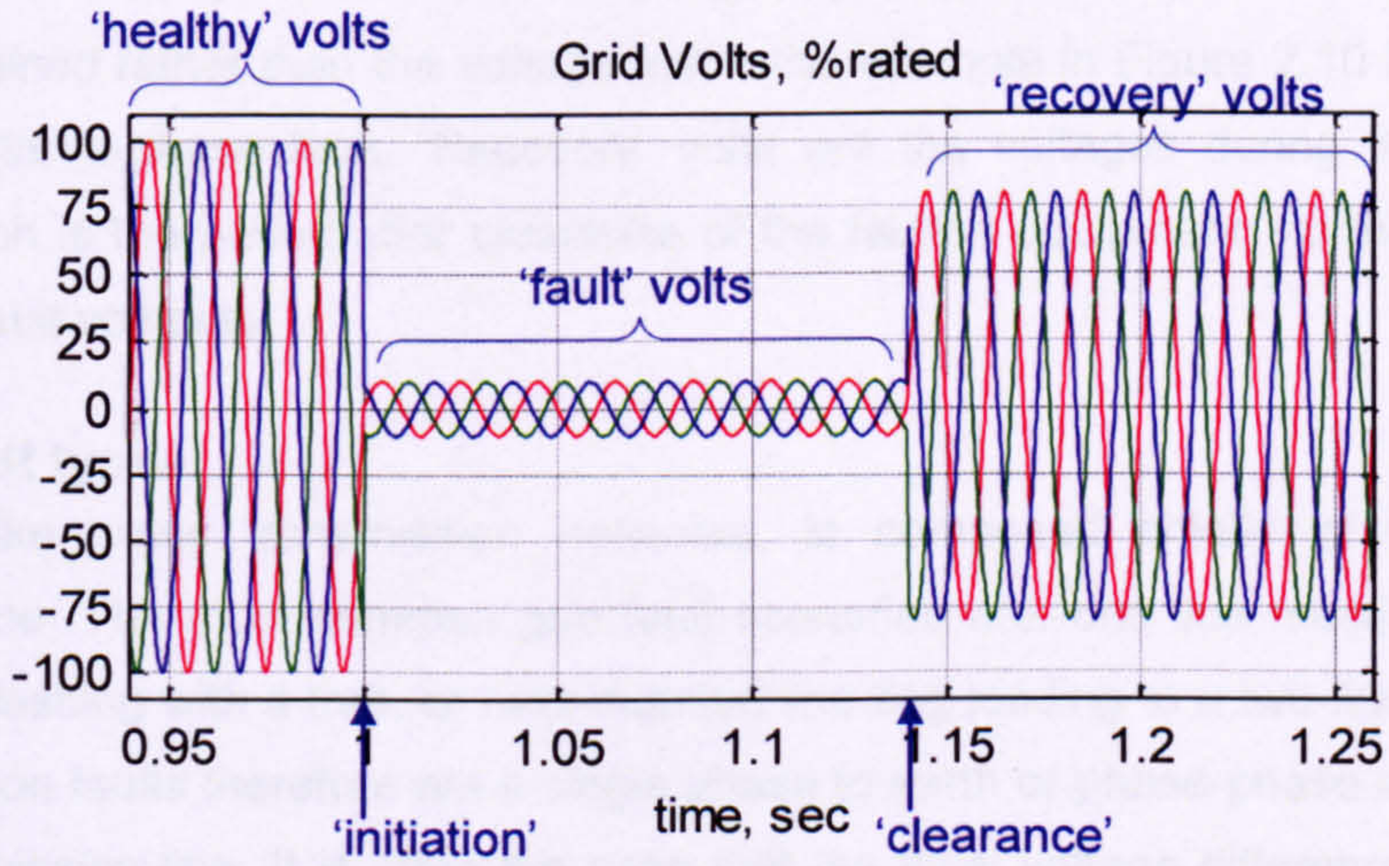

Figure 2.10. Three-phase voltages, balanced grid fault example, 10% fault.

Network connection impedances will vary for each wind turbine, but their overall effect is to lessen the severity of the voltage dip which is seen at the generator terminals.

2.3.5 Wind turbine transformers

To complete the picture of grid faults as experienced by wind turbines, it is worth noting the effect of the wind turbine transformer. Each wind turbine possesses a dedicated power transformer to convert the generator's LV output to a MV wind farm distribution level, typically wound in delta-star formation [12].

This transformer has the effect of phase-shifting the grid supply, minimising asymmetry from unbalanced grid faults [14] and screening the generator from exposure to any zero-sequence components of grid voltage or current [22].

2.3.6 Definitions

Grid faults as experienced by the generation plant are defined as a short-term voltage dips on one or more phases of the transmission system. The fault period is the time for which the voltage dip endures, starting at 'fault initiation' and ending at 'fault clearance'. Fault recovery is the period beginning with the isolation ('clearance') of the faulted equipment and ending when the voltages return to a healthy pre-fault state. The reinstatement of the previously faulted section is accomplished by reclosing the relevant circuit-breakers. This process may be simply referred to as 'reclosure', and (if successful) marks the end of the grid fault event.

Balanced faults are those causing an equal dip in voltage for all three phases. An unbalanced fault is any fault causing unequal voltage dips in the three phases.

'Healthy' volts are the pre-fault operating voltages (defined as 1.0 p.u. volts throughout this work). 'Fault' volts are the voltages during the fault period, expressed as p.u. with respect to the healthy volts. Note that voltage dips are described in this work by the voltage *retained* rather than the voltage *lost* – the example in Figure 2.10 is described as a 10% three-phase fault. 'Recovery' volts are the voltages during the recovery period, which is the period after clearance of the faulted equipment; normally 80-90% of the pre-fault voltages.

2.3.7 Fault types

The UK, like many transmission networks, is composed chiefly of three-phase overhead line. The most common grid fault scenarios are: one line meeting an earth path, e.g. clashing with a tree, or heat-induced line sag leading to a two-line clash. The most common faults therefore are a single phase to earth or phase-phase short circuits on a transmission line. It is often the case that the local voltage difference due to an unbalanced fault leads to arcing across phases. Effectively an asymmetric fault may develop quickly into a 3-phase fault. Faults on transmission pylons typically produce single phase short-circuits [29]. Transformer faults are far rarer and more likely to be 3-

phase. Faults at generator terminals are less frequent still although they are the most severe in nature.

Figure 2.11 shows a breakdown of transmission equipment faults by type during 2006 for the interconnected Scandinavian transmission system managed by NORDEL. The predominant faults were faults on overhead lines, although these were the simplest to remedy and most reclosed automatically. Second most common were faults caused by control equipment failures within substations [29].

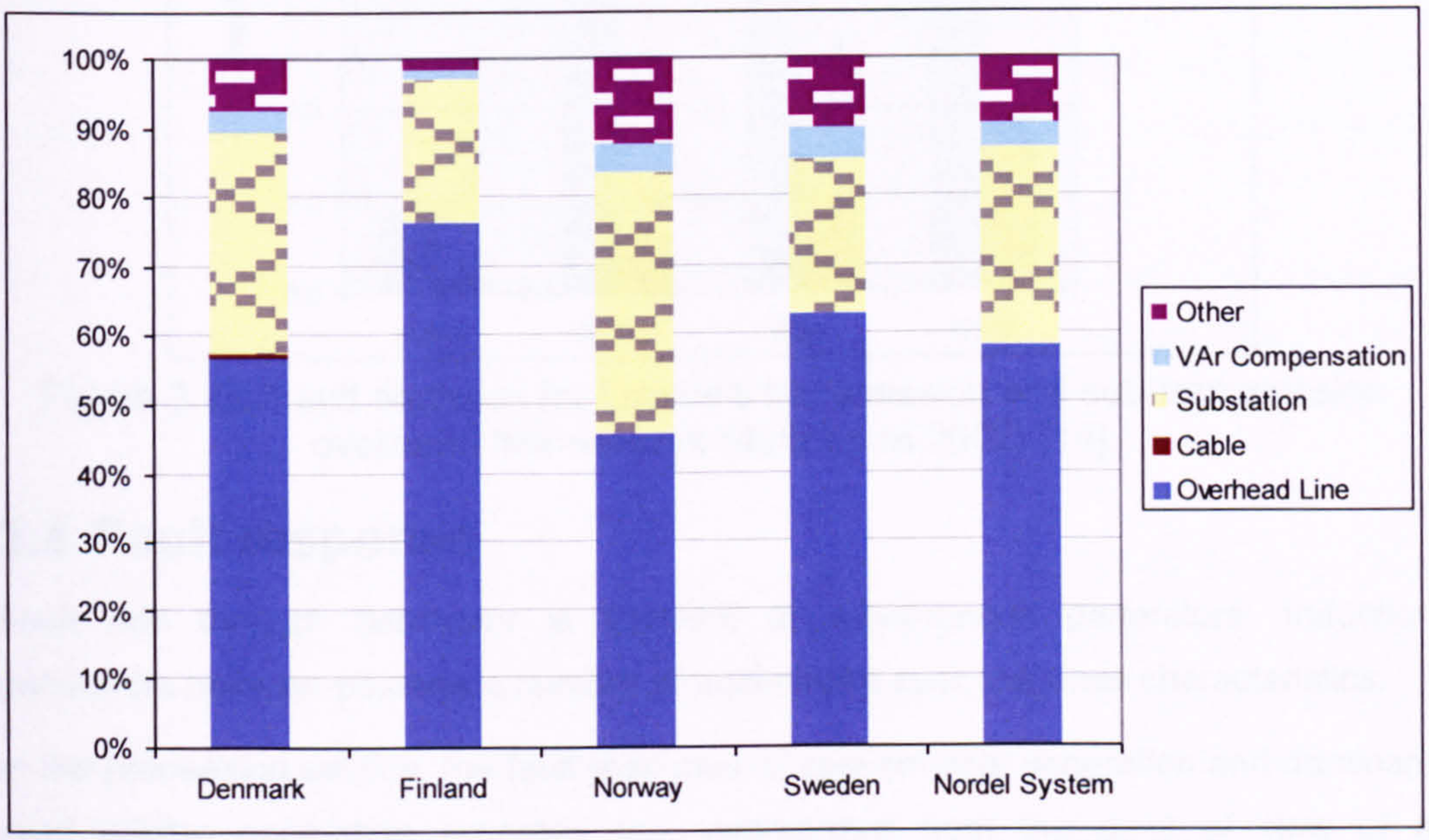

Figure 2.11. Nordel transmission system faults 2006 [29].

2.3.8 Incidence of grid faults

Figure 2.12 shows the relative incidence of voltage disturbance events on France's transmission and sub-transmission networks. This represents approximately 10.5 events per 100km per year at the transmission level (>200kV). Given France's roughly 46,000km of overhead line operated at 225-400kV [30], this equates to roughly 13 such events *per day*.

Although the majority of the faults will be minor (voltage drops no deeper than 70%, say), this highlights the necessity for fault ride through behaviour.

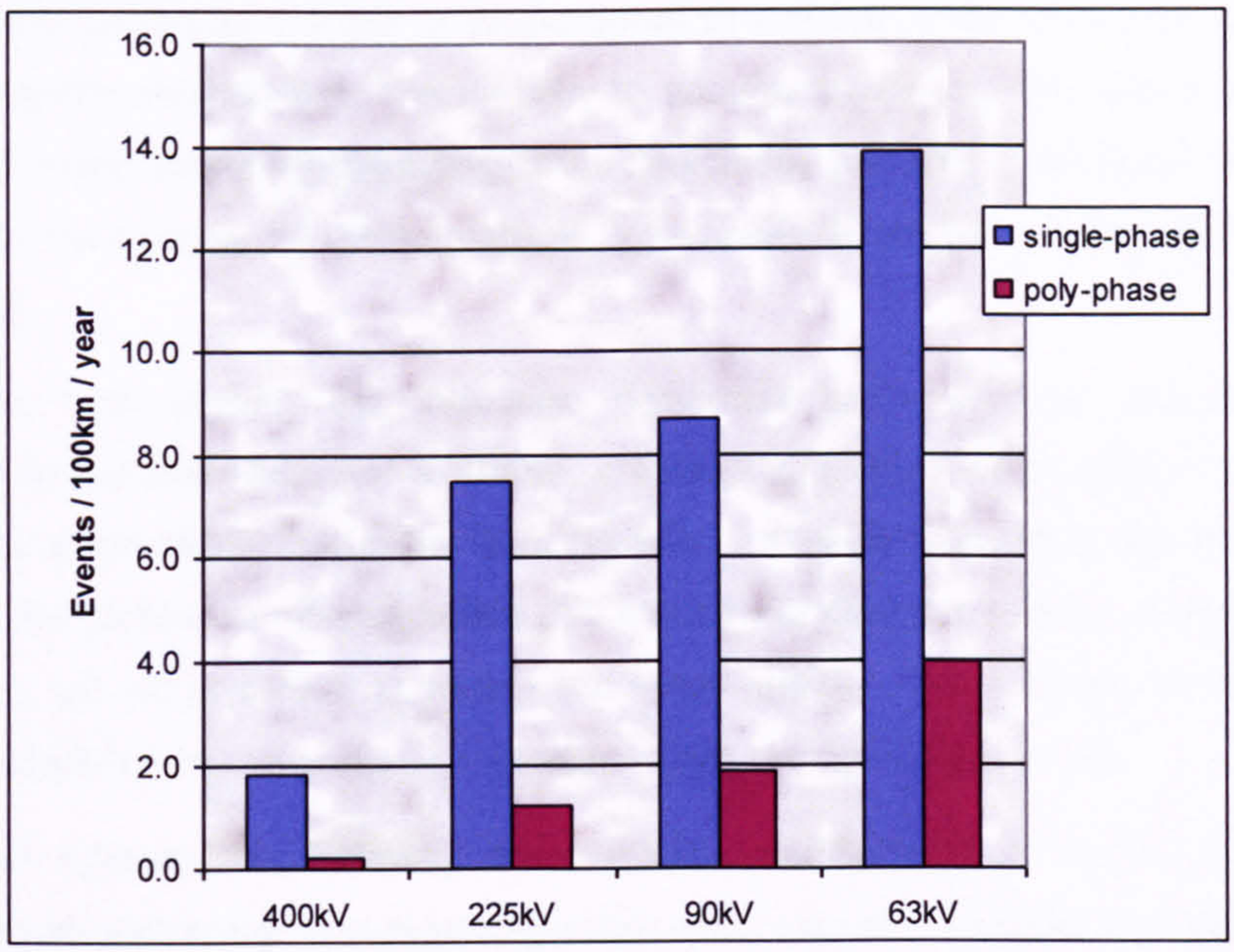

Figure 2.12. Fault statistics for France's transmission and sub-transmission overhead line network (data up to 2002) [14].

2.4 Fault response

Fault ride through behaviour is inherent to synchronous generators. Induction generators however possess a number of undesirable fault response characteristics.

In the proceeding section, the fault response of conventional generation and dominant wind turbine generation schemes are summarised from the point of view of a transmission system operator. Emphasis is placed on the faulted systems' contributions to the electrical network.

2.4.1 Synchronous generation plant

Synchronous generators remain magnetised throughout any credible voltage dip and can maintain continuous operation. Approximately rated emf is produced at the stator terminals, driving a substantial current into a grid fault. Conventional protection schemes use this fault current to recognise grid faults. The generator may continue to provide fault current until the thermal limits of the stator circuit are reached, far longer than credible grid fault durations.

In response to a power shortfall on the grid, the relatively high rotor inertia assists in limiting the rate of change of system frequency, while the governor sets typical speed limits of 94-106% of synchronous speed [31]. Synchronous generators may also deliver reactive power to support the network during a non-zero voltage dip.

2.4.2 SFIG wind turbines

At fault initiation, SFIG wind turbines demagnetise quickly; injecting transient fault currents lasting a few tens of milliseconds. The voltage drop sorely reduces the torque

output of the generator (torque is proportional to voltage squared at a given slip) and the rotor rapidly accelerates. The inability to actively control power output may lead to significant power instability following fault clearance, and the fault-period acceleration of the rotor may cause an unrecoverable over-speed event forcing the wind turbine to trip-off [32].

During the fault period, the induction generator loses internal magnetisation in proportion to the lost volts. For example, a balanced drop to 10% supply volts will lose 90% of the generator's flux. After fault recovery, a large amount of reactive power is drawn by the turbine to re-magnetise the induction generator, which, without external assistance, will act to further suppress the local voltage. The reactive current demand is exacerbated by any rotor speed increase which implies a higher slip.

SFIG wind turbines are typically disconnected during serious faults and restarted following fault clearance. The restart process may require a number of minutes, during which no power is supplied to the grid.

2.4.3 Fully-rated converter wind turbines

Voltage-source converters (VSCs) with fast acting power electronic switches may remain connected and stable during all credible voltage dips [33]. After a transient period of controller readjustment, the generator can deliver current into the network at controllable power factor, although this current is strictly limited by the ratings of the converter's power electronic devices.

The generator in a fully-rated converter wind turbine is screened from the voltage drop by the converter. However, as power export is limited, a large imbalance of power is produced across the converter. The converter must be fitted with a protective power sink in order to maintain continuous operation or else the mechanical input power must be very quickly reduced. While the latter is possible via the wind turbine's blade-pitch control, this may limit the mechanical power available immediately following the fault.

Overall, a fully-rated converter turbine generator may contribute positively during a fault with its continuously controllable current output. However, allowances should be made for the limited magnitude of its fault current contribution.

2.4.4 DFIG wind turbines

Generator response

The standard DFIG system is sensitive to dips in supply voltage. As with the SFIG, the induction generator very quickly loses internal magnetisation in proportion to the lost voltage. The demagnetisation produces large outrush currents on both stator and rotor circuits.

With a sufficiently rated power converter, the DFIG can continuously manage the generator currents, supplying (current-limited) controlled power output during the fault period and stabilising the turbine dynamics.

However, the rotor fault currents are typically far greater than the ratings of the converter's power electronic devices (Chapter 6). The converter must be temporarily disconnected. The length and nature of converter disengagement, together with the speed with which vector control can be resumed, are critical issues with regards to the fault response of DFIG wind turbines. DFIG fault response is considered in greater detail in Chapter 5.

Mechanical stability

As with fully-rated converter wind turbines, it is possible to stabilise the machine speed by limiting the mechanical power input (via blade pitch control). However, if widely implemented, this resulting loss of power into the network due to a fault poses similar problems to generator disconnection. As a result, it is desirable for variable speed wind turbines to not curtail their power input during a grid fault. Grid faults last less than one second, and as a result the speed excursions are not critical for a variable-speed wind turbine [24].

Step changes in electrical torque due to the voltage steps associated with grid faults excite low resonant-frequency oscillations in the wind turbine drive-shaft. These resonances are typically very poorly damped and will impact the power output for many seconds following fault clearance. Nonetheless, a DFIG wind turbine running at rated speed prior to any credible grid fault can safely restore its speed to rated operation after fault clearance.

Fault ride through options

Many techniques have been proposed to satisfy TSO fault ride through requirements, including temporary disconnection, flux damping equipment and rotor circuit crowbar devices. Fault ride through techniques for DFIGs are treated in Chapter 6. There is to date no industry-wide agreement on a solution to the problem of fault ride through, which remains a significant issue for the DFIG system.

2.5 Fault ride through requirements

2.5.1 General transmission system requirements

There are four main issues for FRT from the point of view of the transmission system:

- Stability and the ability to remain grid-connected throughout a grid fault
- Active power output and system frequency support.

- Reactive power output and local voltage support.
- Fault currents for protection scheme activation.

These issues are expanded upon in this section.

Generator stability

As stated in GB Grid Code [26], the primary demand on large generators is to "remain connected and transiently stable" during a credible grid fault.

As explained in Section 2.2.2, a sudden loss of power output to the transmission system may lead to frequency instability. Backup generation, so-called spinning reserve, cannot contribute within grid fault timescales and a wind turbine re-start requires several minutes. As stated in ([24], p.169): "the main challenge is uninterrupted operation rather than short-term voltage stability". Transient operation through grid faults is a necessity for all generators making significant contributions to the grid.

Power control

In addition to remaining connected to the grid, generation plant must maximise power output to prevent the power shortfall from causing an under-frequency event. As the fault periods are very short with respect to the typical system inertia, active power provision is most relevant during the period of fault recovery after the faulted equipment has been isolated. Grid codes must strike a balance between permissible frequency excursion and the practical dynamic power capabilities of generators.

Voltage support during fault conditions

The balance of reactive power between generators and loads affects the voltages on the network. By the inductive nature of transmission impedances, voltage dips can be partially offset by delivering reactive power. This is why TSOs often specify a reactive power export demand for grid fault periods.

Fault current and protection schemes

Most transmission system protection relays are triggered on over-current detection. Fault clearance times vary according to the level of fault current, which will be larger for a more severe fault. This scheme however relies on the fault currents associated with synchronous generators. Induction generators offer fault current for only for a few tens of milliseconds while their internal magnetisation decays [22]. Power electronic converters remain stable and connected but are limited in their current capability by the rating of their components.

Without a redesign, the widespread use of non-synchronous generation plant could inhibit the activation of traditional protection schemes [34]. TSOs may be tempted to demand impractical fault current capability from these generators.

Systems with a high proportion of non-synchronous generation plant require revised protection schemes to account for the different technologies. This could include for example making greater use of voltage sensitive protection, such as impedance relays. Voltage sensitive protection could permit a significant increase in the grid connection of power-converter equipment by precluding onerous demands for short-term over-ratings.

2.5.2 Grid code FRT requirements

Assessments of the numerous TSO grid codes are widely available (e.g. [14][15][16], [34][35][36]). The principle fault ride through requirements for mature grid networks are explained in this section, with examples provided.

Small and relatively isolated transmission systems (e.g. the Irish or GB transmission systems) are most sensitive to frequency deviations caused by unscheduled power shortfalls. As a result their grid codes typically focus on the restoration and management of active power.

Physically large and/or well interconnected systems (e.g. the German or Danish transmission systems) can more easily balance active power flows across their networks. Of greater concern here is the geographical spread of suppliers and consumers. These grid codes instead typically emphasise local voltage control and reactive power contributions during grid faults.

In this section we take a closer look at two grid codes and their requirements for fault response. The British and German codes have undergone rigorous re-examination in recent years and as such offer good examples of FRT requirements; balancing power system needs against generator capabilities.

GB grid code FRT requirements

GB grid code specifies that each generator must remain transiently stable and connected to the system without tripping for faults on the GB transmission system at so-called 'supergrid voltages' [26]. These faults are classified into two main types:

a) Close-up three-phase short-circuit faults and unbalanced short-circuit faults with a total fault clearance time of up to 140 ms. This includes cases where any or all three of the transmission phases experience zero voltage at the point of fault.

b) For clearance times exceeding 140 ms: any faults with a voltage magnitude profile above the voltage limit (the heavy black line) shown in Figure 2.13.

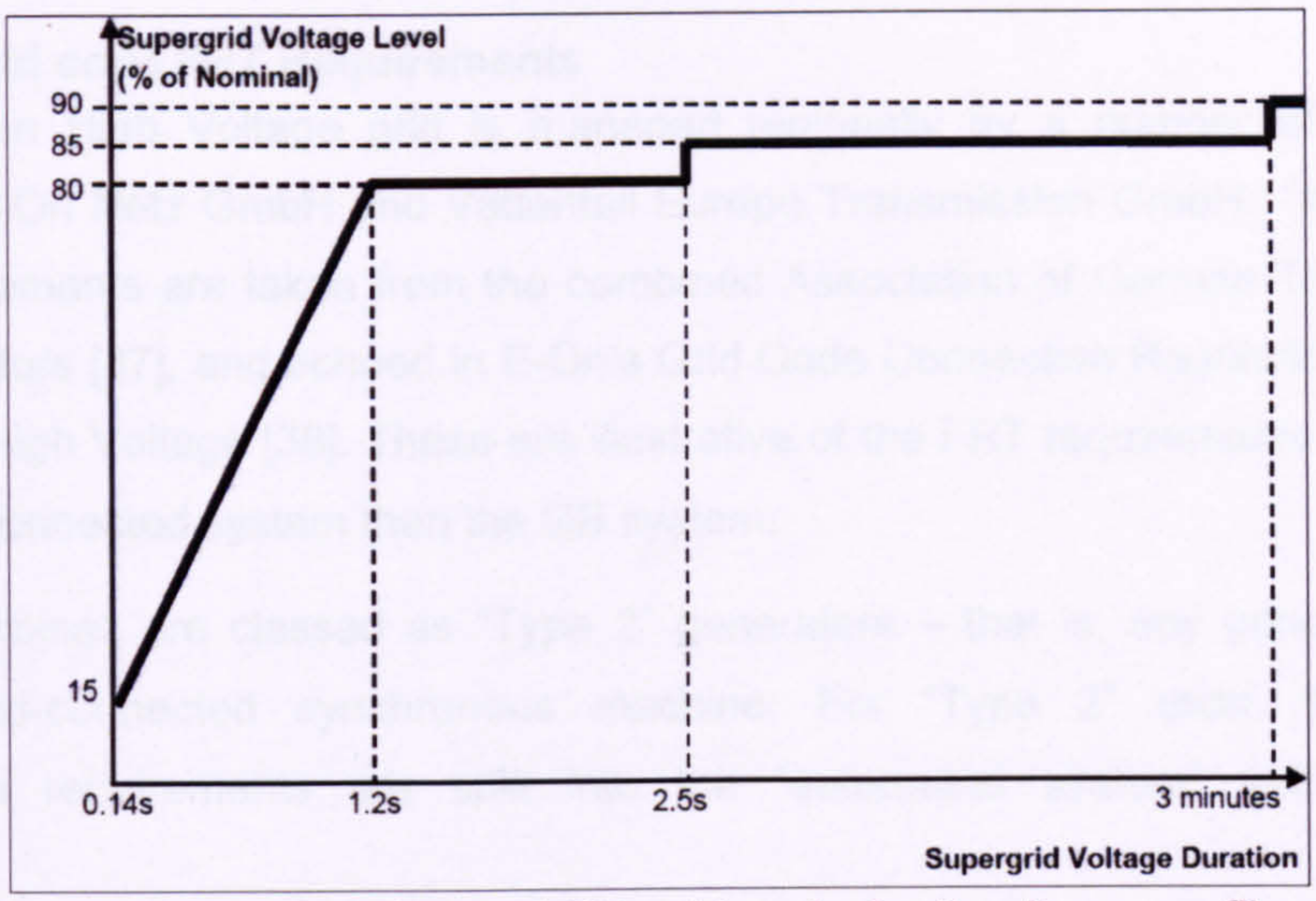

Figure 2.13. Envelope of GB grid code fault voltage profiles.

Using the envelope from Figure 2.13, Figure 2.14 shows one example of a fault voltage magnitude profile, as provided within the Grid Code.

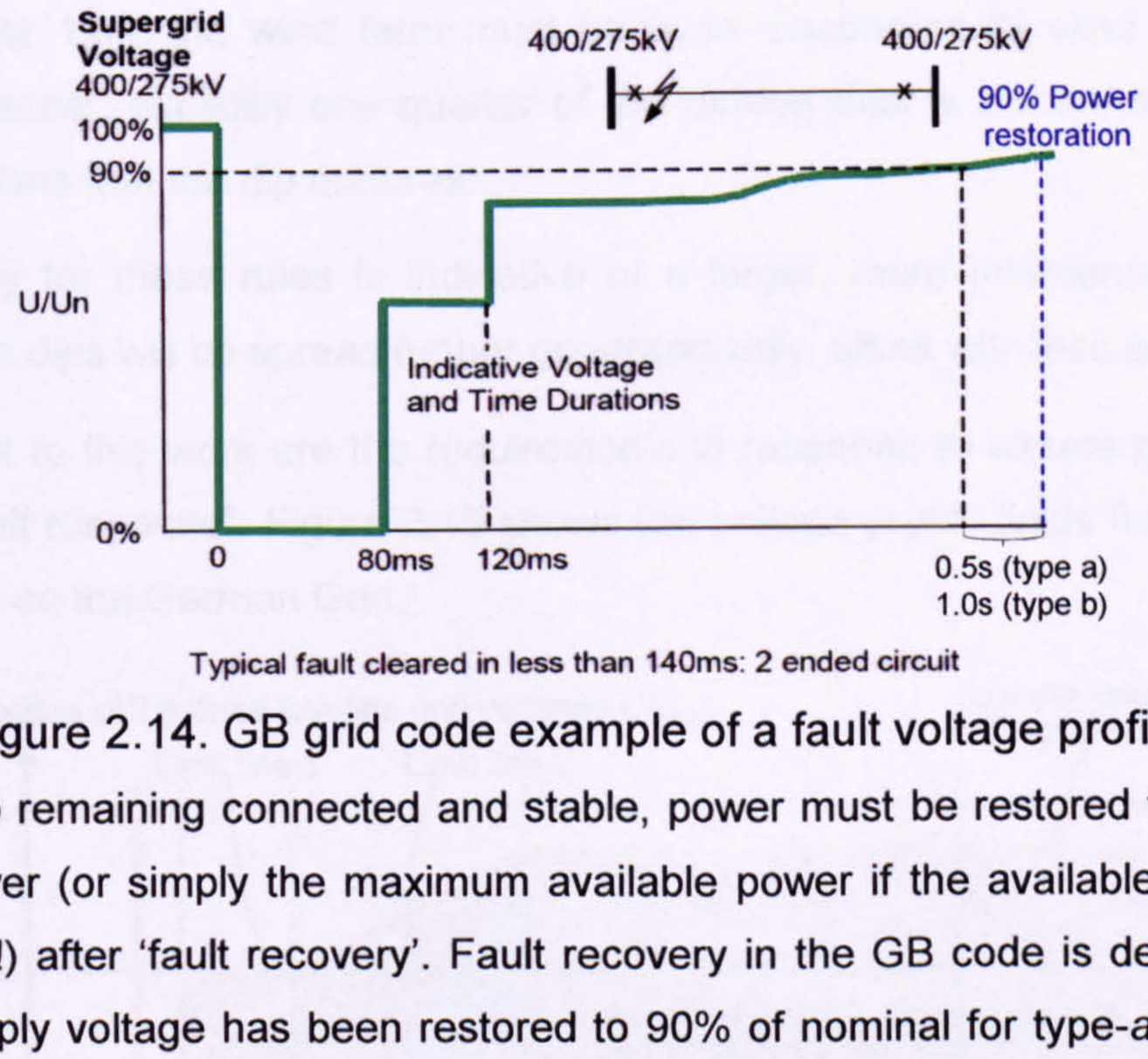

Figure 2.14. GB grid code example of a fault voltage profile.

In addition to remaining connected and stable, power must be restored to 90% of the pre-fault power (or simply the maximum available power if the available wind energy has dropped!) after 'fault recovery'. Fault recovery in the GB code is defined as 0.5s *after* the supply voltage has been restored to 90% of nominal for type-*a* short-circuits (or 1.0s after the 90% target for type-*b* extended-duration faults).

During the fault and recovery periods generators must provide active power in proportion to the retained balanced voltage at the grid connection point. They also must generate the maximum available reactive current without exceeding the generators' transient ratings limits. Derogations to the above regulations exist for Scottish wind

farms built before April 2005. However, these rules otherwise apply to all generator units connecting to the GB transmission system.

German grid code FRT Requirements

The German High Voltage grid is managed regionally by a number of operators, including E-On Netz GmbH and Vattenfall Europe Transmission GmbH. The following FRT requirements are taken from the combined Association of German Transmission Grid Operators [37], and echoed in E-On's Grid Code Connection Regulations for High and Extra High Voltage [38]. These are illustrative of the FRT requirements of a larger, more interconnected system than the GB system.

All wind turbines are classed as "Type 2" generators – that is, any generator not a directly grid-connected synchronous machine. For "Type 2" units, the voltage disturbance requirements are split into the "automated system" and the "fault response".

The "automated system" requirements detail the response to long-duration shallow-voltage dips (or rises) and non-critical long-duration frequency excursions. For example, if a wind farm measures a dip to below 80% rated voltage on its LV system which lasts for 1.5s, the wind farm must begin to disconnect its wind turbines in a staggered manner: explicitly one quarter of the turbine total is disconnected for each additional 300ms that the dip endures.

The necessity for these rules is indicative of a larger, more interconnected system where voltage dips will be spread further geographically, albeit with less severity.

More relevant to this work are the requirements in response to severe grid faults, the so-called "fault response". Figure 2.15 shows the voltage profile limits for credible grid fault voltages on the German Grid.

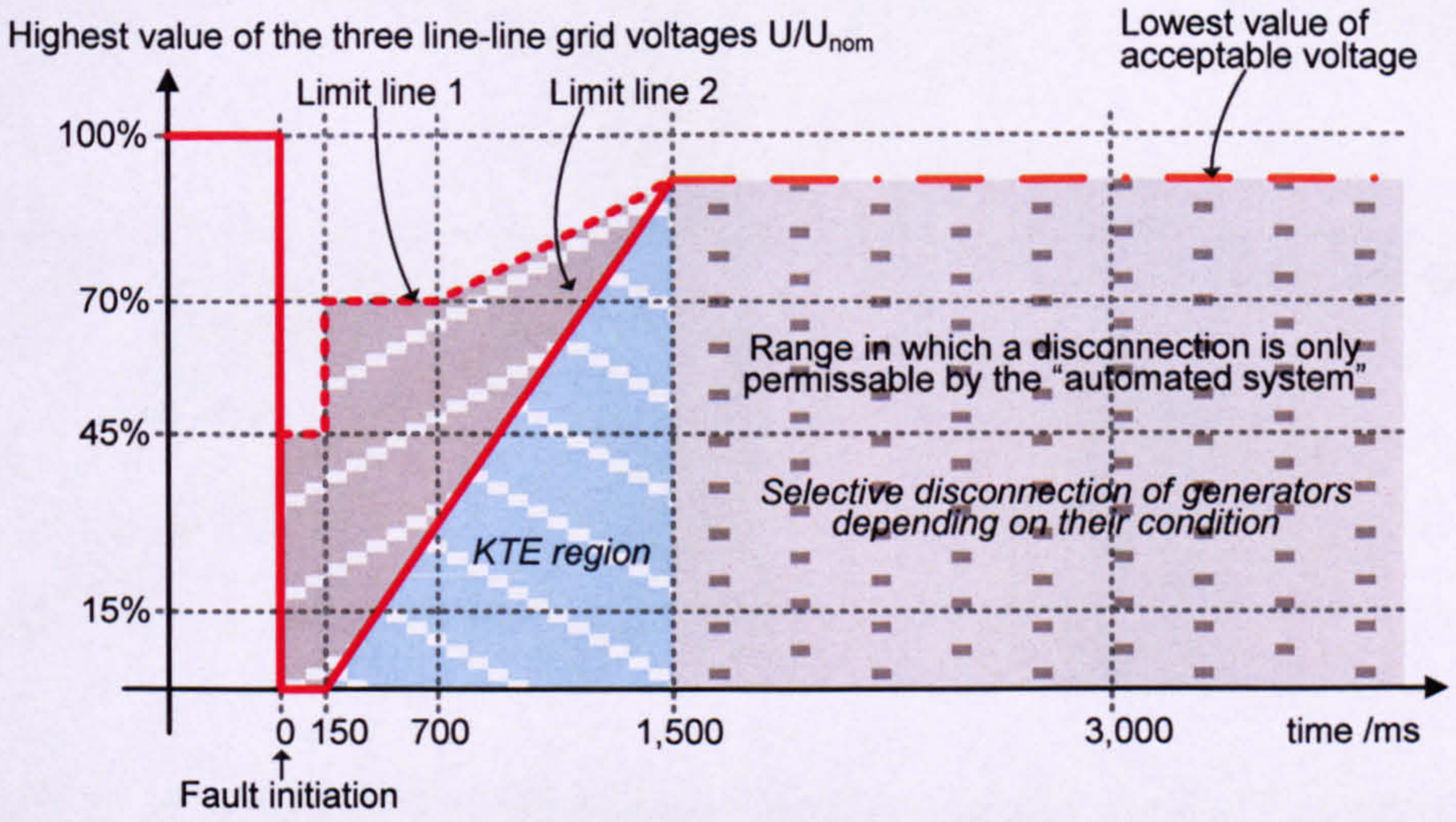

Figure 2.15. Limits of German fault voltage profiles at the grid connection [37].

The code defines a brief grid disconnection event, a so-called "KTE": the turbine is electrically disconnected but reconnected within 2s, after which active power output is restored at a rate of at least 10% rated power per second. With reference to Figure 2.15 therefore, wind turbine fault response requirements are as follows:

- Voltage profile above line 1: no transient instability or disconnection from the grid.
- Voltage profile in shaded area above line 2: generally no disconnection from the grid, although a KTE event may be permitted under special prior arrangement with the TSO. The exact profile of limit line 2 and the specific KTE parameters may also be adjusted with consent of the TSO.
- Voltage profile below line 2: KTE event always permitted.
- Fault voltage exceeding 1,500s: dealt with under the rules for the "automated response".
- If no KTE takes place, the restoration of active power after fault clearance must occur at a rate of at least 20% rated power per second.

During a voltage deviation generator units must also offer voltage support by way of reactive current. For any voltage deviation greater than 10%, the unit must offer 2% capacitive current for each 1% voltage drop (or inductive current for voltage rise), as illustrated in Figure 2.16. After the voltage returns to within the deadband this reactive power support must continue for an additional minimum of 500ms to ensure voltage stability.

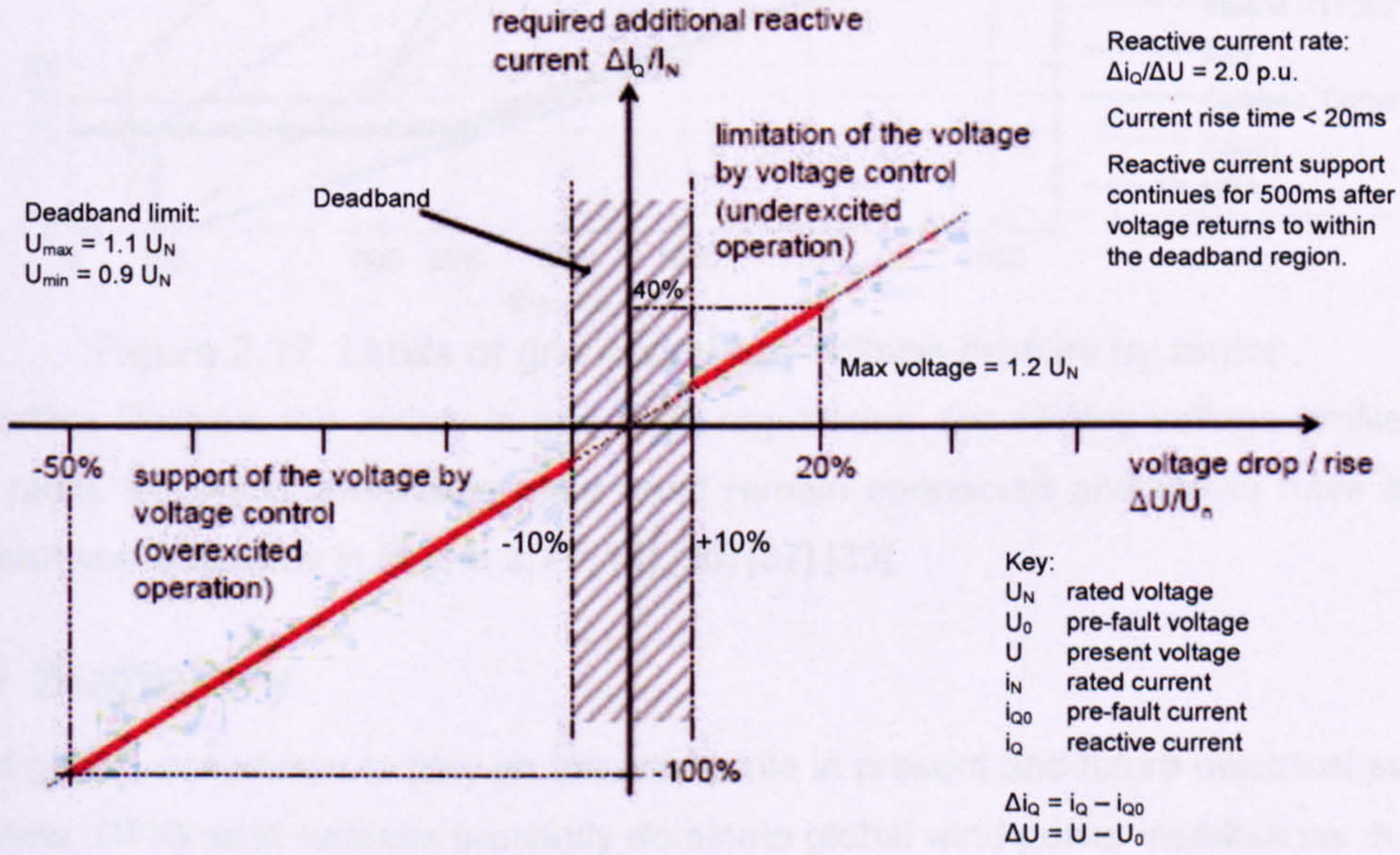

Figure 2.16. Reactive current requirements for voltage support following grid fault events [37].

The emphasis on voltage stability again reflects the needs of a power system which is more geographically spread out than the GB system.

Summary of grid code FRT requirements

Grid codes are evolving constantly, particularly in response to the recent trend towards smaller, more widely distributed generation plant. As such many of the rules laid down to date are subject to revision. Certain countries' codes have made little allowance for non-synchronous technologies and work on a case-by-case basis. Transmission system operators who have taken stock of the fault ride through behaviour of non-synchronous plant (e.g. in Great Britain and Germany) have revised their grid code requirements for fault ride through.

The consensus is that new generation plant connecting to high-voltage grids, notably wind turbines, must remain connected and stable for a range of defined 'credible' grid faults. During the fault and for a period of fault recovery the plant must provide reactive power to support the local voltage. Following fault clearance, active power must be delivered in a matter of seconds.

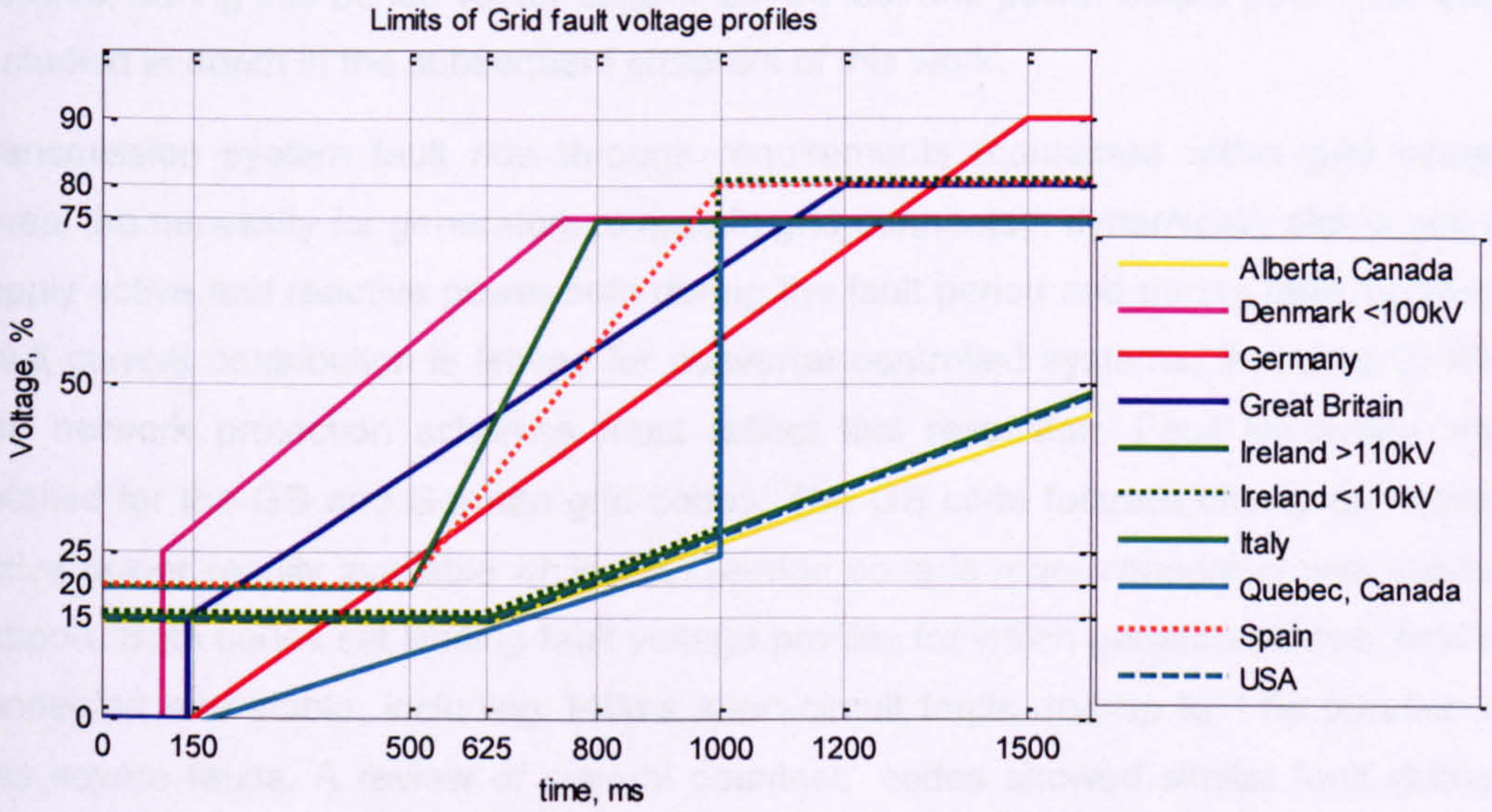

Figure 2.17. Limits of grid code fault-voltage profiles by region.

To further illustrate the variety in grid code regulations, the limiting voltage profiles of grid faults for which generating plant must remain connected and stable have been collated and illustrated in Figure 2.17 [14] [26] [37] [39].

2.6 Summary

Wind power was shown to play an important role in present and future electrical power systems. DFIG wind turbines presently dominate global wind power installations due to the combination of variable speed operation and a relatively cost-effective power

converter. The operation of transmission system networks creates numerous challenges for wind turbines, notably that of grid fault ride through.

Grid fault events were defined, and the danger of cascade generator disconnection due to a transmission system short-circuit was highlighted. Different types, incidences and depths of grid fault were discussed, revealing that grid faults typically last less than 0.5s but may occur several times in one week.

The fault response characteristics of major generation topologies revealed that synchronous machines, and to a lesser extent grid-connecting power-converters, are well-disposed to ride through and support the network during grid faults. Induction generators, including DFIGs, inherently lose a proportion of their magnetisation, producing very short-period transient over-currents and temporarily losing power control. A SFIG may not recover from the resulting period of acceleration, and in any case will suppress the recovery voltage due to its re-magnetisation process. A DFIG offers better control of power export during fault recovery but must take self-protective action during fault transients to protect its power converter from the ensuing rotor over-currents; during this period vector control can be lost and power output poor. This area is studied in depth in the subsequent chapters of this work.

Transmission system fault ride through requirements (contained within grid codes) reveal the necessity for generators to remain grid-connected, dynamically stable and to supply active and reactive power both during the fault period and during fault recovery. Fault current contribution is limited for converter-controlled systems, including DFIGs, and network protection schemes must reflect this restriction. Fault behaviour was detailed for the GB and German grid codes. The GB code focuses chiefly on making active power readily available while the German code is more concerned with voltage support. Both codes set limiting fault voltage profiles for which generators must remain connected and stable, including 140ms short-circuit faults and up to 1.5s duration of less severe faults. A review of several countries' codes showed similar fault voltage limiting profiles.

DFIG CONCEPTS 3

This chapter provides an overview of the theory and principles of DFIG operation and control. The aim is to cover the necessary background to analyse the fault response of a conventional wind turbine DFIG.

The first section introduces the elements of generalised machine theory needed to follow the induction machine fault response description in Chapter 5. Space vector analysis, magnetic field distribution and the physics of torque generation are described. Generalised machine equations are presented followed by the transient time constants which govern the machine's dynamic response to electromagnetic phenomena.

DFIG system elements are explained, including the wind turbine transformer, the wound rotor and the choice of rotor circuit topology. The predominant voltage-source converter scheme is described. Vector control of the DFIG is outlined and the use of PI feedback control is justified. The line-side and rotor-side controllers for the DFIG power converter are studied separately, presenting simple feedback control laws for each. Finally the dynamic control limitations of DFIG rotor control are discussed.

3.1 Induction Machine Principles

To understand the response of the DFIG to voltage dips requires a sound grasp of the fundamentals of magnetic flux and torque production in induction machines. Considerably more literature exists for the singly-fed (commonly squirrel-cage rotor) induction machine. The doubly-fed generator and its control are documented in, for example, [40]. This section introduces general machine theory applicable to either type, although it is worth noting throughout that in normal operation the doubly-fed machine *controls* the magnitude and phase of the rotor's magnetic field, unlike the singly-fed version for which the rotor field is passively induced.

This section presents the essential theory behind the magnetic flux interactions and the generalised machine approach for an idealised three-phase induction generator. This is intended to provide a solid understanding of the machine's internal magnetics before the description of induction machine fault response in Chapter 5. The selection of

machine magnetic theory was made to assist a power-system specialising reader; a machine-specialist reader can safely skip on to Section 3.2.

3.1.1 Space vector analysis

The advantages of space vector analysis are well-documented [41]. The system of space vector representation as used in this work is explained in greater detail in Appendix A and the nomenclature of space vector forms is listed in the glossary. An example of the space vector concept is given below.

In vector analysis, three-phase elements of the electrical system are converted into per-unit orthogonal d-q axes space-vector representations. An example is shown in Figure 3.1 where a stator-current space vector is mapped onto a cross-section of a symmetrical two-pole, three-phase AC machine. The equivalent three-phase a-b-c components and excitation-frame d-q components are drawn, along with a set of stationary three-phase sA-sB-sC axes, stationary sd-sq axes, and excitation reference frame ed-eq axes.

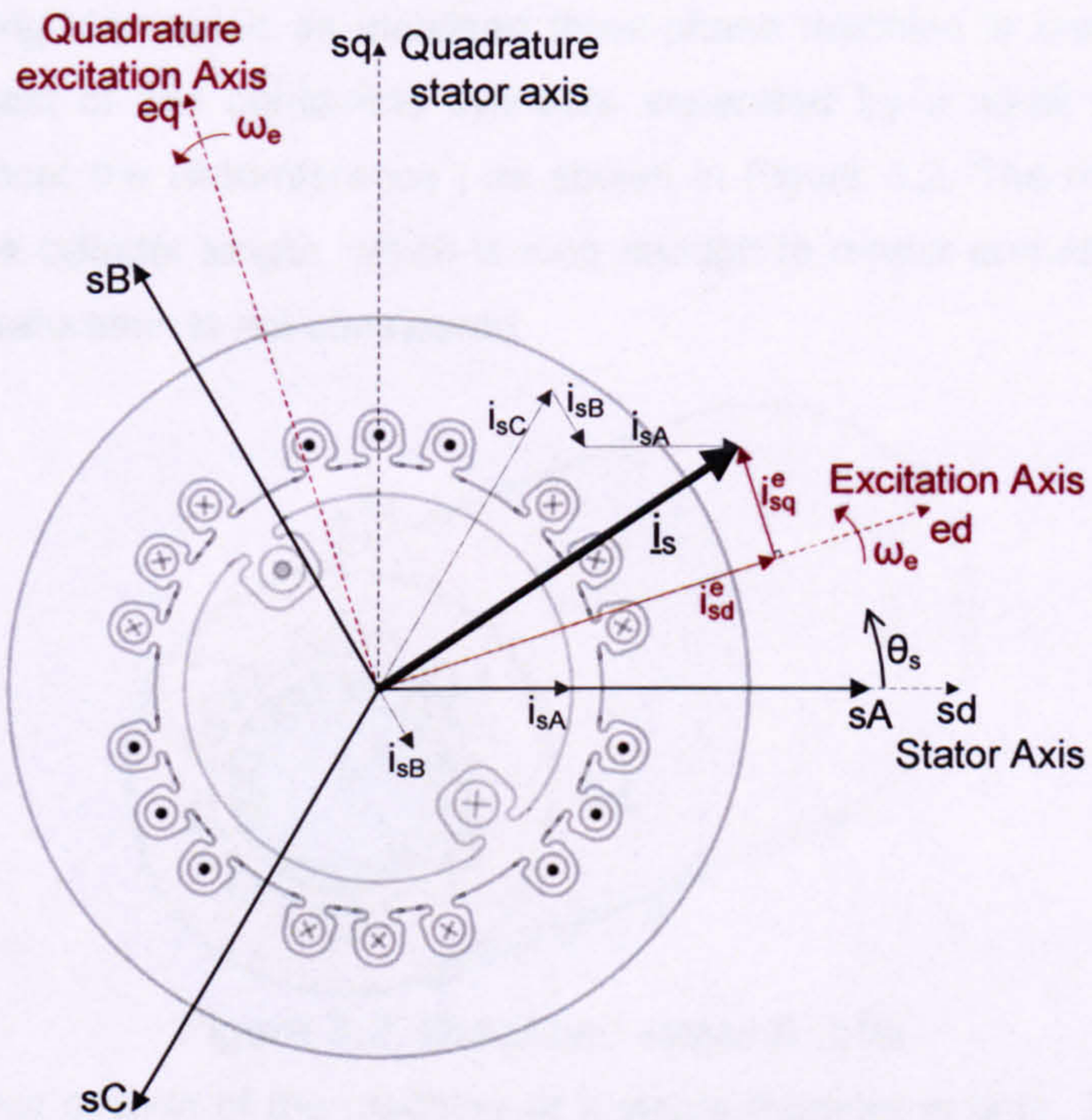

Figure 3.1. Space vector of stator current.

Generalised electrical machine theory, including space vector analysis, depends on the following simplifying assumptions [22], [42]:

- Flux and mmf distributions are represented by their fundamental harmonic component alone.
- Slotting and other geometric winding distribution effects are neglected.
- Commutation effects and brush-connections are idealised.

- The magnetic materials possess negligible eddy currents and hysteresis effects.
- Magnetic saturation is neglected.

The first four are generally reasonable approximations of practical cases. However, magnetic saturation certainly affects all practical machines, limiting the concentration of magnetic flux at any one point. The magnetic simplifications imply linear magnetics, such that different magnetic fields may be linearly superposed. This is needed for certain mathematical solutions, as explained in Chapter 5. This work concentrates on fault response. A direct result of fault response is the decay of machine flux, which lessens any magnetic saturation present in the machine. Practically, if magnetic saturation has any effect on fault response it will limit the transient excesses of current and power. Linear magnetic analysis of fault response will therefore derive a worst case response in terms of over-currents and power output. The DFIG test rig presented in Chapter 4 was used for practical validation.

3.1.2 Magnetic field distribution

For the following discussion an idealised three-phase machine is considered. Stator and rotor consist of two concentric cylinders separated by a small uniform airgap, symmetrical about the circumference[3], as shown in Figure 3.2. The machine coils lie parallel with the cylinder length, which is long enough to render end-effects negligible, and magnetic saturation is not considered.

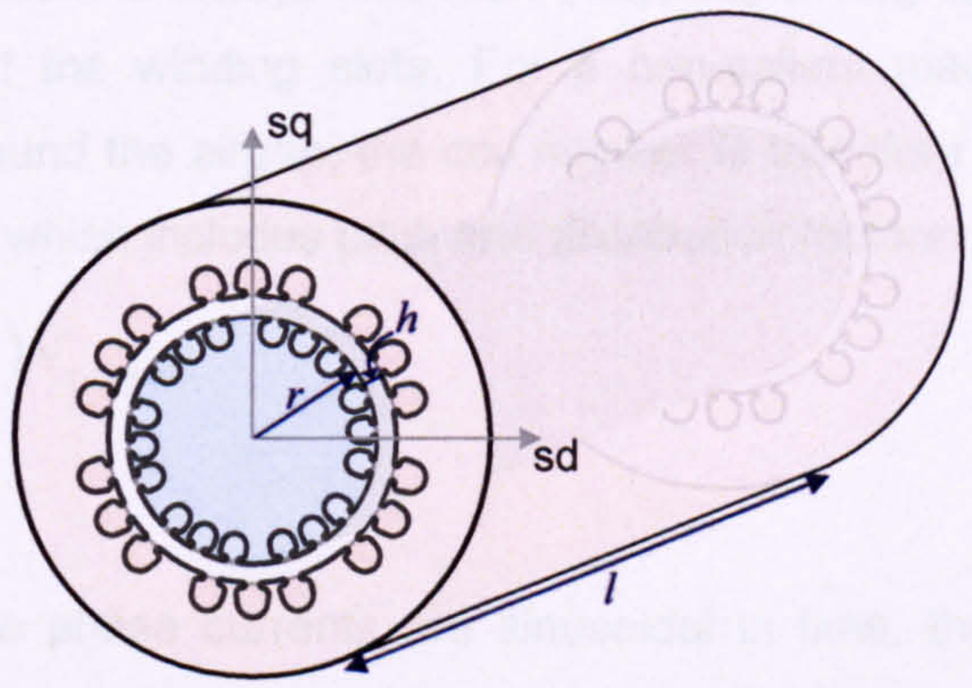

Figure 3.2. Simplified stator & rotor.

Consider a cross section of the machine at a single moment in time. The windings of the machine's stator are distributed in such a manner as to produce an approximately sinusoidal MMF around the airgap when supplied with three balanced currents [43] (Figure 3.3).

[3] Saliency is addressed in Appendix A.

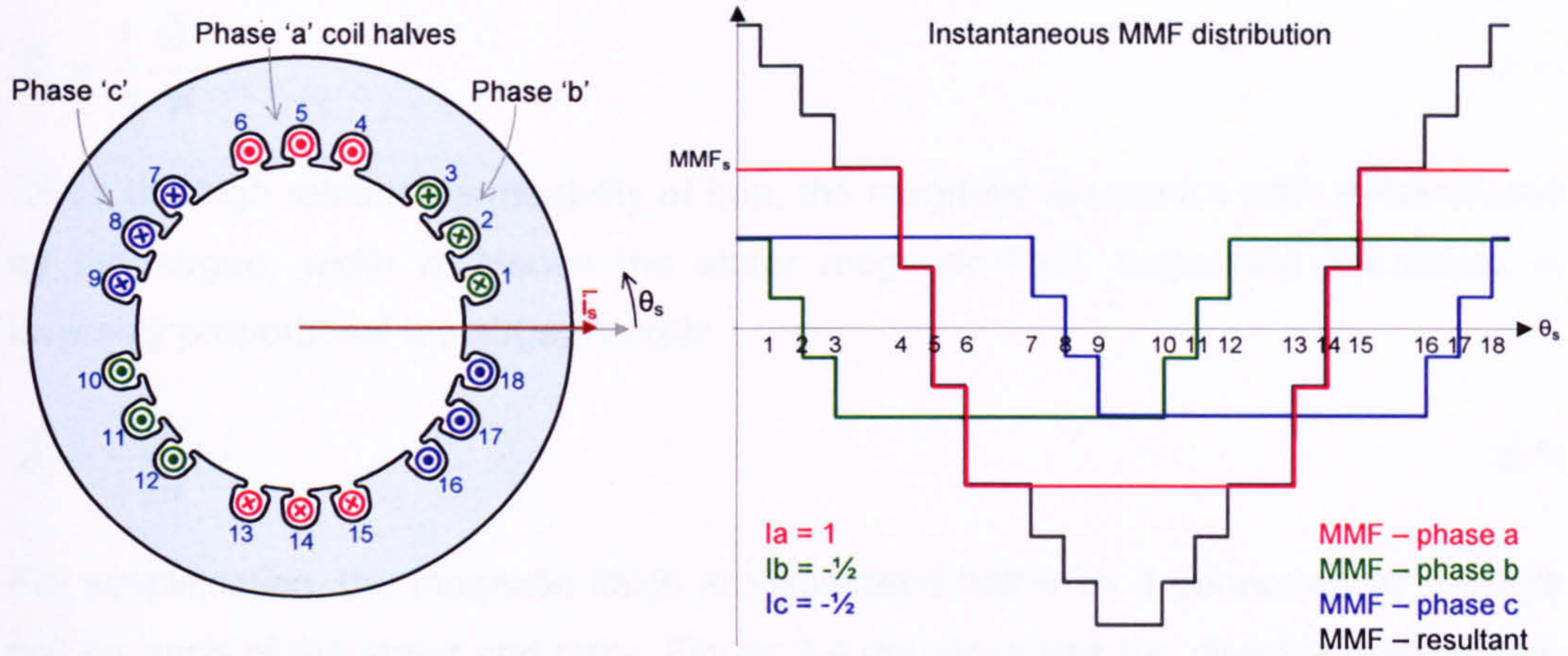

Figure 3.3. Example of stator MMF distribution.

Each phase current contributes a standing wave to the MMF distribution. The sinusoidal quality of MMF depends upon the number and geometric distribution of windings. The space vector of stator MMF is defined as the instantaneous peak of the resultant stator MMF distribution.

The stator MMF space vector can be derived from: the number of coils of each stator phase winding, the space vector of stator current, and a coefficient describing the geometric distribution:

$$\overline{\Theta}_s = k(\theta_s) N_{s,actual} \bar{i}_s \tag{3.1}$$

The geometric coefficient is always less than unity, depending upon the angular pitch and concentration of the winding slots. For a non-salient machine, the coefficient remains constant around the airgap; the coil number is therefore often replaced by an effective coil number which includes pitch and distribution factors:

$$N_s = N_{s,effective} = k(\theta_s) N_{s,actual}$$

$$\overline{\Theta}_s = N_s \bar{i}_s \tag{3.2}$$

Note that if the three phase currents are sinusoidal in time, the MMF will progress around the rotor circumference. The locus of the stator MMF space vector will form a circle, as it rotates with the stator current space vector.

A space vector of rotor MMF may be similarly defined with respect to the peak of the rotor MMF distribution. In terms of the rotor current and effective rotor turns:

$$\overline{\Theta}_r = N_r \bar{i}_r . \tag{3.3}$$

The MMF drives a sinusoidally distributed magnetic flux across the airgap of the machine. Considering the stator flux, the reluctance and area of the airgap flux path:

$$\overline{B}_s = \frac{1}{A}\frac{\overline{\Theta}_s}{\Re} \tag{3.4}$$

Given the high relative permeability of iron, the magnetic reluctance path is dominated by the airgap, width *h*. Hence the stator magnetic field, neglecting saturation, is inversely proportional the airgap length:

$$\overline{B}_s = \frac{\mu_0 N_s}{2h}\bar{i}_s \tag{3.5}$$

For simplification, the magnetic fields are illustrated below as if generated by a single coil on each of the stator and rotor. Figure 3.4 demonstrates the direction and relative strength of the stator component of magnetic field strength around the airgap of an idealised two-pole machine.

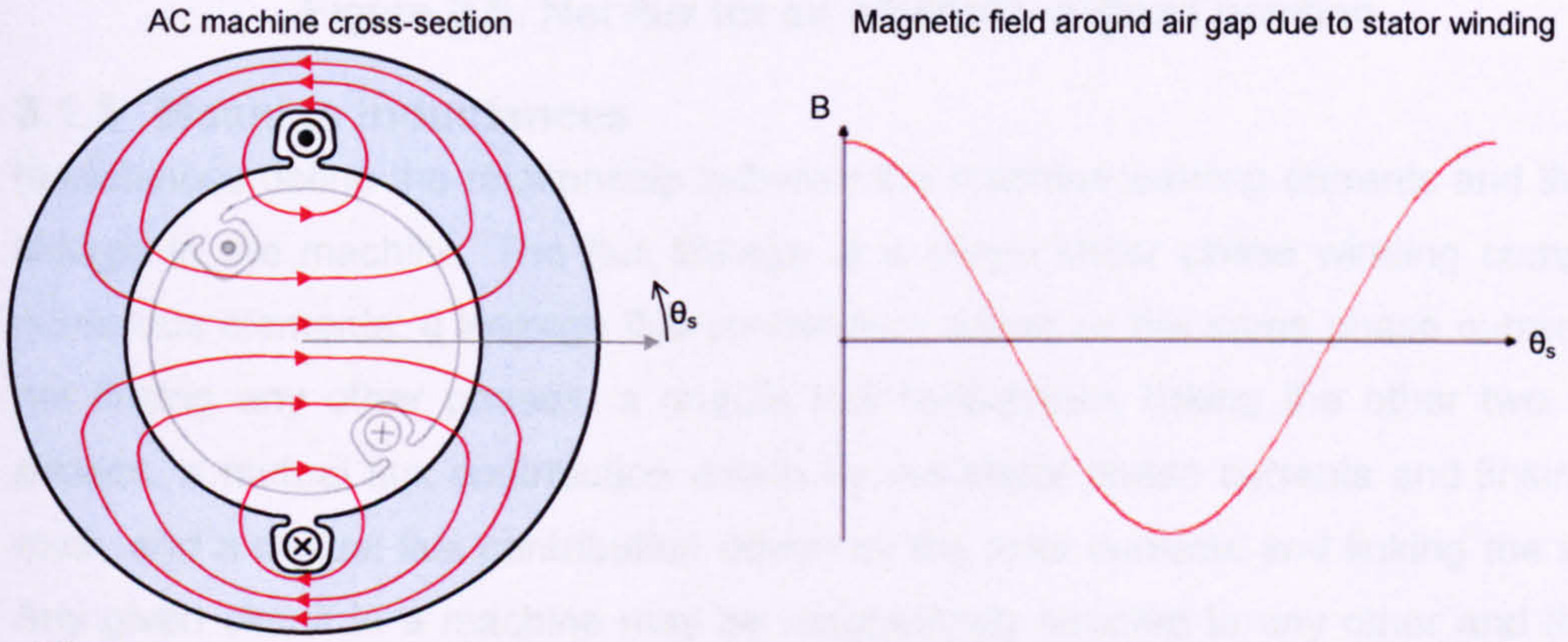

Figure 3.4. Stator contribution to magnetic flux around the circumference of a symmetrical two-pole AC machine.

A similar magnetic field is produced by the rotor circuit MMF, shown by Eq. 3.6 and Figure 3.5.

$$\overline{B}_r = \frac{\mu_0 N_r}{2h}\bar{i}_r \tag{3.6}$$

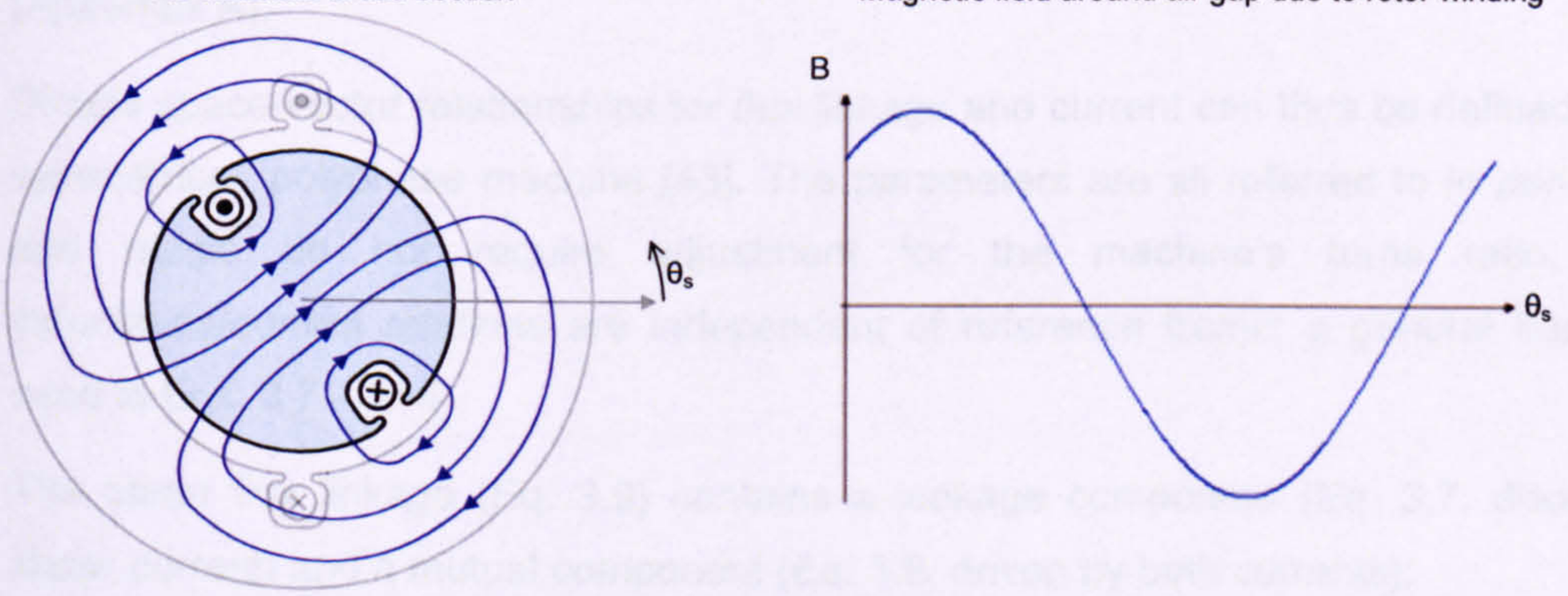

Figure 3.5. Rotor flux distribution.

The resultant flux distribution is a (approximately linear) combination of the two fields (Figure 3.6). Note that the net flux linkage comprises both *leakage* flux paths (which thread stator or rotor alone) and *mutual* flux paths (which thread both rotor and stator).

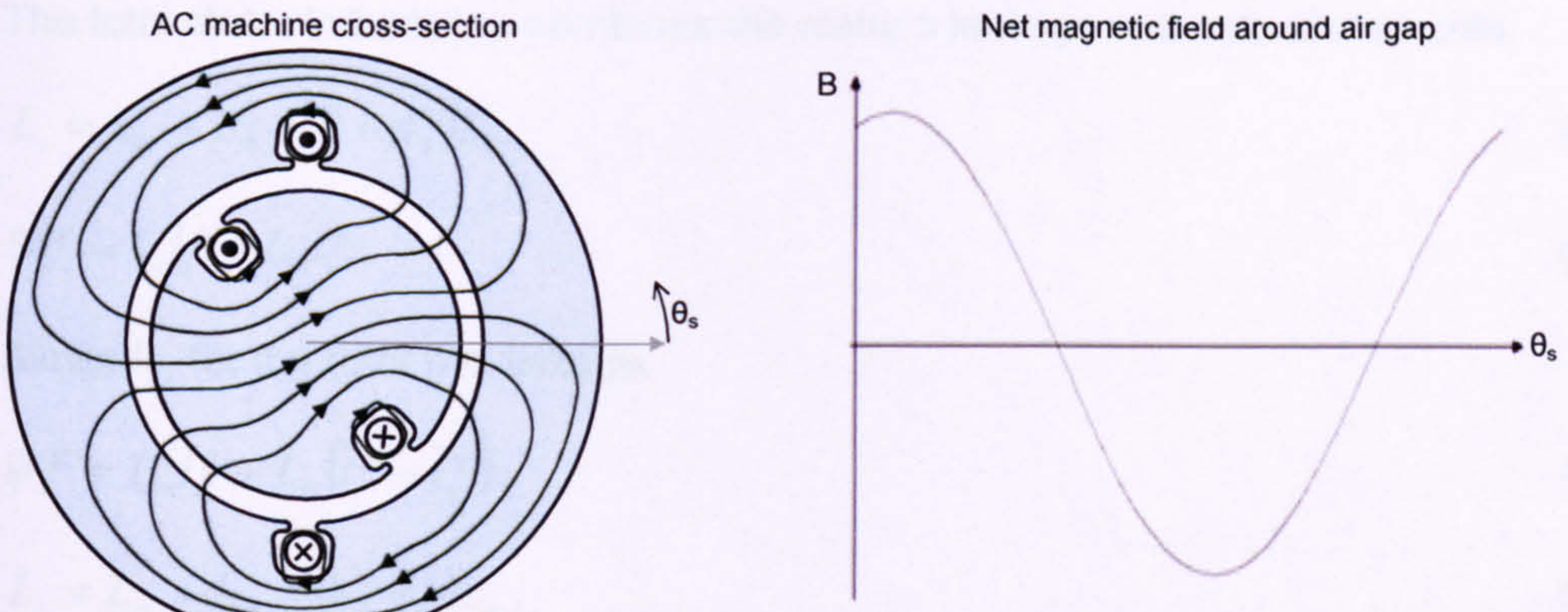

Figure 3.6. Net flux for an arbitrarily aligned position.

3.1.3 Machine inductances

Inductances define the relationship between the machine winding currents and the flux linkage in the machine. The flux linkage of a single stator phase winding comprises numerous elements: a leakage flux contribution driven by the same phase current and not linking any other phases, a mutual flux contribution linking the other two stator phases, a mutual flux contribution driven by the stator phase currents and linking the rotor, and a mutual flux contribution driven by the rotor currents and linking the stator. Any given circuit in a machine may be magnetically coupled to any other and the full formal circuit equations can be complicated [44].

In the manner originally introduced by Park, substantial simplification is made by transforming each circuit to represent the magnetic couplings separately on an orthogonal two-axis representation of the machine [45]. All the magnetic couplings may be described by relevant impedance parameters. With symmetrical machine windings, the inductance parameters do not vary around the airgap or with rotor position (Appendix A).

Simple space-vector relationships for flux linkage and current can thus be defined for a symmetrical, polyphase machine [43]. The parameters are all referred to in *per-units*, and hence do not require adjustment for the machine's turns ratio. The inductance/current relations are independent of reference frame; a general frame is used in Eqs. 3.7 - 3.14.

The stator flux linkage (Eq. 3.9) contains a leakage component (Eq. 3.7, driven by stator current) and a mutual component (Eq. 3.8, driven by both currents):

$$\bar{\psi}_{es}^{g} = L_{es}\bar{i}_{s}^{g}, \tag{3.7}$$

$$\bar{\psi}_m^g = L_m\left(\bar{i}_s^g + \bar{i}_r^g\right), \tag{3.8}$$

$$\bar{\psi}_s^g = L_{es}\bar{i}_s^g + L_m\left(\bar{i}_s^g + \bar{i}_r^g\right) \tag{3.9}$$

The total stator inductance combines the stator's leakage and mutual elements:

$$L_s = L_{es} + L_m = (1+\sigma_s)L_m, \tag{3.10}$$

$$\bar{\psi}_s^g = L_s\bar{i}_s^g + L_m\bar{i}_r^g. \tag{3.11}$$

Similarly, for the rotor flux linkage:

$$\bar{\psi}_r^g = L_{er}\bar{i}_r^g + L_m\left(\bar{i}_r^g + \bar{i}_s^g\right), \tag{3.12}$$

$$L_r = L_{er} + L_m = (1+\sigma_r)L_m, \tag{3.13}$$

$$\bar{\psi}_r^g = L_r\bar{i}_r^g + L_m\bar{i}_s^g. \tag{3.14}$$

Eqs. 3.7 - 3.14 are valid in transient conditions [46]. Where applicable, magnetic saturation may be accounted for in a reduction of the relevant inductance values, although for simpler analysis saturation is often neglected [22]. A useful measure of the relative strength of the leakage and mutual fields in a machine is the derived leakage factor (Eq. 3.15).

$$\sigma = 1 - \frac{L_m^{\,2}}{L_r L_s} \tag{3.15}$$

3.1.4 Torque generation

Torque is generated in all electrical machines via the misalignment of two rotating magnetic fields. The fields associated with each pole-pair on the stator and rotor behave like two magnetic dipoles[4], resulting in an electromagnetic torque dependent upon the strength of each field and the sine of their phase separation. As a generator, the rotor field is effectively dragged ahead of the stator field by the mechanical input torque. The production of induction machine torque is explored below. More formal derivations can be found in [40][46].

Locally, the leakage fields around the conductors in a slot displace the largely radial flux crossing the airgap (Figure 3.7). Torque is produced along the slot edges. The radial components of field produce a strong alignment force normal to the rotor surface (F_n in Figure 3.7), which does not contribute to the rotational force. The displaced fringe

[4] Multipole machines appear physically to have multiple concentric magnetic dipoles. Descriptions of the interactions of magnetic 'hexapoles' and so on have been omitted for clarity! Omitting saturation, the effects are linear: one may consider a single pair of poles and scale the results for multipole machines.

fields produce a far smaller torque-generating force tangential to the rotor surface at the slot edges (F_T in Figure 3.7) (if permanent magnets are used instead of a wound rotor, a similar argument can show torque production at the edge of the magnets).

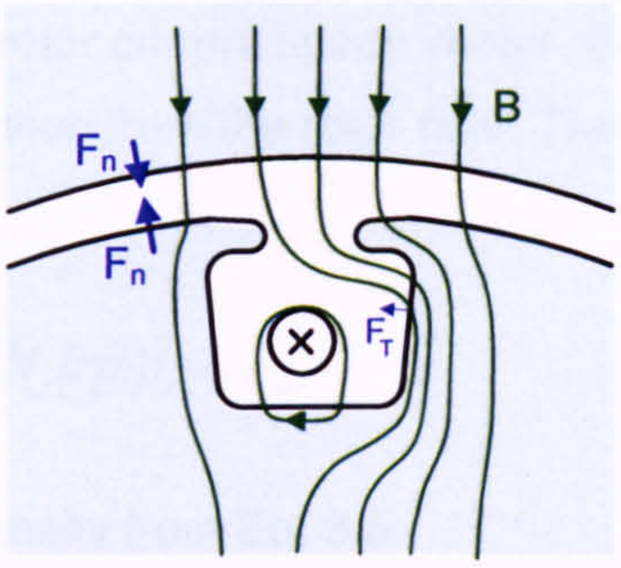

Figure 3.7. Flux path near a rotor slot.

The rotor flux can be considered to *displace* an amount of stator flux. The torque can be calculated as if the rotor current carrying conductors had been placed artificially into the undisturbed magnetic field of the stator (or vice versa) [47]. Figure 3.8 illustrates the force element on a single rotor conductor due to the stator field.

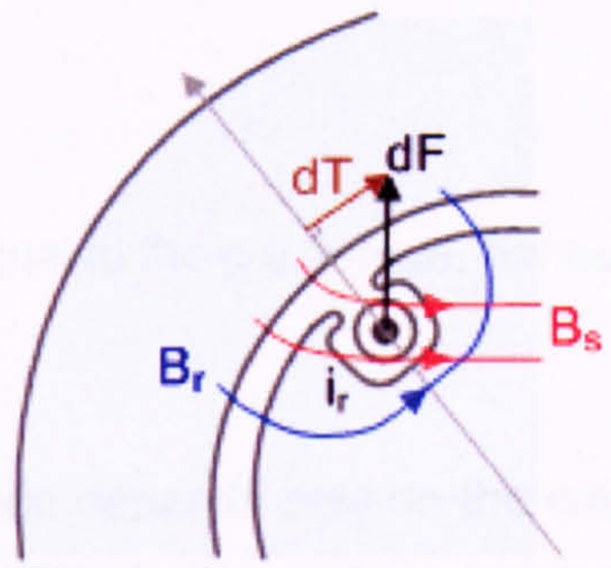

Figure 3.8. Force element on a rotor conductor.

Applying the Lorentz force law to a line current in a magnetic field (Eq. 3.16), the rotor current conductor experiences a force in the radial plane. For a current carrying element of length *dl*:

$$\overline{dF} = i_r \overline{dl} \times \overline{B_s} \quad [5] \tag{3.16}$$

Now, the magnetic field is perpendicular to the axial-direction current element:

$$dF = i_r dl \left| \overline{B_s} \right| \tag{3.17}$$

A torque element is produced by the component of force perpendicular to the radius, *r*, where θ is the angle between the stator field and rotor field:

$$dT = i_r dl \left| \overline{B_s} \right| r \sin\theta \,. \tag{3.18}$$

Forming a summation for all rotor conductors and *p'* pole pairs:

---

[5] Here the operator '×' indicates the *vector cross product* (see Glossary & Symbols)

$$T = 2lrp' \sum_{i=1}^{N_r} i_r \left|\overline{B_s}\right|_i \sin\theta_i \tag{3.19}$$

Now, the rotor field is driven by the rotor MMF, sinusoidally distributed around the airgap and positioned by the rotor current space vector. Each element of the stator field holds the same phase separation from the rotor field. Therefore, using the vector cross product determinant:

$$T = 2lrp' \sum_{i=1}^{N_r} \left|\bar{i}_r\right| \left|\overline{B_s}\right|_i \sin\theta_i = \left(2N_r lrp'\right)\bar{i}_r \wedge \overline{B}_s \tag{3.20}$$

Substituting the stator field density from Eq. 3.5:

$$T = p'\left(\frac{N_s N_r lr\mu_0}{h}\right)\bar{i}_r \wedge \bar{i}_s \tag{3.21}$$

The bracketed coefficient in Eq. 3.21 (containing coil numbers and geometric factors) defines the mutual inductance of the machine, L_m. The torque equation can hence be simplified:

$$T = p' L_m \bar{i}_r \wedge \bar{i}_s \tag{3.22}$$

The torque per pole-pair is equal to the p.u. torque, hence:

$$T = L_m \bar{i}_r \wedge \bar{i}_s \quad (p.u.) \tag{3.23}$$

The resulting torque expression depends only on the cross product of stator and rotor currents, i.e. the sine of the angle between the current space vectors. This correlates with the magnetic dipole alignment description of torque. In the aligned position, the net forces around the airgap cancel, resulting in zero torque. Torque is maximised when the rotor field is perpendicular to the stator field.

The torque can be re-expressed to incorporate the mutual flux linkage (Eq. 3.8) by using the orthogonal nature of the vector cross product:

$$T = \overline{\psi}_m \wedge \bar{i}_s = \bar{i}_r \wedge \overline{\psi}_m \tag{3.24}$$

That is to say that the torque may be *equally* defined by the cross product of the airgap-crossing flux linkage and *either* stator or rotor current vectors (allowing for a sign change). The two sets of currents are independent and experience the influence of the other current exclusively via the airgap-crossing flux.

Note that the torque only depends upon the relative phase of the two vectors, and hence any reference frame may be used. The torque equation (Eq. 3.22) is commonly written in texts in a more complicated form which avoids the vector cross product:

$$T = p' L_m \operatorname{Im}\left\{ \underline{\bar{i}_s} \, \underline{\bar{i}_r}^* \right\}^6 \tag{3.25}$$

3.1.5 Voltage equations

A space vector of voltage can be defined, just as for the currents and flux linkages of Section 3.1.3. In the stationary reference frame, a voltage applied to the stator effectively 'sees' only the stator windings, and therefore comprises only the emf induced by the stator flux and resistive drop of the stator current (Eq. 3.26). The converse applies to the rotor circuit in the rotor reference frame (Eq. 3.27).

$$\bar{u}_s^s = R_s \bar{i}_s^s + \partial \bar{\psi}_s^s \tag{3.26}$$

$$\bar{u}_r^r = R_r \bar{i}_r^r + \partial \bar{\psi}_r^r \tag{3.27}$$

Eqs. 3.26-3.27 are not rotationally symmetric. When viewed from a reference frame rotating with respect to either circuit, a rotational emf term must be included in order to preserve Faraday's law of induction. For example, a dc rotor voltage does not sustain a rotor-coil emf and the rotor flux linkage is constant. When viewed from the stator frame, the apparently rotating rotor voltage must be offset by a rotor-frequency flux-linkage term to maintain constant rotor flux linkage (Eq. 3.29). This rotational term can be derived from the voltage definitions in Eqs. 3.26-3.27, as demonstrated in Eq. 3.28.

$$\bar{u}_r^s = \bar{u}_r^r \exp(+j\omega_r t) = \exp(+j\omega_r t)\left\{ R_r \bar{i}_r^r + \partial\left(\bar{\psi}_r^s \exp(-j\omega_r t) \right) \right\} \tag{3.28}$$

$$\bar{u}_r^s = R_r \bar{i}_r^s + \partial \bar{\psi}_r^s - j\omega_r \bar{\psi}_r^s \tag{3.29}$$

3.1.6 Generalised machine equations

Considering Sections 3.1.3 - 3.1.5, a symmetric polyphase induction machine may be described by the following 5 equations, here referred to the stator reference frame:

$$\bar{u}_s^s = R_s \bar{i}_s^s + \partial \bar{\psi}_s^s \tag{›3.26}$$

$$\bar{u}_r^s = R_r \bar{i}_r^s + \partial \bar{\psi}_r^s - j\omega_r \bar{\psi}_r^s \tag{›3.29}$$

$$\bar{\psi}_s^s = L_s \bar{i}_s^s + L_m \bar{i}_r^s \tag{3.30}$$

$$\bar{\psi}_r^s = L_r \bar{i}_r^s + L_m \bar{i}_s^s \tag{3.31}$$

$$T = p' L_m \, \bar{i}_r \wedge \bar{i}_s \tag{›3.22}$$

These five are often referred to as the governing equations for a 'fifth order' simulation model. They are applied generally in the electrical modelling of induction machines

---

[6] Here the current operator is the *2D direct product* (see Glossary & Symbols)

[40], and form the basis of the solution for DFIG fault response in Chapter 5. These so-called 'generalised machine equations' remain valid in transient conditions [46].

3.1.7 Transient timescales

Dynamic electromagnetic phenomena within electric machines are dominated by the transient time constants - essentially the rate at which magnetic flux linkage may change in a given circuit. In an induction machine there is a single dominant timescale for each of the stator and rotor circuits ([22], [44], Appendix A):

$$\tau_s = \frac{\sigma L_s}{R_s} \tag{3.32}$$

$$\tau_r = \frac{\sigma L_r}{R_r} \tag{3.33}$$

In per-unit terms, a symmetrical wound-rotor induction machine will possess similar inductance and resistance values on its stator and rotor circuits. As a result, the transient time constants will be similar. By way of example, the 7.5kW test rig in Chapter 5 was measured to possess a stator transient time constant of 25.7ms and a rotor transient time constant of 38.7ms. The terms 'rotor/stator time constant' and 'rotor/stator transient time constant' are used interchangeably in this work.

3.2 Doubly-Fed Induction Generator (DFIG)

3.2.1 Principles of DFIG operation

The DFIG concept was introduced in Chapter 2. Unlike a singly-fed machine, a wound-rotor is required to access the rotor phase coils. The rotor currents can be actively controlled with, for example, a voltage-source converter; this permits independent control of the active and reactive power output of the machine (Section 3.3.3).

Wound rotor

In a conventional singly-fed induction machine with a squirrel-cage rotor, the rotor emf is induced on the rotor by the relative movement of its conductor bars in the stator field. In a doubly-fed machine the rotor field is produced by a set of rotor currents impressed onto the rotor windings via a set of slip-rings and brushes. A cutaway section of a wound-rotor three-phase doubly-fed induction machine is shown in Figure 3.9. Note the slip rings and brush connections in the upper-left corner. A voltage between the rotor phase terminals is induced when the lengthwise sections of rotor coil rotate inside the magnetic field established by the stator, and vice versa.

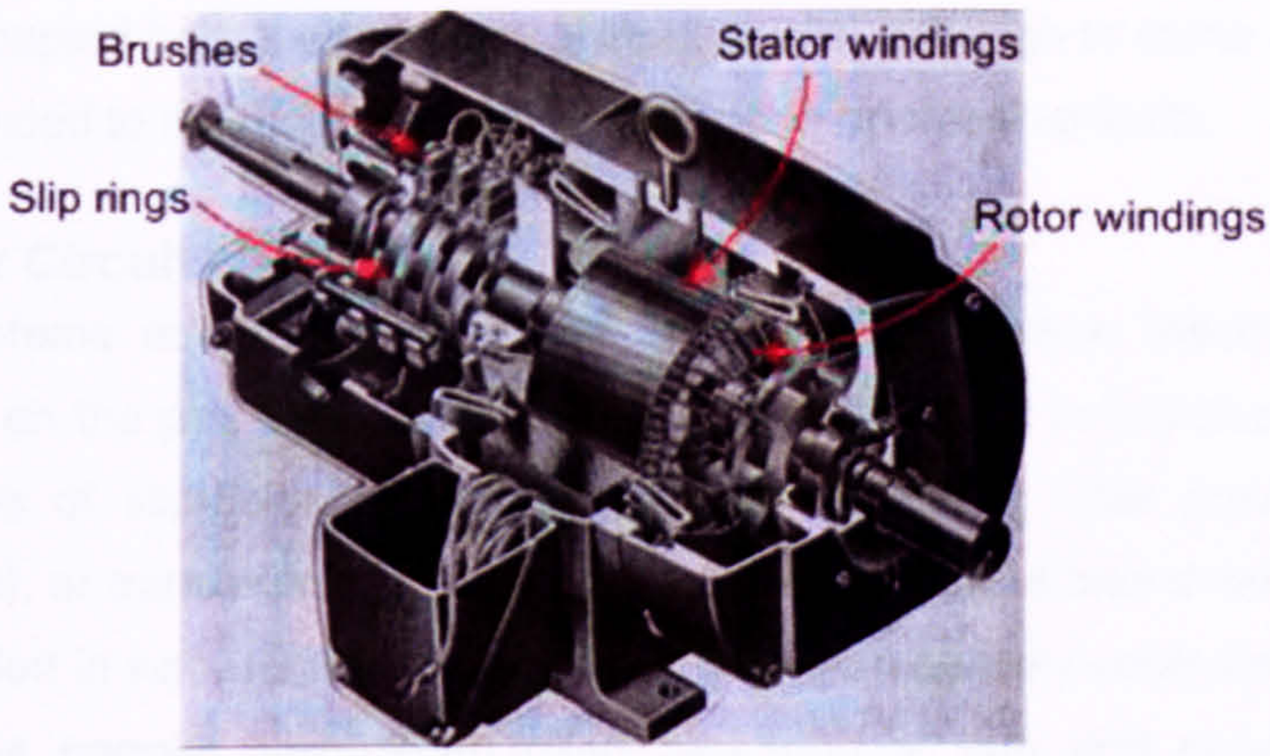

Figure 3.9. Cutaway section of a wound-rotor induction machine [47].

The wound-rotor offers the option of rotor-field control, and with it partial decoupling of the turbine power from the generator's output. This result permits variable speed operation, power factor control and reductions in mechanical shaft stresses. The chief disadvantages are slip-ring and brush maintenance, and the cost of rotor-field control equipment.

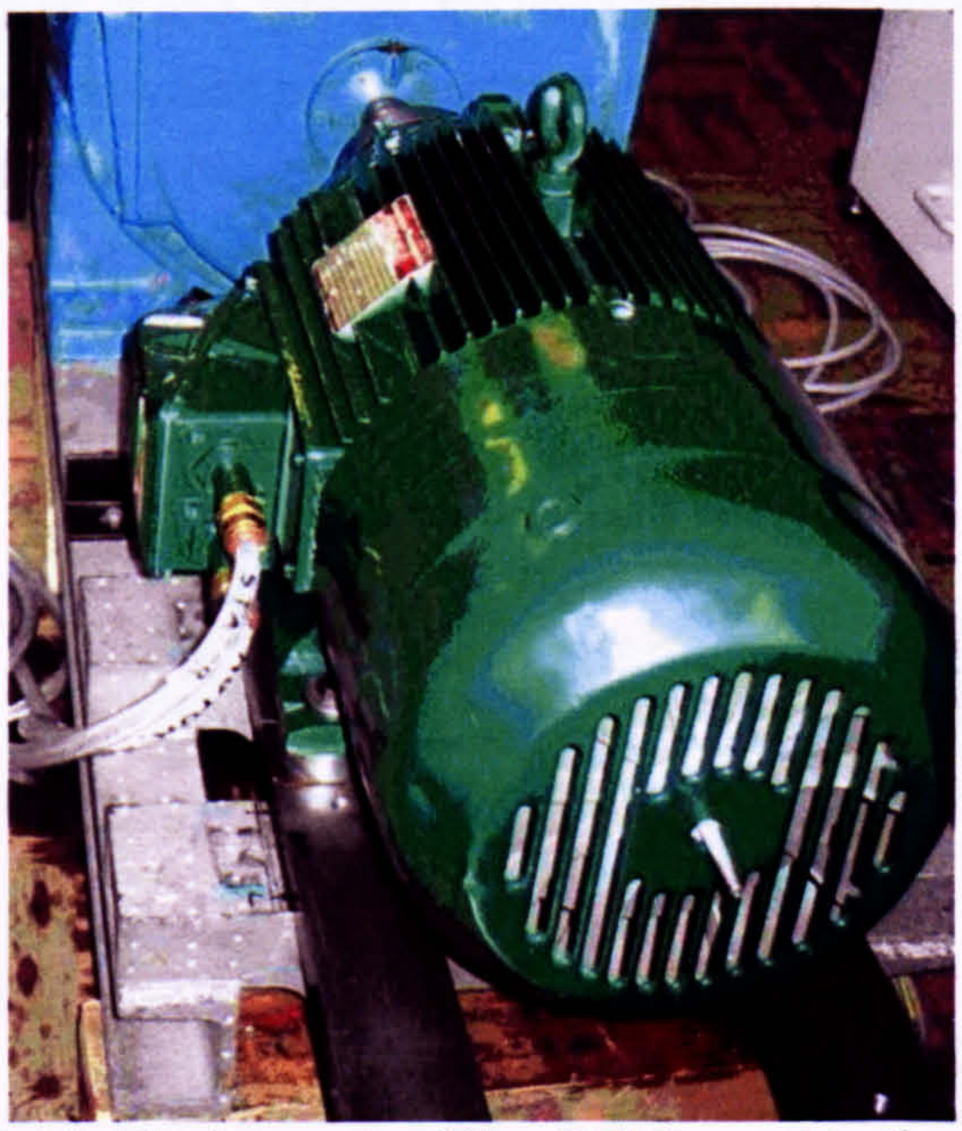

Figure 3.10. Photograph of the DFIG used in the test rig.

Vector control principles

Control of the DFIG with a voltage-source converter can be considered in terms of space vectors. Instant-by-instant the controller can reposition the applied rotor-voltage space vector (within the limits of available converter voltage) to determine the flow of current in the rotor circuit. The rotor current space vector is actively controlled using feedback measurements of the rotor currents. This implies control of the magnitude and relative position of the rotor circuit MMF. In this manner the rotor flux linkage may be constrained to lead, lag, over- or under-excite the stator flux linkage. This allows the DFIG to generate, motor, source or sink reactive power respectively. The DFIG power

output is decoupled from the mechanical input power, although to some degree the two must be balanced to maintain the rotor speed within operational limits.

3.2.2 Rotor Circuit topologies

All DFIG systems employ a polyphase wound-rotor induction machine. This work concentrates on the predominant three-phase machine used in global power systems. Early systems of slip-power recovery included converting rotor power output only (Krämer drive), or transferring bi-directional rotor power (Scherbius drive) [48]. Variable speed operation in wind turbines is fulfilled by using an actively controlled bi-directional converter; this permits current-controlled operation at sub and super-synchronous speeds.

The most dominant, flexible and well-understood rotor circuit arrangement is a pair of three-phase bridge voltage-source inverters fitted back-to-back with a common DC-link. Current-source converters and matrix cycloconverters may be employed instead, but remain insignificant in volume [11]. Current-source topologies typically offer poorer control capabilities than those offered by voltage-source topologies with IGBTs or MOSFETs. Cycloconverters add considerable harmonic content and complexity whilst losing the energy buffer of a DC-link. The most widespread DFIG scheme is illustrated schematically in Figure 3.11.

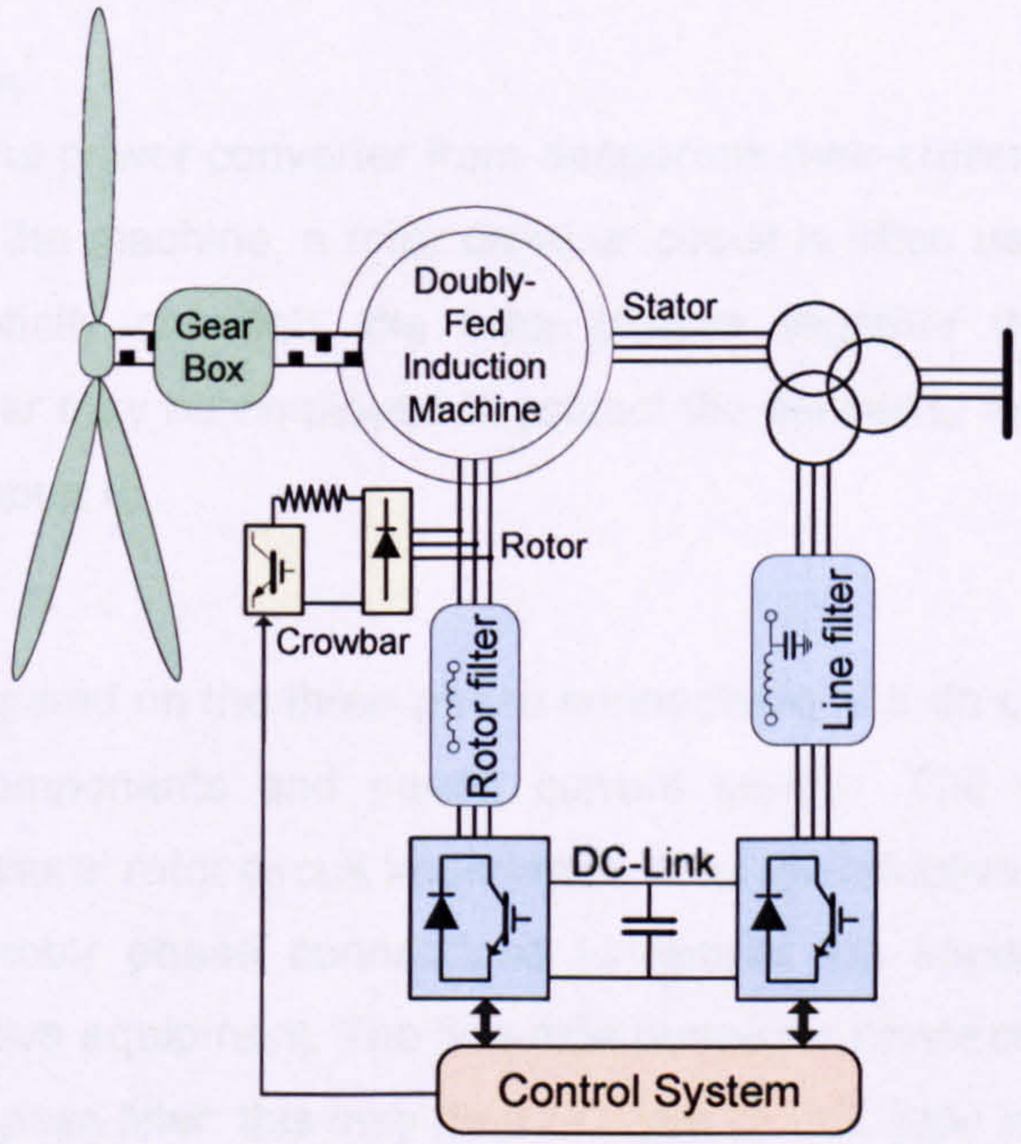

Figure 3.11. Schematic of a wind turbine DFIG including a back-back IGBT power converter.

3.2.3 DFIG Power Converter

Voltage-Source Converter (VSC)

The predominant topology for a wind turbine DFIG power converter is based on three-phase bridge inverters, of which an example is illustrated in Figure 3.12. Two such inverters are connected back-to-back via a capacitive DC-link to form a bi-directional AC power converter. Each inverter is controlled by an independent three-phase PWM source to supply slip-frequency currents to the rotor circuit and system-frequency currents to the grid.

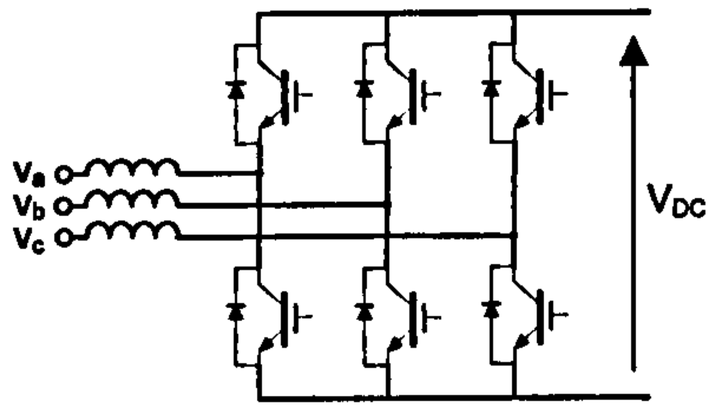

Figure 3.12. Three-phase IGBT bridge converter

The DC-link capacitance maintains the DC-link voltage, providing a small energy buffer and permitting independent control of the two converters. The rotor-side converter (RSC) controls the rotor current and hence the active and reactive power output of the generator. The line-side converter (LSC) through the line-side currents controls the DC-link voltage, conveying rotor power (in either direction) to the grid.

Crowbar protection

In order to protect the power converter from dangerous over-currents and to allow safe demagnetisation of the machine, a rotor crowbar circuit is often used. When engaged, the crowbar essentially connects the rotor phases together through a dedicated resistance. A crowbar may be employed to protect the converter in response to a fault, as discussed in Chapter 6.

Converter filters

Filter circuits are required on the three-phase connections of both converters to remove PWM frequency components and permit current control. The rotor-side converter makes use of the natural rotor circuit impedance. A small inductive filter may be added in series with the rotor phase connections to restrict the impact of PWM voltage transitions on sensitive equipment. The line-side converter connects to the grid voltage via a dedicated low-pass filter: this may be a *LC*-type or *LCL*-type low-pass filter; it may also include high frequency RFI filtering. The example in Figure 3.11 shows an *LC*-filter.

3.2.4 Wind turbine transformer

The Wind turbine generator's output phases are normally restricted to less than 1000V. In fact, most European generators are designed to operate with 690V phase-phase.

This is in part due to safety regulations for a wind turbine tower, and in part due to the flexibility and cost-effectiveness of production for cables and switchgear at low voltages [12]. As a result, all large DFIG wind turbines include a LV:MV transformer to step-up the generator's LV to distribution levels. The three-phase transformer is most commonly wound in Δ -Y form, incidentally shielding the generator from any grid-side DC fault-currents.

3.3 DFIG Control

Conventional PI feedback control of line-side and rotor current space vectors is described in this section. Advanced control schemes are discussed in Chapter 6.

3.3.1 Vector control

Vector control theory for electric drives is well-understood and can be applied to the control of the doubly-fed machine [40]. Control schemes have long been developed for a voltage-source-converter DFIG employed in wind power generation. Unusual control schemes including rotor flux control and state feedback have been proposed [49][50] (although the latter depends strongly upon accurate estimation of constant machine parameters). In general, robust and reliable control can be achieved using PI feedback controllers with machine currents or flux linkages transformed into excitation reference frame d-q space vectors [51][52].

The controller's excitation frame may be aligned in rotation to any particular voltage or flux linkage space-vector such that in steady-state operation all the machine currents and voltages appear as dc commodities. This approach lends itself to the application of PI feedback controllers, in nested control loops, with independent control of active and reactive power. The reader is assumed to be familiar with cascaded PI control and space-vector control schemes. However, for the purposes of clarity an explanation of vector control of voltage-source converters is given in Appendix C.

3.3.2 Line-side converter control

The line-side converter transmits rotor circuit power to or from the grid connection. Its primary function is to manage the DC-link voltage, indirectly balancing power in or out from the rotor-side converter. The vector controller uses measurements of the DC-link voltage, converter currents and stator voltage to control the DC-link voltage and the reactive power exchanged between the converter and the grid.

The line-side current space vector is expressed in Eq. 3.34, defining the direction of current as flowing into the converter from the grid.

$$\bar{i}_c = \frac{\bar{v}_s - \bar{v}_{LSC}}{Z_{filter}} \tag{3.34}$$

In a reference frame aligned with the supply voltage, the steady-state values become constants:

$$\bar{v}_s^e = |v_s| \therefore \bar{i}_c^e = \frac{|v_s| - \bar{v}_{LSC}^e}{Z_{filter}} \tag{3.35}$$

Assuming that the filter is relatively uncomplicated, the simple feedback current control law given in Eq. 3.36 can be used. The feed-forward term on the right-hand side of the equation is optional but helps the converter respond to step-changes in stator voltage. Further feed-forward terms based on the explicit nature of the filter can be used (expanding Eq. 3.34), relying on accurate state measurements to provide incremental improvements in drive performance [53].

$$\bar{v}_{LSC}^{e\,\otimes} = PI\left(-\bar{i}_c^{e\,\otimes} + \bar{i}_c^e\right) + \bar{v}_s^e \tag{3.36}$$

The active and reactive power *in*puts to the LSC are determined by Eqs. 3.37 & 3.38.

$$P_c = |v_s| i_{cd}^e \tag{3.37}$$

$$Q_c = -|v_s| i_{cq}^e \tag{3.38}$$

The active and reactive current components control the active and reactive power inputs independently. The active power directly affects the DC voltage: energy absorbed into the converter is stored on the DC-link, raising the DC voltage. Hence simple version of feedback power control can be derived (Eqs. 3.39-3.40).

$$i_{cd}^{e\,\otimes} = PI\left(V_{dc}^{\otimes} - V_{dc}\right) \tag{3.39}$$

$$i_{cq}^{e\,\otimes} = PI\left(-Q_c^{\otimes} + Q_c\right) \tag{3.40}$$

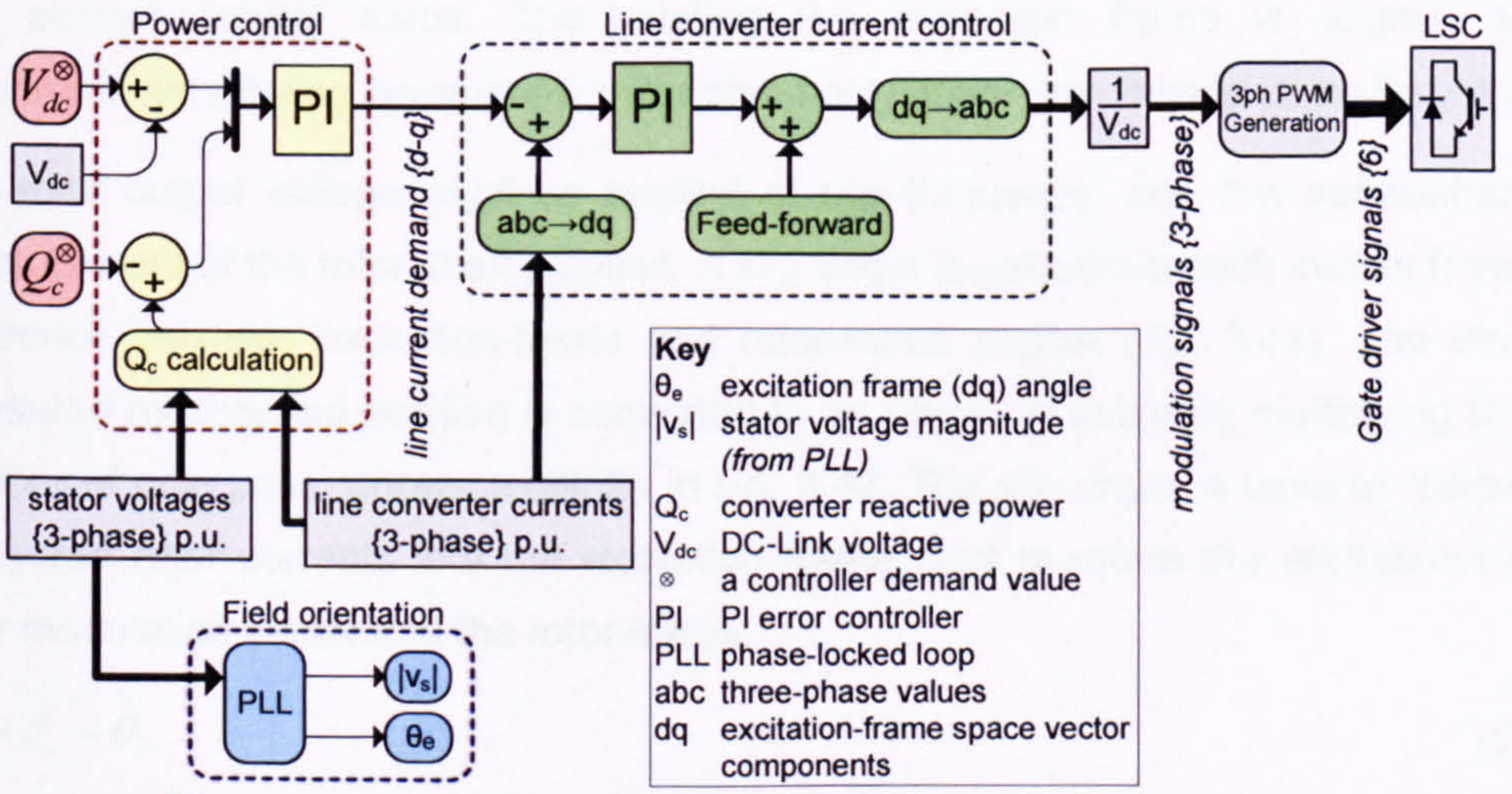

Figure 3.13. A line-side converter vector control scheme.

A typical cascade control arrangement for a line-side converter is shown schematically in Figure 3.13. Note that the current controller's output signal is multiplied by the reciprocal of the DC-link voltage, as this ensures a correct p.u. modulation output and negates the influence of any DC-link variations on the performance of the controller.

The dedicated line-side filter enables the fast-acting current controller to respond to current errors in milliseconds whilst maintaining a stable controlled output. The line-side converter controller can be tuned to respond faster than the rotor-converter's controller, which therefore permits good control of the DC-link voltage.

3.3.3 Rotor-side converter control

The rotor-side converter's vector controller uses measurements of the DC-link voltage, rotor currents, stator currents, stator voltages and rotor shaft position to control the active and reactive stator power.

Power reference

The flexibility of control capabilities permits rotor speed or torque control in place of active power control [54]. In a pitch-controlled wind turbine the power output will normally be set by a master-controller working in conjunction with the turbine's blade-pitch controller. The pitch-controller normally controls the rotor speed, in order to optimise wind energy capture and keep the turbine stable. The master-controller will in turn adjust the generator's power reference, although on a mechanical timescale, which is relatively slow compared with the electromagnetic dynamics of the machine. As a result, The DFIG rotor controller below is based upon active power control, with the active power reference value as an external input.

Alignment

In a similar fashion to the line-side converter, the rotor-side employs cascaded power and current control loops. The rotating d-q excitation frame is aligned to a synchronously rotating commodity; most commonly stator flux-linkage or stator voltage.

The rotor output voltage must be applied at slip frequency, and this necessitates a measurement of the rotor shaft position. A slip angle is calculated each instant from the difference between excitation-frame and rotor-frame angles (Eq. 3.41). The directly measured mechanical position is converted to an electrical angle by multiplying by the number of pole pairs, shown explicitly in Eq. 3.42. The slip angle is used to rotate the measured rotor currents into the excitation frame, and to rotate the excitation-frame rotor modulation vector into the rotor-frame.

$$\theta_\varsigma = \theta_e - \theta_r \tag{3.41}$$

$$\theta_\varsigma = \theta_e - p'\theta_{mech} \tag{3.42}$$

Many DFIG rotor-control schemes use an excitation-frame aligned with the stator flux-linkage [51][52]. This allows clear decoupling between d and q components of rotor current. However, the alignment depends upon accurate positioning of the stator flux-linkage vector. The stator flux linkage cannot be directly measured; typically it is estimated from integrating the stator voltage equation (Eq. 3.26), although the integration process is not without drawbacks. It is possible, making the assumption that stator resistance is small, to assume that the flux-linkage always lies $\pi/2$ radians behind the stator voltage. In this third method one simply uses the relatively stable phase angle provided by a PLL applied to the stator voltage [55]. Alternatively, it is acceptable to align the excitation-frame with the stator voltage space vector, as employed by the line-side converter. The main advantage lies in using only the reliable and stable output of a PLL for the field alignment. The main disadvantage is in requiring approximations in the decoupling aspect of the control laws (see power-control section below). Another possibility is to apply rotor flux-linkage control to the inner loop, as opposed to rotor current control, although this method is not to date widely used. [49].

The following example uses stator voltage alignment, using the reference angle provided by the stator voltage PLL and adding the convenience of using the same field orientation as the line-side converter. This method was used with the DFIG test rig (Chapter 4).

Current control

The control equations can be deduced from the generalised machine equations. First, consider rotor voltage and flux-linkage in the excitation frame:

$$\bar{u}_r^e = R_r \bar{i}_r^e + \partial \bar{\psi}_r^e + j\omega_\varsigma \bar{\psi}_r^e \tag{3.43}$$

$$\bar{\psi}_r^e = L_r \bar{i}_r^e + L_m \bar{i}_s^e \tag{3.44}$$

Eq. 3.45 defines a magnetisation flux-linkage which contains only the mutually-linking flux contributions. With a stiff voltage supply to the stator the internal magnetisation remains roughly constant in the excitation reference frame [40][51].

$$\bar{\psi}_m^e = L_m\left(\bar{i}_r^e + \bar{i}_s^e\right) \tag{3.45}$$

Recalling the total rotor inductance in terms of its leakage and mutual contributions (Eq. 3.46), the rotor voltage can be expressed in terms of rotor current and the pseudo-constant magnetisation flux linkage (Eq. 3.47).

$$L_r = (1+\sigma_r)L_m \tag{3.46}$$

$$\bar{u}_r^e = \left(R_r + \sigma_r L_m \partial + j\omega_\varsigma \sigma_r L_m\right)\bar{i}_r^e + \partial \bar{\psi}_m^e + j\omega_\varsigma \bar{\psi}_m^e \tag{3.47}$$

Eq. 3.47 shows the relationship between rotor voltage and current in a machine with roughly constant magnetisation. A feedback rotor-current error controller can be derived from Eq. 3.47, using PI controllers to determine the appropriate rotor voltage modulation. Any of Eqs. 3.48 - 3.50 may be used as governing control laws, with successively more complex feed-forward terms.

$$\bar{u}_r^{e\otimes} = PI\left(\bar{i}_r^{e\otimes} - \bar{i}_r^{e}\right) \tag{3.48}$$

$$\bar{u}_r^{e\otimes} = PI\left(\bar{i}_r^{e\otimes} - \bar{i}_r^{e}\right) + \partial\bar{\psi}_m^{e} + j\omega_\varsigma\bar{\psi}_m^{e} \tag{3.49}$$

$$\bar{u}_r^{e\otimes} = PI\left(\bar{i}_r^{e\otimes} - \bar{i}_r^{e}\right) + j\omega_\varsigma\sigma_r L_m\bar{i}_r^{e} + \partial\bar{\psi}_m^{e} + j\omega_\varsigma\bar{\psi}_m^{e} \tag{3.50}$$

The relative performance of the inclusion of feed-forward terms depends upon the particular control environment: the speed of the controller, resolution and reliability of the sensors, accuracy of the excitation-frame alignment, and so on. The stability and performance of various rotor-current control schemes has been analysed in [53], including a study of the benefits of feed-forward terms in the PI control scheme.

Power Control

The direction of stator and rotor current in this work is defined as flowing *into* the generator. The apparent stator power in Eq. 3.51 is therefore written in sink convention, implying a negative value for power generation. Similarly, sink convention implies a negative value for reactive power *export* (capacitive behaviour). Sink convention is maintained throughout this work.

$$\bar{S}_s = \bar{v}_s^{e}\bar{i}_s^{e*} \tag{3.51}$$

The dependence of stator power on rotor current can be derived as follows. Stator current in Eq. 3.51 can be substituted using the stator inductance definition from Eq. 3.11:

$$\bar{i}_s^{e} = \frac{\bar{\psi}_s^{e}}{L_s} - \frac{L_m}{L_s}\bar{i}_r^{e} \tag{3.52}$$

$$\bar{S}_s = |v_s|\left(\frac{\bar{\psi}_s^{e}}{L_s} - \frac{L_m}{L_s}\bar{i}_r^{e}\right)^* \tag{3.53}$$

Making the assumption that stator resistance is small, then the p.u. stator flux linkage lays approximately $\pi/2$ radians behind the stator voltage, and is also of constant magnitude in the steady-state. Hence:

$$P_s \approx -\left(|v_s|\frac{L_m}{L_s}\right)i_{rd}^e \tag{3.54}$$

$$Q_s \approx \frac{|v_s|}{L_s}\left(|\psi_s| + L_m i_{rq}^e\right) \tag{3.55}$$

Hence, in this reference frame, the active power is related to the negative value of the direct-component of rotor current. The reactive power is related to the positive value of the quadrature-component of rotor current. This conclusion generates simple feedback control laws for rotor current, such as Eqs. 3.56-3.57.

$$i_{rd}^{e\,\otimes} = PI\left(-P_s^{\otimes} + P_s\right) \tag{3.56}$$

$$i_{rq}^{e\,\otimes} = PI\left(Q_s^{\otimes} - Q_s\right) \tag{3.57}$$

A feed-forward term in reactive power control could be derived to take advantage of the stator flux offset in Eq. 3.55. This is omitted in the example below, where the integral component of the reactive power PI controller winds up to the appropriate level of reactive current.

The overall vector controller bears a similar structure to the line-side converter (Figure 3.14). The line-side and rotor-side controllers are implemented independently, but may save computational effort by sharing information such as the PLL phase and the DC-link voltage measurement.

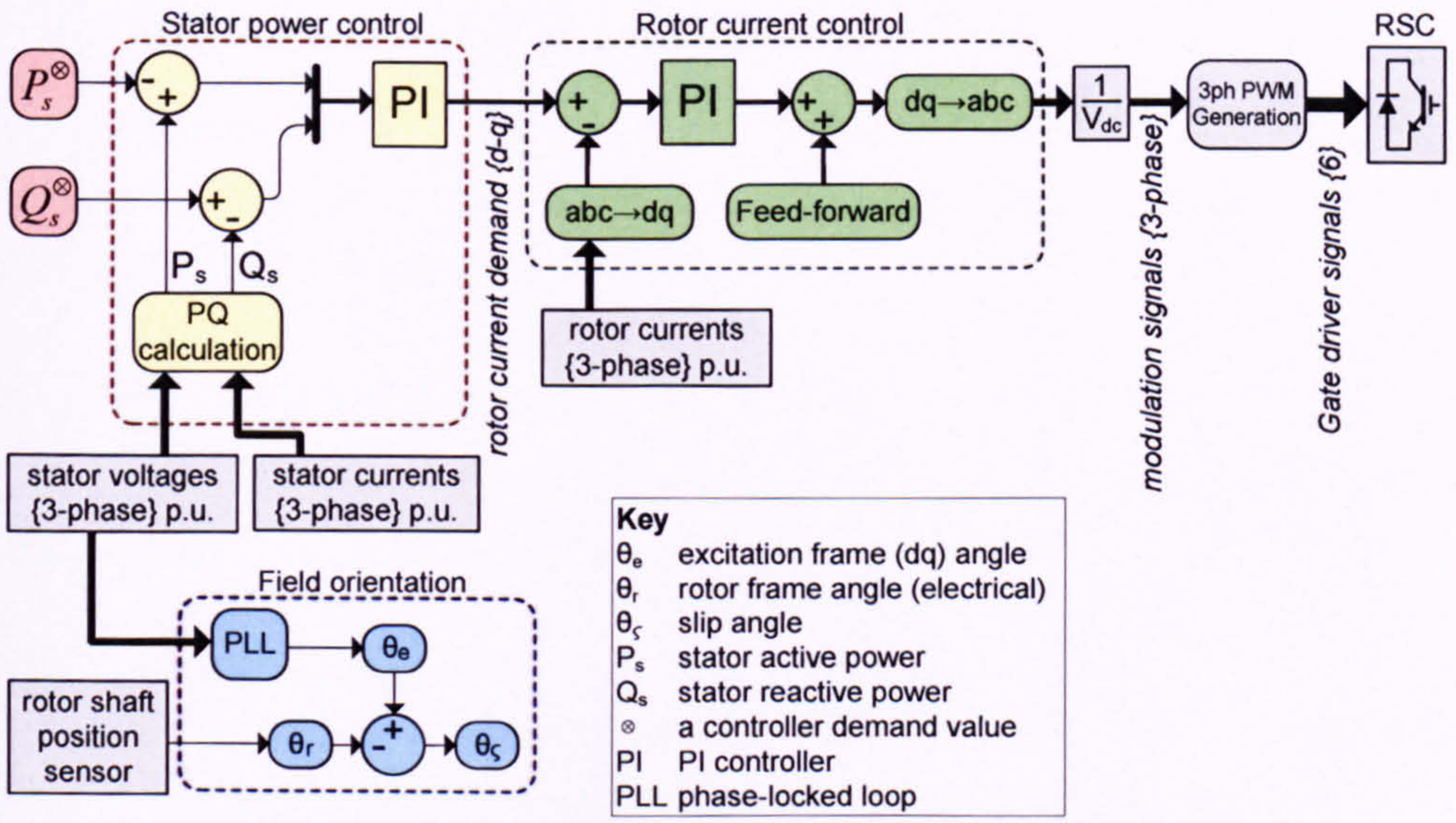

Figure 3.14. A rotor-side converter vector control scheme.

Dynamic control limitations

The control dynamics are limited by the PWM frequency, the relative DC-link voltage, the rotor circuit's transient time constant and the filter circuit (as shown in Appendix C).

The DC-link voltage headroom, i.e. the difference between the DC-link voltage and the typical rotor emf, is roughly constant for different DFIGs for efficiency reasons: the machine rotor turns are typically configured to maximise use of the converter voltage. The PWM frequency capability improves with newer generations of power electronic devices and several kilohertz is common at present. This level poses no significant bottleneck given the relative rates of dynamic machine phenomena, as the control delay from measurement sample to action totals less than 0.5ms.

The transient time constant ultimately determines the rate of change of electromagnetic phenomena on the rotor circuit. The rotor currents cannot be controlled more than perhaps 5-10 times faster than the rotor's transient time constant. For example, tuning of the rotor controller on the test rig with a rotor transient timescale of 40ms provided no better than a roughly 6ms characteristic rise-time in response to a step change in rotor current demand.

3.4 Summary

The principles of torque generation in an induction machine were explored and a set of generalised machine equations were presented. The doubly-fed induction generator (DFIG) concept was introduced in the context of wind power generation. Using the generalised machine equations, vector control of the DFIG system was explained.

EXPERIMENTAL APPARATUS AND SIMULATION MODEL

4

The aim of this chapter is to familiarise the reader with the experimental tools used for the study of DFIG fault response. Primarily, a 7.5kW DFIG test facility was built and commissioned in Newcastle University. Known collectively as the 'test rig', this facility was designed to accommodate the study of wind turbine DFIGs under grid fault conditions. The test rig aims were to include:

- A doubly-fed induction generator to operate with the slip range of a typical variable-speed wind turbine.
- An IGBT power converter capable of withstanding fault test conditions.
- Representation of a wind turbine's mechanical dynamics.
- Application of grid faults in a manner representative of a transmission system.
- The typical grid connection impedance of a wind turbine.
- A flexible control scheme for the rapid prototyping of new control methods or to accommodate hardware modifications.

In support of the test rig, a full dynamic simulation of the DFIG system was prepared in Matlab / Simulink software. This was primarily to pre-screen fault ride through techniques before implementation on the test rig.

4.1 Test rig hardware

This section will provide an introduction to the key elements of the test rig and their function. Detail on the test rig can be found in Appendix D.

4.1.1 Test rig overview

A test rig was designed and built to simulate the elements of a grid-connected DFIG wind turbine. Figure 4.1(a) shows a wind turbine generator scheme while Figure 4.1(b) shows an overview of the test rig facility, with the corresponding elements highlighted.

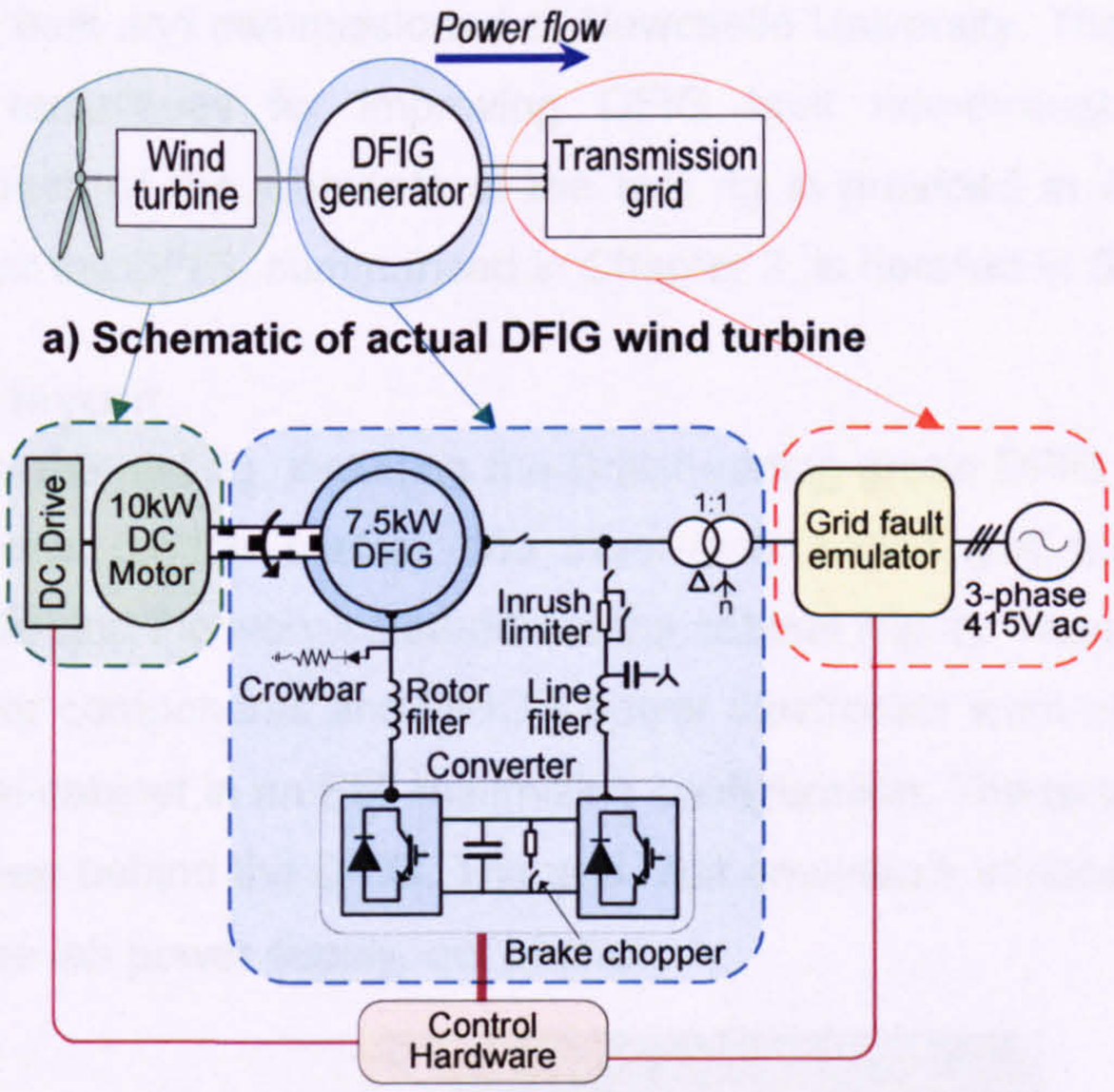

Figure 4.1. DFIG wind turbine generator & test rig overview.

The test rig permitted the experimental evaluation of the DFIG system and its associated controller under a range of grid fault conditions. The test rig comprised four main elements: a wind turbine simulator, a DFIG system, a grid fault emulator and a control hardware assembly.

- The grid fault emulator permitted a flexible approach to the application of grid faults. It allowed a range of balanced voltage-dip profiles to be applied to the terminals of the DFIG via a 1:1 Y-Δ isolation transformer.
- A 10kW DC motor and its drive provided a torque input to the DFIG. Together with a simulated mechanical model executed by the control hardware, this replicated the torque input from a wind turbine rotor, drawing from industry-supplied wind turbine data.
- The 7.5kW DFIG system represented the wind turbine's doubly-fed induction generator, including a custom 50A-rated IGBT power stack employed as a bi-directional power converter. The power stack was deliberately over-rated to accommodate fault conditions without damaging the equipment.
- The control hardware consisted of a combination of analogue protection & interface boards, isolated sensing equipment, proprietary controller development equipment and a dedicated PC. A central electronics board was responsible for the test rig protection system and control signal routing. A dSpace control system was used to execute the DFIG controller, wind turbine simulator and fault test control.

The test rig was built and commissioned at Newcastle University. The rig was used to test promising techniques for improving DFIG fault ride-through. Full technical information for each of the elements of the test rig is provided in Appendix D. The control method for the DFIG, summarised in Chapter 3, is detailed in Section 4.2.

4.1.2 Test rig layout

Figure 4.2 shows the test rig, including the British-racing green DFIG (bottom-left), the sea-blue DC motor (bottom-centre), the silver-grey caged grid fault emulation kit (centre, on bench) and the ivory-coloured control cabinet (right). The control hardware, the DC drive, filter components and DFIG's power electronics were all mounted within the earthed metal cabinet in an EMI minimizing configuration. The isolation transformer is hidden from view behind the DFIG. The grid fault emulator's variacs were kept close to the three-phase lab power supply, out of shot.

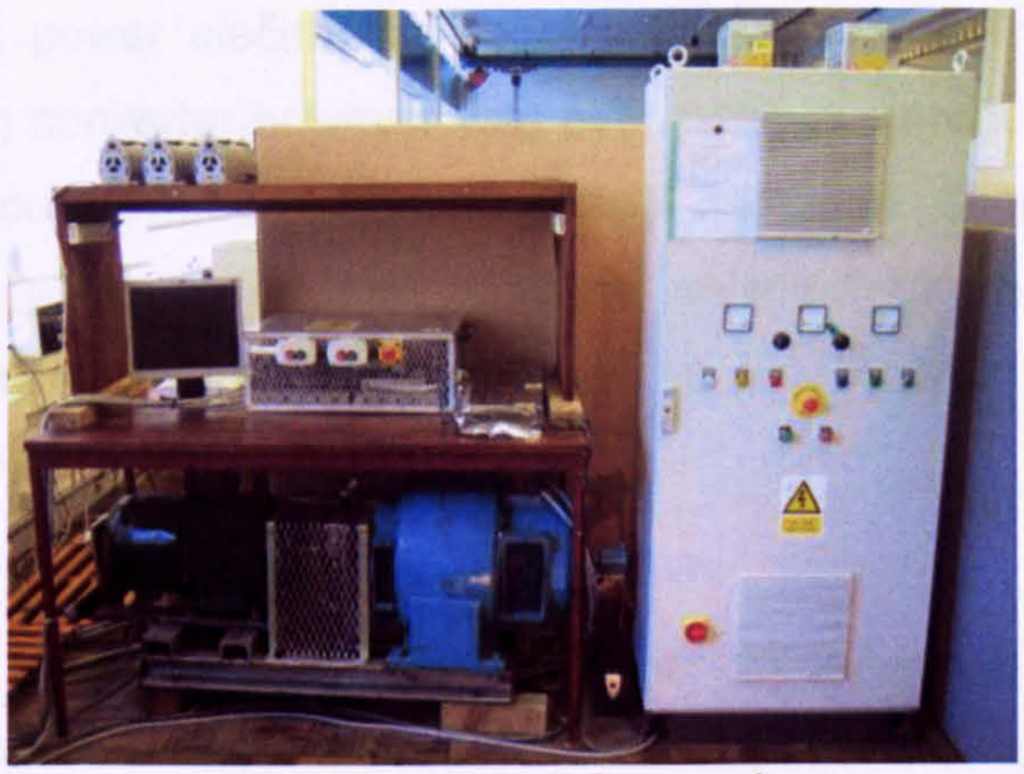

Figure 4.2. DFIG test rig.

4.1.3 DC motor prime mover

A 10kW DC motor was used to replicate the mechanical torque of a wind turbine shaft experienced by its generator. The control hardware computed a mechanical two-mass shaft model nested inside a closed-loop turbine-shaft speed controller to represent the blade-pitch control action of the turbine (Section 4.2.1). The final torque demand was applied to the DC motor by a 75A DC-drive. The dynamics of the simulated model (Appendix D) were derived from industrial data; these compare well with general turbine parameters [24].

A 5000-line optical encoder on the rotor shaft provided detailed rotor position information. A proximity sensor and shaft-mounted nylon drum sent a pulse train to a dedicated over-speed relay for added protection.

4.1.4 Generator and power electronics

Power converter

A 7.5kW, 415V wound-rotor induction machine was used with a custom-built 415VAC, 50A back-to-back IGBT converter, illustrated in Figure 4.3.

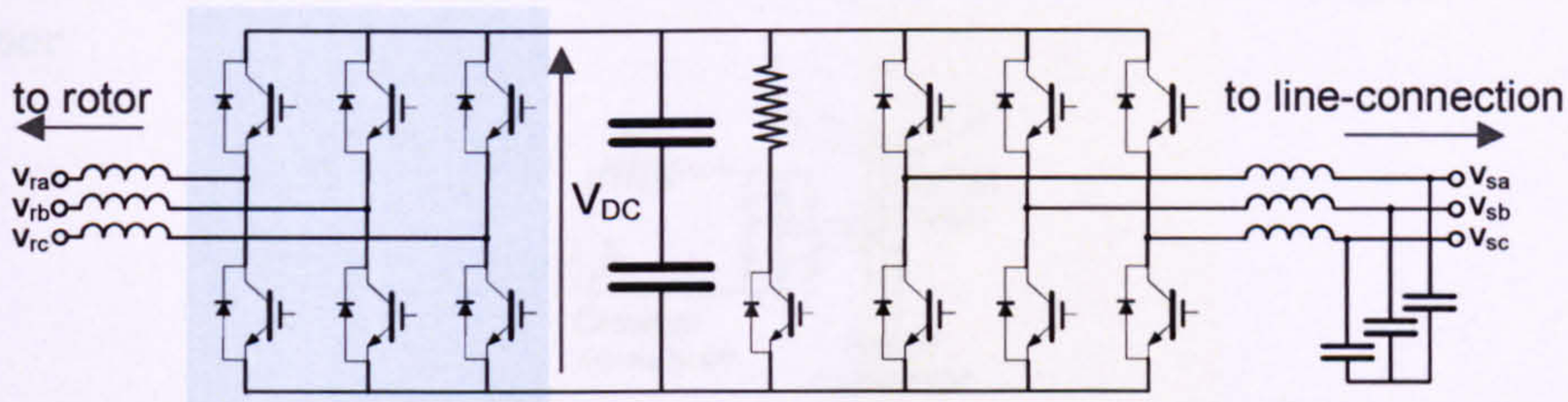

Figure 4.3. DFIG power converter and line filters.

The induction machine's rotor was wound to produce rated converter voltage at a maximum operating slip of ±30% and rated stator voltage. To minimise cost, a commercial DFIG's power electronics would be rated for maximum operating rotor current. The test rig converter however was over-rated in current to permit a range of grid-fault tests without adversely affecting normal operation. Similarly, the electrolytic DC-link capacitors used in the test rig were selected for their additional surge capability, permitting short term excursions of up to 1100Vdc (compared with the 1000Vdc rated value).

Filters

An LC type filter was chosen for the line-side converter with a 1200Hz cut-off frequency. A small three-phase choke was added to the rotor circuit to supplement the rotor's own inductance and limit the impact of PWM voltage switching on the rotor windings. The rotor-side converter (RSC) and the line-side converter (LSC) were controlled independently: the RSC at 5kHz and the LSC at 4.89kHz.

Inrush protection

A set of resistors were included with a bypass circuit to limit the inrush current when pre-charging the DC-link. After a 3 second delay the resistors were bypassed by a timer-controlled contactor.

Brake chopper

The converter's DC-link was protected by a brake chopper: an IGBT switch which shorts the DC-link through a separate high-power resistor. The chopper circuit was mounted in parallel with the DC-link capacitors, as shown in Figure 4.3. The chopper was engaged automatically when measuring a DC-link voltage above 810V, and disengaged when the measurement fell below 795V.

A brake chopper circuit is not a standard protection device in wind turbine DFIG power converters. It was necessary for this test rig in order to ensure safe operation under all

the proposed grid fault test conditions. It is possible to infer the necessity of such a device by extrapolating the test data: the rate of the DC-link voltage rise before brake-chopper application can be so very quick that it is clear that, without the brake chopper, an equivalent power converter would have suffered damage in the test.

Crowbar

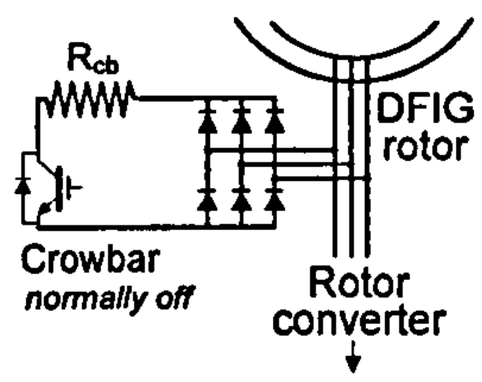

Figure 4.4. Crowbar circuit in test rig.

A crowbar connects the rotor phases together through an external resistor (detailed in Chapter 6). The test rig rotor circuit was protected by a crowbar comprising a three-phase diode rectifier, a resistor and an IGBT switch (Figure 4.4). The IGBT was enabled by either of two triggers: firstly a hardwired error signal (enabled by gate driver error or a measured current exceeding 45A), or secondly a software enabled trigger enabled by the dSpace controller. When the crowbar was engaged, the rotor-side converter switches were turned off.

The crowbar was not normally operational and maybe considered a last-line of defence against extreme over-currents in the test facility – in this manner the crowbar was triggered by test-rig rotor currents above 45A peak (nearly 10 p.u.). The crowbar may, separately, be included in certain fault ride through techniques as explained in Chapter 6. This latter mode was executed by the dSpace controller.

4.1.5 Control hardware

Power converter control and DC-drive control were performed by a dSpace dS1103 single-board computer. The control signals were conditioned and routed through an independent logic analysis 'main' board. The main board housed a PIC microcontroller which performed start-up and shut-down procedures and responded to test rig error detection either by isolating appropriate sections of the circuit, executing a controlled shut-down sequence or by performing an emergency stop. Signal acquisition hardware optically isolated the measurement signals and used adjustable error threshold levels to supply error signals to the main board. Rotor-side PWM was performed by the dSpace controller. Line-side PWM switching was performed by an independent PIC-based interface board, taking its modulation signals directly from the dSpace controller.

4.1.6 Grid fault emulation

The grid fault emulator was produced to apply balanced, rectangular grid fault voltage profiles of the type specified in grid code (Chapter 2).

Three independent voltage levels (healthy, fault and recovery) were prepared in parallel on three (3) three-phase variable auto-transformers (variacs). The three variac outputs were connected by a set of back-to-back IGBT transfer switches controlled from a central switch-control electronics board. A fault test was performed by switching the voltage applied to the generator from one variac source to the next in sequence: from "healthy" to "fault" and then to "recovery" as required. A single line diagram of the grid fault emulator setup is shown in Figure 4.5.

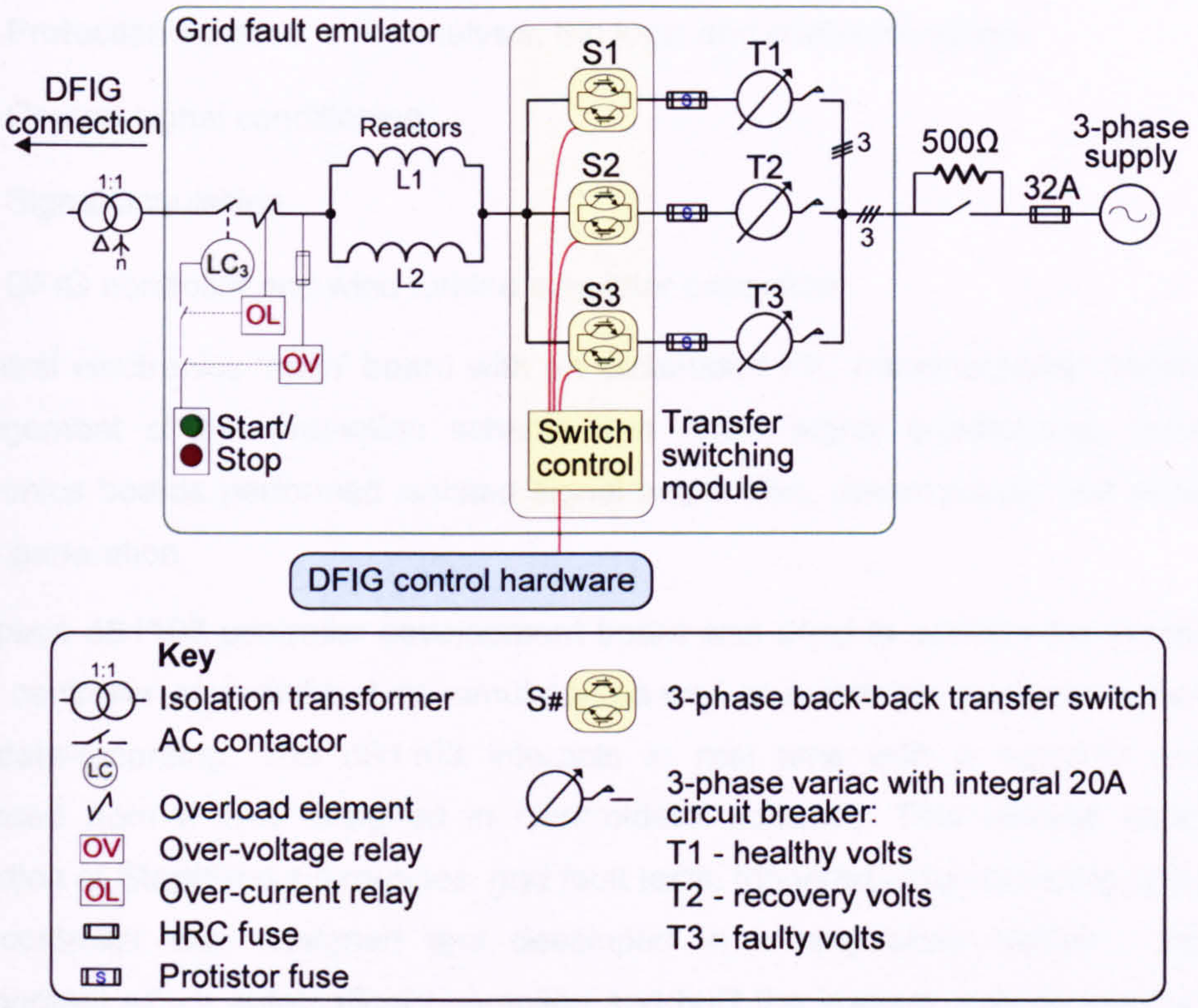

Figure 4.5. Grid fault emulator.

The IGBT switches were rated for 55A each and were protected by a series of fast-acting 30A semiconductor fuses. The status of the switched voltage sources was dictated by a command signal despatched from the dSpace controller. The dedicated switch-control board logic precluded short-circuiting the variacs via simultaneous engagement of multiple switches. The grid fault voltage and recovery voltage magnitudes were manually pre-set on the appropriate variacs before each test.

4.1.7 Grid connection impedance

A grid transformer, connecting a wind farm to the grid, possesses considerable reactance. Additionally, each wind turbine typically has a dedicated step-up transformer and interconnecting cabling. Included in the grid fault emulation kit therefore were a set of three-phase reactors (Figure 4.5) measuring 0.15 p.u. (including the isolation transformer), selected as a representative lumped connection impedance for a wind turbine in a large wind farm [32]. A wind turbine's transformer is most commonly wound

in star-delta form; this behaviour was reproduced by a three-phase star-delta wound 1:1 isolation transformer connected in series between the reactors and the DFIG. An additional benefit was that the interposing reactance inhibited undesirable interactions between the test rig's various switching sources.

4.2 Test rig control

The test rig DFIG system's control hardware comprised four main elements:

- Protection scheme: error analysis, trip logic and contactor action.
- Control signal conditioning.
- Signal acquisition.
- DFIG controller and wind turbine simulator execution.

A central electronics 'main' board with an embedded PIC microcontroller handled the management of the protection scheme and driver signal conditioning. Peripheral electronics boards performed isolated signal acquisition, power supply and secondary PWM generation.

A dSpace dS1103 controller development board was used to perform the functions of DFIG controller and wind turbine simulator, as well as numerous supervisory functions and data-recording. The dS1103 interacts in real time with a host-PC and was accessed from a GUI designed in Controldesk software. This allowed conditional execution of Start/Stop subroutines, grid fault tests, triggered data-recording and so on. The controller was designed and developed in a proprietary Matlab / Simulink environment which automatically compiled and built the custom code for operation on the dSpace controller. This allowed rapid prototyping of modified control schemes.

The complete setup of the control hardware electronics and the test rig protection scheme is detailed in Appendix D. This section will concentrate on the wind turbine simulator and DFIG controller which were developed in Simulink and operated on the dSpace platform. The control scheme detailed below is the base controller, i.e. without adaptations for fault response. Fault ride through modifications for the DFIG controller are discussed in Chapter 6.

4.2.1 DC motor wind turbine simulator

Two-mass model

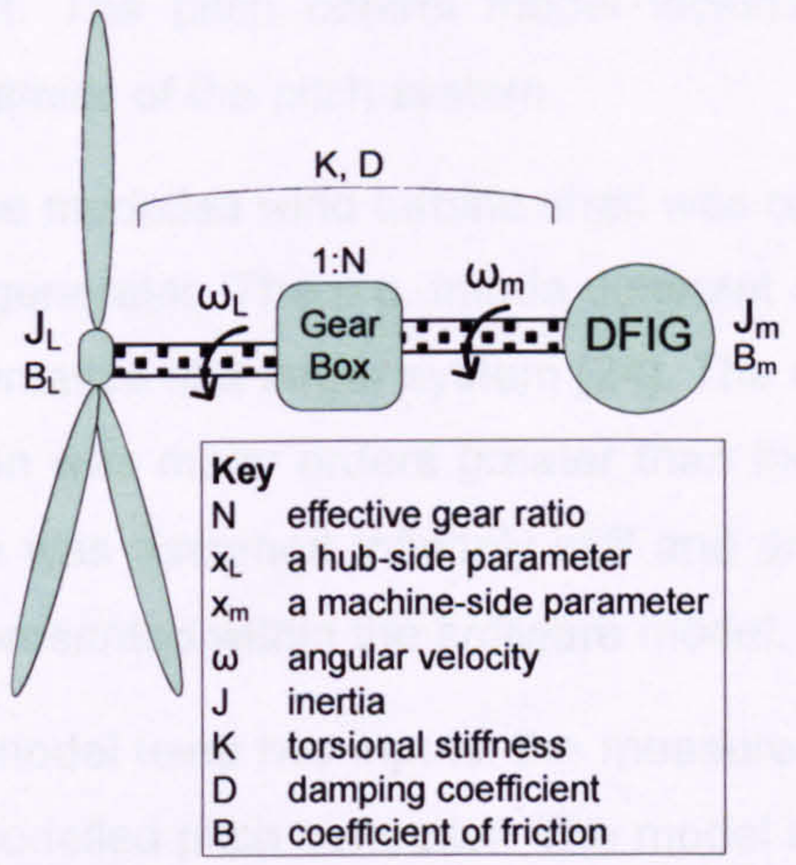

Figure 4.6. Two-mass flexible-coupling wind turbine drive-train model.

A two-mass model is the recommended representation of the wind turbine mechanical dynamics in electrical studies [24]. A two-mass drive-train model is depicted in Figure 4.6, and described by the torque Eqs. 4.1 & 4.2:

$$J_L \frac{d^2\theta_L}{dt^2} + B_L \frac{d\theta_L}{dt} + D(\omega_L - \omega_m) + K(\theta_L - \theta_m) = T_L \tag{4.1}$$

$$J_m \frac{d^2\theta_m}{dt^2} + B_m \frac{d\theta_m}{dt} + D(\omega_m - \omega_L) + K(\theta_m - \theta_L) = T_e \tag{4.2}$$

The two-mass model groups all of the low-speed (wind turbine) components into a single body at the far end of a modelled non-stiff shaft, with the real electrical generator at the near end. In p.u. terms, the gear ratio of the gearbox is neglected and the gearbox only contributes towards the total effective damping coefficient. The test parameters are listed in Appendix D.

Wind turbine simulator

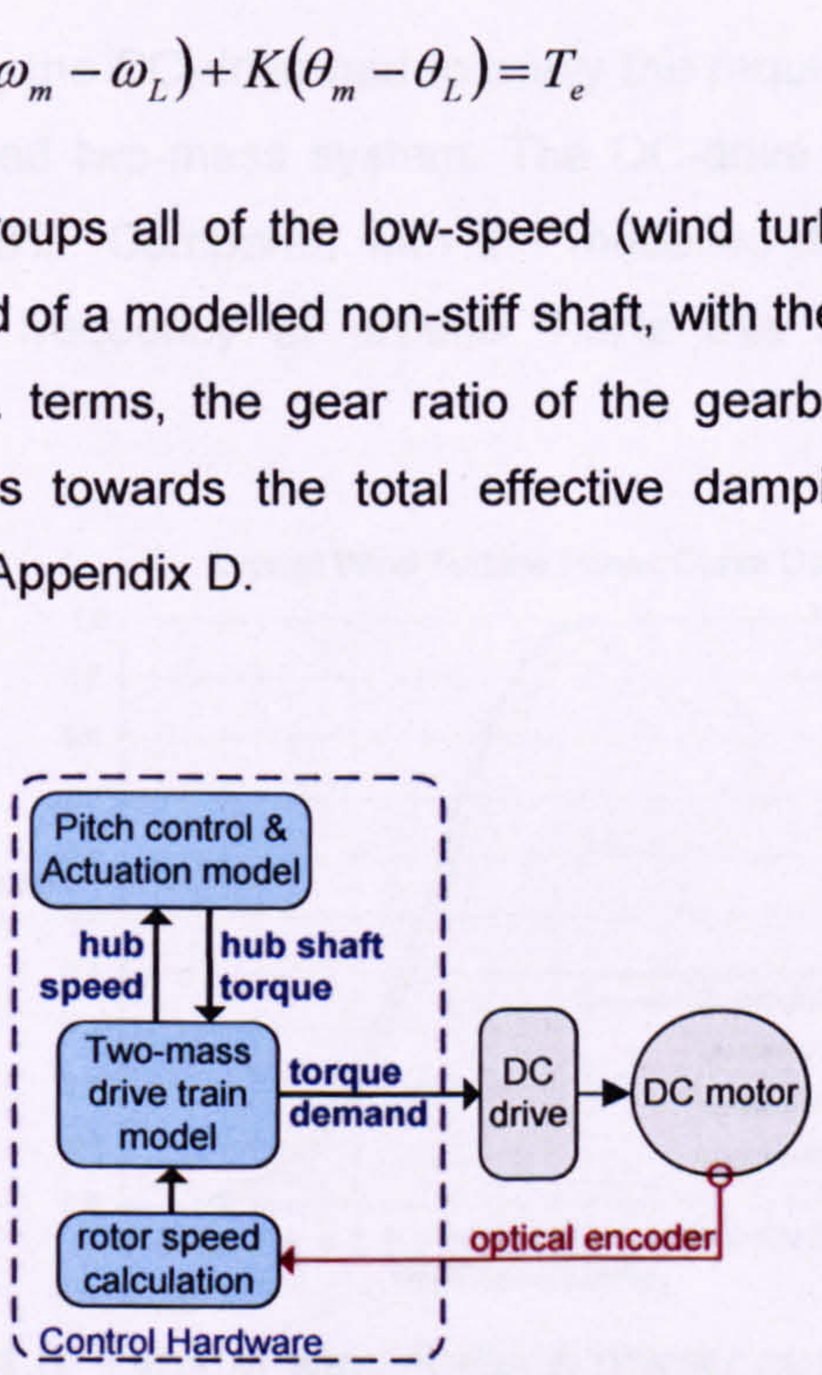

Figure 4.7. DC motor control.

The DC motor was controlled to emulate the dynamics of a wind turbine drive train. A two-mass drive train model was used to represent a complete wind turbine shaft

assembly as described above. The low-speed end of the turbine shaft was modelled along with a blade-pitch control scheme which worked to control the speed of the bladed end of the shaft. The pitch control model included an actuation delay to represent simply the dynamics of the pitch system.

The high-speed end of the modelled wind turbine shaft was represented by the real test rig motor shaft and real generator. The p.u. inertia constant of the generator and shaft were found to be representative of a larger system [24]. The relative stiffness of the DC motor to DFIG connection was many orders greater than the modelled drive-train. As such the real connection was assumed infinitely stiff and any wind turbine drive-train torsions were entirely represented within the software model.

The two-mass software model used two inputs: the measured rotor angle and the load torque output from the modelled pitch controller. The model solved Eq. 4.1 for the high speed angle, θ_L, using the wind turbine mechanical constants in Appendix D. Using this solution, the model's output provided the coupling torque defined in Eq. 4.3. This is the torque exerted on the generator end of the modelled shaft by the wind turbine. In terms of the test rig, this value was the torque applied by the DC motor onto the stiff test rig shaft, and hence onto the DFIG.

$$T_{couple} = D(\omega_L - \omega_m) + K(\theta_L - \theta_m) \tag{4.3}$$

To validate this scheme, the DC-drive had to apply the required torque faster than the dynamics of the modelled two-mass system. The DC-drive application note states a control bandwidth of 80Hz. Compared with the modelled mechanical system with a characteristic resonant frequency at around 1.5Hz this implied sufficient control bandwidth.

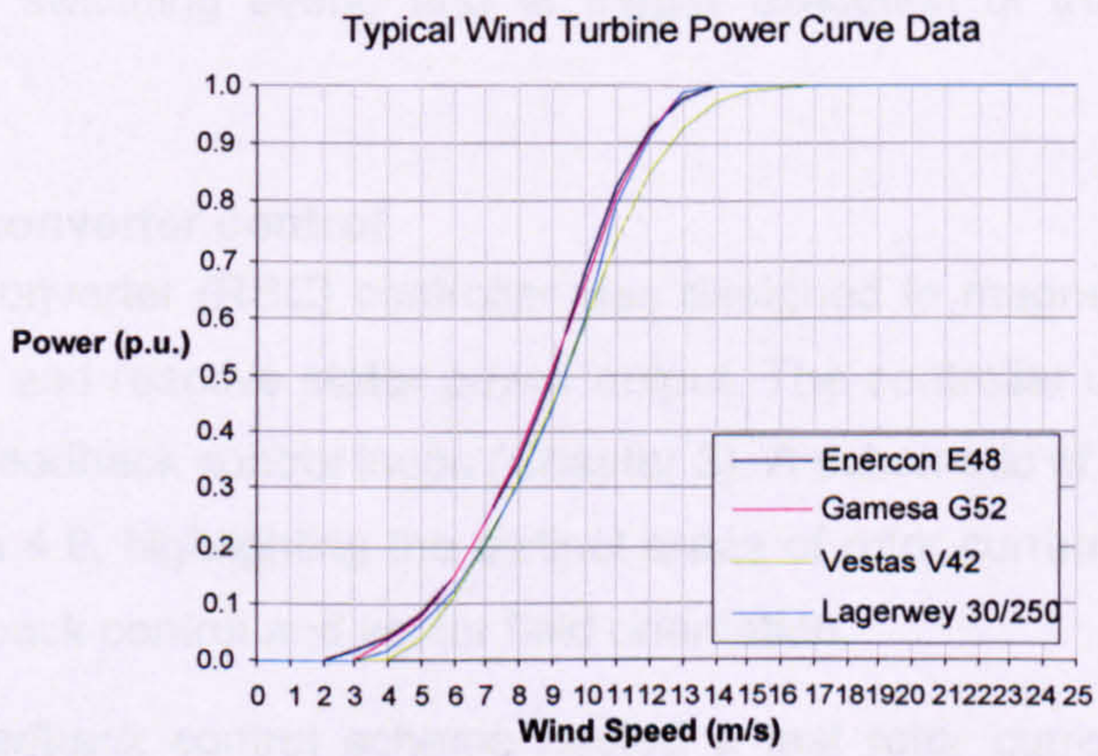

Figure 4.8. Typical wind turbine power curves [57].

Rotor speed and wind conditions

Rotor speed in a wind turbine is maintained chiefly by the turbine blades and pitch control – here performed by DC motor control. The wind turbine power output is normally optimised for the wind conditions: typically wind speed averaged over ten-minute periods [56]. However, grid fault tests require the study of a period of less than 5 seconds. The modelled wind speed and the active stator power demand were therefore each held constant for the duration of the grid fault tests.

[58] gives details of all the offshore wind farms in the UK, showing typical average wind speeds of up to $11ms^{-1}$. Figure 4.8 shows the per unit power output of a range of wind turbines for a given wind speed. For the purposes of understanding fault ride-through a single operating point was chosen to represent a typical healthy pre-fault operating condition: $10ms^{-1}$ wind speed corresponding to 0.67p.u. power output. This equates to 5kW power output from the DFIG test rig.

4.2.2 DFIG controller

The DFIG was controlled using vector control principles, as explained in Chapter 3. Vector control allows separate decoupled control of the active and reactive power outputs, permitting the generator to be fully magnetised from the rotor-side converter and allowing the DFIG to operate at a choice of power factor from its stator terminals.

The rotor-side converter and supervisory functions were controlled at 5kHz, triggered by a hardware interrupt signal from the dSpace's own three-phase PWM generation facility. This signal also triggered almost all of the sensor signal sampling. The line-side converter's PWM modulation was calculated by an independent PIC microcontroller, configured to operate at 4.89kHz. A line-side converter PIC PWM interrupt signal was used to trigger sampling of the line-side currents (only) (in order to avoid sampling the currents during a switching event) and to trigger execution of the line-side current control code.

DFIG rotor-side converter control

The Rotor-Side Converter (RSC) controller was designed to magnetise the generator and control active and reactive stator power output. The controller used vector control principles and PI feedback control loops (Chapter 3). A schematic of the RSC controller is shown in Figure 4.9, highlighting the distinct areas of rotor current feedback control, stator power feedback control and vector field orientation.

The cascaded feedback control scheme nested a fast rotor current PI control loop inside a slower stator power (PQ) PI control loop. A rotating orthogonal d-q controller reference frame (the excitation frame) was defined, aligning with the stator voltage space vector. A digital PLL provided the stator voltage vector angle. The rotor angle

was provided by an optical encoder on the rotor shaft. The power demand was scaled by the p.u. voltage magnitude in order to prevent an over-rated demand of rotor current. Reactive power demand was produced from voltage magnitude by way of a direct lookup table, exporting reactive power during voltage dips. The reactive power controller is explored further in Chapter 6.

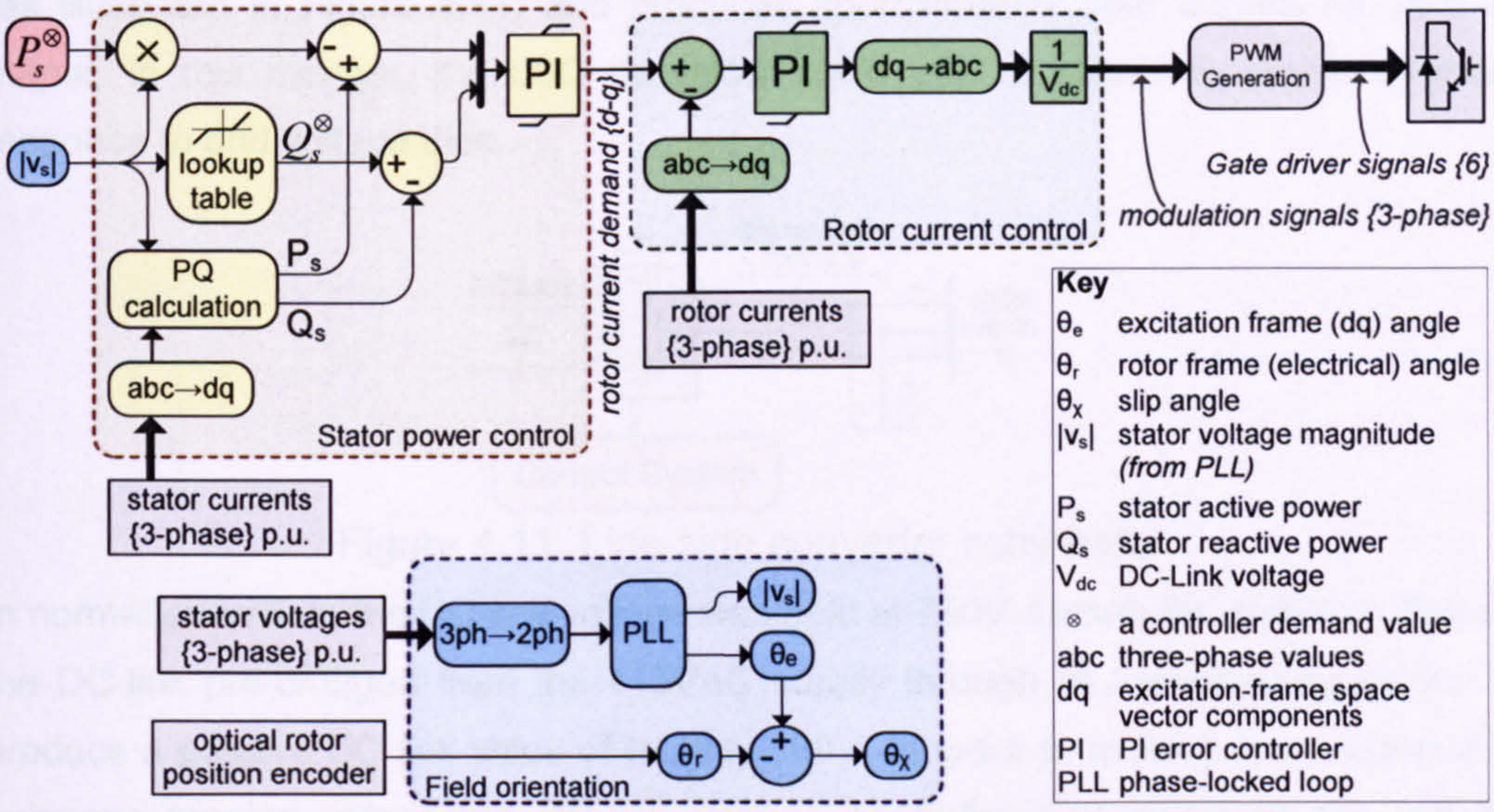

Figure 4.9. Rotor-side converter vector control scheme.

DFIG line-side converter control

The Line-Side Converter (LSC) controller was designed to maintain the DC-link voltage of the converter, indirectly conveying active power between the rotor and the grid connection point. During the test rig startup procedure the DC-link was passively pre-charged through the anti-parallel freewheel diodes in the three-phase bridge converter. A vector control scheme was then engaged which raised the DC-link up to its operational value of 750Vdc.

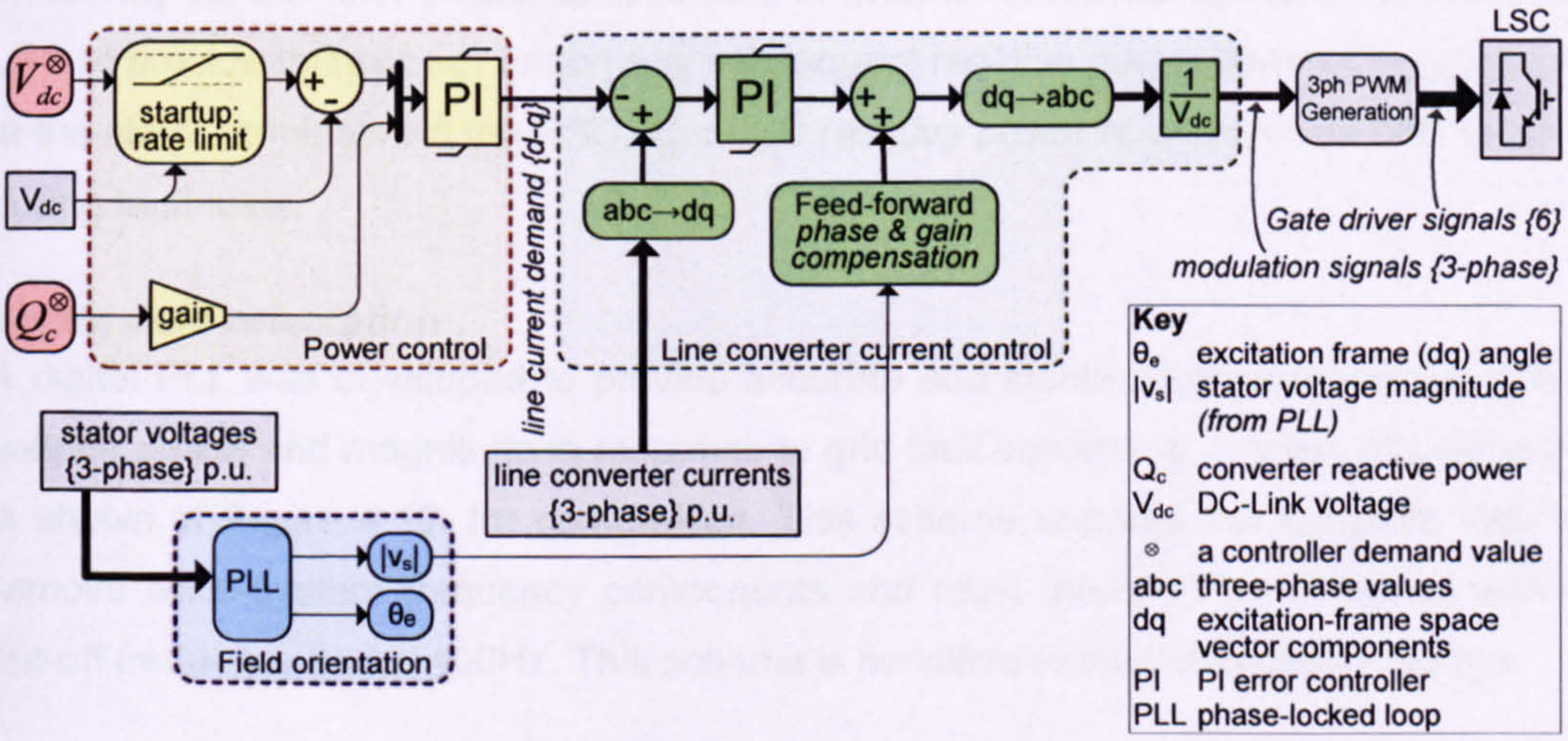

Figure 4.10. Line-side converter vector control scheme.

The d-q reference frame was defined in alignment with the local stator voltage, as for the rotor-side controller. A fast-acting line-side converter current PI control loop was nested inside a slower DC-link voltage PI control loop. The current control loop used a simple feed-forward term based on stator voltage. The feed-forward voltage term approximates the stator voltage: this minimises the potential difference across the filter (as illustrated in Figure 4.11) and produces approximately zero current for zero PI output. In this manner, the LSC converter could offer a more favourable dynamic response to grid voltage dips.

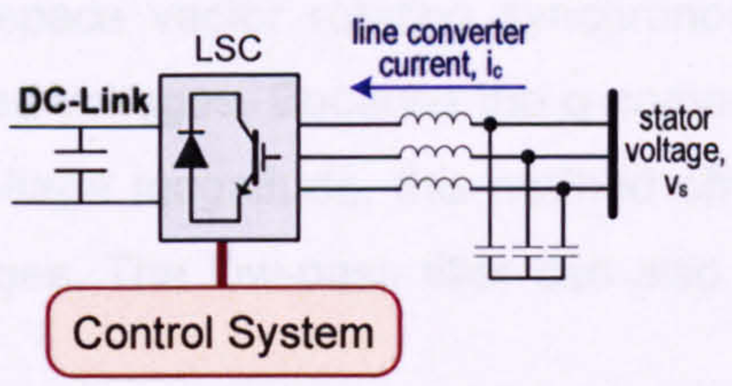

Figure 4.11. Line-side converter schematic.

In normal operation, the DC-link voltage was held at 750V. During the start-up process, the DC-link pre-charged from the 415VAC supply through its freewheeling diodes to produce a passive DC-link value of roughly 560V. In order to avoid current spikes and nuisance tripping, when the DC-link voltage controller was engaged the voltage demand was initially fixed at the last measured voltage. The voltage demand was then ramped up towards rated value at a predetermined rate, taking approximately 3.0 seconds to reach 750Vdc and precluding transient over-currents.

The reactive-component of the outer control loop takes advantage of the direct relationship between line-side converter current and reactive power (Chapter 3). The LSC could have been controlled to exchange reactive power with the grid. However, given the winding arrangement of the machine, reactive current was provided more effectively via the rotor circuit, as explained in Chapter 6. Normal operation is to set the LSC to provide unity power factor; any subsequent reactive power demand is produced at the stator terminals via the RSC. The LSC reactive power reference was held at zero during fault tests.

Vector field orientation

A digital PLL was developed to provide accurate and stable information on the stator voltage phase and magnitude in response to grid fault conditions. A basic PLL scheme is shown in Figure 4.12. for comparison. This scheme requires the low-pass filter to remove twice-system frequency components and must therefore be designed with a cut-off frequency below 100Hz. This scheme is sensitive to step changes in voltage.

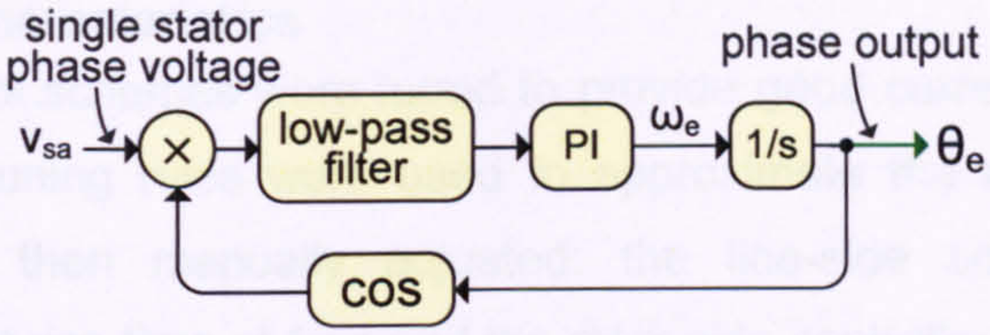

Figure 4.12. Basic PLL scheme.

A vector-based PLL system (VPLL) is shown schematically in Figure 4.13. The excitation frame is aligned with the fundamental stator voltage space vector. As such, the quadrature component of d-q voltage should be zero. This definition is exploited by the VPLL to generate a space vector rotating synchronously with the fundamental component of the measured voltages. Because the q-component of voltage should be zero irrespective of the voltage magnitude, this method offers improved performance against step voltage changes. The low-pass filter can also include a wider frequency pass-band.

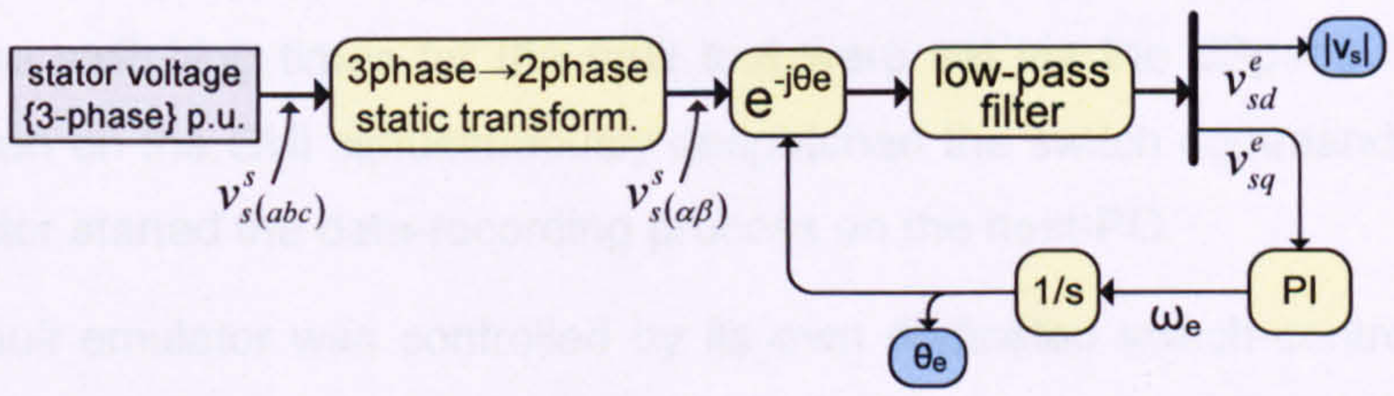

Figure 4.13. Vector-based PLL scheme used in the test rig.

This PLL scheme gave accurate phase estimation for stator voltages as low as one fifth of a percent of rated voltage magnitude (0.5V per-phase ac). Below this level of magnitude the VPLL was configured to artificially generate phase from a fixed source using the last measured frequency (i.e. to hold the frequency output at the last good value). In practice, no test fault voltages triggered this response.

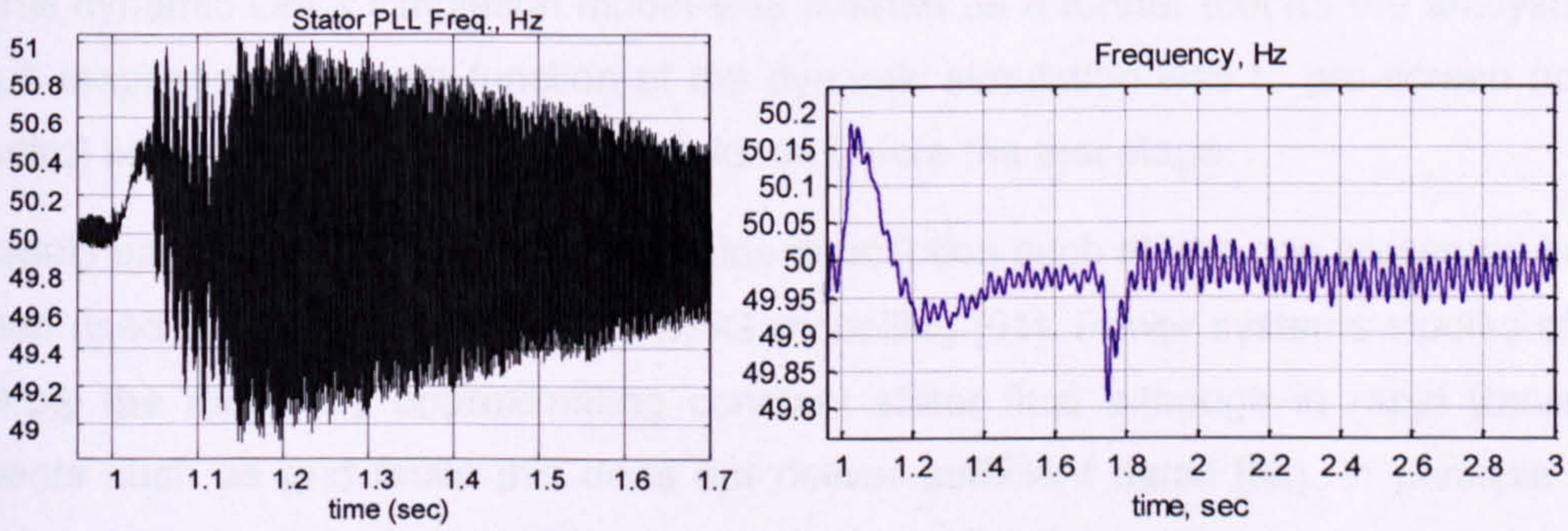

Figure 4.14. PLL performance comparison with test rig 50% fault: basic PLL (left) and VPLL (right).

The performances of the two schemes in response to a 50% fault test are shown in Figure 4.14. The basic PLL employed a 2nd order 80Hz cut-off filter with a 30dB characteristic stop-band gain. The VPLL used a 2nd order filter with a 1,000Hz cut-off and a much steeper 80dB stop-band gain. Both schemes performed adequately to permit vector control, but the vector based scheme produced a much cleaner output.

Dynamic control characteristics

The feedback control schemes were tuned to provide good current control bandwidth. Ziegler-Nichols PI tuning rules were used to approximate the appropriate controller gains which were then manually adjusted: the line-side controller produced a characteristic current rise-time of 1ms and the rotor-side controller 5ms.

The outer power control loop was tuned for a deliberately slower response to ensure stability of current control. The PQ (rotor) controller showed a characteristic power rise-time of 40ms, almost 10 times slower than the rotor current. The DC-link voltage conversely was tuned to ensure good voltage control: the proportional controller gain was increased to the point of instability and then set at 60% of this value, in keeping with the Ziegler-Nichols method [59].

4.2.3 Grid fault test control

The operator first prepared the fault voltage levels manually on the grid fault emulator variacs. The switching times for the fault test were set via the dSpace GUI. A 'Run Test' function on the GUI simultaneously despatched the switch commands to the grid fault emulator started the data-recording process on the host-PC.

The grid fault emulator was controlled by its own dedicated switch-control logic. The dSpace controller despatched a 3-pin digital command signal to dictate the status of the voltage switching kit: "healthy", "fault" or "recovery". For safety, the grid fault emulator was controlled to ignore a change of state if more than one switch signal was sent high.

4.3 DFIG simulation

A full dynamic DFIG simulation model was created as a further tool for the analysis of fault response. The main function of the dynamic simulation was to pre-screen novel control schemes and fault-ride-through ideas before the test stage.

Models based on the generalised machine description such as the one presented have been used successfully in dynamic DFIG modelling [61]. Power systems studies often simply the model by approximating constant stator flux, although in rapid transient events such as grid faults this does not deliver sufficient detail [62]. In principle the parameters can be changed on a test-validated simulation in order to model large generators and fault profiles beyond the capabilities of the test rig; this allows a general impression of proposed schemes at industrial power-levels. However, to detail the response of a large generator from simulation would require considerable confidence in the modelled setup and a detailed study of the non-linear effects imposed by different generation environments. The primary thrust of this work remains in consolidating the analytical concepts against data obtained from the test rig facility.

No results for the model are demonstrated as they do not contribute anything more than the test results presented in Chapters 5 and 6.

4.3.1 Simulink model

A full dynamic computer simulation of a doubly-fed induction generator for use in a wind turbine generator was created, using Matlab / Simulink software. The model included: the induction generator, a bidirectional power electronic converter, a digital controller with cascaded feedback control schemes, a two-mass drive-shaft model to represent the wind turbine mechanical dynamics, a simplified wind turbine controller and a simplified network model. A block diagram of the model is given in Figure 4.15.

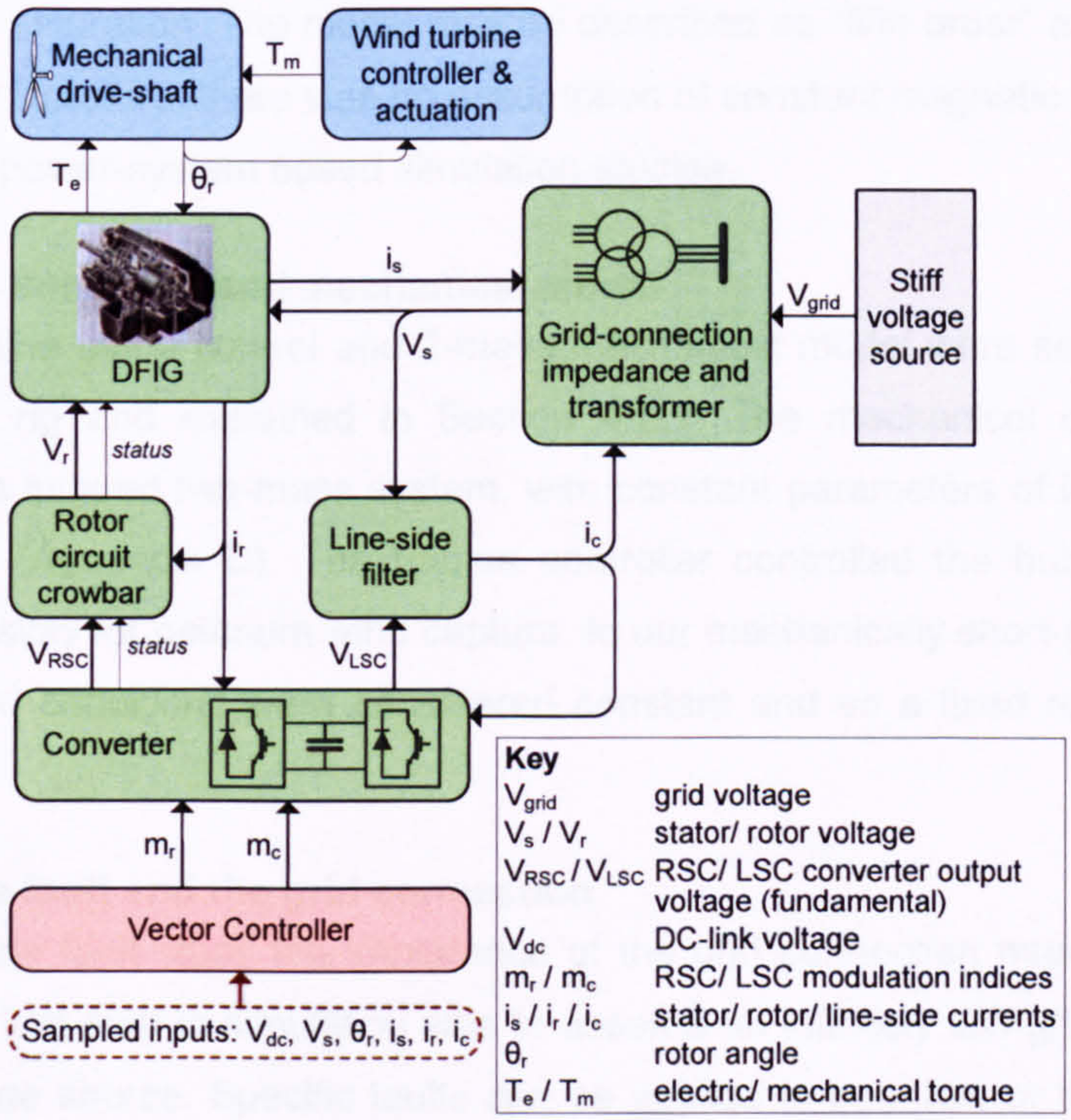

Figure 4.15. Block diagram of the DFIG system Simulink model.

All electrical parameters in the model were represented in rotating space-vector form to simplify the analysis without loss of accuracy [43]. The three phase signals were converted to two-phase representation as per Appendix A, and any zero-sequence component was neglected due to the winding arrangements of the wind turbine's transformer.

Simulation configuration

Simulink was set up to execute a variable-step solution using an "ode23s" type solver, with a maximum time step of 10^{-5}s and a relative tolerance of 10^{-4}. The solver was chosen to best deal with the combination of discrete and non-discrete variables in conjunction with the moderately stiff problem of grid fault application. For comparison,

the simulation was run with a maximum time-step of 5×10^{-7}s, with no discernible difference in the results, and so the larger limit was kept for improved simulation speed.

Generator model

A mathematical model of the DFIG generator was developed based on the basic principles of electrical machines as described in Chapter 3 and numerous standard texts. The model takes stator voltages, rotor voltages and rotor position as inputs and solves the five generalised machine equations (Section 3.1.6) for flux linkages, currents and electric torque.

These governing equations include transient phenomena but neglect spatial harmonics and magnetic saturation. The model may be described as "fifth order" as suggested by contemporary literature; there was no assumption of constant magnetic flux, as is often the case with power-system based simulation studies.

Wind turbine controller and mechanical model

The wind turbine blade control and 2-mass mechanical model were set-up exactly as with the test rig and explained in Section 4.2.1. The mechanical drive-shaft was modelled as a lumped two-mass system, with constant parameters of inertia, stiffness and damping (Appendix D). The turbine controller controlled the hub speed of the turbine, ostensibly for optimum wind capture. In our mechanically short-period grid fault tests, the wind conditions were considered constant and so a fixed reference speed was used.

Modelling the fault and the grid connection

For an accurate fault study the impedance of the grid connection must be taken into account. The first step in simulation was to assume an infinitely stiff grid which entails an ideal voltage source. Specific faults can be applied to one, two or three phases of this supply voltage which is converted from three-phase to d-q representation. In this scenario the modelled voltages were applied directly to the stator connection of the d-q DFIG model.

A second step was to apply the same fault waveforms through a modelled 3-phase transformer. When magnetised, the transformer behaves in p.u. terms just like a series inductance. It was necessary to add a capacitance at the DFIG side of the transformer (or use, for example, the line-side filter's capacitance) to stabilise the simulated stator voltage.

Finally, the grid connection impedance was be modelled. For very long and weak grid connections a full distributed-parameter model would be appropriate. However, for grid fault studies a lumped parameter model for the wind turbine grid connection is sufficient [32]. This, unlike the stiff voltage version, reveals the effect of the fault on local

voltages; a critical issue for fault response behaviour. The DFIG model included 0.15 p.u. of inductance as with the test rig grid fault emulation equipment.

Power converter

Individual switching events were omitted from the model. The controller's modulation indices were scaled by the DC-link voltage and passed through as output voltages, as if the PWM output contained nothing but the desired fundamental component[7]. The main drawback of this method was the neglect of PWM harmonics, although with 5kHz PWM these high-frequency distortions have negligible impact on the DFIG system [60]. The modelling of fundamental PWM output alone delivered a vastly increased simulation speed compared with full PWM-switching modelling. This method does not account for individual device voltage-drops or turn-on/ turn-off behaviour. This work is focused on the broader capabilities for fault ride through rather than the response to individual device failure, and so detailed converter switch modelling was neglected.

In considering the transformation from d-q to three-phase representation, it was conservatively assumed that the magnitude of the rotor current space vector could at any moment be carried in full by a single IGBT device. This permits a worst-case consideration of fault current withstand. The limiting current ratings of the converter devices are discussed in Chapter 6.

DC-link

The DC-link voltage was calculated from the balance of energy in and out of the converter. It was assumed that the net power flow was deposited in (or removed from) the DC-link capacitance, as per Eq. 4.4. The LSC and RSC power values were calculated from their respective voltages and currents. A percentage power loss was estimated for each converter-half for the approximate phase current flowing through each of three active IGBTs, a roughly squared relation shown graphically on the datasheets of the test rig devices [63]. The capacitor banks were considered lossless and the capacitance considered constant.

$$\int \left(P_{LSC} - P_{RSC} - P_{loss}\right) dt = \frac{1}{2} C \left(V_{dc}{}^{2} - V_{dc,initial}{}^{2}\right) \tag{4.4}$$

Brake-chopper

A DC-link brake-chopper was modelled and optionally included in modelled fault tests. This device was set to automatically engage at 810V dc and disengage at 795V dc according to the DC-link voltage, as for the test rig. The effect is to subtract a power loss component P_{BC} from the voltage calculation in Eq. 4.4, such that it acts to reduce the DC-link voltage. The additional loss term was derived in Eq. 4.5, using the known

[7] A unit time-step delay was included to account for the real delay in LSC PIC PWM-generation.

resistance of the brake-chopper as a constant. The model was designed to stop the simulation if at any point the DC-link exceeded 1,000V dc.

$$P_{BC} = \frac{V_{dc}^{\ 2}}{R_{BC}} \tag{4.5}$$

Line-side filter

The line-side filter was a very simple series resistor-inductance model, using the voltage difference between the LSC and the stator to produce line-side current. The capacitance of the L-C filter was actually included in the 'grid-connection' model to stabilise the stator voltage variable.

Rotor circuit crowbar.

A modelled rotor-circuit crowbar could be optionally engaged by the DFIG controller. When engaged, the DFIG rotor voltage was rendered zero and the rotor winding resistance was increased to include the effective per-phase crowbar resistance. When disengaged, the crowbar had no effect on the rotor circuit; the RSC voltage was passed unchanged to the rotor of the DFIG.

Vector control

The DFIG vector control system within the model employed the same cascaded control scheme as the test rig, detailed in Section 4.2.2. The inputs to the controller were all sampled at the main control frequency of 5kHz. Unlike the test rig, the rotor-side and line-side control schemes were executed in a common control period.

The simulated vector controller was used to trial fault ride through modifications and advanced control techniques. However, feedback control tuning using the simulation was considerably easier than on the test rig. The real-world control gains could be necessarily as much as 10 times smaller to avoid instability with the test rig currents.

4.4 Summary

The key elements of a DFIG 'test rig' were described: a 7.5kW DFIG test facility constructed at Newcastle University for testing control schemes and fault ride through techniques for wind turbine doubly-fed induction generators under grid fault conditions. The test rig comprised a wind turbine simulator, a generator system and a grid-fault emulator, all operated from a common flexible control hardware setup. The test rig satisfied the aims laid out in this chapter's introduction.

The DFIG system consisted of a 7.5kW generator and a 50A rated bi-directional IGBT power converter, with an 1100Vdc-capable DC-link and a protective brake-chopper circuit. The converter's three-phase connections were routed through dedicated PWM

filters and signal acquisition sensors. The rotor circuit included a protective crowbar unit and the line-side included inrush-limiting equipment.

A 10kW DC motor and drive were selected to provide a torque input to the DFIG. The DC motor's controller was setup up to simulate a representative two-mass flexible-coupling model of a wind turbine drive-shaft and a simple turbine speed governor.

To permit investigations into fault response a grid fault voltage emulator was built. The voltage output to the generator could be quickly switched between three parallel sources by a set of solid-state transfer switches. This allowed balanced grid fault voltage profiles to be applied to the generator. The DFIG connected to this voltage source through a 1:1 isolation transformer, representing a wind turbine transformer, and a set of 0.15 p.u. reactors, representing typical wind turbine grid-connection impedance.

Control of the rig was chiefly carried out by a dSpace dS1103 control development board. Wind turbine simulation and DFIG vector control schemes were developed in a proprietary Matlab / Simulink environment which automatically created and downloaded the custom code for use on the controller board. The controller was manipulated in real-time from a dedicated GUI on a host-PC.

The protection scheme for the test rig was chiefly operated from a dedicated logic analysis 'main' board which housed a PIC microcontroller. The PIC dictated selected protective actions in response to error signals. Signal acquisition electronics contained error-signal trigger thresholds. The rotor-side converter's PWM generation was performed by the dSpace controller. A second PIC interface board was necessary to perform three-phase PWM modulation for the line-side converter. All of the control and power electronics, contactors and filters were housed in an earthed metal cabinet.

Detail on the rig layout, protection schemes, hardware and electronics configurations are presented in Appendix D.

Section 4.2 presented the base vector control scheme used in tests. This was founded on the vector control concepts explained in Chapter 3. The control reference frame for both converters was aligned with the stator voltage space vector, using a phase angle provided by a software-based PLL. A vector-based PLL was shown to provide a cleaner response to voltage dips, chiefly due to the wider frequency pass-band of its low-pass filter. The current feedback controllers were tuned, producing the following characteristic current rise-times for impulse response: 1ms on the line-side and 5ms on the rotor-side.

A Matlab / Simulink dynamic DFIG Simulation model was presented based on the solutions of the generalised machine equations for the DFIG and including the wind

turbine simulator model used with the test rig. The model neglected both PWM switching and detailed converter device modelling. It was used primarily to pre-screen and develop control-methods and fault ride through techniques before implementation on the test rig.

The fully commissioned rig was used to study the fault response of the machine (Chapter 5) and to test techniques which had been selected from simulation work as holding the greatest potential for improving DFIG fault ride-through performance (Chapter 6).

FAULT RESPONSE 5

This chapter provides a comprehensive study of DFIG fault response. A complete description is needed because DFIG short-circuit response is only partially or summarily treated in contemporary literature [42][43][44][45]. The approach set out below takes three parts: firstly introducing the physical picture from inspection of the machine's magnetic flux behaviour, secondly presenting detailed analytical solutions of the generalised machine equations and thirdly reviewing the analytical assertions with experimental evidence from the DFIG test rig.

Sections 5.1-5.3 focus on the zero rotor voltage 'natural response' of the generator to a stator short-circuit, including the transient currents, their peak values, duration and frequency composition. Section 5.4 introduces the effects of the rotor voltage produced by the DFIG's power converter. Section 5.5 discusses the grid fault response of the power converter.

The DFIG test rig, detailed in Chapter 4, was designed to emulate a wind turbine generator and its grid connection equipment. Experimental evidence from the test rig is presented and discussed in Sections 5.6-5.7. Section 5.6 details a 140ms short-circuit fault applied at a the 'grid-connection' point of the DFIG. Section 5.7 considers non-zero grid faults, detailing examples of a 500ms 15% fault and a 720ms 50% fault. The effects of unbalanced voltage faults are discussed in summary in Section 5.8.

In reviewing the fault response described in this chapter in the context of grid code fault ride through requirements, Section 5.9 concisely presents the key issues for DFIG fault ride through. These issues form the basis of the development of fault ride through techniques discussed subsequently in Chapter 6.

5.1 Flux-based description of induction machine fault response

5.1.1 Interpretation of magnetisation and demagnetisation

Throughout this work the terms 'magnetisation' and 'demagnetisation' are used to describe not only the loss and recovery of magnetic flux in the induction machine due

to a supply voltage dip, but also the associated physical processes: these include rotor-speed change and fault energy throughput.

5.1.2 Flux paths

Consider a two-dimensional distribution of magnetic flux on a cross section of an idealised, three-phase, two-pole induction machine, as introduced in Chapter 3. The rotor windings are short-circuited and the flux linkage is driven around the circumference of the machine by a steady supply voltage at constant frequency. The reference frame for the proceeding description is the excitation-frame, rotating synchronously with the supply voltage (and pre-fault flux linkage). Normal operation implies a continuous distribution of flux: pseudo-constant in this reference frame, well spread over the machine iron and dominated by the mutual flux linking both stator and rotor. The physical coils of the stator and rotor windings rotate relative to the pseudo-stationary flux, but the relative phase of the magnetisation ensures a fixed spatial distribution of flux. The only disturbance to the constant flux comes from the localised leakage paths, centred on each physical coil, representing a small fraction of the total distribution. A snapshot of this pre-fault picture for a simplified machine is shown in Figure 5.1. Only two active coils are highlighted in order to simplify the following description of fault response. These represent the main current-carrying coils (at this snapshot in time) on the stator and rotor respectively.

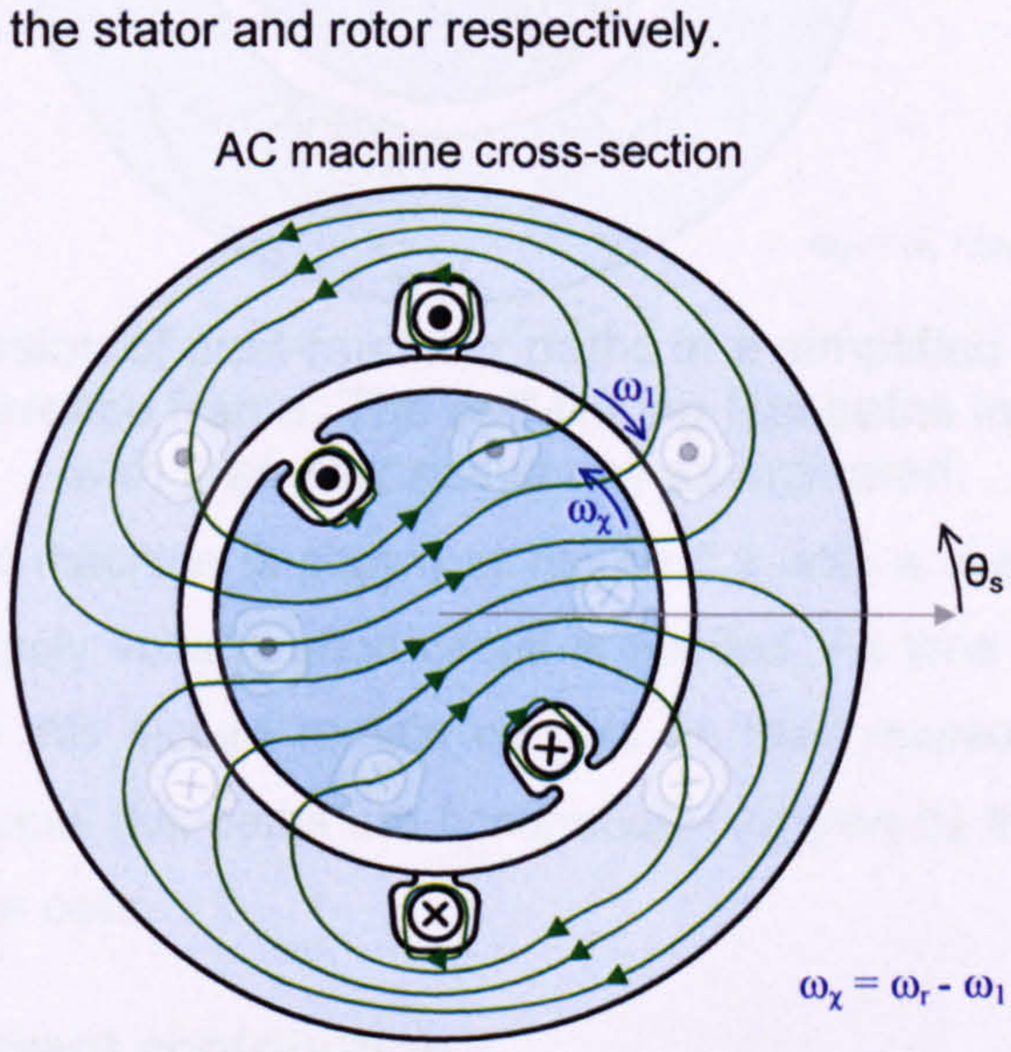

Figure 5.1. Impression of pre-fault flux paths in a simplified machine, viewed in the excitation reference frame, with only two coils highlighted. Flux paths appear *pseudo-stationary* in this picture while the *coils rotate* as indicated.

Now consider an instantaneous short-circuit applied to the stator terminals of the machine. The theorem of continuous flux linkage applies, and the amount of flux linked by each coil immediately following the short-circuit is exactly the same as immediately before. As a result, the flux distribution will initially appear exactly as it did before the fault. Now, from the moment the short circuit begins, the stator flux is no longer driven

around the airgap at synchronous speed. In fact, in the case of a close-up zero-voltage event, the concept of synchronous speed no longer holds any physical meaning. As the fault continues, each element in the flux distribution will begin to encircle the nearest coil and move with it, as mechanical rotation is the only factor forcing a spatial change in flux distribution. The flux concentrates around each coil resulting in very large leakage flux levels. Viewed from the excitation reference frame the stator leakage flux moves away with the stator coils at synchronous speed and the rotor leakage flux moves away with the rotor coils at slip speed. A smaller proportion of flux continues to link both stator and rotor. The airgap-crossing flux paths are continually broken and remade as the rotation continues and the flux lines cluster around the physical rotating coils.

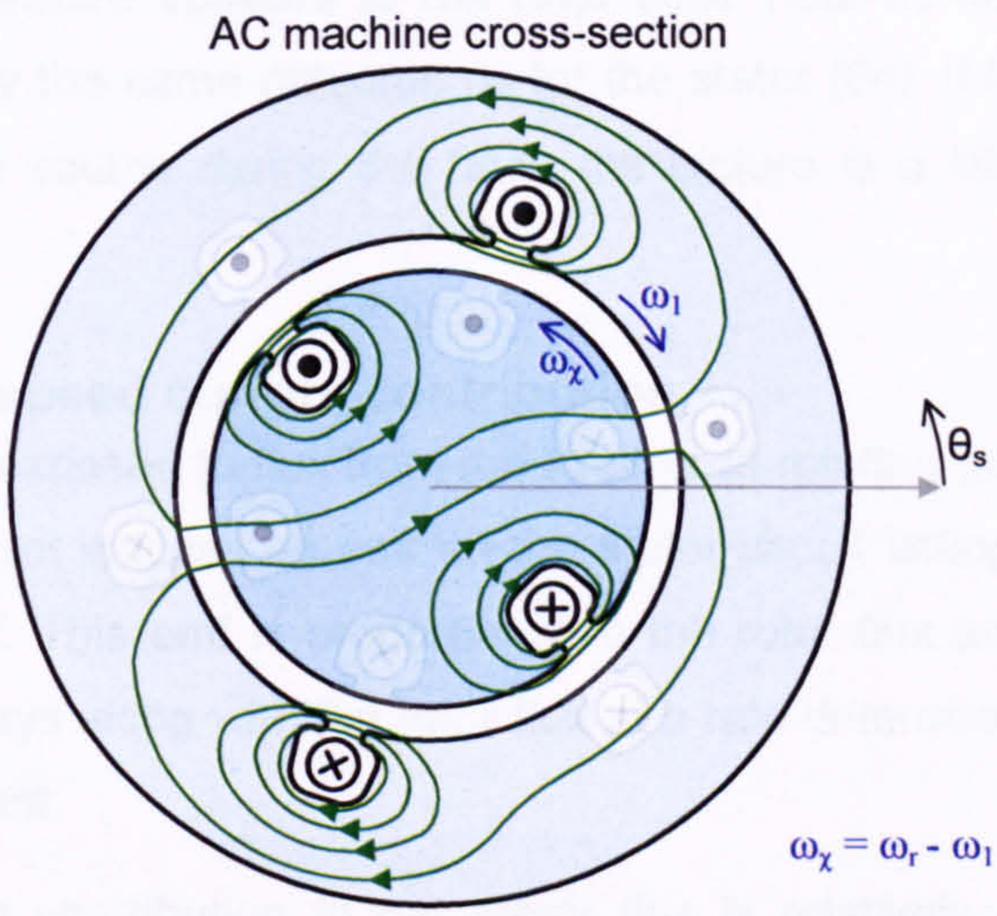

Figure 5.2. Impression of post-fault flux paths in a simplified machine viewed in the excitation reference frame. The self-linking flux paths in this picture *rotate with their respective coil* as indicated.

The same simplified machine is shown in Figure 5.2 with a sketch of the flux paths moments after a supply voltage short-circuit is applied. As time progresses, the self-linking flux paths in this picture remain centred on their respective nearest coil and rotate with them. Mutual flux paths are continuously warped by the relative movement of the stator and rotor coils.

5.1.3 Near-dc current contribution

Without an external emf, the majority of the flux linking each individual coil remains held by that coil and rotates with it; leading to descriptions of 'frozen' or 'trapped' flux concentrated on each coil. These flux contributions dominate the net flux of each of the stator and rotor circuits and their behaviour is governed by the leakage parameters of their respective circuit. A hypothetical superconducting coil would hold on to this flux indefinitely; a real coil on the other hand experiences a near-dc exponential decay of

flux over the coil's own resistance at a rate set by the effective transient time constant of the respective circuit.

The 'trapped' stator flux decays into the short circuit via demagnetising stator currents. The magnitude of this current is dominated by the effective operational reactance of the stator circuit [22]. These currents may develop several times rated value for a number of system cycles (Section 5.6).

With a short-circuited or cage rotor, similar logic applies to the rotor circuit. 'Trapped' rotor flux on each coil decays chiefly by near-dc demagnetising rotor currents, dominated by the rotor's effective transient reactance.

A DFIG connects the rotor to a power converter of practically zero impedance: the power converter therefore appears to the rotor coils' near-dc flux decay as a short-circuit with effectively the same outcome as for the stator [64]. If the DFIG converter is producing a voltage source during the fault, the picture is a little more complicated (Section 5.4).

5.1.4 Near-rotor speed current contribution

The stator coils are exposed to flux from the rotor coils rotating past effectively at rotor speed. This movement induces an emf on the stator circuit acting in opposition to the rotor flux movement. This emf is proportional to the rotor flux and the relative speed (rotor speed); it decays along with the rotor flux at a rate determined by the rotor circuit transient time constant.

This airgap-crossing contribution to net stator *flux* is relatively small. The magnetic paths are longer and, unlike the pre-fault case, the MMF is not being driven across the airgap by a voltage. In terms of the emf induced, this effect is compensated for by the relative speed, such that its contribution to stator current is equivalent to that of the near-dc component.

In a reciprocal fashion, a small amount of stator flux crossing the airgap cuts the rotor coils at rotor speed (in the opposite direction). This stator flux decays with near-dc frequency over the stator transient time constant. The ensuing emf acts on the rotor coils to produce a negative near-rotor speed contribution to current on the rotor circuit.

5.1.5 Transient circuit parameters

For a symmetrical induction machine undergoing rapid magnetic change, each circuit has a limiting transient operational inductance (derived in Appendix B):

$$L_s' = \sigma L_s = L_s - \frac{L_m^{\,2}}{L_r} \tag{5.1}$$

$$L_r' = \sigma L_r = L_r - \frac{L_m^{\,2}}{L_s} \tag{5.2}$$

Eqs. 5.1 & 5.2 incorporate the machine leakage factor:

$$\sigma = 1 - \frac{L_m^{\,2}}{L_r L_s} \tag{5.3}$$

The transient inductance values provide limits on the rate of change of flux in each circuit and as such help to define a timescale for the transient electromagnetic phenomena, as introduced in Chapter 3:

$$\tau_s = \frac{L_s'}{R_s} \tag{5.4}$$

$$\tau_r = \frac{L_r'}{R_r} \tag{5.5}$$

These time constants are important in defining the natural dynamic response of the induction machine to changing electromagnetic conditions. Transient time constant values are roughly 30-150ms for practical machines. Depending on the particular winding arrangement, stator and rotor time constants in a given machine are roughly similar.

As a result of the similarity in time constants, the fault response of a shorted-rotor induction machine is likely to display both near-dc and near-rotor speed contributions to the current at a similar magnitude and decaying within a similar period. Notably, this is the worst combination of parameters in terms of producing the maximum over-current on each circuit.

5.1.6 Estimation of fault currents

The short-circuit current can be estimated, combining the effects described above and using the continuity of magnetic flux. Firstly, initial conditions are defined for stator and rotor flux linkage immediately pre-fault:

$$\bar{\psi}_s^s(t=0) = \bar{\psi}_{s0}^s, \qquad \bar{\psi}_r^s(t=0) = \bar{\psi}_{r0}^s \tag{5.6, 5.7}$$

Now, rearranging the flux linkage definitions from Chapter 3:

$$\tilde{i}_s^s = \frac{1}{L_s'}\left(\bar{\psi}_s^s - \frac{L_m}{L_r}\bar{\psi}_r^s\right) \tag{5.8}$$

Hence, initially:

$$\bar{i}_{s0}^{s} = \frac{1}{L_s'}\left(\overline{\psi}_{s0}^{s} - \frac{L_m}{L_r}\overline{\psi}_{r0}^{s}\right) \tag{5.9}$$

The flux decay characteristics are estimated from the arguments in Sections 5.1.3 & 5.1.4. The stator current will display a near-dc contribution from the stator flux decay and a near-rotor speed contribution from the rotor flux decay. Hence:

$$\bar{i}_{s}^{s}(t) \approx \frac{1}{L_s'}\overline{\psi}_{s0}^{s}\, e^{-t/\tau_s'} - \frac{1}{L_s'}\frac{L_m}{L_r}\overline{\psi}_{r0}^{s}\, e^{-t/\tau_r'} e^{j\omega_r t} \tag{5.10}$$

An expression for rotor current can be inferred by symmetry:

$$\bar{i}_{r}^{r}(t) \approx \frac{1}{L_r'}\overline{\psi}_{r0}^{r}\, e^{-t/\tau_r'} - \frac{1}{L_r'}\frac{L_m}{L_s}\overline{\psi}_{s0}^{r}\, e^{-t/\tau_s'} e^{j\omega_r t} \tag{5.11}$$

5.1.7 Alignment effects

As explained in Chapter 3, the tendency of two concentric magnetic dipoles is to align: the rotor field's rotation will be slowed by the stator field and the stator field accelerated by the passing rotor field. If the short-circuit was maintained and the transient time constants were near-infinite, implying negligible energy loss, then eventually both sets of magnetic flux linkage would align and rotate at a common velocity somewhere between zero and rotor speed.

The impact of this dragging effect depends inversely upon the relative speed of the two fields, i.e. the rotor speed. At high rotor speed the fields barely interact, whereas this alignment-based drag will be more pronounced at lower speeds (Evidence for this is lies in the inverse relation between the frequency adjustment parameter and rotor speed, derived in Section 5.2.2). The effect in most cases is no larger than a few percent, but it provides an explanation for the near-zero and near-rotor frequency components found in experiment (Sections 5.3.2 & 5.3.3).

5.1.8 Fault torque

As explained in Chapter 3, torque can be derived by considering the stator and rotor fields as two magnetic dipoles. The resulting torque is proportional to the vector cross product determinant of the stator and rotor current space vectors, i.e. the sine of the angle between the current vectors. The p.u. torque equation is:

$$T = L_m\, \bar{i}_r \wedge \bar{i}_s \tag{5.12}$$

Rearranging Eq. 5.12 using the flux linkage definitions from the generalised machine equations (Section 3.1.6), the torque can be described by the cross product of the flux linkage space vectors:

$$T = \frac{L_m}{\sigma L_s L_r} \overline{\psi}_r \wedge \overline{\psi}_s \tag{5.13}$$

Before the fault, rated torque is produced by two MMF waves rotating synchronously with a small defined angular separation determining the constant torque:

$$T_{rated} = \frac{L_m}{\sigma L_s L_r} |\overline{\psi}_r| |\overline{\psi}_s| \sin x, \ (x << 1) \tag{5.14}$$

Immediately post-fault the majority of the flux linkage distribution becomes self-linking, concentrated around the individual coils. As explained above, the dominant contributions to the two flux linkage space vectors rotate with respect to each other at approximately rotor speed. The fault torque therefore becomes:

$$T_{fault} \approx \frac{L_m}{\sigma L_s L_r} |\overline{\psi}_r| |\overline{\psi}_s| \sin(\omega_r t) \tag{5.15}$$

The result initially is a very large oscillating torque causing significant stress to the mechanical drive-train. As both sets of flux decay exponentially into the short-circuit, the torque will decay faster still – by approximately twice the rate of either the stator or rotor flux. The fault torque therefore poses no additional mechanical stress after one or two system cycles have elapsed.

5.1.9 Fault clearance

The behaviour at fault clearance is very similar to that at fault initiation. From a purely linear magnetic point of view a step increase of 1 p.u. stator voltage induces the same effects as a 1 p.u. voltage drop: transient decay components of currents at near-dc and near-rotor speed, the peaks of which are inversely proportional to the operational inductance, and which give way to steady-state operation at system frequency. This is illustrated by Eq. 5.16, where the stator current is estimated in the excitation frame as a function of constant stator and rotor voltages. In this frame of reference, the current comprises three components: a system frequency self-linking stator flux transient which decays with the stator time constant, a slip frequency mutual-linking flux transient which decays with the rotor time constant, and a dc steady-state excitation frame current which tends to a constant at a rate determined by the stator time constant. Coefficients k_1 - k_3 are general functions of the applied voltages in the excitation frame.

$$\tilde{i}_s^e(t) \approx \frac{1}{L_s'} k_1(u_s^e, u_r^e) e^{-t/\tau_s'} e^{-j\omega_e t} + \frac{1}{L_s'} k_2(u_s^e, u_r^e) e^{-t/\tau_r'} e^{j(\omega_r - \omega_e)t} + k_3(u_s^e, u_r^e)\left(1 - e^{-t/\tau_s'}\right) \tag{5.16}$$

In practice, fault clearance normally results in a lower connection voltage due to the higher impedance with respect to the fault, as explained in Chapter 2. The transient components are directly proportional to the relative step change in voltage, and so the

current peaks at fault clearance are less severe than at fault initiation. For example, clearance of a 0% fault to 90% of rated voltage will induce current peaks at 90% of the value following fault initiation.

5.2 Analytical solution for induction machine fault response

An analytical solution for fault response can be found for a symmetrical induction machine by solving the generalised machine equations of Section 3.1.6. Firstly, initial conditions are established based upon normal operation of the machine. Then a zero-volts close-up short-circuit fault is implemented by setting the stator voltage to zero. This voltage drop is assumed to occur instantly, or at least far quicker than the machine's transient timescales.

The rotor speed is assumed to remain constant during the fault period (which can last anything up to a few hundred milliseconds), recognising that electromagnetic dynamic phenomena occur on a far shorter time frame than mechanical phenomena in a wind turbine: a DFIG generator's inertia constant is typically of the order of one second [24].

Now, with constant rotor speed the generalised machine equations are reduced to a set of first-order linear differential equations in flux linkage, current and voltage. These can be solved using Laplace transforms to suggest exponentially decaying flux linkage on stator and rotor circuits, concurring with the arguments presented in Section 5.1. A full derivation is given in Appendix B.

Analytical solutions for DFIG fault response have been presented in [64] and [65], with broadly similar results. Both papers omit the complex frequency adjustment explained in Section 5.1.7 but produce similar values of peak transient current.

5.2.1 Assumptions

The key assumptions for the analytical solution are summarised below:

- The generator is a symmetrical (non-salient) polyphase induction machine with a sinusoidal MMF distribution and a smooth, uniform airgap – this validates the use of the generalised machine equations.
- Magnetic saturation is neglected – this effectively renders the machine inductances constant. This assumption is almost certainly false and applied for mathematical convenience. Nonetheless, as flux linkage falls, the impact of saturation cannot be much worse under fault conditions than in normal operation.
- Rotor speed is assumed constant during the fault period. Applied strictly to allow the analytical solution, a small speed change makes little practical difference to the results.

- Voltage drop is assumed to occur far quicker than machine transient timescales. The electromagnetic response would be far less dramatic if the voltage dropped gently; unfortunately grid faults are quick and savage in nature.

5.2.2 Laplace transform solution

Firstly, take the generalised induction machine equations (Section 3.1.6):

$$\bar{u}_s^s = R_s \bar{i}_s^s + \partial \bar{\psi}_s^s \tag{5.17}$$

$$\bar{u}_r^s = R_r \bar{i}_r^s + \partial \bar{\psi}_r^s - j\omega_r \bar{\psi}_r^s \tag{5.18}$$

$$\bar{\psi}_s^s = L_s \bar{i}_s^s + L_m \bar{i}_r^s \tag{5.19}$$

$$\bar{\psi}_r^s = L_r \bar{i}_r^s + L_m \bar{i}_s^s \tag{5.20}$$

Eqs. 5.19 & 5.20 are used to substitute the currents in Eqs. 5.17 & 5.18 with flux linkages, using the transient time constants introduced in Section 5.1.5:

$$\bar{u}_s^s = \frac{1}{\tau_s}\left(\bar{\psi}_s^s - \frac{L_m}{L_r}\bar{\psi}_r^s\right) + \partial \bar{\psi}_s^s \tag{5.21}$$

$$\bar{u}_r^s = \frac{1}{\tau_r}\left(\bar{\psi}_r^s - \frac{L_m}{L_s}\bar{\psi}_s^s\right) + \partial \bar{\psi}_r^s - j\omega_r \bar{\psi}_r^s \tag{5.22}$$

On the assumption of constant rotor speed, Eqs. 5.21 & 5.22 become linear first order differential equations, permitting analytical solution by the method of Laplace transforms. Eq. 5.23 is produced by setting the stator voltage to zero, taking Laplace transforms of the resulting voltage equations and finally rearranging for stator flux linkage.

$$\bar{\Psi}_s^s(\nu) = \frac{\left(\frac{1}{\tau_r} - j\omega_r + \nu\right)\bar{\psi}_{s0}^s + \left(\frac{L_m}{L_r\tau_s}\right)\bar{\psi}_{r0}^s}{(\alpha+\nu)(\beta+\nu)} + \frac{\left(\frac{L_m}{L_r\tau_s}\right)\bar{U}_r^s(\nu)}{(\alpha+\nu)(\beta+\nu)} \tag{5.23}$$

Note that the Laplace variable is defined as ν rather than the more commonly used s to avoid confusion with induction machine slip. Note also that to perform the differential operation with p.u. values for inductance and system angular velocity, 1 p.u. of time is equivalent to (1/100π) seconds. Transient time constants are therefore of the order of 10-50 p.u.

The denominator roots α and β are complex constants. These roots determine the exponential order of the resulting time solution, i.e.:

$$\bar{\psi}_s^s(t) = Ae^{-\alpha t} + Be^{-\beta t} + f\left(\bar{u}_r^r(t)\right) \tag{5.24}$$

where constants A and B are to be determined. Roots α and β determine both the rate of natural flux linkage decay and the dominant frequency components of the solution.

Solution roots and the complex frequency adjustment parameter

The roots of stator flux linkage solution depend upon the transient time constants, the leakage factor and the rotor speed. Solving Eqs. 5.21 - 5.23 as per Appendix B reveals:

$$\alpha = \tau_s^{-1} - \varsigma_f \qquad \beta = \tau_r^{-1} - j\omega_r + \varsigma_f, \tag{5.25, 5.26}$$

where a small complex-frequency-adjustment parameter is defined by Eq. 5.27.

$$\varsigma_f = \frac{(1-\sigma)}{\tau_s \tau_r \left(\tau_r^{-1} - \tau_s^{-1} - j\omega_r\right)} \tag{5.27}$$

The real and imaginary frequency adjustment components can be estimated with the knowledge that the p.u. transient time constants are significantly larger than 1, substituting approximation Eq. 5.28 into the definition 5.27:

$$\tau_s, \tau_r >> 1 \therefore \left\{\frac{1/\tau_r - 1/\tau_s}{\omega_r}\right\} << 1, \tag{5.28}$$

$$\mathrm{Re}(\varsigma_f) = \kappa \approx \frac{(1-\sigma)}{\omega_r^{\,2}\tau_s\tau_r}(1/\tau_r - 1/\tau_s) \tag{5.29}$$

$$\mathrm{Im}(\varsigma_f) = \delta \approx \frac{(1-\sigma)}{\omega_r \tau_r \tau_s} \tag{5.30}$$

This complex frequency adjustment hints at an interaction between the fluxes linked by either set of windings. The introductory description of fault response from Section 5.1 suggested that dc and induced-rotor-speed components of emf decay at rates equal to the stator and rotor time constants respectively. In fact the effective decay frequencies are fractionally *closer* to each other; the difference between the decay frequencies is diminished when compared with isolated stator and rotor circuits. Eq. 5.27 also reveals that δ is a small *positive* number, as indicated by Eqs. (5.33, 5.34):

$$f_{self-linking\,decay} = \delta \qquad f_{mutual-linking\,decay} = (\omega_r - \delta) \tag{5.31, 5.32}$$

$$f_{self-linking\,decay} > 0 \qquad f_{mutual-linking\,decay} < \omega_r \tag{5.33, 5.34}$$

The effective decay frequencies are described in the main text as 'near-dc' and 'near-rotor speed'. They may deviate from pure-dc and rotor-speed by less than one percent for a very low resistance circuit, or over three percent for a highly resistive circuit, such as a DFIG rotor with added crowbar resistance applied (Section 5.3.3).

The real component of the complex frequency adjustment parameter is typically an order of magnitude smaller than the imaginary component, i.e. the effect on the decay frequencies is more pronounced than the negligible impact on the decay time constants. The effect of κ is to increase the difference between the *effective* stator and rotor time constants when compared with the original values (Eq. 5.37).

$$\tau_s'^{-1} = \left(\tau_s{}^{-1} - \kappa\right) \qquad \tau_r'^{-1} = \left(\tau_r{}^{-1} + \kappa\right). \tag{5.35, 5.36}$$

$$\left|\tau_r' - \tau_s'\right| > \left|\tau_r - \tau_s\right| \tag{5.37}$$

The effective frequency adjustment, δ, is of the order of τ_r^{-2}, roughly 1%. However, the effective time-constant adjustment, κ, is of the order of $\delta \times (\tau_r^{-1} - \tau_s^{-1})$, well below 0.05% for a practical machine, with negligible impact.

5.2.3 Natural response analysis

Looking again at the Laplace transform solution for stator flux, there are two main elements: a natural response formed from the initial conditions and a forced response driven by the ongoing rotor voltage (Eq. 5.23). By linear superposition the two elements can be solved separately; the two resulting time-based partial solutions are added to form a final solution.

$$\overline{\Psi}_s^s(\nu) = \overbrace{\frac{\left(\frac{1}{\tau_r} - j\omega_r + \nu\right)\overline{\psi}_{s0}^s + \left(\frac{L_m}{L_r\tau_s}\right)\overline{\psi}_{r0}^s}{(\alpha+\nu)(\beta+\nu)}}^{\text{Natural Response}} + \overbrace{\frac{\left(\frac{L_m}{L_r\tau_s}\right)\overline{U}_r^s(\nu)}{(\alpha+\nu)(\beta+\nu)}}^{\text{Forced Response}} \tag{5.38}$$

The natural response solution is the complete solution for a short-circuited or zero-voltage rotor.

Stator circuit

Solving the natural response term of Eq. 5.38 for stator flux by partial fraction expansion and inverse Laplace transformation (Appendix B) produces:

$$\overline{\psi}_s^s(t) = \overbrace{\left(\overline{\psi}_{s0}^s + A_s^s\right)e^{-t/\tau_s'}e^{j\delta t}}^{\text{Near-DC}} \overbrace{- A_s^s\, e^{-t/\tau_r'}e^{j(\omega_r-\delta)t}}^{\text{Near-rotor speed}} \tag{5.39}$$

where:

$$A_s^s = \frac{(\delta + j\kappa)\overline{\psi}_{s0}^s + j\left(L_m/(L_r\tau_s)\right)\overline{\psi}_{r0}^s}{(\omega_r - 2\delta) + j\left(\tau_r'^{-1} - \tau_s'^{-1}\right)} \tag{5.40}$$

Note that the form of the solution contains two terms, one for each root. Most of the flux is represented by the stator circuit's own leakage decay seen at near-dc frequency and

decaying with the effective stator time constant (left-hand term in Eq. 5.39). A smaller term (right-hand term in Eq. 5.39) represents the mutual decay, transferred from the rotor circuit, seen at near-rotor speed and decaying with the effective rotor time constant.

The stator current can be determined by using the stator circuit equation (Eq. 5.17) with zero voltage:

$$\bar{i}_s^s = \frac{-1}{R_s}\partial\overline{\psi}_s^s \tag{5.41}$$

$$\bar{i}_s^s(t) = \overbrace{\frac{\left(\overline{\psi}_{s0}^s + A_s^s\right)\left(\tau_s'^{-1} - j\delta\right)}{R_s}e^{-t/\tau_s'}e^{j\delta t}}^{\text{Near-dc}} - \overbrace{\frac{A_s^s\left(\tau_r'^{-1} - j\left(\omega_r - \delta\right)\right)}{R_s}e^{-t/\tau_r'}e^{j(\omega_r-\delta)t}}^{\text{Near-rotor speed}} \tag{5.42}$$

This expression can be simplified by using the time constant approximation from Eq. 5.28 and neglecting any coefficient terms of the order τ^{-2} or smaller:

$$A_s^s \approx j\frac{L_m}{L_r\omega_r\tau_s}\overline{\psi}_{r0}^s, \tag{5.43}$$

$$\bar{i}_s^s(t) \approx \frac{1}{L_s'}\overline{\psi}_{s0}^s e^{-t/\tau_s'}e^{j\delta t} - \frac{L_m}{L_s'L_r}\overline{\psi}_{r0}^s e^{-t/\tau_r'}e^{j(\omega_r-\delta)t} \tag{5.44}$$

The approximated stator current expression in Eq. 5.44 is very similar to the original estimate of Eq. 5.10 in Section 5.1.6 based only on the flux-decay description. The main difference is the inclusion of the small complex frequency adjustment term, which relates to alignment effects discussed in Section 5.1.7.

Rotor circuit

Using the same method as for the stator flux linkage solution, the Laplace transforms of Eqs. 5.21 & 5.22 can be solved for rotor flux under conditions of constant rotor speed and applying zero stator voltage. The rotor solution is viewed from the rotor reference frame in Eq. 5.45.

$$\overline{\psi}_r^r(t) = \overbrace{A_r^r e^{-t/\tau_s'}e^{-j(\omega_r-\delta)t}}^{\text{Near-rotor speed}} + \overbrace{\left(\overline{\psi}_{r0}^r - A_r^r\right)e^{-t/\tau_r'}e^{-j\delta t}}^{\text{Near-dc}} \tag{5.45}$$

where:

$$A_r^r = \frac{-\left(\delta + j\kappa\right)\overline{\psi}_{r0}^r + j\left(L_m/\left(L_s\tau_r\right)\right)\overline{\psi}_{s0}^r}{\left(\omega_r - 2\delta\right) + j\left(\tau_r'^{-1} - \tau_s'^{-1}\right)} \tag{5.46}$$

The rotor circuit decay components reciprocate the decay component frequencies of the stator circuit. Comparing Eq. 5.45 with Eq. 5.39 reveals that, on the *rotor* circuit most of the flux decays at near-dc with the *effective rotor* time constant, whilst the mutual contribution decays at near-rotor speed with the effective stator time constant. Also, when viewed from the rotor reference frame the directions of rotation appear reversed; the near-dc frequency appears as $-\delta$ and the near-rotor speed frequency as $-(\omega_r - \delta)$.

For the natural response the rotor voltage is set to zero. As a result, the rotor circuit equation simplifies to Eq. 5.47 and an expression for rotor current can be determined by differentiating Eq. 5.45:

$$\bar{i}_r^r = \frac{-1}{R_r}\partial\overline{\psi}_r^r \tag{5.47}$$

$$\bar{i}_r^r(t) = \overbrace{\frac{\left(\tau_s'^{-1} + j(\omega_r - \delta)\right)A_r^r}{R_r} e^{-t/\tau_s'} e^{-j(\omega_r-\delta)t}}^{\text{Near-rotor speed}} + \overbrace{\frac{\left(\tau_r'^{-1} + j\delta\right)\left(\overline{\psi}_{r0}^r - A_r^r\right)}{R_r} e^{-t/\tau_r'} e^{-j\delta t}}^{\text{Near-DC}} \tag{5.48}$$

The rotor current equation can be simplified by using the time constant approximation from Eq. 5.28 and neglecting any coefficient terms of the order τ^{-2} or smaller:

$$A_r^r \approx j\frac{L_m}{L_s\omega_r\tau_r}\overline{\psi}_{s0}^r, \tag{5.49}$$

$$\bar{i}_r^r(t) \approx \frac{1}{L_r'}\overline{\psi}_{r0}^r e^{-t/\tau_r'} e^{-j\delta t} - \frac{L_m}{L_r'L_s}\overline{\psi}_{s0}^r e^{-t/\tau_s'} e^{-j(\omega_r-\delta)t} \tag{5.50}$$

Again, the approximation from the full derivation here very closely matches the original estimation of Eq. 5.11 in Section 5.1.6 which was based on the flux-decay description alone. The main difference is the small complex frequency adjustment parameter, which chiefly affects the effective frequency composition. The same values of peak fault currents and their duration are predicted by the two expressions.

Fault torque

The torque is found from the cross product of the stator and rotor current space vectors. The expression in Eq. 5.12 can be simplified by using the current approximations from Eqs. 5.44 & 5.50, remembering to transform the space vectors into a common reference frame (detail in Appendix B):

$$T = \left[\frac{-L_m}{\sigma L_s L_r}\left|\overline{\psi}_{r0}\right|\left|\overline{\psi}_{s0}\right| e^{-t/\tau_T'}\right]\sin\left((\omega_r - 2\delta)t + \theta_{\psi_0}\right) \tag{5.51}$$

Eq. 5.51 includes two new parameters. Firstly, the initial phase separation of flux linkage vectors:

$$\theta_{\psi_0} = \theta\left(\overline{\psi}^{g}_{r0}\right) - \theta\left(\overline{\psi}^{g}_{s0}\right) \tag{5.52}$$

Secondly, a torque transient time constant: a parallel combination of the stator and rotor time constants:

$$1/\tau'_T = \left(1/\tau'_r + 1/\tau'_s\right) \tag{5.53}$$

The initial phase angle ensures a torque expression which is continuous in time. The torque time constant is smaller than either circuit's time constant indicating a very rapid decay of torque, perhaps less than a single system cycle. The torque oscillates almost at rotor speed, as described in the flux-based argument in Section 5.1.8.

Eq. 5.51 can be further simplified in order to estimate the peak torque. Assuming that the leakage inductances are far smaller than the mutual inductance, the leakage factor can be approximated as shown in Eq. 5.54.

$$\sigma = 1 - \frac{{L_m}^2}{L_r L_s} \approx \frac{L_{es} + L_{er}}{L_m} \quad \left(L_{es}, L_{er} << L_m\right) \tag{5.54}$$

Further, with small leakage values and pre-fault conditions of torque generation, the product of flux magnitudes is no more than roughly 10% above 1 p.u. Hence:

$$T \approx \left[\frac{-1.1}{L_{es} + L_{er}} e^{-t/\tau'_T}\right] \sin\left(\left(\omega_r - 2\delta\right)t + \theta_{\psi_0}\right) \tag{5.55}$$

Eq. 5.55 indicates a very large peak torque output within one cycle of the short-circuit, which rapidly decays to zero. The peak torque depends very much on the machine's leakage parameters: a typical generator may exhibit 3-5 p.u. peak. This simplification is borne out by the example shown in Figure 5.3.

Example of fault torque

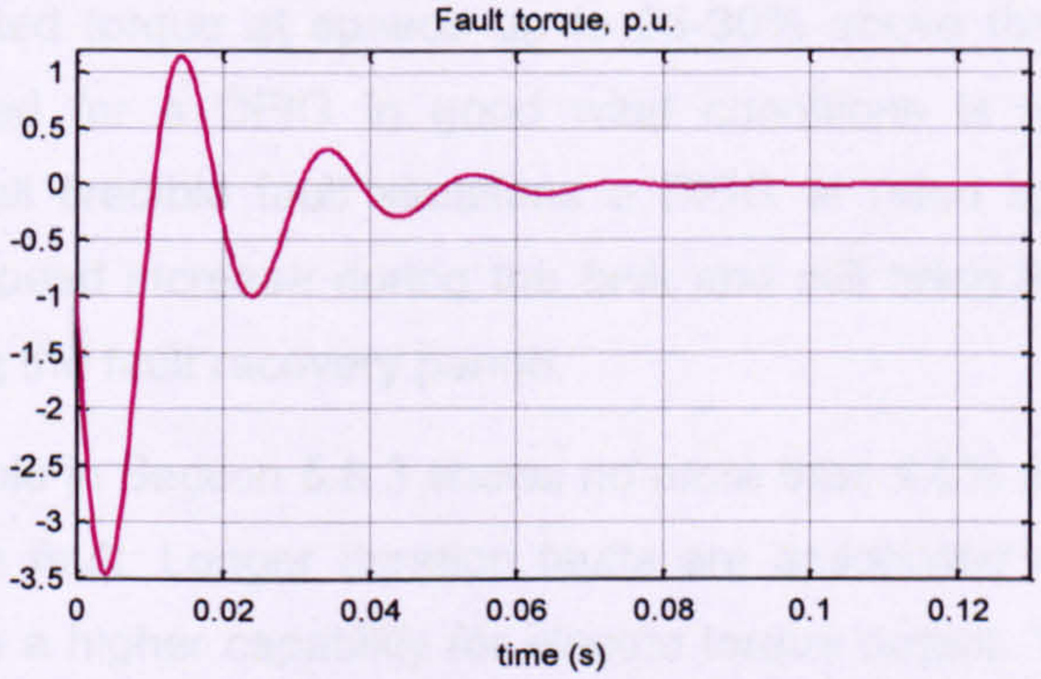

Figure 5.3. Induction machine zero-volts fault response – torque.

An example of the fault torque, calculated using definition Eq. 5.12, is shown in Figure 5.3 for a zero voltage short-circuit fault. The machine parameters were taken from the 7.5kW DFIG test rig (Appendix B). In this example over-rated torque endures for less than 15 ms, inferring a very short-term high mechanical strain. More serious is the fault-long inability to produce electrical braking torque, and hence the potential free acceleration of the rotor. The mean value of electrical torque in Figure 5.3 over 140ms is -0.19 p.u.; assuming the continuation of rated mechanical input power this leaves the generator with an average shortfall of roughly 80% of rated torque during the example 140ms fault period. In general however the brevity of grid fault durations limits the practical speed increase to a handful of percent, as discussed below.

5.2.4 Speed stability

The question of speed stability for wind turbines following grid voltage disturbances is comprehensibly treated in [24]. This work does not repeat his research but summarises the relevant points below.

Given the collapse of electric torque explained above, and without applying very swift restrictions to the generator's input power, a grid fault will cause the rotor to accelerate rapidly. However, a fault duration of no more than roughly 500ms limits a wind turbine's rotor speed increase to no more than roughly five to ten percent. The rotor speed will therefore remain within safe limits for a DFIG entering the fault period with rated speed.

SFIG rotor speed stability

As reported in [24], speed stability is a critical issue for the fault response of singly-fed machines. SFIGs cannot generate significant torque at high slip; indeed they are dynamically unstable at speeds above the pull-out torque. Grid faults may lead the rotor to beyond its maximum stable speed before fault clearance. Fault ride through solutions for SFIGs must tackle the issue of rotor speed stability [32].

DFIG rotor speed stability

A key advantage of the DFIG system is its range of speed operation, with an inherent ability to deliver rated torque at speeds up to 25-30% above the synchronous rotor speed. Rated speed for a DFIG in good wind conditions is roughly 10% super-synchronous. For all credible fault situations a DFIG at rated speed may therefore accept a 15-20% speed increase during the fault and still bring the rotor safely back under control during the fault recovery period.

The 0% fault example in Section 5.6.3 shows no more than 4.5% increase in speed for the 140ms duration fault. Longer duration faults are associated with higher retained voltages and hence a higher capability for electric torque output. This helps the DFIG

limit the rotor's acceleration. The 500ms 15% fault example in Section 5.7.2 showed a maximum speed deviation of 6%.

No credible fault (as described in Chapter 2) will force a DFIG at rated speed into an over-speed event. If the instant of a grid fault coincides with momentary high-rotor speed operation, such as could happen in very gusty wind conditions, it is possible for the rotor speed to be raised above its maximum acceptable limit. This event is sufficiently rare to allow derogation from fault ride-through requirements. Temporarily high rotor speeds will affect no more than a handful of wind turbines at any one time in a large wind farm; it is feasible that these few could be allowed to disconnect without significantly affecting the fault response of the wind farm.

5.3 Experimental validation of the analytical solution

5.3.1 Validation tests

The test rig (introduced in Chapter 4) was used to determine the validity of the analytical solution from Section 5.2. The test rig layout is shown in Figure 4.1, with machine parameters given in Appendix B. In each experimental test the stator voltage was dropped to zero 1.0s after data-recording started.

In order to compare directly with the analytical solution, only the stator and rotor currents from these tests are displayed. Rotor speed, voltage and other commodities of the generator under fault conditions are discussed in Section 5.6.

For each test the corresponding analytical solution for current is calculated from Eqs. 5.42 & 5.48, using the same machine parameters. The d-q component solutions are converted into three-phase representation for direct comparison with the test results. The initial conditions are set using pre-fault steady-state values in the excitation frame, and so an arbitrary initial phase angle is included when transforming into the stator or rotor reference frames.

Note on the limited resolution of the frequency spectra

In order to establish the frequency composition of the results, Fourier analysis was performed using Matlab's discrete fast-Fourier-transform (FFT) function. The FFT was performed on only around 140ms of fault data, which were sampled at 4kHz with the SFIG and 5kHz with the DFIG. By Nyquist's theorem, the upper limit of measurable frequency is therefore 2.0 – 2.5 kHz. With less than 1000 points of data, the frequency resolution is limited to around 1Hz, and hence the FFT spectrum is best used only as an indicator of the relative frequency content.

The specific ac component frequencies were established by inspection of the mean distance between ac peaks. An exponential approximation of the near-dc decay was subtracted from the data to improve readings of the ac peaks.

5.3.2 SFIG fault response test

The first example is of the test rig configured as a singly-fed induction machine, with the three phases of the wound-rotor physically short-circuited using a steel bolt. The machine was setup to generate 7kW at a steady speed of 1.02 p.u (1530rpm) prior to the fault.

Pre-fault conditions

Pre-fault data showed the SFIG operating at (1.020 ± 0.001) p.u. speed, corresponding to a rotor frequency of (51.02 ± 0.05) Hz compared with a (50.0 ± 0.1) Hz supply voltage. The frequency composition of the pre-fault currents is shown in Figure 5.4. Measurements of the mean ac period showed a single frequency contribution to stator current at (49.99 ± 0.40) Hz and to the rotor currents at slip speed of (-1.02 ± 0.40) Hz, as expected. The rotor currents showed a reverse phase order of R-B-Y, confirming a negative slip frequency in keeping with super-synchronous operation.

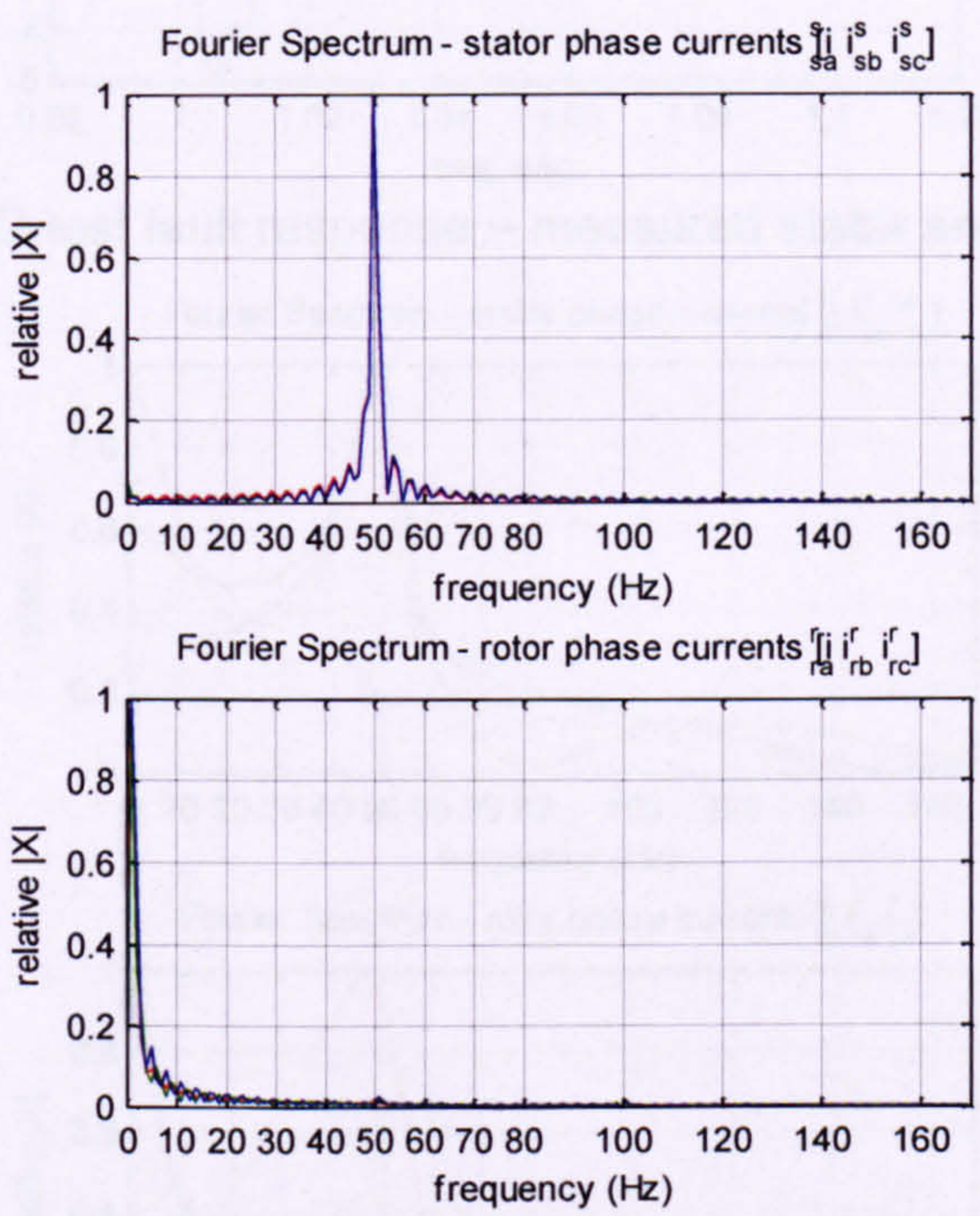

Figure 5.4. SFIG test pre-fault measured frequency composition.

Test currents

The measured stator and rotor currents for the fault test are shown in Figure 5.5. The rotor currents exhibit more dc than ac, indicating that the rotor transient time constant is longer. The near-dc component of the stator currents decays over roughly 25ms, while near-dc on the rotor decays over a timescale closer to 40ms. The peak rotor current is

a little below 5 p.u. The stator current sensors were saturated below peak stator current, although inspection of the waveform indicates a similar peak to that of the rotor currents.

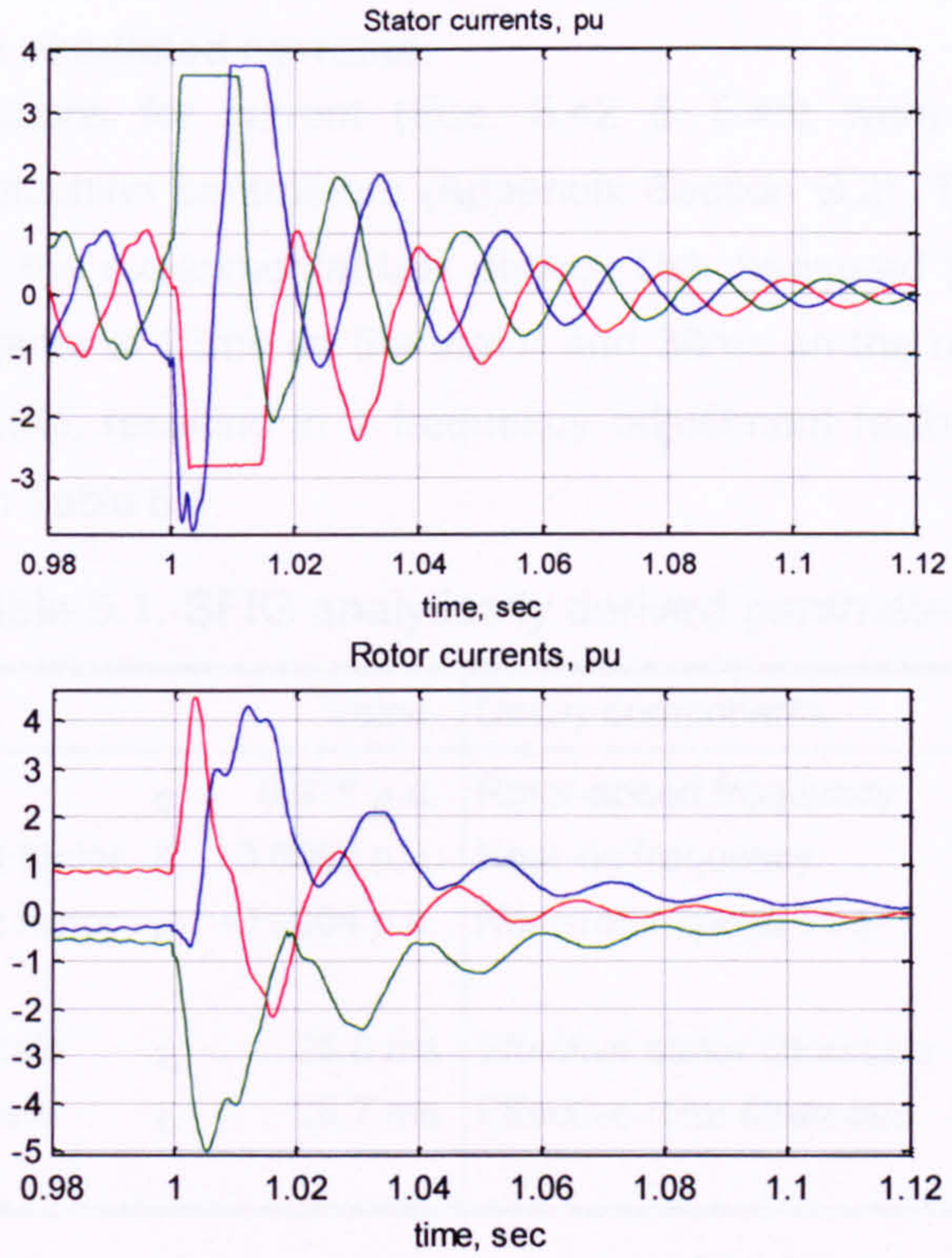

Figure 5.5. SFIG test fault response – measured stator and rotor currents.

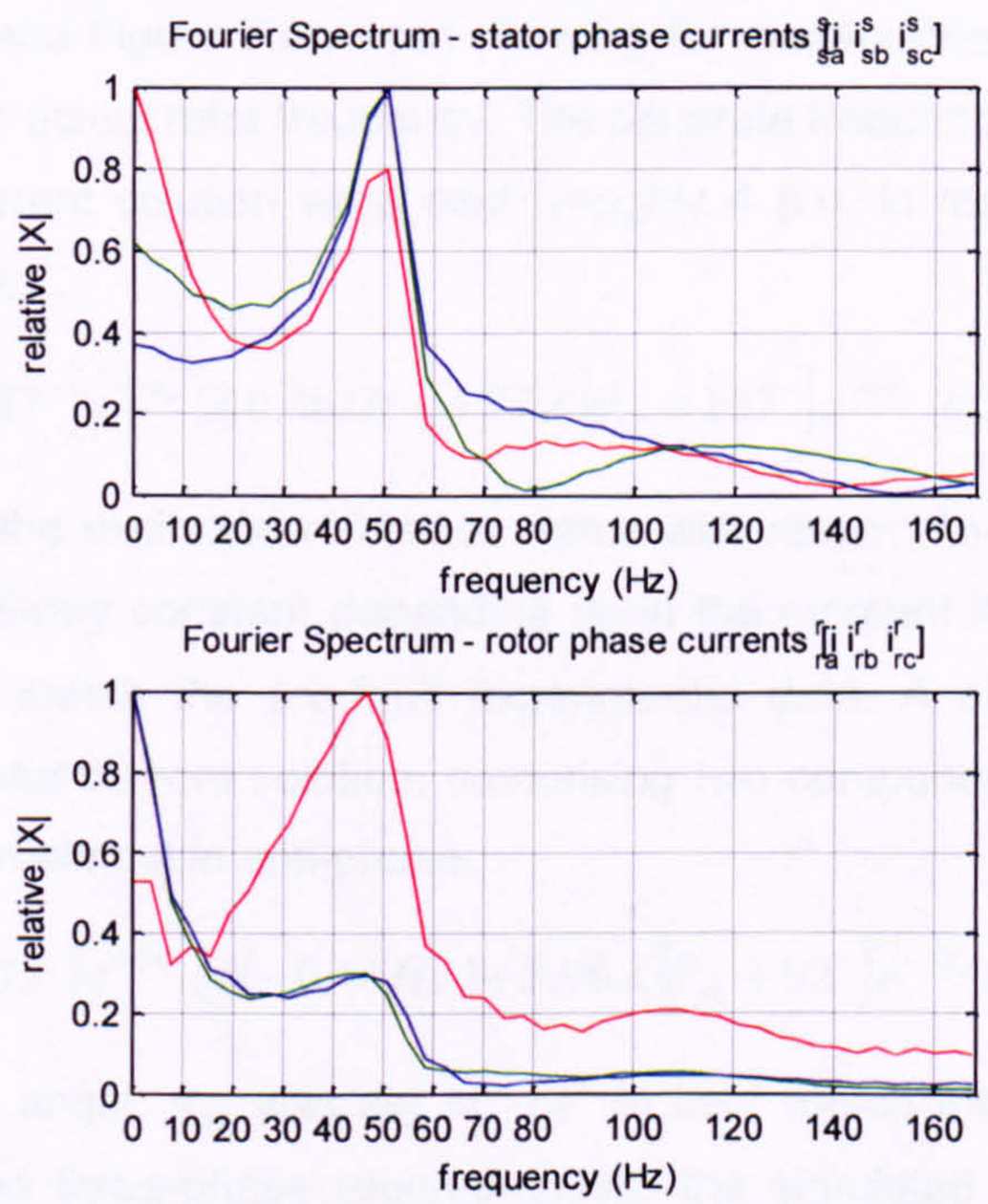

Figure 5.6. SFIG test fault response – measured frequency compositions.

The Fourier spectra in Figure 5.6 indicate two frequency components within each set of currents, as predicted. The near-dc frequency was too low to estimate within the fault

period. The near-rotor speed frequency was (50.50 ± 0.35) Hz in the stator currents and (50.65 ± 0.40) Hz in the rotor currents, each approximately 1% less than the rotor speed.

Analytical solution simulated currents

The analytical solutions for current (Eqs. 5.42 & 5.48) were enumerated using measured test rig machine parameters (Appendix Section B.2). The initial conditions were set up as per the experimental test above. The measured parameters suggest transient time-constants of 26ms on the stator and 39ms on the rotor. The calculated leakage factor is 7.5%, resulting in a frequency adjustment factor of roughly 1%, or 0.46Hz, as shown in Table 5.1.

Table 5.1. SFIG analytically derived parameters.

Derived Parameters		Value	Decay components		Value
Leakage factor	σ	0.075 p.u.	Rotor-speed frequency	f_r	51.02 Hz
Frequency adjustment factor	δ	0.0092 p.u.	Near-dc frequency	f_{self}	0.46 Hz
Timescale adjustment factor	κ	-0.0004 p.u.	Near-rotor speed freq.	f_{mutual}	50.59 Hz
Stator transient timescale	τ_s	25.8 ms	Effective stator timescale	τ_s'	25.7 ms
Rotor transient timescale	τ_r	38.7 ms	Effective rotor timescale	τ_r'	38.9 ms

The near-rotor speed decay frequency shows good agreement with the experimental results (Figure 5.5 and Figure 5.6); even allowing for measurement error this value is noticeably below the actual rotor frequency. The separate frequency components of the simulated stator current solution were each roughly 4 p.u. in magnitude and initially almost in anti-phase:

$$\bar{i}_s^s(t) = 4.06\angle\{\theta_{e0} - 87^\circ\}e^{-t/\tau_s'} @0.46Hz + 3.77\angle\{\theta_{e0} + 107^\circ\}e^{-t/\tau_r'} @55.59Hz \quad (5.56)$$

The initial angle of the excitation reference frame with respect to the stator reference frame, θ_{e0}, is an arbitrary constant depending upon the moment the fault occurs: -84° was found to best match the pre-fault experimental data. A similar result can be calculated for the rotor current solution, comprising two components of roughly 4 p.u. magnitude and again almost in anti-phase:

$$\bar{i}_r^r(t) = 3.87\angle\{\theta_{\varsigma 0} - 73^\circ\}e^{-t/\tau_r'} @(-0.46Hz) + 3.96\angle\{\theta_{\varsigma 0} + 92^\circ\}e^{-t/\tau_s'} @(-55.59Hz) \quad (5.57)$$

The initial rotor slip angle, $\theta_{\varsigma 0}$, was set at -72° to best match the experimental data. After transforming to three-phase representation, the simulated currents appear as shown in Figure 5.7, where the short-circuit has been applied at 0 seconds.

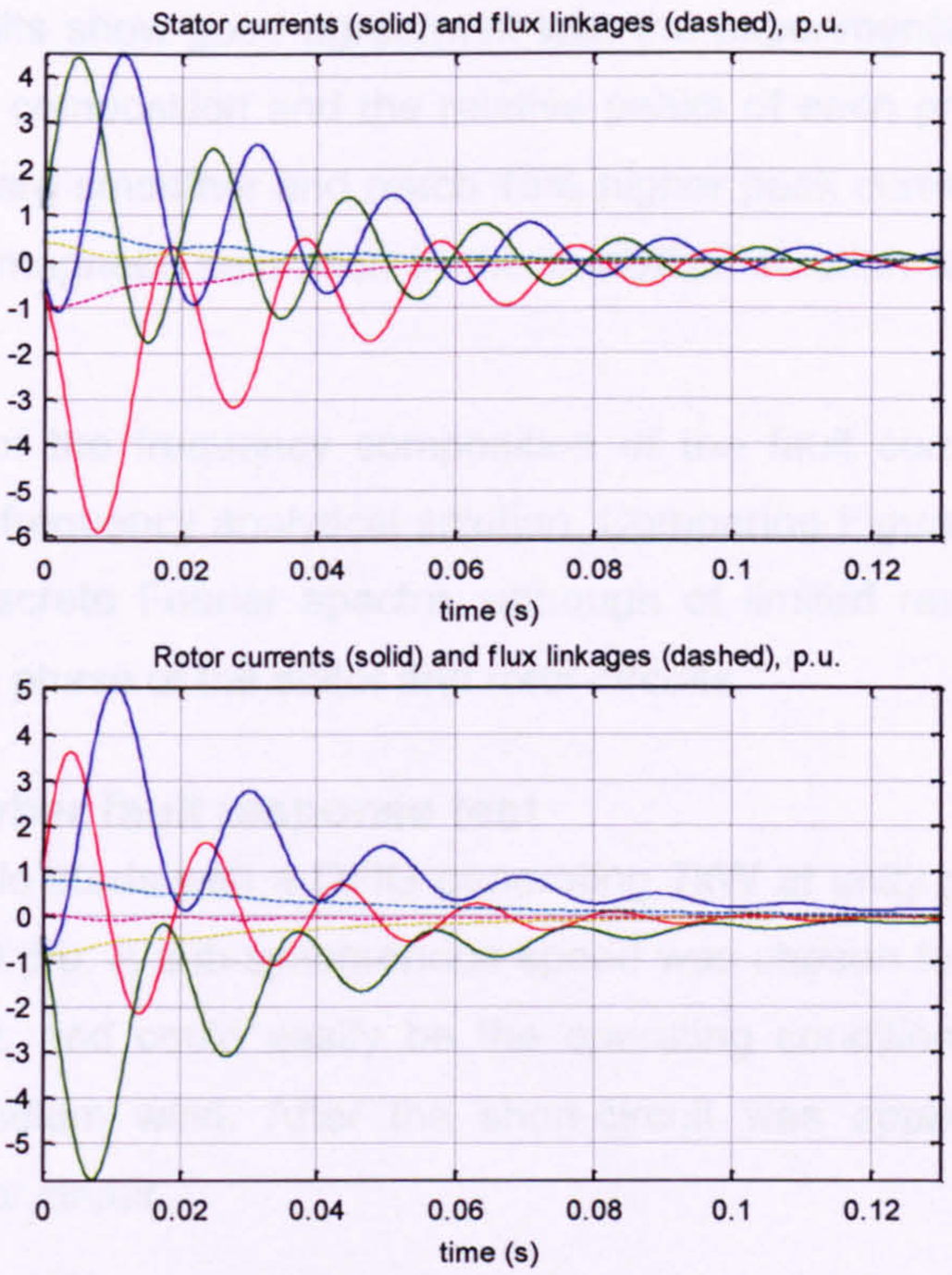

Figure 5.7. SFIG simulated fault response – stator and rotor circuits.

Note that the rough similarity in the time constants of this machine renders the stator and rotor currents similar in per unit terms. The flux linkages are each dominantly dc, decaying continuously to zero from roughly 1 p.u., while the currents on each circuit contain near-dc and near-rotor speed ac components.

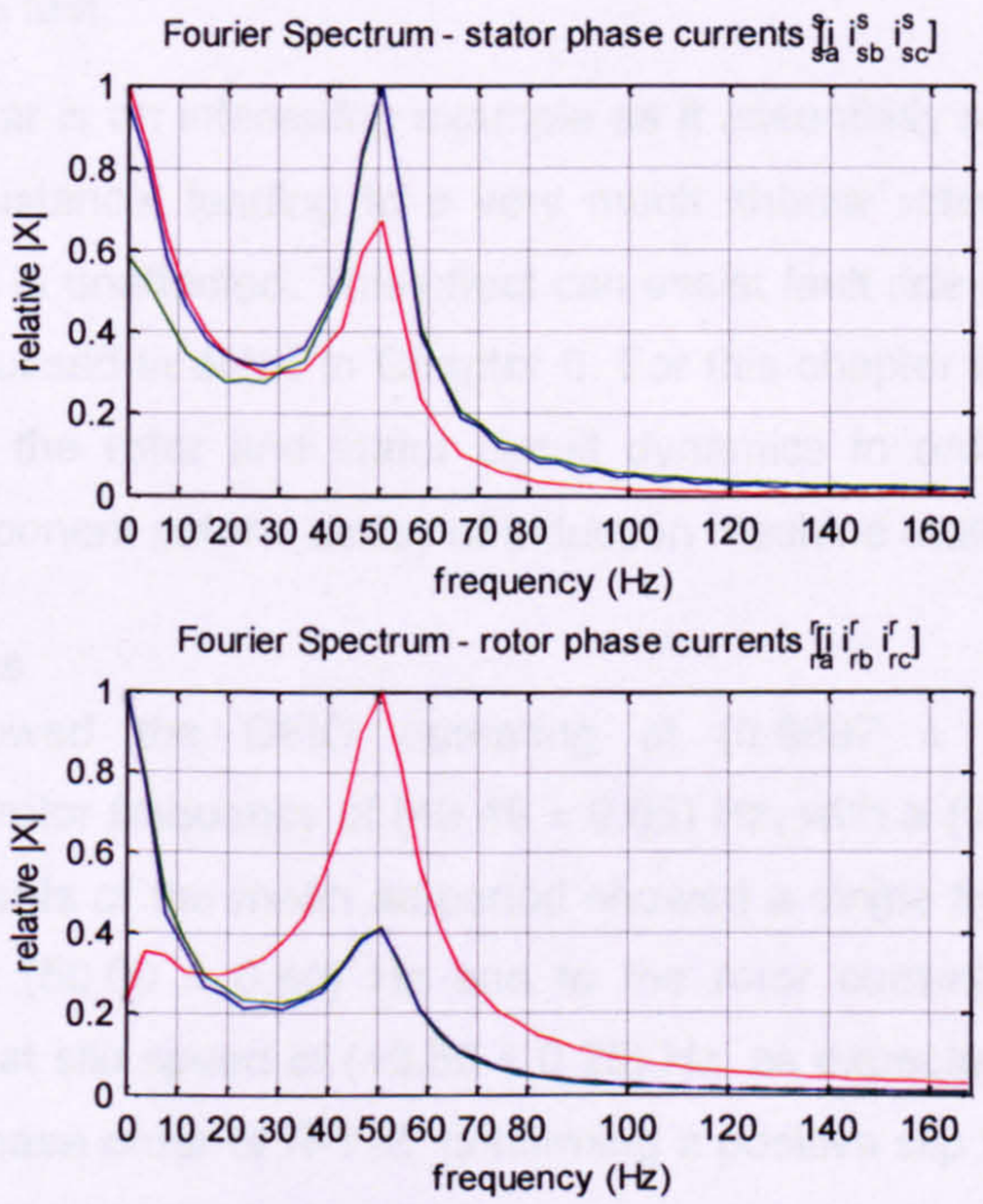

Figure 5.8. SFIG simulated fault response – frequency compositions.

The simulated results show good agreement with the experimental set (Figure 5.5) in terms of frequency composition and the relative peaks of each phase of current. The simulated currents are smoother and reach 15% higher peak current. This is likely due to the omission of magnetic saturation in the analytical solution which would limit the real currents.

Closer inspection of the frequency composition of the fault currents underlines the success of the two-frequency analytical solution. Comparing Figure 5.8 with Figure 5.6 reveals that the discrete Fourier spectra, although of limited resolution, show good agreement for each phase of the stator and rotor circuits.

5.3.3 DFIG Crowbar fault response test

The second example starts with a DFIG generating 7kW at unity power factor with an initial speed of 0.99 p.u. A sub-synchronous speed was chosen to distinguish this test from the SFIG test, and could easily be the operating condition for a wind turbine during a low-to-medium wind. After the short-circuit was applied, a crowbar was engaged on the rotor circuit.

Crowbar circuit and rotor resistance

The crowbar circuit temporarily closes the rotor circuit through a known resistance via a fast-acting IGBT switch. The crowbar was here automatically activated by a specific level of rotor over-current (2.0 p.u.), and held in place for the remaining duration of this test. The crowbar diverted current away from the DFIG's power converter which played no further part in the test.

The use of a crowbar is an interesting example as it essentially significantly increases the rotor circuit resistance, leading to a very much shorter rotor time constant. The stator time constant is unaffected. This effect can assist fault ride through performance and as such is discussed in detail in Chapter 6. For this chapter it serves to break the symmetry between the rotor and stator circuit dynamics in order to illustrate more clearly the two-component natural decay of induction machine fault response.

Pre-fault conditions

Pre-fault data showed the DFIG operating at (0.9897 ± 0.001) p.u. speed, corresponding to a rotor frequency of (49.49 ± 0.05) Hz, with a (50.1 ± 0.1) Hz supply voltage. Measurements of the mean ac period showed a single frequency contribution to stator current at (50.00 ± 0.40) Hz and to the rotor currents (controlled by the converter pre-fault) at slip speed of (+0.56 ± 0.25) Hz, as expected. The rotor currents showed a normal phase order of R-Y-B, confirming a positive slip frequency in keeping with sub-synchronous operation.

Test currents

The measured stator and rotor currents for the fault test are shown in Figure 5.9. Unlike the SFIG test, the rotor currents exhibit a greater ac component than dc component, indicating that the effective rotor transient time constant is shorter than that of the stator. The decay of the rotor-circuit near-dc component is here less than 15ms, while the stator-circuit near-dc decay timescale appears unchanged. The peak rotor current is a little over 5 p.u. The stator current sensors saturate below peak stator current, although inspection of the waveform indicates a similar peak to that of the rotor currents.

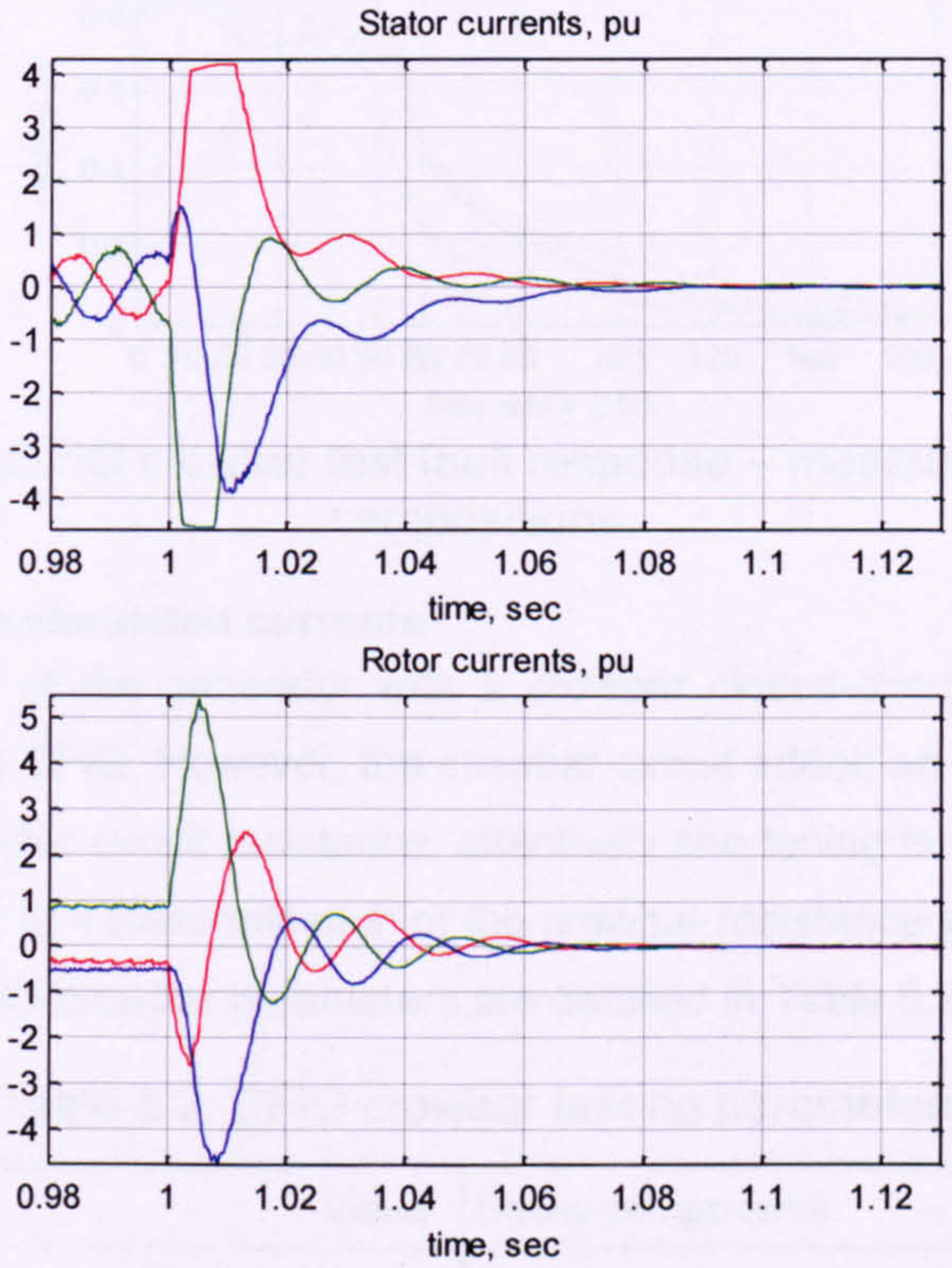

Figure 5.9. DFIG crowbar test fault response – measured stator and rotor currents.

The Fourier spectra in Figure 5.10 indicate two frequency components within each set of currents, as expected. The near-dc frequency was too low to estimate within the fault period. The near-rotor speed frequency was (47.70 ± 0.73) Hz in the stator currents and (48.02 ± 0.55) Hz in the rotor currents, each approximately 3% less than the rotor speed.

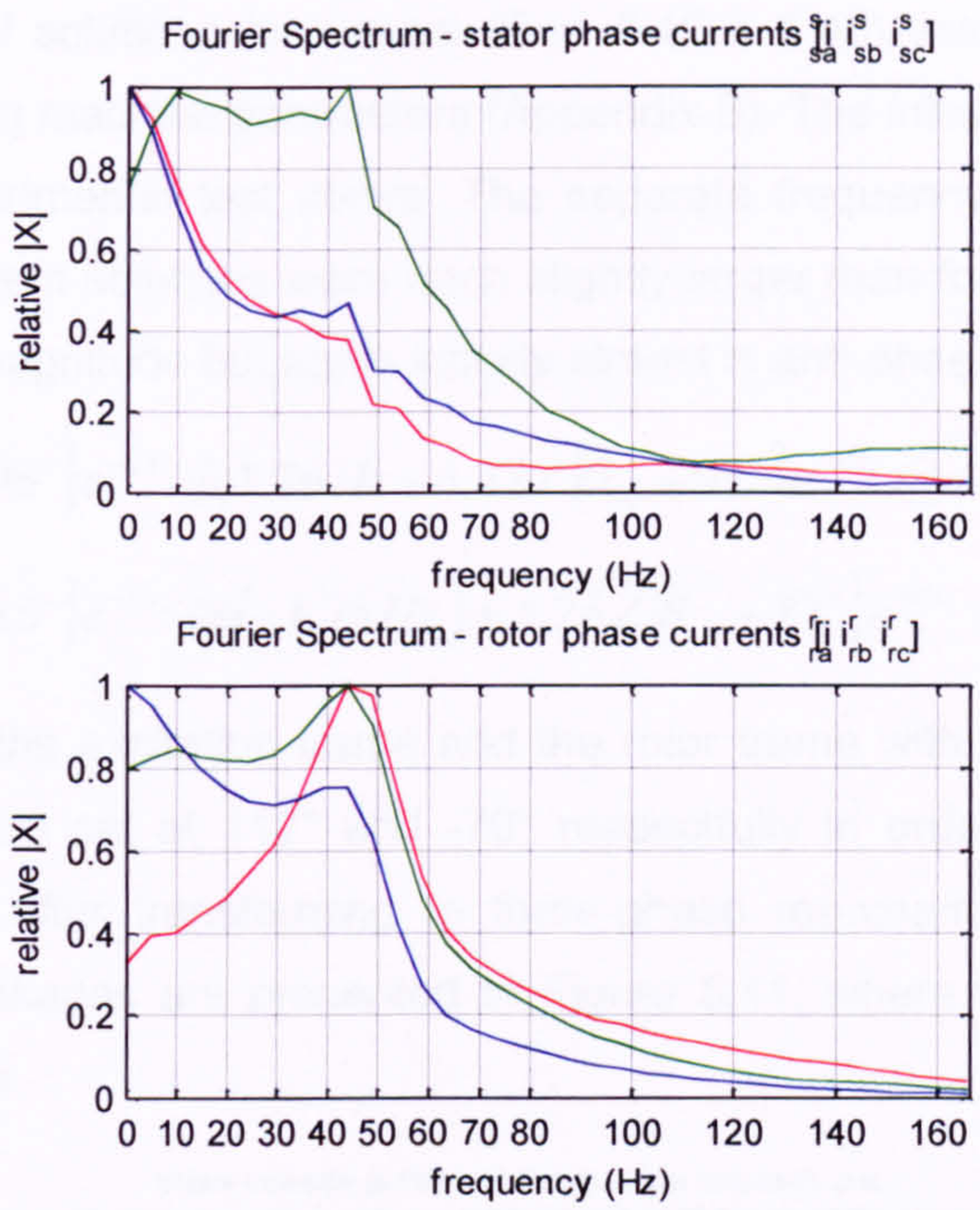

Figure 5.10. DFIG crowbar test fault response – measured frequency compositions.

Analytical solution simulated currents

The fault response of the generator with a crowbar closed-circuit rotor was broadly similar to that of the SFIG. However, the crowbar circuit added an additional 6% to the approximately 2% rotor circuit resistance, effectively shortening the rotor transient time constant by a factor of 4 (determination of the crowbar resistance value is discussed in Chapter 6). The DFIG crowbar parameters are detailed in Table 5.2.

Table 5.2. DFIG crowbar test rig parameters

Derived Parameters		Value	Decay components		Value
Leakage factor	σ	0.075 p.u.	Rotor-speed frequency	f_r	49.49 Hz
Frequency adjustment factor	δ	0.035 p.u.	Near-dc frequency	f_{self}	1.76 Hz
Timescale adjustment factor	κ	0.007 p.u.	Near-rotor speed frequency	f_{mutual}	47.84 Hz
Stator transient timescale	τ_s	25.8 ms	Effective stator timescale	τ_s'	27.3 ms
Rotor transient timescale	τ_r	10.1 ms	Effective rotor timescale	τ_r'	9.8 ms

The drop in transient timescale on the rotor circuit caused a noticeable rise in the complex frequency adjustment parameter to 3.5%, and as a result, the near-rotor speed decay frequency was significantly lower than the rotor speed. This reduced ac frequency showed good agreement with the experimental results; without the proposed magnetic drag effect this contribution at 96% of system frequency could not be easily explained.

Again, the analytical solutions for current (Eqs. 5.42 & 5.48) were enumerated using the measured test rig machine parameters (Appendix B). The initial conditions were set up as per the experimental test above. The separate frequency components of the stator and rotor current solutions were each slightly larger than for the SFIG test: here roughly 4.4 p.u. in magnitude but again initially almost in anti-phase:

$$\bar{i}_s^s(t) = 4.36\angle\{\theta_{e0} - 96^\circ\}e^{-t/\tau_s} @1.76Hz + 4.37\angle\{\theta_{e0} + 97^\circ\}e^{-t/\tau_r} @47.84Hz \quad (5.58)$$

$$\bar{i}_r^r(t) = 4.45\angle\{\theta_{\varsigma 0} - 85^\circ\}e^{-t/\tau_r} @(-1.76Hz) + 4.26\angle\{\theta_{\varsigma 0} + 83^\circ\}e^{-t/\tau_s} @(-47.84Hz) \quad (5.59)$$

The initial angle of the excitation frame and the rotor frame with respect to the stator reference frame were set at 112° and -70° respectfully in order to best match the experimental data. After transforming to three-phase representation, the simulated currents and flux linkages are presented in Figure 5.11, where the short-circuit was applied at 0 seconds.

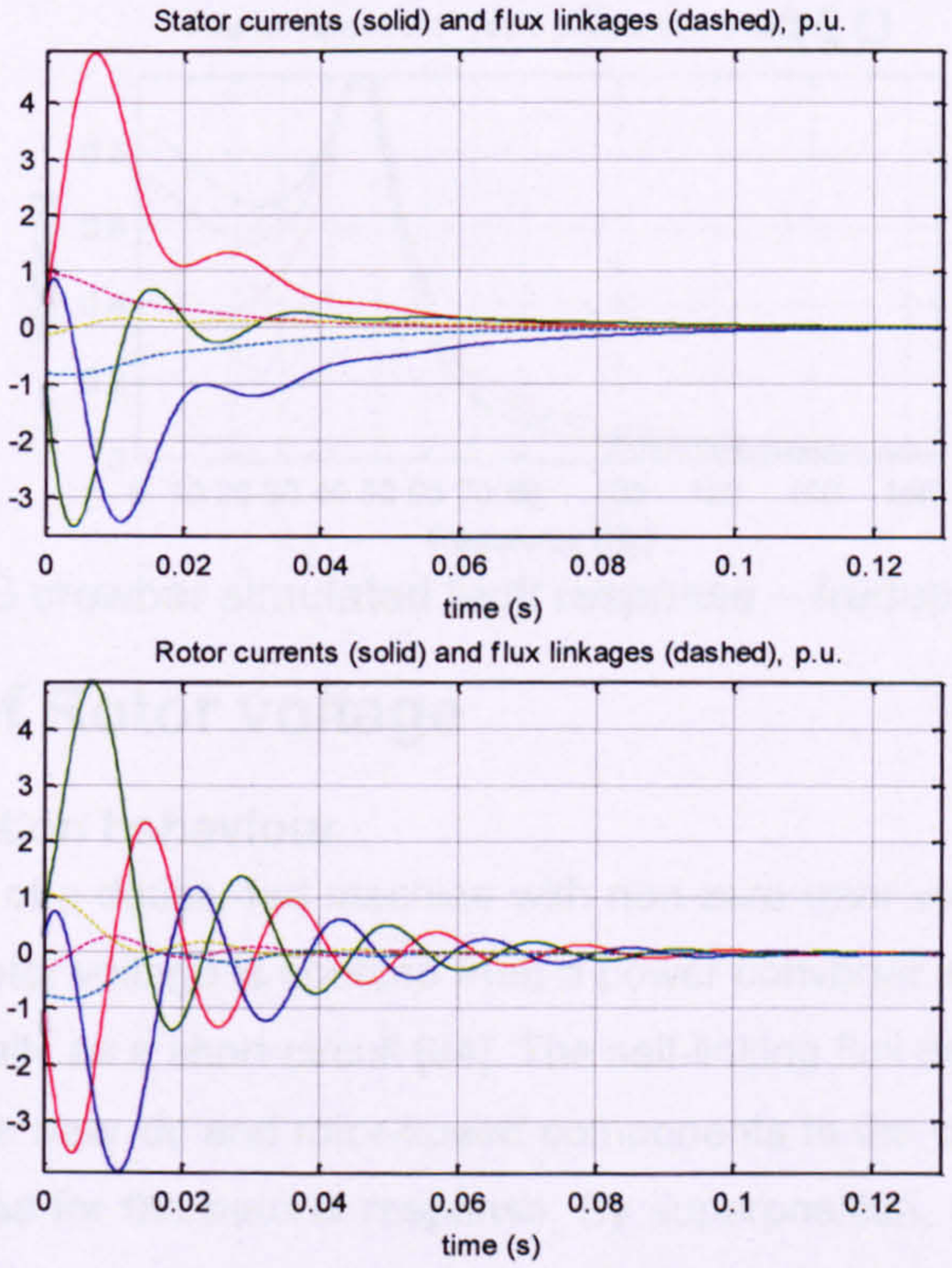

Figure 5.11. DFIG crowbar simulated fault response – stator and rotor circuits.

Figure 5.11 shows the stator and rotor flux linkages collapsing to zero from approximately 1 p.u. magnitude. However, unlike the SFIG example, the high rotor resistance here caused the rotor flux to decay over approximately 10ms.

The simulated currents show reasonable agreement with the experimental data (Figure 5.9). Here the rotor ac component and stator dc components specifically appear to decay around 15% slower than in the experimental data. The fact that these two elements are out by the same margin reinforces the idea that the real components are

physically linked; the rotor's near-rotor speed ac component and the stator's near-dc component are two views of essentially the same element of flux decay.

The frequency composition again supports the twin-frequency component analytical solution. Comparing Figure 5.12 with Figure 5.10 reveals that the discrete Fourier spectra, although of limited resolution, show sound agreement for each phase of the stator and rotor circuits.

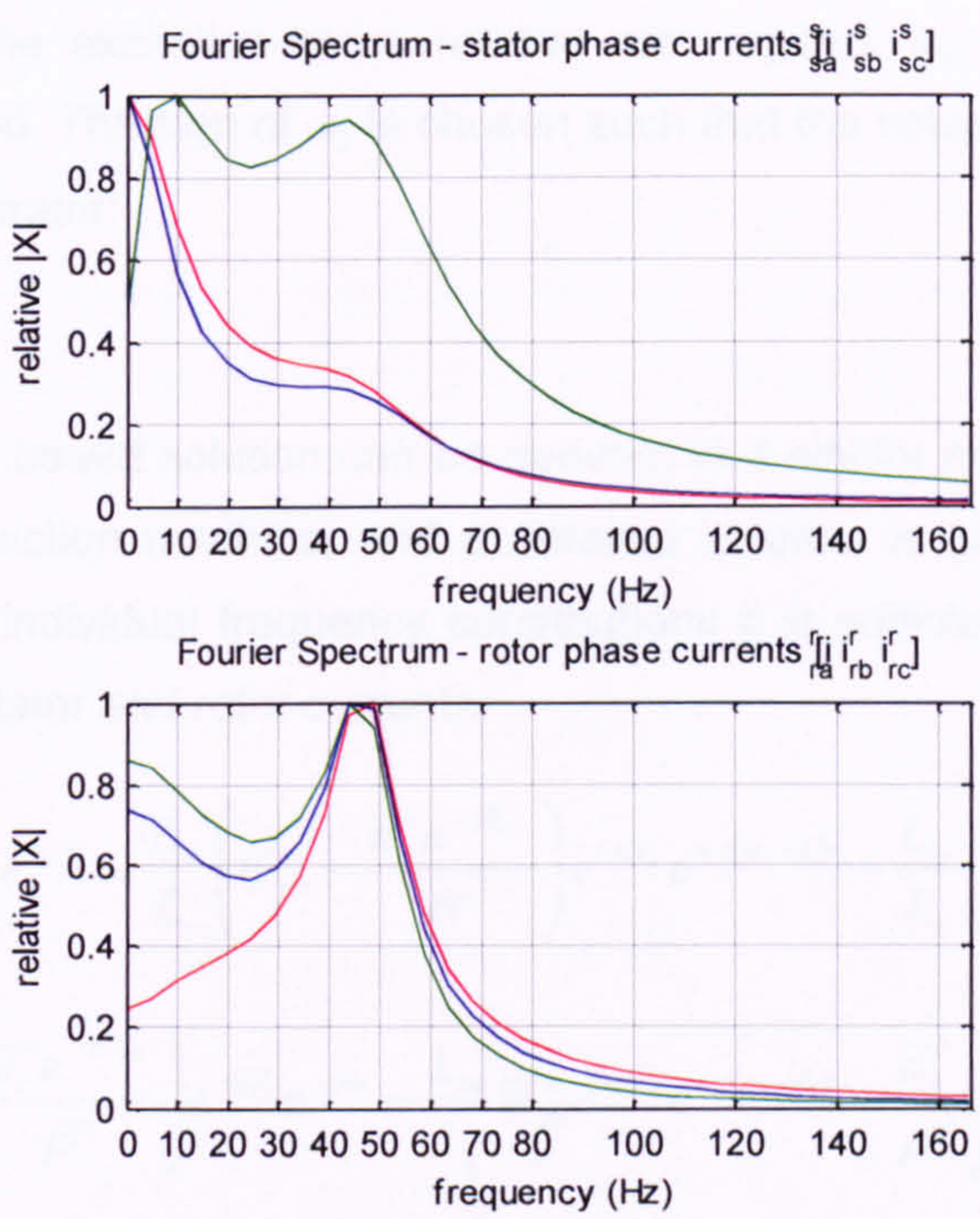

Figure 5.12. DFIG crowbar simulated fault response – frequency compositions.

5.4 Effects of Rotor voltage

5.4.1 Superposition behaviour

The fault response of a doubly-fed machine with non-zero rotor voltage is a little more complicated. The rotor voltage is sourced from a power converter which appears to the rotor circuit essentially as a short-circuit [64]. The self-linking flux decay and mutual flux decay will contribute near-dc and rotor-speed components to the observed currents, in the same manner as for the natural response. By superposition, and for the moment neglecting magnetic saturation, any rotor excitation will contribute an additional component to each current. These contributions may be sustained throughout the fault.

5.4.2 Constant rotor voltage

Stator and rotor current solutions

A good example of forced short-circuit response is to set the rotor voltage constant in the excitation reference frame. This is also the controller's frame; steady-state operation of the DFIG entails a constant excitation-frame rotor voltage. This steady-

state value may be held by the rotor power converter during the fault, producing ac rotor voltage at slip frequency in the rotor reference frame. The induction machine voltage equations in the excitation frame become:

$$R_s\bar{i}_s^e + \partial\overline{\psi}_s^e + j\omega_e\overline{\psi}_s^e = \bar{u}_s^e = 0 \tag{5.60}$$

$$R_r\bar{i}_r^e + \partial\overline{\psi}_r^e - j\omega_\chi\overline{\psi}_r^e = \bar{u}_r^e = const. \tag{5.61}$$

Eq. 5.61 includes the excitation-frame relative rotor speed, ω_χ, which is the exact negative of slip-speed. The sign of ω_χ is chosen such that the value is normally positive for an induction generator:

$$\omega_\chi = \omega_r - \omega_e \tag{5.62}$$

A Laplace transform based solution can be derived, in a similar manner to the natural response of the induction machine, and a detailed solution is given in Appendix B. Without loss of any individual frequency contributions it is sufficient to study the final approximations for stator and rotor currents:

$$\bar{i}_s^s(t) \approx \frac{1}{\sigma L_s}\left(\overline{\psi}_{s0}^s e^{-t/\tau_s'} e^{+j\delta t} - \frac{L_m}{L_r}\left(\overline{\psi}_{r0}^s - \frac{\bar{u}_r^e e^{+j\theta_{e0}}}{\beta^e}\right)e^{-t/\tau_r'} e^{+j(\omega_r-\delta)t} - \frac{L_m}{L_r}\frac{\bar{u}_r^s}{\beta^e}\right) \tag{5.63}$$

$$\bar{i}_r^r(t) \approx \frac{1}{\sigma L_r}\left(\left(\overline{\psi}_{r0}^r - \frac{\bar{u}_r^e e^{-j\theta_{\chi 0}}}{\beta^e}\right)e^{-t/\tau_r'} e^{-j\delta t} - \frac{L_m}{L_s}\overline{\psi}_{s0}^s e^{-t/\tau_s'} e^{-j(\omega_r-\delta)t} + \frac{\bar{u}_r^r}{\beta^e}\right) \tag{5.64}$$

where

$$\bar{u}_r^s = \bar{u}_r^e e^{+j(\omega_e t+\theta_{e0})}, \tag{5.65}$$

$$\bar{u}_r^r = \bar{u}_r^e e^{-j(\omega_\chi t+\theta_{\chi 0})} \tag{5.66}$$

and

$$\beta^e = \left(\tau_r^{-1} + \kappa\right) - j\left(\omega_\chi - \delta\right) \tag{5.67}$$

The expressions for current above show a very similar outcome to the natural response approximations (Eqs. 5.44 & 5.50). The stator-flux sourced decay is approximately unchanged. The rotor-flux sourced decay is somewhat offset in magnitude by the rotor voltage in fault conditions, but obeys the same envelope of decay rate and frequency. The right-hand term featuring rotor voltage is a system frequency driven current.

Fault current estimation from constant rotor voltage

The steady-state rotor voltage in the excitation frame may be roughly estimated from healthy initial conditions, assuming rated stator voltage, small p.u. stator and rotor

resistances and that the p.u. leakage inductances are much smaller than the mutual inductance:

$$\bar{u}_{r0}^{e} \approx \left(\omega_\chi R_s - R_r + j\omega_\chi \left(L_{es} + L_{er}\right)\right)\bar{i}_{s0}^{e} - \omega_\chi - j\,R_s/L_m \tag{5.68}$$

Eq. 5.68 is not readily contractible, but assuming pre-fault unity power factor and neglecting the right-hand-term in stator resistance:

$$\bar{i}_{s0}^{e} = -1 \tag{5.69}$$

$$\bar{u}_{r0}^{e} \approx R_r - \omega_\chi \left(1 + R_s - j\left(L_{es} + L_{er}\right)\right) \tag{5.70}$$

Eq. 5.70 implies that in normal operation at roughly -10% slip the DFIG requires roughly 10% p.u. magnitude of rotor voltage, which fits in with the 'equivalent-circuit' rotor voltage. Eq. 5.70 can be used to estimate the magnitude of the right-hand rotor-voltage-dependent term in the expressions for current in Eqs. 5.63 & 5.64, as follows:

$$\frac{\bar{u}_r^e}{\beta^e} \approx \frac{R_r - \omega_\chi \left(1 + R_s - j\left(L_{es} + L_{er}\right)\right)}{\tau_r'^{-1} - j\omega_\chi} = \begin{cases} \left(\omega_\chi \to 0\right) & \sigma L_r \\ \left(\omega_\chi \to \infty\right) & \left(L_{es} + L_{er} + j\left(1 + R_s\right)\right) \end{cases} \tag{5.71}$$

$$\left|i_r^r\left(\bar{u}_r\right)\right| = \left|\frac{1}{\sigma L_r}\frac{\bar{u}_r^e}{\beta^e}\right| \approx \begin{cases} \left(\omega_\chi \to 0\right) & 1 \\ \left(\omega_\chi \to \infty\right) & \left|1 + j\left(L_{es} + L_{er}\right)\right|/\sigma L_r \end{cases} \tag{5.72}$$

Eq. 5.72 estimates the magnitude of the rotor-voltage-driven component of fault current: approximately 1 p.u. for rotor speeds within a few percent of synchronous, rising towards $(\sigma L_r)^{-1}$ or 3-5 p.u. for very large slip values. This contribution is in addition to the decay transient components of rotor current. As a result it is imperative that DFIG controllers manipulate the rotor voltage in such a way as to minimise the system frequency current. Fortunately, this component is actively managed as a natural response of the PI rotor current controller.

However, the flux-decay components are not restrained by conventional DFIG control. This results in potentially damaging over-currents (explained in Section 5.1), imposing a shut-down or disconnection of the DFIG power converter.

5.5 Power converter fault response

Specific details of power converter fault response depend very strongly on the control setup: the controller sample time, the PWM method, the response of any signal filters, the particular tuning of PI controllers, the effect of feed-forward terms and so on. It is therefore difficult to quantify the response of a general DFIG power converter. The sections that follow concentrate on inescapable physical phenomena which stem from fault response.

5.5.1 Rotor-side converter fault response

Rotor control limitations

In generalising the response of a voltage-source converter, it is tempting to suggest that within the maximum converter voltage limits an ideal power converter can immediately match the emf produced on the rotor windings and prevent a rotor over-current event. In reality, the electromagnetic dynamics of the rotor circuit cannot be influenced much faster than the rotor transient time constant. Despite a controller sampling frequency of several kilohertz, rotor current control is characterised by rise-times no faster than 4-5ms. This action is not faster than the rapid rise of fault current spikes shown in Sections 5.1 - 5.2.4. Rotor over-current events due to grid faults are intrinsically unavoidable and DFIG power converters are forced to take self-protective action.

The PI feedback controller in standard vector control schemes can track the dc or near-dc rotor-circuit emf contributions well, but cannot control the mutual-linking emf decay at near-rotor speed. This ac component in the excitation frame has a half-wave period far smaller than the rotor transient timescale, for which conventional feedback control is difficult to control. As a result, strong near-rotor speed oscillations pervade the rotor currents. Other control approaches are reviewed in Chapter 6: improvements to control performance can be made for the plateau period of fault voltage, but rotor current spikes at fault initiation and clearance are unavoidable.

Converter voltage limits

The power converter's DC-link imposes an upper limit to the ac voltage it can produce. This will be typically matched to the maximum operating slip of the DFIG, roughly 0.3 p.u. (on the machine per-unit base) as explained in Chapter 3. The emf induced on the rotor windings by the decaying flux components can be estimated using the approximations developed in the solution for constant rotor voltage, as follows:

$$emf_r = \partial\overline{\psi}_r^r \approx \frac{1}{\tau_r}\left(\overline{\psi}_{r0}^r - \frac{\overline{u}_r^e e^{-j\theta_{z0}}}{\beta^e}\right)e^{-t/\tau_r'}e^{-j\delta t} - \frac{L_m}{\tau_r L_s}\overline{\psi}_{s0}^s e^{-t/\tau_r'}e^{-j(\omega_r-\delta)t} \tag{5.73}$$

$$\therefore |emf_r| \approx \frac{1}{\tau_r}\left|e^{-t/\tau_r'} - e^{-t/\tau_r'}e^{-j(\omega_r t+\varphi)}\right| \le \frac{2}{\tau_r} \tag{5.74}$$

In this equates to a maximum emf of roughly 0.2 p.u., close but not exceeding the converter voltage limits (~0.3 p.u.). The voltage magnitude therefore does not explicitly impose restrictions on fault response.

Converter disconnection

In any instant where the rotor current threatens to exceed the converter's device ratings, the converter must be disconnected. Conventional DFIG protection involves turning-off of all rotor converter devices and diverting the rotor current into a crowbar circuit (Chapter 6). As a result, the rotor becomes a high-resistance closed-circuit, as demonstrated in Section 5.3.3. The outcome is similar to a poorly-controlled high-slip SFIG.

If the devices are sufficiently rated then the converter can remain connected throughout the fault and offer full control after the initial transient decay. This however requires a power converter rated for higher power than the generator itself, completely negating the cost-efficiency of the DFIG over the full-converter topology. For example, to manage 5 p.u. rotor current on a DFIG rated for up to 25% slip would require a 1.25 p.u. rated power converter, many times more expensive than the original.

For a standard power rating of converter, temporary disconnection of the rotor IGBT devices following a severe fault is unavoidable.

Diode rectifier

If the rotor currents are not diverted through an alternate circuit path, they will flow onto the DC-link via the anti-parallel 'freewheel' diodes that partner each switch in the three-phase converter. With the switches off, the converter appears initially to the rotor circuit as a three-phase rectifier, and a large rise in DC-link voltage may ensue. After the rotor currents reach zero, the diodes become reverse-blocked and no longer conduct. This concept is further explored in Chapter 6.

5.5.2 Line-side converter fault response

At fault initiation the supply voltage drops almost instantaneously. For 2-3 PWM cycles the voltage across the line-side converter filter is large, driving an immediate current rise. Unlike the rotor case, the total flux held by the filter chokes is small and there is no magnetic driver for an extended period of over-currents. The rate of current rise is limited by the time constant of the converter's filter, far longer than the PWM period. The line-side controller rapidly drops its output modulation and the current is brought back under control in 3-4ms. The current spike is unlikely to exceed the protection limits of the converter.

The line-side current may be controlled throughout the fault period as long as the DC-link voltage remains within operational limits. However, the active power in or out of the converter is limited by the retained balanced supply voltage. In the case of a true short-circuit the converter cannot transmit power, only dissipating a maximum of rated current over the resistance of its filter. This realistically sinks not more than a percent of

rated power. In this situation the line-side converter may not be able to balance the rotor circuit power input, leading to a DC-link over-voltage event.

5.5.3 DC-link response

DC-link capacitance

The balance of power in and out of the power converter is buffered by the energy stored on the capacitive DC-link. The capacitance of the DC-link is specific to each converter, but it must be able to balance swings of rated power and stay within safe limits. For a rough estimate, assume that the capacitance of the DC-link is sufficient to absorb a power difference of up to around 1 p.u. (converter-rating) across the converter for one millisecond without changing the DC voltage by more than 5%. This allows the line-side converter to react to changes in rotor conditions within a few PWM cycles and maintain control of the DC-link voltage. This level of voltage ripple sets a capacitance value of roughly 20 p.u. [8], defined against 1 p.u. operational DC voltage and a 1ms time-base.

Rated current

Rated current through the DC-link capacitance is significantly smaller than rated current on the rotor circuit. The rotor p.u. base is given in Eq. 5.75 with regards to the machine power rating, stator line-line voltage and the turns ratio; using the zero subscript to indicate p.u. base values.

$$i_{r0} = \frac{\sqrt{3}P_0 a}{V_{s0}} \tag{5.75}$$

The converter power is set by the maximum operating slip, s_{max}. DC-link capacitor rated current is therefore:

$$i_{dc0} = \frac{P_0 s_{\max}}{V_{dc0}} \tag{5.76}$$

The average value of rectified ac current is 1.35 times the per-phase value [66]. Also, the maximum slip is approximately equal to the turns ratio, hence:

$$\frac{i_{r0}(dc)}{i_{dc0}} \approx \frac{2.34V_{dc0}}{V_{s0}} \tag{5.77}$$

In normal operation, DC-link current from the rotor-side converter is passed through the line-side converter. However, if transient rotor conditions demand a current in excess of the ratings of the line-side converter, the imbalance will flow into the DC-link

[8] For a capacitor, estimation of the voltage change made using $E = \frac{1}{2}CV_{dc}^2$

capacitance. According to Eq. 5.75, with a 415VAC supply and a 750V DC-link each p.u. of rotor over-current equates to 4.2 p.u. current through the DC-link.

Current spikes

Current spikes such as produced by the short-circuit response of the line-side converter can be safely absorbed by the DC-link capacitance. However, grid fault rotor over-currents are sustained for the rotor transient time constant, some tens of milliseconds. Using the dc-current approximation from Eq. 5.75, a rotor over-current of 5 p.u (machine-rating) compared with 1 p.u. line-side converter current leads to over 15 p.u. DC-link transient current, causing a dangerous rise in DC-link voltage. If the converter remains connected to the rotor, a large DC-link voltage spike will occur.

5.6 DFIG response to a grid short-circuit

5.6.1 A short-circuit grid fault

An example of the short circuit fault response of a representative wind turbine DFIG is shown in Figure 5.13 - Figure 5.18. The fault applied was a worst-case zero voltage fault as defined by GB grid code (Section 2.5): a close-up short circuit lasting for 140ms. The recovery voltage was fixed at 0.9 p.u. for the remainder of the test, as per GB grid code.

5.6.2 Test rig setup

The DFIG setup is the 7.5kW test facility, described fully in Chapter 4. The mechanical torque was provided by a DC machine controlled to simulate a wind turbine and its flexible-coupling drive-shaft. The DFIG was controlled to generate at unity power factor under healthy voltage conditions and to export up to 0.67 p.u. of reactive-power producing rotor current in response to voltage drops below 50% (detailed in Chapter 6). Otherwise no special arrangements were made for fault response. Pre-fault conditions consisted of rated rotor speed, specifically 12% above synchronous (1680rpm), and 67% rated power generation (5kW), which corresponds to a typical operational state (Section 4.2.1).

The grid fault was effected by the grid fault-emulation equipment described in Chapter 4, including a 0.15 p.u. series reactance chosen to represent a typical network connection impedance.

5.6.3 Short circuit test response

Stator voltage

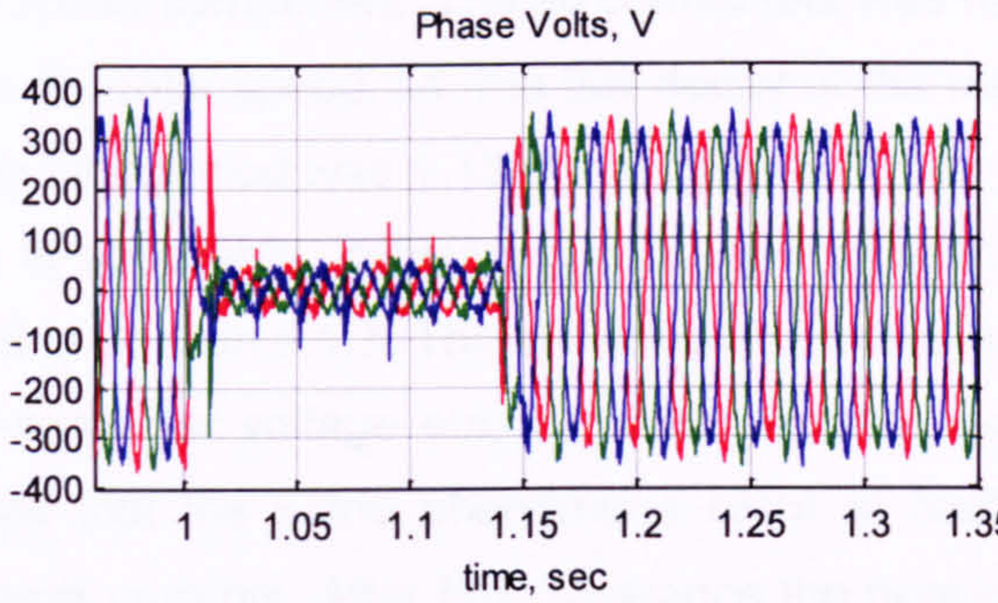

Figure 5.13. DFIG 0% fault response – stator voltages.

The stator voltages show a rapid collapse to below 50V rms per-phase in 2ms (Figure 5.13). The local voltages were maintained at around 30V rms per-phase during the fault. There is a small but not insignificant high frequency (~1kHz) component which makes the signals appear thicker. This frequency corresponds with the high-frequency noise on the line-side converter currents (Figure 5.18) and vanishes after fault clearance.

DFIG currents

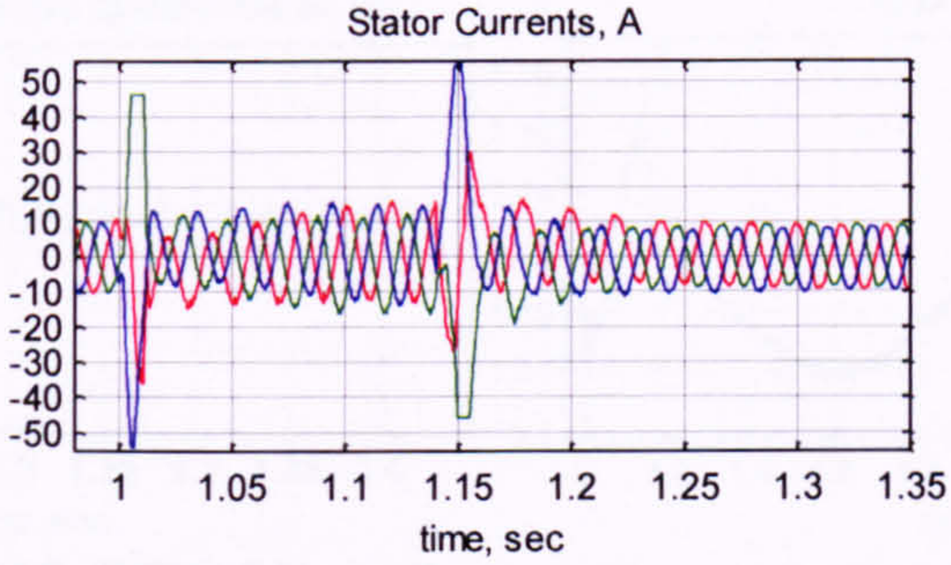

Figure 5.14. DFIG 0% fault response – stator currents.

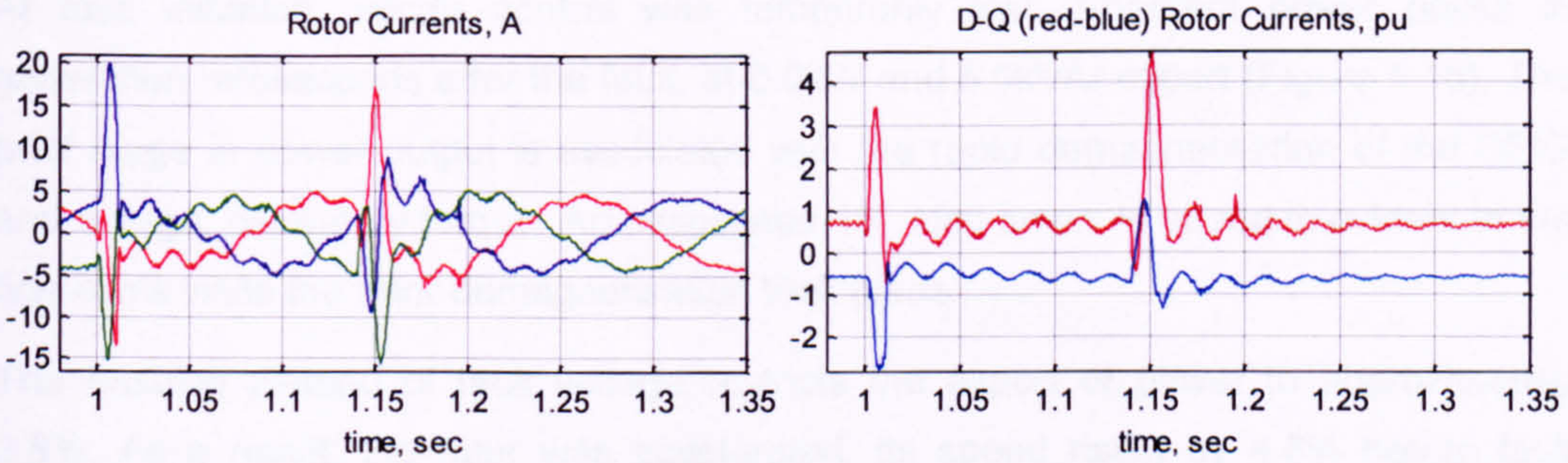

Figure 5.15. DFIG 0% fault response – rotor currents.

The most notable effects are the current spikes on fault initiation and clearance. The rotor currents peak at 20A (4.2 p.u., 4.5 times pre-fault) on fault initiation and 17.5A (3.7 p.u., 4.0 times pre-fault) on fault clearance (Figure 5.15). This is far in excess of a typical DFIG converter's maximum current limit. The stator current peaks exceed 50A in each case, around the saturation level of the test rig current sensors (Figure 5.14).

In the rotor circuit the initial spike lasted less than 20ms, while a 0.23 p.u. ac component seems to extend throughout the fault. These are both superposed on a dominant, 1 p.u. slip speed component. The ac component was measured as 56.0 ±0.6 Hz, and so relates to the rotor speed, i.e. the flux decay of the stator circuit. The mean speed throughout the fault period was 1.13 p.u. (Figure 5.16), or 56.5Hz, and so a 1% frequency reduction is noticeable, concurring with the magnetic-alignment frequency adjustment described in Section 5.1.7. The slip speed contribution is a consequence of the continuing rotor-converter voltage output, which appears roughly constant in the excitation-frame. Note that the same phenomena recur at fault clearance, with 90-100% comparative peak currents. After fault clearance the near-rotor-speed frequency component of rotor current endured for 80ms. Respectable control of rotor current was regained within 50ms of fault clearance.

The stator circuit is very similar, allowing for the relative frequency components in the stationary frame of reference. The initial current spike was extinguished in less than 20ms while a small, near-dc component seems to extend throughout the fault. Both components are superposed on a dominant, near 1 p.u. system frequency component.

Power and speed

Figure 5.16. DFIG 0%-fault response – power and speed.

At fault initiation, vector control was temporarily lost. Apparent power peaks in generation milliseconds after the fault, at 6.0kW and 6.0kVAr export (Figure 5.16). The brief surge in power output is associated with the rapid demagnetisation of the DFIG and a large, oscillatory torque. An associated 1% 'kick-down' in speed is evident in the first 40ms while the rotor demagnetisation took place.

The ensuing plateau of fault voltage restricts the export of power to approximately 2.8%. As a result, the rotor was accelerated, its speed rising by 4.5% before fault clearance. After clearance, the power controller required 500ms to settle the highly oscillatory output, although a mean value of 90% power export was established only 40ms after fault clearance. This capability is in proportion with the magnitude of the recovery voltage and allowed the rotor speed to be stabilised. The modelled wind turbine blade-pitch controller acted to restrain the input power during the recovery

period just sufficiently to return the speed to its rated value. However, the poorly damped rotor-shaft continued to resonate at ~1.1Hz for several seconds. Note that fault clearance triggered a 2% speed kick similar to that at fault initiation. This indicates a burst of power associated with the re-magnetisation of the DFIG.

Similarly, reactive power rose quickly after fault initiation to the same peak level as the active power, 6.0kVAr, before rapidly decaying. The DFIG controller attempted to maximise reactive output during the period of fault voltage: here -0.67 p.u. rotor reactive current on the rotor windings delivered 0.14 p.u. reactive power into the grid connection and a stator voltage of 0.16 p.u. was maintained. Fault clearance produced a very large swing in apparent power. The reactive power surged towards 15kVAr import as the DFIG re-magnetised. However, this effect lasted for less than one system cycle, with only a fleeting impact on the stator voltages (note the minor suppression to the recovery voltages from 1.14s to 1.15s in Figure 5.13).

Power converter

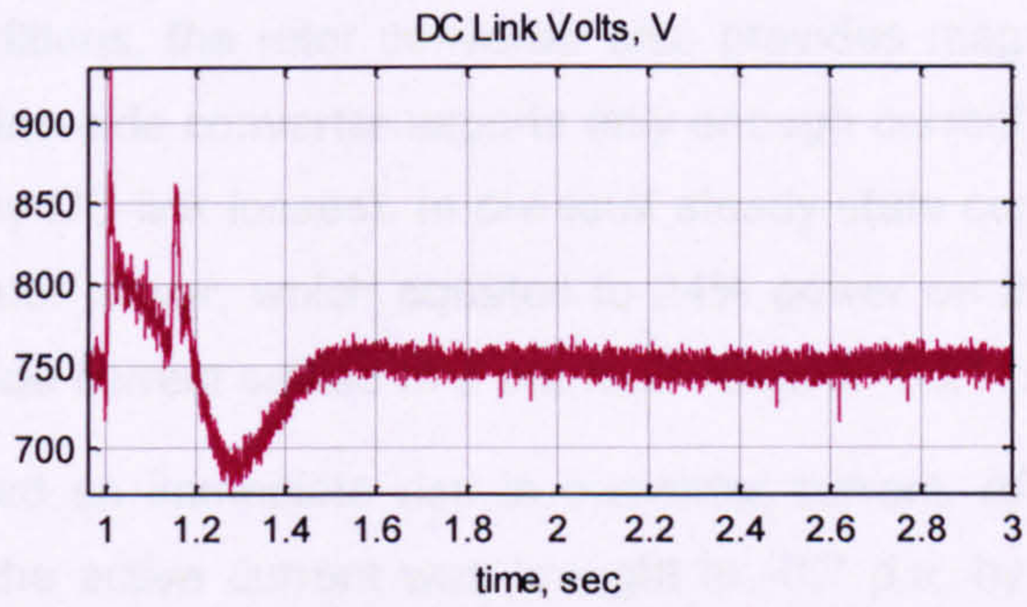

Figure 5.17. DFIG 0% fault response – DC-link voltage.

The Converter's DC link voltage response is shown in Figure 5.17. At fault initiation, the machine generation process caused a massive short-term surge in power output as described in Section 5.5.3. Almost immediately a rapid rise in DC-link voltage was recorded, more than 75V in 2ms, as this energy was deposited onto the DC-link capacitance. At 810V a brake chopper safety device was engaged, adding a parallel resistance across the DC-link to sink excess power. The line-side converter has severely limited power export capability during the fault and the DC voltage was only slowly brought down. The brake chopper is designed to disengage itself below 795V, by which time the rotor flux had mostly decayed. The rotor power was thereafter negligible until fault clearance, while the DC-link voltage was controlled slowly towards 750V. At fault clearance a similar rotor power surge created a second, smaller DC-link voltage spike. During fault recovery however, the line-side converter recovered its power export capability and the DC-link voltage was safely brought under control. The power surge associated with fault clearance can be seen in the active power spike and rotor speed kick at 1.14s in Figure 5.16.

The brake chopper is a non-standard feature on large DC-link power converters. In these tests however, it is clear from the rapid rise of voltage that serious damage would otherwise have been sustained to the converter's capacitors. The brake chopper is discussed in greater detail in Chapter 6.

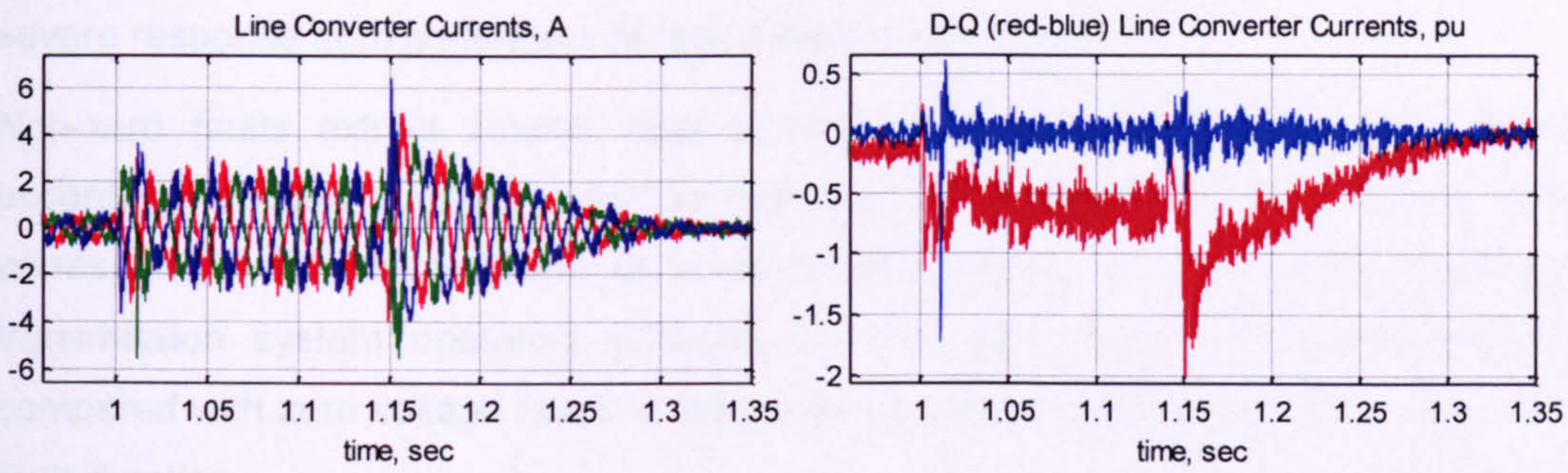

Figure 5.18. DFIG 0% fault response – line-side converter currents.

The line-side converter currents appear thicker with high frequency noise due to the relatively low-impedance low-pass filter fitted to the converter. Note that the pre-fault currents are far smaller than the rotor because only active power is delivered to the grid. In normal conditions, the rotor converter also provides magnetisation current to the generator. The line-side converter exports only enough current to balance the rotor power input (and any DC-link losses). In pre-fault steady-state conditions this leads to 12% of the 67% stator power, which equates to 24% power on the converter. The d-component of line-side current settled to a pre-fault value of -0.21 p.u.

The grid fault caused an immediate rise in converter current. After a small spike in current to 1.1 p.u. the active current was brought to -0.7 p.u. by the controller in an attempt to reduce the DC-link voltage. However, the supply voltage was so low that the resulting power export had little effect. The impact of fault clearance is more pronounced, as the converter could export significant power and bring the DC-link voltage under control. The d-component of current hit -1.5 p.u. before the voltage error was reduced and the current returned towards a controlled steady-state level. This was successfully achieved in a measured fashion over a 200-300ms period following fault clearance.

It is assumed that both converters are rated for the same current, although this may not be necessarily the case as the operational demands on the line-side converter are smaller. In this extreme test of a grid fault short-circuit response, a 75% rated line-side converter would have remained connected and stable throughout the fault period, assuming its devices carried a roughly 2 p.u. short-term over-rating capability (Chapter 6).

5.7 Non-zero fault response

A grid fault may occur at a considerable distance from the generator. As a result of the interposing impedance, the fault voltage experienced by the generator may be anything from zero to rated value, as explained in Chapter 2. These non-zero faults elicit a less severe response from generators at fault initiation and clearance.

Non-zero faults extract smaller fault currents from generators in general, which accordingly require a longer period to trigger power system protection devices. This corresponds with the envelope of credible fault voltage profiles fixed by national transmission system operators (Chapter 2). The key issue with non-zero faults compared with zero voltage faults is therefore a question of stability over an extended fault duration.

5.7.1 Non-zero fault response of a DFIG

Superposition of retained-voltage and lost-voltage elements

The generalised machine equations (Eqs. 3.26 - 3.31) are linear differential equations. Therefore independent solutions for different components of voltage may be linearly combined for a final solution providing they meet all the necessary boundary conditions. Now, a three-phase voltage dip comprises two components: the retained voltage and the 'lost' voltage due to the fault. Assuming (approximately) constant rotor speed as before, the machine equations are solved separately for each of the retained and lost voltage components. The two partial solutions are added to form a complete solution.

The above description does not account for the non-linear response of the power converter, nor the vagaries of magnetic saturation. The analytical solution can be used to generalise the induction machine's non-zero fault response, an approach which compares well with the test rig results presented later in this section.

Description of a 15%-fault response

Consider a grid fault causing the local grid voltage to fall to 15% of rated value for an arbitrary period. The fault response comprises the 15% retained voltage component superposed with the response to a drop of 85%.

15% of the machine's internal mmf will continue to be driven around the airgap by the remaining voltage. 15% of the rotor emf will appear to the converter in the excitation frame exactly as before the fault. Ultimately the DFIG may operate continuously into the fault with 15% currents and 15% voltage, as long as the rotor speed remains stable.

At the same time, 85% of the flux is unsupported by the fault voltage. This 85% will decay, chiefly via leakage flux paths, in the manner described in Section 5.1. Referring to the stator current approximation from Eq. 5.10, an estimate of the 15%-fault response for stator current is shown in Eq. 5.78 (assuming no additional magnetic saturation and a linear control response).

$$\bar{i}_s^s(t) \approx 0.85\left(\frac{\overline{\psi}_{s0}^s}{L_s'}e^{-t/\tau_s'} - \frac{\overline{\psi}_{r0}^s}{L_s'}\frac{L_m}{L_r}e^{-t/\tau_r'}e^{j\omega_r t}\right) + 0.15\bar{i}_{s0}^s e^{j\omega_e t} \tag{5.78}$$

It is clear from this characterisation that the excesses of peak currents and torque output will be proportionally smaller for less severe dips of supply voltage.

5.7.2 15% fault test response

To contrast with the relatively short 140ms zero-voltage fault, the second example was chosen to represent a longer-duration 'deep' fault. The applied fault was a drop to 15% voltage lasting 500ms, approaching the limiting fault voltage profile defined by grid codes for Ireland, USA and Canada (Section 2.5). The recovery voltage was fixed at a grid-code-typical 0.9 p.u. for the remainder of the test.

Fault test setup

The test rig was setup exactly as for the short-circuit test in Section 5.6, with rated speed of 1.12 p.u. (1680rpm) and a power output of 0.67 p.u. (5kW).

Stator voltage

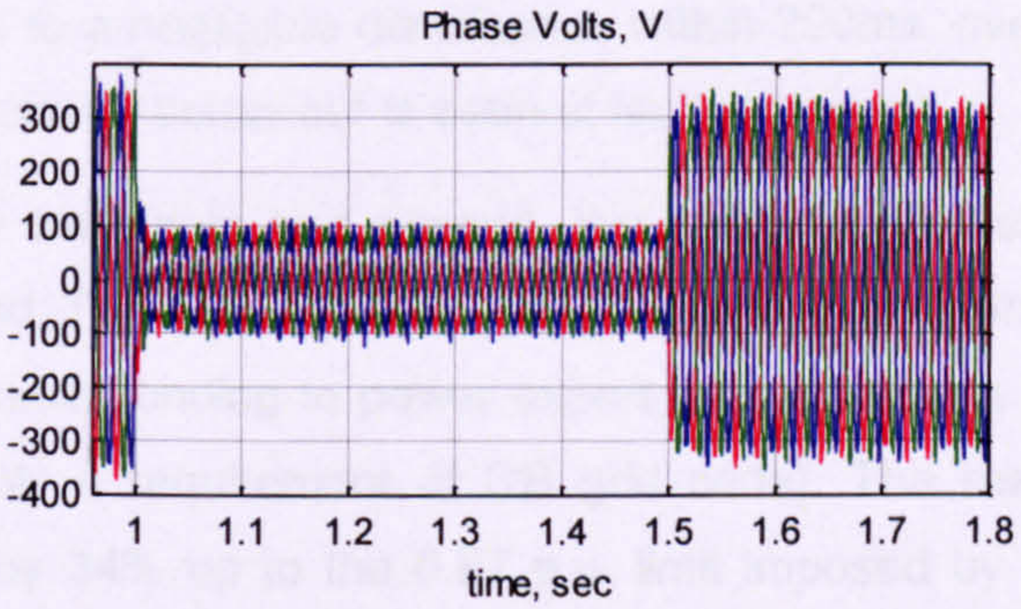

Figure 5.19. DFIG 15% fault response – stator voltages.

The stator voltages show a rapid collapse to 0.26 p.u. (Figure 5.19). After a 50ms settling period, 28% voltage was maintained throughout the fault period.

DFIG currents

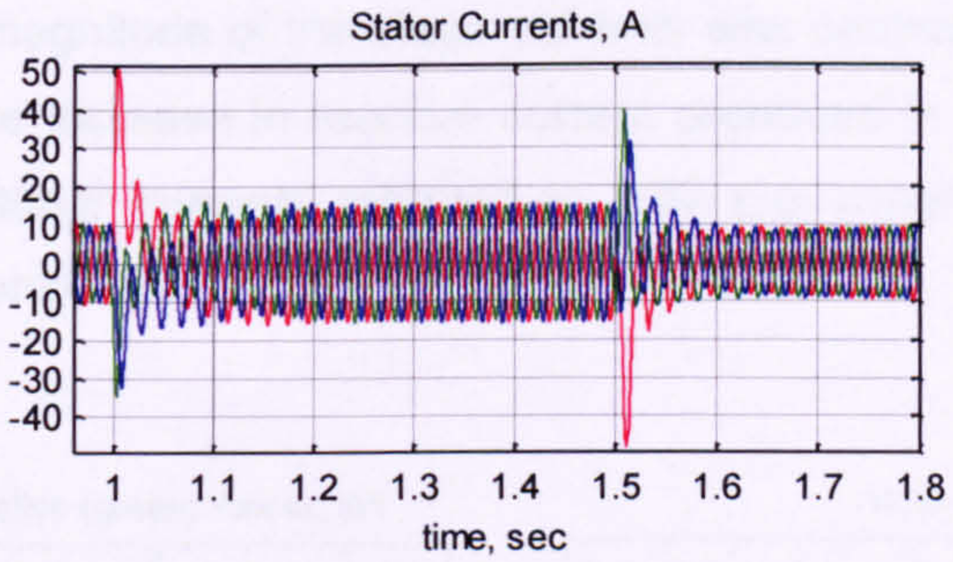

Figure 5.20. DFIG 15% fault response – stator currents.

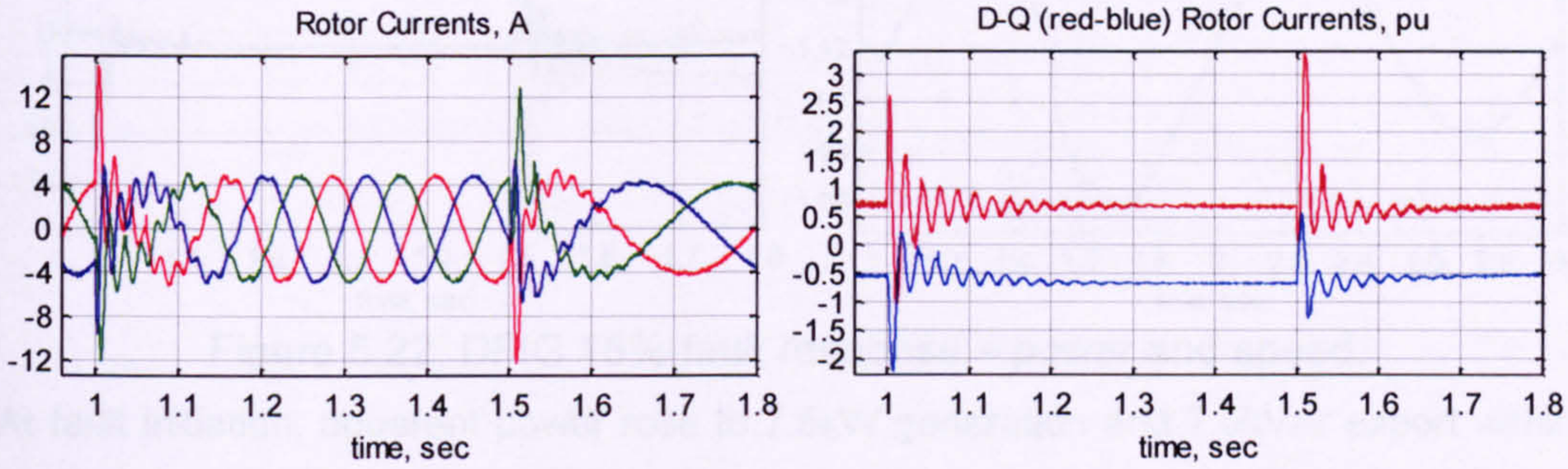

Figure 5.21. DFIG 15% fault response – rotor currents.

The rotor currents behave similarly to the short-circuit case, except with smaller peak values and a clear period of good control prior to fault clearance. Rotor peaks were 15.2A (3.2 p.u.) on fault initiation and 13.0A (2.7 p.u.) on fault clearance (Figure 5.21). This is well beyond the short-term capabilities of a typical DFIG converter. The ac contribution was measured at 55.5 ±0.6 Hz, at least 1% below the equivalent rotor speed, and decayed to a negligible disturbance within 200ms, over a time constant of roughly 30ms. Very similar behaviour is seen at fault clearance.

After the flux decay transients had passed, the rotor currents showed good control during the fault period. The active component of current was maintained at the pre-fault value of -0.7 p.u., corresponding to power export in proportion to the retained voltage (Figure 5.22) (notably a requirement of GB grid code). The reactive component of current was raised by 34% up to the 0.67 p.u. limit imposed by the DFIG controller. This created an over-magnetisation of the rotor and generated 18% reactive power at the stator terminals. This boosted the stator voltage by 13% above the grid fault voltage (Figure 5.19).

The stator currents each show a substantial near-dc offset at fault initiation and fault clearance in Figure 5.20. The twin-component flux decay description suggests a contribution at near-rotor speed, but this component is very difficult to distinguish from the continued 50Hz fundamental driven by the controlled rotor excitation. The near-dc component decayed over a timescale of approximately 30ms, just as with the near-rotor speed component of the rotor current response. Peak stator currents reached 49A

(3.3 p.u., 5.0 times pre-fault) on fault initiation and a fraction less at fault clearance. During the fault, the magnitude of the stator currents was controlled to just over 1 p.u. This is because of the increase in reactive current produced in the fault period. After fault clearance, the stator currents returned to 0.67 p.u. magnitude delivering unity power factor. Good control was restored in a little over 0.1s.

Power and Speed

Figure 5.22. DFIG 15%-fault response – power and speed.

At fault initiation, apparent power rose to 7.5kW generation and 7.5kVAr export within 10ms, before exhibiting a near-dc and near-rotor speed ac twin-frequency composition which died away after around 200ms (Figure 5.22). Active power settled to 1.5kW output and reactive power to 1.3kVAr export until fault clearance. As discussed, the reactive component augmented the stator terminal voltage by 13%, which in turn permitted greater power output during the fault period. Fault clearance triggered more challenging peaks of 19.6kW power output and 12.9kVAr reactive import, each lasting no more than 10ms. The highly oscillatory transient components rapidly deteriorated over a timescale of roughly 30ms once more, while the mean value was brought steadily towards pre-fault values during the proceeding 0.5s.

The speed plot (Figure 5.22) reveals a speed kick-down of 0.25% associated with the brief surge in power output following fault initiation. After this transient, the sustained electrical power output was roughly in proportion to the retained balanced voltage, i.e. 28%, a shortfall of 39% compared with the input power during the fault period. As a result the rotor accelerated sharply, completing a 2.5% rise in 100ms. However, in this period the torsion of the modelled rotor-shaft winds up relative to the slow moving wind turbine end. The acceleration was checked and the speed response became dominated by a drive-train resonant frequency at 1.1Hz which did not settle for many seconds. A second speed step-down of 1.0% immediately followed from fault clearance, in-phase with the mechanical resonance, which led to the peak speed deviation of 6% below rated. The peak of rotor speed was no more than 4.5% above the pre-fault value.

Power converter

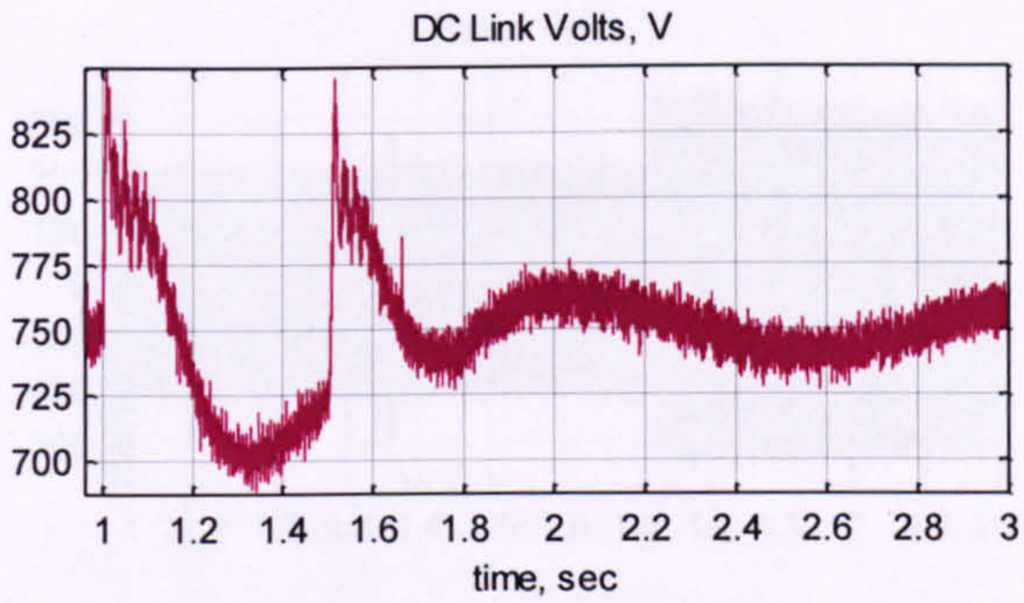

Figure 5.23. DFIG 15% fault response – DC-link voltage.

The power surge following fault initiation and clearance again prompted a rapid DC-link voltage rise, here roughly 75V at initiation and clearance (Figure 5.23). The first voltage rise triggered the brake chopper which recovered voltage stability and disengaged after 40ms when the voltage dropped below 795V. The line-side converter's PI controller undershot by 7% in resuming voltage control, with the accidental benefit of restricting the maximum DC-link voltage experienced at fault clearance to 800V.

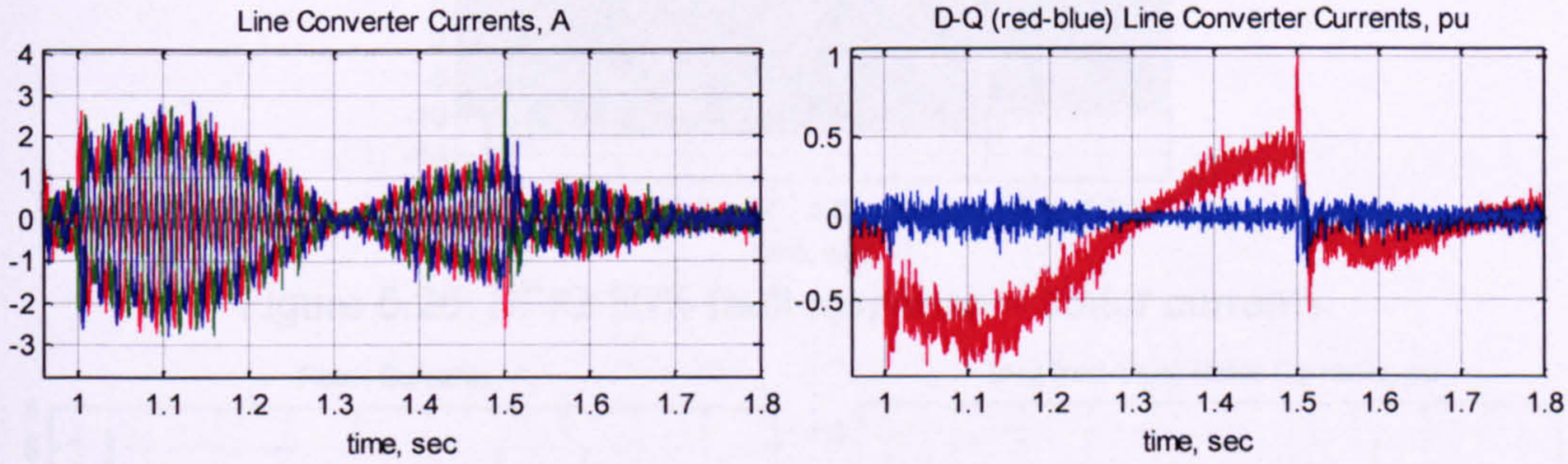

Figure 5.24. DFIG 15% fault response – line-side converter currents.

The line-side currents of Figure 5.24 show graphically the overcompensation of the DFIG controller in attempting to regain control of the DC-link voltage during the fault period. The reactive component remained controlled to zero throughout the test. The magnitude of the three-phase currents nowhere exceeded the converter's rated limits.

5.7.3 50% fault test response

The final example was chosen to represent a credible mid-depth fault. The applied fault was a 50% fault of the longest duration defined by GB grid code (Section 2.5), 720ms. The recovery voltage was fixed at 0.9 p.u. for the remainder of the test, in line with GB grid code.

Fault test setup

The test rig was setup exactly as for the short-circuit test in Section 5.6, with rated speed of 1.12 p.u. (1680rpm) and a power output of 0.67 p.u. (5kW).

Stator voltage

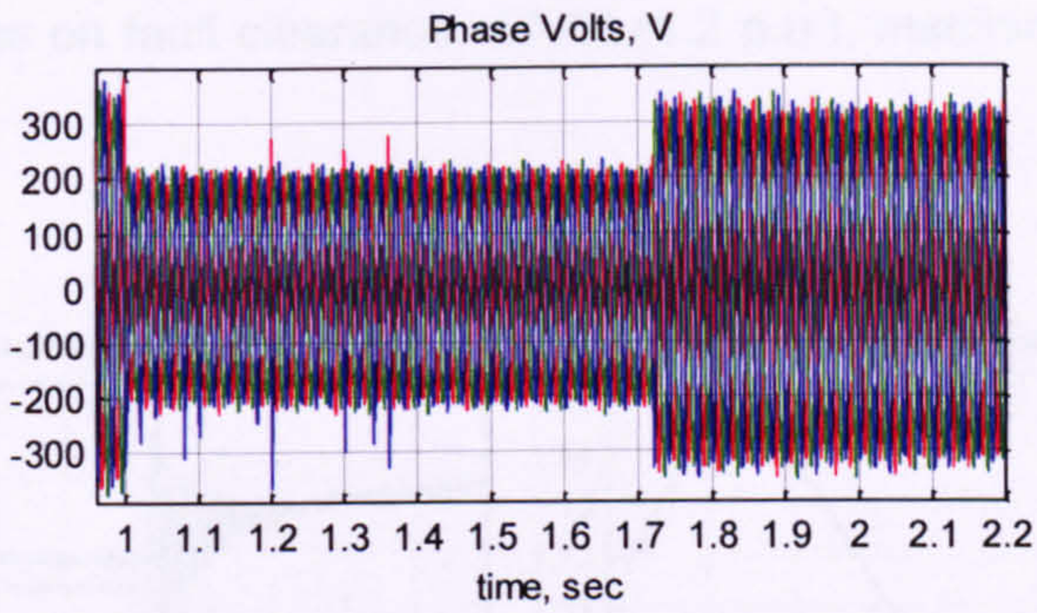

Figure 5.25. DFIG 50% fault response – stator voltages.

The stator voltages show a rapid collapse to approximately 0.65 p.u. (Figure 5.25). This level was maintained throughout the fault.

DFIG currents

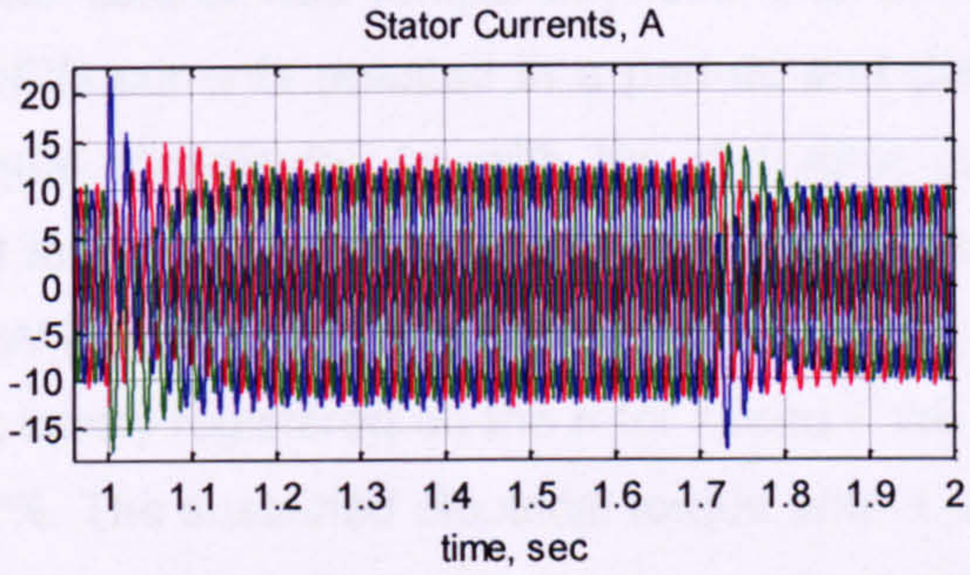

Figure 5.26. DFIG 50% fault response – stator currents.

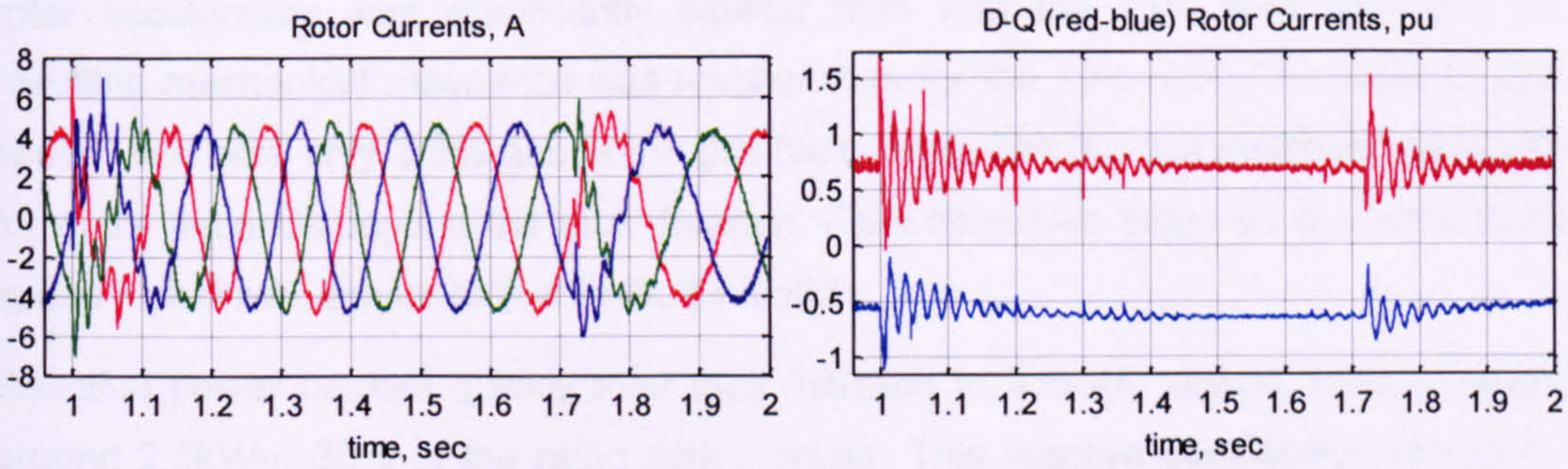

Figure 5.27. DFIG 50% fault response – rotor currents.

The maximum currents on the three phase measurements are very much smaller than for the short-circuit 0% fault. The rotor currents here register a maximum spike at 7.1A (1.5 p.u.) on initiation and 5.9A (1.2 p.u.) on clearance (Figure 5.27). This is well within the short-term capabilities of a typical DFIG converter. For a 200ms period after fault initiation and fault clearance a small near-rotor speed contribution is superposed on the rotor currents without exceeding the rated limits. The frequency of this component was measured as (55.9 ±0.6) Hz, very similar to that of the short-circuit response. This ac component is most noticeable on the d-q graph, which also presents a 30% in-fault increase of the reactive (q-) component of rotor current. The mean value of this over-magnetisation component steadily returned towards its pre-fault value after fault

clearance. In Figure 5.26 stator current spikes touch 21.6A (1.5 p.u.) on fault initiation and substantially less on fault clearance, 17.4A (1.2 p.u.), matching the rotor currents in p.u. terms.

Power and speed

Figure 5.28. DFIG 50%-fault response – power and speed.

At fault initiation, vector control was temporarily lost. The combination of frequency components on the DFIG currents resulted in a part-dc and part-ac apparent power, initially of roughly equal magnitude. As with the d-q rotor current, the oscillatory contributions decayed inside 200ms. Active power peaked in generation milliseconds after the fault, at 6.0kW (Figure 5.28), and slowly settled to 3kW generation. The brief surge in power output barely registered on the rotor speed – the associated kick-down in speed was only 0.2%. The sustained electrical torque output was proportional to the retained balanced voltage, offering 0.65 p.u. throughout the fault period. The resultant rotor acceleration was significantly smaller than with the 15% fault test, and the resulting mechanical resonance was weaker than for the 15% fault. The peak of rotor speed was here only 2.5% above the pre-fault value. The 1.1 Hz oscillation extended for many seconds beyond the fault duration. Fault clearance triggered a modest 0.2% speed kick-down, similar to that at fault initiation.

Reactive power peaked quickly after fault initiation to 3.8kVAr export, before settling around 2.3kVAr, 30% of the rated active power. This reactive contribution raised the stator voltage by 15% above the grid fault voltage, as shown in Figure 5.25. Fault clearance produced an immediate swing in apparent power; the reactive power plot displays instantaneous peaks at 2.4kVAr import and again 3.8kVAr export. This reactive contribution was steadily controlled to zero in approximately 0.5s. The highly oscillatory contributions decayed in approximately 200ms, just as for fault initiation. Overall, neglecting sub-20ms oscillations in instantaneous power, the power output was well-controlled and contributed positively during the fault.

Power converter

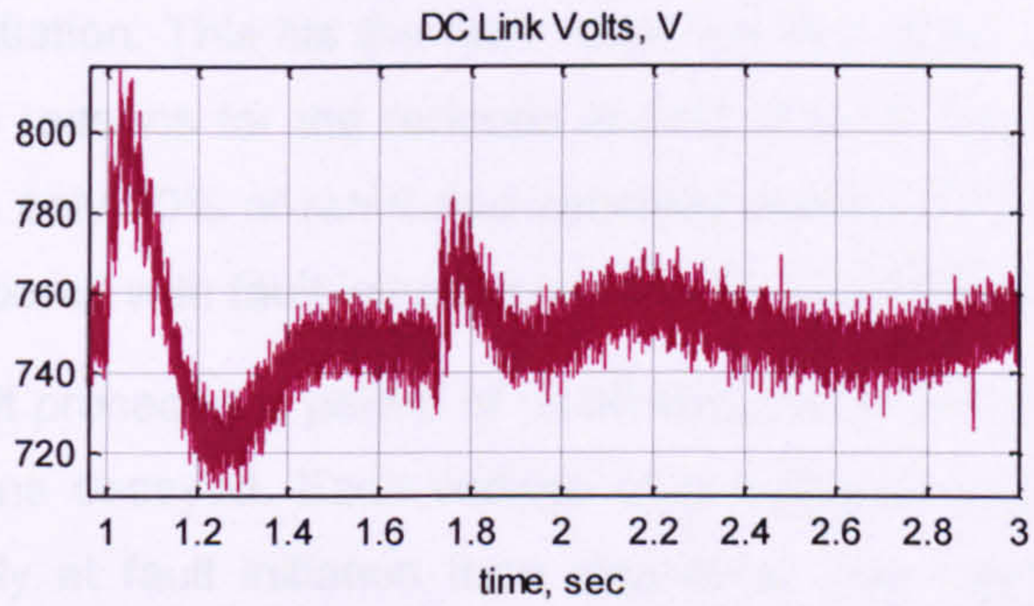

Figure 5.29. DFIG 50% fault response – DC-link voltage.

The Converter's DC link voltage response is shown in Figure 5.29. At fault initiation, the short-term surge in power output caused a surge in DC-link voltage, almost 40V in 2ms, roughly half the rate seen during the 0% fault test. With 65% voltage retained at the stator connection, the power export capability of the line-side converter was sufficient to bring the DC-link voltage back under control without exceeding 810V. Fault clearance instigated a 25V spike, following which the voltage was comfortably brought back under control.

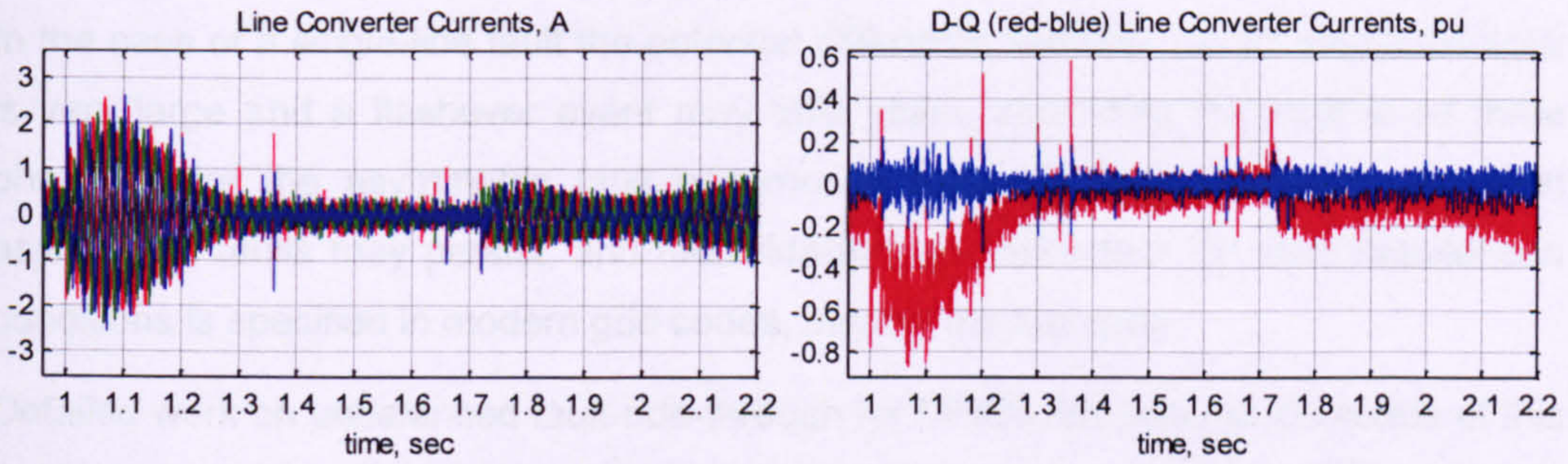

Figure 5.30. DFIG 50% fault response – line-side converter currents.

The grid fault elicited an immediate rise in the direct (d-) component of line-converter current, to -0.7 p.u. peak, after which the DC-link voltage was restored to 750V. The phase currents remained well within converter ratings.

5.7.4 Summary of test response

The non-zero faults each exhibited the twin-frequency decay transients and continuous system frequency contributions as described in Section 5.4. The current spikes at fault initiation were somewhat lower than the proportional voltage drop in each case: compared with the short-circuit rotor current peak of 4.5 p.u., the 15% fault experienced 3.2 p.u. (71%) and the 50% fault 1.5 p.u. (33%). The lower proportion of demagnetisation in fact allowed the DFIG controller to restrict the current rise (a little). The 50% fault in fact provoked a mild fault response which required no fault ride through intervention for converter protection.

In these non-zero fault tests fault clearance produced current spikes of roughly 80% the value at fault initiation. This fits the fault response description of a smaller voltage step. There are two reasons for the reduced impact of fault clearance: firstly that the clearance voltage is only 90% of rated and secondly that the DFIG controller lifted the in-fault voltage compared with fault initiation by means of controlled reactive output.

In each test the fault preceded a period of oscillatory power and current output as the transient contributions decayed. Each voltage step triggered a rapid DC-link voltage rise, more noticeably at fault initiation than clearance. The rapid power fluctuations excited low-speed resonance in the turbine rotor, although the worst deviation was 6%, comfortably within safe operating limits during fault recovery.

5.8 Unbalanced fault response

As explained in Chapter 2, the largest proportion of grid faults concern individual transmission lines, the most common being a single-line-to-ground fault. Most faults are therefore asymmetrical in nature, providing additional challenges for fault-ride-through behaviour.

In the case of a single-line fault the potential difference between the transmission lines is very large and a flashover event may take place, spreading the fault to all three phases; here the asymmetric fault becomes a balanced fault. However, stubborn asymmetric faults may persist, and fault ride through behaviour for such unbalanced conditions is specified in modern grid codes, notably the GB code.

Detailed work on unbalanced fault-ride-through for DFIGs lies beyond the scope of this work. An overview of the key points is given below. Techniques for DFIG control in unbalanced conditions are reviewed in Chapter 6.

5.8.1 Sequence components

Any unbalanced three-phase system may be described as a combination of three sequence components: a positive-sequence set rotating at +50Hz, a negative-sequence set rotating at -50Hz and a dc-offset zero-sequence set [22]. The degree of unbalance is indicated by the amount of negative sequence with respect to the positive. The different types of unbalanced faults experienced by a power system are characterised in [19].

In space vector terms the locus of supply voltage changes from a circle to an ellipse, as shown in Figure 5.31. The zero-sequence component is considered separately.

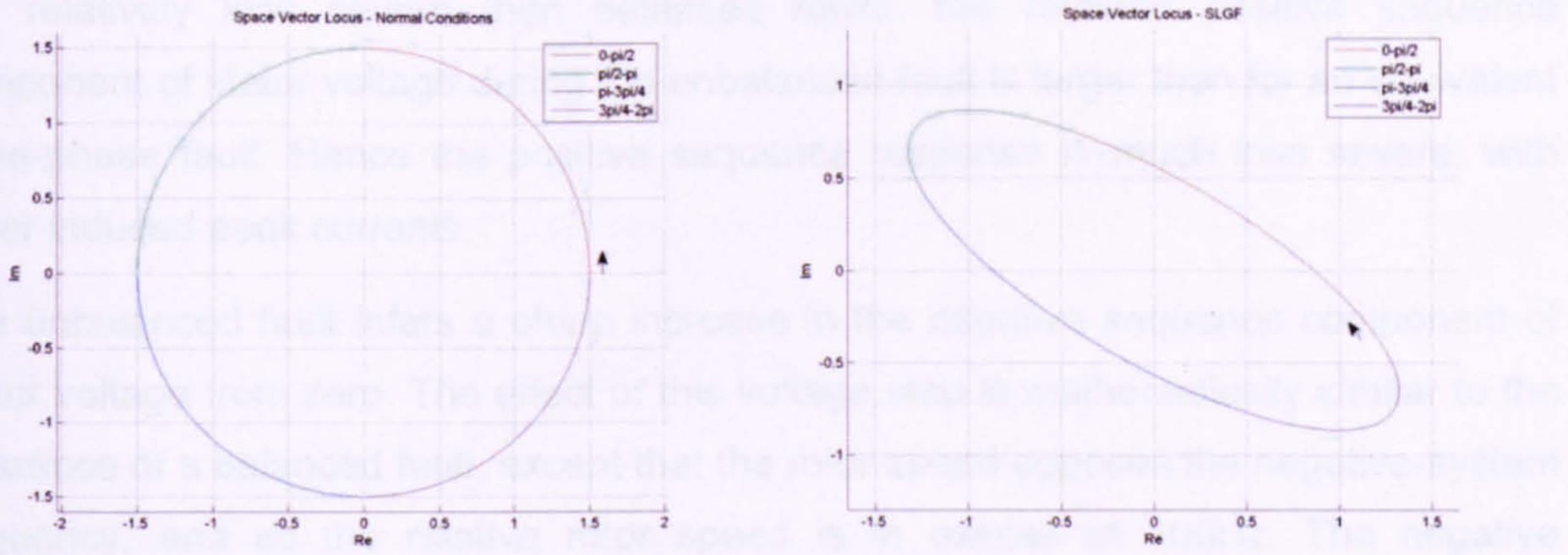

Figure 5.31. Space vector loci of voltage under: (left) balanced conditions (right) a single-line-to-ground fault.

5.8.2 DFIG response to unbalanced conditions

General response

Power and current control of a DFIG with a standard vector controller in response to an unbalanced voltage fault is far poorer than for a balanced fault, throughout the fault and for a considerable period into fault recovery. This is largely due to the unmanaged negative sequence presence imposing twice system frequency oscillations on the stator currents and equivalent frequency oscillations on the rotor currents. However, the net internal magnetisation lost is less than for an equivalent percentage voltage drop in *all three* phases. The peak currents on fault initiation and clearance are therefore not as severe, and there is less immediate danger to the converter devices.

No zero-sequence

As explained in Chapter 3, all large DFIG wind turbines include a LV:MV transformer to step-up the generator's LV to distribution levels. This three-phase transformer will include a version of the Y-Δ winding arrangement. As a consequence, no zero-sequence component may be transmitted from one side of the transformer to the other. In other words, from any unbalanced grid fault the wind turbine generator experiences no zero-sequence component. Any unbalanced grid fault with a zero sequence contribution will appear less severe at the generator's LV terminals.

Induction machine response

The response to positive and negative sequence components of supply voltage can be considered as mathematically independent solutions, using the same assumptions as for the balanced fault solution in Section 5.2.1. The linearised machine equations can be solved for each sequence component and the two partial solutions superposed.

The positive sequence response is mathematically the same as for the balanced fault, driving transient currents associated with flux decay and a system frequency contribution to current driven by the residual voltage (Section 5.4). Unbalanced faults

are relatively less severe than balanced faults: the retained positive sequence component of stator voltage during the unbalanced fault is larger than for an equivalent three-phase fault. Hence the positive sequence response is much less severe, with lower induced peak currents.

The unbalanced fault infers a sharp increase in the negative sequence component of stator voltage from zero. The effect of this voltage step is mathematically similar to the clearance of a balanced fault, except that the rotor speed opposes the negative-system frequency, and so the relative rotor speed is in excess of 100Hz. The negative sequence voltage drives a certain amount of flux linking stator and rotor around the airgap of the machine at -50Hz with respect to the stator. This induces a roughly 105-110Hz component on the rotor circuit, outside of the normal control range and continuing throughout the fault period.

The negative sequence voltage response, like the voltage recovery process for a balanced fault, provides three fault response components of current on both circuits: one for each of the stator and rotor circuits' flux-transients and a continuous negative-system frequency contribution. This is superposed onto the three fault-response components of current due to the positive sequence voltage drop. The result is a four-frequency component fault current. In the stator frame these are: the near-dc transient, the near-rotor speed transient, the system frequency and twice system frequency contributions.

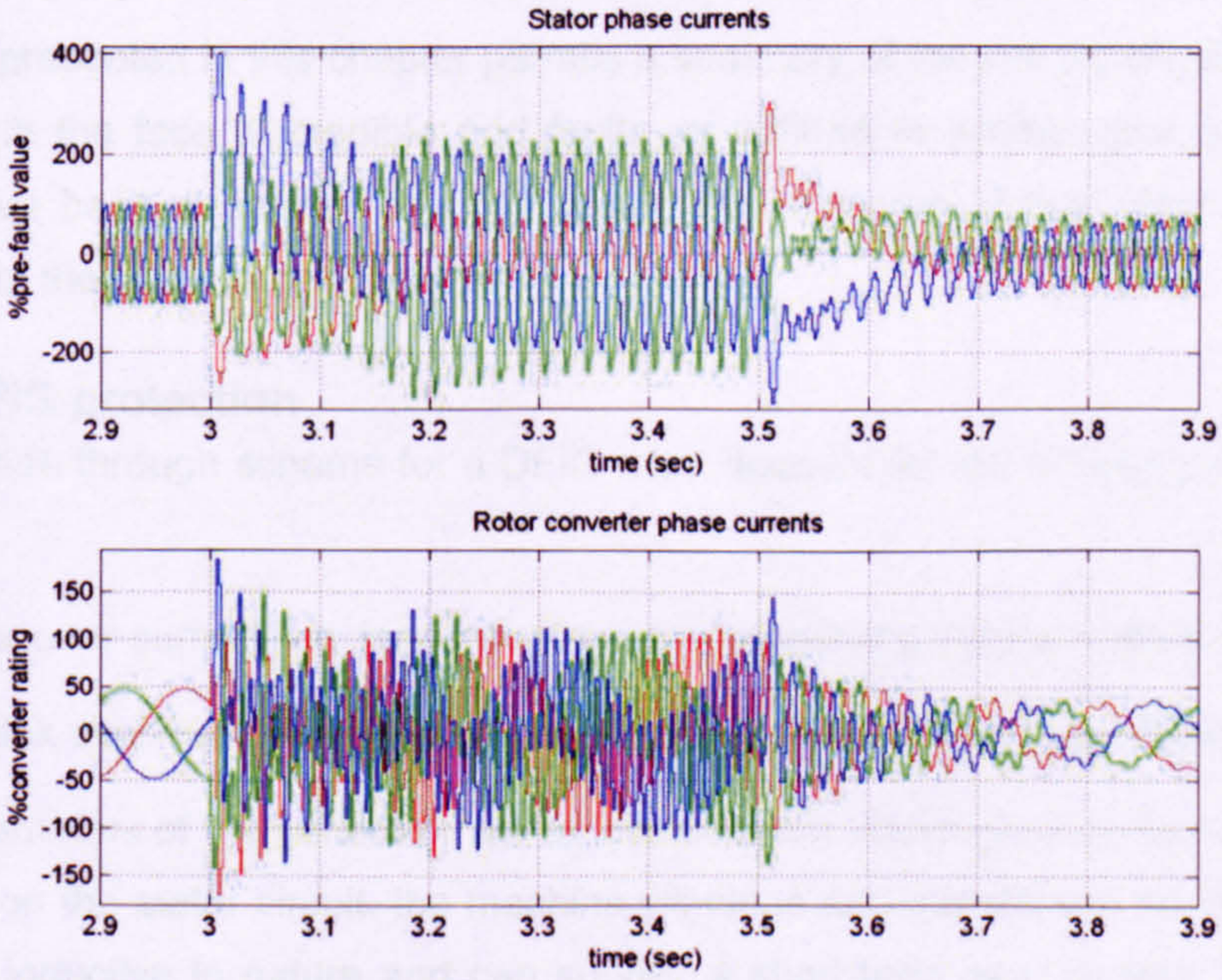

Figure 5.32. Simulated DFIG currents in response to a single-line fault.

To illustrate this point, a single-line-to-ground fault was simulated at the grid connection of a wind turbine DFIG using the Matlab / Simulink simulation model described in

Section 4.3. The DFIG stator and rotor currents are presented in Figure 5.32, where the fault was initiated at 3.0s and cleared at 3.5s. The DFIG was setup to operate at rated speed and 0.40 p.u. power output prior to the fault, while the controller used a conventional PLL scheme for field orientation and the control setup detailed in Chapter 4. Note that the quality of current control during the fault is very poor, although the peaks of rotor current do not exceed 2.0 p.u.

DFIG control response

Standard vector control assumes balanced conditions at the terminals and will neglect any negative sequence component. This may lead the vector controller to mis-position the excitation of the machine and drive unwanted oscillations. In terms of the space vector locus in Figure 5.31, a standard vector controller will approximate a best fit circular locus in positioning its generator emf. This will alternately lead and lag in phase from the elliptical locus of unbalanced voltage, producing the 100Hz oscillatory current described above.

The DFIG may be better controlled by allowing for the negative sequence component. Options for improved vector control of the DFIG in response to unbalanced voltages are reviewed in Chapter 6. In terms of vector control orientation, a digital PLL was developed on the test rig to improve vector field alignment in response to step changes in voltage (Section 4.2.2).

5.9 Key Issues for DFIG fault ride-through behaviour

The work presented in this chapter permits a summary of the key issues for DFIG fault response in the face of credible grid faults as defined in various grid codes. These issues have been separated into two areas: the concerns of the generator and the concerns of the grid system operator.

5.9.1 DFIG protection

Any fault ride-through scheme for a DFIG must account for the following two essential problems:

- Rotor over-current – a danger to the rotor converter's transistor devices.
- DC-link over-voltage – a danger to the converter's DC-link capacitance.

Other parameters of the generator are of less concern. Although over-currents are also produced on the stator circuit, the machine windings and transformer connections of a DFIG are inductive in nature and can survive a short-term over-current. No ac over-voltage can occur, unlike a shunt-capacitor compensated SFIG. A rotor speed excursion may occur, but is very unlikely to rise beyond the limiting capability of the DFIG which can restore speed control during the period of fault recovery.

5.9.2 Transmission system contribution

Grid code fault ride-through requirements were introduced in Chapter 2. Comparing these with the DFIG's standard fault response reveals two key issues: firstly for the generator to remain stable and avoid disconnection, and secondly to provide appropriate power control during the fault period and during fault recovery.

Grid faults inevitably cause a momentary loss of instantaneous power control, but the resulting oscillations in instantaneous power can last less than 1-2 system cycles. The requirements for power control are based on a realistic rms average power output.

Generalising the respective grid code requirements, the DFIG must:

- Remain connected throughout the fault and dynamically stable.
- Not absorb active power. After transients of fault initiation and clearance the DFIG must deliver active power in proportion to the retained balanced voltage.
- Not absorb reactive power. During the fault the DFIG must maximise reactive current output and thereby support local voltages, within rated limits.

Note that the demands for active and reactive power differ. The active power requirement is restricted to proportionality with the retained balanced voltage. The transmission system would naturally benefit from a maximised output to prevent a power shortfall, however, it is deemed unreasonable to demand above rated-current from the generator. On the other hand, the reactive requirement is simply for as much support as can be delivered. A trade-off between active and reactive power priorities must be made in utilising the current limits set by the power converter, a feature discussed in Chapter 6.

5.10 Summary

Summary

A comprehensive treatment of DFIG fault response was presented, starting with the natural flux-driven short-circuit response of the machine before superposing the effects of adding rotor-voltage from the power converter. The power converter's fault response was discussed. Experimental results were presented from tests representing 0%, 15% and 50% grid fault voltages. The effects of voltage unbalance were discussed. Finally, the key issues for DFIG fault ride through were deduced from the work presented in this chapter with reference to the grid code requirements discussed in Chapter 2.

Short-circuit fault response

The voltage drop caused by a grid fault triggers a decay of flux linkage in the induction machine. The natural response of the stator and rotor circuits each comprise two transient decay components: a near-dc decay of self-linking flux and a near-rotor speed

decay of mutual flux. These contribute roughly equal components to the fault currents on each circuit. The stator currents' near-dc component decays with the stator transient time constant, 26ms on the test rig, and the near-rotor speed component decays with the rotor transient time constant, 39ms on the test rig. The converse applies to the rotor circuit currents.

The frequencies of the decay components of current deviate from pure-dc and rotor-speed due to alignment effects in the magnetic fields. This deviation is roughly 1% for a typical machine, but can be over 3.5% with a very high rotor resistance; such as is the case with a crowbar resistance shorted across the DFIG's rotor windings.

The first peaks of over-current on the rotor and stator reach 4-5 p.u. in a typical induction machine experiencing a zero voltage fault, roughly 5ms after the initiation of the fault. This current level is dangerous for the power converter's IGBT devices. Rotor over-currents which flow onto the DC-link cannot be dealt with adequately by the line-side converter and a dangerous rise in DC-link voltage results. The line-side converter however safely manages the line-side currents throughout the fault.

The electric torque in response to a grid fault oscillates at sub-rotor speed, peaking at 3-5 p.u. braking torque and decaying very rapidly with a time constant roughly half that of either the rotor or stator transient time constant. No torque is supported during the plateau of a close-up short-circuit. During the fault the rotor is accelerated by the wind power input, although the maximum speed increase in tests was no more than 6%, leaving the post-fault DFIG well within its normal operating range. The torque difference caused by the fault instigates a low-frequency shaft resonant oscillation which continues for several seconds after the fault has cleared.

The DFIG controller can stabilise vector control of the power output during the fault, but cannot prevent spikes of over-current at fault initiation and clearance. Power export is limited in proportion to the retained balanced stator voltage, as the power converter can offer no more than rated current output.

Fault clearance instigates a step increase in voltage, normally only 80-90% compared with fault initiation. The same principles of transient decay components apply as for fault initiation, although the current peaks are proportionally smaller.

General fault response

Non-zero fault voltages present shorter drops in voltage and therefore a proportionally smaller drop in the internal magnetisation of the generator. Peak over-currents in test proved to be 65-80% of the proportional voltage lost (e.g. 33% peak for a 50% voltage drop when compared with the short-circuit response). Unbalanced faults offer serious problems for standard vector control schemes, but the fundamental positive sequence

response is no worse than for balanced faults. Both types of fault require a topological modification to protect the power converter's devices.

Key issues

The key issues for DFIG fault ride through were established as: protection of the DFIG from both rotor over-current and DC-link over-voltage, to remain grid-connected and dynamically stable, and to offer controlled active and reactive power output both during the fault period and during fault recovery.

FAULT RIDE THROUGH TECHNIQUES 6

This chapter presents possible solutions to the problems posed by fault ride through. Drawing from the understanding of voltage dip response established in Chapter 5, DFIG fault response is summarised in Section 6.1; where special attention is paid to the limitations of the conventional setup and the challenges posed for both protection of the generator and a positive grid contribution. These limitations include most importantly the maximum current capability of the DFIG power converter.

This information is used to produce a set of design aims for any fault ride through solution. The designs aims as listed in Section 6.2 deal with minimising the severity of the fault, protecting the DFIG from the voltage-step induced transients and the delivery of appropriate apparent power during the grid fault.

Section 6.3 reviews and references a range of proposed fault ride through techniques. The potential of each technique is evaluated against the design aims from Section 6.2. The three most promising of these were taken on for development and application on the test rig. The standard test setup is discussed in Section 6.4, including an explanation of the per unit system used with the test rig and vector control nomenclature.

Sections 6.5-6.7 detail the development of three potential techniques for improving fault ride through behaviour. The test results presented are summarised below:

- Reactive power delivery: Reference results vs. VAr-support control.
- DFIG crowbar methods: Timer crowbar and Minimum threshold crowbar.
- DFIG DC-link brake methods: Minimum threshold and Control-delay techniques.

The chapter concludes by reviewing the comparative performances of the highlighted techniques and discussing their potential application to high-powered wind turbine installations.

6.1 Fault response

Chapter 5 looked in detail into the fault response of a doubly-fed machine in a wind turbine. A symmetrical machine with linear magnetic properties and approximately

constant rotor speed was considered under the influence of a very swift drop in grid voltage. Analysis of the ideal machine established the twin leakage component composition of the natural fault response and superposed the effects of an applied rotor voltage. The key points for fault ride through are visited below, with a view to developing techniques for grid fault ride through improvements.

6.1.1 Transient periods of fault initiation and clearance

Over-currents

The transient period immediately following fault initiation and fault recovery revealed a rapid de/re-magnetisation of the induction machine which generates over-currents in stator and rotor currents as shown in Eqs. 6.1 & 6.2. These solutions assume a close-up zero-voltage fault; the peak currents will be proportionally smaller for a less severe voltage dip.

$$\left|\bar{i}_s\right|_{peak} = \frac{1}{\sigma L_s} \approx 5\,p.u. \tag{6.1}$$

$$\left|\bar{i}_r\right|_{peak} = \frac{1}{\sigma L_r} \approx 5\,p.u. \tag{6.2}$$

The over-current endures for a period approximately equal to the stator or rotor transient time constant, whichever is the longer. The peak rotor currents are dangerously high for the power converter's IGBT devices, which possess typical surge capabilities of no more than 2 p.u. (Section 6.1.4).

Rotor controller dynamic limitations

The rotor currents here contain three significant frequency components: a near-dc contribution of self-linking flux decay, a near rotor-frequency contribution of mutual flux decay and a forced contribution from the applied rotor voltage. The natural response components possess a rise-time far smaller than the rotor's transient time constant. As such it is hard to conceive of a practical feedback controller which could reliably manage all three components to within safe operating limits at all times.

DC-link

If the rotor over-currents are permitted to flow into the DC-link (even with rotor-side PWM disabled, the anti-parallel diodes in the bridge converter will behave as a three-phase rectifier) this demagnetisation energy is deposited onto the DC-link capacitance far quicker than it can be dispatched via the line-side converter. The DC-link voltage rises rapidly. Electrolytic capacitors are very limited in their voltage withstand capabilities (commonly limited to 450Vdc each, or 900Vdc for a series-pair) and can easily be damaged by this voltage rise.

Fault current

A grid fault will bring about large transient stator currents. These types of currents from conventional generators are used to trigger power system protection; however, induction machine transients are too short to be incorporated into existing power system protection schemes [34].

Electrical stability upon voltage recovery

Care has to be taken in the DFIG vector controller's response to voltage recovery. A misalignment of control, or control failure, may see the machine behave like a demagnetised singly-fed induction machine at high slip faced with a step increase in supply voltage. This will induce very large reactive power absorption from the grid, sufficient to significantly depress the local voltage. This in turn would adversely affect the fault response of other locally grid-connected plant.

6.1.2 Fault plateau period between initiation and clearance

Provided that the current demanded of the power converter is no greater than its normal ratings, in terms of both active and reactive contributions, the DFIG can remain electrically stable, controlled and connected to the network indefinitely. Mechanical stability is considered separately.

A controlled response

After the natural response components have decayed, the DFIG faces an indeterminate plateau period with a roughly constant low voltage supply. It has been shown that the rotor-side converter can successfully manage the machine currents in this period (Section 5.7). Reactive current can be supplied up to the nominal ratings of the converter to augment the local voltage. Active current can be supplied up to the normal ratings of the converter to extract electrical power in proportion to the residual local voltage.

DC-link management

The line-side converter can successfully control its output current into any constant low voltage. Power export is limited by the magnitude of the residual voltage. Meanwhile, active power on the rotor circuit is proportional to the machine slip, a potential problem if full electrical power is maintained. The DC-link voltage can be managed indefinitely provided that the residual voltage p.u. magnitude exceeds the machine slip. Given the reactive current output capability via the stator terminals, VAr-export control of the DFIG should always permit at least a 15% magnitude of local voltage with a 15% grid connection impedance (Section 6.5). When compared with a rated slip of roughly -10% this implies safe management of the DC-link throughout the plateau of fault voltage.

Mechanical stability

As the power export is limited, the rotor will accelerate during this period. A turbine blade-pitch control system may slowly respond in reducing the power input, which will aid stability. However, in a close up zero-voltage fault the acceleration will be very rapid, supplying 1 p.u. power to a generator with inertia of 1-2 p.u.

In practice however, credible zero-voltage faults as defined by grid codes last less than 150ms. Longer lasting faults have almost-proportionally larger residual voltage and hence power export capability. The resulting speed rise is no more than 5-10% [24]. After fault recovery, the DFIG can respond with a short-term over-export of power to restore the rotor speed. The mechanical stability of a DFIG wind turbine in response to grid faults is demonstrated in [23].

One argument is that, at the moment a grid fault occurs, the DFIG may be operating at close to its maximum possible speed, or within 5-10% of the maximum, such that any resultant acceleration goes beyond the safe operating limits of the generator. It is clear from the wind speed vs. rotor speed charts in Section 4.2.1 that a continuous high speed wind will nonetheless cause the DFIG to operate at *rated* speed. It is very rare that the DFIG will be operating at 10-15% over its rated speed, far rarer still that a grid fault will occur at the same instant. In these improbable conditions the specific wind turbine can be safely allowed to trip-off from the power system. In a large wind farm the great majority of DFIG turbines will be operating near enough to rated speed (~10% super-synchronous) for the acceleration effects to be minor.

6.1.3 Test rig evidence

The description of fault response outlined above was supported by test results from the 7.5kW test facility, as shown in Chapter 4. These results form the basis for the discussions on fault ride through solutions that follow.

6.1.4 Converter current limits

Maximum current

The fault response of the DFIG leads to dangerously high rotor over-currents. The most sensitive devices to over-rated current are the IGBTs in the DFIG power converter. In this type of application IGBTs are typically chosen to be able to carry twice the rated current, based on the maximum current pulses delivered at a 50% duty cycle. In this case the maximum permissible instantaneous current through any one switch is twice the rated current [63].

The power converter in the DFIG is assumed to be rated for the same current as the DFIG rotor circuit. Throughout this work therefore, the maximum permissible IGBT current for any fault ride through technique was set at 2.0 p.u. The specific ratings of

the power electronics in a particular converter may allow short-term operation at a higher rating. However, the 2.0 p.u. benchmark was used throughout in order to readily compare the proposed techniques.

Cost of current rating

A formal survey of the relative cost of power conversion equipment to wind turbine total cost was not readily obtainable, but it is certain that the power converter contributes a significant proportion of the overall wind turbine cost. A stated in [67] "Even with low priced power electronics, doubly-fed technology has a substantial cost advantage as compared to the conversion of full power". Scanning the catalogues of commercial vendors of power semiconductor devices reveals a rough proportionality between current rating and cost. Up-rating of the DFIG power converter is avoided on cost grounds.

6.2 Fault ride through solution aims

6.2.1 Key criteria for fault ride through solutions

In summarising the fault response of the DFIG and the fault-ride through requirements of a grid operator, key issues for fault-ride through behaviour are reiterated below, as explained in Chapter 5. Non-critical issues are omitted; these include areas that are within the normal capabilities of a wind turbine DFIG, such as mechanical stability and line-side converter current management.

Generator protection

The DFIG must:

1. Protect its power converter devices from the rotor circuit over-currents.
2. Protect its DC-link capacitance from a damaging over-voltage event.

Transmission system contribution

The DFIG must:

3. Remain dynamically stable and not trip-off.
4. Export active power in proportion to the retained balanced voltage and never motor.
5. Export reactive current up to the limits of the converter and never absorb significant amounts of reactive power.

In light of the power system requirements, it is important to clarify the definitions of tripping-off and practical power output. In this context, to trip-off involves a full electrical shut down of the wind turbine, with a deceleration of the rotor-shaft. It is possible that a very short electrical disconnection (lasting some tens of milliseconds) may be

permissible under certain circumstances, providing that full control could be restored in much less than a second (Section 2.5). The calculation of power in a practical sense involves the rms average of sampled currents and voltages [19][56]. As a result, any instantaneous power oscillations occurring within a single system cycle of 20ms should not have a significant impact on the grid system.

6.2.2 Design aims

With knowledge of the natural fault response of the DFIG and the key issues for fault ride through, any proposed fault ride through technique must cover at least one of the following three broad aims:

A. Minimize the voltage drop experienced by the generator

The degree of demagnetisation, the size of over-currents and the limits of power export are all determined by the severity of voltage dip experienced by the generator. Any technique which minimises the voltage drop experienced by the generator will aid fault ride through and expand the range of faults for which desperate protective action is avoided.

B. Divert rotor over-currents away from the converter's devices, or negate over-currents altogether

The surge capability of each IGBT in the power converter is approximately 2.0 p.u. (Section 6.1.4). Any fault ride through scheme must ensure that the currents carried by the IGBTs remain below this level. The transient rotor over-currents of the natural fault response peak at up to 5 p.u., and so these currents must be either heavily reduced or diverted from the converter's devices.

This problem can be solved at a stroke by over-rating all the IGBT/diode pairs in the rotor-side converter by a factor of three, ensuring ride through capability for all grid faults. However, this would almost prohibitively raise the overall price of the power converter. For example, 1200V rated power electronics devices in a 2MW wind turbine DFIG could be expected to be rated at approximately 500A. Replacing the rotor-side devices with 1,500A versions would be very costly; perhaps three times the unit cost for each IGBT module.

The fault response of the DC-link voltage is very much tied-in with the rotor's fault currents. It is the transient rotor over-currents which force a DC-link over-voltage. A scheme which successfully diverts or reduces the rotor over-currents can also prevent a DC over-voltage event.

C. Produce appropriate power output during faults

After the transient periods of fault initiation and recovery, a vector control scheme can deliver current at a specified power factor into a grid fault. However, an individual

generators' dynamic control response varies from turbine to turbine; depending strongly upon the particular circuit parameters, connection situation, PWM type, thermal sensitivity, controller method and so on. The dynamic response of the DFIG controller will limit the rate at which apparent power control can be restored, and hence perhaps limit the grid code compliance of the turbine

What is clear is that instances of fault initiation and clearance impose very strenuous disturbances on a standard feedback control scheme; this entails some instability and temporary loss of vector control orientation. On the other hand, during the plateau of a grid fault it is possible to safely deliver power in proportion to the residual balanced voltage and (up to) rated current's worth of reactive power support.

The specific requirements for apparent power output are an area of contention. Any proposed fault ride through scheme must restore apparent power control very swiftly following fault initiation and clearance in order to contribute to system frequency stability. On the other hand, reactive power output can improve the fault response of other locally-connected equipment. Neither can be controlled by a DFIG in the immediate transient period of a few ms after fault initiation. Specific regulations notwithstanding, the controlled export of apparent power within 2-3 cycles (40-60ms) of a serious voltage disturbance would represent a very favourable fault response.

6.3 Proposed fault ride through techniques

In this section numerous fault ride through solution proposals are discussed. Where appropriate these are referred to the three design aims listed in Section 6.2.2

6.3.1 Fault ride through control

Fault ride through control is an attempt to safely manage transient rotor currents and improve the controlled power output. Despite the rapidity of the demagnetisation forced by the drop in supply voltage, a number of efforts have been made to limit the after-effects via improved DFIG control, mostly in simulation. However, there is no strong experimental evidence that fault ride through issues can be resolved with control measures alone.

Decay component control

In a comprehensive approach to fault ride through control, Xiang et al [68] proposes precise positioning of the rotor converter voltage to negate or at least minimise the effects of dc and rotor speed ac components of flux decay. By estimating the separate frequency contributions of flux, the transient over-currents are limited in simulation to within 2.0 p.u. for grid faults with apparent residual voltages as low as 20%.

Experimental verification is however limited to no-load conditions and the pre-fault voltage supply is required to be below 85% of rated.

The controller's ability to damp over-currents is strongly linked to the size of the rotor's leakage inductance, L_{er}; it is worth noting that [68] reports a similar transient situation for the characteristic DFIG fault response to that detailed in Section 5.1.

Other control methods

The importance of field orientation in the controller's response is stressed in Yikang et al [69] with slight improvements reported in a Matlab/Simulink model. The same software is used by Serban et al [70]; where reduced over-currents are reported for a simulated controller which throttles back the reference current demand. However, reactive power appears to dominate the voltage recovery process with a period of 1.5 p.u. VAr absorption. Rathi et al [71] reports reduced over-currents using "H_∞ control synthesis", although DC-link voltage deviations appear dangerously to extend to 100% above rated and 50% below rated.

On a broader note, tighter control performance is reported using rotor-flux feedback control rather than rotor-current feedback control in Hughes et al [49]. However, as yet this concept has not been extended to grid fault response.

Necessity for topological modification

As explained in Chapter 5, the characteristic over-current rise-time at fault initiation and recovery is a fraction of the transient time constant of the rotor circuit, and faster than the controlled rise-time response of the rotor converter's current controller. It seems that control alone cannot adequately curtail the over-currents caused by a close-up grid fault. However, in periods longer than the characteristic response-time of the rotor converter controller (perhaps 0.5-2 times the rotor's transient time constant) the rotor converter can play an active part in fault response, particularly in terms of apparent power control and overall stability.

The immediate over-currents produced by grid faults demand a topological modification which protects the power converter whilst allowing the converter to resume control at the earliest possible opportunity. This requirement exists also for unbalanced faults, which are explored briefly in Section 6.3.9.

6.3.2 VAr support

Reactive power export can help to minimise the voltage dip experienced by the generator.

Reactive power control

As explained in Chapter 3, the DFIG offers a respectable range of power factor of operation. When control is resumed after the transients of fault response, the DFIG may contribute reactive power from both converters, up to the rated currents of its devices.

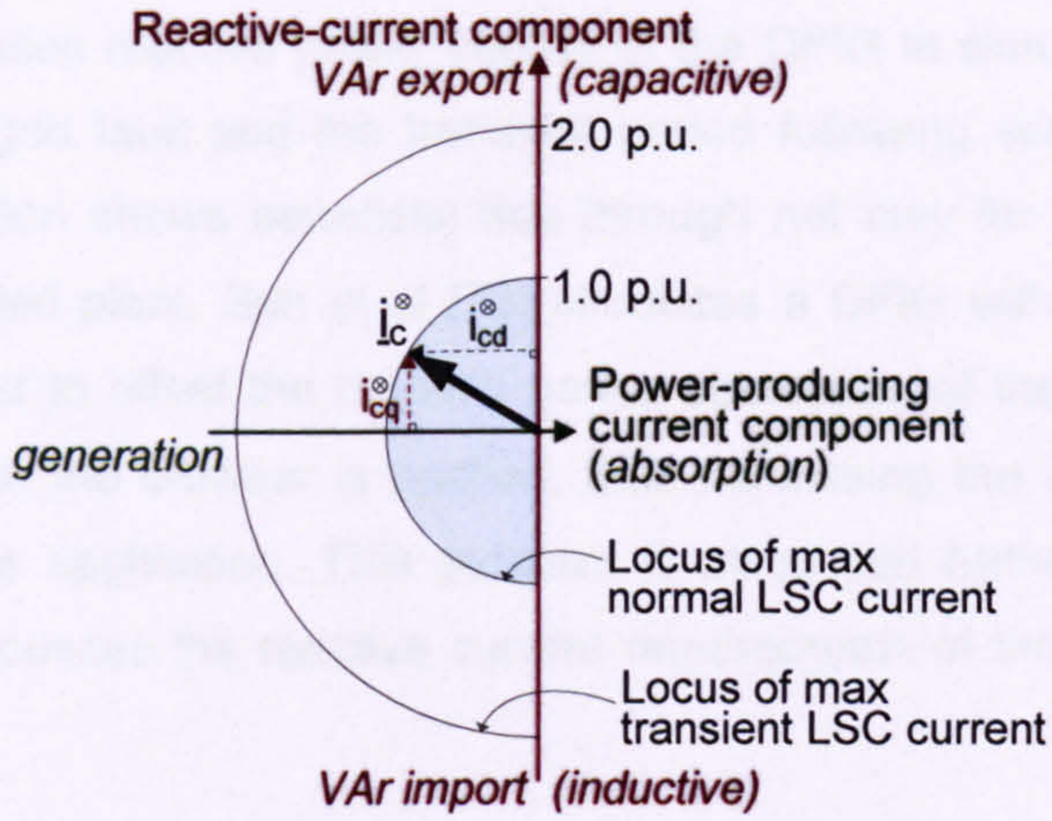

Figure 6.1. Loci of line-side converter current reference limits.

In practice, the rated current must be shared between the direct power-producing and quadrature reactive components. Figure 6.1 illustrates this concept using the example of the line-side converter, although the principle applies to both converters. Although four-quadrant control is perfectly technically feasible, normal operational settings can restrict the currents to avoid motoring and the diagram only displays the generation half-plane.

For the line-side converter, the power-producing component must be prioritised to maintain the DC-link voltage within safe limits, while the reactive current component can take up the rest of the allowance. The respective values can be recalculated at each control step.

In the rotor-side converter the operator may choose the relative priority of reactive and active power output. Due to the rotor-biased turns ratio of a typical doubly-fed generator, rated rotor current is smaller than on the stator circuit. As a result, the power converter ratings achieve greater p.u. reactive current at the stator terminals via the rotor than direct reactive current from the line-side converter. During grid faults it can be argued that reactive current should take a higher priority over the power-producing component, as, irrespective of the short-term electrical power export, mechanical stability can normally be restored soon after fault clearance.

Normal reference currents should remain within rated 1 p.u. magnitude to prevent over-heating of the converter. However, short-term excursions beyond this zone are permissible, for example in response to grid faults. The maximum surge current is 2.0

p.u. in either converter, as explained in Section 6.1.4. The reference currents in the vector controller must stay well below this limit. In the control methods in Sections 6.5-6.7 the d and q components of rotor current are independently limited to no more than 1 p.u. each, ensuring a total demand of no more than 1.4 p.u. in magnitude.

Examples

Hansen et al [72] uses reactive power control of the DFIG in simulation to raise local voltages during a grid fault and the transient period following voltage recovery. The DIgSILENT simulation shows beneficial ride-through not only for the DFIG but other locally grid-connected plant. Sun et al [73] simulates a DFIG with line-side converter reactive power used to offset the reactive power absorption of the induction machine during periods when the crowbar is applied, thus minimising the voltage suppression induced by crowbar application. This problem is discussed further in Section 6.6.4. Erlich et al [74] discusses the reactive current requirements of the German grid code during grid faults.

Review of VAr control measures

VAr control is useful aid to fault response, without solving the critical issues of managing the transient over-currents. In all cases, it is clear that up to rated rotor reactive current can be pressed into a DFIG during a grid fault while the power converter is safely involved in DFIG control, and that this can be applied irrespective of topological fault ride through modifications, at no extra cost. The key limitation is the rate at which control can be restored following the short-circuit transients associated with a grid fault, an area explored further with the tested fault ride through techniques in Sections 6.5 - 6.7.

Parallel VAr generation

A final option for minimising the voltage drop experienced by the generator is to install parallel capacitance on the stator circuit or wind farm connection. This would help to maintain the magnetisation of the DFIG during a grid fault.

It would be difficult to 'switch-in' a large capacitive unit exclusively in grid fault conditions. The sudden imposition of a large capacitance will induce such an inrush of current as to worsen the grid fault situation, while if successive steps of capacitance were included they would not be introduced quickly enough to prevent machine demagnetisation. A STATCOM-type device is essentially already included in the form of the line-side converter, and the reactive power capabilities of this unit should be used to their full. However, the line-side converter is rated for a fraction of the DFIG stator current (such is the economic attraction of a DFIG over a fully-rated converter

scheme). The cost of over-rating of the line-side converter or adding rated-power STATCOM equipment would be very significant.

It is possible to include a local shunt capacitance in the continuous operation of the DFIG, exactly as for many existing SFIG installations. This technology has the advantage of being relatively cheap and already widely-used in wind power installations. Care has to be taken to prevent any possibilities of over-voltage spiking at the capacitor terminals. The minor benefit of fault voltage support may be offset economically by the maintenance implications and voltage protection equipment required.

Such a scheme may offer assistance during grid faults, but could not prevent the fundamental demagnetisation process and its danger to the power converter. As a result this method is not considered in further detail in this work.

6.3.3 Rotor circuit crowbar

Overview

Crowbar operation is a temporary measure widely employed in rotor-circuit error conditions to protect the power electronic components in the DFIG converter. It involves connecting the rotor phases together through a designated resistance, diverting current from the rotor-side converter and rapidly de-energising the rotor. The crowbar absorbs the initial energy outflow from the machine, while the resistance shortens the effective decay timescale of the rotor flux decay, hence hastening the de-magnetisation process. Conventionally the crowbar is applied for an extended duration to fully demagnetise the rotor (see 'Examples'). The crowbar can also be referred to as a rotor flux-damper device.

Unfortunately, vector control is lost while the crowbar is applied and the induction machine must draw its magnetisation from the stator side, producing a high-slip reactive power demand which works to suppress the stator voltage.

Crowbar circuit configurations

The crowbar was developed as a rotor circuit protection device long before the advent of wind turbine grid code regulations. The title incorporates any device which connects together the rotor windings of a wound rotor machine in a closed circuit, bypassing the power converter. Example crowbar layouts are shown in Figure 6.2. This section analyses the common forms of crowbar from the point of view of stator voltage dip response.

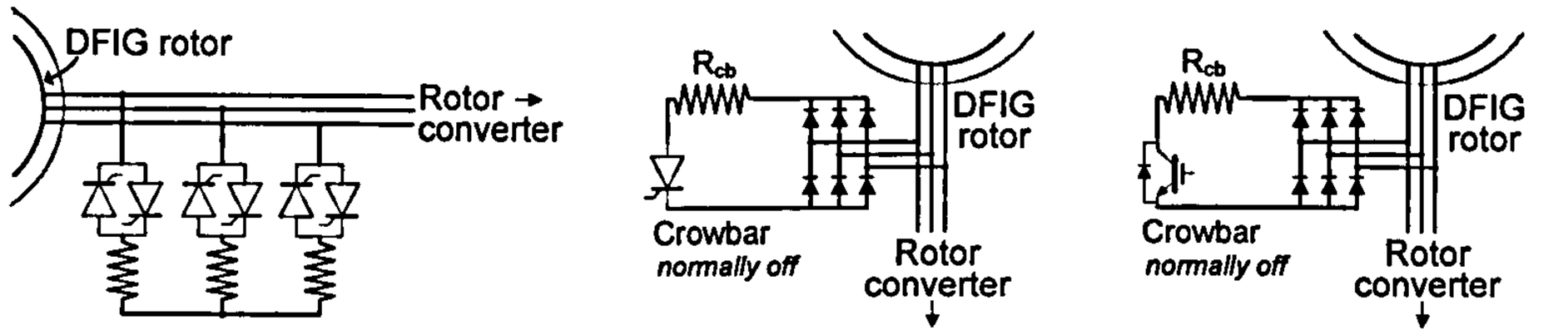

a) Three-phase triac crowbar b) Rectifier and thryristor crowbar c) Rectifier and IGBT crowbar

Figure 6.2. Crowbar circuit.

Referring to Figure 6.2, each SCR in configuration (a) must be rated to block maximum rotor voltage and to carry worst-case rotor over-currents. The thyristor switches can be fired by a current fed gate signal, but can only be turned off at a through-switch current zero. Alternatively, GTO thyristors offer better turn-off capabilities, but demand a far higher turn-off gate current. Configuration (a) is simulated in [75].

A rectifier-SCR configuration, Figure 4.4 (b) uses only one switching device. This device must be able to block roughly 140% of rotor phase-phase voltage and carry the peak of rotor over-currents almost continuously for 50-100ms. Each diode in the bridge must carry the same ratings as for the SCRs in configuration (a). Overall, given the relative cost of diodes, diode rectifier configurations offer a major cost saving. The single resistor in (b) and (c) must carry an average current 135% of the value carried by each resistor in case a). Thermally however, grid faults cover a very short period and hence the single resistor is not rated much higher than three separate resistors. The rectifier-SCR configuration is used in [76]. Turn-off of the SCR device in configuration (b) must wait for a rectified current zero; this will only occur once the rotor circuit flux has completely decayed.

Near-instantaneous turn-on and turn-off can be achieved by using an IGBT power switch, as shown in the rectifier-IGBT configuration in Figure 4.4 (c). The IGBT is current-rated as for the thyristor in configuration (b), with a considerable increase in single device cost. However, the swift turn-off ability of an IGBT is necessary for certain fault ride through control methods, as detailed in Section 6.6. Configuration (c) is employed on the test rig used in this work; its behaviour is considered in further detail in Section 6.6.

In any configuration, turn-off of the crowbar can be followed up with the resumption of rotor-converter PWM and rotor current control. The speed at which control may be resumed depends upon the state of the machine at crowbar turn-off, the availability of the DC-link voltage and the individual settings of the controller.

High-slip SFIG behaviour

When the crowbar is engaged, the DFIG resembles a high-resistance singly-fed machine, typically at very high slip (relative to standard induction generator operation).

This temporary configuration is a worst case combination of poor torque output and very high reactive current demand. This reactive power absorption can only occur on the stator, acting to suppress the local fault voltage. The poor torque output worsens the mechanical stability. It is therefore necessary that crowbar application periods are minimised.

Examples

A crowbar system is used very successfully to protect the generator from grid fault effects in simulation in [76], using configuration (b) from Figure 4.4. However, the thyristor turn-off point is delayed until rotor transients have decayed to zero; each crowbar activation period lasts roughly 120ms. In the case of fault recovery this leads to a 100ms post-fault period of at least 50% reactive power absorption and associated voltage suppression. In the words of the author: "a second crowbar firing should be avoided in all possible cases". [77] Simulates an actively controlled DFIG Crowbar using Matlab / Simulink software.

A DFIG is protected from grid fault over-currents in simulation in [78]. Here the author uses configuration (a) from Figure 4.4, referred to as "DFIG bypass resistors". Here, the crowbar activation on fault recovery leads to a 500ms period of at least 20% reactive power absorption, undesirable from a grid point of view. The value of appropriate crowbar resistance is considered in [75].

[3] discusses the failure of a DFIG system to meet fault ride through requirements when using a crowbar for periods of 100ms or more. [72] refers to the crowbar system as a standard DFIG protection package but stresses the problem of turning the DFIG into a high-resistance SFIG.

At least as important as the structure of the crowbar is the approach of the DFIG controller in restoring control after the crowbar is released. [79] resets the integral components of the rotor's feedback PI controllers to zero before the crowbar is released to restrict windup of the controller's integrators. [78] forces the feedback PI controllers to restart with a current reference equal to the last measured current. From here a soft restoration of control can be achieved by gradually leading the current demand towards the normal reference at a limited rate. By way of illustration, this soft-engagement of feedback control is the same method used in the DC-link voltage control of the test rig, shown in Chapter 4.

Variable crowbar

The crowbar's resistance can be varied to provide limited control over the decay of rotor flux and hence some control over the resulting current magnitude. Using

configuration (c) from Figure 4.4, a chopper circuit can be used to drive the IGBT at a calculated duty cycle to impose a variable crowbar resistance onto the rotor windings.

This could be useful for example in minimising the immediate impact of crowbar engagement, after which the resistance could be ramped up to fully de-energise the rotor. A variable resistance concept is understood to be used in Gamesa's commercial "Active Crowbar" fault ride through offering. After simulation, research on varying the crowbar resistance in this work was relegated in favour of the ultimately successful minimum threshold crowbar method, whose aim was simply to minimise the length of crowbar application periods (Section 6.6.6).

Review of crowbar systems

Overall, the crowbar system is a cost-effective and reliable method of protecting the DFIG's power converter from rotor over-currents and indirectly protects its DC-link. However, extended periods of crowbar operation lead to poor power quality, especially high reactive power absorption, which is undesirable for the grid.

6.3.4 DC-link brake

Overview

A DC-link brake is used to contain the DC-link voltage while accepting transient rotor over-currents. The DC-link brake appears somewhat similar to the rectifier-IGBT crowbar configuration. Instead of a separate rectifier, the six anti-parallel diodes in the DFIG's rotor-side converter are up-rated to handle short-circuit currents. A power resistor and series switch are placed in parallel with the DC-link capacitance to sink power as required. While this rectifier and resistor arrangement is similar to the crowbar circuit, the key difference is the presence of the DC-link capacitance. This method re-uses a conventional DC-link voltage protection device known as a brake chopper [80].

Brake chopper

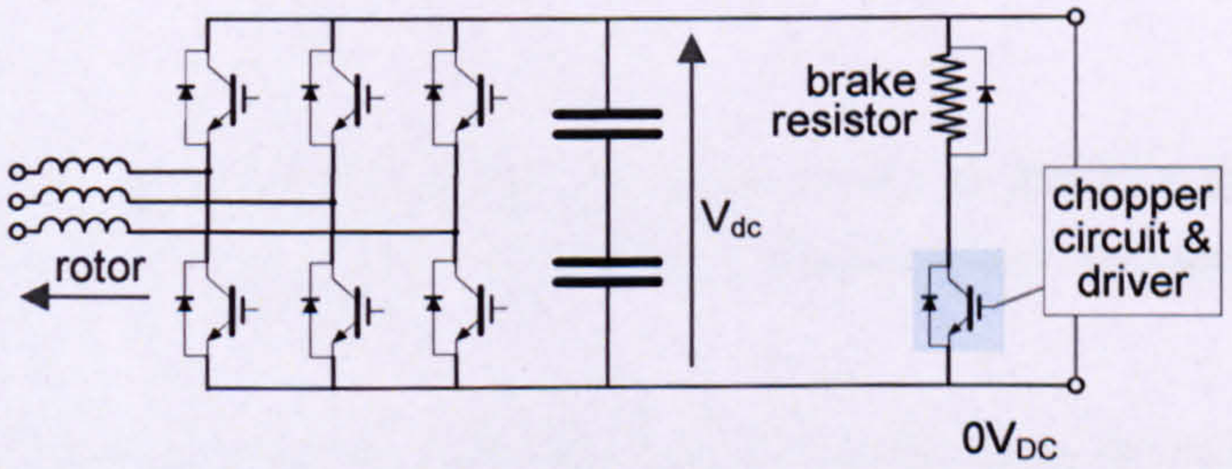

Figure 6.3. Rotor converter with DC-link brake chopper.

A DC-link brake chopper is shown schematically in Figure 6.3, added across the DC-link of a DFIG converter. Only the rotor-side converter is pictured, as this is the focus of DFIG fault response.

The brake chopper logic circuit monitors the DC-link voltage and activates the brake if the voltage exceeds a certain threshold. The driver chops the IGBT on/off with a duty cycle determined by the magnitude of over-voltage. The duty cycle of the chopper is increased as the over-voltage increases up to a maximum permanently-on state. During the off-periods, an anti-parallel diode carries residual current in the resistor. The chopper works on a hysteresis band, i.e. the turn-off voltage is set below the turn-on threshold.

Fault response

As for the crowbar method, the rotor-side PWM may be disabled in case of transient over-currents: all of the rotor converter's IGBTs are switched off. Without an alternative circuit path, the transient rotor currents are forced to conduct through the rotor converter diodes. Rotor demagnetisation energy is dumped on the converter's DC-link, causing the DC-link voltage to rise rapidly. The brake switch is automatically engaged from its own voltage measurement logic, sinking power through the brake resistor and helping to prevent a dangerous over-voltage event on the DC-link. When the rotor transients have sufficiently decayed, rotor-side PWM and rotor current control may be re-engaged.

If the rotor converter switches are held off for long enough for the unsupported rotor flux to decay, then the DC-link voltage will reverse-block the converter's diodes. The diodes will cease conducting from the next current zero, and the rotor currents are then held at zero until IGBT switching is resumed.

Ratings

The resistor must be small enough and rated for sufficiently high current to protect the DC-link from the worst case of fault induced rotor over-currents. The current rating of the brake resistor and switch is determined by the maximum permissible DC-link voltage, as shown in Eq. 6.3.

$$i_{brake} \leq \frac{V_{dc,\max}}{R_{brake}} \tag{6.3}$$

The switch must have an appropriate snubber circuit to prevent the emergence of dangerous voltage spikes on turn-off, which may otherwise threaten the integrity of local equipment.

The anti-parallel freewheel diodes in the rotor converter must be capable of handling rotor fault currents, up to roughly 5 p.u. The DC-link capacitance must be rated to withstand the rectified form of these over-currents, for periods where the brake resistor is not engaged. This translates to roughly 7 p.u. current (on a machine-rotor p.u. base).

The capacitor current rating is unlikely to form an onerous equipment restriction. The key issue is whether the DC-brake can prevent the voltage from exceeding the capacitors' maximum voltage capabilities; this can be secured with an appropriate choice of brake resistor.

Examples

In fault ride-through simulations, a brake chopper is used successfully in conjunction with a crowbar in [76]. Specifically, the simulated rotor over-currents do not demand crowbar action in the demonstrated cases where the stator voltage recovery is rather slow. The authors note the power quality problems of long-periods of crowbar application. A DC-link brake resistor is used in a 15kW test setup in [81]. However, no active switch is used, and control can only be resumed after the DC-link currents are forced to zero (after the diodes have become reverse-blocked).

The IGBT crowbar, brake chopper and their joint use are arguably covered by a US patent [82], specifying that either or both should be applied in case of a grid fault to "draw out the rotor short circuit energy" and then "switched off once the short circuit current has decayed". [82] also states that the brake chopper ratings can be reduced by simultaneously employing a crowbar.

Overall

The DC brake offers a relatively cost-effective means of protecting the power converter in the wake of grid faults and rotor over-currents[9]. DC-brake action for fault ride through is studied in further detail in Section 6.7.

6.3.5 DC-link battery

It has been suggested that the DC-link voltage could be maintained in grid faults by use of a large battery [83]. On a larger scale, some form of UPS supply could be attached in parallel to the DC-link to maintain the DC-link voltage during grid faults. With a necessary rating of 900V and perhaps 1,000A for an industrial application, this is perhaps the least economic proposal reviewed, whilst at the same time not protecting the converter from damaging over-currents.

6.3.6 Temporary disconnection

One option to protect the generator in a grid fault is to rapidly disconnect the stator from the grid as shown in Figure 6.4. With the stator open-circuit, the stator flux is interrupted; the machine is rapidly de-energised and restarted via the rotor converter soon after the de-energisation [84].

[9] Cost-effective compared primarily with over-rating the DC-link capacitor voltages.

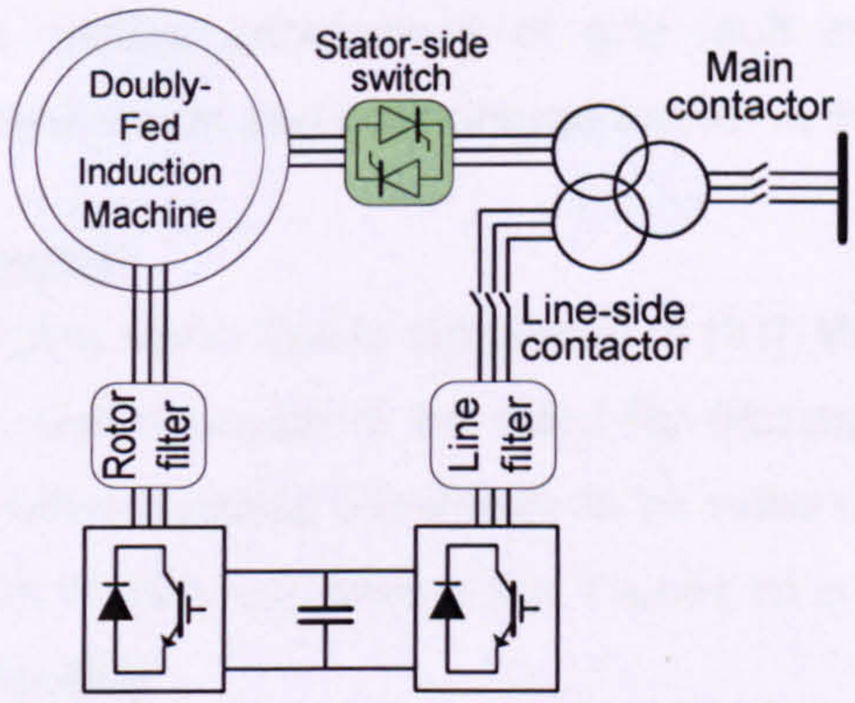

Figure 6.4. Stator-side switch.

The type of device used in the switch is discussed in [84] and [82]. A fast-acting contactor is lossless in normal operation, but requires at the very least 40ms to operate, too slow to help the converter survive demagnetisation currents. NPT type IGBTs have sufficient blocking capabilities and can be switched quickly, however they carry an uneconomic 2% typical on-state loss per device. [84] and [85] use anti-parallel thyristor pairs, as indicated in Figure 6.4, as the best compromise of power handling, turn-off behaviour and cost.

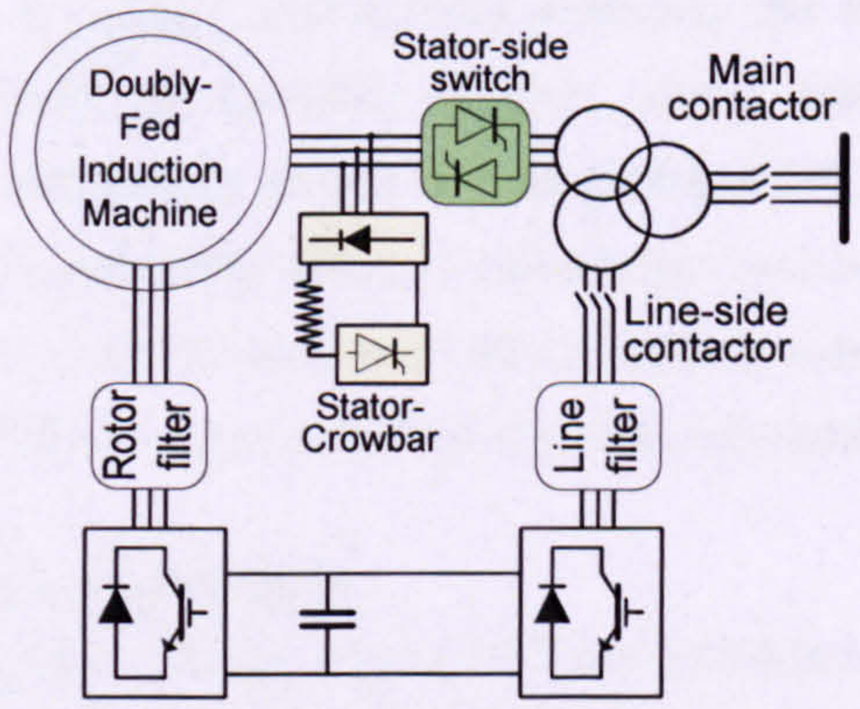

Figure 6.5. Stator-side switch and stator crowbar.

[85] goes further to add a stator-side crowbar to aid the turn-off of this stator-side switch, as shown in Figure 6.5. This stator-side crowbar quickens the decay of stator flux in exactly the same way that the rotor crowbar does for the rotor flux. Note that in this case, the stator crowbar devices must all be rated for the worst case of stator over-current: 5 times rated stator current and hence 20 times the ratings of the converter's devices – at a considerable cost.

Calculations of the on-state losses for a three-phase anti-parallel thyristor switch, as proposed in [84], were made for the suggested SKT2400 Semikron SCR devices, as well as (for comparison) a set of International rectifier ST700C12L SCRs, using publicly available data-sheets; each device carrying 1640A at 690V (as for a 2MW system). The on-state losses were calculated using the typical on-state voltage drop from the respective datasheets, indicating approximately 1% continuous power loss for this

switch type. Given the relative infrequency of grid fault events, this method was considered ultimately uneconomic and not pursued further in this work.

6.3.7 Stator flux damper

A further method of damping stator flux is suggested in [81]. Whereas the crowbar-type arrangement requires a switch device to be rated for demagnetisation over-currents, this normally-on configuration requires the device to be rated only for normal operation. The setup is illustrated in Figure 6.6, where the Y-point of a set of stator windings is routed through a diode rectifier.

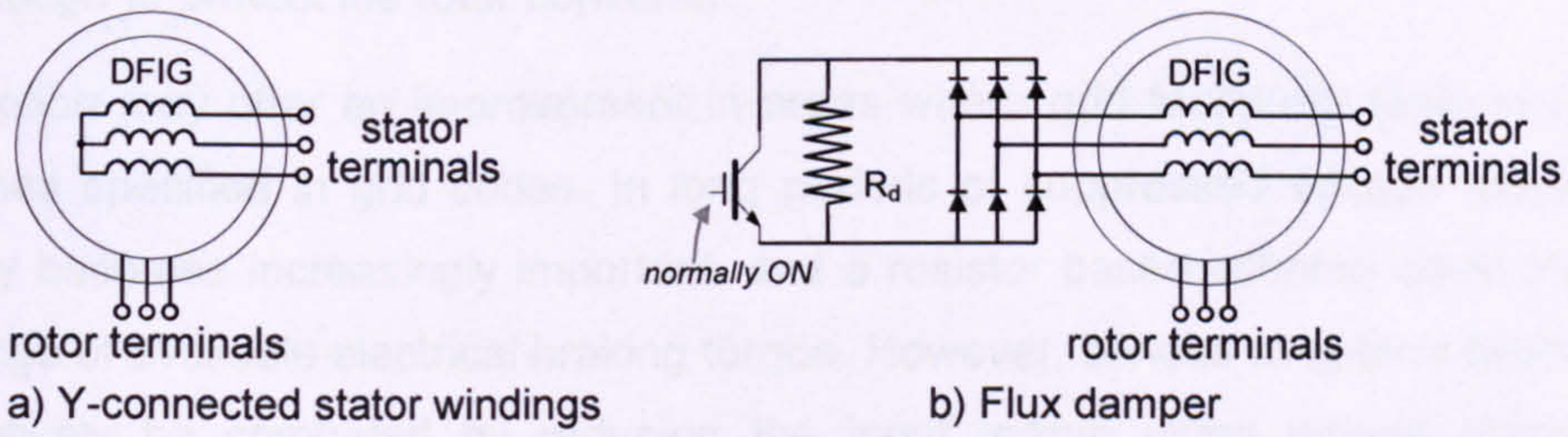

Figure 6.6. Stator flux damper.

Here, the instance of a grid fault causes the damper switch to be opened, forcing the stator currents through a resistor and quickly damping the stator flux. However, this involves the IGBT switch as carrying rectified stator current throughout normal operation, leading to a continuous power loss of perhaps 2%. Considering the relative infrequency of grid fault events, this effect is considered too uneconomical to be of use. Alternatively, the switch could be replaced with a lossless contactor, although it would not be able to open quickly enough to protect the rotor converter from over-currents.

6.3.8 Switched series impedance

One method of reducing the voltage drop is to insert impedance between the fault and the generator. The action of passing fault current through this impedance will raise the relative voltage at the generator terminals. The approximate setup is illustrated in Figure 6.7.

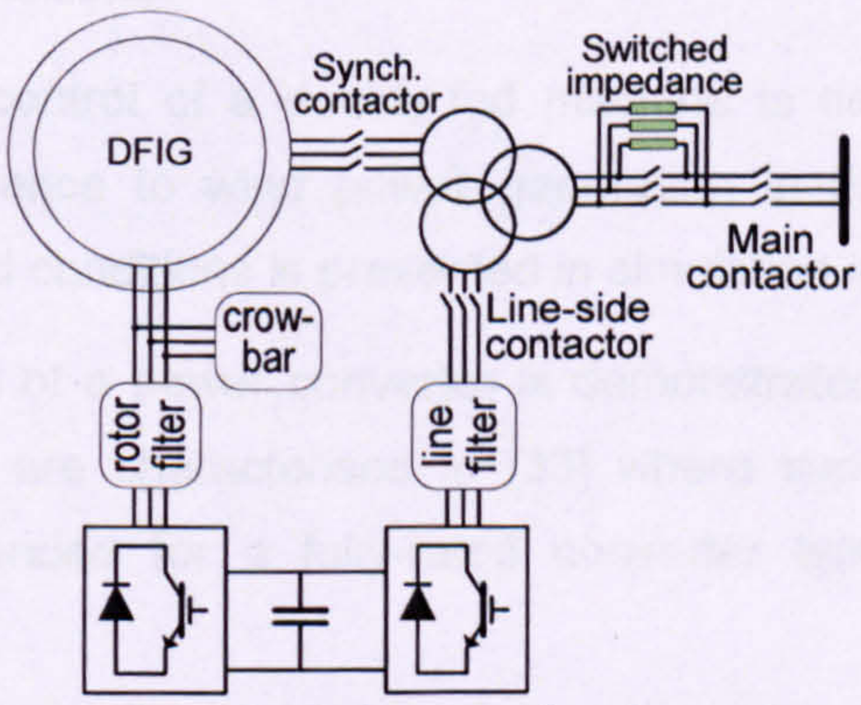

Figure 6.7. Switched series impedance.

A similar scheme has been shown to assist the ride-through of SFIG-type wind turbines, which are intrinsically more sensitive to the local voltage. [32] uses fast-acting contactors and parallel resistors to temporarily improve the stator voltage during a fault.

In practice, the switch could be placed either side of the transformer (to take advantage of low-voltage equipment) and contain a combination of resistive and perhaps capacitive or inductive components. Nonetheless, the switching element suffers from the same drawbacks as explained in Section 6.3.6, namely connection speed versus on-state power loss. The only lossless switching option is a contactor, which will not act fast enough to protect the rotor converter.

This option may offer an improvement in areas where grid faults are likely to exceed the times specified in grid codes. In long periods of suppressed voltage mechanical stability becomes increasingly important, and a resistor based scheme could increase the range of available electrical braking torque. However, serious long-term faults could alternatively be combated by reducing the input torque using turbine blade pitch control. This work focuses on protection from the immediate transient effects of fault response, while looking to avoid additional on-state losses. As a result the series switched impedance scheme is not further considered in this work.

6.3.9 Unbalanced fault response

As explained in Chapter 2, the most common grid fault type at initiation is unbalanced in nature. Efforts have been made to demonstrate sequence component control of voltage-sourced converters in the face of such asymmetric conditions. To date however, no test results have been presented for a DFIG showing improved fault response to grid-code defined unbalanced faults.

In practice, the decomposition of measured currents requires some kind of band-pass filter which then limits the dynamic response of the rotor current feedback controller. Sequence component controllers must however produce adequate dynamic response under balanced fault conditions.

Sequence component control of a doubly-fed machine is detailed in [86], [87] and implemented with reference to wind power generation in [88]. An improved DFIG controller for unbalanced conditions is presented in simulation in [89].

Dual-component control of a power converter is demonstrated experimentally in [90]. Unbalanced grid faults are characterised in [33] where improved converter control schemes are recommended for a fully-rated converter type variable speed wind turbine.

The test rig facility introduced in Chapter 4 is limited to the application of balanced faults alone, and so unbalanced fault response is not pursued experimentally in this

work. Research in this area suggests that improved power output can technically be produced in response to a continuous unbalance present in the generator's supply voltage. However, none of the schemes can eliminate the problem of machine demagnetisation and the resulting over-currents. Any symmetrical component controller would have to work in conjunction with a topological modification designed to protect the DFIG from the worst case of balanced faults.

6.3.10 Summary

From all the concepts reviewed, the most favourable in terms of cost-effectiveness and scope for a practical solution are: VAr support control, the rotor-circuit crowbar and the DC-link brake. These three methods were selected for further development and testing on the DFIG test rig.

6.4 Standard test setup notes

6.4.1 Test conditions

For comparison of fault ride through schemes, a standard test setup was determined. This is the same setup as used for the three DFIG fault response tests presented in Chapter 5, based on the test rig detailed in Chapter 4. Pre-fault conditions consisted of rated rotor speed, specifically 12% above synchronous (1680rpm), and 67% rated power generation (5kW). The DFIG was controlled to generate at unity power factor under healthy voltage conditions.

6.4.2 Fault voltage profiles

For each method studied in this chapter the first test shown is for a 15% fault voltage lasting for 500ms. This fault is severe enough to cause problematic over-currents, and endures for significantly longer than the transient time constant of either the stator or the rotor. This reveals the response of the DFIG during the near-steady-state conditions of a low voltage plateau. Secondly, the most severe fault test of 0% is shown: a short-circuit test lasting for 140ms. In the reactive power control section a 50%, 720ms fault test is included. The over-currents in this test did not exceed converter limits and so the results for 50% dips are not shown for the other techniques. In all cases, the recovery voltage was fixed at 90% for the remainder of the test.

The 0% and 50% fault voltage profiles were drawn from GB grid code. The 15% fault voltage profile was chosen in comparison with the 0% fault to represent a longer-duration severe fault, approaching the limiting profile set by US and Irish grid codes (Section 2.5).

6.4.3 Per units

For easy comparison between tests, the per-unit system is often referred to. For clarification, stator-circuit per units refer to a 7.5kW, 415V (line-line rms) base, which implies 10.4A per-phase rms current. The rotor-circuit per-unit base is taken from the machine windings: 1,290V (line-line rms, at standstill or unity slip) and 3.35A rms. It is assumed that the rotor converter would normally be chosen to match this rating of current. Hence the power converter leg currents (line-side and rotor) are described with the same per unit current base as the rotor windings. Now, the DC-link voltage is determined chiefly by the standard ratings of the power electronics, where 600V/1200V/1700V are common upper limits. The test rig used 1200V-limited IGBT devices. The DC-link was operated at 750V dc, which is designated as the DC-link per-unit voltage base.

It is worth noting that the test rig power converter employed 75A max-rated electronic devices for safety, a comfortable 22.4 times the rating described above. However, the fault response results in the proceeding sections are discussed with reference to a standard, machine-rotor per-unit rated power converter: the aim is therefore to limit device currents to below 2.0 p.u. throughout the tests, as described in Section 6.1.4. It is worth noting that on the test rig rotor circuit, the 2.0 p.u. surge limit corresponds to 9.5A peak in each phase.

6.4.4 Rotor-side vector control and saturation limits

Vector control terms and limits

For familiarity with the frequently repeated terms relating to vector control of the rotor converter, a simplified version of the control scheme is presented in Figure 6.8, naming the key elements and saturation limits.

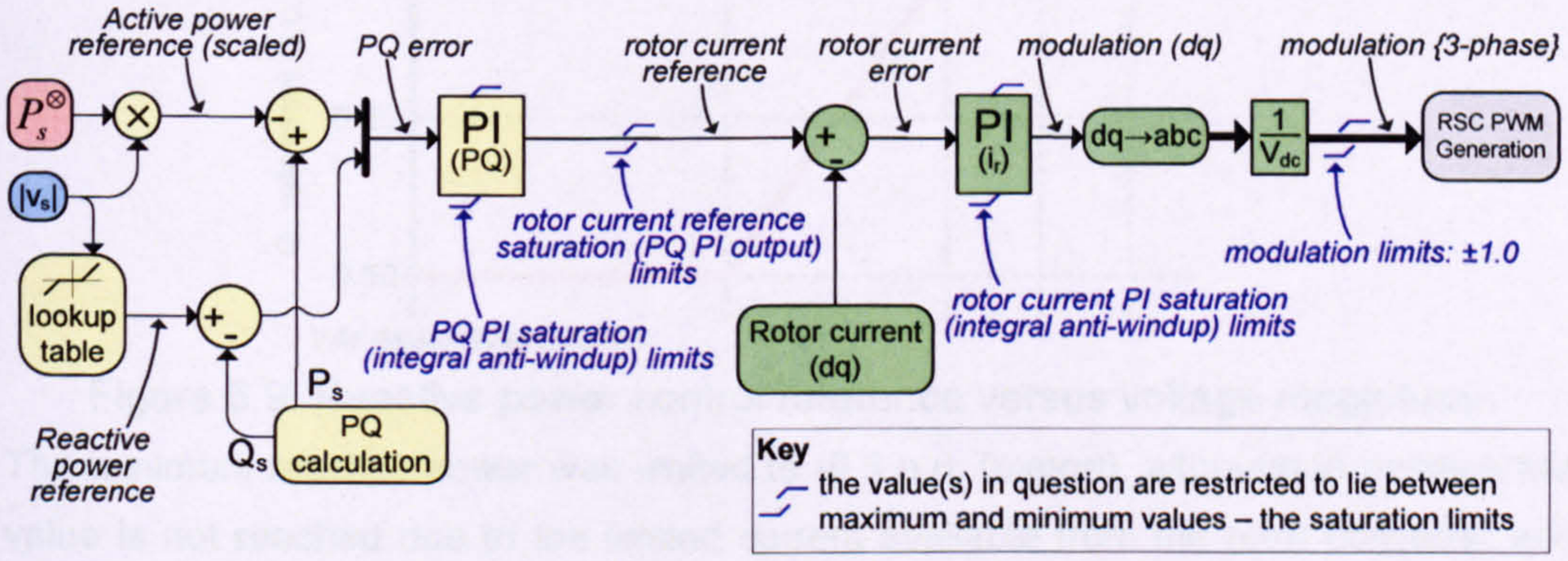

Figure 6.8. Simplified RSC vector control diagram with saturation limits.

The stator power reference is scaled by the magnitude of the stator voltage in order to commit only rated active-power-producing current from the converter in the event of sudden voltage disturbances. Each of the PI controller's integral components are saturation-limited to prevent integral windup. The rotor current reference is limited to

avoid an out-of-range current demand. Finally, the modulation indices are limited for the maximum IGBT duty cycle.

The rotor current PI integral anti-windup limits are set for all tests at ±1.0 p.u. in line with the maximum modulation output. The PQ controller limits and rotor current reference limits depend upon the particular control method, as discussed in Sections 6.5 – 6.7.

Dynamic control performance

The feedback current controllers were tuned for performance on the test rig, as follows. The rotor current PI controller produced at best a 5ms characteristic impulse response rise-time with an overshoot below 5%. This reaction was far slower than the simulated version due to the poor quality of the lab supply voltage. The response is put into context by the 39ms rotor transient time constant. The PQ controller was tuned for a characteristic 40ms rise-time, deliberately 8 times slower than the rotor current controller to ensure dynamic stability.

6.5 A VAr-support method

6.5.1 VAr-support control setup

To demonstrate the controlled response of the DFIG in grid faults, the test rig controller was setup to contribute VArs in response to dips in stator voltage magnitude. The rotor converter's reactive power reference value was determined by a lookup table with voltage magnitude as its input, as shown in Figure 6.9. This reference value is dispatched to the PQ PI controllers as indicated in Figure 6.8.

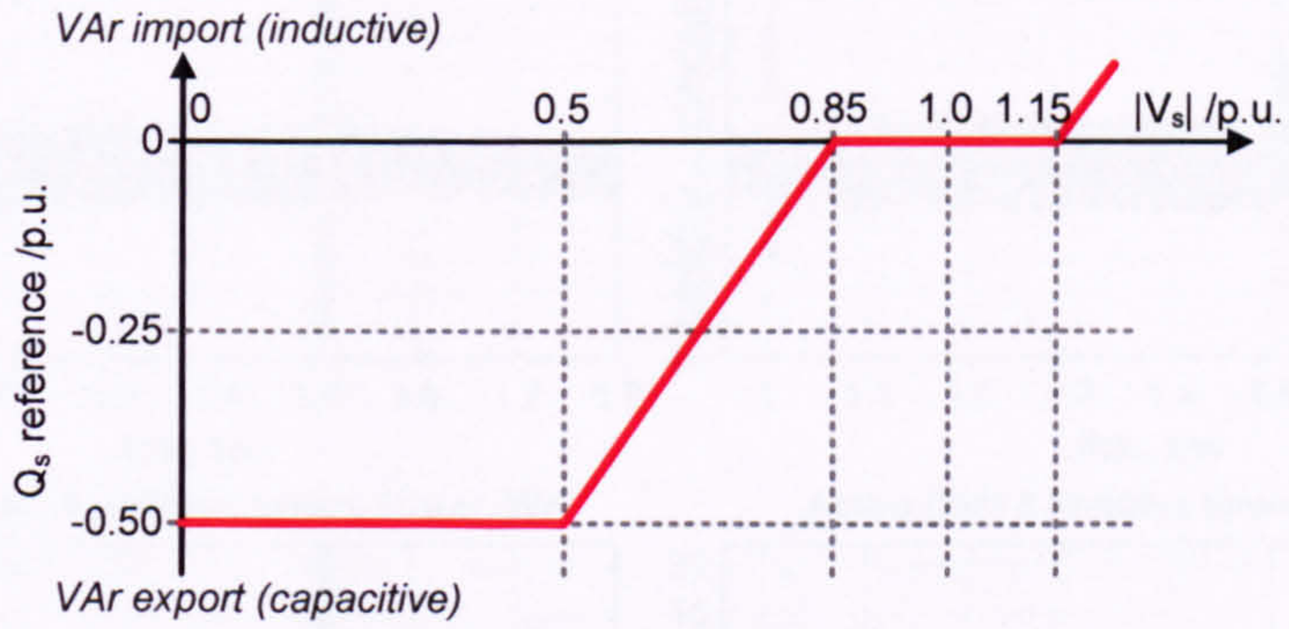

Figure 6.9. Reactive power control reference versus voltage magnitude.

The minimum reactive power was limited to -0.5 p.u. (export), although in practice this value is not reached due to the limited current available from the rotor converter and the magnetisation demands of the induction machine. In operation, the rotor's reactive-current-reference calculated by the PQ PI controller may lie beyond the safe operating range of the converter. This reference value is therefore saturated (limited in magnitude). The PQ PI integral component (anti-windup limits) and the PQ PI output

reference are each configured to limit the reactive-current component to ±0.67 p.u while the active power component is limited to ±1.0 p.u. This ensures a maximum short-term current reference magnitude of well below the transient surge limit of 2.0 p.u. Generous headroom below the maximum current magnitude was included to allow for overshoot in the current response and to prevent continuous operation at above 1.0 p.u. magnitude.

For example: in order to generate 0.5 p.u. of reactive power with a 20% retained fault voltage the machine would require a 2.5 p.u. reactive current reference. However, the rotor-current-reference magnitude can be no higher than 0.67 p.u. This prevents integral windup in the PI controllers while delivering a certain amount of reactive power into the fault.

6.5.2 Fault tests

VAr-support test – 15% fault

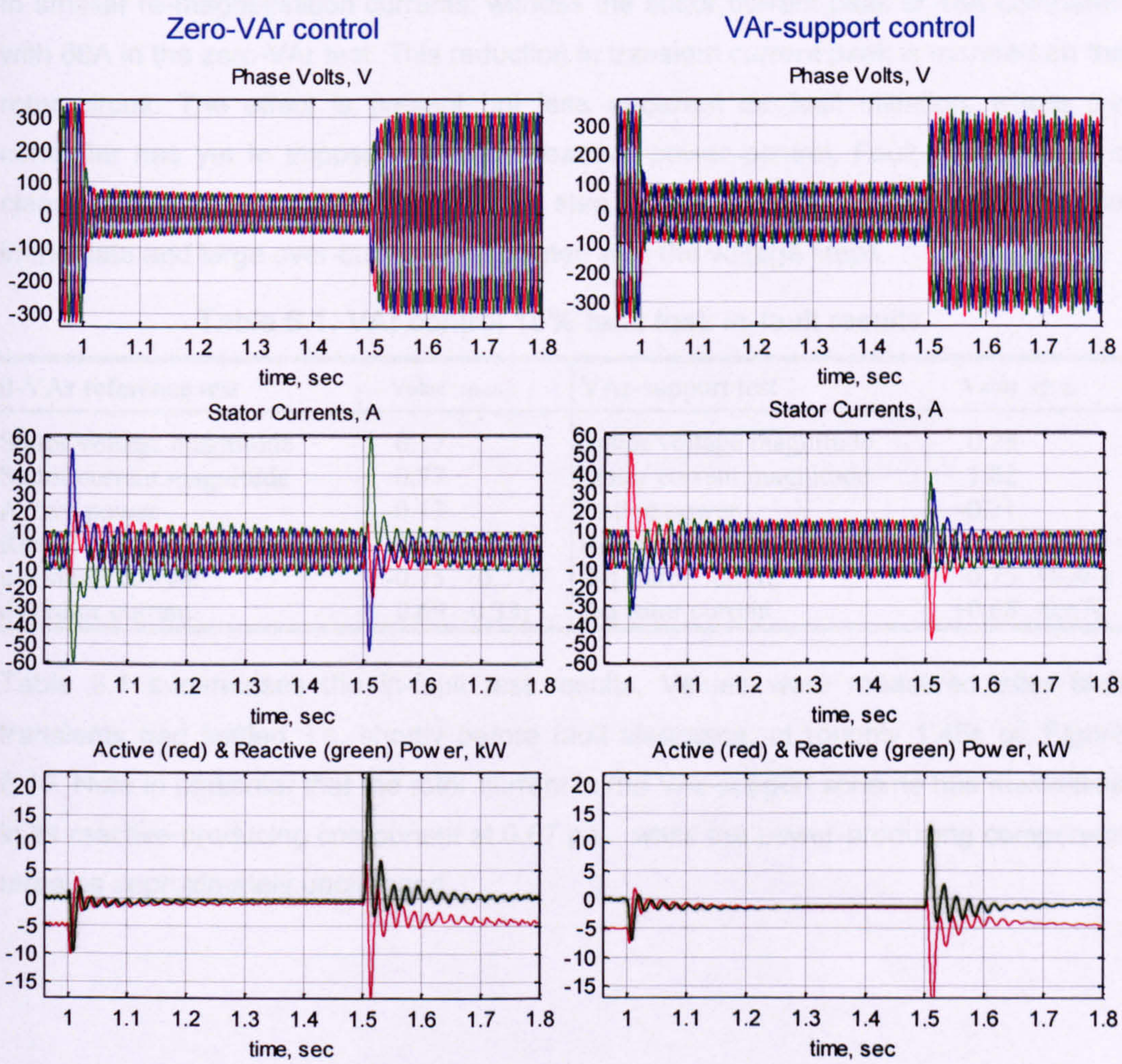

Figure 6.10. 15% fault tests: left zero-VAr control, right VAr-support control.

The VAr-support method above is tested under the three standard fault conditions introduced in 6.4.2. The relevant results are displayed in the right-hand columns of

Figure 6.10, Figure 6.11 and Figure 6.12: including stator voltages, stator currents and stator power. The left hand columns in these figures display the results of comparative 'zero-VAr' tests where the PQ PI reactive power reference was held at zero throughout.

The zero-VAr test revealed a fairly steady in-fault peak voltage of almost 60V compared with the pre-fault 340V: 17% of rated. Stator current transients touched 60A (4p.u.) peak before running at 11A peak (0.77p.u). The in-fault active power settled at 970W (13% rated), whilst the reactive power settled on a trivial 350W (4.7%).

By comparison, the DFIG fared better in the VAr-support test. Peak voltage was almost 95V (28%), an increase of roughly 11%. The stator currents were managed at 14.7A peak during the fault period, i.e. 1p.u. magnitude. However, the increased voltage permitted 1.6kW (21%) and 1.3kVAr (18%) of generation.

Note that because of the relatively higher in-fault voltage during the VAr-support tests, the step in voltage on fault clearance is smaller than for the zero-VAr tests. This leads to smaller re-magnetisation currents: witness the stator current peak of 48A compared with 60A in the zero-VAr test. This reduction in transient current peak is mirrored on the rotor circuit. The effect is present but less apparent on fault initiation, where the controller has yet to impose deliberate reactive power control. Fault ride through is clearly aided by restricting the voltage step, but it cannot altogether negate the immediate and large over-currents associated with the voltage steps.

Table 6.1. VAr control 15% fault test: in-fault results.

0-VAr reference test	Value /p.u.	VAr-support test	Value /p.u.
Stator voltage magnitude	0.17	Stator voltage magnitude	0.28
Stator current magnitude	0.77	Stator current magnitude	1.02
Active power	-0.13	Active power	-0.21
Reactive power	-0.05	Reactive power	-0.18
d-q stator current	-0.75 +0.31j	d-q stator current	-0.75 +0.64j
d-q rotor current	0.69 -0.33j	d-q rotor current	+0.68 -0.67j

Table 6.1 summarises the in-fault test results. Values were measured after fault transients had settled, i.e. shortly before fault clearance, at roughly 1.45s on Figure 6.10. Note in particular that the rotor current in the VAr-support scheme has maximised in its reactive-producing component at 0.67 p.u., while the power-producing component remains approximately unchanged.

VAr-support test – 50% fault

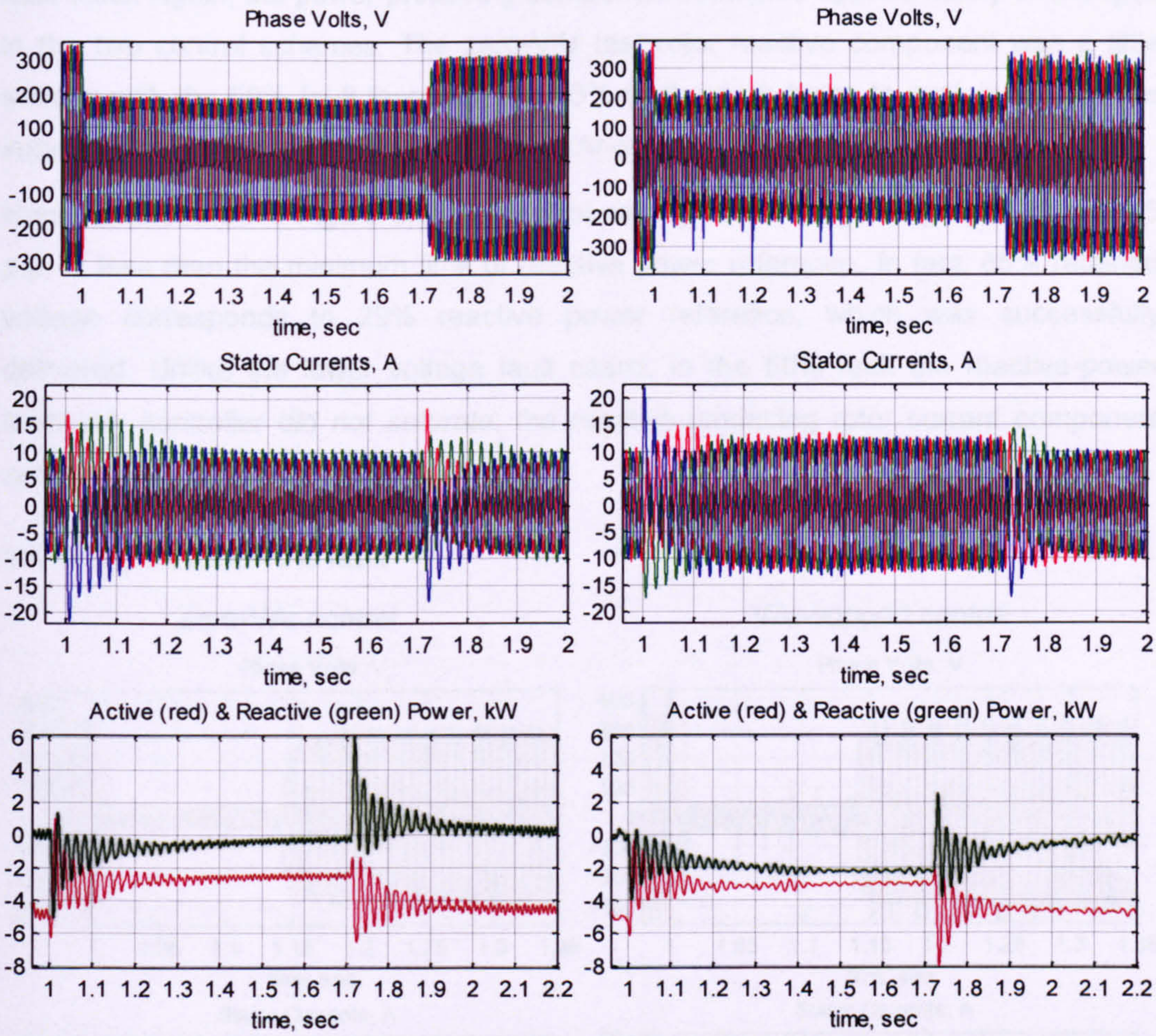

Figure 6.11. 50% fault tests: left zero-VAr control, right VAr-support control.

Results for the 50% fault tests are shown in Figure 6.11. In-fault results are summarised in Table 6.2, sampled at a point roughly 1.65s into the recorded data. The VAr-support test reveals a significant 14% improvement in fault voltage, which permitted a perhaps disappointing 6% increase in active power output. Again, the smaller step voltage at fault clearance reduced the transient peak currents: one phase reaching 16A rather than two phases reaching 18A. As shown in Chapter 5, the 50% fault turned out to be mild enough for the DFIG controller to manage safely without modifications.

Table 6.2. VAr control 50% fault test: in-fault results.

0-VAr reference test	Value /p.u.	VAr-support test	Value /p.u.
Stator voltage magnitude	0.51	Stator voltage magnitude	0.65
Stator current magnitude	0.64	Stator current magnitude	0.83
Active power	-0.34	Active power	-0.40
Reactive power	-0.03	Reactive power	-0.30
d-q stator current	-0.66 +0.06j	d-q stator current	-0.61 +0.46j
d-q rotor current	+0.66 -0.30j	d-q rotor current	+0.68 -0.64j

Interestingly, the in-fault rotor currents (Table 6.2) were each similar those the 15% fault tests. Again, the power-producing component remained approximately unchanged in the two control schemes. The zero-VAr test rotor reactive component was a little smaller with the 50% fault than with the 15% fault, which helps to explain the greater improvement in voltage magnitude in this VAr-support test.

Now, as illustrated in Figure 6.9, the control setting for a voltage magnitude above 0.5 p.u. is less than the minimum limit of reactive power reference. In fact, 65% retained voltage corresponds to 29% reactive power reference, which was successfully delivered. Unlike the lower voltage fault cases, in the 50% fault the reactive-power feedback controller *did not saturate*; the reactive-producing rotor current component settled at a controlled 64%.

VAr-support test – 0% fault

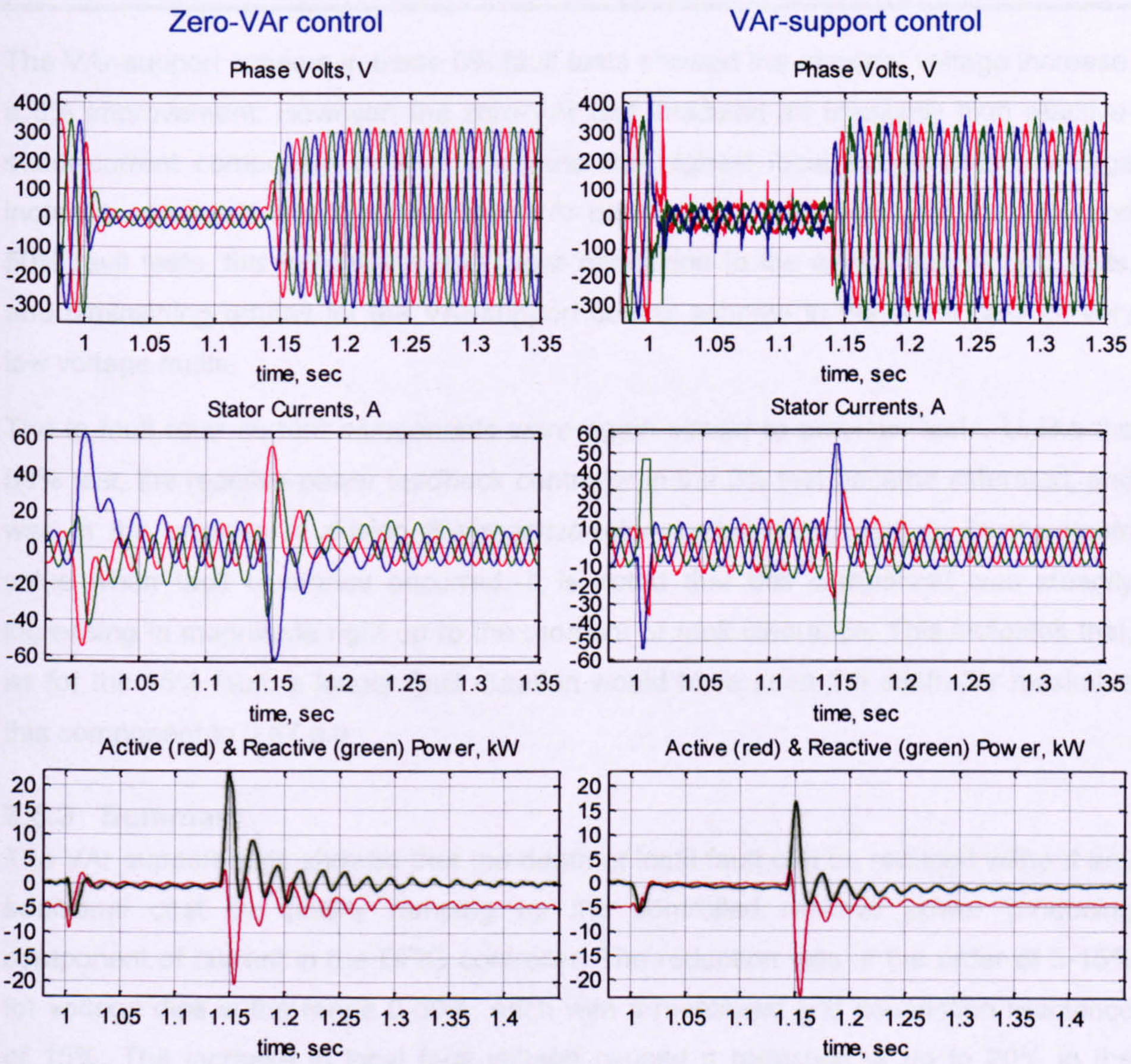

Figure 6.12. 0% fault tests: left zero-VAr control, right VAr-support control.

Results for the 0% fault tests are shown in Figure 6.12. In these short faults the transient currents did not fully decay before fault clearance in either case. There

appears to be considerable dc-offset in the zero-VAr test currents, which is further evident in the extended 50Hz oscillations of power. The low voltage in the VAr-support test brought about undesirable high frequency noise from elements in the grid fault emulation equipment. This noise is not apparent in the zero-VAr test, a test performed some months earlier, and is attributed to equipment deterioration. Nonetheless the 50Hz fundamental can be seen clearly in both tests. The pre-clearance values of the mean fundamental components are recorded in Table 6.3.

Table 6.3. VAr control 0% fault test: in-fault results.

0-VAr reference test	Value /p.u.	VAr-support test	Value /p.u.
Stator voltage magnitude	0.10	Stator voltage magnitude	0.16
Stator current magnitude	0.93	Stator current magnitude	0.96
Active power	-0.02	Active power	-0.03
Reactive power	-0.09	Reactive power	-0.14
d-q stator current	-0.20 +0.87j	d-q stator current	-0.18 +0.89j
d-q rotor current	+0.76 -0.39j	d-q rotor current	+0.66 -0.65j

The VAr-support scheme in these 0% fault tests showed the smallest voltage increase, a 6% improvement. However, the zero-VAr test indicated an unusually high reactive-stator-current component at 0.87 p.u. (and the highest local-voltage-to-fault-voltage increase compared with the other zero-VAr base tests). Compared with the 15% and 50% fault tests, this indicates a non-linear opposition to the application of zero volts, and diminishing returns for the VAr-support control scheme in the worst case of very low voltage faults.

The in-fault rotor current components were again similar to previous tests. Unlike the 50% test, the reactive-power feedback controller in the 0% test became saturated, and was in the process of driving the reactive-rotor-current-component to its maximum value when fault clearance occurred. It is noted that this component was steadily increasing in magnitude right up to the moment of fault clearance. This indicates that, as for the 15% fault, a longer fault duration would have seen the controller maximise this component to 0.67 p.u.

6.5.3 Summary

The VAr support tests showed that the depth of local fault can be reduced without any additional cost by quickly ramping up the controlled reactive power producing component of current in the DFIG controller. The reduction was of the order of 5-15% for voltage dips in the range 0-50%, each with a measured grid connection reactance of 15%. The increase in local fault voltage caused a reduction of up to 20% in the recorded peak over-currents upon fault recovery.

This does not negate the problem of transient currents on fault initiation and recovery, but shows that the DFIG can remain stable and contribute a limited amount of voltage support during grid faults. The quantification of voltage support depends strongly on the specific grid connection impedance. Although the precise power cannot be explicitly prescribed, it is recommended that the rotor converter maximise its reactive-power producing component of current in response to voltage dips below 50%. This contribution should be prioritised over the active power-producing component until the transients of fault recovery begin to decay, after which active power and mechanical stability can become steadily a higher priority.

In light of these results, the VAr-support control scheme was kept in place for all other fault tests in this work, including the crowbar and brake chopper tests which follow. Having established the stability of the VAr-support control scheme, the saturation limits on the reactive-component of rotor current reference were increased from ±0.67 to ±1.0 p.u. for the ensuing tests. Together with the power-producing component, this may produce transient rotor current reference magnitudes above 1.0 p.u. but still well below the 2.0 p.u. surge limit. The VAr-support test results became the 'base test' benchmark to which the crowbar and DC-brake schemes were compared.

With or without VAr-support, the 50% fault did not elicit transient currents in excess of the stated transient limit of 2.0 p.u. Further fault ride through schemes are not tested for this relatively shallow fault.

The reactive power feedback controller should ensure that reactive-current contributions are maximised (within safe limits) during grid faults. With hindsight it seems plausible to override the *reactive power* feedback controller in the instance of the fault and instead apply *reactive-component of stator current* feedback control. This would more easily account for the change in voltage, and allow direct comparison with the reactive-current fault response demands of, for example, German grid code. Unfortunately, time restrictions and a late spate of problems with the grid fault emulation equipment prevented these tests from being repeated with a new reactive current control scheme.

Nonetheless, these results clearly indicate that the reactive-current capabilities of the DFIG's converter can be used to improve fault ride through behaviour, particularly at voltage recovery, without explicitly solving the underlying problems of rapid demagnetisation.

6.6 Crowbar methods

6.6.1 The crowbar in detail

The rotor-circuit crowbar was introduced in Section 6.3.3, where its use in terms of DFIG fault response was outlined. This section explores the action of the crowbar in more detail and proposes criteria for the selection of appropriate crowbar resistance. The crowbar circuit used in the test rig is formed of a three phase rectifier, power resistor and series IGBT switch as shown in Figure 6.13.

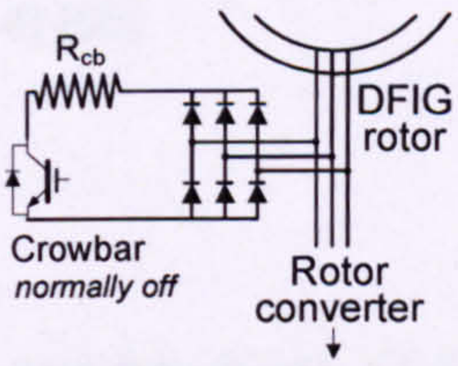

Figure 6.13. Rectifier-IGBT crowbar in the DFIG rotor circuit.

Principle of rectifier crowbar operation

The crowbar is normally off and does not contribute to normal operation. When engaged, the crowbar draws rectified current in proportion to the rectified voltage. A simple simulation of the rectifier-switch crowbar provides the current waveforms shown in Figure 6.14. The simulation was setup using Simulink using its Power Systems toolbox, with nominal values for snubber circuits and forward-conduction losses. Here, a 590Vph AC source was shorted through an IGBT-rectifier crowbar with a 25Ω resistor; a situation not dissimilar to test rig fault conditions. The simulated crowbar was energised at 0 seconds.

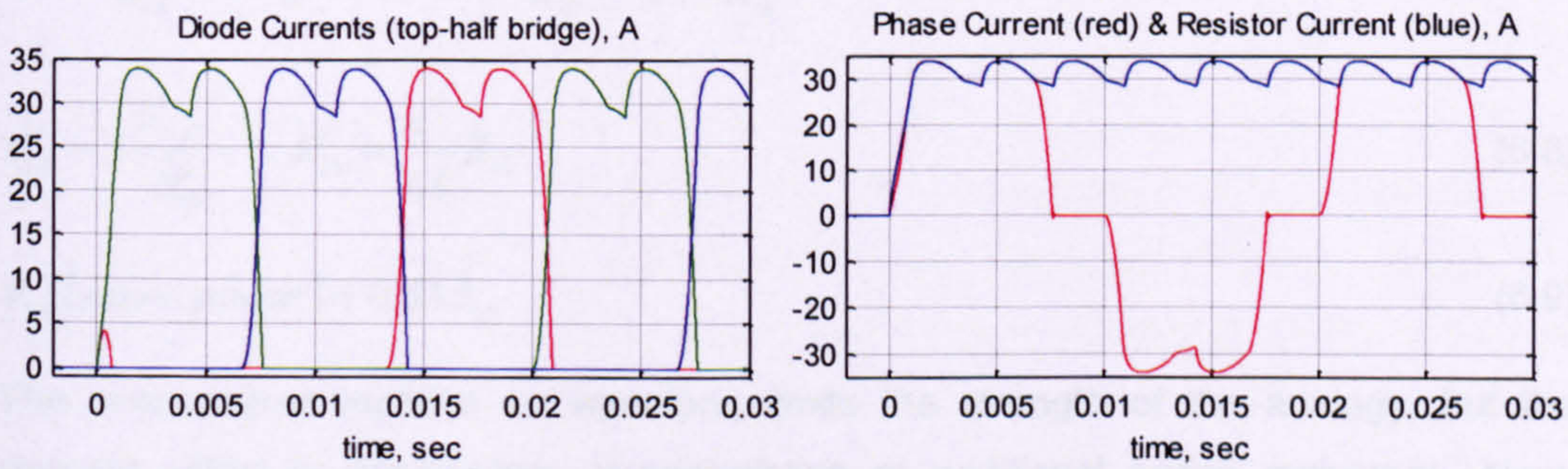

Figure 6.14. Crowbar simulation.

The diodes of the crowbar continuously conduct while the crowbar is engaged. As noted in Section 6.3.3, with a thyristor switch the rotor currents must decay to zero before the crowbar can be turned off. With a GTO thyristor or IGBT, the switch may interrupt the crowbar current when required.

Equivalent phase resistance

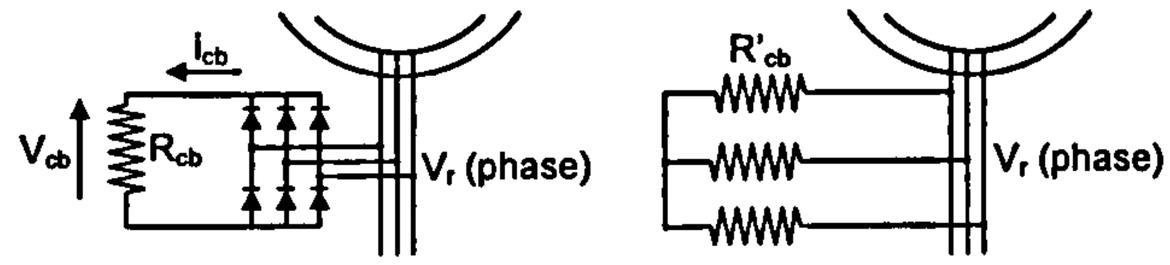

Figure 6.15. Approximate crowbar-resistance analogy

With the switch engaged, the crowbar resistance behaves similarly to the addition of three phase resistors to zero volts in series with the rotor's windings (Figure 6.15). An equivalent 'per-phase' resistance of the crowbar can be approximated using this analogy. Firstly, note that an ideal rectifier provides an average dc voltage of 1.35 times the line-line voltage (Eq. 6.4) [66]:

$$\langle V_{dc} \rangle = \left(\frac{3\sqrt{2}}{\pi} \right) V_{ac,ph-ph.rms} \tag{6.4}$$

In terms of *average current*, the crowbar draws √3 times more current than the same resistance in series (Eq. 6.5).

$$i_{cb} = \left(\frac{3\sqrt{2}}{\pi} \right) i_r = \frac{v_{cb}}{R_{cb}} = \left(\frac{3\sqrt{2}}{\pi} \right) \frac{\sqrt{3} V_{r,ph}}{R_{cb}} \therefore i_r = \frac{\sqrt{3} V_{r,ph}}{R_{cb}} \therefore R'_{cb} = \frac{R_{cb}}{\sqrt{3}} \tag{6.5}$$

$$R'_{cb}(equiv.current) = 0.58 R_{cb} \tag{6.6}$$

In terms of *average power* dissipated, the equivalent series resistance produces a similar relationship:

$$P_{cb} = \frac{{v_{cb}}^2}{R_{cb}} = \left(\frac{3\sqrt{2}}{\pi} \sqrt{3} V_{r,ph} \right)^2 \frac{1}{R_{cb}} = \frac{54}{\pi^2} \frac{{V_{r,ph}}^2}{R_{cb}} \tag{6.7}$$

$$P'_{cb} = 3 \frac{{V_{r,ph}}^2}{R'_{cb}} \therefore R'_{cb} = \frac{\pi^2}{18} R_{cb} \tag{6.8}$$

$$R'_{cb}(equiv.power) = 0.55 R_{cb} \tag{6.9}$$

The unsmoothed rectified ac waveform limits the strength of the analogy, but the average effect is nonetheless representative of additional series resistance. Now, considering the flux decay time constants as defined in Chapter 3, this resistance shortens the effective rotor transient time constant (Eq. 6.10).

$$\tau_r = \frac{\sigma L r}{R_r} \rightarrow \frac{\sigma L r}{R_r + R'_{cb}} \tag{6.10}$$

A well chosen resistance can extinguish the self-linking rotor flux in a handful of milliseconds, as discussed in Section 6.6.7. After the rotor transients have decayed, the crowbar can be disabled and rotor-converter control can be resumed.

Effects of changing the crowbar resistance

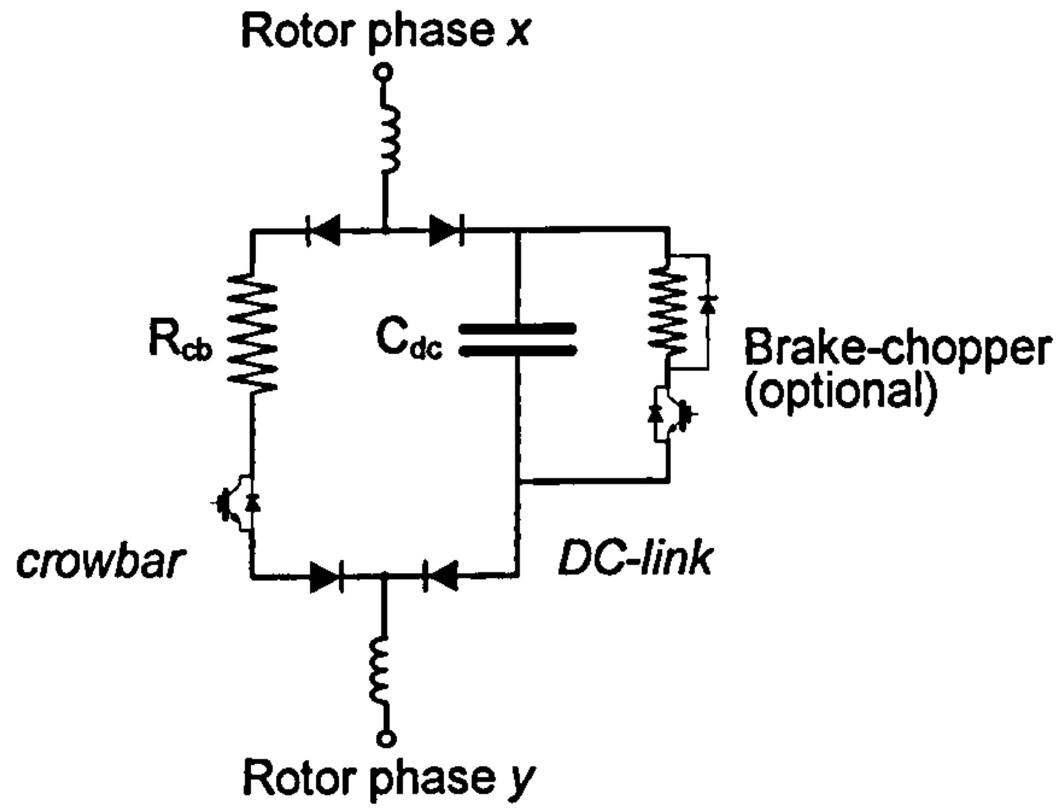

Figure 6.16. Circuit paths for fault-transient rotor currents.

The impact of changing the crowbar resistance with respect to DFIG fault response is best illustrated by referring to Figure 6.16. This depicts the circuit path options for rotor currents faced with a PWM-disabled rotor converter and an active crowbar, flowing between two arbitrary rotor phases.

With zero or very low resistance, the crowbar simply shorts the rotor windings and has scant effect on the natural dynamics of rotor circuit decay. The rotor converter's diodes are fully blocked and there is no current flow onto the DC-link. As the crowbar resistance is increased, the rotor time constant is reduced; the crowbar accepts the shortened periods of over-current while the DC-link remains blocked. At greater than twice the rotor winding resistance or more, the crowbar starts to dominate the rotor circuit, sinking the majority of the rotor magnetisation energy after a severe grid fault. Above a certain resistance, the iR potential across the crowbar indicates sufficient phase-phase rotor voltage to drive current through the rotor-converter diodes and through the DC-link capacitance. At successively higher crowbar resistance the share of current is increasingly taken by the DC-link capacitor and the DC-link voltage is forced higher. If present, the action of a brake chopper helps to limit the DC-link voltage rise, but does not directly influence the nature of the rotor flux decay.

In order to prevent a DC-over-voltage event, the crowbar resistance should be limited to prevent or at least minimise conduction through the converter's DC-link; a restriction described by Eq. 6.11

$$i_{cb}R_{cb} < V_{dc} \tag{6.11}$$

Recognising the average value of rectified current from Eq. 6.5:

$$R_{cb} < \frac{V_{dc}}{1.35 i_r} \tag{6.12}$$

Eq. 6.12 describes the maximum crowbar resistance in SI units. Caution should be applied when comparing p.u. bases of the machine and the converter's DC-link. Also, this limit is somewhat imprecise because it depends upon the average value of current and whether the converter's DC-link can manage a small level of conduction; this in turn depends upon the relative size of the capacitance, the presence of a protective brake chopper and the ability of the line-side converter to sink power from the DC-link through the residual fault voltage.

Chapter 5 established maximum transient rotor currents of roughly 5 p.u. An approximation of the limit in Eq. 6.12 is therefore:

$$R_{cb} < \frac{V_{dc}}{6.75 i_{r,base}} \tag{6.13}$$

Overall, the crowbar resistance should be maximised to improve its relative ability to hasten the decay of rotor flux, but should remain safely below the maximum limit imposed by Eq. 6.12.

6.6.2 Test rig crowbar value

Using the operational DC-link voltage of 750V dc and the base rotor current of 3.35A Eq. 6.13 suggests a maximum crowbar resistance of 33Ω.

The crowbar resistance was chosen to reduce the rotor transient time constant to 10ms, which is roughly ¼ of the test machine's original value. According to Eq. 6.10, with a rotor winding resistance measured at 0.02 p.u., this required an additional 0.06 p.u. of equivalent per-phase resistance: 13.4Ω using machine rotor base values. Using the equal power approximation of Eq. 6.9 this equates to 23.0Ω of dc crowbar resistance. A 25Ω, 0.6kW power resistor was selected for this purpose. The relatively low thermal power rating is acceptable because the crowbar is used for such short durations. Note that the chosen resistance is still 25% below the estimated maximum limit. The new DFIG fault decay parameters with the 25Ω crowbar applied were detailed in Table 5.2 in Chapter 5.

6.6.3 Crowbar tests overview

Crowbar tests

The test rig crowbar used an IGBT-plus-rectifier configuration, as shown in Figure 4.4 (c). This was originally chosen for its simplicity and flexibility of operation; however the IGBT's turn-off capability becomes implicit in the minimum threshold control method described in Section 6.6.6.

The test rig crowbar was hardwired to self-energise in the case of dangerous test rig rotor currents (over 45A peak, or 9 p.u.), irrespective of the test or controller settings. In the following fault ride through methods the crowbar was activated by the DFIG control scheme via a separate software-driven trigger signal, used for lower, more representative rotor current values.

The first method involves a timer-controlled crowbar. This safety-first method involves the total de-energisation of the rotor circuit. The crowbar is engaged for a timed period, chosen to comfortably exceed rotor transients, after which the crowbar is disabled and the rotor converter is quickly re-engaged onto a rotor circuit with zero current.

Secondly, crowbar operation is developed to minimise the duration for which the crowbar is applied, focussing chiefly on the stability of resuming vector control. Finally a successfully applied minimum-time threshold crowbar method is presented.

Trigger signal

Primarily, the crowbar is designed to protect the power converter devices from over-rated currents. Originally therefore the crowbar was planned to be triggered by any one of three rotor phases exceeding a threshold limit. However, it is worth noting that due to the winding arrangement of the rotor, no zero-sequence current can flow. Therefore the d-q form of rotor current contains all the magnitude information from the three-phases. Hence the crowbar is triggered if the d-q current magnitude exceeds the p.u. threshold limit. On the test rig, this simple software trigger sends a digital on/off signal from the DFIG dSpace controller to the crowbar, via opto-isolation on the main protection board. On the test rig, this dSpace signal proved 100% reliable. However, in practice, a trigger signal circuit could be built instead using analogue electronics if increased reliability were an issue.

6.6.4 Timer action crowbar

General operation

The crowbar is activated when the magnitude of the rotor current exceeds a threshold value (Eq. 6.14). As for all the crowbar tests, this threshold was set for the stated maximum IGBT pulse current of 2.0 p.u.

Crowbar turn-on: $|\vec{i}_r| > 2.0\,\text{p.u.}$ (6.14)

The crowbar then remains engaged for a fixed time, τ_{cb}. While the crowbar is engaged, rotor-side PWM is disengaged (all switches 'off'). The rotor current and power PI controllers are all reset to zero output. The line-side converter's controllers remain unaffected.

After τ_{cb} has elapsed, the crowbar is released. The crowbar timer is reset-dominant, which means that it will disengage before it re-engages. If a rotor over-current persists, the crowbar is re-engaged for an additional τ_{cb} period.

When the crowbar is released, rotor-side PWM and rotor current PI control are immediately resumed. Power control is resumed after a specified delay, to allow the current controllers to settle. In the meantime, the current controllers are fed constant reference values. These interim values are deliberately constant to minimise the settling time of the current controllers. The PQ control delay should not become onerous as the interim reference currents will in any case deliver a reasonable power factor and will not act to destabilise the controller. A key trick for stability is to initialise the PQ PI feedback controllers' integral components with values set equal to the interim reference values. This helps to smooth the resumption of outer-loop feedback control. In a further smoothing mechanism, changes to the reference currents are rate-limited such that any sharp transitions cannot destabilise the current control loops.

Timer crowbar control details

The parameters of the final timer crowbar test are given in Table 6.4. The crowbar duration was set to ensure de-energisation of the rotor.

Table 6.4. Timer crowbar settings.

Threshold / p.u.	Crowbar duration /ms	PQ controller delay /ms	d-q current ref. rate-limit
2.0	120	40	1.50 p.u./s

A delay in activating the crowbar could lead to currents exceeding the transient safety threshold. The crowbar IGBT can be fired in tens of microseconds and so the largest bottleneck on crowbar activation is the control cycle time of 200μs (5kHz PWM). If the worst case transient rotor currents can rise to 5 p.u. in 20ms (Section 5.2), then the maximum current increase during crowbar activation is roughly 5%, in the worst case where a rotor current sample is taken immediately prior to an instantaneous voltage drop. In practice this rise could be accounted for in a 5% threshold limit reduction, although this was deemed negligible on the test rig.

The interim rotor current reference is set to deliver approximate reference power and reactive power (Eq. 6.15).

$$\bar{i}_r^{e\otimes}(interim\ ref) = \left[-1.00P_{ref} + 0.64|V_s|j\right] \tag{6.15}$$

The active power reference was held constant during the fault: -0.67 p.u. for 5kW nominal generation, which implies that the d-component of interim rotor current reference was also held at +0.67 constant. This d-component compares favourably

with the actively controlled rotor current values recorded in each of the VAr-support tests in Section 6.5.

The q-component was smaller here because no offset has been added to magnetise the machine at zero voltage. This was a cautious approach assuming the possibility of zero voltage on the stator and set in order to minimise the current reference, noting that the rotor is completely de-energised after 120ms of crowbar engagement.

As PQ PI control is resumed, note that the rotor current reference value changes were rate-limited to no more than 1.50 p.u./s to ensure current feedback control stability. Finally, the reactive-current reference saturation limits had been raised to ±1.0 p.u. in response to the VAr support tests.

Timer crowbar – 15% fault test

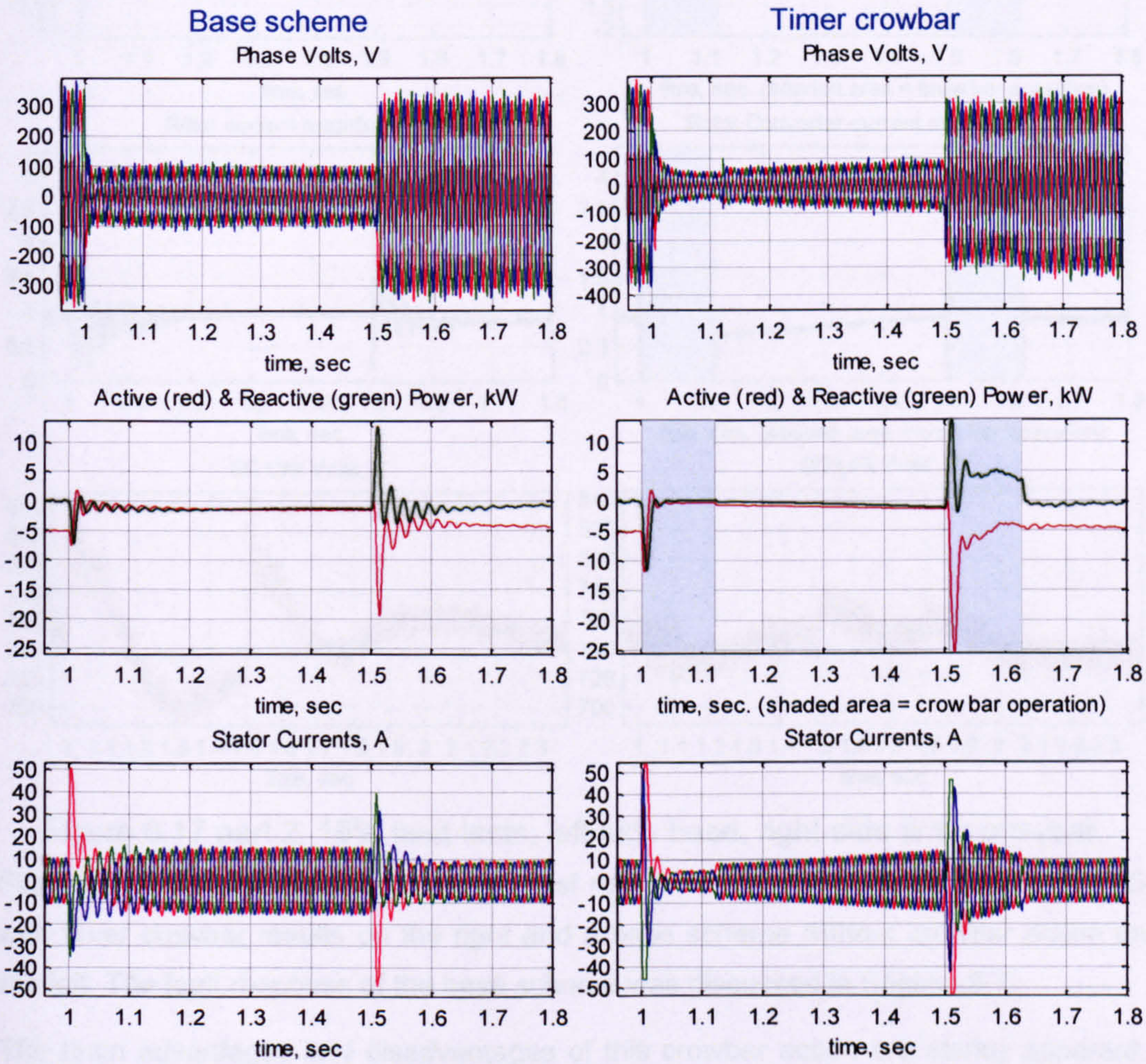

Figure 6.17 part 1. 15% fault tests: left-side base, right-side timer crowbar.

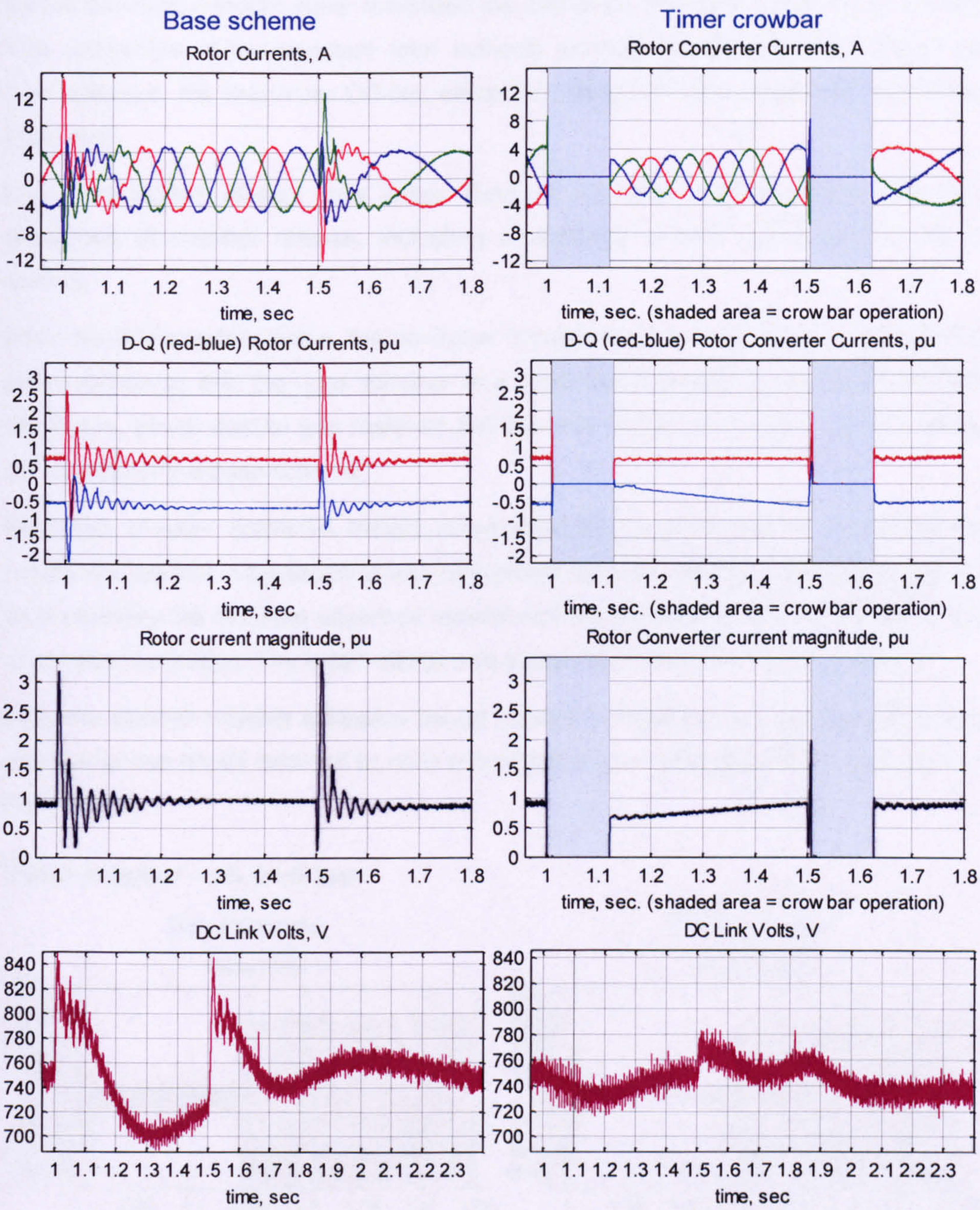

Figure 6.17 part 2. 15% fault tests: left-side base, right-side timer crowbar.

Figure 6.17 directly compares differing test results for a 15% fault applied to a DFIG with timer crowbar results on the right and a base scheme without crowbar action on the left. The fault response of the base scheme was discussed in Section 5.7.

The main advantages and disadvantages of this crowbar action are starkly apparent. On a positive note, crowbar activation immediately redirected the rotor currents. In these tests the current sensors were placed at the output of the rotor-converter's series filter chokes, between the crowbar and the converter. It is clear from this data that the converter leg currents were forced to zero throughout the crowbar period. The close-up graph of rotor current magnitude shows the 2 p.u. limit in effect. During the whole fault

period the rotor currents never exceeded the calculated maximum limit of 9.5A (peak). The redirection of the transient rotor currents protects the DC-link from dangerous over-voltages; the maximum DC-link excursion being 30V compared with 90V in the base test.

Close inspection reveals very minor kicks in d-q rotor current 40ms after both occasions of crowbar release, indicating a relatively smooth resumption of PQ PI control.

After the first crowbar action, the controller brought the d-q rotor currents towards the same values as with the base scheme, at a controlled rate-limit of 1.5 $p.u.s^{-1}$. By fault clearance, power control was restored and the local voltage boosted to 25%, close to the voltage of the base scheme.

However, crowbar activation initially suppressed the local voltage to 13% while the machine's internal magnetisation was demanded from the stator circuit. Worse still, on fault recovery the machine absorbed more than 50% reactive power for the full 120ms of crowbar activation. The local voltage was suppressed to 84% during this period.

After the second crowbar activation period, control is regained very quickly; active and reactive power levels returned to unity power factor and 5kW generation within tens of milliseconds.

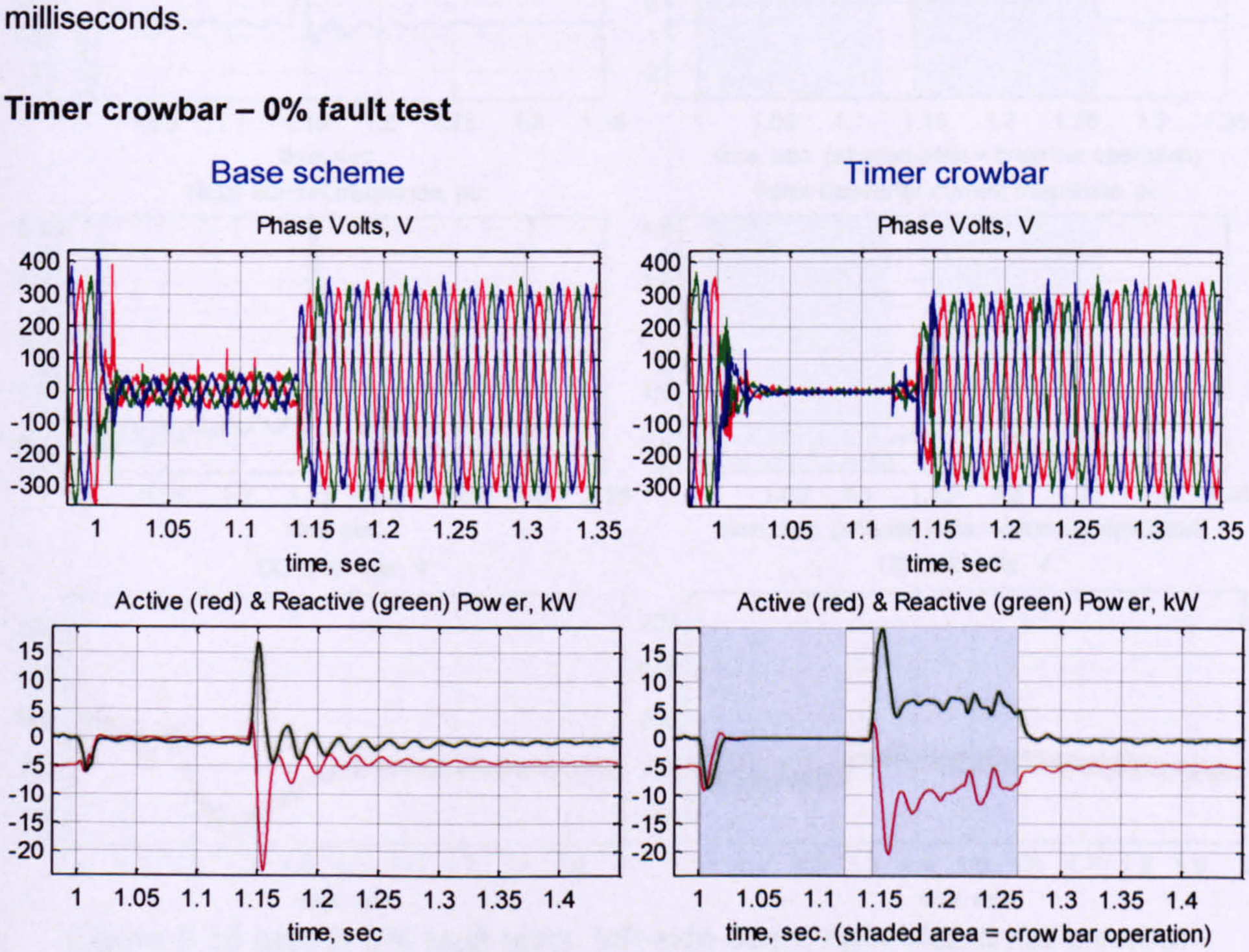

Figure 6.18 part 1. 0% fault tests: left-side base, right-side timer crowbar.

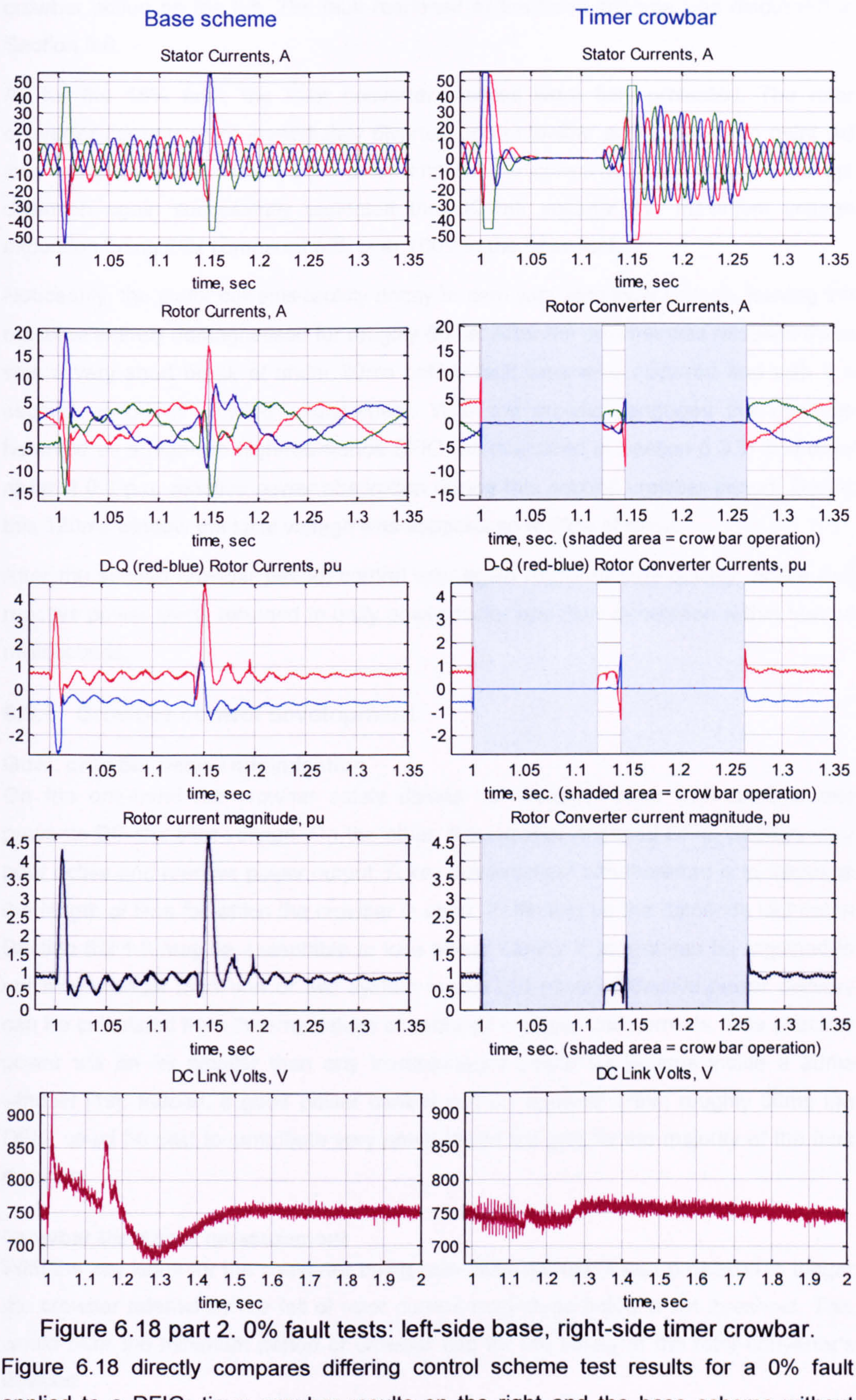

Figure 6.18 part 2. 0% fault tests: left-side base, right-side timer crowbar.

Figure 6.18 directly compares differing control scheme test results for a 0% fault applied to a DFIG: timer crowbar results on the right and the base scheme without

crowbar action on the left. The fault response of the base scheme was discussed in Section 5.6.

As for the 15% fault, the rotor converter devices were fully protected. The rotor converter currents were immediately diverted upon crowbar activation; at no point did they exceed the calculated 9.5A peak limit for the converter. The transient current diversion again successfully protected the DC-link voltage; the maximum voltage excursion being 20V compared with over 100V in the base test.

Noticeably, the stator currents rapidly decay to zero with zero local voltage, leaving the machine entirely demagnetised for roughly 80ms. After the crowbar was released there was a very short break of under 20ms before fault clearance occurred and with it a second period of crowbar engagement. With the crowbar engaged the machine behaved as a high-slip high-resistance SFIG (as described in Section 6.3.3) and drew at least 0.8 p.u. reactive power absorption during this second crowbar period. During this 120ms window the local voltage was suppressed to 82% of rated.

After the second crowbar period, control was again regained very quickly; active and reactive power levels returned to unity power factor and 5kW generation within tens of milliseconds.

6.6.5 Crowbar control development

Goal: crowbar period minimisation

On the one-hand the crowbar safely diverts the transient rotor over-currents and prevents DC-link over-voltage. On the other, the crowbar-engaged DFIG displays very poor active and reactive power output. A key development aim therefore is to minimise the length of time for which the crowbar is used. Reflecting on the demands laid out in Section 6.2.1 it may be acceptable to lose power control if control can be regained in not much longer than one or two system cycles (20-40ms). Effective power delivery can be calculated from the rms values of sampled voltages and currents. This effective power will be far smaller than any instantaneous power oscillations inside a 20ms window [19]. Indeed, if good power control can be restored within roughly 50ms the DFIG could be said to contribute very positively to the grid for the majority of the fault duration.

Crowbar threshold measurement

With the key issue for the converter being rotor over-current, it was proposed to trigger the crowbar release by the fall of rotor current magnitude below a set threshold. This would offer the minimum period of crowbar use for the safety of the rotor-converter's devices.

In order to measure the rotor currents throughout the crowbar-engaged period, the sensors in the rotor circuit were moved to between the crowbar and the rotor terminals (as shown in the test rig layout drawing Figure D.33 in Appendix D). The rotor-converter leg currents can be assumed zero during crowbar operation, provided the DC-link voltage does not rise rapidly after the crowbar is applied, as illustrated in the timer crowbar tests (Figure 6.17 & Figure 6.18) and discussed in Section 6.6.1.

Control stability

There are problems with releasing the crowbar close to its turn-on threshold of current magnitude: the ac element from the stator flux decay, uncertainties in the grid voltage plus any kicks from feedback control resumption could all threaten to re-trigger the crowbar. A certain amount of headroom was required to ensure stability with the threshold method, and this headroom by its nature is inexact.

A number of control schemes promised excellent control in simulation. The true test of stability lay in practical application to the test rig, where the vagaries of system noise and low-quality voltage supply imposed far tougher standards.

Crowbar turn-off

Initially, a deadband period was included such that release of the crowbar depended upon the rotor current magnitude remaining below the turn-on threshold for a defined time. This built an unfortunate delay into the turn-off process. To avoid this, it was noted with the natural decay and crowbar case that the rotor current magnitude drops strongly after the first peak (Section 5.3.3). The turn-off threshold was therefore set a little below the turn-on threshold: to minimise the crowbar period while avoiding nuisance re-triggering (Eq. 6.16).

Crowbar turn-off: $|\bar{i}_r| < 1.9$ p.u. (6.16)

This 5% threshold reduction (when compared with the turn-on threshold) prevented nuisance retriggering of the crowbar.

Interim reference current

When rotor current PI control was resumed before PQ PI control, the inner control loop could be fed by constant interim reference currents to contribute a reasonable power factor output while the current controllers are steadied. The interim reference introduced in Eq. 6.15 for the timer method did not include a reactive-component offset for machine magnetisation because the rotor currents were zero upon timer crowbar release. The threshold method resumes converter control onto a partially magnetised machine and the interim currents must be recalculated accordingly, as shown in Eq.

6.17. The reactive component was calculated by aggregating the zero-VAr and VAr-support test rig rotor currents for 15% and 0% faults (Section 6.5.2).

$$\bar{i}_r^{e\otimes}(interim\ ref) = \left[-1.00P_{ref} + \left(0.64Q_{ref} - 0.36\right)j\right] \tag{6.17}$$

The active power reference was held constant during the fault, at -0.67 p.u. for 5kW generation. The reactive power reference saturated at -0.5 p.u. for any voltage dip below 50%. Hence, for any serious fault:

$$\bar{i}_r^{e\otimes}(interim\ ref) = \left[0.67 - 0.68j\right] \tag{6.18}$$

Further, the onerous reference-current rate-limit from the timer crowbar control scheme was removed from the controller.

Threshold method development example

In documenting the struggle to stabilise DFIG control after crowbar application, an example of the development of the threshold crowbar method is shown below. As discussed above, the crowbar is activated and deactivated by rotor current magnitude. As before, while the crowbar is engaged, rotor-side PWM was disengaged and all IGBTs were 'off'.

After the crowbar was released, rotor-side PWM and rotor current PI control were immediately resumed. PQ control was resumed after a specified delay to allow the current controller state variables to settle. Interim current references were supplied to the rotor current controllers during the delay period. To smooth the resumption of PQ control, these interim currents were used to initialise the PQ PI controllers. The reference currents were not rate-limited. The specific parameters are given in Table 6.5.

Table 6.5. Threshold method development example.

Crowbar thresholds / p.u. ON (OFF)	PQ controller delay /ms	interim d-q current ref.
2.0 (1.9)	10	[+0.67 -0.68j]

Threshold method development example – 0% fault test

Results are shown in Figure 6.19. Overall, the rotor currents were rendered safe with respect to the converter. However, PQ PI control was not very successfully restored during the fault. The reference current outputs saturated and the rotor current controllers mismanaged the rotor currents. As a result the crowbar was triggered 3 times during the fault, each activation resulting in a period of SFIG operation which yielded undesirable power output and poor fault response behaviour.

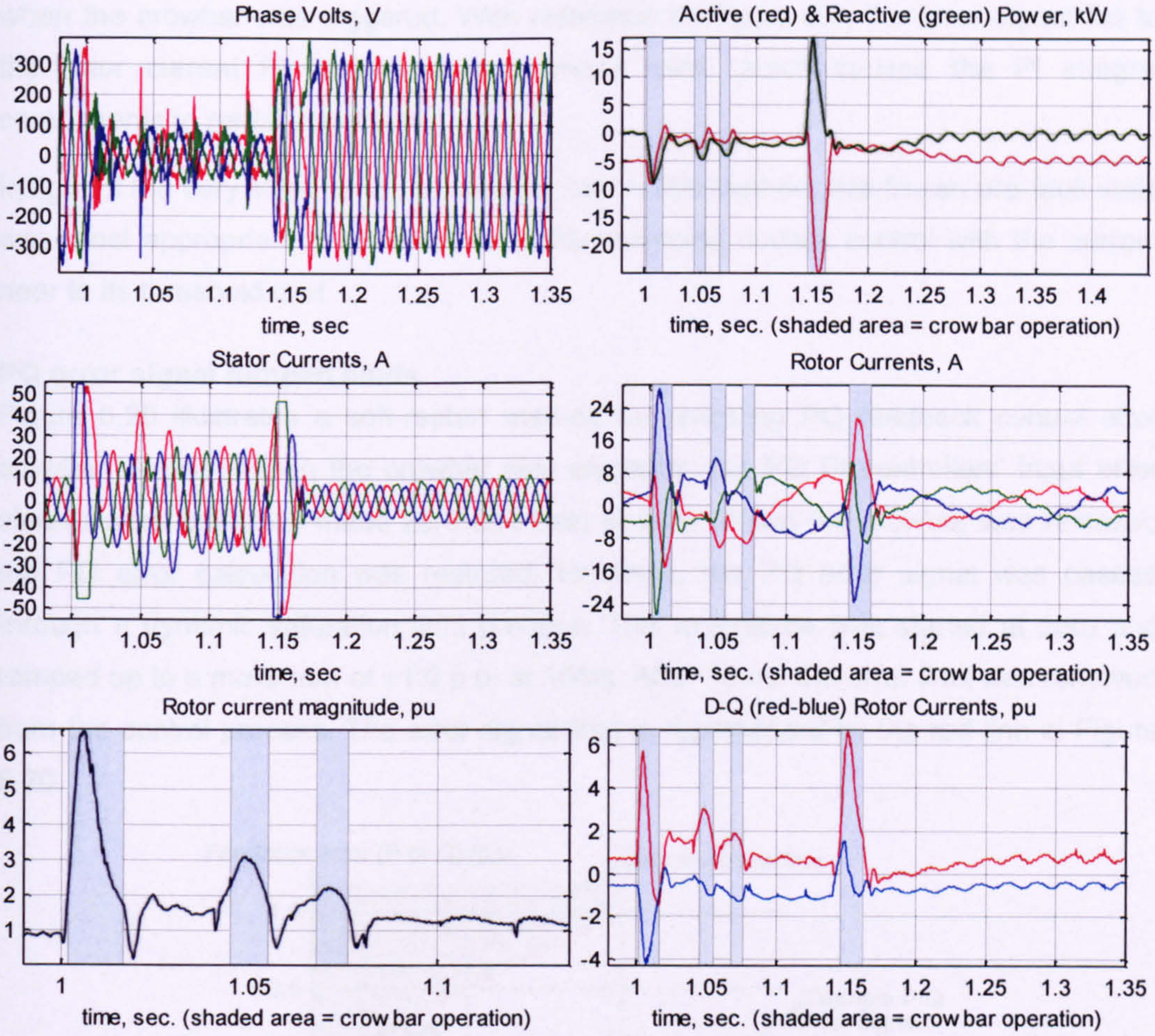

Figure 6.19. 0% fault test: Minimum threshold crowbar development.

Nonetheless, rotor current magnitude continued to fall immediately following each release of the crowbar. This left the rotor currents within controllable limits for tens of milliseconds between each crowbar application. A better suited control method should therefore manage these currents without forcing repeated applications of the crowbar.

The unwelcome spikes in stator voltage during the fault were not related to the crowbar on/off transitions. These were caused by degradation of the transfer switch equipment causing, for example, the small spike in rotor current magnitude at 1.040s.

6.6.6 Minimum threshold crowbar

A number of improvements were made to the original threshold crowbar control method to produce a stable and reliable fault ride through technique. These include 'freezing' rather than resetting the rotor current PI controllers and soft-restarting the PQ controllers by means of an error signal ramp.

Rotor current PI controller freeze

Some of the instability following resumption of rotor current PI control lay in the stabilisation of its state variables, i.e. the PI integral components. Rather than reset to zero, the PI states were 'frozen' by immediately suspending the input d-q error signal

when the crowbar was triggered. With reference to Figure 6.8, the error signal fed to the rotor current PI controllers were made zero, which caused the PI integral components to remain constant.

In light of the very short period of crowbar use in this method, this frozen pre-fault state was most appropriate in terms of smoothly resuming current control with the current near to its threshold limit.

PQ error signal ramped limits

Figure 6.20 illustrates a soft-restart method for restoring PQ feedback control after crowbar release. When the crowbar was engaged, the PQ PI controllers' input error signals were artificially made zero and held at zero. When the crowbar was released the PQ error calculation was restored. However, the PQ error signal was passed through a dynamic saturation limit process. This magnitude limit started at zero and ramped up to a maximum of ±1.0 p.u. at 10ms. After 10ms, the error limit was removed from the control process. The error signal limit is represented by the red line in Figure 6.20.

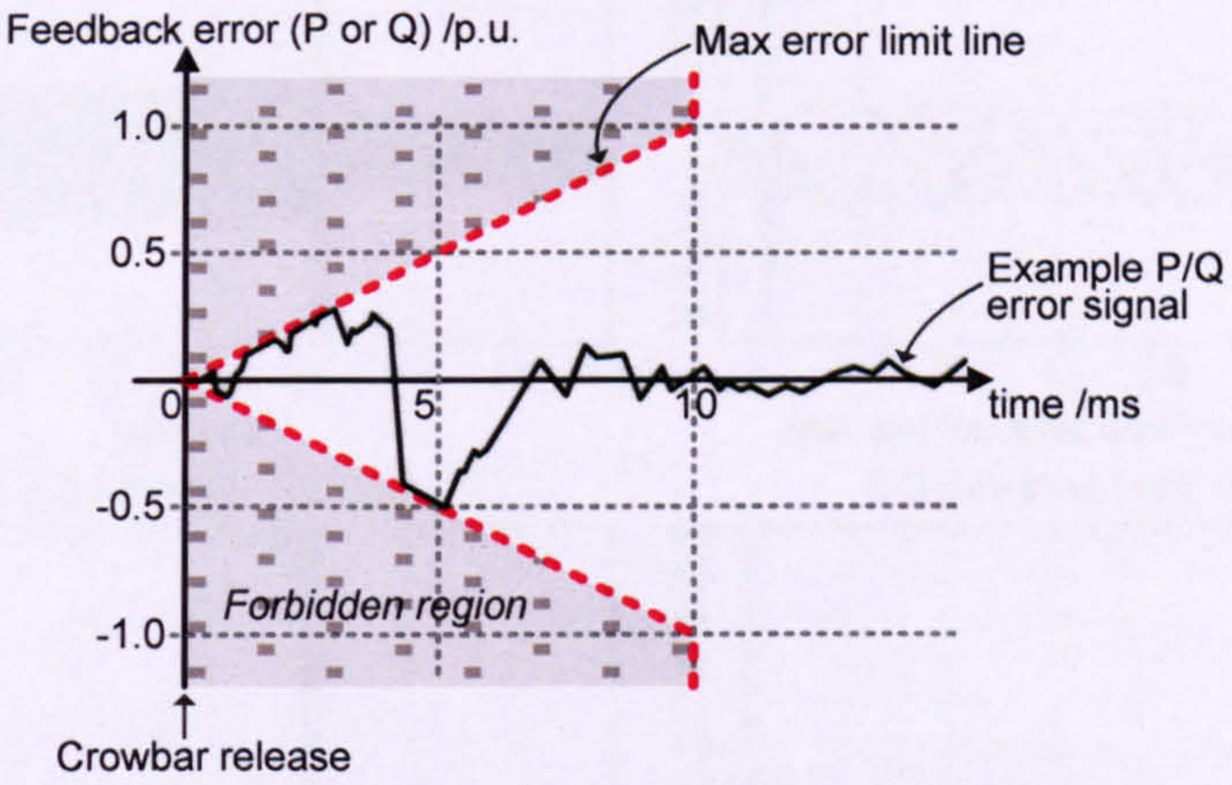

Figure 6.20. PQ error limiting soft-restart method.

When the crowbar was released the PQ PI controllers' integral components were artificially reset to output the most recent measurement of rotor current. As a result the rotor current PI controllers restarted with approximately zero error input, minimising any kick in current associated with the resumption of feedback control. 10ms was chosen for the ramp duration as a value comfortably between the characteristic rise-times of the two control loops (5ms for rotor current control and 40ms for PQ control). This method replaced the interim current reference method used in previous tests.

Minimum threshold crowbar control details

The minimum threshold control scheme parameters are summarised in Table 6.6. This method was designed to allow the controller to smoothly resume vector control of a

partially energised machine. In this manner the length of the crowbar application periods could be minimised.

Table 6.6. Minimum threshold parameters.

Crowbar thresholds / p.u. ON (OFF)	PQ controller error limit ramp rate / $p.u.s^{-1}$	PQ controller error limit duration / ms.
2.0 (1.9)	100	10

Minimum threshold crowbar – 15% fault test

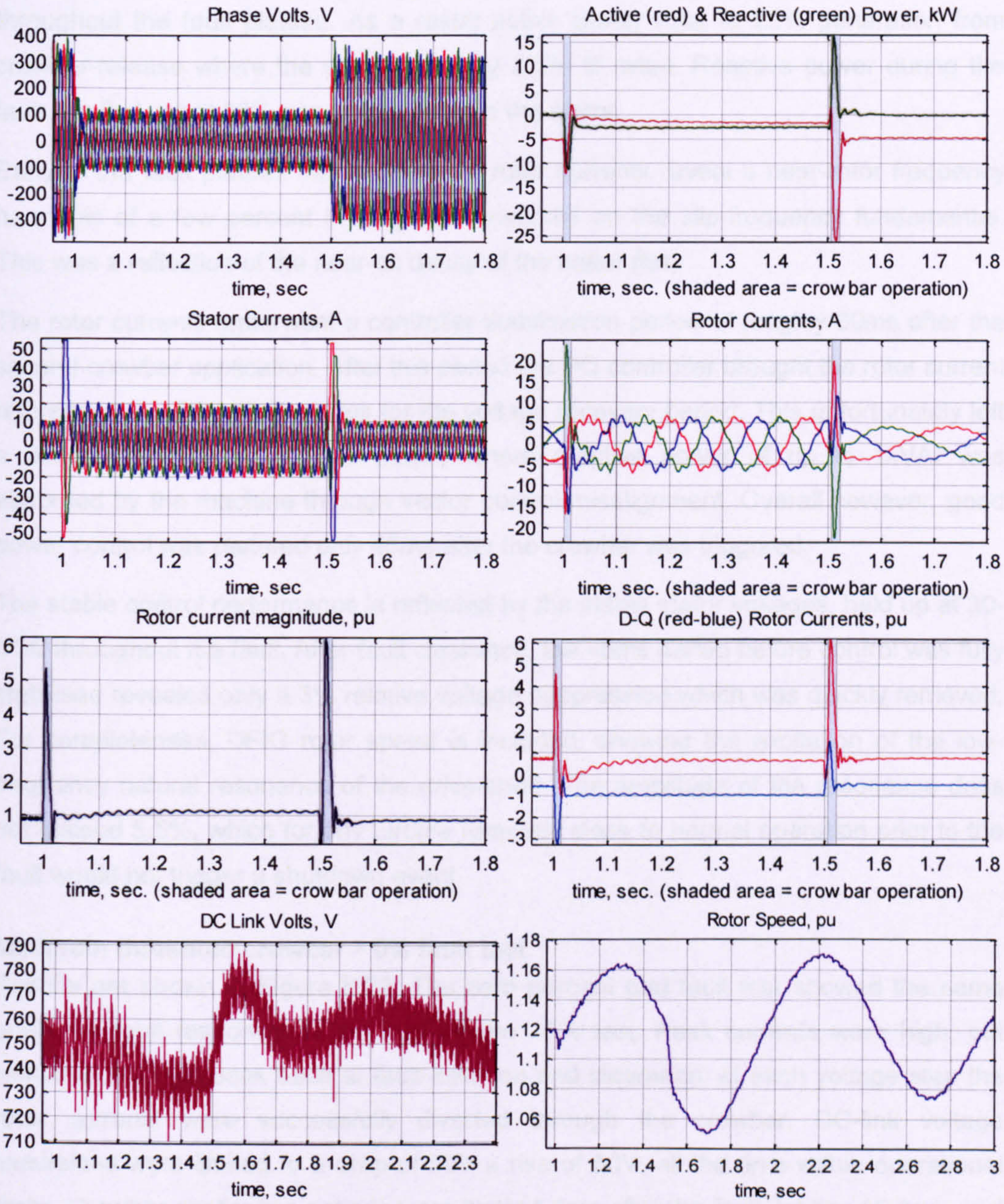

Figure 6.21. 15% Fault test: Minimum threshold crowbar.

Results are shown in Figure 6.21. As previously, the rotor currents flowing through the converter remained below 2 p.u. for the whole test. The first instance of crowbar

application was so quick that the DC-link voltage barely registered the event. The second led to a safe excursion of only 30V. The first application, 1.2ms after the fault, lasted for 13.0ms. The second crowbar application, 6.6ms after fault clearance, lasted for 15.6ms.

The d-q rotor currents show stable control established no more than 10ms following the first crowbar release. The PQ controller led the d-component to a +0.67 p.u. reference in a first-order-lag type response, showing the controller's 40ms characteristic rise-time. The q-component rose to the maximum limit of -1.0 p.u. which was held throughout the fault plateau. As a result active power rose to 22% generation from crowbar-release where the value was only 2.5% of rated. Reactive power during the fault levelled out at 33% generation through the stator.

Early in the fault plateau the three-phase rotor currents reveal a near-rotor frequency harmonic of a few percent in magnitude overlaid on the slip-frequency fundamental. This was a reflection of the near-dc decay of the stator flux.

The rotor currents underwent a controller stabilisation period of roughly 30ms after the second crowbar application. After this period the PQ controller brought the rotor current references to appropriate values for the voltage recovery period. This unfortunately left a 30ms post-crowbar release period where reactive power of up to 1kVAr was absorbed by the machine through vector control misalignment. Overall however, good power control was restored only 45ms after the crowbar was triggered.

The stable control performance is reflected by the stable stator voltages, held up at 30-31% throughout the fault. After fault clearance, the 45ms period before control was fully stabilised revealed only a 3% relative voltage suppression which was quickly removed. For completeness, DFIG rotor speed is included, showing the excitation of the low-frequency natural resonance of the drive-shaft. The amplitude of the resonance does not exceed 5.5%, which for any turbine remotely close to normal operation prior to the fault would not trigger a shutdown event.

Minimum threshold crowbar – 0% fault test

Results are shown in Figure 6.22. The zero percent grid fault test showed the same quality of fault response as the less severe 15% test. Peak currents were high, but limited to a single peak each at fault initiation and clearance; at each voltage step the rotor currents were successfully diverted through the crowbar. DC-link voltage excursions were limited to a drop of 30V a rise of 50V, all the time within operational limits. Crowbar application periods were firstly 1.0ms after the fault, lasting 15.0ms, and secondly 8.4ms after fault clearance, lasting 10.8ms.

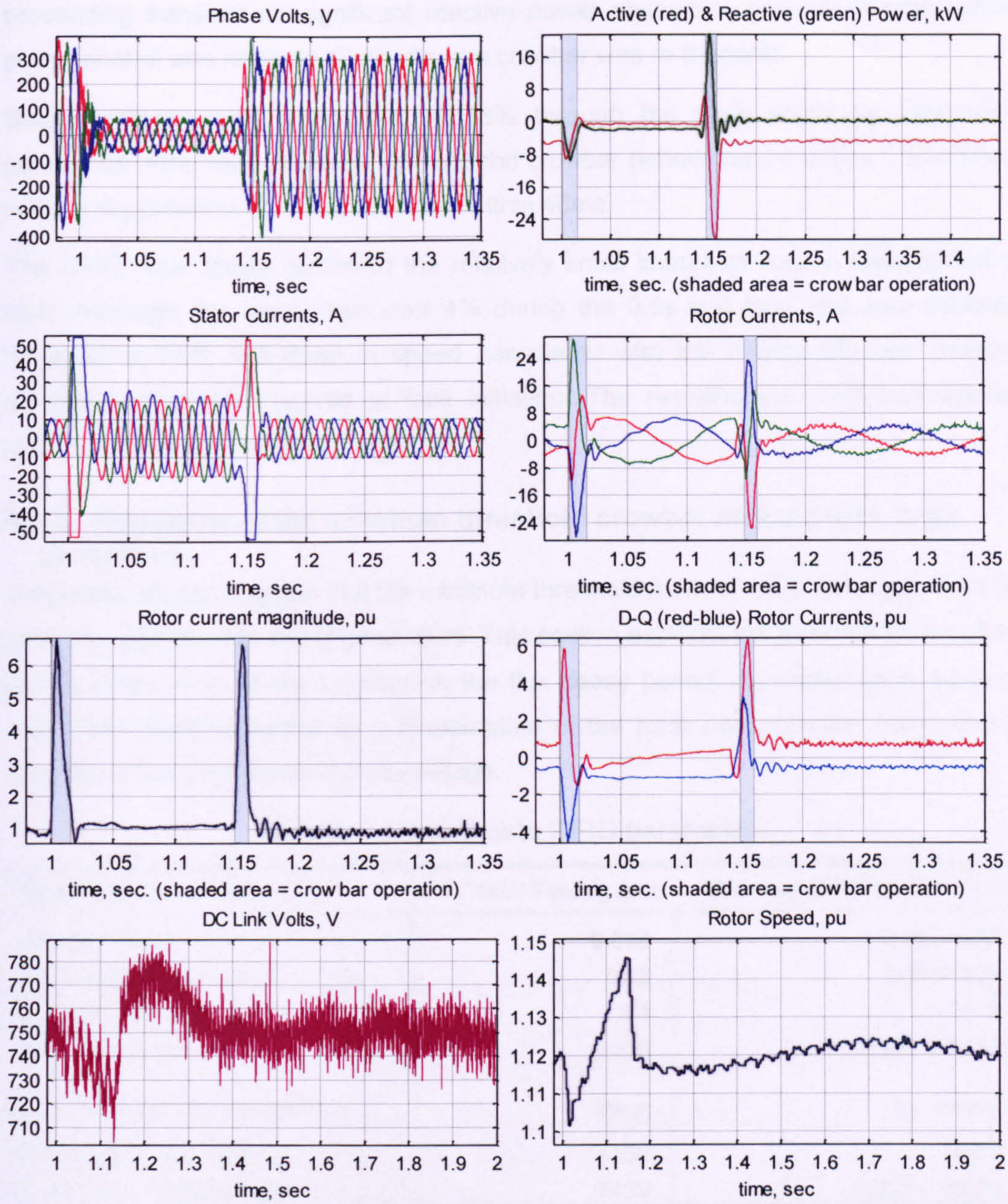

Figure 6.22. 0% Fault test: Minimum threshold crowbar.

Good control of rotor currents can be seen within 15ms after the crowbar is first released. The PQ controller led the d-component towards a +0.67 p.u. reference over the proceeding 100ms, while the q-component again marked the maximum limit of -1.0 p.u. Correspondingly, active power rose to 8.4% generation from a crowbar-release value at 3.9% of rated. Reactive power during the fault rose from a respectable 21% to 25% export.

On voltage recovery, the second crowbar period again led to a roughly 30ms period of control re-stabilisation. However, here the reactive power incidentally held a position of roughly 1 p.u. export at exactly the moment the crowbar was released, and in the

proceeding transient no significant reactive power absorption ensued. Overall, good power control was restored 40ms after the crowbar was re-triggered.

Stable voltages were maintained at 18% through the fault, solely by local VAr generation. After fault clearance, the second crowbar period caused only a 1% relative voltage suppression which was relieved within 40ms.

The DFIG rotor speed confirmed the relatively small impact of such a short duration fault. Although the speed rose over 4% during the 0.5s grid fault, this was partially offset by a 1.5% kick-down in speed associated with the demagnetisation energy dissipated from the machine at fault initiation. The resulting low frequency speed oscillation was very small in magnitude.

6.6.7 Feasibility of the minimum threshold crowbar method with large generators.

Simulation studies suggest that the minimum threshold method used in Section 6.6.6 is perfectly applicable to larger generators. This section explores the potential for crowbar use in terms of its ability to minimise the flux decay period. As explained in Section 6.6.1, this ability is limited by a combination of the rotor over-currents, the crowbar resistance and the relative DC-link voltage.

Table 6.7. Approximate DFIG parameters.

Parameter		7.5kW Test rig /p.u.	MW class DFIG (approx) /p.u.
Leakage factor	σ	0.075	0.04 – 0.08
Rotor leakage inductance	X_{es}	0.12	0.09 – 0.12
Mutual Inductance	X_m	3.1	3 – 6
Rotor resistance	R_r	0.020	0.005 – 0.010
Rotor transient time constant	τ_r	39ms	70 – 140ms
Stator voltage (line-line)	v_{s0}	415V	690V
Rotor phase-voltage base	$v_{r0,ph}$	745V	1000 – 1200V

Unfortunately, the wind turbine generator machine data that I had access to is restricted by confidentiality agreements, and cannot be referenced here. I will however make some generalised comments on larger machines, which I trust will not run contrary to the reader's experience. Firstly, larger generators are generally more efficient. For example, end-winding effects become less significant and slot filling can be improved. In terms of the idealised induction machine the per unit leakage inductances are similar to small machines, indeed a certain amount can be deliberately maintained to permit current control of the rotor circuit. The mutual inductance can be enhanced somewhat with better overlap of stator and rotor fields. The resistances possess the most significant change: smaller per unit resistances can be realised, with

economic benefits of reduced losses. Approximate machine parameters are shown in Table 6.7, with reference to the 7.5kW test rig.

The most marked difference is the larger resistance of the test rig windings, and hence the test rig's smaller transient time constant. For the minimum threshold crowbar method to be attractive with large generators, the crowbar resistance must be able to reduce the effective rotor flux decay time constant to below 40ms, or preferably below 20ms.

Now, the maximum crowbar resistance can be estimated as explained in Section 6.6.1 (Eq. 6.12). To generalise this expression the commodities are converted into machine-rotor per units. The results is shown in Eq. 6.19, with the SI measurement of crowbar compared to the rotor circuit base resistance and the maximum rotor current denoted with a '^'.

$$\frac{R_{cb,SI}}{R_{r0}} < \frac{\left(V_{dc}/v_{r0,ph}\right)}{1.35\hat{i}_{r,pu}} \tag{6.19}$$

The equivalent power approximation for a 'per-phase' crowbar resistance (Eq. 6.9) permits an estimate of the upper limit of per-unit resistance that can be added by a crowbar:

$$R'_{cb,pu} < \frac{0.55\left(V_{dc}/v_{r0,ph}\right)}{1.35\hat{i}_{r,pu}} \tag{6.20}$$

Now, worst case over-currents have been shown to be roughly 5 p.u. Further, all converters based on standard 1200V IGBT devices will operate a DC-link voltage in the region of 800V. This gives a rough measure of the maximum 'per-phase' crowbar resistance: 8.7% on the test rig, 5.4%-6.5% for a larger machine with a 690V stator connection. Assume therefore that an equivalent of 5% rotor resistance is added by means of a crowbar: with the values of rotor resistance in Table 6.7 this crowbar resistance can reduce rotor transient time constants by a factor of 6-11. Now, the high-end time constants mentioned in Table 6.7 correlate with the low-end of quoted rotor resistance. As a result, the crowbar may deliver effective rotor flux decay timescales of less than 20ms for all of the machines considered.

This being the case, the minimum threshold crowbar method of Section 6.6.6 offers the best combination of rotor-converter protection and swift restoration of apparent power control, with crowbar application periods lasting less than 20ms each at fault initiation and voltage recovery.

6.6.8 Crowbar method Summary

The minimum threshold crowbar method was shown to safely divert rotor over-currents and prevent a DC-link over-voltage in response to a 15% voltage, 500ms fault and a 0% voltage, 140ms fault. Periods of crowbar application lasted 11-16ms, once each at fault initiation and recovery. Good power control was restored in 40-45ms following each voltage step and sustained throughout the plateau of fault voltage. Finally, estimations of the parameters of large generators suggest that a similar performance can be achieved with an appropriate, maximised value of crowbar resistance.

6.7 DC-link brake methods

6.7.1 The DC-link brake in detail

The DC-link brake chopper was introduced in Section 6.3.4, where the use of such a device in response to grid faults was outlined. This section explores the fault response of such equipment in more detail and considers the appropriate value of brake resistance.

Brake chopper concept

The brake chopper is a simple DC-link protection device which shorts the DC-link through a power resistor when the DC-link voltage exceeds a fixed threshold. In place of a discrete on/off system, a chopper circuit is used with an IGBT to rapidly engage and disengage the resistor. As explained in Section 6.3.4, the duty cycle of the chopper can be increased as the over-voltage increases.

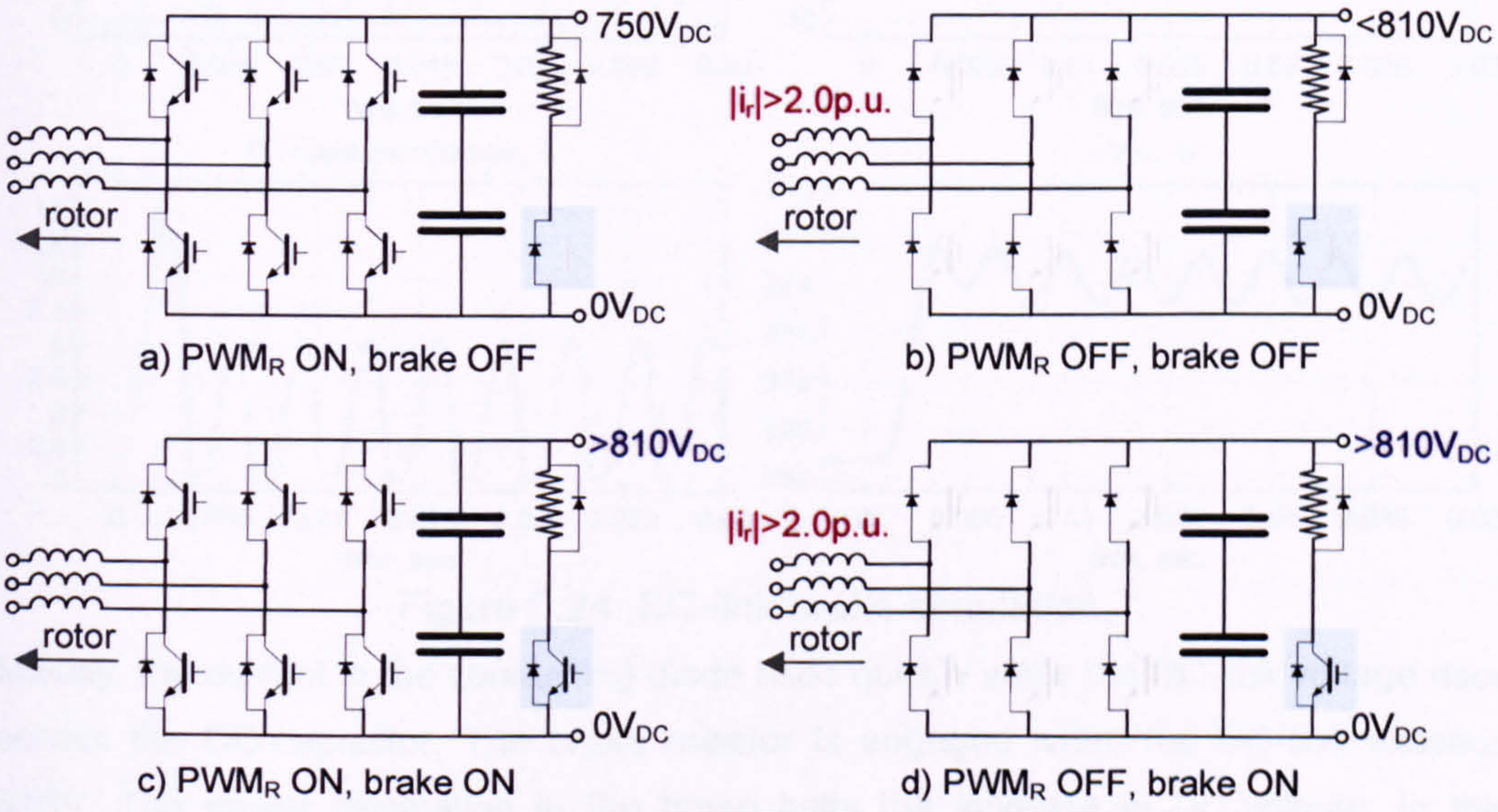

Figure 6.23. Brake chopper modes (values indicative).

Brake chopper modes are shown in Figure 6.23, with reference to the protection threshold limits used in the test rig. Figure 6.23 (a) illustrates normal operation with the

brake chopper off. If the DC-link voltage rises above 810V, the brake is engaged as shown in (c). Figure 6.23 (b) and (d) refer to DC-link brake grid fault operation, detailed below.

Brake chopper use during grid faults

In response to grid faults, transient rotor over-currents force the DC-link voltage to rise rapidly. To protect the converter's switches from the over-currents, they are turned-off, although the currents will still flow through the freewheel diodes, as shown in Figure 6.23 (b). The resulting DC-link voltage rise will trigger the brake, as shown in (d). PWM is resumed when the rotor current returns below a threshold limit.

A simple simulation of the brake chopper produces the waveforms shown in Figure 6.24. The simulation was setup using Simulink and its Power Systems toolbox, with nominal values for snubber circuits and forward-conduction losses. Here, a 590V AC source was ramped up to simulate a fault condition. The DC-link model used a capacitance of 705μF and an 180Ω brake resistor to match the test rig. In this example the transient power into the modelled DC-link is sufficiently high to raise the chopper duty ratio to 1, i.e. the brake resistor is held permanently on.

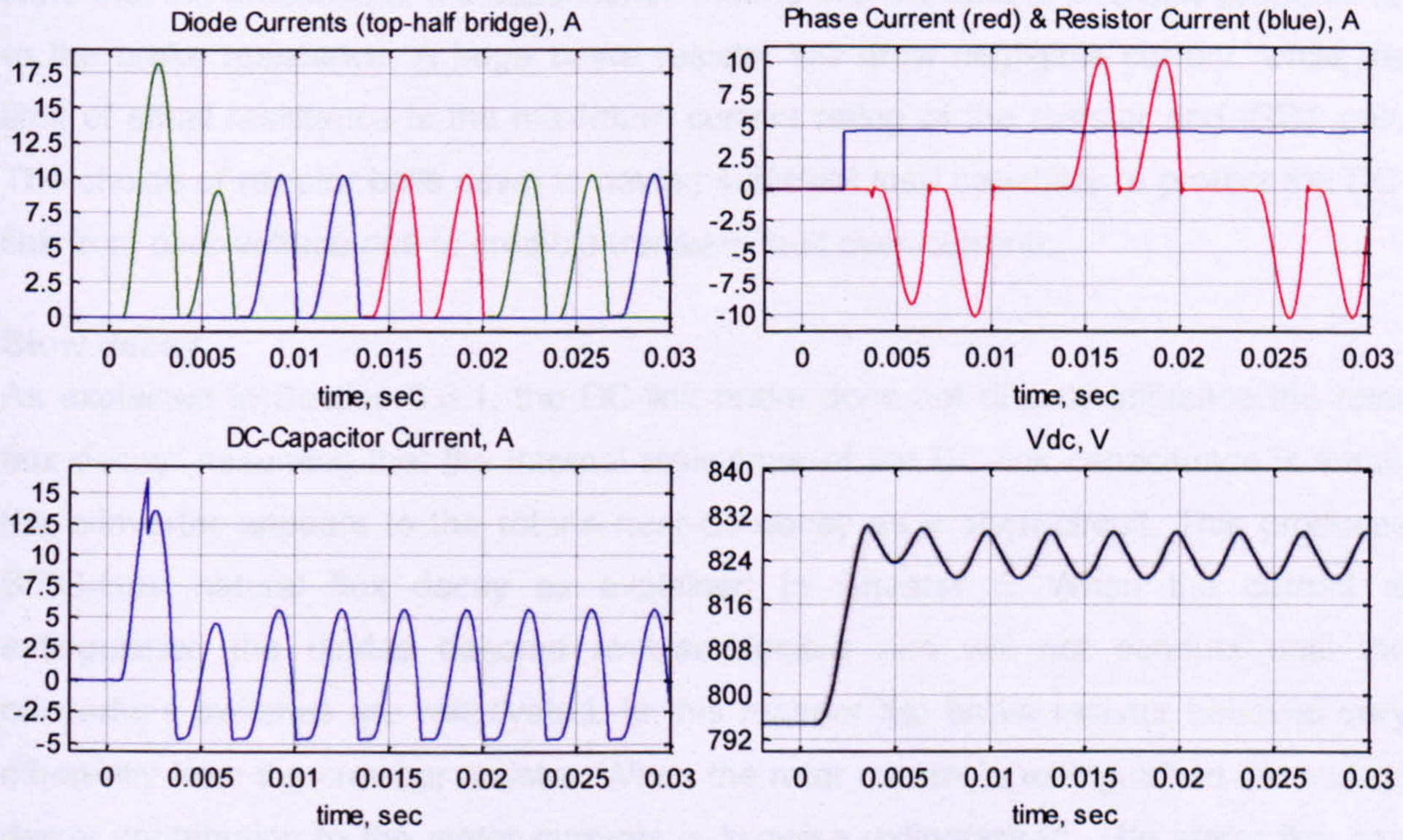

Figure 6.24. DC-link brake simulation.

Initially, the current in the conducting diode rises quickly while the DC-link voltage rises across the DC-capacitor. The brake resistor is engaged when the DC-link exceeds 810V. The power dissipation in the brake halts the increase in DC-voltage. In this example the power balance is conveniently exact – in a practical case the voltage will go one of two ways: either to continue to increase (at a slower rate) until the converter trips-off at its maximum voltage threshold, or fall back to the chopper on/off threshold.

In either eventuality, the DC voltage is smoothed by the capacitor and the brake resistor will draw DC current as indicated in Figure 6.24. This DC-current is the mean value of the sum of the three currents flowing through the three diodes in the top-half of the converter. The oscillatory current contributions flow in and out of the capacitor, causing the 6 times system frequency DC-voltage ripple observed.

The brake resistor is disengaged if the voltage remains below the lower hysteresis threshold level, set at 795Vdc in the test rig. Independently, rotor-side PWM can be resumed whenever the measured rotor currents fall within safe operating values.

Brake resistance

Any change in DC-link voltage is chiefly limited by the DC-link capacitance. The voltage across the brake resistor will remain roughly constant, in the range 800-850V in the example of our test rig. The brake can be considered as an approximately constant load, sinking power according to Eq. 6.21.

$$P_{brake} = \frac{V_{dc}^{\ 2}}{R_{brake}} \tag{6.21}$$

Note that the presence of the capacitance means that the load is inversely proportional to the brake resistance. A large brake resistor will draw negligible current, while the limit of small resistance is the maximum current rating of the resistor and IGBT pair. The choice of resistor boils down to having sufficient load capability to protect the DC-link from over-voltage due to credible transient fault over-currents.

Slow decay

As explained in Section 6.6.1, the DC-link brake does not directly influence the rotor flux decay. Assuming that the internal resistance of the DC-link capacitance is small, the converter appears to the rotor's near-dc decay as a short-circuit. This produces SFIG-type natural flux decay as explained in Chapter 5. When the current is extinguished the diodes become reverse-blocked and will not conduct until the converter's switches are reactivated. In this manner the brake resistor behaves very differently from the crowbar resistor. When the rotor current is extinguished the mutual decay contribution to the stator currents is likewise extinguished. The stator flux can now only decay through its own circuit and the effective stator time constant is lengthened. In practice, the stator currents hold a slower-decaying near-dc component alone until rotor currents flow is restored.

6.7.2 Test rig brake resistor value

From simulation tests, two multiples of operational rotor power dissipated from the DC-link was sufficient to maintain the DC-link voltage below 1,000V in grid fault situations.

The test rig brake resistor was sized to sink twice the maximum operational converter power continuously during grid faults, which equated to 0.5 p.u. power on the machine p.u. base, or 3.75kW. Using Eq. 6.21, with a brake chopper cut-in value of 810V, this equates to 175Ω. An 180Ω, 0.6kW resistor was chosen; the low (essentially thermal) power rating is acceptable because the grid fault durations are so relatively short.

The brake resistor needed to be small enough to keep the DC-link voltage below the limits of the converter, particularly the breakdown voltage of the capacitance. The specific value of the resistor however does not directly influence the decay characteristics of the machine.

6.7.3 DC-link brake tests overview

The rotor converter's anti-parallel diodes must be rated sufficiently high to accommodate the maximum rotor over-currents. No crowbar is employed in any of the following tests. The brake chopper employed on the DC-link operates its own hysteresis controller using a DC-link voltage measurement independent from the one recorded by the dSpace controller.

In the same manner as for the crowbar method, when the measured rotor current magnitude exceeds the threshold value the rotor-side PWM is disengaged, i.e. all switches are turned 'off' (Eq. 6.22). The criterion for the resumption of rotor-side PWM varied with the particular methods shown later.

Rotor PWM turn-off: $|\bar{i}_r| > 2.0\,\text{p.u.}$ (6.22)

The period for which the rotor PWM was turned-off and vector control suspended is known as the rectification period, because any rotor currents flowing were rectified by the diodes in the rotor side converter.

The first method presented is a failed minimum-rectification-period method for which the performance and challenges are discussed. Secondly, a successful implementation of the DC-link brake is presented, which required longer periods of rectification operation.

6.7.4 Minimum threshold rectification

The cumbersome title was chosen to mimic the minimum threshold crowbar method of Section 6.6.6. The vector controller here is setup exactly as for that crowbar method, all bar the external crowbar trigger signal. In the case of the crowbar, this control setup proved to be favourable for the swift resumption of vector control.

Notably, the rotor-current PI controllers are not reset because the rectification duration is short. The PQ PI controllers are reset using the last measured rotor current for the PI

integral components. The PQ error signal is gradually reintroduced after PWM is resumed, as shown in Figure 6.20.

The criterion for the resumption of PWM and vector control is the same as for the minimum threshold crowbar method (Eq. 6.23):

Rotor PWM resumed: $|\bar{i}_r| > 1.9$ p.u. (6.23)

Minimum threshold rectification trial – 0% fault test

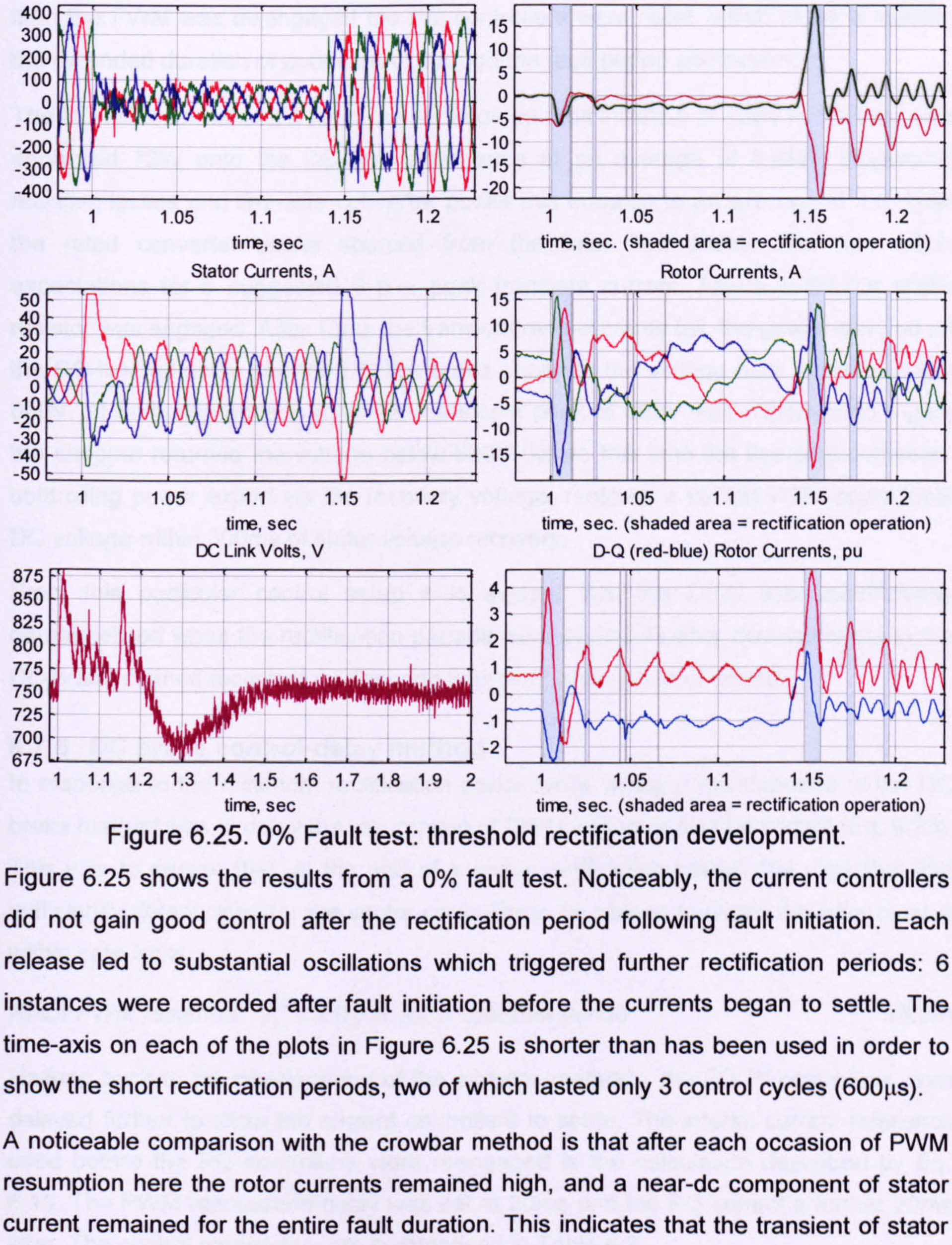

Figure 6.25. 0% Fault test: threshold rectification development.

Figure 6.25 shows the results from a 0% fault test. Noticeably, the current controllers did not gain good control after the rectification period following fault initiation. Each release led to substantial oscillations which triggered further rectification periods: 6 instances were recorded after fault initiation before the currents began to settle. The time-axis on each of the plots in Figure 6.25 is shorter than has been used in order to show the short rectification periods, two of which lasted only 3 control cycles (600μs).

A noticeable comparison with the crowbar method is that after each occasion of PWM resumption here the rotor currents remained high, and a near-dc component of stator current remained for the entire fault duration. This indicates that the transient of stator

flux decay had not passed and that unsupported flux remained in the machine. This also imposed a near-rotor speed oscillation on the rotor currents and rendered the control environment more difficult. Sharp spikes of rotor current were produced as the current references pulled sharply to and from their saturation limits – note that the quadrature PI integral component of reference rotor current was limited to within ±1 p.u. and that the measured reactive component oscillated just beyond this limit.

A similar pattern emerged from voltage recovery where three rectification periods were triggered by the rotor currents and the power output became highly oscillatory. Each time the PWM was disengaged the PQ controllers were reset, which helps to explain the extended duration of poor control through the fault period and beyond.

The DC-link experienced a rapid over-voltage on fault initiation of 126V in 12.8ms. This deposited 72W onto the DC-link capacitance at an average of 5.6kW. Neglecting resistive losses and line-side converter power this equates to an average of 3.0 times the rated converter power sourced from the rotor flux decay. This lies within expectations for a suggested 5 p.u. peak transient current. Above 810V the brake resistor was engaged. After 13ms the transient over-currents fell, the power dumped on the DC-link fell away and the DC-link brake chopped the voltage back down to under 800V. At fault clearance in a similar manner a peak of 862V was experienced. Again the chopper returned the voltage below 800V before this time the line-side converter, controlling power export via the recovery voltage, restored a settled 750V operational DC voltage within 300ms of stator voltage recovery.

From this particular control setup it is evident that the DFIG was insufficiently demagnetised when the rectification periods were ended. Further developments in the DC-brake method focussed on ensuring improved resumption of control.

6.7.5 DC brake control-delay method

In response to the minimum rectification period tests, a major development of the DC brake method was to delay the resumption of PWM and rotor current control (Eq. 6.23). This was to ensure that, at the end of a given rectification period, the rotor flux had sufficiently deteriorated for the vector controller to be able to maintain the rotor current within safe limits.

Rotor PWM resumed: $|\bar{i}_r| < 2.0$ p.u. *for a specified period* (6.24)

Harking back to the development of the crowbar methods, the PQ PI controllers were delayed further to allow the current controllers to settle. The interim current reference used before the PQ controllers were reengaged is the calculation described by Eq. 6.15. The PWM reactivation delay was set at 20ms and the PQ control a further 20ms later. The control parameters are summarised in Table 6.8.

Table 6.8. DC brake control-delay method parameters.

Threshold / p.u.	Reactivation delay /ms	PQ controller delay /ms
2.0	20	20

As for the earlier methods, results for a 15% fault are given below. However, from all the tests performed, no good data was recorded for a 0% fault using this method, which has therefore been omitted from this section. The problem originated with sensor equipment rather than the fault ride through technique.

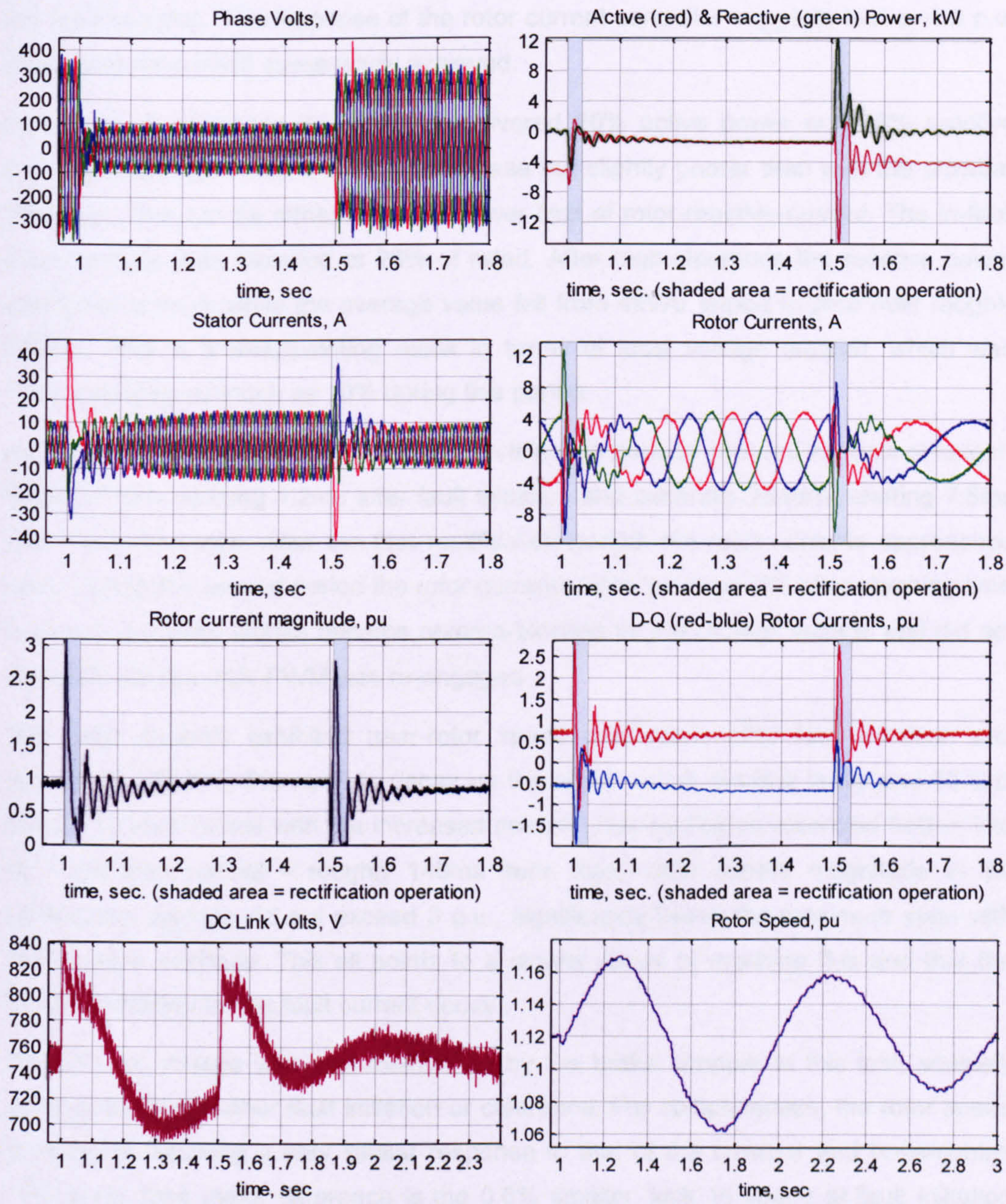

Figure 6.26. 15% Fault test: DC-brake control-delay method.

Results for the 15% fault test are shown in Figure 6.26. This method showed an improved response in triggering only a single rectification period following each of fault initiation and clearance. As before, the transient rotor over-currents were diverted from the IGBTs. Near-dc components of rotor current decayed within the rectification periods, although the stator circuit near-dc decay extends well into the fault and recovery periods.

Good rotor current control is exhibited roughly 80ms after each rectification period. The d-component of rotor current was controlled mid-fault to 0.67 p.u. as in previous tests. The q-component was saturated at -0.70 p.u. here, a belatedly discovered mistake in the control setup. The response of the rotor current controller suggests that a -1.0 p.u. limit could have been successfully achieved.

Prior to fault clearance the machine delivered 20% active power and 18% reactive power generation, better than the base case but slightly poorer than with the crowbar methods. This can be attributed to the lower limit of rotor reactive-current. The in-fault stator voltage was steadied at 28% of rated. After fault clearance the reactive power oscillated strongly while the average value fell from 4kVAr *import* to zero over roughly 100ms. This is a disappointing result in terms of local voltage support, which was suppressed by as much as 10% during this period.

As a result of the reactivation delay, the rectification periods endured somewhat longer: firstly 27.6ms, starting 1.2ms after fault initiation and secondly 25.6ms, starting 7.8ms after fault clearance. After the first rectification period, the rotor currents approached zero. During the second period the rotor currents were 'pinched off': after reaching zero the rotor-converter diodes became reverse-blocked by the DC-link voltage and did not conduct until the rotor PWM was re-engaged.

The rotor currents exhibited near-rotor speed oscillations after fault initiation and clearance reflecting the near-dc decay on the stator circuit (54.5Hz firstly and 55.5Hz latterly, in accordance with the increased speed). This oscillation extended further into the fault than normal – roughly 140ms here. Also, rotor current magnitude in the rectification periods did not exceed 3 p.u., significantly below the maximum seen with the crowbar methods. This all points to a slower decay of machine flux and that the DC-link inhibited the ac fault current decay.

The DC-link voltage was well maintained by the brake chopper in this test, scarcely passing 820V on either fault initiation or clearance. For completeness, the rotor speed is included, showing a very similar response to that of the crowbar and base-control 15% tests. One minor difference is the 0.6% smaller 'kick' in speed at fault initiation when compared with the crowbar tests, reflecting the slower dissipation of

demagnetisation energy. Otherwise the mechanical response was similar to that of the base and crowbar control methods.

6.7.6 DC-brake Summary

The DC-link brake was shown to successfully maintain the DC-link voltage within safe limits for a 500ms 15% voltage fault, while potentially dangerous rotor over-currents where allowed to conduct safely through (over-rated) rotor converter diodes. Power control was restored within roughly 80ms of each disengagement of the rotor converter's switches, which occurred once for each voltage step of fault initiation and clearance.

However, the periods of converter disengagement and the length of time required to restore power control were each roughly double the examples presented for the minimum threshold crowbar control method. This is because the DC-link brake fundamentally does not assist the demagnetisation process of the machine, whereas the crowbar can shorten the rotor decay timescale. The DC-brake fully demagnetises the rotor before forcing the characteristic slow stator flux decay. The result is a delayed resumption in control.

6.8 Summary

Fault response and ride through aims

The principle design aims for a DFIG fault ride through technique were established. An improvement must be based on at least one of the following:

A. Minimize the voltage drop experienced by the generator.

B. Divert or negate the transient rotor over-currents.

C. Produce maximum reactive power output and proportional active power output during faults.

These goals were concluded from inspection of the complete fault response of the DFIG in Chapter 5 and the transmission system requirements in Chapter 2.

During the plateau of a grid fault, a roughly constant voltage, it was argued that a DFIG can remain stable, grid-connected and control its current output. The principle challenge identified for DFIG fault response is to cope with the transient currents inevitably associated with a step-change in the supply voltage. For a conventional DFIG setup, demagnetisation of the generator could force up to 5 p.u. currents through rotor-converter devices and instigate a dangerous surge in the DC-link voltage. The dynamic response of the DFIG controller is limited and it cannot prevent a spike of rotor current at fault initiation and clearance.

It is assumed that the power converter is rated for 1 p.u. rotor current. Although individual IGBT modules vary, a typically single-device maximum current of 2.0 p.u was chosen as a safe-operation boundary limit throughout this work [63].

Review of proposed solutions

A range of proposed fault ride through techniques were reviewed and discussed.

Advanced control techniques offer potential improvements for in-fault control, recovering from the transient or managing the response to an unbalanced fault. None have to date shown the ability to prevent the immediate rotor over-currents induced by severe dips from rated voltage.

Setting the DFIG controller to commit reactive-current and hence generate VArs during the fault can raise the local fault voltage by a significant amount: aiding the fault response of other local equipment and reducing the step-voltage impact at fault clearance. Due to the winding arrangements, more reactive power can be delivered from the rotor-converter than from the line-side converter. However, the rotor-side current reference, limited in magnitude by the converter, must balance the priorities of reactive and active power output. Some over-rating capability of the power converter devices could be used to maximise the impact of this method. This method has previously been demonstrated successfully in simulation. Static reactive support devices on the other hand come with considerable cost implications and generally cannot prevent the transient rotor over-currents.

A rotor crowbar circuit can divert the transient over-currents of fault response and shorten the flux decay timescale of the rotor circuit. In this manner the DFIG can 'ride through' the transient and resume control during the remaining fault or recovery period. However, during the period that the crowbar is applied the DFIG appears as a high-slip high-resistance SFIG – with associated problems of poorly controlled output and severe stator-circuit magnetisation demands, resulting in suppressed stator voltages. The crowbar is nonetheless referred to as a standard DFIG protection device.

A DC-link brake allows the anti-parallel diodes in the rotor-side converter to conduct the transient rotor over-currents while the transistor switches are turned off. This causes the DC-link voltage to rise rapidly. The brake device is triggered above a set voltage threshold, shorting a dedicated resistance across the DC-link and arresting the DC-link voltage rise. DFIG control may be resumed once the rotor currents decay to within the maximum permissible limits. For this method the rotor converter's diodes must be up-rated for approximately five times the rated current. This method has previously been demonstrated successfully in simulation, when used in conjunction with a rotor crowbar. The brake circuit has also been specified in a US patent.

Temporary disconnection of the DFIG, stator flux damping circuits and switched-in series impedances were all considered, all requiring in-circuit main-power line switch devices. Fast-acting solid state switches were shown to be uneconomical for their steady-state losses while lossless contactor devices are too slow to prevent transient rotor over-currents.

VAr-support control tests

The VAr-support control tests revealed in-fault stator voltage increases of 6%, 11% and 14% respectively for 0%, 15% and 50% fault voltages when compared with a zero-VAr reference control scheme. This resulted in proportional improvements in power output during the fault and a roughly 20% reduction in the peak fault currents at fault clearance for each VAr-support test. This confirmed that the impact of a grid fault can be partially mitigated at no extra cost through maximising the reactive-power output of the DFIG.

Rotor crowbar

The crowbar was shown to behave similarly to a three-phase rotor closed-circuit through a higher per-phase resistance. This has the impact of shortening the transient time constant of the rotor circuit. The equivalent crowbar resistance was defined and a maximum limit of crowbar resistance determined in order to avoid conduction through the rotor-converter. The 25Ω test rig crowbar resistor reduced the effective rotor decay timescale from 39ms to 10ms.

The timer crowbar method engaged the crowbar for 120ms when the measured rotor current exceeded the threshold value of 2.0 p.u. This successfully diverted the transient rotor currents and fully de-energised the machine. The redirection of rotor currents also meant that the DC-link voltage rose by no more than 30V in response to either a 15% or 0% fault. However, during the crowbar periods the DFIG showed poor power output and a 6-8% suppression of stator voltage during the recovery period.

A minimum threshold method was developed to reduce the length of crowbar application periods and optimise the resumption of power control. In 15% and 0% fault tests this method resulted in a single crowbar application at fault initiation and at fault clearance, each time successfully diverting the over-rated currents. The crowbar periods were 11-16ms in duration and good power control was evident approximately 30ms later in each case. During the brief settling period the reactive power at worst absorbed 1.0kVAr, causing 3% suppression in stator voltage. The raised limits of rotor current reference saw the DFIG deliver 22% active power and 33% reactive power into the 15% fault; 8% and 25% respectively into the 0% fault. The key outcome was that the DFIG presented good power output within 45ms of each voltage step.

The crowbar is a relatively well-known wound-rotor protection device and would be relatively straightforward to retro-fit to an existing DFIG system. The cost of the unit depends chiefly on the single IGBT switch module, which must be capable of perhaps 7 p.u. current for sporadic 20ms bursts. In the context of the whole system this is a cost effective solution with no impact on normal operation of the DFIG.

The potential application of the crowbar circuit to a high-powered generator was reviewed. The larger machine was assumed to operate with a 690V stator, 1200V power electronic devices and a roughly 800V DC-link voltage. The major difference in per unit machine parameters for a larger machine is an estimated 2-4 times reduction in winding resistance, producing a roughly 2-4 times longer transient time constant than the test rig. However, the maximum per-phase equivalent rotor crowbar resistance is 6%, producing an effective transient time constant below 20ms. As a result, performance similar to that shown with the test rig can be expected. This confirms the use of a rotor crowbar with a minimum-time control method as an attractive tool for fault ride through in wind turbine DFIGs.

DC-brake

The use of a brake-chopper circuit in response to grid faults was detailed and the choice of brake resistance explained. Unlike the crowbar, the brake resistor does not directly influence the decay rate of the rotor circuit. The fault currents flow through the converter's anti-parallel diodes until they reach zero, at which point the diodes become reverse-blocked by the DC-link voltage and the rotor currents are held at zero until PWM is resumed. Once the rotor currents are extinguished, the stator flux decay becomes restricted and the stator currents comprise only a slow-decaying near-dc component.

The slower demagnetisation is reflected in the fault test results. A minimum threshold type controller (similar to the crowbar method) revealed that stable vector control could not be established immediately after the first peak of rotor current.

A control-delay method successfully managed the rotor currents and restricted the DC-link voltage to below 850V in the face of 15% fault voltages, with a single rectification period at fault initiation and at fault clearance. The required rectification periods were 26-29ms. In each test the fault clearance rectification period preceded a 50% reactive power import which suppressed the stator voltage by around 11%. The controller required roughly 100ms in each case to return to unity power factor.

The DC-brake chopper is a well-known stand-alone protection device and could be relatively easily retro-fitted to an existing DFIG converter. A more complicated problem would be the replacement of the rotor converter's anti-parallel freewheel diodes. The

unit costs may total less than the crowbar: the IGBT brake switch need only be rated for little more than 1 p.u. rotor current (determined by the maximum DC-link voltage and the brake resistor) while up-rating individual diodes is relatively cheap. However, the non-standard converter design required to house the non-standard diodes would add a considerable overhead.

Overall, as a stand-alone method the crowbar is preferred; particularly in terms of the rapidity with which full control can be restored. A DC-brake may nonetheless be considered valuable for converters with low values of DC-link capacitance; these may be more sensitive to incoming over-currents.

7 CONCLUSIONS

7.1 Conclusions and Recommendations

7.1.1 Short-circuit fault response

The voltage drop caused by a grid fault triggers a decay of flux linkage in the induction machine. The natural response of the stator and rotor circuits each comprise two transient decay components: a near-dc decay of self-linking flux and a near-rotor speed decay of mutual flux. These contribute roughly equal components to the fault currents on each circuit. The rotor currents' near-dc component decays with the effective rotor transient time constant, 39ms on the test rig, and the near-rotor speed component decays with the effective stator transient time constant, 26ms on the test rig. This is illustrated by Eq. 7.1, with algebraic terms specified in Chapter 5. The converse applies to the stator circuit currents.

$$\bar{i}_r^r(t) = \overbrace{\frac{\left(\tau_s'^{-1} + j(\omega_r - \delta)\right)A_r^r}{R_r} e^{-t/\tau_s'} e^{-j(\omega_r-\delta)t}}^{\text{Near-rotor speed}} + \overbrace{\frac{\left(\tau_r'^{-1} + j\delta\right)\left(\overline{\psi}_{r0}^r - A_r^r\right)}{R_r} e^{-t/\tau_r'} e^{-j\delta t}}^{\text{Near-DC}} \tag{7.1}$$

The frequencies of the decay components of current deviate from pure-dc and rotor-speed due to drag effects in the magnetic fields. This deviation is roughly 1% for a typical machine, but can be over 3.5% with a very high rotor resistance; such as is the case with a crowbar resistance shorted across the DFIG's rotor windings.

$$\bar{i}_r^r(t) \approx \frac{1}{\sigma L_r} \overline{\psi}_{r0}^r e^{-t/\tau_r'} e^{-j\delta t} - \frac{L_m}{\sigma L_r L_s} \overline{\psi}_{s0}^r e^{-t/\tau_s'} e^{-j(\omega_r-\delta)t} \tag{7.2}$$

The rotor current expression in Eq. 7.1 can be simplified on the assumption that the transient time constants are significantly larger than 3.2ms, resulting in Eq. 7.2. This reveals the dependence of the transient currents on the reciprocal of the operational inductance, leading to over-current peaks on the rotor (and stator) circuits of 4-5 p.u. in a typical induction machine experiencing a zero voltage fault. The peak is reached roughly 5ms after the initiation of the fault. This current level is dangerous for the power converter's IGBT devices. Rotor over-currents which are permitted to flow onto the DC-

link instigate a dangerous rise in DC-link voltage. The line-side converter however safely manages the line-side currents throughout the fault.

During the fault the torque output is minimal and the rotor is accelerated by the wind power input, although the maximum speed increase in tests was no more than 6%, leaving the post-fault DFIG well within its normal operating range.

$$\bar{i}_r^r(t) \approx \frac{1}{\sigma L_r}\left(\left(\overline{\psi}_{r0}^r - \frac{\overline{u}_r^e e^{-j\theta_{x0}}}{\beta^e}\right)e^{-t/\tau_r'}e^{-j\delta t} - \frac{L_m}{L_s}\overline{\psi}_{s0}^s e^{-t/\tau_s'}e^{-j(\omega_r-\delta)t} + \frac{\overline{u}_r^r}{\beta^e}\right) \quad (7.3)$$

The application of rotor voltage via the power converter superposes a slip frequency component onto the rotor currents, as illustrated by Eq. 7.3[10]. Using the pre-fault steady-state controller modulation output the net outcome is to add a roughly 1 p.u. slip fundamental component to the existing transient currents. The limits of controller dynamics and the driven flux decay mean that spikes of over-current at fault initiation and recovery cannot be prevented. The DFIG controller can however stabilise vector control of the power output during the remaining fault and recovery periods. Power export is limited in proportion to the retained balanced stator voltage, as the power converters can offer no more than rated current output.

The same principles of transient decay components from fault initiation apply at fault clearance by symmetry. However, the step increase in voltage at fault clearance is normally only 80-90% of the drop at fault initiation, with correspondingly lower peak currents.

7.1.2 General fault response

Non-zero fault voltages present shorter drops in voltage and therefore a proportionally smaller drop in the internal magnetisation of the generator. Peak over-currents in test proved to be 65-90% of that predicted by Eq. 7.2 for the *proportional* voltage lost; for example the 15% fault test revealed a 3.2 p.u. rotor current peak, 76% of the 0% fault peak, as shown in Figure 7.1. This equates to 90% of the calculated natural response for 85% voltage lost. The reason is that the decay transients of shallower voltage drops can be more readily combated by the DFIG controller.

[10] Algebraic terms specified in Chapter 5.

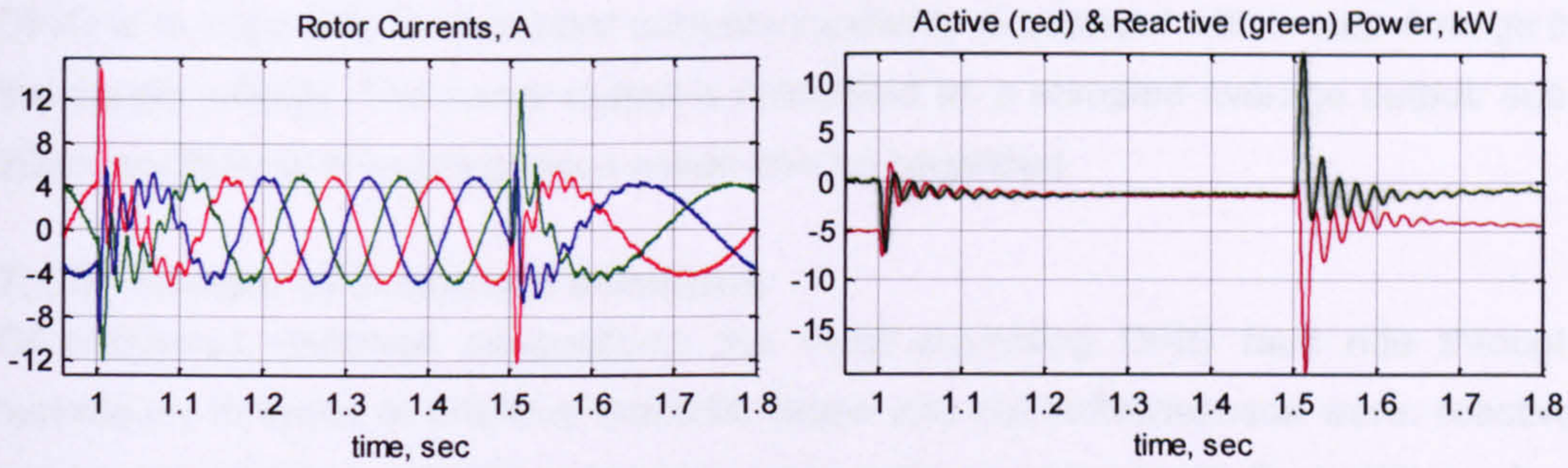

Figure 7.1. Basic DFIG 15% fault test – rotor currents and stator power.

For a standard power rating of converter, temporary disconnection of the rotor devices following a fault below 50% retained voltage is unavoidable. Unbalanced faults offer serious problems for standard vector control schemes, but the fundamental positive sequence response is no worse than for balanced faults. Both types of fault require a topological modification to protect the power converter's devices.

7.1.3 Key Issues for wind turbine DFIG fault response

The most critical problems which can be experienced by a DFIG during a grid fault are listed below:

- Rotor over-current, risking rotor converter power electronic component damage.
- DC link over-voltage and capacitor failure.
- Temporary loss of control of wind turbine active and reactive power output, and oscillations in these outputs.
- Extended suppression of local voltages due to reactive power consumption during fault recovery, or due to loss of control of reactive power.

These problems can be seen at fault initiation and at fault clearance. In order to remain grid-connected the first two points must be met without infringing the DFIGs ability to meet the second two points.

7.1.4 Fault ride through design aims

An improvement on DFIG fault ride through behaviour must be based on at least one of the following:

A. Minimize the voltage drop experienced by the generator.

B. Divert or negate the transient rotor over-currents.

C. Produce maximum reactive power output and proportional active power output during faults.

During the plateau of a grid fault, a roughly constant voltage, a DFIG can remain stable, grid-connected and control its current output. The principle challenge for the

DFIG is to cope with the transient currents inevitably associated with a step-change in the supply voltage. The power output is calculated on a sampled average output; sub-20ms oscillations in instantaneous power can be neglected.

7.1.5 Review of proposed solutions

Of numerous reviewed suggestions, the most promising DFIG fault ride through techniques in terms of practical implementation and cost-effectiveness were: reactive power control output, DC-link brake circuit and rotor crowbar circuit. Each of these has previously been proposed in some form, but not optimised for practical implementation or adequately demonstrated in test.

On the alternatives: generally, advanced control schemes can assist in-fault behaviour, but cannot prevent spikes of rotor over-current during the transients. Techniques involving series stator-circuit switches are either too loss-making or too slow. Additional VAr-source equipment offers relatively little reward in terms of fault response to justify the cost.

7.1.6 Controlled in-fault reactive power contribution

Raising the local voltage during the fault has two main benefits: reducing the step-voltage impact at fault clearance and aiding the fault response of other local equipment. The DFIG controller can commit reactive-current and hence generate VArs during the fault, raising the local fault voltage by an amount dependent upon the intervening grid impedance and the current limits of the DFIG's converter. In short, a simple recommendation is for the DFIG to maximise its reactive-current output during any fault below 50% retained voltage. This technique is the most-cost effective, as it is essentially free.

Any possibility for short-term over-rating of the current magnitude should be taken. For example, it is assumed that the power converter is rated for 1 p.u. rotor current. Although individual power modules vary, the IGBTs are typically chosen to carry an instantaneous maximum of twice rated current, i.e. 2.0 p.u. (Section 6.1.4). In this case the reactive-current reference can be safely set at 1 p.u. independently of the power-producing component of current (which should also be limited to no more than 1 p.u.).

VAr-support control tests

This concept has been previously demonstrated in simulation, but not on a test facility such as the one presented as part of this thesis. The VAr-support control tests revealed in-fault stator voltage increases of 6%, 11% and 14% respectively for 0%, 15% and 50% fault voltages when compared with a zero-VAr reference control scheme. Each test included a representative 0.15 p.u. 'grid-connection' reactance and limited the rotor's reactive-current to 0.67 p.u. to avoid an above-rated reference value. This

resulted in 1%-9% improvements to in-fault power output and a roughly 20% reduction in the peak fault currents at fault clearance in each test.

7.1.7 DC-brake methods

A DC-link brake allows the anti-parallel diodes in the rotor-side converter to conduct transient rotor over-currents while the transistor switches are turned off; the DC-link voltage rises rapidly, triggering a brake resistance device which arrests the DC-link voltage rise. DFIG control may be resumed once the rotor currents decay to within the maximum permissible limits. A DC-link brake layout is shown in Figure 6.3.

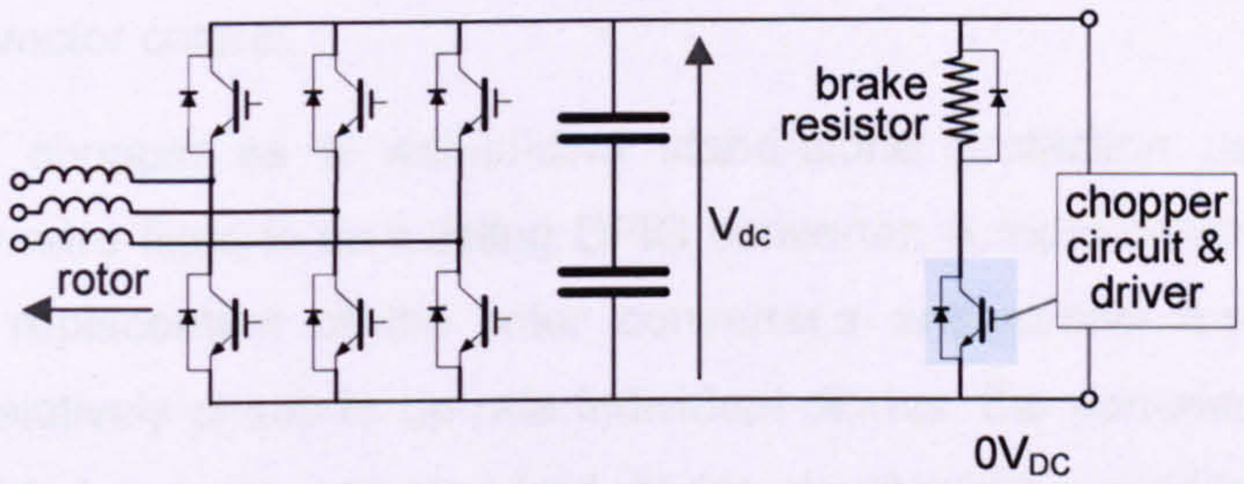

Figure 7.2. Rotor converter with DC-link brake circuit.

For this method the rotor converter's diodes must be up-rated for approximately five times the rated current. The brake-chopper itself is a well-known DC-link protection device, although its application to grid fault ride through has been relatively unexamined. This method has previously been demonstrated successfully in simulation, when used in conjunction with a rotor crowbar, and mentioned in a US patent.

DC-brake tests

A 'control-delay' method successfully managed the rotor currents (Figure 7.3) and restricted the DC-link voltage to below 850V in response to 15% and 10% grid faults, with a single rectification period at each of fault initiation and fault clearance. The required rectification periods were 26-29ms; at fault clearance in each test this preceded a 50% reactive power import which suppressed the stator voltage by around 11%. The controller required roughly 100ms in each case to return to unity power factor.

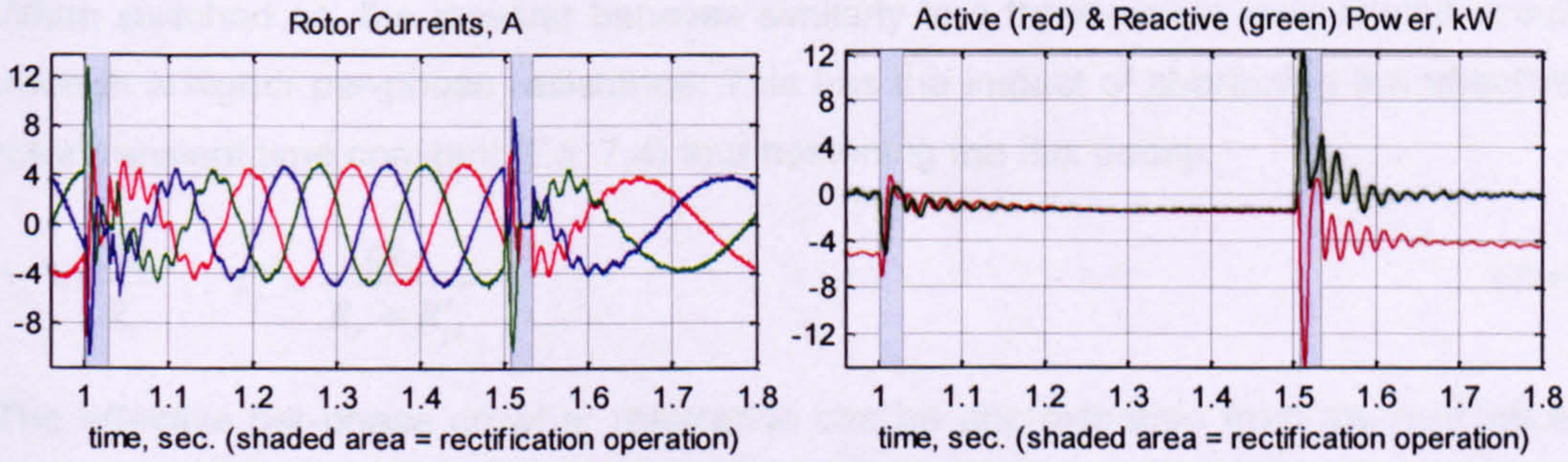

Figure 7.3. 15% Fault test: DC-brake control-delay method.

DC-brake discussion

Unlike the crowbar, the brake resistor does not directly influence the decay rate of the rotor circuit. The fault currents flow through the converter's anti-parallel diodes until they reach zero, at which point the diodes become reverse-blocked by the DC-link voltage; the rotor currents are then held at zero until PWM is resumed. Once the rotor currents are extinguished, the stator flux decay becomes restricted and the stator currents comprise only a slow-decaying near-dc component. This effect is reflected in the fault test results, where the turn-off period for the IGBT switches was necessarily 80-100% longer than the minimum threshold crowbar method in order to be able to resume stable vector control.

The DC-brake chopper as a well-known stand-alone protection device could be relatively easily retro-fitted to an existing DFIG converter. A more complicated problem would be the replacement of the rotor converter's anti-parallel freewheel diodes. Although it is relatively cheap to up-rate individual diodes, the non-standard converter design required to house the non-standard diodes would add a considerable overhead.

7.1.8 Rotor crowbar methods

A rotor crowbar connects the rotor-windings together through an external resistance, diverting the rotor currents away from the converter. In this manner the DFIG can 'ride through' the transients of fault response and resume control during the remaining period of the fault or voltage recovery. However, during the period that the crowbar is applied the DFIG appears as a high-slip high-resistance SFIG – with associated problems of poorly controlled output and severe stator-circuit magnetisation demands, resulting in suppressed stator voltages. An example of a crowbar circuit is shown in Figure 7.4.

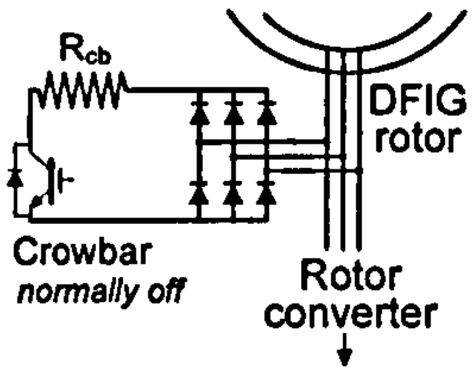

Figure 7.4. Rotor-circuit crowbar including IGBT switch.

When switched on, the crowbar behaves similarly to a three-phase rotor closed-circuit through a higher per-phase resistance. This has the impact of shortening the effective rotor transient time constant (Eq. 7.4) and hastening the flux decay.

$$\tau_r = \frac{\sigma L_r}{R_r} \therefore \tau_r' = \frac{\sigma L_r}{R_r + R_{cb}'} \tag{7.4}$$

The effective per-phase crowbar resistance can be approximated from the real value using Eq. 7.5:

$$R'_{cb} \approx 0.55 R_{cb} \tag{7.5}$$

The maximum crowbar resistance is set by the maximum rotor current: above a certain limit the potential drop in the crowbar exceeds the DC-link voltage and the rotor converter's diodes would conduct (Eq. 7.6). This limit equates to 33Ω on the DFIG test rig, where the crowbar resistor was fixed at 25Ω, reducing the effective rotor decay timescale from 39ms to 10ms.

Poor response with long-duration crowbar application

Certain examples of crowbar use involve complete demagnetisation of the rotor. This is particularly the case for thyristor-based crowbar circuits, which cannot be disengaged before the current becomes zero. This leads to roughly 100ms periods of crowbar application, during which the flux-sustaining reactive-current for the induction machine must be supplied from the stator, hindering voltage recovery.

On the test rig, a timer crowbar method engaged the crowbar for 120ms at fault initiation and at fault clearance: this caused 6-8% suppression of stator voltage during recovery period and relatively poor power output for a considerable period following crowbar release.

Successful minimum threshold crowbar method

A minimum threshold method was developed to minimise the length of crowbar application periods and optimise the resumption of power control. This involved partial suspension of the rotor current PI controllers and a soft-restart function for the PQ outer-loop PI controllers. The crowbar was engaged and disengaged strictly according to the rotor current magnitude, taking advantage of a single-peak characteristic of the hastened crowbar-induced rotor flux decay. An example of the rotor currents and stator power performance of this method from test is shown in Figure 7.5.

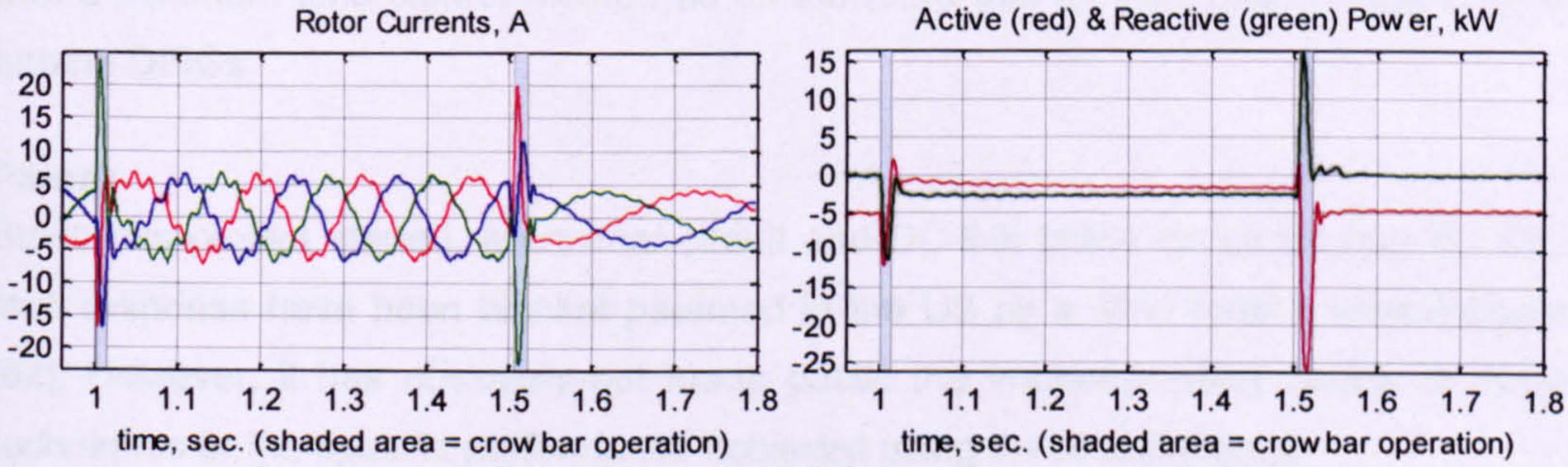

Figure 7.5. 15% Fault test: Minimum threshold crowbar.

In 15% and 0% fault tests this method successfully diverted the over-rated transient currents and presented good power output within 45ms of each voltage step. The crowbar periods were 11-16ms in duration, once each at fault initiation and at fault clearance. During the brief settling period after crowbar release the worst

instantaneous reactive power was 1.0kVAr import in fault recovery, causing a brief 3% suppression in stator voltage; unity power factor was restored in roughly 30ms. During the fault period the raised rotor reactive-current limit of 1.0 p.u. allowed 33% reactive power and hence 22% active power output during the 15% fault test.

Overall, as a stand-alone method the crowbar is preferred; particularly in terms of the rapidity with which full control can be restored. A DC-brake may nonetheless be considered valuable for converters with low values of DC-link capacitance; these may be more sensitive to incoming over-currents.

Rotor crowbar application to high-power DFIGs

The crowbar circuit is a well-known DFIG protection device and would be relatively straightforward to retro-fit to an existing DFIG system. The cost of the unit depends chiefly on the single IGBT switch module, which must be capable of perhaps a maximum 7 p.u. rotor current for sporadic 20ms bursts. In the context of the whole DFIG system this is a cost-effective solution with no impact on normal operation.

$$R'_{cb,pu} < \frac{0.55\left(V_{dc}/v_{r0,ph}\right)}{1.35\hat{i}_{r,pu}} \tag{7.6}$$

A commercial MW-class DFIG is assumed to operate with a 690V stator, 1200V power electronic devices and a roughly 800V DC-link voltage. The major difference from the test rig in per-unit machine parameters is an estimated 2-4 times reduction in winding resistance, producing a roughly 2-4 times longer transient time constant in the larger machine. However, assuming 5 p.u. peak rotor currents, the maximum per-phase equivalent rotor crowbar resistance is 6% (Eq. 7.6), producing an effective DFIG-plus-crowbar transient time constant well below 20ms. As a result, performance similar to that shown with the test rig can be expected. This confirms the use of a rotor crowbar with a minimum-time control method as an attractive tool for fault ride through in wind turbine DFIGs.

Patent

Since this project started, a crowbar-circuit and DC-link brake circuit for use in DFIG fault response have been blanket patented in the US by a wind turbine manufacturer [82]. However, it has obviously not made public the implementation details of these techniques or the specific performance achieved using these techniques.

7.2 Review of the research objectives

The objectives of the research project from Chapter 1 are reviewed below:

- A comprehensive description of the grid fault response of wind turbine DFIGs was presented in Chapter 5. This description was validated using test results.

- The limitations of wind turbine DFIG fault response centres on the inability to handle the transient rotor over-currents. This can induce a poorly controlled power output. The key challenges were summarised in Section 7.1.3.
- A 7.5kW test facility was developed and used to investigate DFIG fault response.
- A number of potential fault ride through improvements were analysed and three were developed for practical implementation: VAr-support control, DC-link brake and rotor crowbar.
- In evaluation using the test rig, both the DC-brake and the rotor crowbar could protect the generator and its converter from fault transient effects. The DC-brake alone could not restore good control of the power output within 80ms of fault initiation or clearance. However, the crowbar application periods could be minimised to 11-16ms and good power control was restored with 40-45ms of both fault initiation and clearance.
- In evaluation on the test rig, a VAr-support control method could produce stator voltages 6-14% greater than the applied grid fault voltage, resulting in roughly 20% reductions in peak current at fault clearance.
- It is recommended that wind turbines DFIGs maximise their reactive-current output during grid faults. During the fault period itself, this component should be prioritised over the active power-producing component, and any permissible short-term over-rating of current output should be used. During the fault recovery period the active-power producing component can be set in proportion to the retained balanced voltage to deliver satisfactory power output.
- It is recommended that wind turbine DFIGs employ a rotor crowbar with a resistance optimised to reduce the effective rotor transient time constant to below 20ms. This crowbar should be used with a minimum-time control scheme which can safely release the crowbar and re-establish good power control within 50ms of the voltage step due to either fault initiation or clearance.

7.3 Suggestions for further work

7.3.1 Unbalanced fault control

As explained in Chapter 2, the most common type of grid fault is unbalanced in nature, eliciting a poorly controlled response from a conventional vector control setup. As reviewed in Chapter 6, there is significant room for an improved response to unbalanced fault conditions; a condition now included in, for example, GB grid code. Asymmetric control was one of the originally considered goals of this research project, unfortunately precluded by the available equipment and time restrictions.

7.3.2 Test facility for the study of unbalanced fault response

The grid fault emulation equipment used in the DFIG test rig described in this thesis was capable of producing only balanced three-phase voltage-dip profiles. Any improvements in DFIG control during unbalanced fault response should be backed up by results from an appropriate test facility.

7.3.3 Extension of the dynamic DFIG wind turbine simulation

The dynamic simulation of a DFIG wind turbine system presented in Chapter 4 could be extended for general application to a wide range of DFIG wind turbines. This would require a rigorous validation process using sampled data from a number of high-power DFIG wind turbines.

7.3.4 High-power DFIG test for the minimum threshold crowbar method

The minimum threshold crowbar method presented in Chapter 6 produced a very good response to severe grid faults on the 7.5kW test rig. Studies of the crowbar resistance value presented in the same chapter suggest that this method could be perfectly applicable to high-power systems, although of course proof of this would require actual testing on a high-power DFIG facility.

7.3.5 Wind farm DFIG fault ride through

This thesis concentrated on meeting transmission system fault ride through requirements on an individual wind turbine basis. It could well be cost-effective to provide a blanket solution at a wind farm's grid connection point, which would require further study.

REFERENCES

[1] G. Pannell, R. Kemsley, "Consultation Report", *Cost-Effective Improvements in DFIG Performance Under Fault Conditions for Offshore Applications*, prepared for the DTI New and Renewable Energy Technology Programme, Contract no. K/EL/00335/00/REP, Econnect Ventures Ltd., October 2004.

[2] G. Pannell, R. Kemsley, C. Barbier, *Cost-Effective Improvements in DFIG Performance Under Fault Conditions for Offshore Applications*, prepared for the DTI New and Renewable Energy Technology Programme, Contract no. K/EL/00335/00/REP, Econnect Ventures Ltd., 2007.

[3] G. Pannell, D. J. Atkinson, R. Kemsley, L. Holdsworth, P. Taylor, and O. Moja, "DFIG Control Performance under Fault Conditions for Offshore Wind Farms", presented at *CIRED: 18th International Conference on Electricity Distribution*, Turin, 2005.

[4] D. Millborrow, "Assimilating Wind", *IEE Review*, 2002, pp. 9-13.

[5] *Costs of Wind Power Generation*, in Wind Background, UK Strategic Environmental Assessment (SEA), 2008, available from: http://www.offshore-sea.org.uk/site/

[6] *Dynamics of GB Electricity Generation Investment*, Consultation Document, Redpoint Energy Limited and Energy Strategies Limited, May 2007, available from: http://www.berr.gov.uk/files/file38972.pdf

[7] "Wind Power in Europe", *EU Power magazine*, European Wind Energy Association (EWEA), 5 October 2007.

[8] *UK Renewable Energy Strategy*, Department for Business Enterprise Reform, available from: http://www.berr.gov.uk/energy/sources/renewables/index.html

[9] *Wind and the UK's 10% Target*, BWEA briefing sheet, The British Wind Energy Association, 2002, available from: http://www.bwea.com/energy/briefing-sheets.html

[10] A.D. Hansen, F. Iov, F. Blaabjerg, L.H. Hansen, "Review of contemporary wind turbine concepts and their market penetration", *Journal of Wind Engineering*, 28(3), 2004, pp. 247-263.

[11] L.H. Hansen *et al*, *Conceptual survey of Generators and Power Electronics for Wind Turbines*, Risø National Laboratory, Roskilde, Denmark, December 2001.

[12] T. Burton, D. Sharpe, N. Jenkins, E. Bossanyi, *Wind Energy Handbook*: John Wiley & Sons, 2001.

[13] *The Grid Code Preface*, Issue 3, Revision 25, September 2005, National Grid Electricity Transmission plc, available from: http://www.nationalgrid.com/uk/Electricity/Codes/gridcode/gridcodedocs/

[14] F. Iov, A.D. Hansen, P. Sørensen, N.A. Cutululis, *Mapping of grid faults and grid codes*, Risø National Laboratory, Technical University of Denmark, July 2007.

[15] F. Santjer and R. Klosse, "New Supplementary Regulations for Grid Connection by E.On Netz GmbH", *DEWI Magazin*, vol. 22, 2003.

[16] *Grid Code Changes to Incorporate New Generation Technologies and DC Inter-Connectors (Generic Provisions),* Background information to Grid Code

Consultation Document D/03, National Grid Electricity Transmission plc, June 2003.

[17] *Guidance Note for the Connection of Windfarms*, Scottish Power Transmission and Distribution and S. H. Electric, 17 December 2002.

[18] N. Mohan, T. M. Undeland, W. P. Robbins, *Power electronics: converters, applications, and design*: John Wiley & Sons, 2003.

[19] M. H. J. Bollen, *Understanding Power Quality Problems: Voltage Sags and Interruptions*: IEEE Press, 2000.

[20] S. Muller, M. Deicke, R.W. De Doncker,"Adjustable speed generators for wind turbines based on doubly-fed induction machines and 4-quadrant IGBT converters linked to the rotor", *Record of the IEEE Industry Applications Conference*, Vol.4 pp. 2249-2254 October 2003.

[21] J. B. Ekanayake, L. Holdsworth, and N. Jenkins, "Control of Doubly Fed Induction Generator (DFIG) Wind Turbines," *IEE Power Engineer*, vol. February, 2003, pp. 28-32.

[22] P. Kundur, *Power System Stability and Control*: McGraw-Hill, 1994.

[23] T. Sun, Z. Chen, and F. Blaabjerg, "Transient Stability of DFIG Wind Turbines at an External Short-circuit Fault", *Wind Energy*, Issue 8, pp. 345-360 August 2005.

[24] V. Akhmatov, *Analysis of Dynamic Behaviour of Electrical Power Systems with Large Amount of Wind Power*, PhD thesis, Ørsted DTU, Technical University of Denmark, 2003.

[25] B. M. Weedy and B. J. Cory, *Electric Power Systems*, 4 ed.: John Wiley & Sons, 1998.

[26] *The Grid Code*, Issue 3, Revision 25, February 2008, National Grid Electricity Transmission plc, available from: http://www.nationalgrid.com/uk/Electricity/Codes/gridcode/gridcodedocs/

[27] M. Rasmussen, Grid Compliance and how Vestas turbines can meet the new grid Code demands, Vesta A/S, available from: http://www.ofgem.gov.uk/LICENSING/ELECCODES/GRIDCODE/MODS/Documents1/6817-Vestas.pdf

[28] H. Urdal, *Addendum to Guidance Notes for Generators Compliance Process for Wind Farms greater than 100MW*, issue 1, National Grid Electricity Transmission plc, January 2004.

[29] *Grid Disturbance and Fault Statistics*, Nordel, 2006, available from: http://www.nordel.org

[30] *Overview of the Potential for Undergrounding the Electricity Networks in Europe*, Prepared for the DG TREN/European Commission, Study Contract No 2002/009/C2, ICF Consulting Ltd, February 2003.

[31] P. Kiameh, *Power Generation Handbook: Selection Application, Operation and Maintenance*: McGraw Hill, 2002.

[32] A. Causebrook, D.J. Atkinson and A.G. Jack, "Fault Ride-Through of Large Wind Farms Using Series Dynamic Braking Resistors", *IEEE Transactions on Power Systems*, vol. 22, no. 3, August 2007, pp. 966-975.

[33] G. Saccomando, J. Svensson and A. Sannino, "Improving Voltage Disturbance Rejection for Variable-Speed Wind Turbines", *IEEE Transactions on Energy Conversion*, vol. 17, no. 3, September 2002, pp. 422-428.

[34] B.M. Buchholz, Z.A. Styczynski and W. Winter, "Dynamic simulation of renewable energy sources and requirements on fault ride through behavior", *IEEE Power Engineering Society General Meeting*, 18-22 June 2006.

[35] *Proposed Grid Code changes to incorporate new Generation Technologies and DC Interconnectors*, Document H/04, National Grid Electricity Transmission plc, September 2004.

[36] *Specifications for Connecting Wind Farms to the Transmission Network (ELT1999-411a)*, Eltra Transmission System Planning, Document 74557, 26 April 2000.

[37] *TransmissionCode 2007* – Network and System Rules of the German Transmission System Operators, Verband der Netzbetreiber VDN e.V. beim BDEW, August 2007, available from: http://www.bdew.de/

[38] *Grid Code for High and Extra High Voltage*, E.On Netz GmbH, 1 April 2006, available from: http://www.eon-netz.com/

[39] *Technical Regulations 3.2.6: Wind Turbines connected to Grids with Voltages below 100 kV – UK version*, Elkraft System and Eltra, 25 May 2004, available from: http://www.energinet.dk/en

[40] W. Leonhard, *Control of Electric Drives*, 3 Ed: Springer, 2001.

[41] P. Vas, *Vector control of AC machines*: Oxford University Press, 1990.

[42] D. O'Kelly and S. Simmons, *Introduction to Generalized Electrical Machine Theory*: McGraw-Hill, 1968.

[43] P. C. Krause, *Analysis of Electrical Machinery*: McGraw-Hill, 1986.

[44] I. Boldea and S.A. Nasar, *Electric Machine Dynamics*: New York, Macmillan, 1986.

[45] M.G. Say, *Alternating Current Machines*, 5 ed.: Longman Scientific and Technical, 1983.

[46] P. Vas, *Sensorless Vector and Direct Torque Control*: Oxford University Press, 1998.

[47] A. E. Fitzgerald, C Kingsley Jr., S. D. Umans, *Electric Machinery*, 6 ed.: McGraw-Hill, 2003.

[48] B.L. Jones and J.E. Brown, 'Electrical Variable Speed Drives'. *Proceedings of. IEE*, vol 131, pt A, no 7, 1984, pp 516-558.

[49] F.M. Hughes, O. Anaya-Lara, N. Jenkins, G. Strbac, "Control of DFIG-based Wind Generation for Power Network Support", *IEEE Transactions on Power Systems*, Vol. 20, no. 4, November 2005.

[50] R. Peña, R. Cárdenas, D. Soto, J. Proboste, R. Blasco-Gimenez, "Control Strategy for Doubly-Fed Induction Machine Based on State Feedback", *10th European Conference on Power Electronics and Applications (EPE2003)*, Toulouse, France, 2-4 September 2003.

[51] R. Pena, J.C.Clare, G.M. Asher, "Doubly Fed Induction Generator using back-to-back PWM Converters and its Application to Variable-Speed Wind-energy Generation", *IEE Proceedings on Electric Power Applications*, Vol. 143, no. 3, May 1996.

[52] D. J. Atkinson, R. A. Lakin, and R. Jones, "A Vector-Controlled Doubly-Fed Induction Generator for a Variable-Speed Wind Turbine Application", *IEEE Transactions of the Institute of Measurement and Control*, vol. 19, 1997.

[53] A. Petersson, L. Harnefors, T. Thiringer, "Evaluation of Current Control Methods for Wind Turbines using Doubly-Fed Induction Machines", *IEEE Transactions on Power Electronics*, Vol. 20, no. 1, January 2005, pp. 227-235.

[54] G. Tapia, A. Tapia, "Wind Generation Optimisation Algorithm for a Doubly-Fed Induction Generator", *IEE Proceedings on Generation, Transmission and Distribution*, Vol. 152, no. 2, March 2005.

[55] B. Hopfensberger, *Field Oriented Control of Single and Cascaded Doubly-Fed Induction Machines*, PhD thesis, Department of Electrical and Electronic Engineering, Newcastle University, 1998.

[56] *Measurement and assessment of power quality characteristics of grid connected wind turbines*, International Electrotechnical Commission (IEC) wind turbine standard: IEC 61400-21, 1999.

[57] RETScreen® International, "Clean Energy Project Analysis software", National Resources Canada, 2008, available from: http://www.retscreen.net/ang/home.php

[58] *UK Wind Energy Database*, The British Wind Energy Association, 2008, available from: http://www.bwea.com/ukwed/index.asp

[59] V.VanDoren, "Ziegler-Nichols Methods Facilitate Loop Tuning", *Control Engineering Magazine*, August 1998.

[60] S. Chondrogiannis, M. Barnes, M. Aten, P. Cartwright, "Modelling and GB Grid Code Compliance Studies of Offshore Wind Farms with Doubly-Fed Induction Generators", *The 3rd IET International Conference on Power Electronics, Machines and Drives*, Mar. 2006 pp. 22 – 26.

[61] S. Heier, *Grid integration of Wind Energy Conversion Systems*, Chichester, UK: John Wiley & Sons Ltd., 1998.

[62] V. Akhmatov, H. Knudsen, A.H. Nielsen, "Advanced simulation of windmills in the electric power supply", *International Journal of Electrical Power & Energy Systems*, vol.22 no.6, pp.421-434, 2000.

[63] Semikron IGBT Application notes, available from http://www.semikron.com.

[64] M.S. Vicatos and J.A. Tegopoulos, "Transient State Analysis of a Doubly-Fed Induction Generator under Three-Phase Short Circuit", *IEEE Transactions on Energy Conversion,* Vol.6, no.1, March 1991, pp. 62-68.

[65] D.D. Li, "Analysis of Short-circuit Current of Wind Turbine – Doubly Fed Induction Generator", *1st IEEE Conference on Industrial Electronics and Applications*, 2006.

[66] T. Wildi, Electrical Machines, Drives, and Power Systems: 4th Ed. Prentice Hall, 2000.

[67] F. Iov, F. Blaabjerg, *Converter Applications in Future European Electricity Network*, Areva T&D Technology Centre, EC Contract n°: 019794 (SES6), 2007.

[68] D. Xiang, L. Ran, P. Tavner, and S. Yang, "Control of Doubly Fed Induction Generator in a Wind Turbine during Grid Fault Ride-through", *IEEE Transactions on Energy Conversion,* Vol.21, no.3, September 2006, pp. 652-662.

[69] He Yikang, Hu Jiabing, Zhao Rende, "Modeling and control of wind-turbine used DFIG under network fault conditions", *Proceedings of the Eighth International Conference on Electrical Machines and Systems*, ICEMS 2005. Vol. 2, pp. 986 – 991, September 2005.

[70] I. Serban, F. Blaabjerg, I. Boldea, Zhe Chen, "A Study of the Doubly-Fed Wind Power Generator Under Power System Faults", *10th European Conference on Power Electronics and Applications EPE 2003*, Toulouse France EPE 2003.

[71] M. Rathi, N. Mohan, "A novel robust low voltage and fault ride through for wind turbine application operating in weak grids" 31st Annual Conference of IEEE Industrial Electronics Society, IECON 2005, November 2005.

[72] A. D. Hansen, G. Michalke, P. Sørensen, T. Lund, F. Iov, "Co-ordinated Voltage Control of DFIG Wind Turbines in Uninterrupted Operation during Grid Faults", Wind Energy, Issue 6. 2006.

[73] T. Sun, Z. Chen, F. Blaabjerg, "Voltage Recovery of Grid-Connected Wind Turbines with DFIG After a Short-Circuit Fault", 35th Annual IEEE Power Electronics Specialists Conference, Aachen, Germany, 2004.

[74] Erlich and U. Bachmann, "Grid code requirements concerning connection and operation of wind turbines in Germany", *Power Engineering Society General Meeting*, 2005. IEEE, vol. 2, pp. 1253 - 1257, 12-16 June 2005.

[75] J. Morren, S.W.H. de Haan, "Short-Circuit Current of Wind Turbines With Doubly Fed Induction Generator", *IEEE Transaction on Energy Conversion*, Volume 22, Issue 1, March 2007 pp. 174 – 180.

[76] I. Erlich, H. Wrede, C. Feltes, "Dynamic Behaviour of DFIG-Based Wind Turbines during Grid Faults", *IEEE Power Conversion Conference (PCC 07)*, Nagoya, 2007.

[77] Zhou Peng, He Yikang, "Control strategy of an active crowbar for DFIG based wind turbine under grid voltage dips", *International Conference on Electrical Machines and Systems*, ICEMS 2007, pp. 259 – 264, October 2007.

[78] J. Morren, S.W.H. de Haan, "Ridethrough of Wind Turbines with Doubly-Fed Induction Generator During a Voltage Dip", IEEE Transactions on Energy Conversion, Vol. 20, No. 2, pp. 435-441, June 2005.

[79] Bing Xie, B. Fox and D. Flynn, "Study of Fault Ride-Through For DFIG Based Wind Turbines", *IEEE International Conference on Electric Utility Deregulation, Restructuring and Power Technologies (DWT2004)*, Hong Kong, April 2004.

[80] W. Drury, *The control techniques drives and control handbook*, IEE power and energy series 35, 2001.

[81] M. Molinas, B. Naess, W. Gullvik, T. Undeland, "Cage Induction Generators for Wind Turbines with Power Electronics Converters in the Light of the New Grid Codes" *2005 European Conference on Power Electronics and Applications*, 11-14 Sept. 2005.

[82] L. Feddersen, "Circuit Arrangement and Methods for use in a Wind Energy Installation, US Patent 7,102,247-B2, Vestas Wind Systems A/S (DK), September 2006.

[83] P. La Seta, P. Schegner, "Comparison of stabilizing methods for doubly-fed induction generators for wind turbines", *2005 International Conference on Future Power Systems*, 16-18 Nov. 2005.

[84] A. Petersson, S. Lundberg and T. Thiringer, "A DFIG Wind Turbine Ride-through System. Influence on the Energy Production", Wind Energy Issue 8. pp. 251–263, 2005.

[85] A. Dittrich, A. Stoev, "Grid Voltage Fault Proof Doubly-Fed Induction Generator System", *10th European Conference on Power Electronics and Applications EPE 2003*, Toulouse France EPE 2003.

[86] M. Chomat, J. Bendl, and L. Schreier, "Extended vector control of doubly fed machine under unbalanced power network conditions," *IEE Conference Proceedings*, vol. 487, pp. 329-334, 2002.

[87] J. Bendl, M. Chomat, L. Schreier, "Independent control of positive- and negative-sequence current components in a doubly fed machine", *European Transactions on Electrical Power*, Vol. 15: pp. 191–202, 2005.

[88] H. Azaza, A. Masmoudi, "Implementation of a dual vector control strategy in a doubly-fed machine drive", *European Transactions on Electrical Power*, Vol. 15: pp. 541–555, 2005.

[89] F. A. Magueed, A. Sannino, J. Svensson, "Design of Robust Converter Interface for Wind Power Applications", *Nordic Wind Power Conference*, Chalmers University of Technology, Sweden; March, 2004.

[90] H.-S. Song and K. Nam, "Dual Current Control Scheme for PWM Converter Under Unbalanced Input Voltage Conditions," *IEEE Transactions on Industrial Electronics*, vol. 46, pp. 953-959, 1999.

[91] R. Dorf, R. Bishop, *Modern Control Systems*, 9 Ed: Prentice Hall, 2001.

[92] D. Atkinson, "Cost-effective Improvements in DFIG Performance under Fault Conditions for Offshore Applications" K/EL/00335, *Test Rig Design Report*, January 2005.

[93] "IEEE Standard Test Procedure for Polyphase Induction Motors and Generators" ANSI/IEEE Std.112-1984, 1984.

[94] User guide, "Control Techniques Mentor II", DC drives 25A to 1850A output, Issue 10, May 2000.

[95] Schaffner Components short form catalogue, Three-Phase Filters and Line reactors, http://www.schaffner.com.

[96] S. Turner, "Low power virtual power system", project report, Newcastle University, revision 1.145, August 2004.

GENERALISED INDUCTION MACHINE ANALYSIS

A

A.1 Space vector representation

A.1.1 Space vector description

The space vector is a mathematical abstraction convenient for machine analysis wherein three-phase electrical elements such as voltage and current can be described using an orthogonal two-axis reference frame. The orthogonal representation is useful in permitting simpler vector-based manipulations of the electrical quantities.

The space vector representation, including the zero sequence component, contains all the information of the real three-phase waveforms. These may be resolved at any instant via a reverse matrix transformation. The space vector model is "valid for any instantaneous variation of voltage and current and adequately describes the performance of the machine under both steady-state and transient operation" [46]. Space vector representation has been extensively described for use in machine analysis.

It is important to recognize that space-vectors, representing the peak of a spatial sinusoidal distribution, are not physically the same as the time-vectors of the power system. However, both representations used in combination satisfy the elementary per-phase impedance equations and may be used interchangeably for analysis.

A.1.2 AC machine MMF distribution

Consider a three-phase non-salient ac machine, with a symmetrical three-phase distribution of windings. The resulting MMF produced by the phase currents describes a sinusoidal distribution around the periphery of the machine. The peak of this MMF distribution follows the space vector of current. The space vector is defined by:

$$\bar{i}(t) = i_a(t) + a\,i_b(t) + a^2\,i_c(t), \tag{A.1}$$

where

$$a = \exp(-j\,2\pi/3). \tag{A.2}$$

This applies to any instantaneous set of three-phase currents. However, owing to the symmetrical winding distribution any zero-sequence component of stator current does not contribute to the net MMF, and may be neglected:

$$i_a + i_b + i_c = 0 \tag{A.3}$$

An example of space vector representation, using stator windings and stator currents in a non-salient machine, is depicted in Figure A.1.

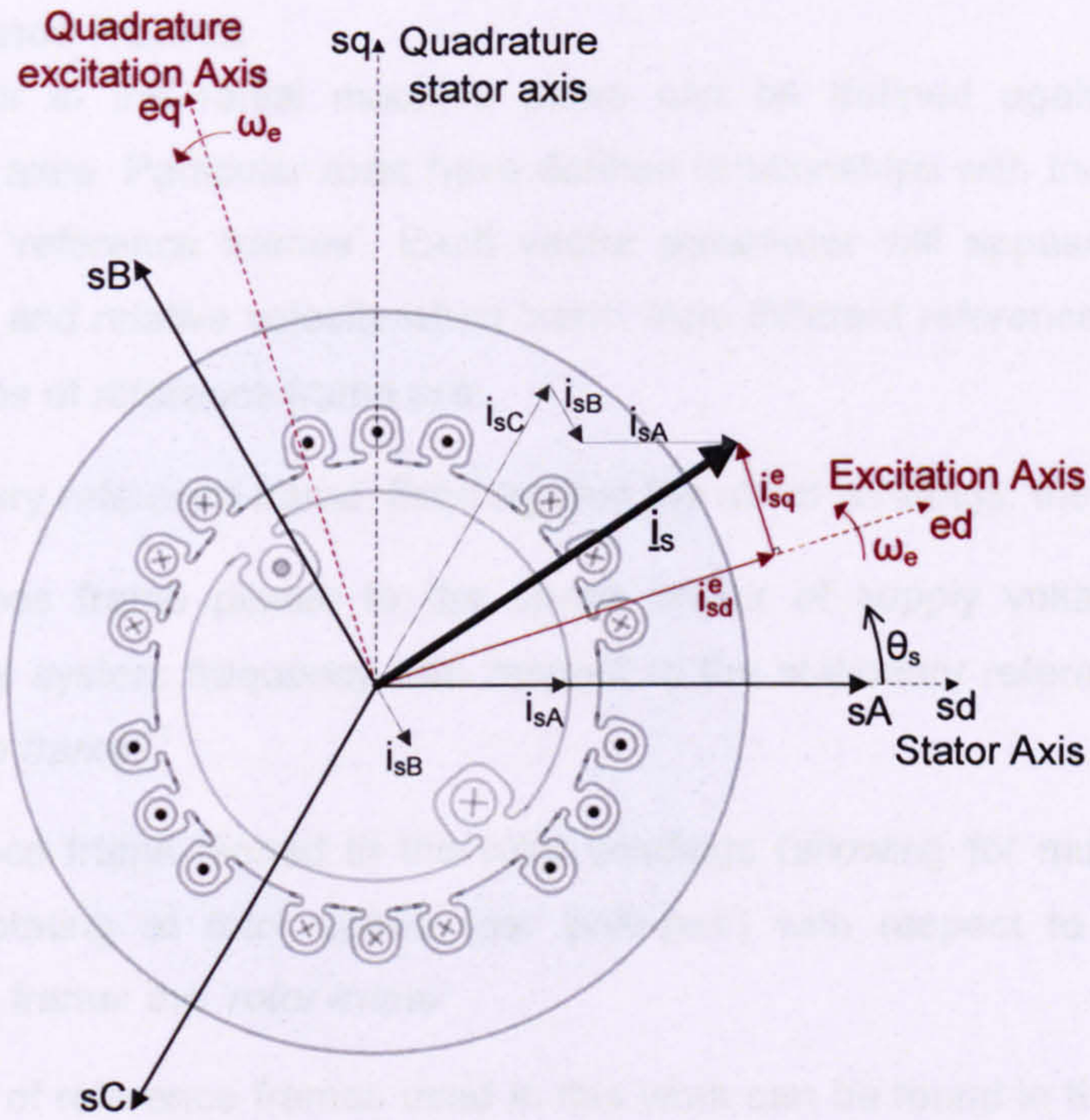

Figure A.1. Space vector of stator current.

The resultant space vector of stator current may be resolved against a set of orthogonal d-q axes aligned with the stator's phase-a windings (axis sA). This stationary reference frame is marked with the superscript 's':

$$\begin{bmatrix} i^s_{sd} \\ i^s_{sq} \end{bmatrix} = \frac{2}{3}\begin{bmatrix} 1 & -1/2 & -1/2 \\ 0 & +\sqrt{3}/2 & -\sqrt{3}/2 \end{bmatrix}\begin{bmatrix} i_{sA} \\ i_{sB} \\ i_{sC} \end{bmatrix} \tag{A.4}$$

As shown in Figure A.1, A particular d-q reference frame may rotate with respect to the stator windings.

A.1.3 Voltage vector

By analogy, a vector of voltage may be defined from a three-phase set:

$$\bar{v}(t) = v_a(t) + a v_b(t) + a^2 v_c(t), \tag{A.5}$$

This voltage vector does not have a physical basis in the manner of stator current and MMF distributions. It is useful however, in that it satisfies elementary impedance relations in combination with space-vectors of current and flux linkage. Eq. A.6 shows the relationship for a three-phase set of machine windings:

$$\bar{v} = R\bar{i} + \frac{\partial \bar{\psi}}{\partial t} \tag{A.6}$$

A.2 Reference frames and transformations

A.2.1 Reference frames

A space vector in the radial machine plane can be defined against any set of orthogonal d-q axes. Particular axes have defined relationships with the machine, and are known as 'reference frames'. Each vector parameter will appear to possess a different phase and relative velocity when 'seen' from different reference frames. Three common choices of reference frame are:

- A stationary reference frame, fixed against the stator windings: the *'stator frame'*
- A reference frame pinned to the space vector of supply voltage and hence rotating at system frequency with respect to the stationary reference frame: the *'excitation frame'*[11]
- A reference frame pinned to the rotor windings (allowing for multiple magnetic poles), rotating at rotor speed (per pole-pair) with respect to the stationary reference frame: the *'rotor frame'*

A complete list of reference frames used in this work can be found in the glossary. An example of changing reference frames is shown in Figure A.2, where the stator current is given angle ξ with respect to the stator reference frame.

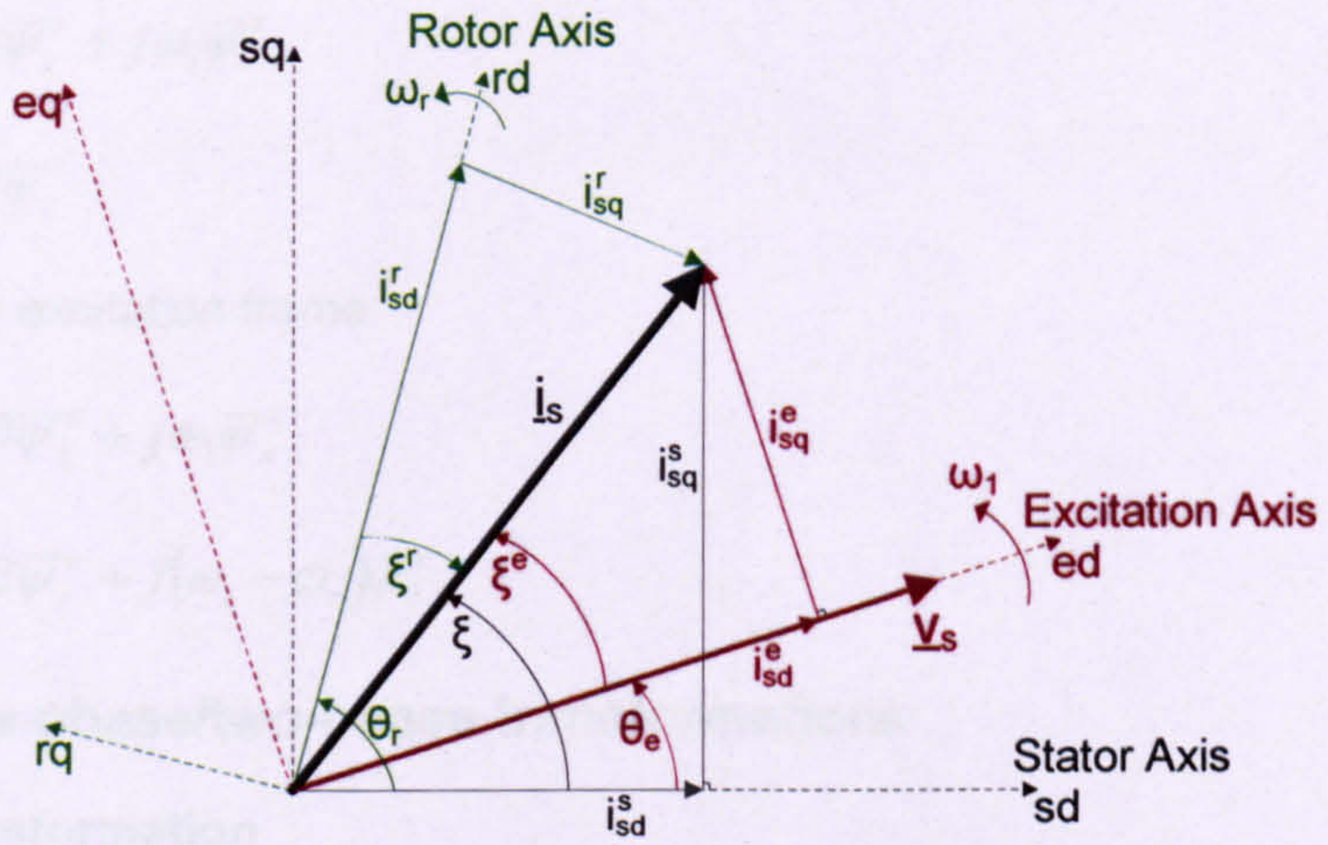

Figure A.2. Space vector of stator current in various reference frames

The stator current space vector appears with a different phase angle when viewed in each of the aforementioned reference frames (Eqs. A.7-A.9). It may be seen to rotate

[11] In certain texts the excitation frame may be pinned against the stator flux rather than stator voltage. A certain amount of caution is necessary in comparing references!

at 50Hz in the stationary frame, appear pseudo-stationary in the excitation frame, and to rotate at slip frequency when viewed from the rotor frame.

$$\bar{i}_s^s(t) = |i_s| \exp(j\xi) = i_{sd}^s + j\, i_{sq}^s, \tag{A.7}$$

$$\bar{i}_s^e(t) = |i_s| \exp(j\xi^e) = |i_s| \exp(j\{\xi - \theta_e\}) = i_{sd}^e + j\, i_{sq}^e, \tag{A.8}$$

$$\bar{i}_s^r(t) = |i_s| \exp(j\xi^r) = |i_s| \exp(j\{\xi - \theta_r\}) = i_{sd}^r + j\, i_{sq}^r. \tag{A.9}$$

The d-q components are all scalar quantities by definition. The vector operator *j* is used to position the quadrature-axis components with respect to the direct-axis components.

A.2.2 General machine voltage equations in three reference frames

Machine coils will appear to "cut" flux at different rates in various reference frames. For completeness we must include an emf which depends on the relative motion of the reference frame and the relevant coil. Only in a frame stationary with respect to the coil will a rotational emf not be apparent. To illustrate, Eqs. A.10 - A.15 express the same stator and rotor voltage vectors of a symmetrical machine viewed in three different reference frames. Firstly in the stator frame:

$$\bar{u}_s^s = R_s \bar{i}_s^s + \partial \bar{\psi}_s^s, \tag{A.10}$$

$$\bar{u}_r^s = R_r \bar{i}_r^s + \partial \bar{\psi}_r^s - j\omega_r \bar{\psi}_r^s. \tag{A.11}$$

Secondly, in the rotor frame:

$$\bar{u}_s^r = R_s \bar{i}_s^r + \partial \bar{\psi}_s^r + j\omega_r \bar{\psi}_s^r, \tag{A.12}$$

$$\bar{u}_r^r = R_r \bar{i}_r^r + \partial \bar{\psi}_r^r. \tag{A.13}$$

Finally, in the excitation frame:

$$\bar{u}_s^e = R_s \bar{i}_s^e + \partial \bar{\psi}_s^e + j\omega_1 \bar{\psi}_s^e \tag{A.14}$$

$$\bar{u}_r^e = R_r \bar{i}_r^e + \partial \bar{\psi}_r^e + j(\omega_1 - \omega_r) \bar{\psi}_r^e \tag{A.15}$$

A.2.3 Three-phase/two-phase transformations

General transformation

Consider a general three-phase system *abc*. Reference axes *sA*, *sB* and *sC* are defined as shown in figure a.3. Axis *sB* is β ahead of *sA*, and *sC* is γ ahead of *sA*.

A 3:2 transformation allows representation of any three-phase variable in an arbitrary orthogonal reference frame *dq0*. The '0' or 'zero-sequence' component of *dq0* accounts for the net DC component from the three phase representation. The zero-sequence can be thought of as independent of the space vector picture and represented along a

third orthogonal axis perpendicular to the space vector plane. The d-q components define the remaining two-dimensional contributions. The relationship between the radial-plane axes is shown in Figure A.3.

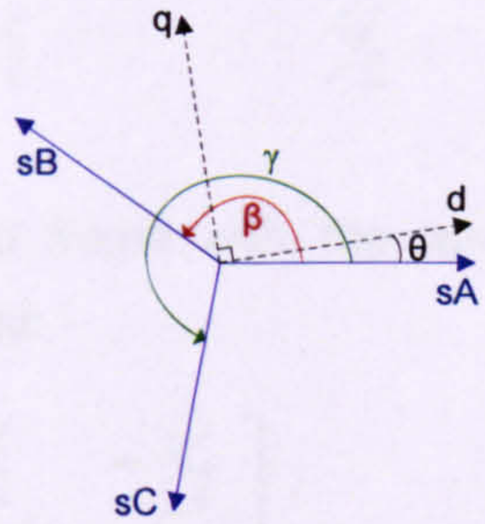

Figure A.3 Orthogonal vs. Three-phase Reference Frame

The q- (quadrature) axis is defined as π/2 radians ahead of the d-axis. The d- (direct) axis is commonly aligned with a particular space vector, for example the space vector of stator voltage, to define a specific *dq0* reference frame. In the following example, an axis *d* is chosen to lie θ ahead of the axis *sA*.

Consider a space vector of voltage, produced by three phase voltages:

$$\bar{v}(t) = v_a(t) + v_b(t)\exp(-j\beta) + v_c(t)\exp(-j\gamma) \tag{A.16}$$

Define the *abc* and *dq0* representations:

$$[v_{abc}] = \begin{bmatrix} v_a \\ v_b \\ v_c \end{bmatrix}, \; [v_{dq0}] = \begin{bmatrix} v_d \\ v_q \\ v_0 \end{bmatrix} \tag{A.17}$$

A general transformation matrix can be derived to resolve the *abc* voltages into the *dq0* representation:

$$[v_{dq0}] = k_C [C]_{gen} [v_{abc}], \tag{A.18}$$

where:

$$[C]_{gen} = \begin{bmatrix} \cos\theta & \cos(\theta-\beta) & \cos(\theta-\gamma) \\ -\sin(\theta) & -\sin(\theta-\beta) & -\sin(\theta-\gamma) \\ 1/2 & 1/2 & 1/2 \end{bmatrix} \tag{A.19}$$

The scaling coefficient, k_C, is an arbitrary constant.

Balanced three-phase systems

Now, for a balanced 3-phase system β = 2π/3 rad, γ = 4π/3 rad. Inserting these into Eq. A.19:

$$[C]_{abc-anydq0} = \begin{bmatrix} \cos\theta & \cos\left(\theta - \frac{2\pi}{3}\right) & \cos\left(\theta + \frac{2\pi}{3}\right) \\ -\sin(\theta) & -\sin\left(\theta - \frac{2\pi}{3}\right) & -\sin\left(\theta + \frac{2\pi}{3}\right) \\ 1/2 & 1/2 & 1/2 \end{bmatrix} \quad \text{(A.20)}$$

If we choose to align the *dq0* frame with the *abc* frame such that θ = 0, The transformation is further simplified:

$$[C]_{abc-dq0\,aligned} = C = \begin{bmatrix} 1 & -1/2 & -1/2 \\ 0 & +\sqrt{3}/2 & -\sqrt{3}/2 \\ 1/2 & 1/2 & 1/2 \end{bmatrix} \quad \text{(A.21)}$$

This matrix is used throughout this work to transform electrical 3-phase variables into stationary *dq0* equivalents (Eq. A.22).

$$[v_{dq0}] = k_C [C][v_{abc}] \quad \text{(A.22)}$$

Inverse transformation

An inverse transformation is used to reconvert dq0-components into 3-phase-components. Note that the inverse process utilises the transpose of the three/two-phase transformation matrix:

$$[v_{abc}] = k_{C-1} [C]^T [v_{dq0}], \quad \text{(A.23)}$$

where

$$[C]^T = \begin{bmatrix} 1 & 0 & 1/2 \\ -1/2 & +\sqrt{3}/2 & 1/2 \\ -1/2 & -\sqrt{3}/2 & 1/2 \end{bmatrix}. \quad \text{(A.24)}$$

A.2.4 Transformation standards

Transformation coefficients

To invert the transformation, the coefficients of Eqs. A.22 and A.23 must satisfy:

$$k_C k_{C-1} [C]^T [C] = [I], \quad \text{(A.25)}$$

where I is the identity matrix. As a result, coefficients k_C and k_{C-1} must obey:

$$k_C k_{C-1} = \frac{2}{3} \quad \text{(A.26)}$$

In practice, a number of different standards can be used.

Equivalent-coil transformations

Each representative two-phase (d-q) machine coil has the same impedance a single real three-phase coil, carrying the same current and same voltage. Hence:

$$k_C = \frac{2}{3},\ k_{C-1} = 1. \tag{A.27}$$

However, the real-world total machine power must be scaled up accordingly from the product of d-q voltage and current vectors:

$$\bar{S} = \frac{3}{2}\left[v_{dq}\right]\left[i_{dq}\right]^* \tag{A.28}$$

Power invariant transformations

Each representative two-phase (d-q) machine coil has 2/3 the impedance of a real three-phase coil. Each d-q coil carries 3/2 times more current for the same voltage, with the result that the two systems do not need a scaling coefficient for power calculations. For voltage transformations:

$$k_{C,V} = \frac{2}{3},\ k_{C-1,V} = 1. \tag{A.29}$$

For current and flux linkage transformations:

$$k_{C,I} = 1,\ k_{C-1,I} = \frac{2}{3} \tag{A.30}$$

Resulting in:

$$\bar{S} = \left[v_{dq}\right]\left[i_{dq}\right]^* \tag{A.31}$$

Symmetrical transformations

A less well used system is included purely for its mathematical simplicity. For forward and reverse transformations:

$$k_C = k_{C-1} = \sqrt{\frac{2}{3}} \tag{A.32}$$

Per Unit transformations

Whilst not strictly a different transformation system, I have included this to avoid the pitfalls of confusing the above three. The transformations are carried out as per the equivalent coil representation; however, the two-axis variables are always converted into per-units. This negates the question of power invariance, as shown in Equation A.33.

$$\bar{S}_{pu} = \left[v_{dq}\right]_{pu}\left[i_{dq}\right]_{pu}^{*} \tag{A.33}$$

In the test rig controller (Section 4.2), wherever a 3:2 phase transformation is used it is post-multiplied by a dedicated per-unit scalar. This results in, for example, rated three phase voltage becoming 1.0 p.u. d-q voltage. This p.u. system is used throughout this work.

A.3 Saliency

In a salient wound rotor machine the capability for linking flux varies around the rotor surface. The magnetic flux path reluctance is dominated by the effective airgap, which may lengthen across large or deep winding slots. As a result inductance values will vary with rotor alignment [42]. An example is shown in Figure A.4. Here, the flux linkage along a flux path parallel to the qr-axis will be far less than the linkage parallel to the dr-axis, as there is far less iron in a qr-axis path and hence a far greater magnetic reluctance.

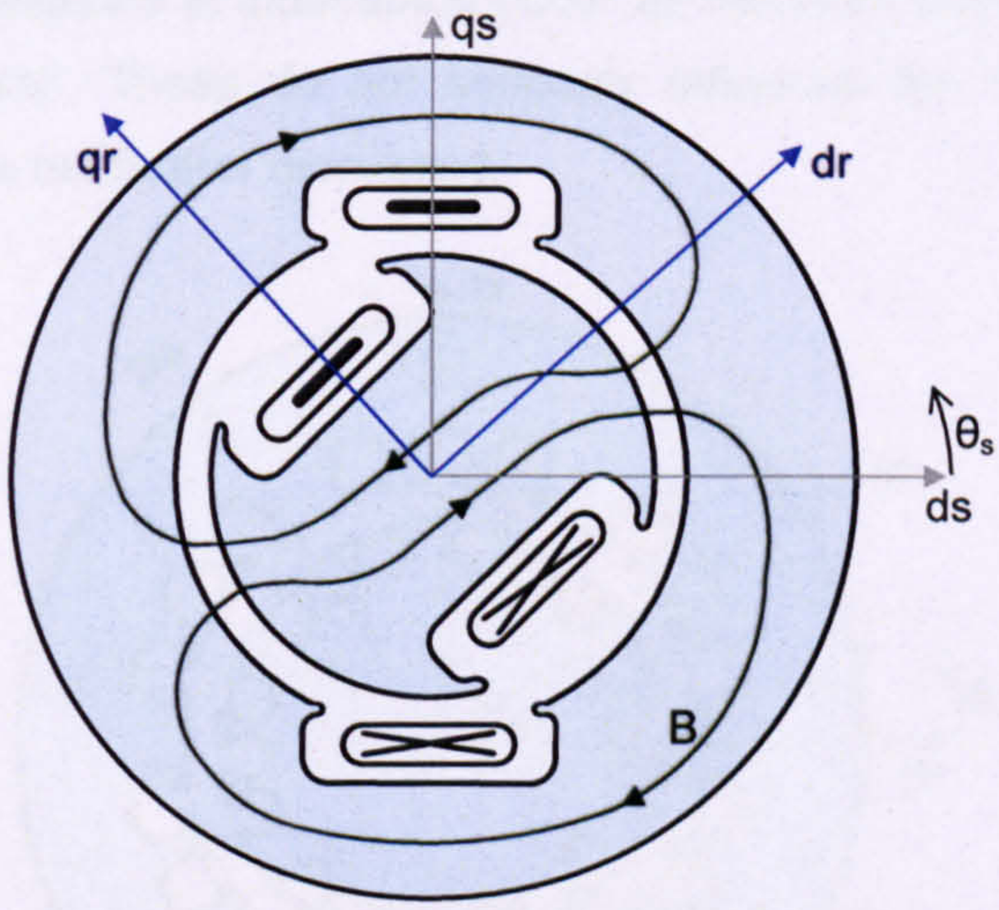

Figure A.4. Salient rotor-pole machine example.

The governing machine equations, viewed in the rotor reference frame, become:

$$\bar{u}_s^r = R_s\bar{i}_s^r + \partial\bar{\psi}_s^r + j\omega_r\bar{\psi}_s^r \tag{›A.12}$$

$$\bar{u}_r^r = R_r\bar{i}_r^r + \partial\bar{\psi}_r^r \tag{›A.13}$$

$$\bar{\psi}_s^r = L_s(\theta_r)\bar{i}_s^s + L_m(\theta_r)\bar{i}_r^s \tag{A.34}$$

$$\bar{\psi}_r^s = L_r(\theta_r)\bar{i}_r^s + L_m(\theta_r)\bar{i}_s^s \tag{A.35}$$

The machine inductances may be resolved against the rotor and stator axes. This leads to a complicated expression for impedance. With all terms viewed in the rotor reference frame and 'L_m' replaced by 'M' for clarity:

$$\begin{bmatrix} u_{sd} \\ u_{sq} \\ \cdots \\ u_{rd} \\ u_{rq} \end{bmatrix} = \begin{bmatrix} \left(R_{s\to dr} + L_{s\to dr}\partial\right) & +\omega_r M_{ds-qs} & M_{ds-dr}\partial & +\omega_r M_{ds-qr} \\ -\omega_r M_{qs-ds} & \left(R_{s\to qr} + L_{s\to qr}\partial\right) & -\omega_r M_{qs-dr} & M_{qs-qr}\partial \\ \cdots & \cdots & \cdots & \cdots \\ M_{dr-ds}\partial & 0 & \left(R_{r\to dr} + L_{r\to dr}\partial\right) & 0 \\ 0 & M_{qr-qs}\partial & 0 & \left(R_{r\to qr} + L_{r\to qr}\partial\right) \end{bmatrix} \begin{bmatrix} i_{sd} \\ i_{sq} \\ \cdots \\ i_{rd} \\ i_{rq} \end{bmatrix} \quad \text{(A.36)}$$

For a polyphase winding distribution, with multiple slots per phase and a small, consistent airgap width, the aggregate effect of saliency is diminished, as can be seen from Figure A.5. Inductance values vary negligibly with position and can be considered approximately constant (Eq. A.37).

$$L(\theta_r) = L \quad \text{(A.37)}$$

This result allows use of the more general non-salient machine flux linkage equations:

$$\bar{\psi}_s^r = L_s \bar{i}_s^s + L_m \bar{i}_r^s \quad \text{(A.38)}$$

$$\bar{\psi}_r^s = L_r \bar{i}_r^s + L_m \bar{i}_s^s \quad \text{(A.39)}$$

Small, ripple-like deviations in inductance occur as the slots align and mis-align in so-called 'slotting effects'. These do not seriously influence the fault response of AC machines and so are not further discussed.

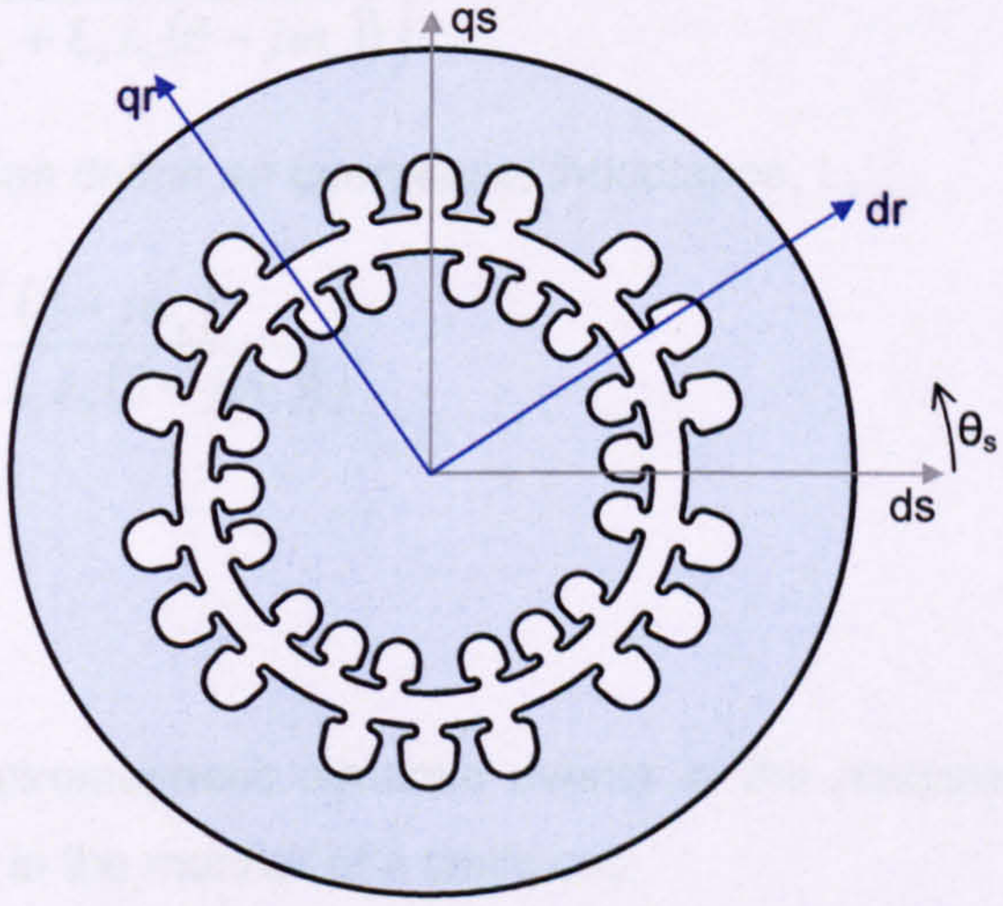

Figure A.5. Low-saliency machine.

All wind turbine DFIGs are polyphase induction machines and typically use high slot- and winding-numbers, with a small smooth airgap to maximise efficiency [47]. All wind turbine DFIGs therefore possess minimal saliency and throughout this work the machine inductances are assumed to be independent of rotor position. This important result allows us to consider the inductances as constant when viewed in a stator, rotor or synchronously-rotating reference frame.

A.4 Transient Timescale Derivation

The transient timescale governs electromagnetic dynamic phenomena over which the rotor speed remains constant. The following derivation is based on one shown in [44]. Consider an induction machine with a short-circuited rotor:

$$0 = R_r \bar{i}_r^s + \partial \overline{\psi}_r^s - j\omega_r \overline{\psi}_r^s \tag{A.40}$$

Substituting for flux linkage (Eq. A.38):

$$0 = R_r \bar{i}_r^s + (\partial - j\omega_r)(L_r \bar{i}_r^s + L_m \bar{i}_s^s) \tag{A.41}$$

$$0 = (R_r + L_r\partial - j\omega_r L_r)\bar{i}_r^s + (L_m\partial - j\omega_r L_m)\bar{i}_s^s \tag{A.42}$$

$$\bar{i}_r^s = -\frac{L_m(\partial - j\omega_r)}{(R_r + L_r(\partial - j\omega_r))}\bar{i}_s^s \tag{A.43}$$

Substituting rotor current (Eq. A.43) into the expression for stator flux (Eq. A.38):

$$\overline{\psi}_s^s = \bar{i}_s^s\left(L_s - \frac{{L_m}^2(\partial - j\omega_r)}{(R_r + L_r(\partial - j\omega_r))}\right) \tag{A.44}$$

$$\overline{\psi}_s^s = \bar{i}_s^s L_s\left(1 - \frac{{L_m}^2(\partial - j\omega_r)}{(R_r L_s + L_r L_s(\partial - j\omega_r))}\right) \tag{A.45}$$

Using Eq. A.45 we can define an *operational inductance*, L_s':

$$L_s' = L_s\left(1 - \frac{{L_m}^2(\partial - j\omega_r)}{(R_r L_s + L_r L_s(\partial - j\omega_r))}\right), \tag{A.46}$$

such that:

$$\overline{\psi}_s^s = \bar{i}_s^s L_s' \tag{A.47}$$

A timescale for electromagnetic dynamic events in the machine's stator circuit can therefore be derived in the manner of a static coil:

$$\tau_{IM,stator} = \frac{L_s'}{R_s} \tag{A.48}$$

From initial value theorem the operational inductance at the initial time (t→0) becomes:

$$L_{s,transient}' = \lim_{\partial \to \infty}(L_s') = L_s\left(1 - \frac{{L_m}^2(\partial - j\omega_r)}{(R_r L_s + L_r L_s(\partial - j\omega_r))}\right) = L_s\left(1 - \frac{{L_m}^2}{L_r L_s}\right) \tag{A.49}$$

Now, using the leakage constant definition:

$$\sigma = \left(1 - \frac{L_m{}^2}{L_r L_s}\right) \tag{A.50}$$

$$L'_{s,transient} = L_s\left(1 - \frac{L_m{}^2}{L_r L_s}\right) = \sigma L_s \tag{A.51}$$

The transient timescale for electrical response on the stator circuit becomes:

$$\tau_s = \frac{\sigma L_s}{R_s} \tag{A.52}$$

Similarly, the transient time constant for the rotor circuit can be derived using a shorted-stator circuit:

$$\tau_r = \frac{\sigma L_r}{R_r} \tag{A.53}$$

The transient time constants specify the time required for a unit of flux on either circuit to decay to 1/e of its value in the event of a close-up short-circuit.

Transient equivalent circuit

It is worth noting that the transient operational inductance (Eq. A.51) can be reproduced by a transient equivalent circuit with parallel paths of mutual inductance and rotor leakage inductance (Figure A.6). This helps to obtain the form of the transient time constant, although it can be misleading in terms of the flux behaviour during fault response.

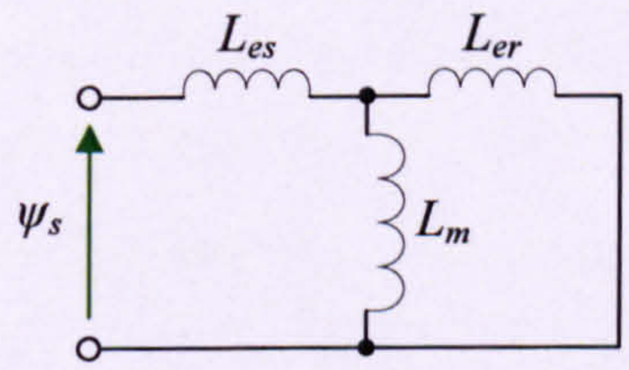

Figure A.6. Stator transient equivalent circuit.

The operational stator inductance from Figure A.6 is:

$$L'_{s,transient} = (L_{es}) + (L_{er} \,//\, L_m) = L_s\left(1 - \frac{L_m{}^2}{L_r L_s}\right) = \sigma L_s \tag{A.54}$$

The converse applies for the rotor circuit.

ANALYTICAL SOLUTION FOR FAULT RESPONSE

B

B.1 Analytical solution for a zero voltage fault

B.1.1 Generalised equations

Consider a non-salient DFIG with a small, uniform airgap. The governing machine equations in space vector form are reproduced here from Section 3.1.6, where all parameters have been referred to the stator reference frame:

$$\bar{u}_s^s = R_s \bar{i}_s^s + \partial \bar{\psi}_s^s \tag{B.1}$$

$$\bar{u}_r^s = R_r \bar{i}_r^s + \partial \bar{\psi}_r^s - j\omega_r \bar{\psi}_r^s \tag{B.2}$$

$$\bar{\psi}_s^s = L_s \bar{i}_s^s + L_m \bar{i}_r^s \tag{B.3}$$

$$\bar{\psi}_r^s = L_r \bar{i}_r^s + L_m \bar{i}_s^s \tag{B.4}$$

Eqs.(B.3, B.4) may be rearranged for stator current, using the leakage parameter, σ, as follows:

$$\sigma = 1 - \frac{L_m{}^2}{L_r L_s} \tag{B.5}$$

$$\bar{i}_s^s = \frac{1}{\sigma L_s}\left(\bar{\psi}_s^s - \frac{L_m}{L_r}\bar{\psi}_r^s\right) \tag{B.6}$$

Similarly, for rotor current:

$$\bar{i}_r^s = \frac{1}{\sigma L_r}\left(\bar{\psi}_r^s - \frac{L_m}{L_s}\bar{\psi}_s^s\right) \tag{B.7}$$

Current equations (B.6, B.7) are substituted into the voltage equations (B.1, B.2), using transient time constants defined in Appendix A:

$$\tau_s = \frac{L_s'}{R_s} = \frac{\sigma L_s}{R_s}, \qquad \tau_r = \frac{L_r'}{R_r} = \frac{\sigma L_r}{R_r} \tag{B.8, B.9}$$

$$\bar{u}_s^s = \frac{1}{\tau_s}\left(\bar{\psi}_s^s - \frac{L_m}{L_r}\bar{\psi}_r^s\right) + \partial \bar{\psi}_s^s \tag{B.10}$$

$$\bar{u}_r^s = \frac{1}{\tau_r}\left(\bar{\psi}_r^s - \frac{L_m}{L_s}\bar{\psi}_s^s\right) + \partial\bar{\psi}_r^s - j\omega_r\bar{\psi}_r^s \tag{B.11}$$

Voltage-flux equations of Eqs. B.10 & B.11 are useful in the proceeding derivations.

B.1.2 Laplace Transform solution for stator flux linkage

A solution to these first order differential equations (B.10, B.11) may be found using the Laplace transform. Now, consider the general Laplace transform and the Laplace transform of a time differential [91]:

$$F(\nu) = \int_{0-}^{\infty} f(t)e^{-\nu t}\,dt = \Gamma\{f(t)\} \tag{B.12}$$

$$\Gamma\left\{\frac{df(t)}{dt}\right\} = \nu F(\nu) - f(0) \tag{B.13}$$

Note that the Laplace variable is chosen to be 'ν' instead of the more common 's' to avoid confusion with induction machine slip. The linearity of the Laplace transform allows its application on complex numbers. The transformed parameters are defined with relevant capitalisation (e.g. Eqs. B.14, B.15) and the initial conditions are defined with a zero in the subscript (e.g. Eqs. B.16, B.17).

$$\Gamma\{\bar{\psi}(t)\} = \bar{\Psi}(\nu), \qquad \Gamma\{\bar{u}(t)\} = \bar{U}(\nu) \tag{B.14, B.15}$$

$$\bar{\psi}_s^s(t=0) = \bar{\psi}_{s0}^s, \qquad \bar{\psi}_r^s(t=0) = \bar{\psi}_{r0}^s \tag{B.16, B.17}$$

Fault conditions are defined here as an instantaneous stator voltage drop to zero volts occurring at time zero. Given the relative mechanical and electromagnetic time-constants, rotor speed changes will occur far slower than magnetic flux changes. Rotor speed is assumed roughly constant over the grid fault interval.

Taking zero stator voltage and using constant rotor speed, the Laplace transforms of Eqs. (B.10, B.11):

$$0 = \frac{1}{\tau_s}\left(\bar{\Psi}_s^s - \frac{L_m}{L_r}\bar{\Psi}_r^s\right) + \left(\nu\bar{\Psi}_s^s - \bar{\psi}_{s0}^s\right) \tag{B.18}$$

$$\bar{U}_r^s(\nu) = \frac{1}{\tau_r}\left(\bar{\Psi}_r^s - \frac{L_m}{L_s}\bar{\Psi}_s^s\right) + \left(\nu\bar{\Psi}_r^s - \bar{\psi}_{r0}^s\right) - j\omega_r\bar{\Psi}_r^s \tag{B.19}$$

Rearranging for stator flux in terms of the initial conditions and rotor voltage:

$$\frac{L_m}{L_r\tau_s}\left(\bar{U}_r^s(\nu) + \bar{\psi}_{r0}^s\right) + \left(\frac{1}{\tau_r} - j\omega_r + \nu\right)\bar{\psi}_{s0}^s = \left[\left(\frac{1}{\tau_r} - j\omega_r + \nu\right)\left(\frac{1}{\tau_s} + \nu\right) - (1-\sigma)\frac{1}{\tau_s\tau_r}\right]\bar{\Psi}_s^s(\nu) \tag{B.20}$$

$$\overline{\Psi}_s^s(\nu)=\frac{\left(\frac{1}{\tau_r}-j\omega_r+\nu\right)\overline{\psi}_{s0}^s+\frac{L_m}{L_r\tau_s}\overline{\psi}_{r0}^s}{\left[\left(\frac{1}{\tau_r}-j\omega_r+\nu\right)\left(\frac{1}{\tau_s}+\nu\right)-\frac{(1-\sigma)}{\tau_s\tau_r}\right]}+\frac{\frac{L_m}{L_r\tau_s}\overline{U}_r^s(\nu)}{\left[\left(\frac{1}{\tau_r}-j\omega_r+\nu\right)\left(\frac{1}{\tau_s}+\nu\right)-\frac{(1-\sigma)}{\tau_s\tau_r}\right]} \quad \text{(B.21)}$$

This form can be simplified, defining certain numeric and complex constants (Eqs. B.22, B.23, B.24), (B.25):

$$\rho_s=\frac{1}{\tau_s},\quad \rho_r=\frac{1}{\tau_r}-j\omega_r,\quad k_\sigma=\frac{(1-\sigma)}{\tau_s\tau_r} \quad \text{(B.22, B.23, B.24)}$$

$$k_r=\frac{L_m}{L_r} \quad \text{(B.25)}$$

$$\overline{\Psi}_s^s=\overbrace{\frac{(\rho_r+\nu)\overline{\psi}_{s0}^s+(k_r/\tau_s)\overline{\psi}_{r0}^s}{(\rho_r+\nu)(\rho_s+\nu)-k_\sigma}}^{\text{Natural Response}}+\overbrace{\frac{(k_r/\tau_s)\overline{U}_r^s(\nu)}{(\rho_r+\nu)(\rho_s+\nu)-k_\sigma}}^{\text{Forced Response}} \quad \text{(B.26)}$$

Eq. B.26 describes the stator flux linkage – consisting of a natural response (term containing the initial conditions) and a forced response (term containing the rotor voltage). The natural response contains the whole solution in a singly-fed machine, or with a doubly-fed machine where the rotor circuit has been short-circuited.

B.1.3 Natural response solution for stator flux linkage

Inverse Laplace transform

Eq. B.26 showed the stator flux to comprise of a natural and forced response. By linear superposition, the real-time solution for stator flux linkage is the sum of the solutions for each independent response:

$$\overline{\psi}_s^s(t)=\Gamma^{-1}\left\{\overline{\Psi}_s^s(\nu)\right\}=\Gamma^{-1}\left\{\frac{(\rho_r+\nu)\overline{\psi}_{s0}^s+(k_r/\tau_s)\overline{\psi}_{r0}^s}{(\rho_r+\nu)(\rho_s+\nu)-k_\sigma}\right\}+\Gamma^{-1}\left\{\frac{(k_r/\tau_s)\overline{U}_r^s(\nu)}{(\rho_r+\nu)(\rho_s+\nu)-k_\sigma}\right\} \quad \text{(B.27)}$$

Looking at the natural response alone, we see a first order numerator and a second order denominator. This form suggests a two-part exponential solution as shown by the following inverse-Laplace transform, where α,β,A,B may be complex:

$$\Gamma^{-1}\left\{\frac{k_1\nu+k_2}{(\alpha+\nu)(\beta+\nu)}\right\}=\Gamma^{-1}\left\{\frac{A}{(\alpha+\nu)}+\frac{B}{(\beta+\nu)}\right\}=Ae^{-\alpha t}+Be^{-\beta t} \quad \text{(B.28)}$$

Natural response roots

Equating Eq. B.28 with the natural response term from Eq. B.27:

$$\frac{k_1 \nu + k_2}{(\alpha+\nu)(\beta+\nu)} = \frac{(\rho_r+\nu)\overline{\psi}^s_{s0} + (k_r/\tau_s)\overline{\psi}^s_{r0}}{(\rho_r+\nu)(\rho_s+\nu)-k_\sigma} \tag{B.29}$$

The denominators of Eq.(B.29) can be solved to find the roots α,β:

$$(\alpha+\nu)(\beta+\nu) = (\rho_r+\nu)(\rho_s+\nu)-k_\sigma \tag{B.30}$$

$$0 = \alpha^2 - (\rho_r+\rho_s)\alpha + (\rho_r\rho_s - k_\sigma) \tag{B.31}$$

$$\alpha = +\frac{(\rho_r+\rho_s)}{2} \pm \frac{1}{2}(\rho_r-\rho_s)\sqrt{\left(1+\frac{4k_\sigma}{(\rho_r-\rho_s)^2}\right)} \tag{B.32}$$

Induction machine transient time constants are no smaller than tens of milliseconds, which equates to roughly 10 p.u. or more on this p.u. base[12]. As such we can make the general assumption:

$$\frac{1}{\tau_{s,r}^{\ 2}} << \omega_r \approx 1 \tag{B.33}$$

and hence:

$$|\rho_r - \rho_s| = \left|\left(\tau_r^{-1} - \tau_s^{-1}\right) - j\omega_r\right| \approx \omega_r >> k_\sigma \tag{B.34}$$

Therefore, using a Taylor Series expansion for the square root term:

$$(1+x)^{1/2} = 1 + (1/2)x + \{f(x^{k>1}) \to 0\} \tag{B.35}$$

$$\sqrt{\left(1+\frac{4k_\sigma}{(\rho_r-\rho_s)^2}\right)} \approx 1 + \frac{2k_\sigma}{(\rho_r-\rho_s)^2} \tag{B.36}$$

$$\alpha = \rho_s - \frac{k_\sigma}{(\rho_r-\rho_s)}, \quad \beta = \rho_r + \frac{k_\sigma}{(\rho_r-\rho_s)} \tag{B.37, B.38}$$

Complex frequency adjustment

We can define the complex frequency adjustment in terms of its real and imaginary parts:

$$\varsigma_f = \frac{k_\sigma}{(\rho_r-\rho_s)} = \kappa + j\delta, \tag{B.39}$$

where κ and δ are both real and small; κ vanishingly so if the two time constants are very close. Note also that the imaginary part δ is always positive. An expansion in terms of the transient time constants is given in Eq. B.40.

[12] 1 p.u. of time = $(100*\pi)^{-1}$ seconds, such that ω_1 = 1 p.u.

$$\varsigma_f = \frac{k_\sigma}{|\rho_r - \rho_s|}\angle -\{\rho_r - \rho_s\} = \frac{(1-\sigma)/\tau_s\tau_r}{|1/\tau_r - 1/\tau_s - j\omega_r|}\angle \arctan\left\{\frac{\omega_r}{1/\tau_r - 1/\tau_s}\right\} \quad \text{(B.40)}$$

The frequency adjustment parameter helps to rewrite the roots of the stator flux linkage solution (from Eqs. B.37, B.38):

$$\alpha = \tau_s^{-1} - \varsigma_f \qquad \beta = \tau_r^{-1} - j\omega_r + \varsigma_f, \quad \text{(B.41, B.42)}$$

$$\alpha = \left(\tau_s^{-1} - \kappa\right) - j\delta \qquad \beta = \left(\tau_r^{-1} + \kappa\right) - j(\omega_r - \delta), \quad \text{(B.43, B.44)}$$

The effective transient time constants take into account the fractional adjustment caused by the complex frequency adjustment term:

$$\tau_s'^{-1} = \left(\tau_s^{-1} - \kappa\right) \qquad \tau_r'^{-1} = \left(\tau_r^{-1} + \kappa\right). \quad \text{(B.45, B.46)}$$

The effective decay frequencies (described in the main text as 'near-dc' and 'near-rotor speed') are closer in value as a result, remembering that δ is always positive:

$$f_{own-circuit} = \delta \qquad f_{mutual} = (\omega_r - \delta) \quad \text{(B.47, B.48)}$$

We can approximate the complex frequency adjustment in the case where the transient timescales for stator and rotor are similar. Here the adjustment parameter ς_f is almost purely imaginary. Using the approximation from Eq. B.34:

$$\varsigma_f \approx \frac{(1-\sigma)/\tau_s\tau_r}{\omega_r}\angle\left(90 - \arctan\left\{\frac{1/\tau_r - 1/\tau_s}{\omega_r}\right\}\right), \quad \text{(B.49)}$$

$$\tau_s \approx \tau_r >> 1 \therefore \left\{\frac{1/\tau_r - 1/\tau_s}{\omega_r}\right\} << 1, \quad \text{(B.50)}$$

$$\varsigma_f \approx \frac{(1-\sigma)}{\omega_r\tau_s\tau_r}\left(\left\{\frac{1/\tau_r - 1/\tau_s}{\omega_r}\right\} + j\right) \quad \text{(B.51)}$$

Therefore, estimating the real and imaginary frequency-adjustment parameters:

$$\kappa \approx \frac{(1-\sigma)}{\omega_r^{\,2}\tau_s\tau_r}(1/\tau_r - 1/\tau_s) \quad \text{(B.52)}$$

$$\delta \approx \frac{(1-\sigma)}{\omega_r\tau_r\tau_s} \quad \text{(B.53)}$$

The real part, κ, is of the order of τ_r^{-3} and therefore has negligible impact. Using the imaginary frequency adjustment from Eq. B.53 therefore, denominator roots approximate to:

$$\alpha \approx \tau_s^{-1} - j\frac{(1-\sigma)}{\omega_r \tau_r \tau_s} \qquad \beta \approx \tau_r^{-1} - j\omega_r\left(1 - \frac{(1-\sigma)}{\omega_r^{2}\tau_r\tau_s}\right) \tag{B.54, B.55}$$

Form of the solution

Substituting the denominator roots (Eqs. B.43, B.44) into the trial solution (Eq. B.28), we see these roots determining the characteristic time-evolution of the natural response of stator flux decay:

Near-DC Near-rotor speed

$$\overline{\psi}_s^s(t) = Ae^{-t/\tau_s'}e^{j\delta t} + Be^{-t/\tau_r'}e^{j(\omega_r-\delta)t} \tag{B.56}$$

In physical terms, we see two components of decaying stator flux. Firstly, unsupported flux decays from its pre-fault value on the stator circuit at near-dc frequency over the stator transient timescale. Secondly, unsupported flux decays on the rotor circuit at near-dc frequency over the rotor transient timescale. This rotor flux linkage decay induces a decaying emf on the stator circuit, acting to oppose the rotor flux decay. The emf appears from the stator windings to possess near-rotor-speed. This produces a near-rotor-frequency contribution to the stator flux, which decays over the rotor leakage timescale. This painfully verbose text is better illustrated by inspection of Eq. B.56.

The twin components make sense intuitively as the rotor windings "cut" the stator flux at rotor speed, and vice versa. If we first accept that each circuit in its own frame will see a dc collapse of unsupported flux (as would an isolated stationary inductive coil), the mutual coupling of rotor and stator will necessitate an induced ac component reflecting the other circuit's dc decay.

The ac component is at near-rotor speed (*electrical* radians/s, accounting for the number of poles). Now, without the supply voltage neither the 50Hz excitation-frame nor machine-slip hold any physical meaning with respect to the short-circuited machine.

The complex frequency adjustment hints at an interaction between the fluxes linked by either set of windings. As explained in the section on torque generation, the tendency of two concentric magnetic dipoles is to align: the rotor flux's rotation will be slowed by the stator field and the stator field accelerated by the passing rotor field. If time constants were near-infinite, implying minimal energy loss, eventually both sets of fluxes would align and rotate at a common velocity somewhere between zero and rotor speed.

$$f_{own\text{-}circuit} > 0 \qquad f_{mutual} < \omega_r \tag{B.57, B.58}$$

The magnitude of this dragging effect depends upon the relative speed of the two fields – i.e. the rotor speed. With high rotor speed the fields barely interact, whereas this alignment-force-drag will be more pronounced at lower speeds. This is evident in the inverse relation between the frequency adjustment parameter and rotor speed (Eq. B.53).

The effect on the effective flux-decay time constants is to increase the difference between them. Put mathematically:

$$\left|\tau_r' - \tau_s'\right| > \left|\tau_r - \tau_s\right| \tag{B.59}$$

However, the percentage difference is of the order of $\delta \times (\tau_r\text{-}1 - \tau_s\text{-}1)$, well below 0.5% for a practical machine and as a result bearing little impact.

Stator flux solution

The coefficients of the trial solution (Eq. B.56) may be obtained from a partial fraction expansion of Eq. B.29:

$$\overline{\Psi}_s^s = \frac{(\rho_r + \nu)\overline{\psi}_{s0}^s + (k_r/\tau_s)\overline{\psi}_{r0}^s}{(\alpha + \nu)(\beta + \nu)} = \frac{A}{(\alpha + \nu)} + \frac{B}{(\beta + \nu)} \tag{B.60}$$

A convenient redefinition of constant A helps the trial solution as follows:

$$\frac{A}{(\alpha + \nu)} + \frac{B}{(\beta + \nu)} = \frac{\overline{\psi}_{s0}^s + A_s^s}{(\alpha + \nu)} + \frac{B}{(\beta + \nu)}, \tag{B.61}$$

$$\left(\overline{\psi}_{s0}^s + A_s^s\right)(\beta + \nu) + B(\alpha + \nu) = (\rho_r + \nu)\overline{\psi}_{s0}^s + (k_r/\tau_s)\overline{\psi}_{r0}^s \tag{B.62}$$

Equating the first order terms in ν:

$$B = -A_s^s \tag{B.63}$$

Equating the zero order terms in ν:

$$A_s^s = \frac{(\rho_r - \beta)\overline{\psi}_{s0}^s + (k_r/\tau_s)\overline{\psi}_{r0}^s}{(\beta - \alpha)} \tag{B.64}$$

Using the frequency adjustment parameters with the root definitions (Eqs. B.43, B.44):

$$A_s^s = \frac{(\delta + j\kappa)\overline{\psi}_{s0}^s + j(k_r/\tau_s)\overline{\psi}_{r0}^s}{(\omega_r - 2\delta) + j\left(\tau_r'^{-1} - \tau_s'^{-1}\right)} \tag{B.65}$$

Note the addition of the superscript to the coefficient; the coefficient depends on initial conditions of flux linkage as measured in the stator reference frame. Initial conditions in their own reference frame must be transformed by the initial rotor frame angle at the instant of short-circuit, for example:

$$A_s^s = \frac{(\delta + j\kappa)\overline{\psi}_{s0}^s + j(k_r/\tau_s)\left(\overline{\psi}_{r0}^r e^{+j\theta_{r0}}\right)}{(\omega_r - 2\delta) + j\left(\tau_r'^{-1} - \tau_s'^{-1}\right)} \tag{B.66}$$

As previously discussed, the reciprocals of the transient machine timescales are far smaller than rotor speed. Using the approximation from Eq. B.34 therefore:

$$A_s^s \approx j\frac{k_r}{\omega_r \tau_s}\overline{\psi}_{r0}^s \tag{B.67}$$

The full expansion produces a description of the natural response of the stator flux linkage, with certain derived parameters repeated below for clarity:

$$\overline{\psi}_s^s(t) = \overbrace{\left(\overline{\psi}_{s0}^s + A_s^s\right)e^{-t/\tau_s'}e^{j\delta t}}^{\text{Near-DC}} - \overbrace{A_s^s\, e^{-t/\tau_r'}e^{j(\omega_r-\delta)t}}^{\text{Near-rotor speed}} \tag{B.68}$$

$$\tau_s = \frac{\sigma L_s}{R_s}, \qquad \tau_r = \frac{\sigma L_r}{R_r} \tag{›B.8, B.9}$$

$$\tau_s'^{-1} = \left(\tau_s^{-1} - \kappa\right) \qquad \tau_r'^{-1} = \left(\tau_r^{-1} + \kappa\right). \tag{›B.45, B.46}$$

$$\overline{\psi}_s^s(t=0) = \overline{\psi}_{s0}^s, \qquad \overline{\psi}_r^s(t=0) = \overline{\psi}_{r0}^s \tag{›B.16, B.17}$$

$$\kappa \approx 0 \tag{›B.52}$$

$$\delta \approx \frac{(1-\sigma)}{\omega_r \tau_r \tau_s} \tag{›B.53}$$

$$A_s^s \approx j\frac{k_r}{\omega_r \tau_s}\overline{\psi}_{r0}^s \tag{›B.67}$$

N.B. As a sanity check, the above solution (B.68) satisfies the initial conditions:

$$\overline{\psi}_s^s(t=0) = \overline{\psi}_{s0}^s \tag{›B.16}$$

B.1.4 Stator current natural response

The stator circuit equation (Eq. B.1) with zero stator voltage:

$$0 = R_s\bar{i}_s^s + \partial\overline{\psi}_s^s \tag{B.69}$$

Using (B.69) and differentiating the stator flux derivation (B.68) therefore:

$$\bar{i}_s^s(t) = \frac{\left(\overline{\psi}_{s0}^s + A_s^s\right)\alpha}{R_s}e^{-\alpha t} - \frac{A_s^s\beta}{R_s}e^{-\beta t} \tag{B.70}$$

$$\bar{i}_s^s(t) = \frac{\left(\overline{\psi}_{s0}^s + A_s^s\right)\left(\tau_s'^{-1} - j\delta\right)}{R_s}e^{-t/\tau_s'}e^{j\delta t} - \frac{A_s^s\left(\tau_r'^{-1} - j(\omega_r - \delta)\right)}{R_s}e^{-t/\tau_r'}e^{j(\omega_r-\delta)t} \tag{B.71}$$

This shows the stator current to display the same frequency components as the stator flux linkage although with different coefficients. Neglecting the small frequency adjustment parameters and terms of the order τ^{-2}:

$$\delta \approx \frac{(1-\sigma)}{\omega_r \tau_r \tau_s} \approx \frac{1}{\tau_x^{\,2}} \approx 0, \tag{B.72}$$

and noting the transient operational inductance:

$$\tau_s = \frac{L'_s}{R_s} \tag{›B.8}$$

the stator current approximates to a simpler form relating chiefly to the effective transient inductance:

$$\bar{i}_s^s(t) \approx \frac{1}{L'_s}\bar{\psi}_{s0}^s e^{-t/\tau'_s} e^{j\delta t} - \frac{k_r}{L'_s}\bar{\psi}_{r0}^s e^{-t/\tau'_r} e^{j(\omega_r-\delta)t} \tag{B.73}$$

or, equally:

$$\bar{i}_s^s(t) \approx \frac{1}{L'_s}\bar{\psi}_{s0}^s e^{-t/\tau'_s} e^{j\delta t} - \frac{k_s}{L'_r}\bar{\psi}_{r0}^s e^{-t/\tau'_r} e^{j(\omega_r-\delta)t} \tag{B.74}$$

Initial conditions

One can check the derivation Eq. B.71 against the initial conditions, using the earlier definitions of A_s, α and β:

$$\bar{i}_s^s(t=0) = \frac{\left(\bar{\psi}_{s0}^s + A_s^s\right)\alpha}{R_s} - \frac{A_s^s \beta}{R_s}, \tag{B.75}$$

$$\bar{i}_s^s(t=0) = \frac{\bar{\psi}_{s0}^s \alpha}{R_s} + \frac{1}{R_s}\left(\bar{k}_f \bar{\psi}_{s0}^s - \frac{k_r}{\tau_s}\bar{\psi}_{r0}^r\right), \tag{B.76}$$

$$\bar{i}_s^s(t=0) = \frac{1}{\sigma L_s}\left(\bar{\psi}_{s0}^s - \frac{L_m}{L_r}\bar{\psi}_{r0}^r\right). \tag{B.77}$$

The validity of Eq. B.77 is evident from the flux linkage definitions (Eqs. B.3 & B.4) and the leakage constant definition (Eq. B.5).

B.1.5 Rotor flux linkage natural response

Similarly to the solution for stator flux linkage in Section B.1.2, Eqs. B.18 & B.19 can be solved for rotor flux linkage.

$$\rho_s = \frac{1}{\tau_s}, \quad \rho_r = \frac{1}{\tau_r} - j\omega_r, \quad k_\sigma = \frac{(1-\sigma)}{\tau_s \tau_r} \tag{›B.22, B.23, B.24}$$

$$k_s = \frac{L_m}{L_s} \tag{B.78}$$

$$\overline{\Psi}_r^s = \frac{(\rho_s + \nu)\overline{\psi}_{r0}^s + (k_s/\tau_r)\overline{\psi}_{s0}^s}{(\rho_r + \nu)(\rho_s + \nu) - k_\sigma} + \frac{(\rho_s + \nu)\overline{U}_r^s(\nu)}{(\rho_r + \nu)(\rho_s + \nu) - k_\sigma} \tag{B.79}$$

Which has the same form as Eq. B.26. Using a partial fraction expansion as before:

$$\overline{\Psi}_{r\ natural}^s = \frac{(\rho_s + \nu)\overline{\psi}_{r0}^s + (k_s/\tau_r)\overline{\psi}_{s0}^s}{(\alpha + \nu)(\beta + \nu)} = \frac{A_r^s}{(\alpha + \nu)} + \frac{\overline{\psi}_{r0}^s + B_r^{'}}{(\beta + \nu)}, \tag{B.80}$$

Equating the first order terms in ν:

$$B_r^{'} = -A_r^s \tag{B.81}$$

Equating the zero order terms in ν:

$$A_r^s = \frac{(\rho_s - \alpha)\overline{\psi}_{r0}^s + (k_s/\tau_r)\overline{\psi}_{s0}^s}{(\beta - \alpha)} \tag{B.82}$$

Using the frequency adjustment parameters (Eqs. B.39) with the root definitions (Eqs. B.43, B.44):

$$A_r^s = \frac{-(\delta + j\kappa)\overline{\psi}_{r0}^s + j(k_s/\tau_r)\overline{\psi}_{s0}^s}{(\omega_r - 2\delta) + j\left(\tau_r^{'-1} - \tau_s^{'-1}\right)} \tag{B.83}$$

As previously discussed, the reciprocals of the transient machine time constants are far smaller than rotor speed. Using the approximation from Eq. B.34 therefore:

$$A_r^s \approx j\frac{k_s}{\omega_r \tau_r}\overline{\psi}_{s0}^s \tag{B.84}$$

The natural response (or zero rotor voltage response) of rotor flux linkage in the stator reference frame becomes:

$$\overline{\psi}_r^s(t) = A_r^s e^{-t/\tau_s'} e^{j\delta t} + \left(\overline{\psi}_{r0}^s - A_r^s\right)e^{-t/\tau_r'} e^{j(\omega_r - \delta)t} \tag{B.85}$$

Transforming into the rotor reference frame:

$$\overline{\psi}_r^r = \overline{\psi}_r^s e^{-j(\omega_r t - \theta_{r0})} \tag{B.86}$$

hence

$$A_r^r = \frac{-(\delta + j\kappa)\overline{\psi}_{r0}^r + j(k_s/\tau_r)\overline{\psi}_{s0}^r}{(\omega_r - 2\delta) + j\left(\tau_r^{'-1} - \tau_s^{'-1}\right)} \tag{B.87}$$

and finally:

$$\overline{\psi}_r^r(t) = A_r^r\, e^{-t/\tau_s'} e^{-j(\omega_r-\delta)t} + \left(\overline{\psi}_{r0}^r - A_r^r\right) e^{-t/\tau_r'} e^{-j\delta t} \tag{B.88}$$

Or, redefining roots α,β for the rotor reference frame:

$$\alpha^r = \tau_s'^{-1} + j(\omega_r - \delta), \quad \beta^r = \tau_r'^{-1} + j\delta \tag{B.89, B.90}$$

Hence the natural response of the rotor flux in the rotor reference frame approximates to:

$$\overline{\psi}_r^r(t) = \left(\overline{\psi}_{r0}^r - A_r^r\right) e^{-\beta^r t} + A_r^r\, e^{-\alpha^r t} \tag{B.91}$$

B.1.6 Rotor current natural response

Using the rotor voltage equation in the rotor reference frame (Eq. B.92) and the rotor flux derivation (Eq. B.91), the natural response (or zero rotor voltage response) of the rotor current can then be derived:

$$0 = R_r \bar{i}_r^r + \partial \overline{\psi}_r^r \tag{B.92}$$

$$\bar{i}_r^r(t) = \overbrace{\frac{\beta^r}{R_r}\left(\overline{\psi}_{r0}^r - A_r^r\right) e^{-t/\tau_r'} e^{-j\delta t}}^{\text{Near-DC}} + \overbrace{\frac{\alpha^r}{R_r} A_r^r\, e^{-t/\tau_s'} e^{-j(\omega_r-\delta)t}}^{\text{Near-rotor speed}} \tag{B.93}$$

This shows that the rotor current frequency components will exhibit the same time-dependence as the stator current, although the directions of rotation are reversed with respect to the stator. Explicitly, this involves a near-dc (negative) frequency component decaying with the rotor leakage time-constant and a near-rotor-frequency (negative) component decaying with the stator leakage time-constant.

Neglecting the frequency adjustment parameter and terms of the order τ^{-2} as for the stator:

$$\delta \approx \frac{(1-\sigma)}{\omega_r \tau_r \tau_s} \approx \frac{1}{\tau_x^{\,2}} \approx 0, \tag{›B.72}$$

and noting the transient operational inductance:

$$\tau_r = \frac{L_r'}{R_r} \tag{›B.9}$$

the rotor current therefore approximates to a simpler form:

$$\bar{i}_r^r(t) \approx \frac{1}{L_r'} \overline{\psi}_{r0}^r\, e^{-t/\tau_r'} e^{-j\delta t} - \frac{k_s}{L_r'} \overline{\psi}_{s0}^r\, e^{-t/\tau_s'} e^{-j(\omega_r-\delta)t} \tag{B.94}$$

B.1.7 Torque during a short circuit

As explained in chapter 3, torque can be derived by considering the stator and rotor fields as two magnetic dipoles. The result is proportional to the vector cross product determinant, i.e. the sine of the angle between the current vectors. The p.u. torque is equal to the torque per pole-pair:

$$T = L_m \bar{i}_r \wedge \bar{i}_s \tag{B.95}$$

The full derivation of torque as a function of initial flux linkages is lengthy. A reasonable estimate can be made by using the approximate expressions for rotor and stator current from Eqs. B.74 & B.94. Converting the rotor current approximation into the stator reference frame and noting that the cross product of a vector with itself is zero:

$$\bar{i}_r \wedge \bar{i}_s = \left[\frac{\overline{\psi}^s_{r0}}{L'_r} e^{-t/\tau'_r} e^{j(\omega_r-\delta)t} - \frac{L_m \overline{\psi}^s_{s0}}{L_r L'_s} e^{-t/\tau'_s} e^{j\delta t}\right] \wedge \left[\frac{\overline{\psi}^s_{s0}}{L'_s} e^{-t/\tau'_s} e^{j\delta t} - \frac{L_m \overline{\psi}^s_{r0}}{L_s L'_r} e^{-t/\tau'_r} e^{j(\omega_r-\delta)t}\right] \tag{B.96}$$

$$\bar{i}_r \wedge \bar{i}_s = \left[\frac{-L_m}{L_s L'^2_r} e^{-2t/\tau'_r}\right]\left(\overline{\psi}^s_{r0} \wedge \overline{\psi}^s_{r0}\right) + \left[\frac{-L_m}{L_r L'^2_s} e^{-2t/\tau'_s}\right]\left(\overline{\psi}^s_{s0} \wedge \overline{\psi}^s_{s0}\right) + \ldots$$

$$\ldots + \left[\frac{1}{L'_s L'_r} e^{-(1/\tau'_r + 1/\tau'_s)t}\right]\left[1 - \frac{L_m{}^2}{L_s L_r}\right]\left(\overline{\psi}^s_{r0} e^{j(\omega_r-\delta)t} \wedge \overline{\psi}^s_{s0} e^{j\delta t}\right) \tag{B.97}$$

$$\bar{i}_r \wedge \bar{i}_s = \left[\frac{\sigma}{L'_s L'_r} e^{-(1/\tau'_r + 1/\tau'_s)t}\right]\left(\overline{\psi}^s_{r0} e^{j(\omega_r-2\delta)t} \wedge \overline{\psi}^s_{s0}\right) \tag{B.98}$$

and finally:

$$T = \left[\frac{L_m}{\sigma L_s L_r}\left|\overline{\psi}_{r0}\right|\left|\overline{\psi}_{s0}\right| e^{-t/\tau'_T}\right] \sin\left(-(\omega_r - 2\delta)t - \theta_{\psi_0}\right) \tag{B.99}$$

$$T = \left[\frac{-L_m}{\sigma L_s L_r}\left|\overline{\psi}_{r0}\right|\left|\overline{\psi}_{s0}\right| e^{-t/\tau'_T}\right] \sin\left((\omega_r - 2\delta)t + \theta_{\psi_0}\right) \tag{B.100}$$

where we have defined the initial phase separation of the rotor and stator flux linkages and a torque transient timescale. The initial flux separation angle is:

$$\theta_{\psi_0} = \theta\left(\overline{\psi}^g_{r0}\right) - \theta\left(\overline{\psi}^g_{s0}\right) \tag{B.101}$$

The torque transient timescale is a parallel combination of the stator and rotor timescales indicating a very fast decay of torque:

$$1/\tau'_T = \left(1/\tau'_r + 1/\tau'_s\right) \tag{B.102}$$

Leakage parameter approximation

The leakage inductance values are significantly smaller than the mutual inductance for all practical machines. As such we can approximate the value of the leakage parameter, utilising a unit-less variable for the leakage inductance:

$$L_s = (1 + x_s) L_m \tag{B.103}$$

$$L_s = (1 + x_s) L_m \tag{B.104}$$

$$x_s, x_r << 1 \tag{B.105}$$

Returning to the leakage parameter definition:

$$\sigma = 1 - \frac{L_m^{\ 2}}{L_r L_s} \tag{›B.5}$$

$$\sigma = 1 - (1 + x_s)^{-1} (1 + x_r)^{-1} \tag{B.106}$$

Using a Taylor series expansion:

$$\sigma \approx 1 - (1 - x_s - x_r) \tag{B.107}$$

$$\sigma \approx x_s + x_r = \frac{L_{es} + L_{er}}{L_m} \tag{B.108}$$

Torque approximation

Chapter 5 introduced an approximation for the torque expression using the leakage parameter approximation from Eq. B.108 and by estimating the pre-fault flux magnitude product at 1.1 p.u. This approximation is reproduced in Eq. B.109.

$$T \approx \left[\frac{-1.1}{L_{es} + L_{er}} e^{-t/\tau_T'} \right] \sin\left((\omega_r - 2\delta) t + \theta_{\psi_0} \right) \tag{B.109}$$

The quality of the approximation is shown in Figure B.1, including an example of the calculated fault response torque for the (zero rotor voltage) DFIG test rig using the test rig parameters listed in Section B.2.1. The formal derivation from Eq. B.95 is shown solid and the torque approximation from Eq. B.109 is shown dashed.

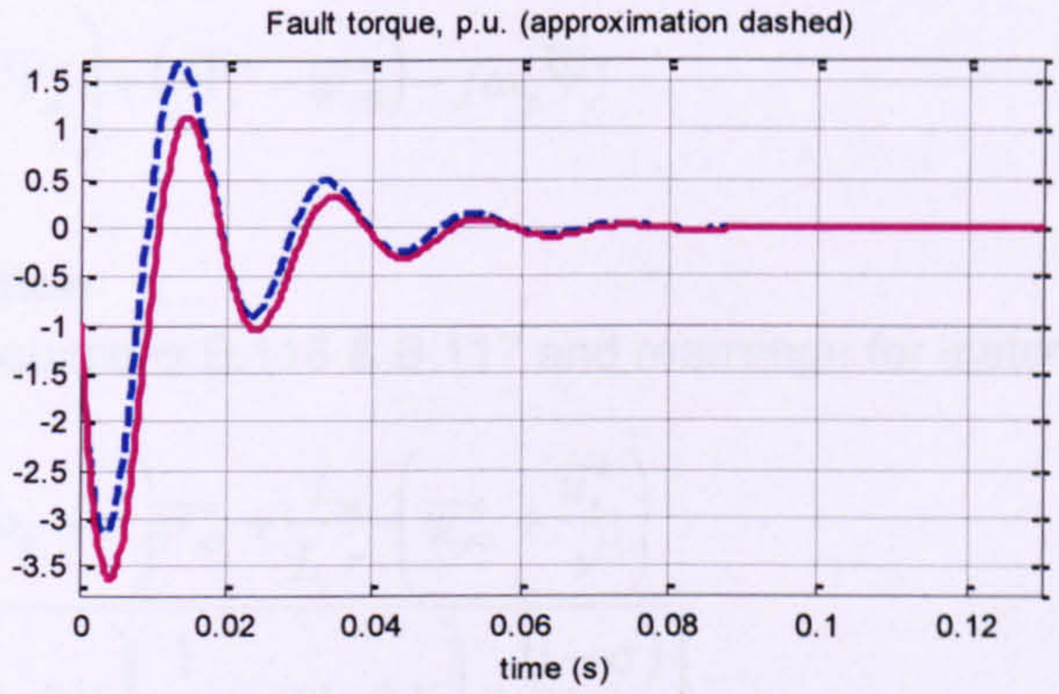

Figure B.1. DFIG test rig fault response torque and torque approximation.

B.1.8 Forced response – non-zero rotor voltage

Here the doubly-fed induction machine is fed with a slip-speed rotating voltage to maintain stable operation in the steady-state. In the excitation reference frame, the rotor voltage vector will appear constant. A Laplace transform solution can be derived, similar to the natural response above, this time starting in the excitation reference frame:

$$\bar{u}_s^e = R_s \bar{i}_s^e + \partial \bar{\psi}_s^e + j\omega_e \bar{\psi}_s^e \tag{B.110}$$

$$\bar{u}_r^e = R_r \bar{i}_r^e + \partial \bar{\psi}_r^e - j\omega_\chi \bar{\psi}_r^e \tag{B.111}$$

Eq. B.111 includes the excitation-frame relative rotor speed, ω_χ (the exact negative of slip-speed). The sign of ω_χ is chosen such that the value is normally positive for a generator.

$$\omega_\chi = \omega_r - \omega_e \tag{B.112}$$

Substituting for current using the inductance definitions B.3 & B.4 and using the transient time constant definitions:

$$\bar{u}_s^e = \frac{1}{\tau_s}\left(\bar{\psi}_s^e - \frac{L_m}{L_r}\bar{\psi}_r^e\right) + \partial \bar{\psi}_s^e + j\omega_e \bar{\psi}_s^e \tag{B.113}$$

$$\bar{u}_r^e = \frac{1}{\tau_r}\left(\bar{\psi}_r^e - \frac{L_m}{L_s}\bar{\psi}_s^e\right) + \partial \bar{\psi}_r^e - j\omega_\chi \bar{\psi}_r^e \tag{B.114}$$

Now, setting the excitation-frame rotor voltage to be constant, and taking Laplace transforms of Eqs. B.10 & B.11:

$$\Gamma\left\{\bar{u}_r^e = const.\right\} = \frac{\bar{u}_r^e}{\nu} \tag{B.115}$$

$$0 = \frac{1}{\tau_s}\left(\bar{\Psi}_s^e - \frac{L_m}{L_r}\bar{\Psi}_r^e\right) + \left(\nu\bar{\Psi}_s^e - \bar{\psi}_{s0}^e\right) + j\omega_e \bar{\Psi}_s^e \tag{B.116}$$

$$\frac{\overline{u}_r^e}{\nu} = \frac{1}{\tau_r}\left(\overline{\Psi}_r^e - \frac{L_m}{L_s}\overline{\Psi}_s^e\right) + \left(\nu\overline{\Psi}_r^e - \overline{\psi}_{r0}^e\right) - j\omega_\chi\overline{\Psi}_r^e \tag{B.117}$$

Stator circuit solution

Take the Laplace equations B.116 & B.117 and rearrange for stator flux:

$$\overline{\Psi}_s^e(\nu) = \frac{\left(\frac{1}{\tau_r} - j\omega_\chi + \nu\right)\overline{\psi}_{s0}^e + \frac{L_m}{L_r\tau_s}\left(\overline{\psi}_{r0}^e + \frac{\overline{u}_r^e}{\nu}\right)}{\left[\left(\frac{1}{\tau_s} + j\omega_e + \nu\right)\left(\frac{1}{\tau_r} - j\omega_\chi + \nu\right) - \frac{(1-\sigma)}{\tau_s\tau_r}\right]} \tag{B.118}$$

This form can be simplified, using certain constants as introduced in Section B.1.2 and defining the complex roots in the excitation frame:

$$\rho_s^e = \frac{1}{\tau_s} + j\omega_e, \quad \rho_r^e = \frac{1}{\tau_r} - j\omega_\chi \tag{B.119, B.120}$$

$$k_r' = \frac{L_m}{L_r\tau_s} \tag{B.121}$$

$$\overline{\Psi}_s^e(\nu) = \frac{(\rho_r^e + \nu)\overline{\psi}_{s0}^e + k_r'\left(\overline{\psi}_{r0}^e + \overline{u}_r^e/\nu\right)}{\left[(\rho_s^e + \nu)(\rho_r^e + \nu) - k_\sigma\right]} \tag{B.122}$$

The denominator of Eq. B.122 lends itself to the 'natural response roots' and 'complex frequency adjustment' of Section B.1.3. The roots are here in the excitation-frame, rotated by $\omega_e t$ radians with respect to the stator-frame roots of Section B.1.3. The complex frequency adjustment has exactly the same form.

$$(\rho_s^e + \nu)(\rho_r^e + \nu) - k_\sigma = (\alpha^e + \nu)(\beta^e + \nu) \tag{B.123}$$

where:

$$\alpha^e = \left(\tau_s^{-1} - \kappa\right) + j(\omega_e - \delta), \qquad \beta^e = \left(\tau_r^{-1} + \kappa\right) - j(\omega_\chi - \delta) \tag{B.124, B.125}$$

and

$$\varsigma_f = \frac{(1-\sigma)/\tau_s\tau_r}{(1/\tau_r - 1/\tau_s - j\omega_r)} = \kappa + j\delta, \qquad (\kappa, \delta) \in \mathrm{Re} \tag{B.126}$$

Hence:

$$\overline{\Psi}_s^e(\nu) = \frac{(\rho_r^e + \nu)\overline{\psi}_{s0}^e\nu + k_r'\left(\overline{\psi}_{r0}^e\nu + \overline{u}_r^e\right)}{(\alpha^e + \nu)(\beta^e + \nu)\nu} \tag{B.127}$$

Eq. B.127 can be solved by partial fractions:

$$\overline{\Psi}_s^e(\nu)=\frac{(\rho_r^e+\nu)\overline{\psi}_{s0}^e\nu+k_r'(\overline{\psi}_{r0}^e\nu+\overline{u}_r^e)}{(\alpha^e+\nu)(\beta^e+\nu)\nu}=\frac{A_1^e}{(\alpha^e+\nu)}+\frac{B_1^e}{(\beta^e+\nu)}+\frac{C_1^e}{\nu} \tag{B.128}$$

resulting in:

$$A_1^e=\left(1-\frac{\varsigma_f}{(\beta^e-\alpha^e)}\right)\overline{\psi}_{s0}^e+\frac{k_r'}{(\beta^e-\alpha^e)}\left(\overline{\psi}_{r0}^e-\frac{\overline{u}_r^e}{\alpha^e}\right), \tag{B.129}$$

$$B_1^e=\frac{\varsigma_f}{(\beta^e-\alpha^e)}\overline{\psi}_{s0}^e-\frac{k_r'}{(\beta^e-\alpha^e)}\left(\overline{\psi}_{r0}^e-\frac{\overline{u}_r^e}{\beta^e}\right), \tag{B.130}$$

$$C_1^e=\frac{k_r'}{\alpha^e\beta^e}\overline{u}_r^e \tag{B.131}$$

The coefficients of Eqs. B.129 - B.131 provide the coefficients of the stator flux linkage solution:

$$\overline{\psi}_s^e(t)=A_1^e e^{-\alpha^e t}+B_1^e e^{-\beta^e t}+\frac{k_r'}{\alpha^e\beta^e}\overline{u}_r^e \tag{B.132}$$

In the stator reference frame, this becomes:

$$\overline{\psi}_s^s(t)=A_1^s e^{-\alpha t}+B_1^s e^{-\beta t}+\frac{k_r'}{\alpha^e\beta^e}\overline{u}_r^e e^{+j(\omega_e t+\theta_{e0})} \tag{B.133}$$

with,

$$A_1^s=\left(1-\frac{\varsigma_f}{(\beta^e-\alpha^e)}\right)\overline{\psi}_{s0}^s+\frac{k_r'}{(\beta^e-\alpha^e)}\left(\overline{\psi}_{r0}^s-\frac{\overline{u}_r^e e^{+j\theta_{e0}}}{\alpha^e}\right), \tag{B.134}$$

$$B_1^s=\frac{\varsigma_f}{(\beta^e-\alpha^e)}\overline{\psi}_{s0}^s-\frac{k_r'}{(\beta^e-\alpha^e)}\left(\overline{\psi}_{r0}^s-\frac{\overline{u}_r^e e^{+j\theta_{e0}}}{\beta^e}\right), \tag{B.135}$$

or, more explicitly:

$$\overline{\psi}_s^s(t)=A_1^s e^{-t/\tau_s'}e^{+j\delta t}+B_1^s e^{-t/\tau_r'}e^{+j(\omega_r-\delta)t}+\frac{L_m}{L_r\tau_s\alpha^e\beta^e}\overline{u}_r^s \tag{B.136}$$

with:

$$\overline{u}_r^s=\overline{u}_r^e e^{+j(\omega_e t+\theta_{e0})}, \tag{B.137}$$

The expression for stator flux linkage therefore contains two decay components (at near-dc and near-rotor speed) and a continuous term driven by the rotor excitation. The two decay components have the same roots and are similar in magnitude to those of the natural response solution. Using the stator voltage equation, we can derive the stator current:

$$\bar{i}_s^s = \frac{-1}{R_s}\partial\bar{\psi}_s^s \tag{B.138}$$

$$\bar{i}_s^s(t) = \frac{\alpha A_1^s}{R_s}e^{-t/\tau_s'}e^{+j\delta} + \frac{\beta B_1^s}{R_s}e^{-t/\tau_r'}e^{+j(\omega_r-\delta)t} - \frac{j\omega_e L_m}{\sigma L_s L_r \alpha^e \beta^e}\bar{u}_r^s \tag{B.139}$$

Making approximations as per Section B.1.4, neglecting terms of the order τ^{-2} and approximating the product of the natural response roots (Eq. B.140) we can produce a simpler form of the stator current solution (Eq. B.145).

$$\alpha^e\beta^e \approx j\omega_e\beta^e \tag{B.140}$$

$$A_1^s \approx \bar{\psi}_{s0}^s \tag{B.141}$$

$$\ldots \frac{\alpha A_1^s}{R_s} \approx \frac{\bar{\psi}_{s0}^s}{\tau_s' R_s} = \frac{\bar{\psi}_{s0}^s}{\sigma L_s} \tag{B.142}$$

$$B_1^s \approx \frac{-jk_r}{\tau_s\omega_r}\left(\bar{\psi}_{r0}^s - \frac{\bar{u}_r^e e^{+j\theta_{e0}}}{\beta^e}\right) \tag{B.143}$$

$$\ldots \frac{\beta B_1^s}{R_s} \approx \frac{-j\omega_r(-jk_r)}{R_s\tau_s\omega_r}\left(\bar{\psi}_{r0}^s - \frac{\bar{u}_r^e e^{+j\theta_{e0}}}{\beta^e}\right) = \frac{-k_r}{\sigma L_s}\left(\bar{\psi}_{r0}^s - \frac{\bar{u}_r^e e^{+j\theta_{e0}}}{\beta^e}\right) \tag{B.144}$$

Hence:

$$\bar{i}_s^s(t) \approx \frac{1}{\sigma L_s}\left(\bar{\psi}_{s0}^s e^{-t/\tau_s'}e^{+j\delta} - \frac{L_m}{L_r}\left(\bar{\psi}_{r0}^s - \frac{\bar{u}_r^e e^{+j\theta_{e0}}}{\beta^e}\right)e^{-t/\tau_r'}e^{+j(\omega_r-\delta)t} - \frac{L_m}{L_r}\frac{\bar{u}_r^s}{\beta^e}\right) \tag{B.145}$$

Rotor circuit solution

In the same manner as above, we take Laplace transforms of voltage equations in the excitation frame (B.113 & B.114) with constant rotor voltage. The resulting Laplace equations (Eqs. B.116 & B.117) are rearranged for rotor flux linkage, using the following derived parameters:

$$\rho_s^e = \frac{1}{\tau_s} + j\omega_e, \quad \rho_r^e = \frac{1}{\tau_r} - j\omega_\chi \tag{›B.119, ›B.120}$$

$$k_s' = \frac{L_m}{L_s\tau_r} \tag{B.146}$$

$$\bar{\Psi}_r^e(\nu) = \frac{(\rho_s^e+\nu)(\bar{\psi}_{r0}^e + \bar{u}_r^e/\nu) + k_s'\bar{\psi}_{s0}^e}{\left[(\rho_s^e+\nu)(\rho_r^e+\nu) - k_\sigma\right]} \tag{B.147}$$

This rotor flux linkage expression can be solved with partial fractions, using the natural response roots and complex frequency adjustment exactly as shown for the stator circuit (Eqs. B.123 - B.126):

$$\overline{\Psi}_r^e(\nu)=\frac{(\rho_s^e+\nu)(\overline{\psi}_{r0}^e+\overline{u}_r^e/\nu)+k_s'\overline{\psi}_{s0}^e}{(\alpha^e+\nu)(\beta^e+\nu)\nu}=\frac{A_2^e}{(\alpha^e+\nu)}+\frac{B_2^e}{(\beta^e+\nu)}+\frac{C_2^e}{\nu} \tag{B.148}$$

resulting in:

$$A_2^e=\frac{\varsigma_f}{(\beta^e-\alpha^e)}\left(\overline{\psi}_{r0}^e-\frac{\overline{u}_r^e}{\alpha^e}\right)+\frac{k_s'}{(\beta^e-\alpha^e)}\overline{\psi}_{s0}^e \tag{B.149}$$

$$B_2^e=\left(1-\frac{\varsigma_f}{(\beta^e-\alpha^e)}\right)\left(\overline{\psi}_{r0}^e-\frac{\overline{u}_r^e}{\beta^e}\right)-\frac{k_s'}{(\beta^e-\alpha^e)}\overline{\psi}_{s0}^e \tag{B.150}$$

$$C_2^e=\frac{\rho_s^e}{\alpha^e\beta^e}\overline{u}_r^e \tag{B.151}$$

The coefficients of Eqs. B.149 - B.151 provide the coefficients of the rotor flux linkage solution:

$$\overline{\psi}_r^e(t)=A_2^e e^{-\alpha^e t}+B_2^e e^{-\beta^e t}+\frac{\rho_s^e}{\alpha^e\beta^e}\overline{u}_r^e \tag{B.152}$$

In the rotor reference frame, this becomes:

$$\overline{\psi}_r^r(t)=A_2^r e^{-\alpha^r t}+B_2^r e^{-\beta^r t}+\frac{\rho_s^e}{\alpha^e\beta^e}\overline{u}_r^e e^{-j(\omega_x t+\theta_{x0})} \tag{B.153}$$

where

$$\alpha^r=\frac{1}{\tau_s'}+j(\omega_r-\delta),\quad \beta^r=\frac{1}{\tau_r'}+j\delta \tag{›B.89, ›B.90}$$

and

$$A_2^r=\frac{\varsigma_f}{(\beta^e-\alpha^e)}\left(\overline{\psi}_{r0}^r-\frac{\overline{u}_r^e e^{-j\theta_{x0}}}{\alpha^e}\right)+\frac{k_s'}{(\beta^e-\alpha^e)}\overline{\psi}_{s0}^r \tag{B.154}$$

$$B_2^r=\left(1-\frac{\varsigma_f}{(\beta^e-\alpha^e)}\right)\left(\overline{\psi}_{r0}^r-\frac{\overline{u}_r^e e^{-j\theta_{x0}}}{\beta^e}\right)-\frac{k_s'}{(\beta^e-\alpha^e)}\overline{\psi}_{s0}^r \tag{B.155}$$

or explicitly:

$$\overline{\psi}_r^r(t)=B_2^r e^{-t/\tau_r'}e^{-j\delta t}+A_2^r e^{-t/\tau_s'}e^{-j(\omega_r-\delta)t}+\frac{\left(\tau_s^{-1}+j\omega_e\right)}{\alpha^e\beta^e}\overline{u}_r^r \tag{B.156}$$

with:

$$\bar{u}_r^r = \bar{u}_r^e e^{-j(\omega_\chi t + \theta_{\chi 0})}, \tag{B.157}$$

The expression for rotor flux linkage, just as for the stator, contains two decay components (at near-dc and near-rotor speed) and a continuous term driven by the rotor excitation. The two decay components have the same roots and are similar in magnitude to those of the natural response solution. Using the rotor voltage equation, we can derive the rotor current:

$$\bar{i}_r^r = \frac{1}{R_r}\left(\bar{u}_r^r - \partial\bar{\psi}_r^r\right) \tag{B.158}$$

$$\bar{i}_r^r(t) = \frac{\beta^r B_2^r}{R_r} e^{-t/\tau_r'} e^{-j\delta} + \frac{\alpha^r A_2^r}{R_r} e^{-t/\tau_r'} e^{-j(\omega_r - \delta)t} + \frac{1}{R_r}\left(1 + \frac{j\omega_\chi \rho_s^e}{\alpha^e \beta^e}\right)\bar{u}_r^r \tag{B.159}$$

Making approximations as per Section B.1.4, neglecting terms of the order τ^{-2}, we can produce a simpler form of the rotor current solution (Eq. B.165).

$$\frac{1}{R_r}\left(1 + \frac{j\omega_\chi \rho_s^e}{\alpha^e \beta^e}\right) = \frac{1}{R_r}\left(\frac{\alpha^e \beta^e + \left(\tau_r^{-1} + \varsigma_f - \beta^e\right)\left(\alpha^e + \varsigma_f\right)}{\alpha^e \beta^e}\right) \approx \frac{1}{R_r}\left(\frac{\tau_r^{-1}\alpha^e}{\alpha^e \beta^e}\right) = \frac{1}{\sigma L_r \beta^e} \tag{B.160}$$

$$A_2^r \approx \frac{jk_s}{\tau_r \omega_r}\bar{\psi}_{s0}^r \tag{B.161}$$

$$\therefore \frac{\alpha^r A_2^r}{R_r} \approx \frac{+j\omega_r (jk_s)}{R_r \tau_r \omega_r}\bar{\psi}_{s0}^r = \frac{-k_s}{\sigma L_r}\bar{\psi}_{s0}^r \tag{B.162}$$

$$B_2^r \approx \left(\bar{\psi}_{r0}^r - \frac{\bar{u}_r^e e^{-j\theta_{\chi 0}}}{\beta^e}\right) \tag{B.163}$$

$$\therefore \frac{\beta^r B_2^r}{R_r} \approx \frac{1}{\tau_r R_r}\left(\bar{\psi}_{r0}^r - \frac{\bar{u}_r^e e^{-j\theta_{\chi 0}}}{\beta^e}\right) = \frac{1}{\sigma L_r}\left(\bar{\psi}_{r0}^r - \frac{\bar{u}_r^e e^{-j\theta_{\chi 0}}}{\beta^e}\right) \tag{B.164}$$

Hence:

$$\bar{i}_r^r(t) \approx \frac{1}{\sigma L_r}\left(\left(\bar{\psi}_{r0}^r - \frac{\bar{u}_r^e e^{-j\theta_{\chi 0}}}{\beta^e}\right) e^{-t/\tau_r'} e^{-j\delta} - \frac{L_m}{L_s}\bar{\psi}_{s0}^s e^{-t/\tau_r'} e^{-j(\omega_r - \delta)t} + \frac{\bar{u}_r^r}{\beta^e}\right) \tag{B.165}$$

B.2 Numeric solutions using DFIG test rig model

B.2.1 Test rig parameters

For validation of the analytical solutions, the expressions were enumerated using measured parameters and compared with test results presented in Chapter 5. The

calculations were performed in Matlab and results reproduced below. The parameters were measured from the DFIG test rig and listed below:

```
% test rig p.u. data.
Rs = 0.030;
Rr = 0.020;
Xes = 0.124;
Xer = 0.124;
Xm = 3.1;
Xs = Xes+Xm;
Xr = Xer+Xm;
```

Transient time-constants are derived: approximately 26ms on the rotor and 39ms on the stator:

```
% time constants /s
t_s = 0.0258
t_r = 0.0387
```

B.2.2 Initial phase

At the instant of fault initiation, rotor and stator frames each hold an arbitrary initial phase difference with respect to the excitation frame, defined by Eqs. B.166 & B.167. The solution can be found by setting the phase to zero, solving the analytical solutions and adding the relative initial phase to the respective solutions.

$$\theta_e(t=0)=\theta_{e0} \tag{B.166}$$

$$\theta_r(t=0)=\theta_{r0} \tag{B.167}$$

A slip angle is defined, separating the rotor and excitation frame at the instant of fault initiation:

$$\theta_\varsigma=\theta_e-\theta_r \tag{B.168}$$

The pre-fault space vectors can be determined in each frame by rotation of the excitation frame steady-state values, accounting for the initial phase separation. For example:

$$\overline{\psi}_s^s(t=0)=\overline{\psi}_{s\,(steady\text{-}state)}^e e^{+j\theta_{e0}} \tag{B.169}$$

$$\overline{\psi}_r^r(t=0)=\overline{\psi}_{r\,(steady\text{-}state)}^e e^{+j\theta_{\varsigma 0}} \tag{B.170}$$

These example rotations are repeated for the other flux linkages and currents, as appropriate.

B.2.3 SFIG test

Initial Conditions

The first example is of a singly-fed generator, illustrating the natural machine response with zero rotor voltage. Initial steady-state conditions are used: 1.0 p.u. stator voltage and 0.93 p.u. power generation to match the 7kW experimental test, this sets the d-component of stator current at -0.93 p.u.

```
%initial conditions - excitation frame
vs = 1;
isd0 = -0.93;
```

The machine equations can be solved for the steady-state case, in this case all time derivatives are set to zero. Solving Eqs. B.3-B.4 & B.110-B.111 (excitation-frame per-unit machine equations) for slip, s, (noting that $\omega_1 = 1$ p.u.):

$$\left(\left\{(\sigma L_s L_r)^2 + (R_s L_r)^2\right\} i^e_{sd0} - R_s L_r{}^2 u_{s0}\right)s^2 + (1-\sigma)R_r L_s L_r\left(2R_s i^e_{sd0} - u_{s0}\right)s...$$

$$...+\left(R_r{}^2 R_s\left(R_s i^e_{sd0} - u_{s0}\right) + (R_r L_s)^2 i^e_{sd0}\right) = 0 \qquad \text{(B.171)}$$

This quadratic function of slip will give two solutions – as can be deduced from the characteristic hump of an induction machine torque-slip curve. The smallest absolute slip is chosen as this value coincides with normal (stable) operation. Using this initial slip value, the other circuit parameters follow:

$$\bar{i}^e_{s0} = \frac{(R_r + jsL_r)u_{s0}}{(R_s R_r - s\sigma L_s L_r) + j(R_r L_s + sR_s L_r)} \qquad \text{(B.172)}$$

$$\overline{\psi}^e_{s0} = -j\left(u_{s0} - R_s \bar{i}^e_{s0}\right) \qquad \text{(B.173)}$$

$$\bar{i}^e_{r0} = \frac{1}{L_m}\left(\overline{\psi}^e_{s0} - L_s \bar{i}^e_{s0}\right) \qquad \text{(B.174)}$$

$$\overline{\psi}^e_{r0} = L_r \bar{i}^e_{r0} + L_m \bar{i}^e_{s0} \qquad \text{(B.175)}$$

The real component of Eq. B.172 is used to verify the initial power conditions before the other parameters are derived.

SFIG response solution

The complex frequency adjustment (Eq. B.39) is almost entirely imaginary: timescale adjustment constant $\kappa < 10^{-3}$ and frequency adjustment constant $\delta \sim 1\%$:

```
kappa = -0.0004
delta =  0.0092
```

Referring to the stator flux natural response Eq. B.56, the effective time constants remain at approximately 26ms and 39ms whilst the effective decay frequencies are calculated at 0.46Hz and 55.59Hz.

```
%adjusted frequencies /Hz
f_own =  0.46
f_mut = 50.59
%adjusted timescales /s
t_s2 = 0.0257
t_r2 = 0.0389
```

The flux magnitude coefficients A_s and A_r (Eqs. B.64, B.82) were calculated and used to evaluate the flux and current coefficients in Eqs. B.68, B.70, B.88 & B.93. Hence, reproducing the individual frequency coefficients in polar form:

$$\bar{\psi}_s^s(t) = 1.01\angle\{\theta_{e0} - 83^\circ\}e^{-t/\tau_s} @0.46Hz + 0.11\angle\{\theta_{e0} - 167^\circ\}e^{-t/\tau_r} @55.59Hz \quad \text{(B.176)}$$

$$\bar{i}_s^s(t) = 4.06\angle\{\theta_{e0} - 87^\circ\}e^{-t/\tau_s} @0.46Hz + 3.77\angle\{\theta_{e0} + 107^\circ\}e^{-t/\tau_r} @55.59Hz \quad \text{(B.177)}$$

$$\bar{\psi}_r^r(t) = 0.97\angle\{\theta_{\varsigma 0} - 80^\circ\}e^{-t/\tau_r} @(-0.46Hz) + 0.08\angle\{\theta_{\varsigma 0} + 9^\circ\}e^{-t/\tau_s} @(-55.59Hz) \quad \text{(B.178)}$$

$$\bar{i}_r^r(t) = 3.87\angle\{\theta_{\varsigma 0} - 73^\circ\}e^{-t/\tau_r} @(-0.46Hz) + 3.96\angle\{\theta_{\varsigma 0} + 92^\circ\}e^{-t/\tau_s} @(-55.59Hz) \quad \text{(B.179)}$$

These results are illustrated in Chapter 5.

B.2.4 DFIG crowbar test

DFIG parameters

The DFIG test rig parameters are listed in Section B.2.1.

Initial Conditions

With the DFIG, initial steady-state conditions are somewhat different. Before the fault the DFIG is controlled to unity power factor and the stator current can be specified directly. The pre-fault speed is set at 0.99 p.u. to match the experimental data.

```
%initial conditions /p.u.
wr = 0.9897;
%initial conditions - excitation frame /p.u.
vs = 1;
is0 = -0.93;
vr0 = 0;
```

Rotor current and flux linkages are derived using the excitation frame machine equations in the steady-state, i.e. with time derivatives set to zero, as for the previous SFIG solution.

$$\bar{u}_s^e = R_s\bar{i}_s^e + \partial\bar{\psi}_s^e + j\omega_1\bar{\psi}_s^e = 1 \quad \text{(B.180)}$$

$$\bar{\psi}_{s0}^e = -j\left(u_{s0}^e - R_s\bar{i}_{s0}^e\right) \quad \text{(›B.173)}$$

$$\bar{i}_{r0}^{e} = \frac{1}{L_m}\left(\bar{\psi}_{s0}^{e} - L_s \bar{i}_{s0}^{e}\right) \quad (\text{B.174})$$

$$\bar{\psi}_{r0}^{e} = L_r \bar{i}_{r0}^{e} + L_m \bar{i}_{s0}^{e} \quad (\text{B.175})$$

Rotor circuit crowbar

At the instant of fault occurrence, a crowbar circuit is assumed to engage instantaneously. This fixes the modelled rotor circuit to zero rotor volts with an increased rotor resistance.

```
% effective crowbar circuit rotor resistance /p.u.
Rcb= 0.057;
Rr = Rr + Rcb;
vr0 = 0;
```

The resulting rotor-circuit transient time constant is reduced to 10ms.

```
% crowbarred DFIG time constants /s
t_s = 0.0258
t_r = 0.0101
```

DFIG crowbar response solution

The complex frequency adjustment (Eq. B.39) is far larger with the crowbar when compared with the SFIG case. The timescale adjustment remains relatively small but the frequency adjustment constant is over 3.5%:

```
kappa = +0.0069
delta =  0.0351
```

The flux and current coefficients in Eqs. B.68, B.70, B.88 & B.93 were calculated and reproduced in the solutions below in polar form:

$$\bar{\psi}_s^s(t) = 1.07\angle\{\theta_{e0} - 82^\circ\}e^{-t/\tau_s} @1.76Hz + 0.15\angle\{\theta_{e0} - 172^\circ\}e^{-t/\tau_r} @47.84Hz \quad (\text{B.181})$$

$$\bar{i}_s^s(t) = 4.36\angle\{\theta_{e0} - 96^\circ\}e^{-t/\tau_s} @1.76Hz + 4.37\angle\{\theta_{e0} + 97^\circ\}e^{-t/\tau_r} @47.84Hz \quad (\text{B.182})$$

$$\bar{\psi}_r^r(t) = 1.06\angle\{\theta_{\varsigma 0} - 92^\circ\}e^{-t/\tau_r} @(-1.76Hz) + 0.27\angle\{\theta_{\varsigma 0} + 1^\circ\}e^{-t/\tau_s} @(-47.84Hz) \quad (\text{B.183})$$

$$\bar{i}_r^r(t) = 4.45\angle\{\theta_{\varsigma 0} - 85^\circ\}e^{-t/\tau_r} @(-1.76Hz) + 4.26\angle\{\theta_{\varsigma 0} + 83^\circ\}e^{-t/\tau_s} @(-47.84Hz) \quad (\text{B.184})$$

These results are illustrated in Chapter 5..

VOLTAGE SOURCE CONVERTER CONTROL

C

C.1 Vector control

The reader is assumed to be familiar with PI control and space-vector control schemes, both of which are well-covered by a variety of undergraduate texts. Differences in nomenclature exist as well as differences in approach and functionality. In the interests of clarity an introduction to certain elementary control concepts is given below. This section provides the building blocks for the DFIG control techniques described in the body of this work.

C.1.1 Current control with a voltage source converter

Voltage-source converter circuit

In general, a voltage source converter (VSC) works against a supply voltage or emf to control its output current. This concept is illustrated in Figure C.1. An alternating voltage signal is produced at the three-phase terminals by PWM switching techniques. The fundamental ac voltage output produced nearly matches the measured supply voltage. The difference between these two voltage sources determines the flow of current through the interposing filter impedance.

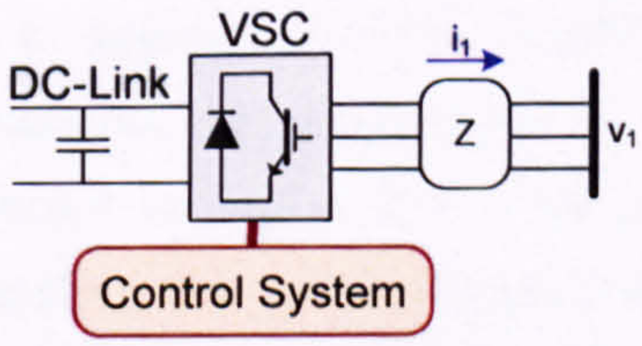

Figure C.1. Voltage-source converter connections.

Defining the VSC output by its fundamental ac component, v_{conv}, the current is determined by the voltage difference across the impedance:

$$\bar{i}_1 = \frac{\bar{v}_{conv} - \bar{v}_1}{Z} \tag{C.1}$$

The current is controlled via a PI controller using current feedback. If either component of vector current is too small, the error between desired and measured current grows. This error signal is fed through the PI controller and the appropriate modulation index component builds up until the current error is negated.

Control scheme

In the excitation frame, here aligned with the supply voltage, the currents appear pseudo-dc and the required voltage can be produced by a PI controller. The basic control law is given in Eq. C.2., with reference to the fundamental circuit equation of Eq. C.1.

$$\bar{v}_{conv}^{e\ \otimes} = PI\left(\bar{i}_1^{e\otimes} - \bar{i}_1^{e}\right) \tag{C.2}$$

In order to implement the PI controller the measured current must be transformed into its space vector form and rotated into the excitation frame. The output of the PI controller meanwhile must be re-converted from a d-q excitation-frame vector to a stationary-frame 3-phase output before the signals are sent to the 3-phase converter. A schematic of such a vector control scheme is shown in Figure C.2.

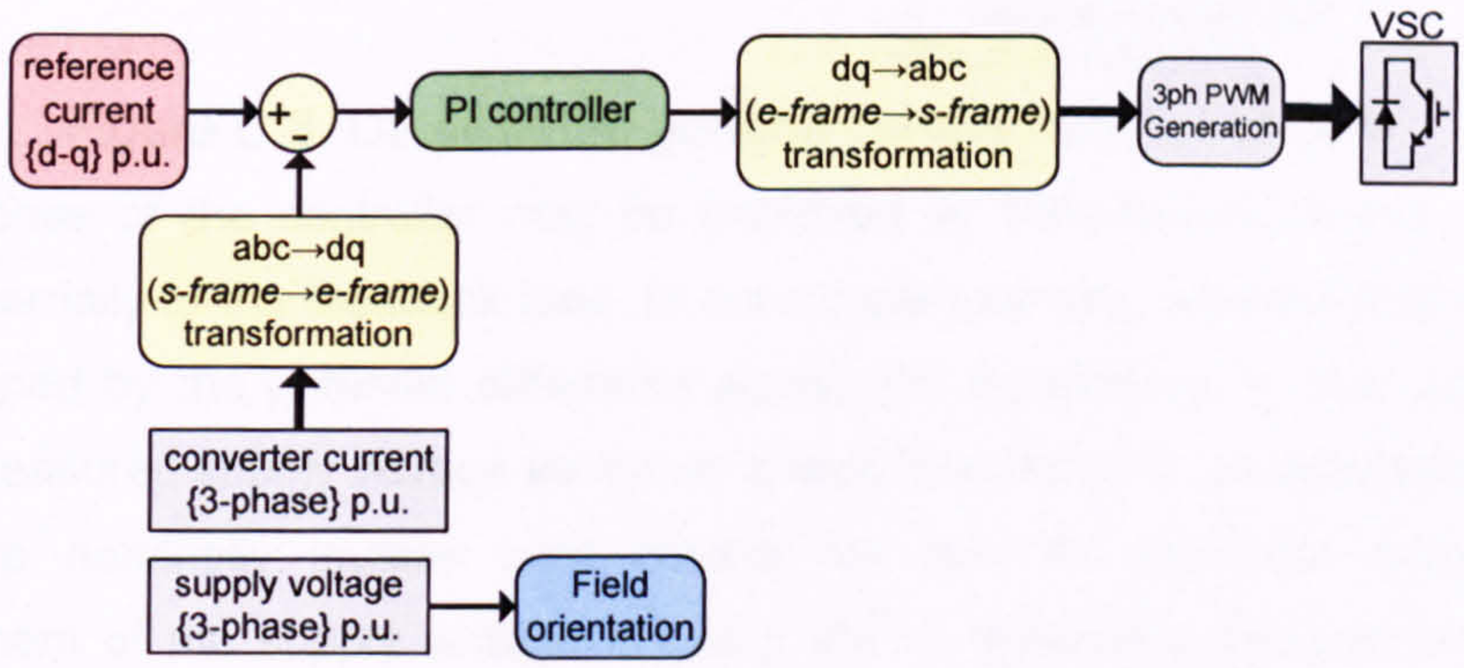

Figure C.2. General current control scheme.

The reference frame transformations are implemented by two separate processes: a stationary three-phase to two-phase matrix transformation and a vector-rotation transformation, as explained in Appendix A. The excitation frame angle is determined by applying a PLL to the measured supply voltages. A more detailed version of the same vector controller is shown in Figure C.3. The rotational transformations are represented by an 'e^{θ}' operator. The proportional-integral controller is expanded, revealing saturation features to prevent either integral windup or an out-of-limits voltage demand.

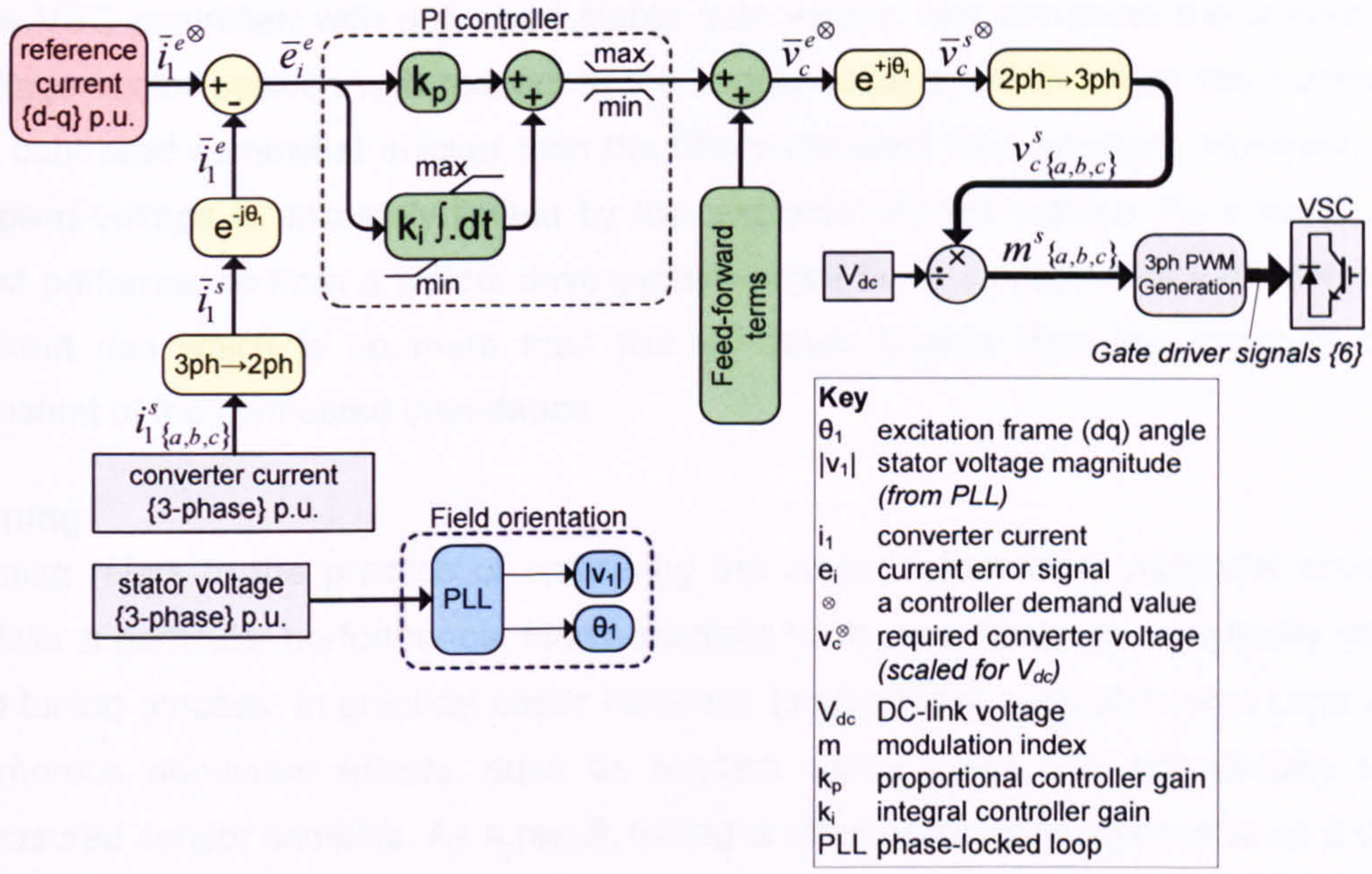

Figure C.3. Detail of the general current control scheme.

The response of the controller may be improved by feed-forward terms, which are added externally to the feedback loop. In our simple example, we note that the current is determined by the potential *difference* across the impedance. In this case we can add the measured supply voltage vector as a feed-forward term, as detailed in Eq. C.3. This setup nominally implies zero current for zero PI controller output. If the measurement of the supply voltage is good, the PI controllers perform less work in establishing a steady-state operating condition, and the overall controller can respond better to sudden changes in supply voltage.

$$\bar{v}_{conv}^{e\,\otimes} = PI\left(\bar{i}_1^{e\otimes} - \bar{i}_1^{e}\right) + \bar{v}_1^{e} \tag{C.3}$$

The p.u. voltage demand can be scaled directly using appropriate gain values to produce modulation index demand values. Further, the modulation index output can compensate for any DC-link voltage deviation by including a reciprocal DC-link voltage gain in series with the output.

Speed of controlled current response

The PWM voltage can be changed instant by instant via the fast-acting transistor switches in response to controller demands. The time delay from measurement to controller reaction to the update of PWM gate signals takes no more than 1-3 control cycles, a fraction of a millisecond. Assuming that the PWM frequency is sufficiently high, normally greater than a few kHz, then the rate of change of current is more likely to be limited by the dynamics of the interposing impedance. The transient time constant of a doubly-fed induction machine's rotor circuit, for example, is of the order of tens of milliseconds.

The VSC controller, with optimised stable gain values, can maximise the converter's voltage vector position with respect to the supply voltage, which allows the current to be controlled somewhat quicker than the filter's transient time constant. However, the applied voltage is ultimately limited by the available DC-link voltage. As a result, the best performance from a typical drive system might be to achieve a rate of controlled current rise which is no more than five-ten times shorter than the transient time constant of the connected impedance.

Tuning

Tuning refers to the practice of optimising the control gains for a particular drive to deliver a particular performance. Many attempts have been made to analytically refine the tuning process. In practical cases however, the feedback controller must cope with numerous non-linear effects, such as random signal noise and occasionally mis-measured sensor samples. As a result, tuning is often colloquially referred to as a dark and mysterious art.

C.1.2 Power control

Cascaded control

With an idealised fast-acting current controller, it is possible to view the VSC as a current source. With this picture we can set the current demand from the VSC to control the power flow from the converter, using the apparent power equation:

$$S_1 = \bar{v}_1 \bar{i}_1^* \tag{C.4}$$

Hence, in an excitation frame aligned with the supply voltage:

$$P_1 = v_{1d}^e i_{1d}^e \tag{C.5}$$

$$Q_1 = -v_{1d}^e i_{1q}^e \tag{C.6}$$

In general, the power output is a direct function of the converter current, and we can use a power feedback error controller to determine the precise current demand.

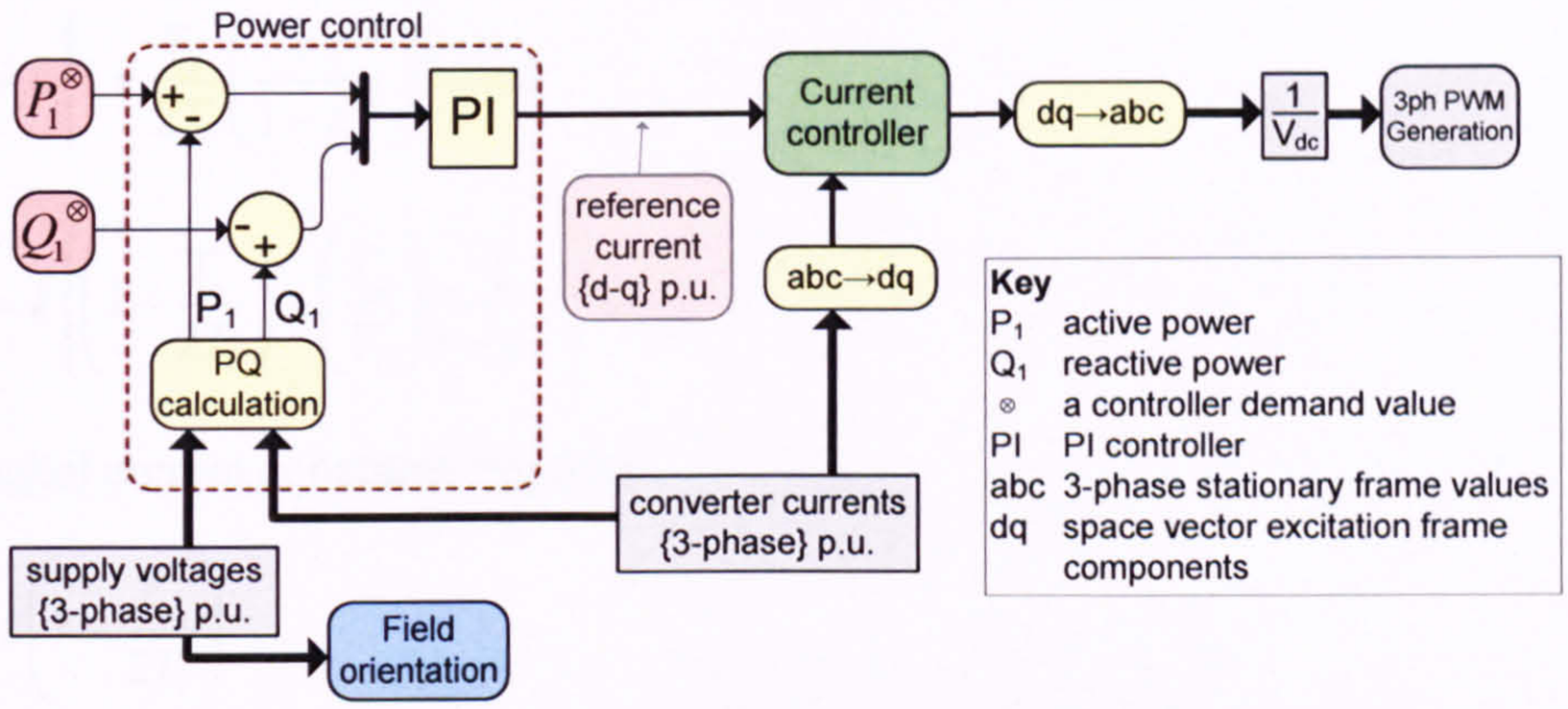

Figure C.4. Power control loop with inner current controller.

Figure C.4 shows a power control feedback loop producing the current reference vector for a current control loop. Note the signs of the power feedback error components with respect to Eqs. C.5 & C.6. The arrangement where one slower control loop feeds its output to the input of a second faster loop is known as cascaded control. The current control loop is said to be nested inside the power control loop.

Speed of controlled power response

In order for the cascaded arrangement (demonstrated in Figure C.4) to function without instability, the output of the power control loop must not change faster than the stable dynamic response of the current control loop. As a rule of thumb, the power controller should be tuned to respond 5-10 times slower to power-error changes than the current controller responds to current-error changes.

C.2 Digital implementation of PI control

A standard feedback error 'PI' controller has following time domain form:

$$u(t) = k\left\{e(t) + \frac{1}{T_i}\int e(t)dt\right\} \tag{C.7}$$

In the Laplace domain this becomes:

$$u(s) = k\left\{1 + \frac{1}{sT_i} + T_d s\right\}e(s) \tag{C.8}$$

It is possible to converting to discrete time domain using an approximation for the discrete time operator [91]. Using Tustin's (bilinear) approximation:

$$z \approx \frac{1+sT_s/2}{1-sT_s/2} \therefore s \approx \frac{2}{T_s}\left(\frac{1-z^{-1}}{1+z^{-1}}\right) \tag{C.9}$$

Hence;

$$U(z)=k\left\{1+\frac{T_s}{2T_i}\left(\frac{1+z^{-1}}{1-z^{-1}}\right)\right\}E(z) \tag{C.10}$$

$$U(z)=k\left\{\left(1-\frac{T_s}{2T_i}\right)+\left(\frac{T_s}{T_i}\right)\frac{1}{1-z^{-1}}\right\}E(z) \tag{C.11}$$

The digital control constants become:

$$K_p=k\left(1-\frac{T_s}{2T_i}\right) \tag{C.12}$$

$$K_i=k\left(\frac{T_s}{T_i}\right) \tag{C.13}$$

Such that the overall control equation simplifies to:

$$U(z)=\left\{K_p+\frac{K_i}{1-z^{-1}}\right\}E(z) \tag{C.14}$$

Eq. C.14 describes a digital PI controller. Eqs. C.12-C.13 allow us to transform real-time controller gains into discrete-time controller gains.

In practical application we can break the discrete controller equation (Eq. C.14) down into separate proportional and integral components:

$$u[k]=u_p[k]+u_i[k] \tag{C.15}$$

Proportional component:

$$u_p[k]=K_p e[k] \tag{C.16}$$

Integral Component:

$$u_i[k]=K_i e[k]+u_i[k-1] \tag{C.17}$$

It is necessary to define an initial state for the integral component, normally zero. In order to prevent windup of the integral component, its value is limited in software to lie within a specific range.

DFIG Test Rig

D

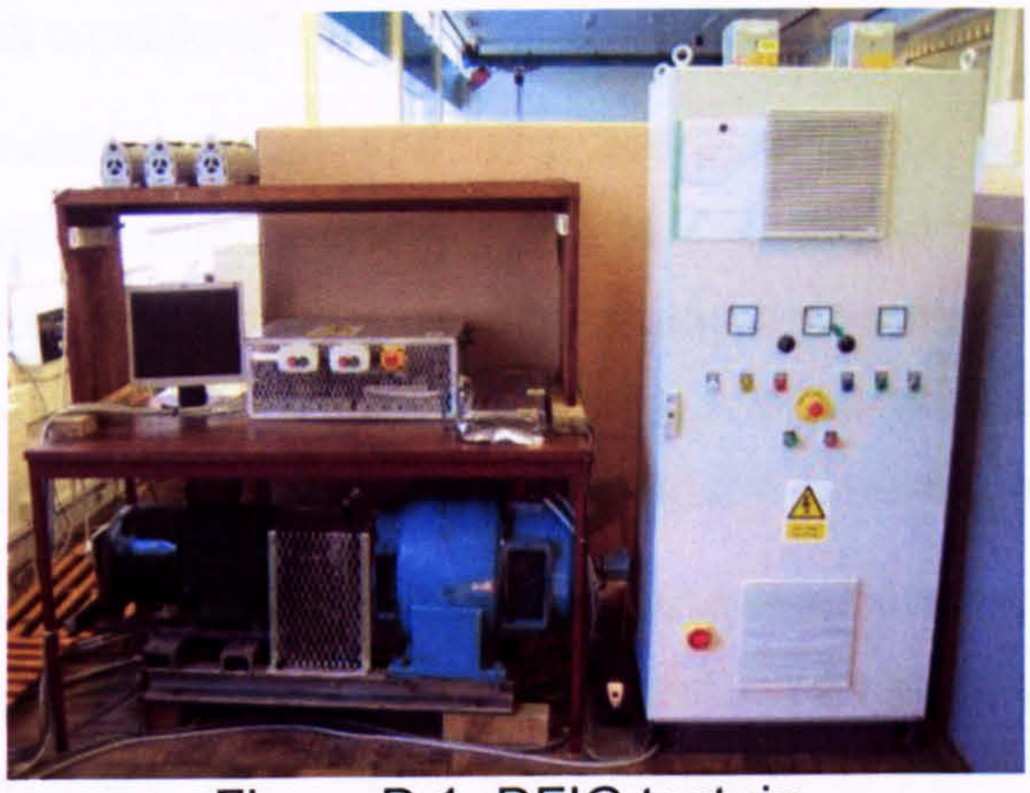

Figure D.1. DFIG test rig.

D.1 Test rig overview

As introduced in Chapter 4, a test rig was designed to simulate the elements of a DFIG wind turbine. Figure D.2 shows an overview of the test rig facility with key components labelled.

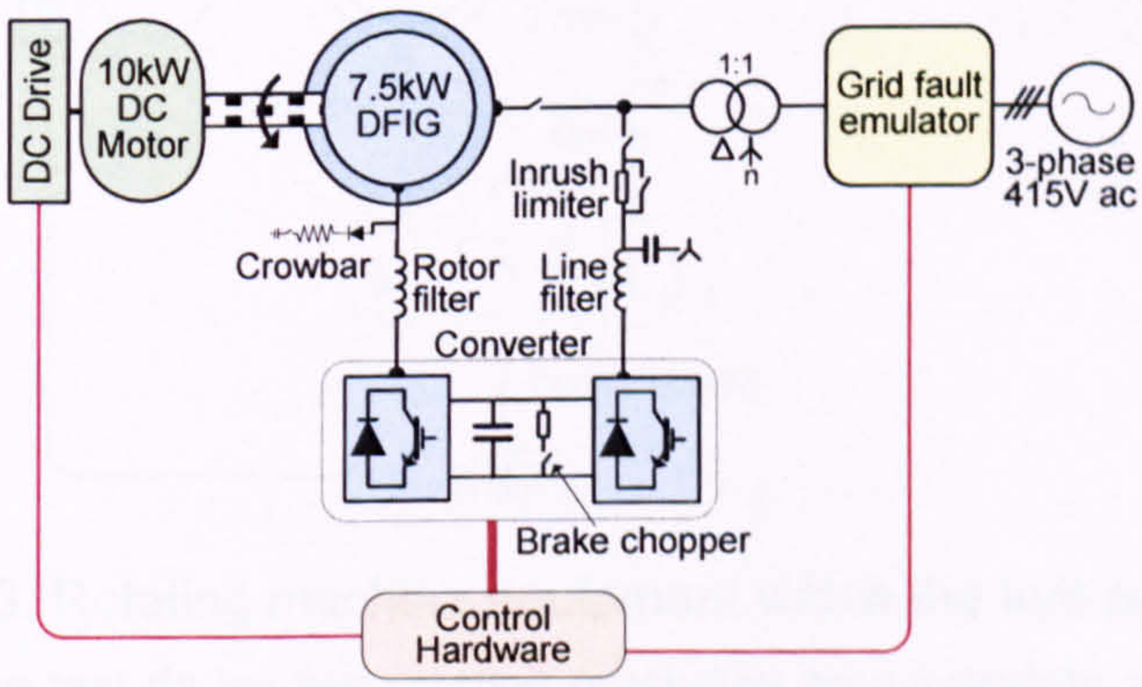

Figure D.2. Test rig schematic.

The test rig permitted the experimental evaluation of the DFIG system and its associated control under a range of grid fault conditions. The test rig comprised four main elements: a grid fault emulator, a wind turbine simulator, a DFIG system and a control hardware assembly.

- The grid fault emulator permitted a flexible approach to the application of grid faults. It allowed a range of balanced voltage-dip profiles to be applied to the terminals of the 7.5kW DFIG via a 1:1 Y-Δ isolation transformer.

- A 10kW DC motor and its drive provided a torque input to the DFIG. Together with a simulated mechanical model executed by the control hardware, this replicated the torque input from a wind turbine's rotor.
- The 7.5kW DFIG system represented the wind turbine's doubly-fed induction generator, including a custom 50A-rated IGBT power stack employed as a bi-directional power converter. The power stack was deliberately over-rated to reproduce fault conditions without damaging the equipment.
- The control hardware consisted of a combination of analogue protection & interface boards, isolated sensing equipment, controller development equipment and a dedicated PC. A central electronics board was responsible for the test rig protection system and control signal routing. A dSpace control system was used to put into effect the DFIG controller, wind turbine simulator and fault test control.

The rig was used to test the most promising techniques for improving DFIG fault ride-through. This chapter presents the technical information for each of the elements of the test rig. Where appropriate, each element is referred to its place within the schematic diagram of Figure D.2.

D.2 Rotating machinery

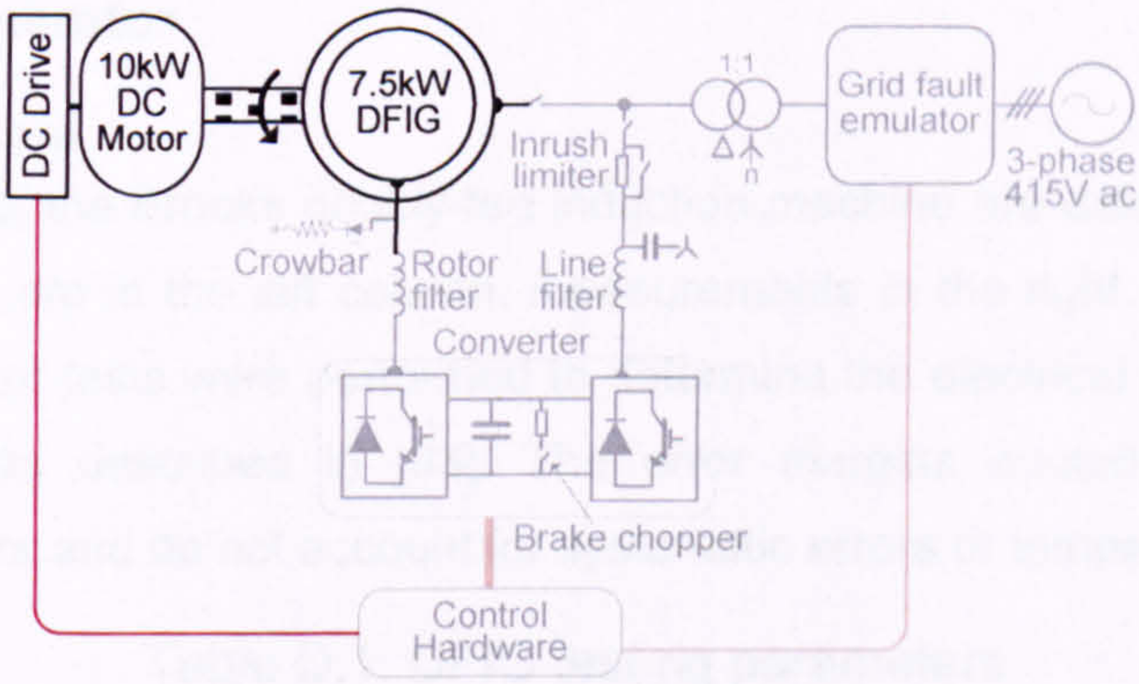

Figure D.3. Rotating machine equipment within the test rig overview.

At the heart of the test rig lay two rotating machines on a common axis with their rotor shafts joined by a short, stiff coupling. A 10kW, 240V, 1500rpm-rated Higgs DC motor provided a torque input to a 7.5kW, 415V, 4-pole Brooks DFIG. The DC motor was controlled by a four-quadrant 75A Control Techniques Mentor II DC-drive. A photo of the two rotating machines along with the DC-drive is shown in Figure D.4.

Figure D.4. Wind turbine simulator test rig motors

The doubly-fed induction generator lies in the foreground painted in British-racing-green. Stator and rotor connection cables can be seen, feeding into a common terminal box on the generator's left flank. Further back on the plinth is the sea-blue DC motor. The DC-drive is depicted at the back, mounted temporarily on a stool. Not pictured are the over-speed-relay's approximate speed sensor (mounted over the central coupling) and a 5000-line optical shaft-position encoder.

D.2.1 DFIG generator

Test rig parameters

The parameters of the Brooks doubly-fed induction machine are detailed in Table D.1. The rated values are in the left column, measurements in the right. Locked rotor and short-circuited rotor tests were performed to determine the electrical parameters of the DFIG windings as described in [93]. The error margins quoted are for random measurement error and do not account for systematic errors or temperature variations.

Table D.1. DFIG test rig parameters

Rated Values		Value	DFIM Parameters from test (per-phase, stator-referred)		Value
Power	kW	7.5	Resistance, stator	Ω	0.68 ±0.005
Pole number		4	Resistance, rotor	Ω	0.46 ±0.005
Operational speed	rpm	1,680	Leakage inductance, stator	mH	9.04 ±0.08
Stator voltage, line	V	415	Leakage inductance, rotor	mH	9.04 ±0.08
Stator current, phase (thermal)	A	14.7	Mutual inductance	mH	226 ±11
Stator current, phase	A	10.4	Turns ratio, stator: rotor		0.32 ±0.01
Rotor voltage, line (zero-speed)	V	1,290			
Rotor current, phase (thermal)	A	3.60			
Rotor current, phase	A	3.35			

The rotor of the original induction machine was rewound to achieve a stator/rotor turns ratio of 0.32, permitting an approximate operational speed range of ±30% based on the turns ratio and the power converter's operational DC-link voltage. At maximum speed the rotor emf magnitude equates with the stator voltage, which corresponds to the operational ac voltage of the line-side converter (using the same DC-link). The new rotor windings' thermal rating of 3.6A per-phase was comfortably above the normal operating requirements.

D.2.2 Wind turbine simulator

A 'wind turbine simulator' was formed by the DC motor, DC-drive and a simulated mechanical model executed by the dSpace controller. This setup was designed to replicate the torque input from a wind turbine's drive-shaft, as explained in Chapter 4. The wind turbine simulator parameters and real DFIG shaft parameters are given in Table D.2 (with reference to Figure D.5)

Table D.2. Wind turbine simulator parameters

Simulated turbine values		Value	Modelled turbine speed PI controller		Value
Rated power		7.5 kW	Control frequency		200 Hz
Rated speed		1,680 rpm	proportional gain	k_p	60
			integral gain	k_i	0.4
referred to high-speed end:		Value /p.u.	DFIG Parameters from test		Value /p.u.
Turbine inertia	J_L	5.25	DFIG & shaft inertia	J_m	1.44 ±0.13
Turbine friction	B_L	0	Friction coefficient	B_m	0.12 ±0.01
Flexible-coupling stiffness	K	98	DFIG shaft stiffness	K_{rig}	∞ [13]
Flexible-coupling damping	D	1.0			

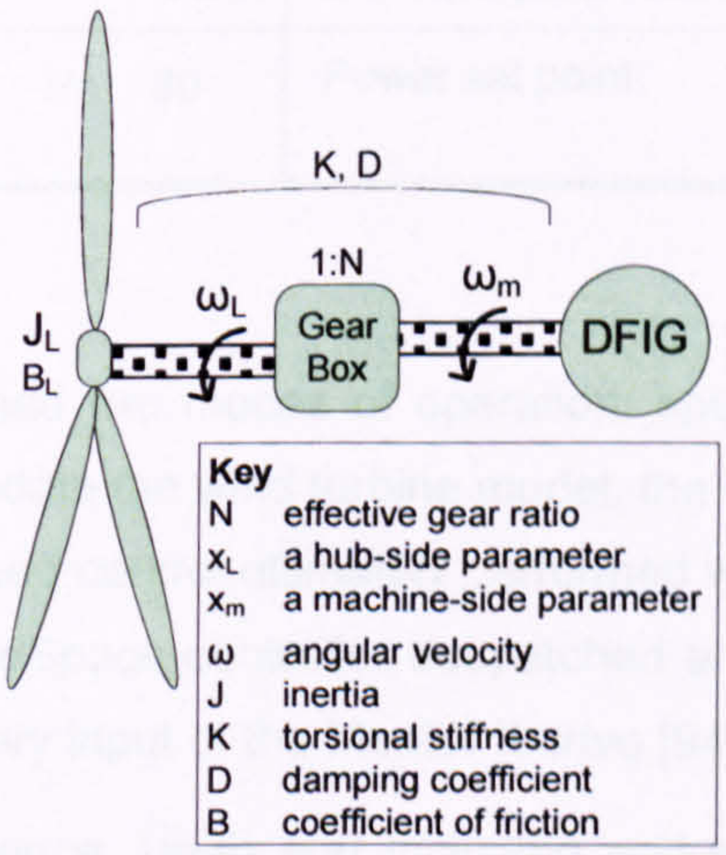

Figure D.5. Two-mass flexible-coupling wind turbine drive-train model.

[13] too high to measure

The dSpace simulation included a two-mass drive-shaft model; accounting for the gearbox, coupling and low-speed end of a wind turbine. It also included a simplified wind turbine blade-pitch controller with responsibility for turbine speed control. The control scheme is described in Chapter 4. The dSpace controller used rotor position information from the position encoder and calculated a torque value for the equivalent high-speed end of the modelled drive-shaft. This torque reference was scaled for the DC-drive and fed to a DAC output.

The DC-drive was set for torque control, i.e. direct control of armature current. The DC-drive picked up the analogue torque reference signal from the dSpace controller via an auxiliary input port and applied the appropriate armature current to the DC motor.

D.2.3 DC motor and drive

Test rig parameters

Wind turbine shaft torque was recreated by a prime mover, the 10kW Higgs DC machine, driven by a four quadrant Control Techniques Mentor II DC-drive. The main parameters of the DC machine and DC drive are given in Table D.3.

Table D.3. DC motor & DC-drive test rig parameters

DC motor rated values		Value	DC motor parameters		Value
Power	kW	10.0	Resistance, armature	Ω	0.31 ±0.03
Speed	rpm	1,650	Resistance, field	Ω	218 ±1
Armature voltage	V	240	Torque constant	Nm/A	1.166 ±0.06
Armature current (thermal)	A	49	EMF constant	V/rad.s	1.166 ±0.03
Field voltage	V	108			
DC-drive rated values		**Value**	**DC-drive parameters**		
Current control bandwidth	Hz	80	Power set point	kW	10

DC-drive operation

The Mentor II DC drive had two modes of operation: speed or torque control modes [94]. In order to accommodate the wind turbine model, the drive was permanently set to torque mode, with the speed control ultimately performed within the dSpace controller's wind turbine model. The dSpace controller despatched an analogue torque reference signal directly to an auxiliary input of the Mentor II drive [94].

During the start-up sequence, up-to and including grid-synchronisation, the dSpace controller operated a tight speed control loop, using rotor speed feedback. After successfully synchronising with the supply voltage, the wind turbine model was engaged. The mechanical model was not engaged earlier because the rapid

acceleration would excite a poorly damped resonance in the simulated drive-train, causing the real speed to oscillate wildly. In case of dangerous over-speed, a rough proximity sensor estimated the speed and triggered an emergency stop via an over-speed relay (Section 0.)

D.2.4 Drive-shaft

Mechanical parameters

The combined DFIG and DC machine rotor shaft had measurable properties as shown in Table D.2. Firstly, the friction measurement was calculated by providing a fixed torque from the DC machine with the DFIG unpowered and the rotor allowed to accelerate under no-load conditions. The final speed reached on the first-order-lag shaped speed graph is inversely proportional to the coefficient of friction. The coefficient of friction may vary somewhat with speed. The fixed torque input was estimated to provide near-rated speed, so that the friction coefficient calculated is the most useful operational value.

To avoid stiction at zero speed, an inertia test was performed at near-rated speed. The combined system was driven to rated speed by the DC machine and held constant for a short period. The DC machine power supply was then interrupted (CON_{DCM} de-energised). The PC recorded speed values from the encoder as the rotor coasted down to zero speed. For a stiff shaft without input torque, the inertia (J) can be calculated from a first order lag model with knowledge of the coefficient of friction (B), as shown in Eqs. D.1 & D.2. Again, the coefficient of friction may not be truly constant, which is why the test was carried out at operational speed; in order to use a friction value that corresponds with rated speed operation.

$$\omega = \omega_{initial} \exp\left(-\frac{t}{\tau}\right) \tag{D.1}$$

$$\tau = \frac{J}{B} \tag{D.2}$$

The p.u. inertia of the overall machine at 1.44 p.u. is comparable with typical wind turbine generator values. The stiffness of the coupling was so great there was no observable speed difference between the ends of the shaft. This useful outcome simplified the two-mass wind turbine simulation model performed by the dSpace controller; the real rotor shaft was considered infinitely stiff when compared with the modelled flexible coupling.

Position encoder

A 5000-line optical encoder on the rotor shaft provided detailed rotor position information. The encoder connected directly into a dedicated dSpace controller DSP

input port, which allowed the dSpace main processor to sample the rotor position at each control cycle.

Speed override trip and proximity sensor

In addition to the encoder, a proximity sensor was used as a rudimentary speed estimation device. The sensor worked by detecting the passing of metal screws embedded around the diameter of a nylon drum fitted to the rotor shaft. This speed estimate was hardwired to an over-speed trip device, as detailed in Section 0. The proximity sensor is detailed in additional drawing Figure D.41.

D.2.5 Earthing insulation test

Both machines were subjected to a standard insulation test using a Megger BM223 insulation tester at 1kV. In the DFIG, rotor and stator winding to earth/chassis resistance was measured to be >999 MΩ. The same test was performed on the DC machine measuring the resistance between the armature or field winding and earth and resulted in >200 MΩ.

D.3 Grid fault voltage emulation

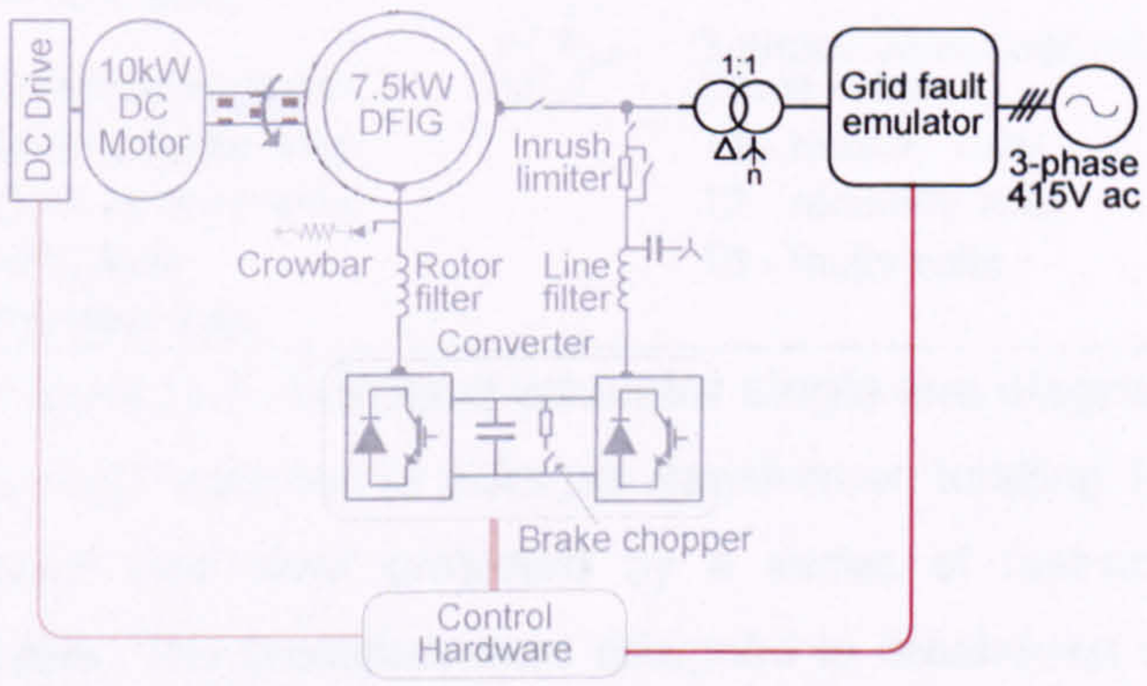

Figure D.6. Grid fault emulation equipment within the test rig overview.

The grid fault emulator was produced to apply balanced grid fault voltage profiles of the type specified by Grid Code. These typically demand an immediate drop to a specified 'fault' voltage for a specified duration followed by a swift rise to a specified 'recovery' voltage, as explained in Chapter 2.

The grid fault emulator connected to the DFIG via an isolation transformer, representing the LV/MV transformer of a typical industrial wind turbine generator, and a 0.15 p.u. set of three-phase reactors.

D.3.1 Setup

In this scheme three independent voltage levels (healthy, fault and recovery) were prepared in parallel on 3 three-phase variable auto-transformers (variacs). The three voltages were connected at their output by a set of back-to-back IGBT transfer

switches. These switches were controlled from a central switch-control electronics board. A fault test was performed by switching the voltage applied to the generator from one variac source to the next in sequence: healthy volts → fault volts → recovery volts → healthy volts. A single line diagram of the grid fault emulator setup is shown in Figure D.7.

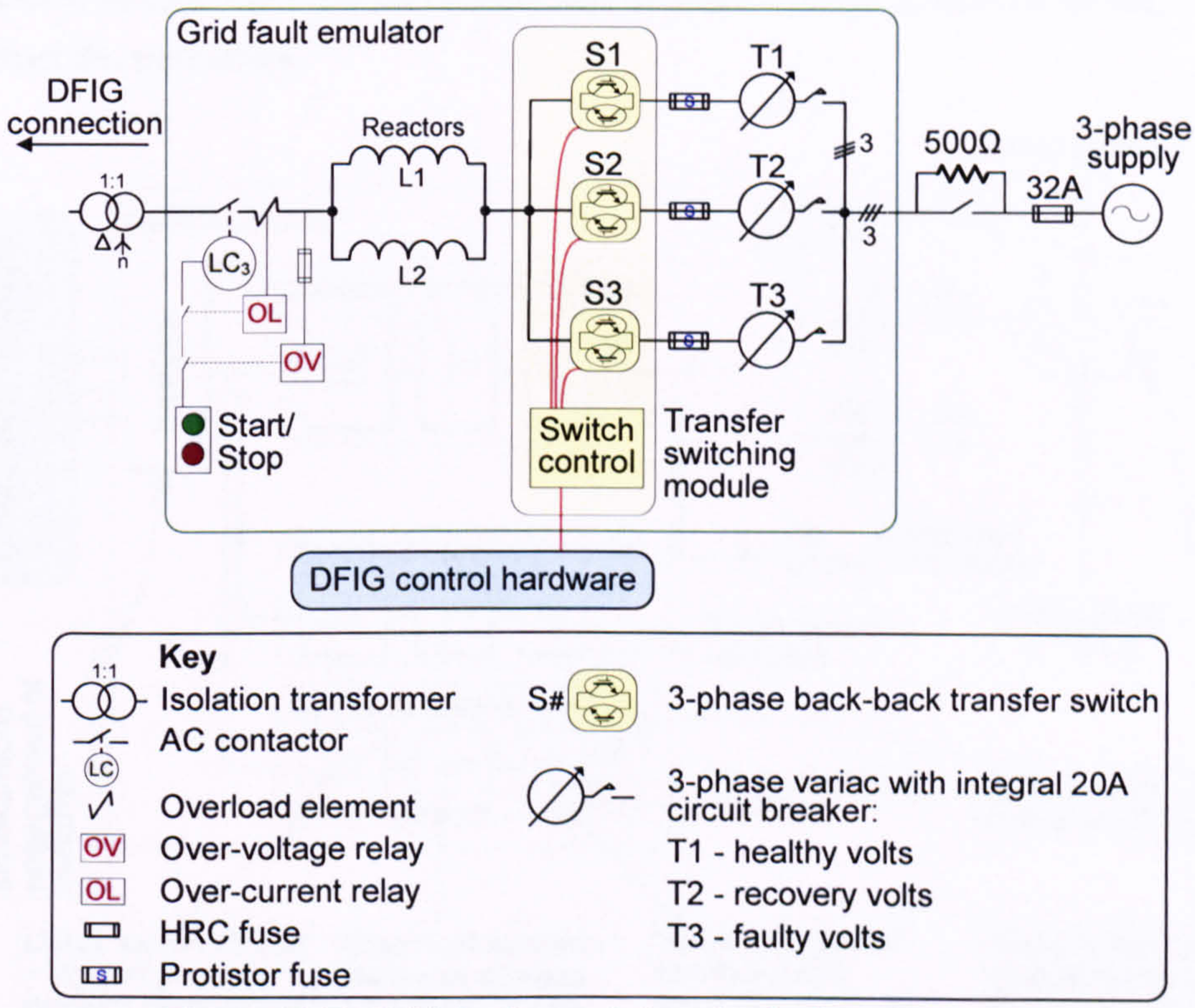

Figure D.7. Grid fault emulator single line diagram.

The back-to-back IGBT switches (3 pairs per transformer, totalling 18 transistors) were rated for 55A each and were protected by a series of fast-acting 30A protistor semiconductor fuses. The protistors were designed to breakdown very quickly above the rated current in order to protect the silicon devices connected in series. The dedicated switch-control board prevents simultaneous engagement of multiple switch sets in order to avoid short-circuiting the variacs.

The grid fault emulator was manually engaged with the DFIG via a Start/Stop button. Over-voltage and over-current devices were each hardwired to de-energise the Start/Stop contactor if their error thresholds were breached.

The switch-control board accepted ON/OFF logic signals for each switch S1-S3 from the digital output of the dSpace controller. In this manner the timings of the voltage switching could be readily controlled from the dSpace controller's GUI. The grid fault and recovery voltages were manually set on the variacs before each test.

D.3.2 Transfer switching

The solid-state IGBT switches allowed practically instantaneous switching between voltage levels and were rated for transient current. While a turn-OFF command was processed immediately, all the switches had a hardwired 10μs turn-ON delay in order to prevent a short-circuit between the switch sets. During the brief switching interval, the current through each switch module was diverted through a 420Vac-limiting varistor to protect the transistors.

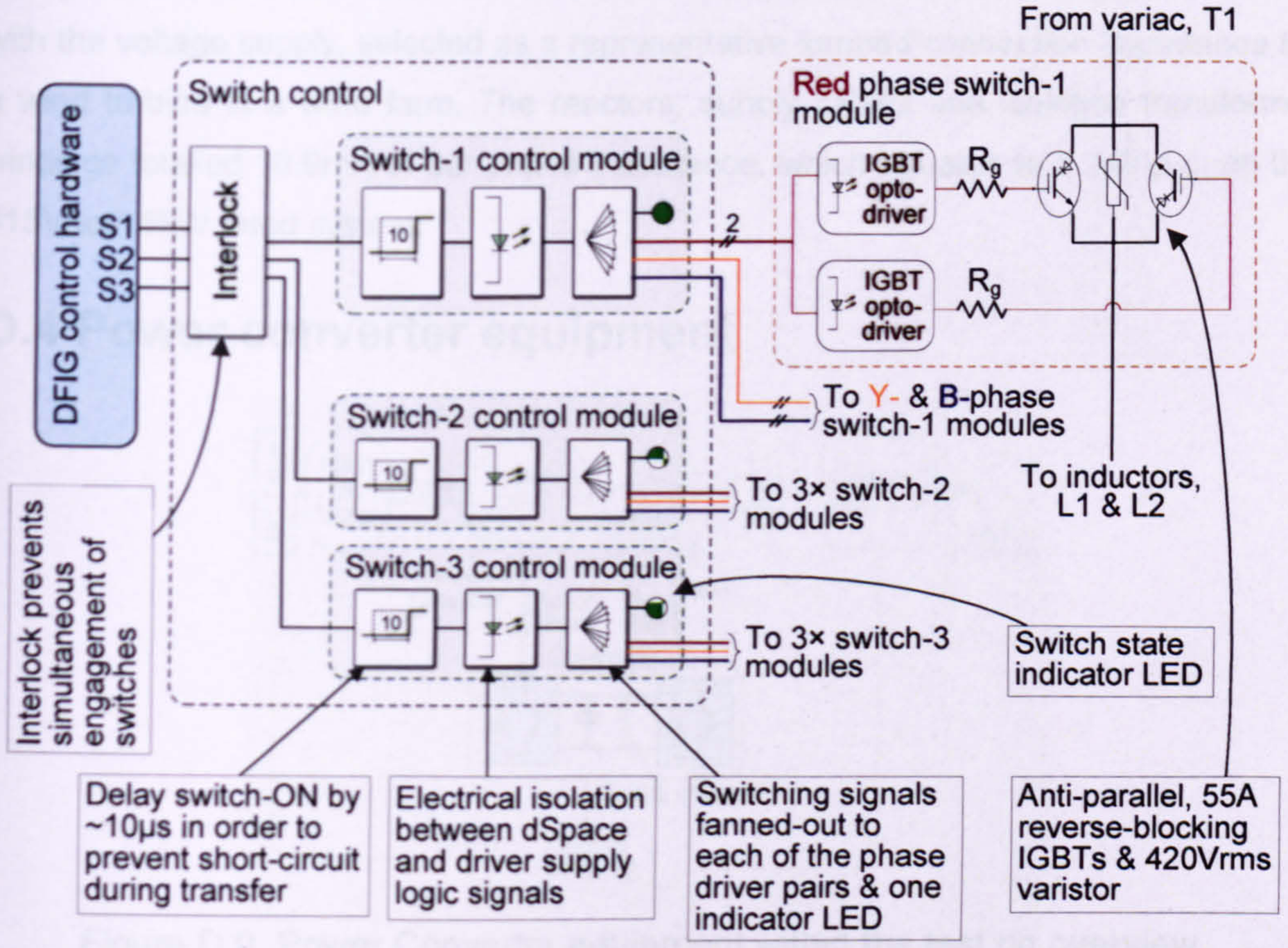

Figure D.8. Grid fault emulator transfer switch scheme.

D.3.3 About the voltage switching equipment

The original voltage switching equipment was designed and built at Newcastle University for another PhD project. This setup was later modified for integration with the DFIG system. The main advantage was the simple, robust design of the switching apparatus. The main disadvantage was the limited flexibility in that only balanced voltage dips could be applied to the generator.

D.3.4 Isolation transformer

The 10kVA isolation transformer served three purposes:

- It represented the winding arrangement on a typical wind turbine's LV/MV transformer.
- It reduced potential harmonic distortion from the thyristor controlled DC-drive.

- It limited the effect on the lab supply and DC-drive of any voltage imbalances arising from the grid-fault tests.

The transformer's three-phase voltage was centred by connecting its input Y-neutral to the lab power supply's neutral. The output Δ-windings fed into the control cabinet and the main contactor (CON_{main}), as shown in the electrical layout Figure D.33.

D.3.5 Grid connection impedance

The grid fault emulator also included a set *of three-phase 10.56mH* reactors in series with the voltage supply, selected as a representative lumped connection impedance for a wind turbine in a wind farm. The reactors, supply cables and isolation transformer windings totalled 10.9mH of per-phase inductance, which equates to 0.149 p.u. on the 415Vac/7.5kW rated system.

D.4 Power converter equipment

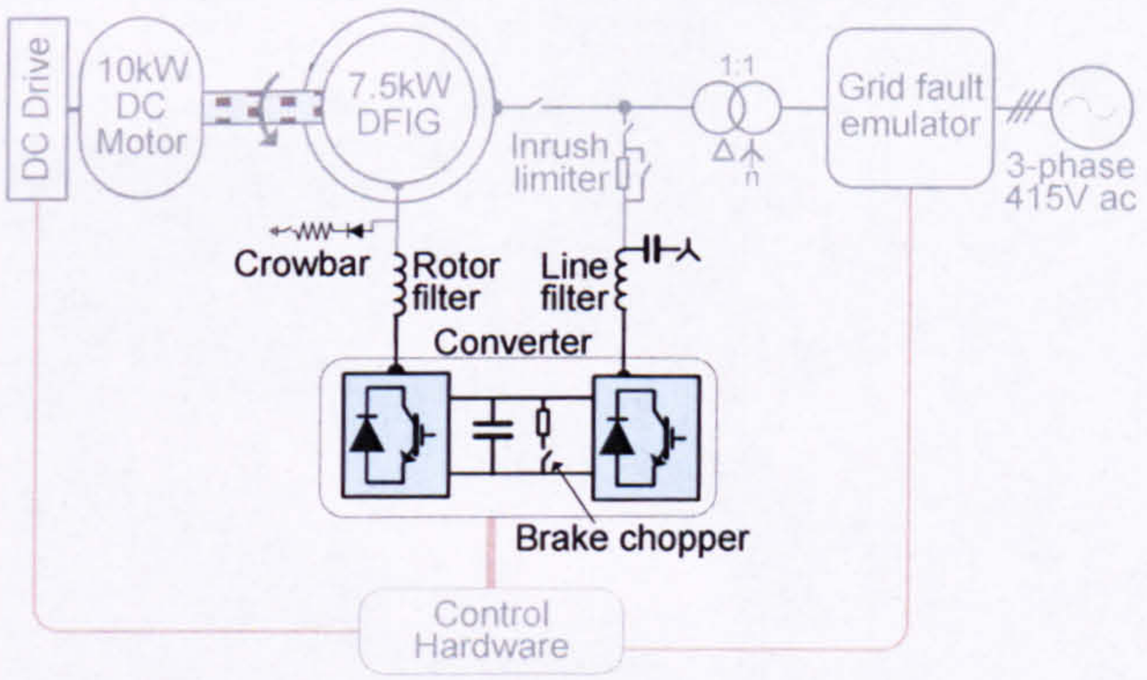

Figure D.9. Power Converter equipment within the test rig overview.

D.4.1 DFIG rotor bi-directional converter

The DFIG's rotor circuit included a bi-directional power converter based on two back-to-back IGBT bridge converters. A schematic of the converter is shown in Figure D.10.

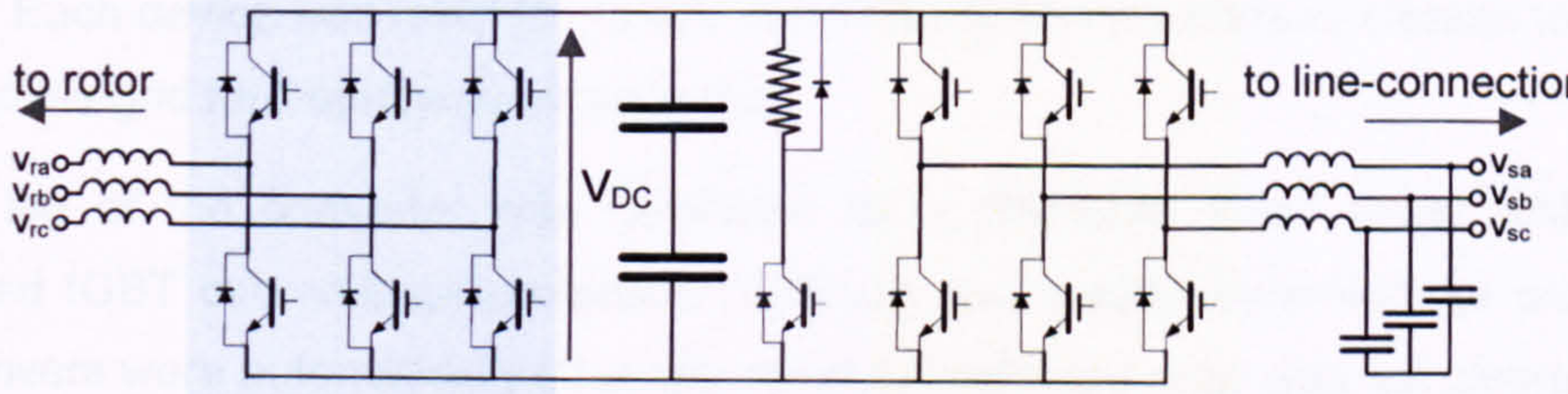

Figure D.10. Converter schematic including filters and brake chopper.

The transistor switches, DC-link, capacitor bank and brake-chopper were all mounted on a common heat sink. This electronics stack is hereon referred to as 'the converter'. Photos of the converter (front and back) are shown in Figure D.11 and Figure D.12.

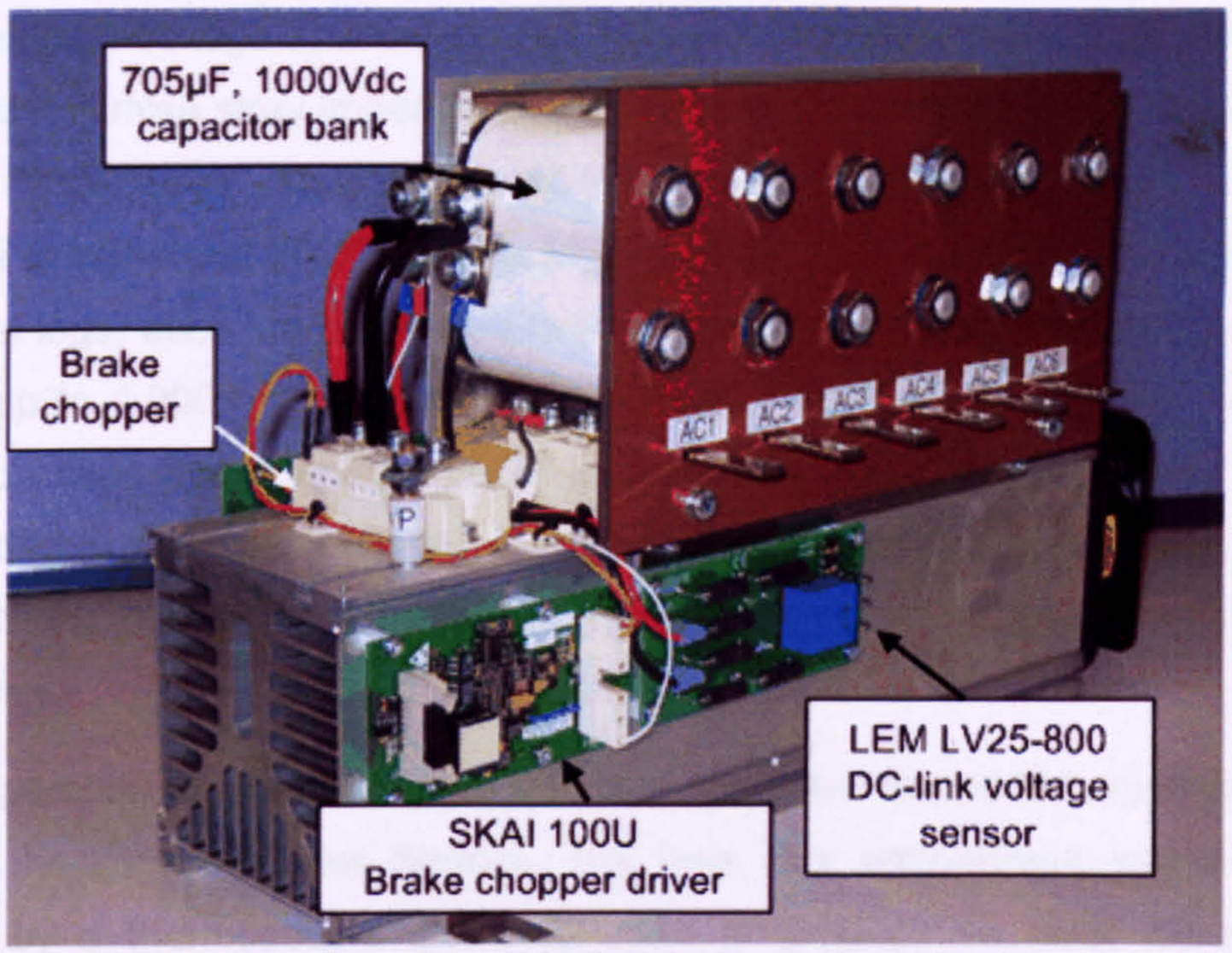

Figure D.11. *Semikron* back-to-back converter stack – front view.

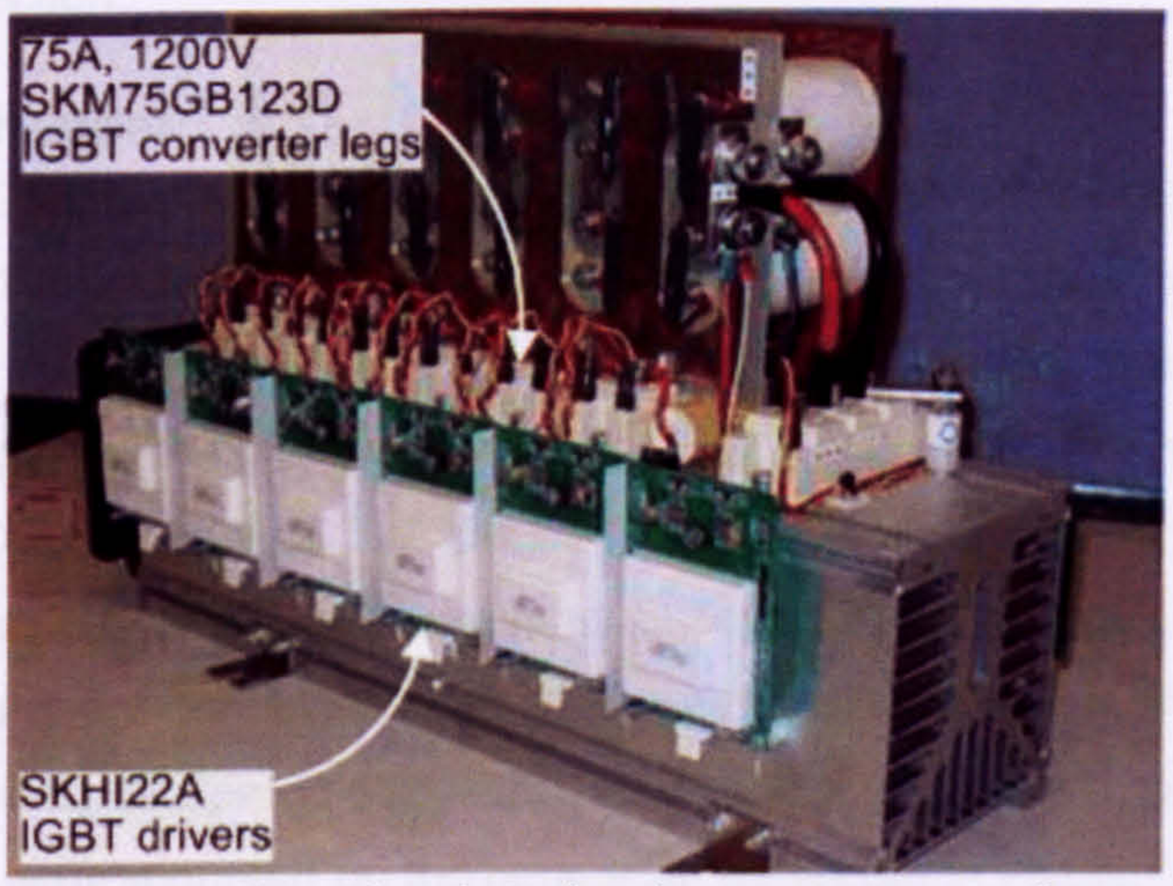

Figure D.12. Semikron back-to-back converter stack – rear view.

The converter was a custom-build Semikron IGBT stack built around 6 SKM75GB123D converter "legs"; each leg containing two IGBT/ freewheel diode pairs (see Figure D.10). Each device was rated for 1200V and 75A continuous current, chosen to exceed all credible grid fault test requirements [63].

Each leg of the converter was controlled by a SKHI22A IGBT driver which also included IGBT over-voltage protection (VCEsat) and supply under-voltage protection. The drivers were automatically internally reset if a detected error was not cleared within 9µs. A sustained error needed to be externally reset through a specially designed circuit as shown in additional drawing Figure D.37. Each SKHI22A driver used 3 CMOS signals to operate: one upper and one lower driver signal plus an error output. These signals were enabled by trip logic and differentially isolated for increased noise immunity.

The DC link high-voltage and low-voltage rails were formed of two large laminar plates arranged to minimise stray impedance. The capacitor bank was built into the Semikron converter stack. Each individual capacitor was rated at 470μF/500Vdc, with surge capabilities to withstand 550V dc for a few seconds. The six capacitors were arranged in 3 parallel legs, each leg containing two series pairs, producing a net capacitance of 705μF at up to 1,000V dc (1,100V dc surge). 11kΩ balancing resistors were placed across each capacitor to ensure equal sharing of voltage. Voltage surge capabilities were included to help the converter survive strenuous grid fault conditions; at the time of construction, most off-the-shelf electrolytic capacitors were rated at no higher than 450Vdc each.

Reliable operation of the power electronics converter depended upon the efficient cooling of the semiconductor devices. The heat sink temperature was continuously monitored by a thermocouple and was used to produce an error signal on over-temperature detection.

D.4.2 Brake chopper

A 1200V/100A IGBT was used with a Semikron SKAI100U brake chopper driver board and a Cressall 180Ω power resistor to limit the dc-link voltage to 810V. The brake chopper driver board made its own measurement of the DC-link voltage and automatically engaged the IGBT if the DC-link rises above 810V. The brake chopper cut out if the DC-link voltage fell below 795V. The IGBT connected a dedicated Cressall power resistor in parallel across the DC-link to sink excess power. The power resistor was mounted externally to the DFIG control cabinet for better heat dissipation. An anti-parallel diode dissipated stray current on the resistor. The brake chopper switch and driver board were mounted on the converter, as shown in Figure D.11.

D.4.3 Crowbar circuit

A crowbar based on a 75A 3-phase rectifier, a SKM75GAL123D 75A IGBT, a SKAI100U driver board and a Cressall 25Ω power resistor was used to short circuit the DFIG rotor circuit during an over-current or other rotor-circuit error condition. The crowbar was activated by externally triggering the Semikron driver board upon rotor-side over-current or driver error detection. The crowbar circuit is shown in Figure D.13.

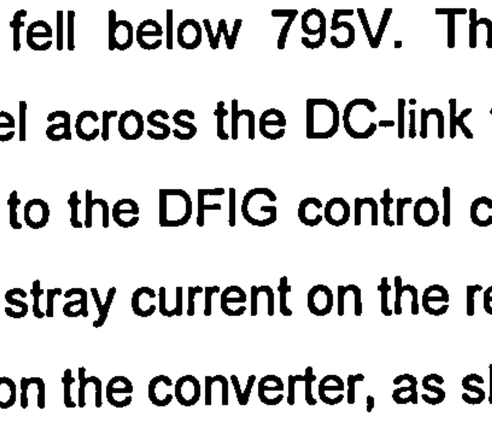

Figure D.13. Crowbar schematic

Activation of the crowbar connected the rotor phases together through a dedicated Cressall power resistor. As with the brake-chopper resistor, this resistor was mounted

externally to the DFIG control cabinet for better heat dissipation. The power electronics hardware and heat sink is pictured in Figure D.14.

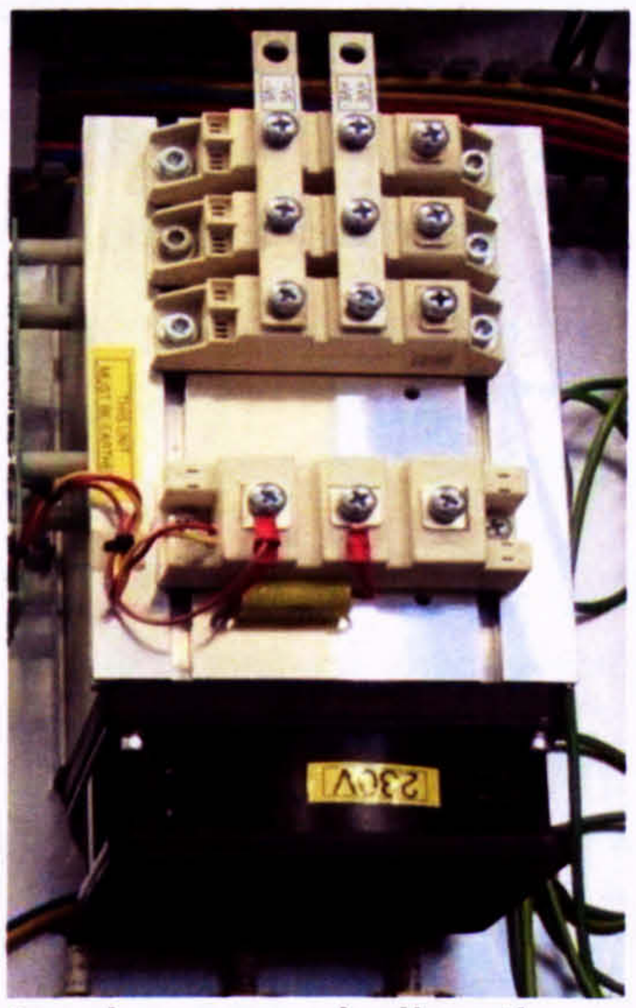

Figure D.14. Crowbar hardware excluding the external power resistor.

Details of the crowbar activation circuit are given in Section D.6.3. The operational details of the crowbar are given in additional drawing Figure D.38.

D.4.4 Chokes and filters

Line filters were needed to suppress undesirable high frequency EMI effects from PWM voltages generated by the inverter. The L-C filter placed between the inverter and grid consisted of series three-phase 10.56mH/10A line chokes with parallel three-phase 1.5 mF/450Vac capacitors connected in star (Figure D.10). This provided a low-pass filter with a cut-off frequency of 1200Hz. A second, small three-phase choke (0.4 mH/16A) was used in the rotor circuit to supplement DFIG rotor inductance. A dedicated EMI filter was used in series with the thyristor controlled DC-drive, in accordance with [95].

D.5 Control electronics

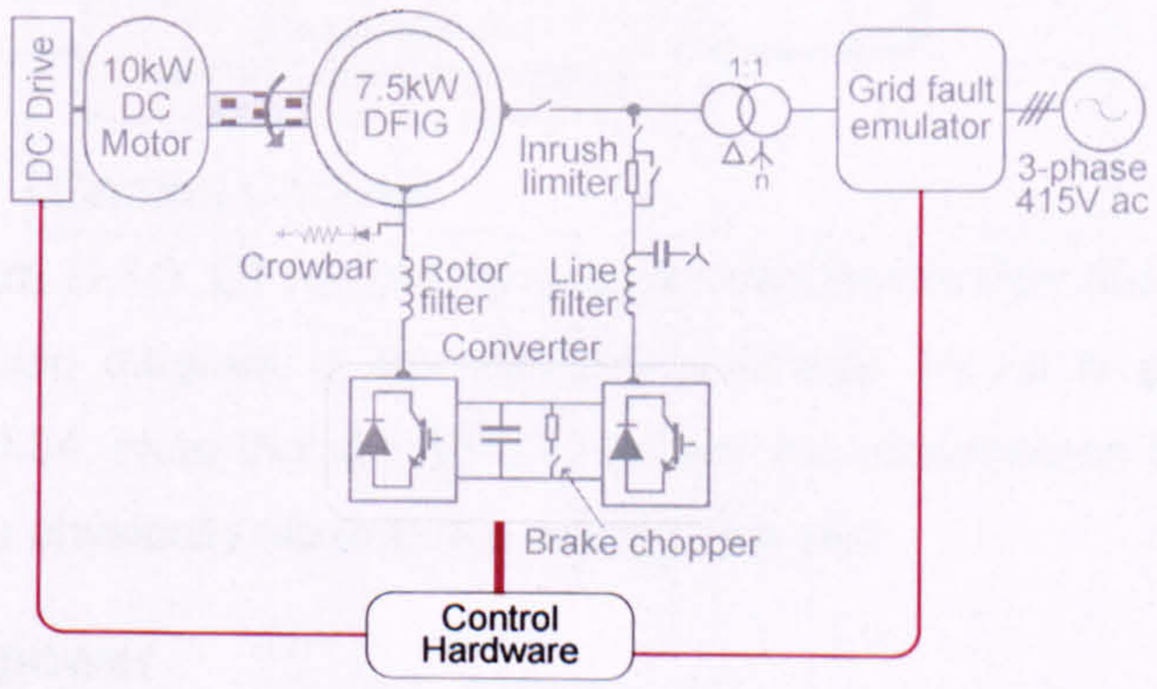

Figure D.15. Control equipment within the test rig overview.

D.5.1 Control overview

Control of the test rig system was carried out by interconnected control electronics hardware, essentially comprising four constituent subsystems:

- dSpace controller & host PC.
- Main board & error logic electronics.
- PWM & interface board.
- Signal acquisition boards with error threshold detection.

The resultant system is shown in Figure D.16. Controlled subsystems received instructions from either the main board or the dSpace controller. These recipient subsystems include: the IGBT driver boards, the DC-drive, all the protective contactors and the grid-fault emulator's electronic switch control system. The DC-drive control functions, system reset and system ESTOP were all available outside of the cabinet – both on the cabinet door and on a remote control box. Figure D.16 places the systems which were housed in the control cabinet approximately as they were located physically in the cabinet, as illustrated in Figure D.28.

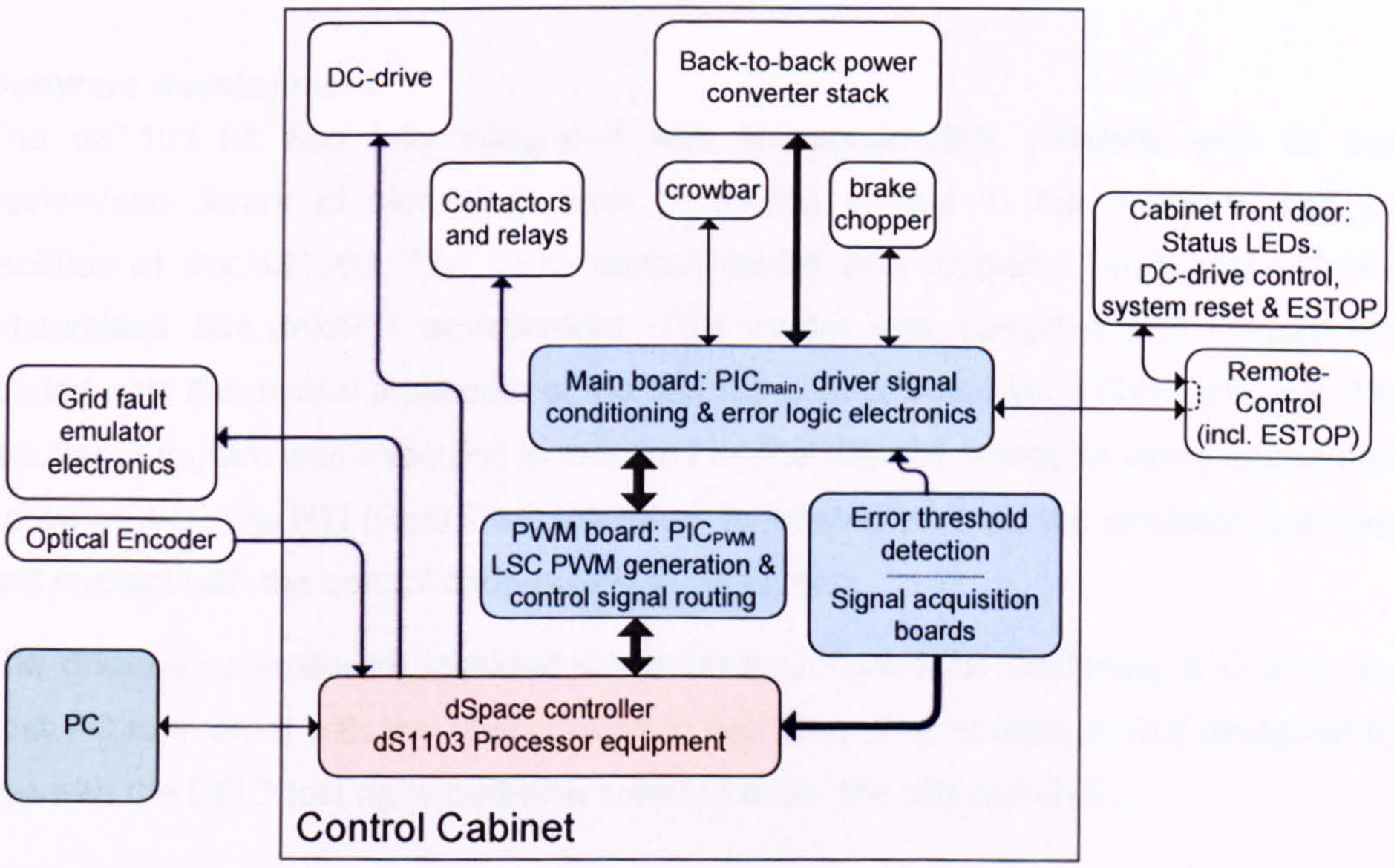

Figure D.16. DFIG control signal interconnection diagram.

A far more detailed diagram of the electronics boards' layout is given in additional drawing Figure D.34. Note that an ESTOP button was mounted on the remote control box in order to be physically close to the test rig operator.

D.5.2 Control power

All PCB control electronics and IGBT drivers were powered from an isolated power supply board with 24V and 15V dc outputs. This power supply board (along with the

dSpace controller) drew its supply from a Trust 14395-series 240V 400VA UPS. The UPS was used in order to prevent dangerous loss of control power or data-recording ability during the grid-fault tests.

D.5.3 dSpace controller and host PC

dSpace hardware

The dSpace controller executed the control algorithms for the DFIG control model and the wind turbine simulator along with other supervisory tasks. The system comes in 3 parts: a dS1103 single board computer housed in a PX4 expansion box, an I/O connector panel (CP1103) and a PCI card to provide a fibre optic interface (DS817) between a host PC and the PX4 expansion box.

The dS1103 used 2 processors: a Motorola PowerPC 640e master processor for floating point operations (used for the DFIG control scheme) and a TMS320F240 16-bit floating point DSP providing peripheral functions (e.g. three-phase PWM generation).

Analogue and digital inputs & outputs for the single-board computer were accessed from the connector panel (pictured in Figure D.18). Test rig I/O connections to the dS1103 are shown in additional drawing Figure D.34.

Software development

The dS1103 kit was fully integrated with Matlab/Simulink software, with its own customised library of simulation tools permitting access to the functions and I/O facilities of the dS1103. The DFIG control model was prepared on a host PC in a customised Simulink/RTI environment. This model was compiled into C-code and loaded onto the central processor of the dS1103 control board via a fibre-optic link. The resultant program was executed in real time by the dSpace computer using appropriate hardware I/O. The RTI (Real Time Interface) functionality allows the operator to access and interact with the control code during its execution.

The dSpace controller kit included Controldesk software for designing a GUI on the host PC to interact with the control code in real time. The multipage GUI designed for use with the DFIG test rig is hereafter referred to as 'the dSpace GUI'.

D.5.4 Main board and error electronics

Interface and error analysis electronics

A master control board, known as the main board, dealt with test rig error analysis and signal conditioning. This board included a Microchip 18F2550 PIC microcontroller (PIC_{main}), error logic, output relays, differential transmission and receiving circuitry, opto-isolation and IGBT driver interface electronics.

A photograph of the main board is shown in Figure D.17, including PIC_{main} near the bottom-left corner, contactor relays in a row along the bottom and driver interface ports near the top-right.

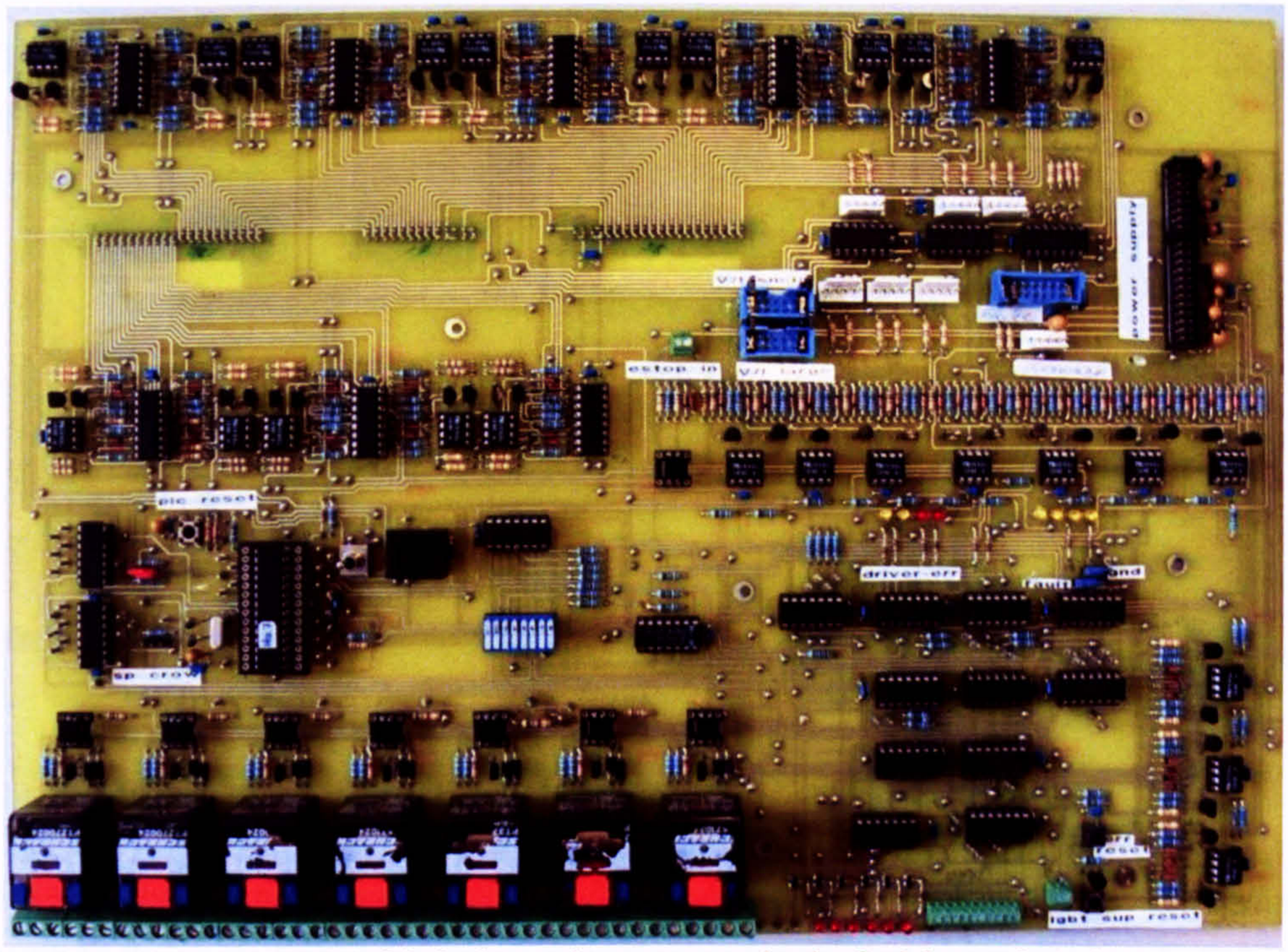

Figure D.17. Main board: error analysis & driver signals.

Main board functions

PWM Modulation signals from both the dSpace controller and from the PWM board were conditioned and fed to the appropriate driver output port.

Critical error signals were isolated and routed to the appropriate relay output, as explained in Section D.6.1. Sub-critical error signals were fed to PIC_{main} for conditional error processing. The test rig protection scheme is discussed in greater detail in Section D.6.

PIC_{main} acquired dSpace command signals (including brake-chopper and crowbar activation commands), sub-critical error signals and various device-status signals to perform conditional error analysis and supervisory control. PIC_{main} also executed pre-programmed start-up and shut-down subroutines on command (See Sections D.6.5 & D.7).

D.5.5 PWM board

The dSpace controller's DSP computed PWM signals for one half of the DFIG's power converter. A dedicated Microchip PIC18F4331 microcontroller (PIC_{PWM}) computed PWM signals for the other half. This PIC was hosted on a dedicated PCB, referred to as the PWM board. The PWM board is shown in close-up in Figure D.18.

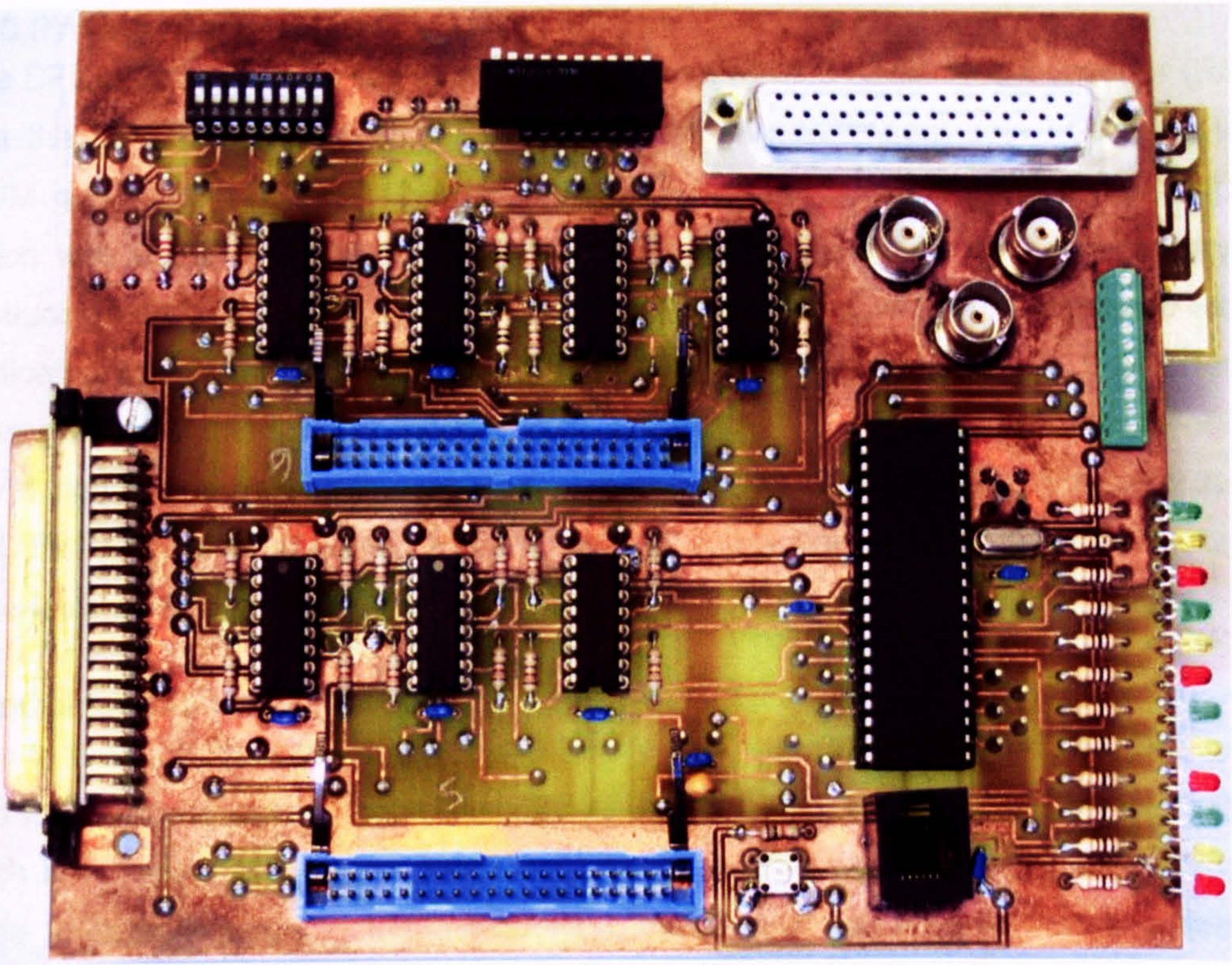

Figure D.18. PWM generation & dSpace interface board.

The PWM board aggregated all the PWM signals and routed them appropriately through to the main board for signal conditioning before they were sent on to the IGBT driver boards. The PWM board also used its digital I/O to direct dSpace commands between the PWM board and PIC_{main}. The PWM board was mounted directly onto the dSpace I/O board as shown in Figure D.19.

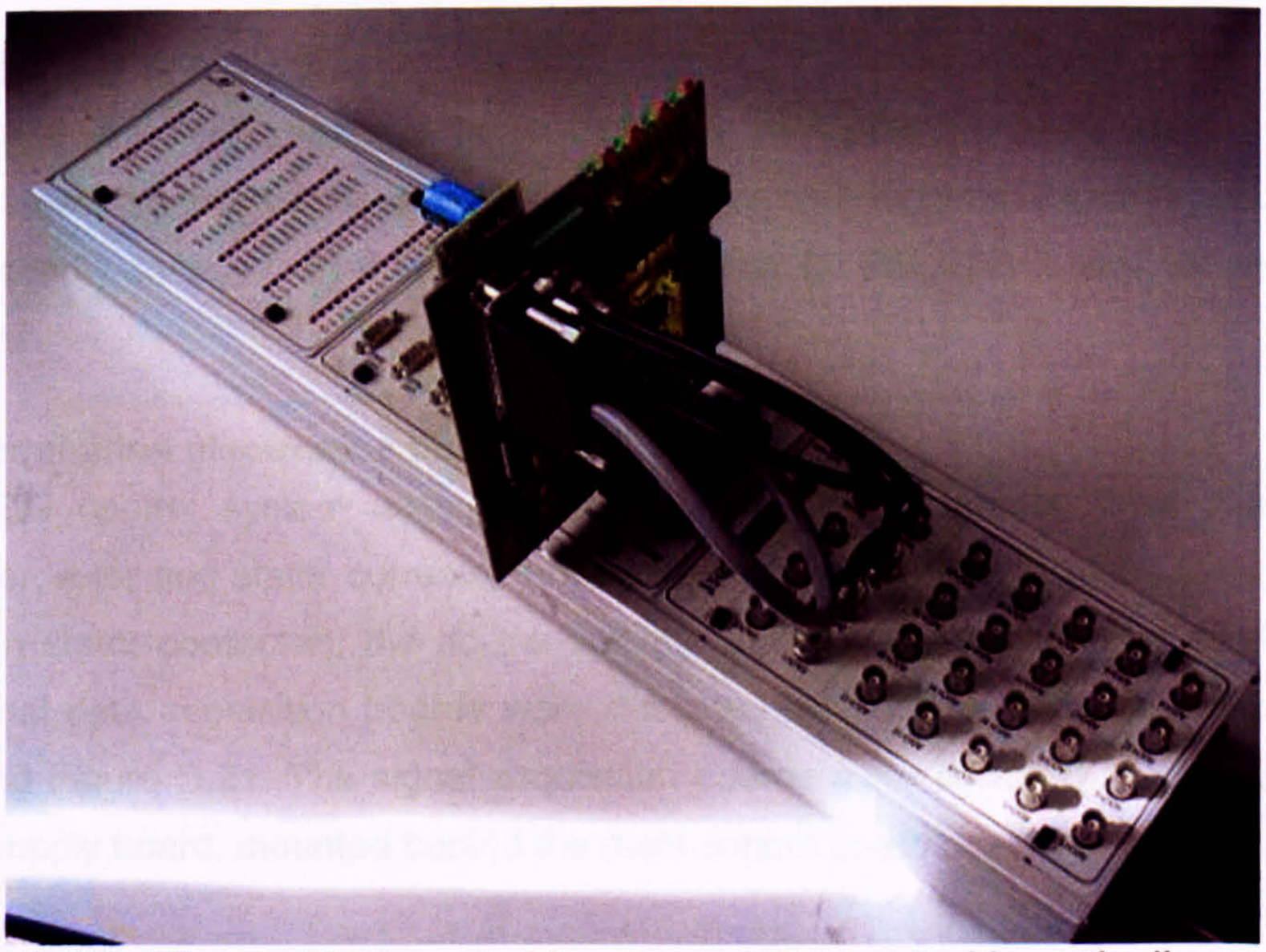

Figure D.19. dSpace 1103 control hardware I/O board with vertically-mounted custom PWM generation PIC board.

LSC PWM

The DFIG system had two three-phase IGBT bridges, the Rotor-Side Converter (RSC) and the Line-Side Converter (LSC), requiring two independent sets of three-phase PWM generation. The dS1103 hardware had one set of three-phase PWM outputs which was used to generate IGBT driver signals for the RSC. It was necessary to produce an additional three-phase PWM output for the LSC, which was achieved with a dedicated PIC board. A Microchip PIC18F4331 microcontroller (PIC_{PWM}) collected 3 analogue PWM modulation indices from the dS1103, calculated digital three-phase PWM signals and passed these to the main board. The main board opto-isolated these LSC PWM signals and passed these to the IGBT gate driver boards, in parallel with its opto-isolated RSC PWM output.

Control tasks and conflict

Due to the independent PWM generation sources, the dSpace DFIG-controller's code and PIC_{PWM} code could not be executed simultaneously, nor could the time periods of each be considered identical. However, PIC_{PWM} was required to interrupt the dSpace code to demand updated LSC modulation indices and flag safe periods in which to perform ADC sampling of the line-side currents.

As such care had to be taken in ensuring the timings of the two tasks did not cause computational errors, whilst minimising the time delay between sensor measurement sampling and PWM update. This tricky problem of control methodology was solved by careful assignment of task priorities in dSpace, customised PWM code on the PIC_{PWM} and minimisation of execution time for both sets of code.

D.5.6 Signal acquisition

The signal acquisition boards performed two functions: firstly to send analogue measurement signals to the dSpace controller for data-logging and control purposes, and secondly to send error-threshold trip signals to the main board for protection purposes.

Data acquisition electronics boards

The DFIG control system uses seventeen measurement inputs: three-phase line-converter, rotor and stator currents; three phase stator and grid voltages (each side of the main stator contactor); the dc-link voltage and the cabinet temperature. For this, two signal data acquisition boards were designed and built and are shown in Figure D.20 and Figure D.21. The signal acquisition boards were powered from a dedicated power supply board, mounted behind the main control board.

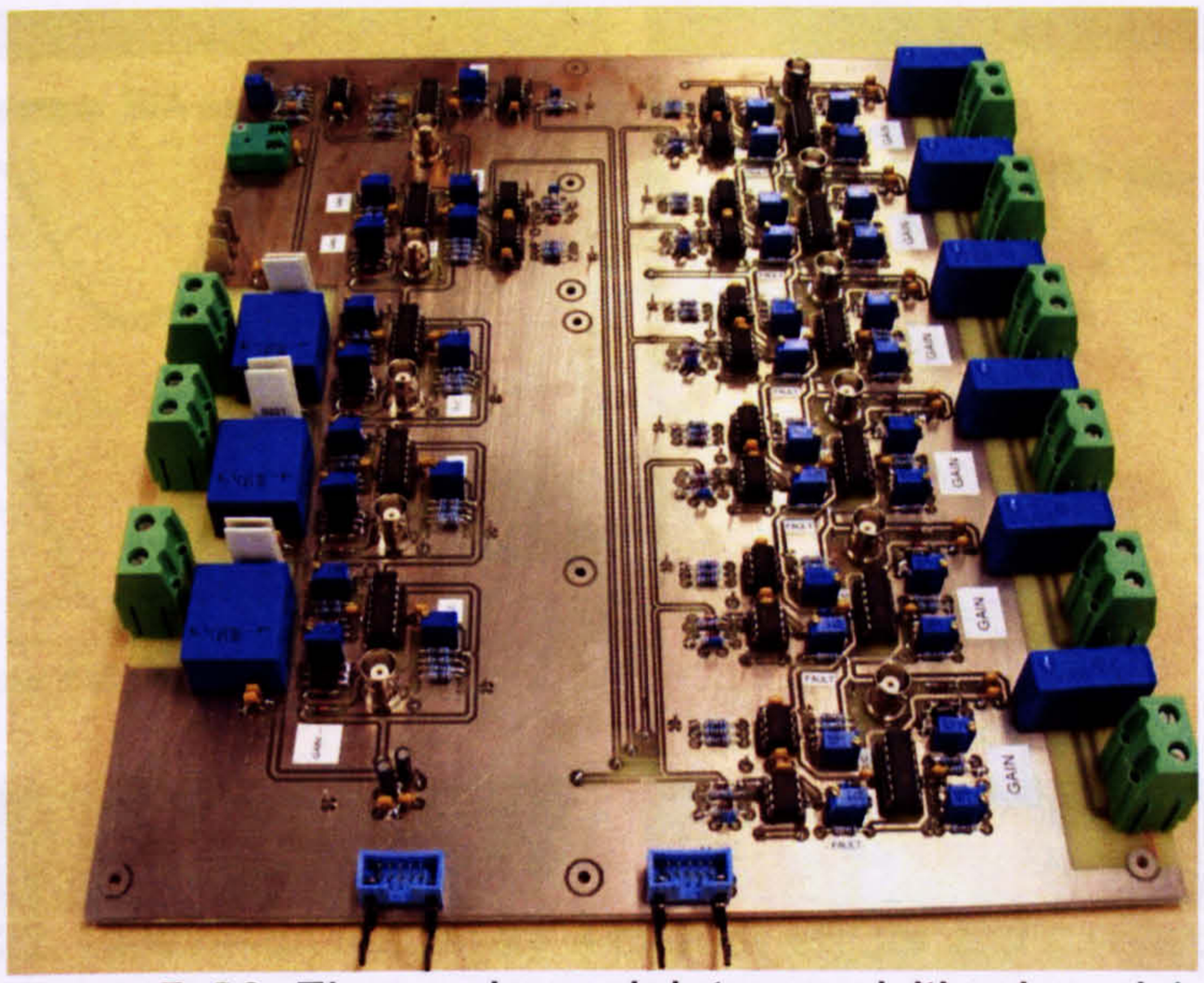

Figure D.20. Eleven-channel data acquisition board 1.

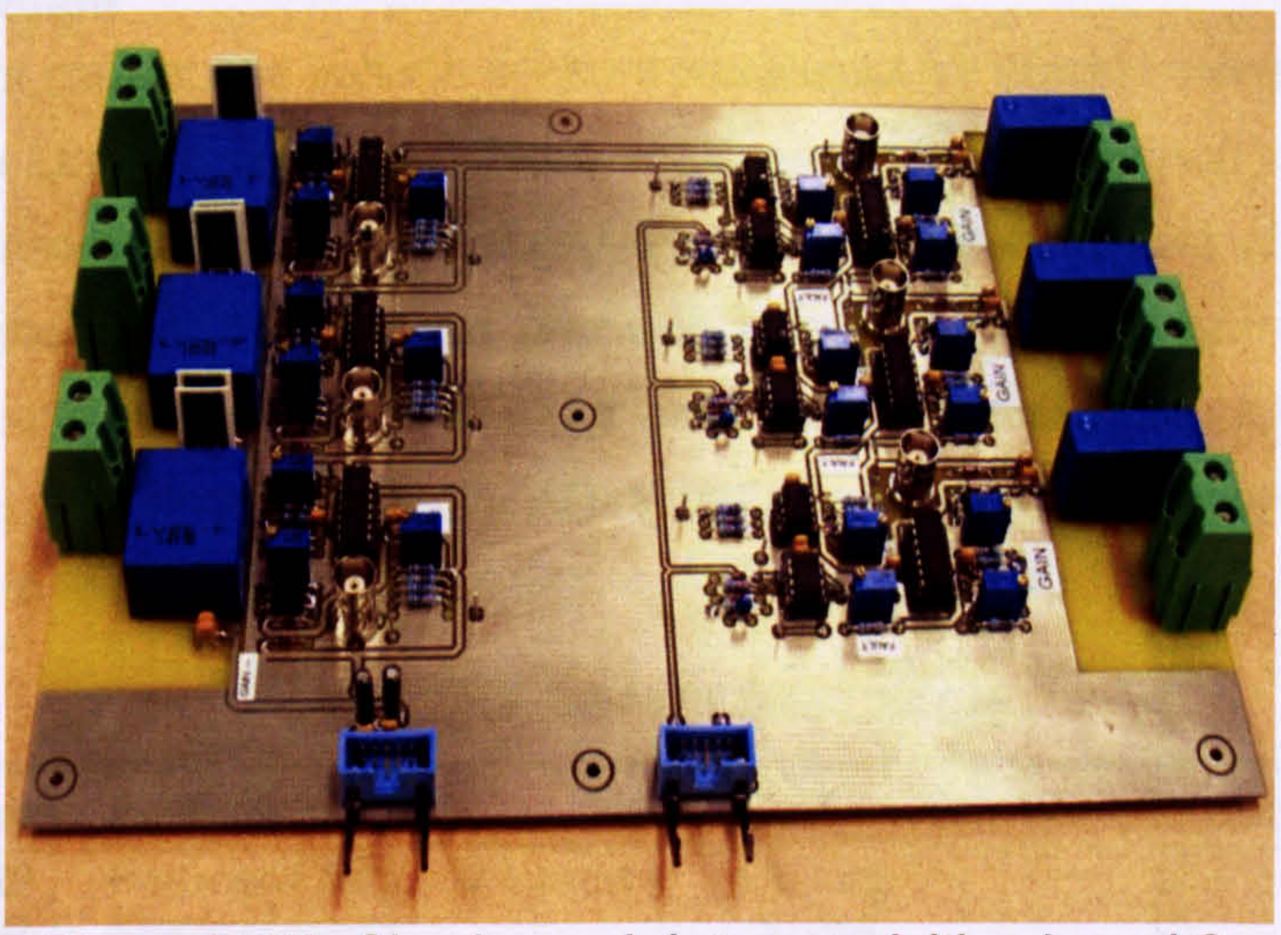

Figure D.21. Six-channel data acquisition board 2.

Acquisition board 1 contained 6 current sensing channels, 4 voltage sensing channels and a heat sink temperature sensing circuit. The second acquisition board included 3 further voltage sensing channels (used for DFIG grid synchronization) and 3 current sensing channels to acquire stator current signals. All the channels except the voltage synchronisation channels included an error threshold detection circuit which activated upon over-current/over-voltage/over-temperature detection. The outputs of these threshold circuits latched separate error signals which were routed to the main board. The same circuit was used to reset the error trips, as detailed in additional drawing Figure D.37. Trip logic circuitry is detailed in additional drawing Figure D.36.

The signal boards were carefully calibrated to measure 3-phase current, voltage and heat sink temperature. Oscilloscope traces of current and voltage measurement channels are shown below in Figure D.22.

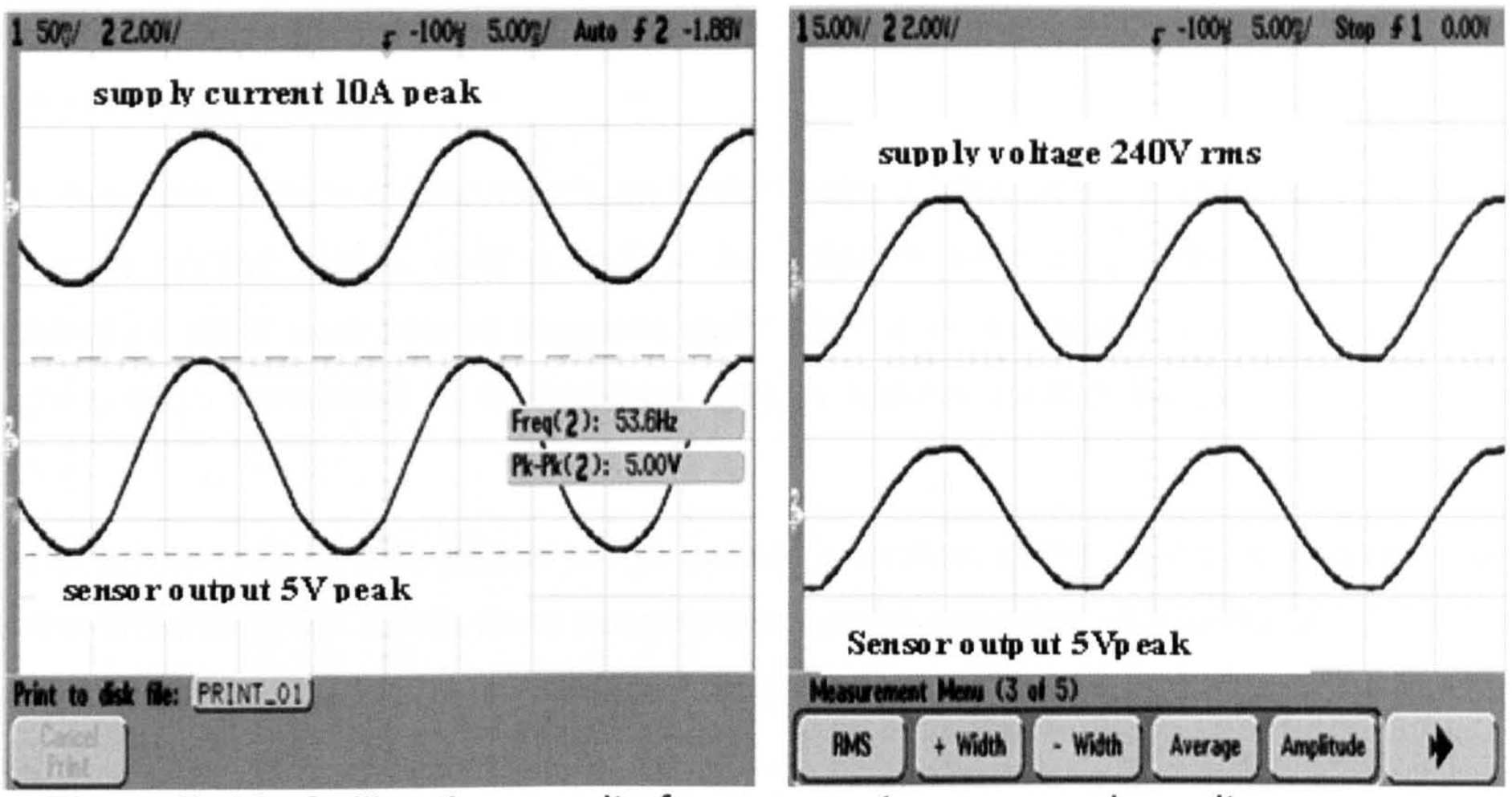

Figure D.22. Calibration results for a current sensor and a voltage sensor.

Sensor equipment

LEM Hall-effect current and voltage sensors were used for electric measurement in the test rig (Table D.4). In order to achieve maximum output resolution, rotor, line and stator side sensors were wired differently to obtain different scales of measurement [96]. It was noted that the required precision levels in measurement were achieved when sensors and measurement resistors were maintained at an ambient temperature of 25C+/-10%. The boards were therefore mounted in the lower half of the control cabinet, close to the ventilation fan.

Table D.4. Sensor parameters

Sensor type	Application	Unit	Nominal val.	Peak value
LAH25-NP	Rotor and line-side currents	A, rms	12	± 27
LTS25-NP	Stator currents	A, rms	25	± 40
LV25-P	Stator voltages	V, rms	415	± 800
LV25-800	DC-link voltage	V, dc	800	± 1200

All data acquisition electronics with threshold detection circuitry were fully opto-isolated to eliminate undesirable noise effects arising from ground loops (additional drawing Figure D.35).

D.6 Protection scheme

The design aim of the error analysis and protection circuit was to segregate errors according to their criticality and activate trip logic according to the specific error. In this manner operational continuity of the overall system could be maintained for non-critical errors. Critical errors were handled by a *hard protection* scheme, generally acting through a series of contactors for a swift error-response. Most non-critical errors were handled by *soft protection,* analysed by the PIC_{main} microcontroller. Certain non-critical

conditional errors were handled by the dSpace controller, making use of its programmable flexibility.

For example, critical over-currents on stator, rotor or line-side converter circuits, over-voltages on the stator, over-speed of the rotor or over-temperature of the control cabinet or IGBT switches all triggered error signals in analogue circuitry. These error signals were hardwired to de-energise certain test-rig contactors as shown in Table D.5.

Other errors may be less critical to the normal operation of the rig. For example, failure of the crowbar IGBT driver does not prevent normal operation of the test rig. The error signal was noted by PIC_{main} and flagged on the dSpace GUI, without tripping off the test rig.

In addition to these provisions, a set of interlocks were added into the contactor scheme to ensure safe start/stop operations. These are detailed in the relevant sections (see also additional drawings Figure D.36 & Figure D.39).

The DFIG system devices were included in the main board protection zone and so all DFIG related control and status signals were routed through the main board. A more detailed diagram is shown in additional drawing Figure D.34.

The grid fault emulator and the DC-drive operated their own safety logic schemes and so were not covered by the main board's safety scheme. The DC-drive's self-protection mechanism was interlocked with the DFIG system's emergency stop, assuring mutual safety. If the grid fault emulator's protection was triggered, it cut-off the grid voltage supplied to the DFIG. This was not an emergency situation for the DFIG; in fact it would replicate the very grid fault situations for which it was designed to study. Any danger to the DFIG would manifest itself in an over-current or over-speed event which would have triggered the DFIG's own protection devices. If these were not triggered, the DC-drive control performed by the dSpace controller would control the rotor to rated speed in a no-load minimum-torque situation.

The hard protection scheme covered errors which were dealt with by hard-wired analogue circuitry. The soft protection scheme covered conditional responses to errors, where the error response was determined in microcontroller software using PIC_{main} or dSpace.

D.6.1 Hard protection (including interlocks)

(Additional drawing Figure D.39.)

Hard protection rules

- Emergency stop will be triggered IF:

ESTOP button is pressed OR DFIG over-speed OR DFIG overload OR power converter overheats OR crowbar resistor overheats OR brake resistor overheats. In this situation, the DFIG-converter loop and the DC-drive are isolated, whilst PIC_{main} activates the crowbar and dc-link brake chopper to discharge all circuits.

- All contactors are all nominally-off, such that an effective ESTOP scenario occurs if the control electronics' power supply fails. The DC-drive contactor must be reset via the cabinet front panel or remote control box buttons to prevent an accidental restart. DFIG contactors must be reset in software before a restart can be attempted.

- System RESET can be executed only after ESTOP is reset. System RESET is interlocked with the dc-link discharge, crowbar trigger and main contactor CON_{main}.

- System RESET is interlocked with CON_{main} for a period of three seconds. This avoids repetitive resetting whilst the system is energized.

- DFIG is synchronised (CON_S ON) only IF:

  DC machine is ON AND line side converter is grid-connected AND DFIG model's external synchronisation trigger moves to ON (i.e. the external CON_S trigger signal MUST be manually reset before grid-synchronisation). This prevents the DFIG being accidentally grid-connected, avoiding potentially dangerous stator currents or dangerously high induced rotor voltages.

- Rotor side PWM is disabled IF rotor-side converter error OR rotor over-current error.

- Line side PWM is disabled IF line-side converter error OR line over-current error.

- Crowbar ON if rotor-side converter error OR rotor over-current OR command from PIC_{main} ON.

Relays

Figure D.23 and Figure D.24 show photographs of the protective relays and contactors for both the DC drive and the DFIG system.

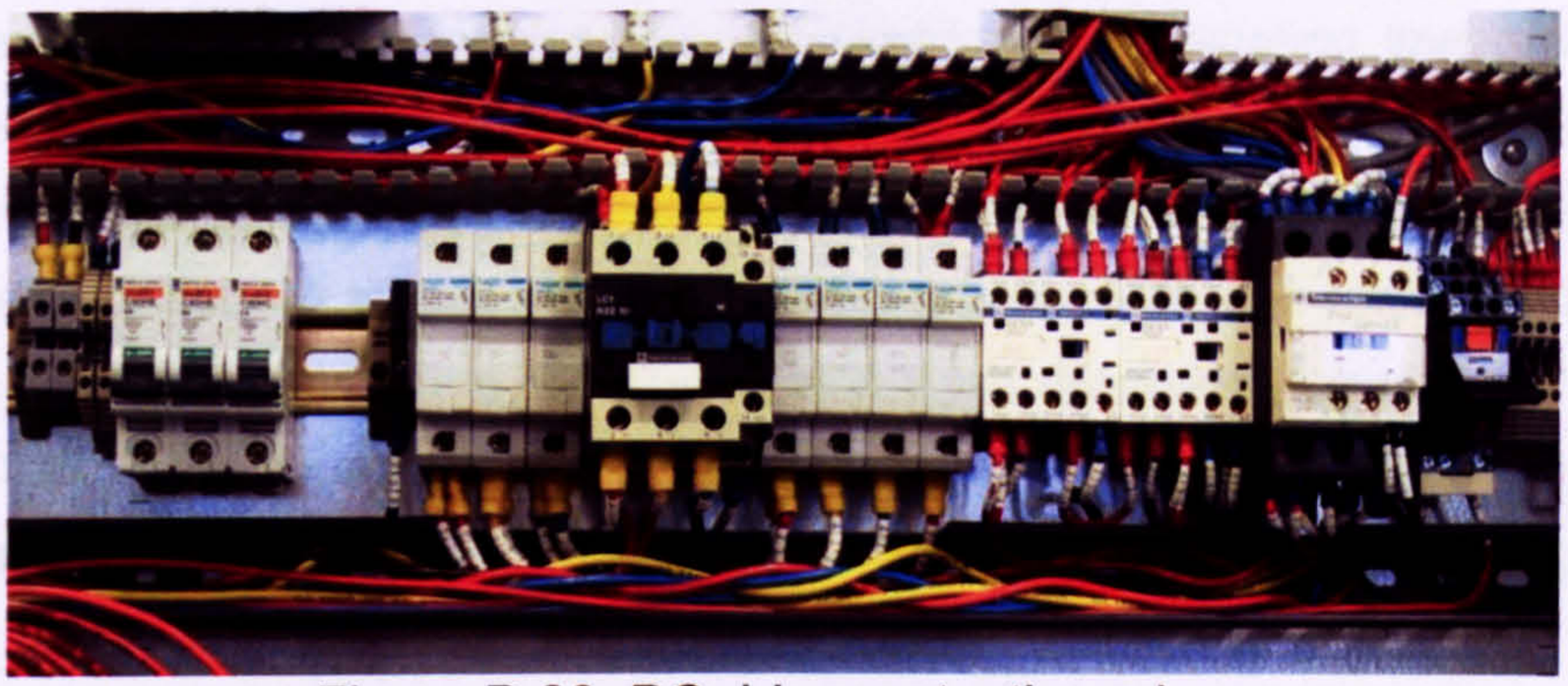

Figure D.23. DC drive protective relays

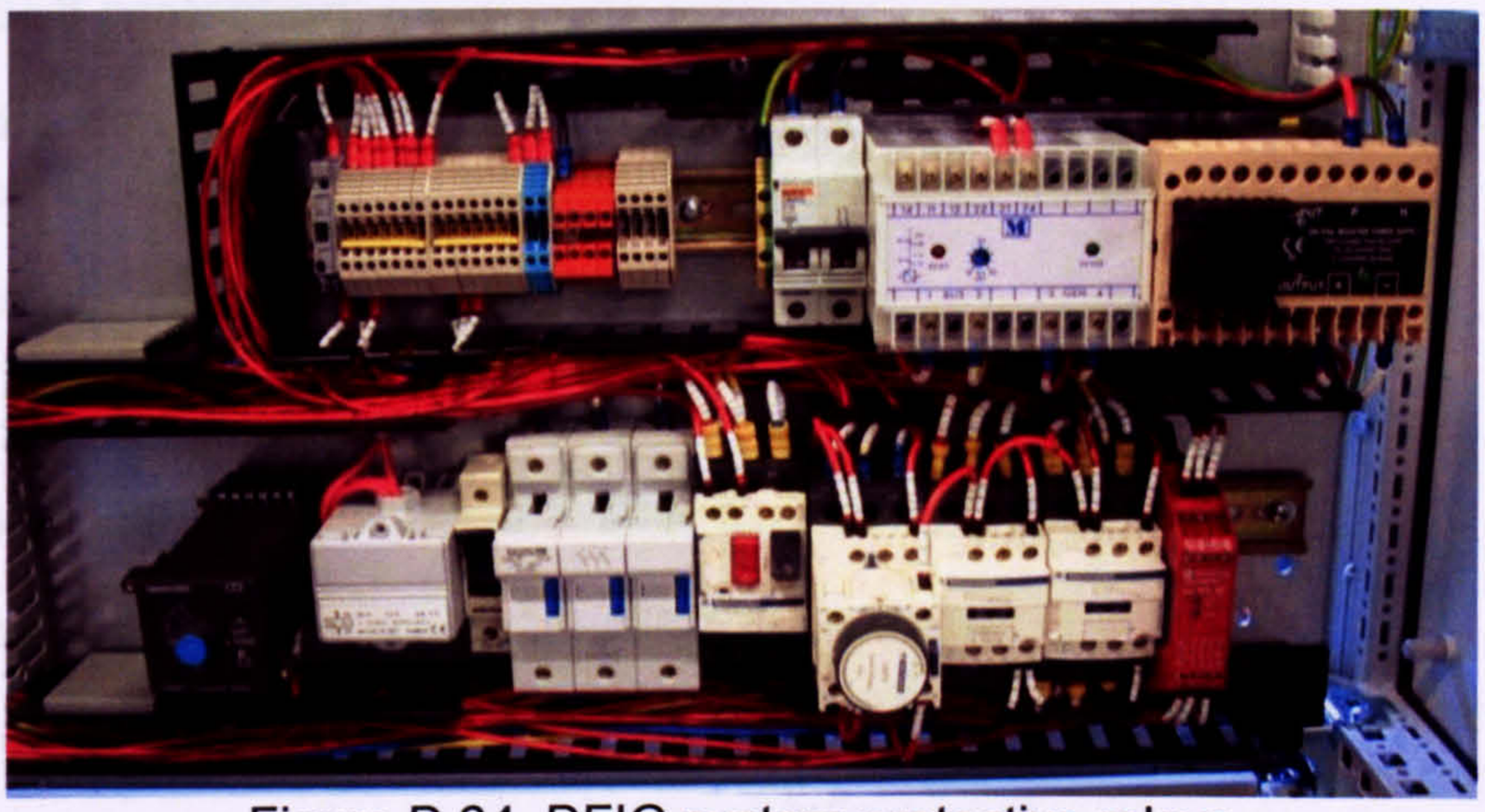

Figure D.24. DFIG system protective relays

Over-speed trip

During a DFIG stator voltage dip, the loss of electromagnetic braking torque induces a sharp acceleration in speed posing a particular safety issue. The dSpace controller calculated speed from the optical position encoder interface, and this speed was used in software to apply a controlled shutdown for over- (or under-) speed events. However, a hardwired over-speed system was also included in case of software failure. The over-speed trip triggered an Estop event as described in Section D.6.4. The over-speed trip was set for a higher threshold than the software trip.

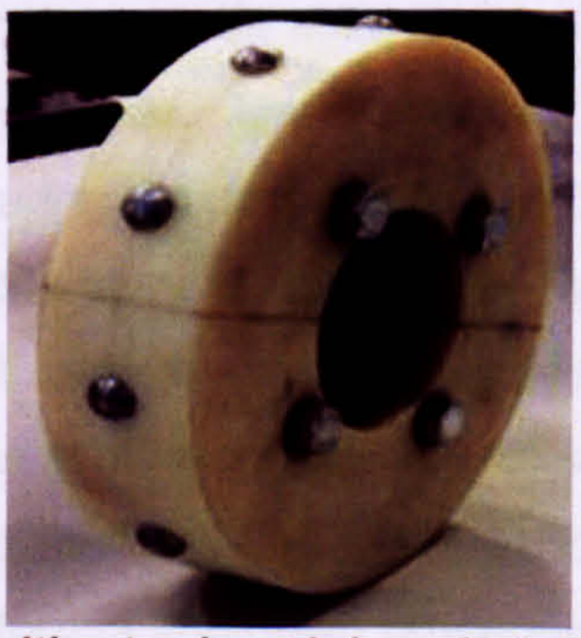

Figure D.25. Nylon drum with steel peripheral studs used for the over-speed trip.

The over-speed estimator was constructed based on a Tempatron speed detection relay and a proximity sensor. Steel studs were threaded into a nylon drum mounted on the rotor shaft to elicit pulses from a proximity sensor at each tenth of a revolution. The speed relay calculated a speed from the resulting pulse train and compared it with a reference value, triggering the emergency stop if the measured speed was too high. Figure D.25 shows the steel-studded nylon drum used in the speed estimation process. Detail on the mechanical speed estimator can be found in additional drawing Figure D.41.

D.6.2 Soft protection

Soft protection rules

The following list summarises soft protection tasks designed into the system:

- Activate crowbar on command from $PIC_{main.}$
- DC-link discharge function.
- Segregate rotor side converter on PIC_{main} command.
- Segregate line side converter on PIC_{main} command.
- Crowbar trigger on PIC_{main} command.
- Operational speed range. During normal operation (i.e. with CON_S ON) dSpace controller checks the rotor speed against an operational range of ±30%. Speed outside range causes dSpace to issue a STOP command to PIC_{main}.

Certain protection commands originated from the dSpace controller e.g. crowbar activation, but all were passed through PIC_{main} so that PIC_{main} held the full status of the DFIG system.

D.6.3 Crowbar activation

(Additional drawing Figure D.38)

The crowbar was hardwired for automatic activation on rotor-side over-current and/or rotor converter-driver error detection. This facilitated the absorption of excessive energy from the DFIG rotor during a critical grid fault or a rotor-side converter error. The hardwire crowbar thresholds were set at 45A, far and above simulated grid fault-ride through values in order to avoid unwanted crowbar activation during grid fault tests, but low enough to prevent damage to the rotor converter's power electronic devices. If the local error condition remained after 315ms (timed by PIC_{main}) then the DFIG system was made to perform a shutdown procedure (Section D.6.5).

Alternatively, the crowbar could also be activated by an external trigger signal from the dSpace control hardware. The external trigger signal was routed through PIC_{main} to

correctly establish crowbar on/off status. Using this external trigger, the crowbar could be involved in grid fault ride-through tests by including crowbar activation logic within a DFIG control scheme (Chapter 6).

D.6.4 Emergency stop (Estop)

If the Estop button on either the cabinet door or the remote control box was pressed then all DFIG system contactors were de-energised immediately (full list on Table D.5). This isolated the DFIG-converter loop from the supply voltage and isolated the DC drive from its supply. The rotor-side and line-side converters' PWM units were disabled. The crowbar and brake-chopper drivers however were both activated by PIC_{main} in order to fully de-energise the system. The Estop and contactor system is illustrated in additional drawing Figure D.39.

The Estop could also be triggered by a DFIG overload, over-speed or over-temperature event. Such an event was registered by a Telemecanique XPS-AC relay, which would de-energise the main contactors and send an Estop trigger signal to PIC_{main} (Figure D.39).

D.6.5 Shut down sequence

The shut down sequence is shown in Figure D.26. Shut down was initiated by a dSpace STOP command, which triggered a shut down sequence in PIC_{main}. The STOP command safely disabled the machine whilst also preparing the dSpace DFIG controller to repeat the startup sequence, whereas an Estop event required the operator to manually reset individual elements of the dSpace DFIG controller or to perform a complete restart of the control software package. Unlike Estop, STOP did not involve the XPS-AC relay.

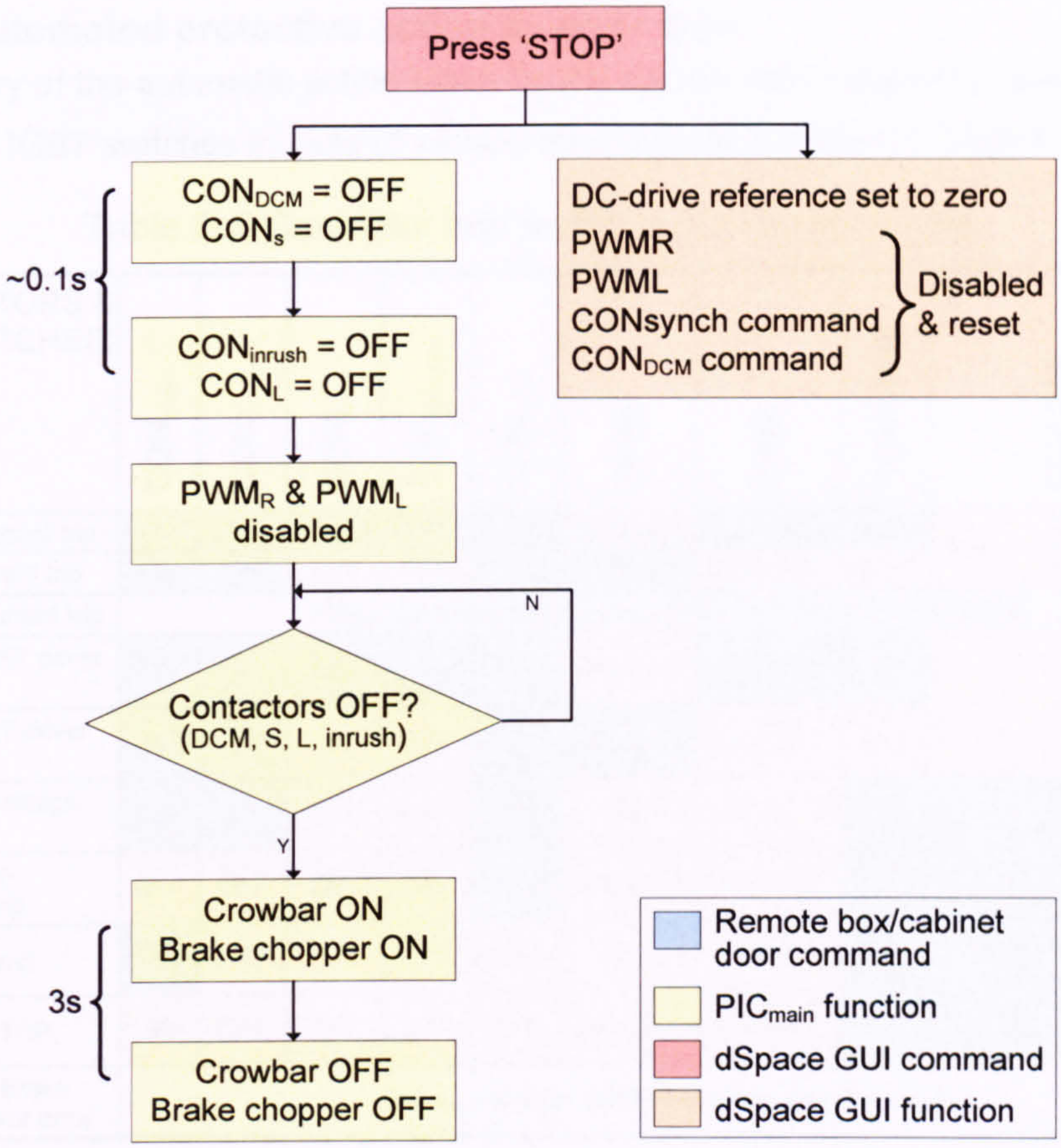

Figure D.26. Test rig shut down sequence

In the dSpace controller software, STOP disabled the DC-machine, both sets of PWM generation and the CON_{synch} command. The analogue reference signal sent to the DC-drive was reset to zero. Note that the software disablement of the PWM signals was different to the hardwired force-disable carried out on the main board.

The shut down sequence in PIC_{main} began with de-energising the CON_S, CON_{DCM}, CON_{inrush} and CON_L contactors, but *not* CON_{main}. CON_{DCM} was de-energised first, quickly followed by CON_S. This ensured that the main power path was disabled and allowed the rotor shaft to coast down to zero speed. The other contactors were de-energised within a short delay. Staggered de-energisation of the contactors helped to ensure reliable operation of the STOP process.

PIC_{main} continued by disabling the PWM signals (which should already have been disabled in software by dSpace). The crowbar and brake-chopper were both engaged for three seconds to de-energise the machine windings and the DC-link respectively.

It is worth noting that the 'DFIG–converter loop' remained energised (with CON_{main} on) after executing the shut down sequence. Startup could readily be re-initiated from this state via dSpace. After the STOP command was completed, the operator could resume the startup procedure from the position "DFIG START" in Figure D.27. However, if the system needed to be completely de-energised, then Estop could be pressed.

D.6.6 Automated protective action by error type

A summary of the automatic action taken by the system with regards to contactors and protective IGBT switches in case of various error signals is shown in Table D.5.

Table D.5 Contactor and switch action by error type.

CONTACTORS & SWITCHES: / ERRORS:	CON_{main}	CON_S	CON_L	CON_{INRUSH}	CON_{DCM}	PWM_R	PWM_L	CROWBAR	DC-LINK DISCHARGE
Rotor over-current trip	ON	ON	ON	ON	ON	DISABLE	ENABLE	ON	OFF
Line over-current trip	ON	ON	OFF	OFF	ON	ENABLE	DISABLE	OFF	OFF
Stator over-current trip	PIC_{main} executes **Emergency STOP** sequence (Section D.6.4)								
Rotor-side IGBT driver error	ON	ON	ON	ON	ON	DISABLE	*ENABLE*	*ON*	OFF
Line-side IGBT driver error	ON	ON	OFF	OFF	ON	ENABLE	DISABLE	OFF	OFF
DC-link over-voltage trip (>1000V)	ON	ON	OFF	OFF	ON	OFF	OFF	ON	ON (IF PWM_R AND CON_L=OFF)
Heat sink over-temperature trip	OFF	OFF	OFF	OFF	ON	DISABLE	DISABLE	ON	ON (IF PWM_R AND CON_L=OFF)
STOP command	ON	OFF	OFF	OFF	OFF	OFF	OFF	ON (3s)	ON (3s) (IF PWM_R AND CON_L=OFF)
Emergency STOP	OFF	OFF	OFF	OFF	OFF	DISABLE	DISABLE	ON	ON (IF PWM_R AND CON_L=OFF)
Crowbar/ Brake chopper driver error	PIC_{main} executes **STOP** sequence (Section D.6.5)								

D.7 System startup

Due to the complex nature of interconnections of sensitive subsystems in the DFIG test rig, the startup operation had to follow a carefully planned sequence. The execution of the startup sequence was shared between the PIC_{main} and dSpace controllers. A flowchart of the startup process is given in Figure D.27. The layout of key components, notably contactors such as CON_{main}, is shown in the test rig single line diagram (Additional drawings, Figure D.33).

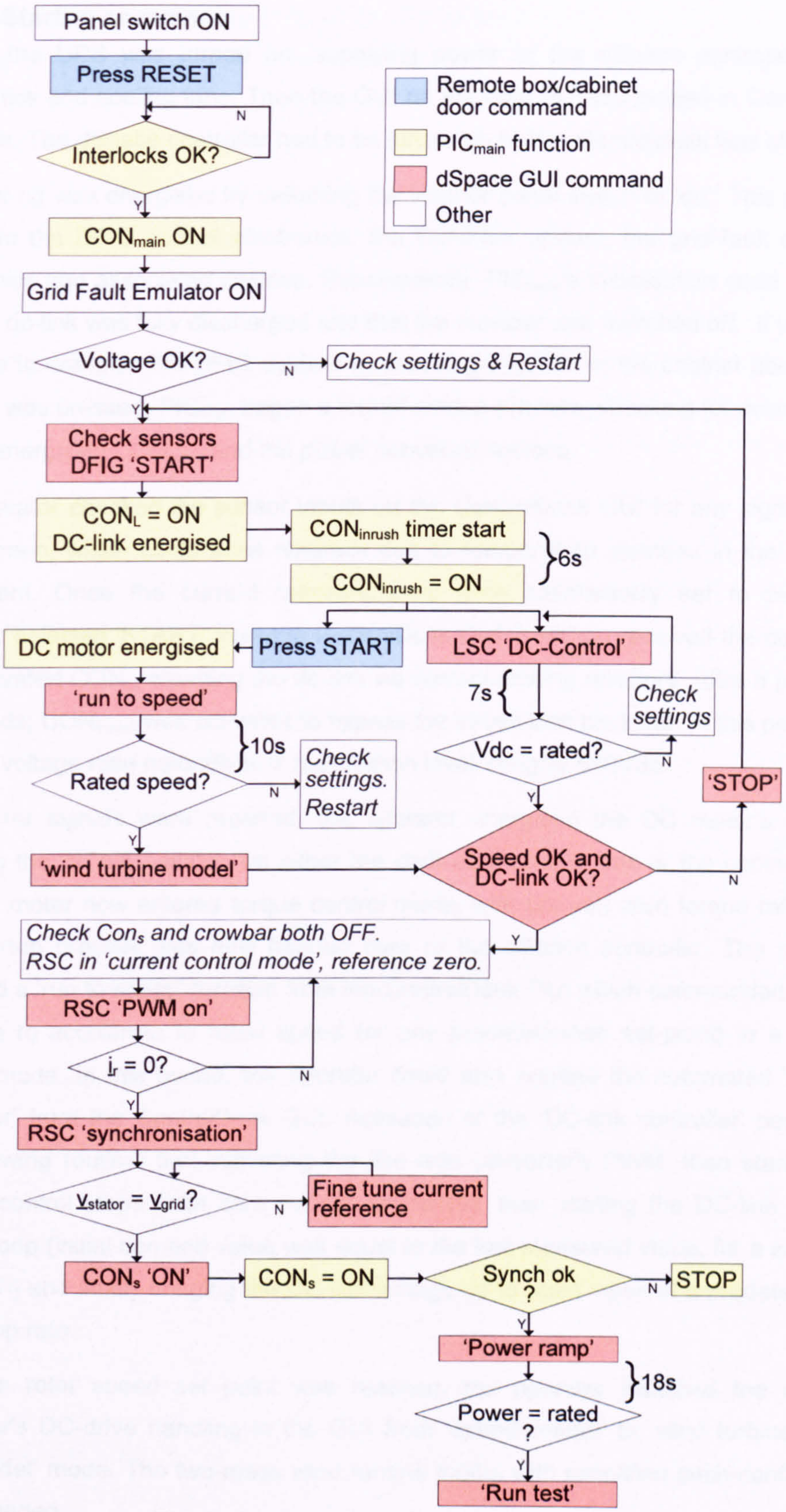

Figure D.27. Test rig start up sequence

D.7.1 Startup sequence

Firstly, the UPS was turned on, supplying power to the dSpace controller, DFIG electronics and cooling fans. Then the GUI on the host PC was loaded in Controldesk software. The dSpace controller had to be turned on before Controldesk was started.

The test rig was energised by switching the isolator panel switch to 'on'. This provided power to the DFIG control electronics, the DC-drive system, the grid fault emulator electronics and associated devices. Subsequently, PIC_{main}'s initialisation code ensured that the dc-link was fully discharged and that the crowbar was switched off. It was then possible to energise the DFIG system by pressing RESET on the cabinet door. Once RESET was pressed, PIC_{main} began a formal startup process, checking for error signals before energising CON_{main} and the power converter devices.

The operator checked the sensor inputs on the ControlDesk GUI for any signs of DC offset creep, which could arise naturally due to temperature changes in the sensing equipment. Once the current measurements were satisfactorily set to zero, the operator selected 'START' from the ControlDesk GUI[14]. PIC_{main} received the command and activated CON_L, charging the dc-link via current-limiting resistors. After a period of 3 seconds, CON_{inrush} was activated to bypass the inrush limit resistors. In this period the DC-link voltage rose naturally to a rectification level, roughly 560Vdc.

If no error signals were reported, the operator energised the DC motor's field by pressing the 'START' button on either the dedicated remote box or the cabinet door. The DC motor now entered torque control mode, with (as yet) zero torque reference. The startup process was now handed over to the dSpace controller. The operator engaged a 'run to speed' function from the ControlDesk GUI which commanded the DC machine to accelerate to rated speed (or any predetermined set-point) in a speed-control mode. In this period, the operator could also engage the automated 'DC-link controller' from the ControlDesk GUI. Activation of the 'DC-link controller' performed the following routine: first activating the line-side converter's PWM, then starting the current control loops (with zero current reference), then starting the DC-link voltage control loop (initial demand value was equal to the last measured value, for a soft-start approach) and finally bringing the DC-link voltage up to rated value at a predetermined safe ramp rate.

After the rotor speed set point was reached, the operator switched the dSpace controller's DC-drive handling in the GUI from 'speed-control' to 'wind turbine drive-train model' mode. The two-mass wind turbine model with simplified pitch-control was then engaged.

---

[14] The dSpace START function is disabled if PIC_{main} reports any system errors.

The operator then navigated to the rotor converter section of the GUI and selected 'synchronisation' mode. This successively activated the rotor-side PWM, then the rotor current control loops (at zero current reference values) and finally led the rotor current space vector components from zero to predetermined synchronisation values. These values were calculated to fully magnetise the generator and provide a stator emf which approximately matched the supply voltage. The stator emf could then be fine-tuned in real-time to accurately match the supply voltage by adjusting the rotor current demand values. When a good match was achieved, the DFIG stator contactor CON_S could be energised with the appropriate button on the GUI. If the synchronisation process generated too high a spike in stator current, an automatic shutdown event would be triggered, and the above process had to be repeated. If the stator current was ok, the startup procedure continued.

When successfully synchronised, the DFIG could start to generate electrical power. The operator selects 'power ramp' function from the GUI which brought the controller's stator power demand up to a predetermined value (normally 5kW generation). The power demand value was ramped up at a limited rate to avoid exciting the natural resonance of the wind turbine model and thereby incurring large speed oscillations. As the electric power increase pulled down the rotor speed the modelled wind turbine controller responded by raising its torque input to control the modelled turbine speed. This in turn raised the modelled drive-shaft coupling torque – the torque reference issued to the DC-drive. This process roughly simulated the pitching-in of wind turbine blades to capture more energy, and was facilitated by a slow-acting turbine-hub speed controller. When the fixed electric power value was reached and the rotor speed was sufficiently steady, the grid fault test could be executed.

D.8 Test rig layout

A detailed single line drawing featuring the electrical layout of all the test rig components is shown in additional drawing Figure D.33. The grid fault emulation equipment was enclosed on a workbench above the rotating machines, with the variac three-phase voltage sources to one side. As for the DFIG system: all the control electronics, contactor hardware, filter equipment, DC-drive and so on were housed in a dedicated metal control cabinet.

D.8.1 Control cabinet

All components except the 10kVA isolation transformer, the DC-motor, induction machine and grid fault emulation equipment were housed in a Rittal TS series cabinet as shown diagrammatically in Figure D.28 and in the photo Figure D.29. The crowbar and brake resistors were mounted externally on the roof of the cabinet for the efficient

dissipation of heat. Careful consideration was given to the cabinet wiring and component placement, separating power and signal cables to maintain noise immunity. Cables carrying high frequency mains voltages were each screened and earthed at one end.

Internal layout

The design of the internal layout of the cabinet is shown in Figure D.28. A photo of the completed cabinet internal layout is shown in Figure D.29.

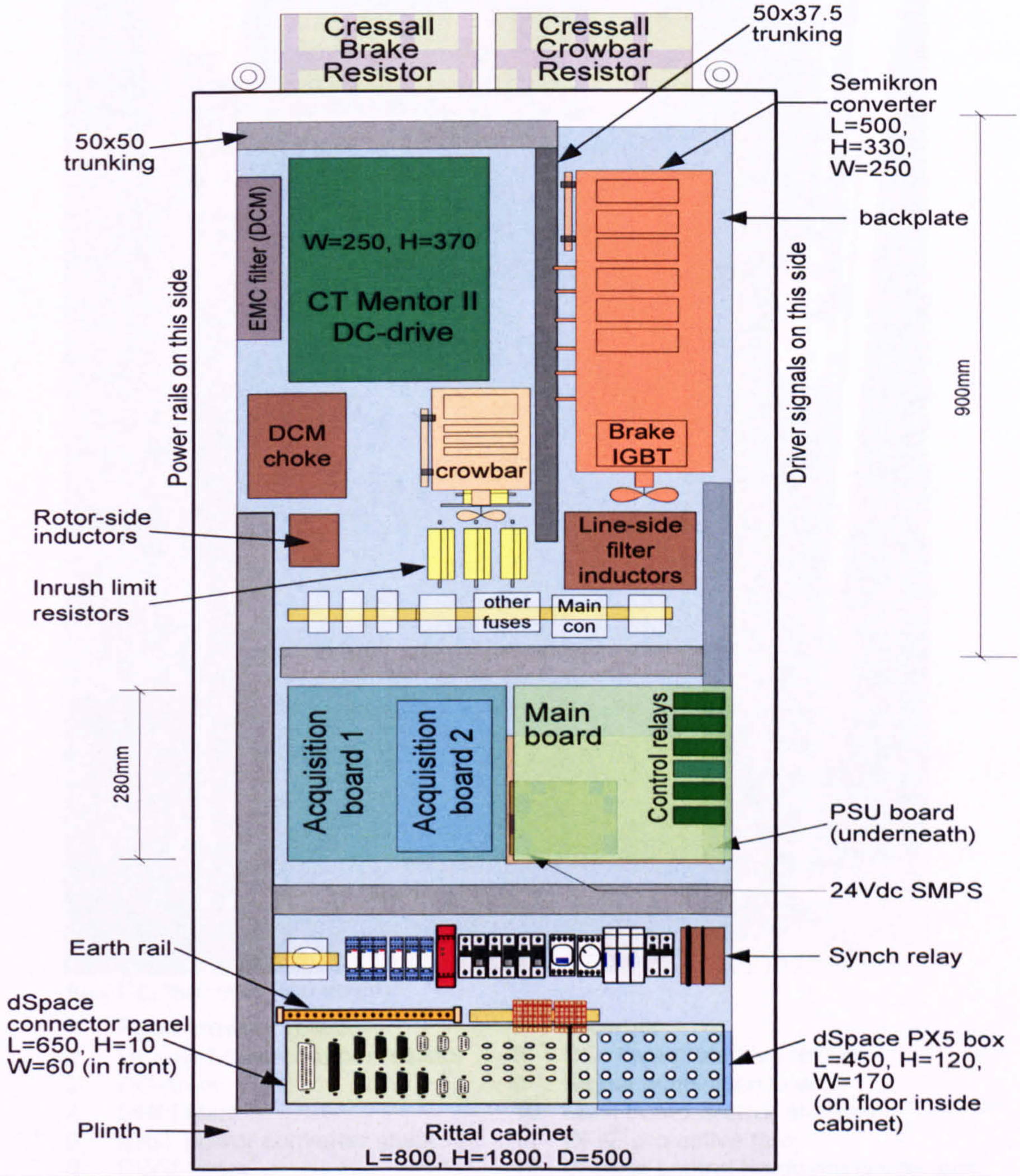

1. 3-phase line outs from the converter are screened. The screen is connected at both ends to the cabinet.
2. The sheath glands terminate <150mm from the converter terminal connection.
3. No sensitive circuitry or wiring resides within 300 mm of the converters.
4. PCBs in two layers are separated by earthed aluminium screens for EMI suppression
5. Main error analysis board is mounted on a hinged aluminium plate. The plate swivels out to provide access the boards behind.
6. Fixed EMI glands are positioned at the cable entry points into the cabinet

All dimensions in mm

Figure D.28. Control cabinet internal layout.

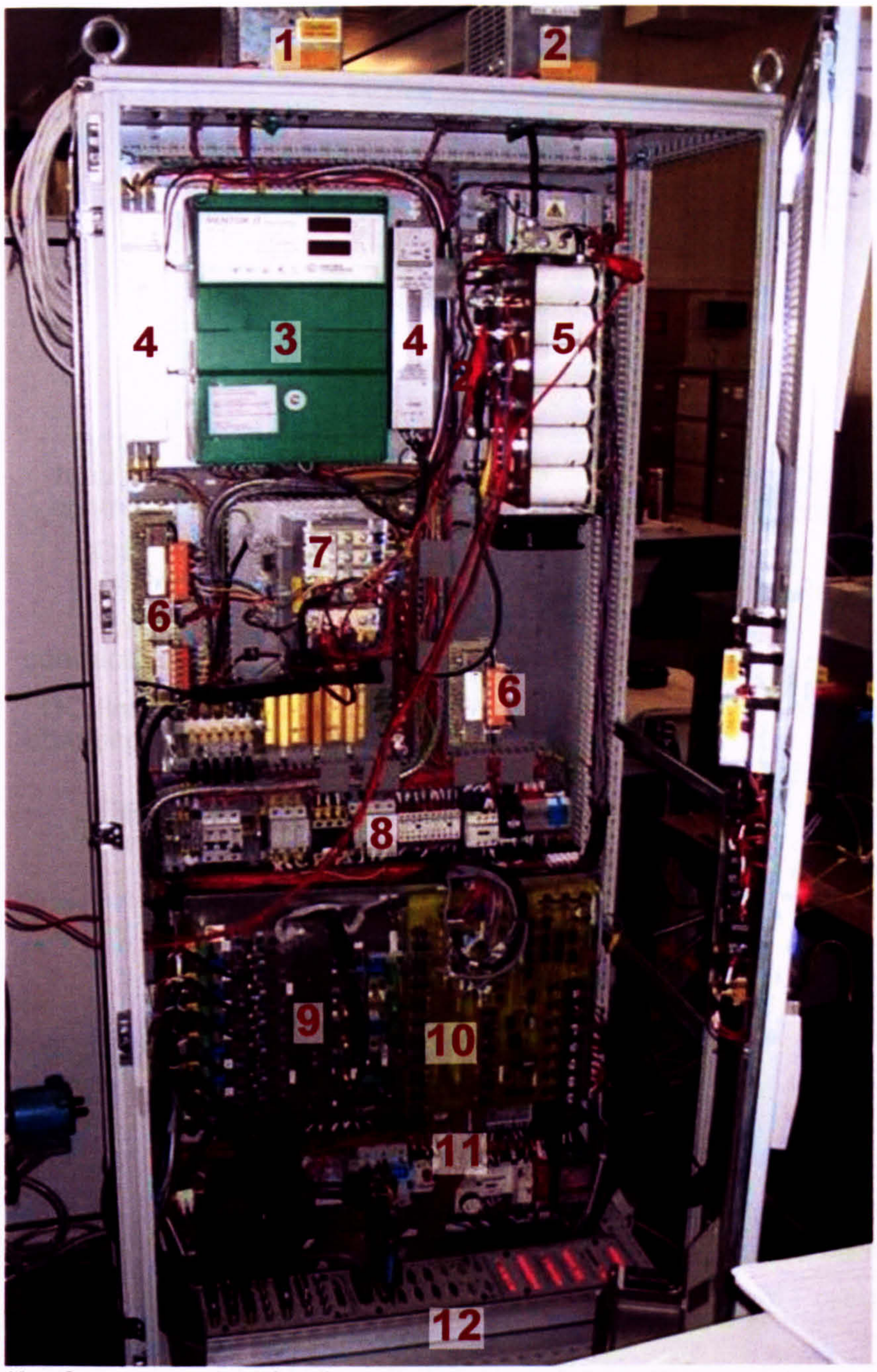

Key Components (top down):

1	Rotor crowbar resistor	7	Crowbar
2	DC-link brake-chopper resistor	8	DC-drive protective relays
3	DC-drive	9	Signal acquisition boards
4	EMI Filters	10	Main board & error analysis
5	IGBT power converter stack	11	DFIG protective relays
6	PWM filters	12	dSpace control hardware & interface

Figure D.29. DFIG control cabinet internal photo.

External layout

A number of safety features, DC-drive control features and DFIG system indicators were designed into the control cabinet's front door for easy access. The door plan is shown in Figure D.30 and a photo of the completed cabinet in Figure D.31.

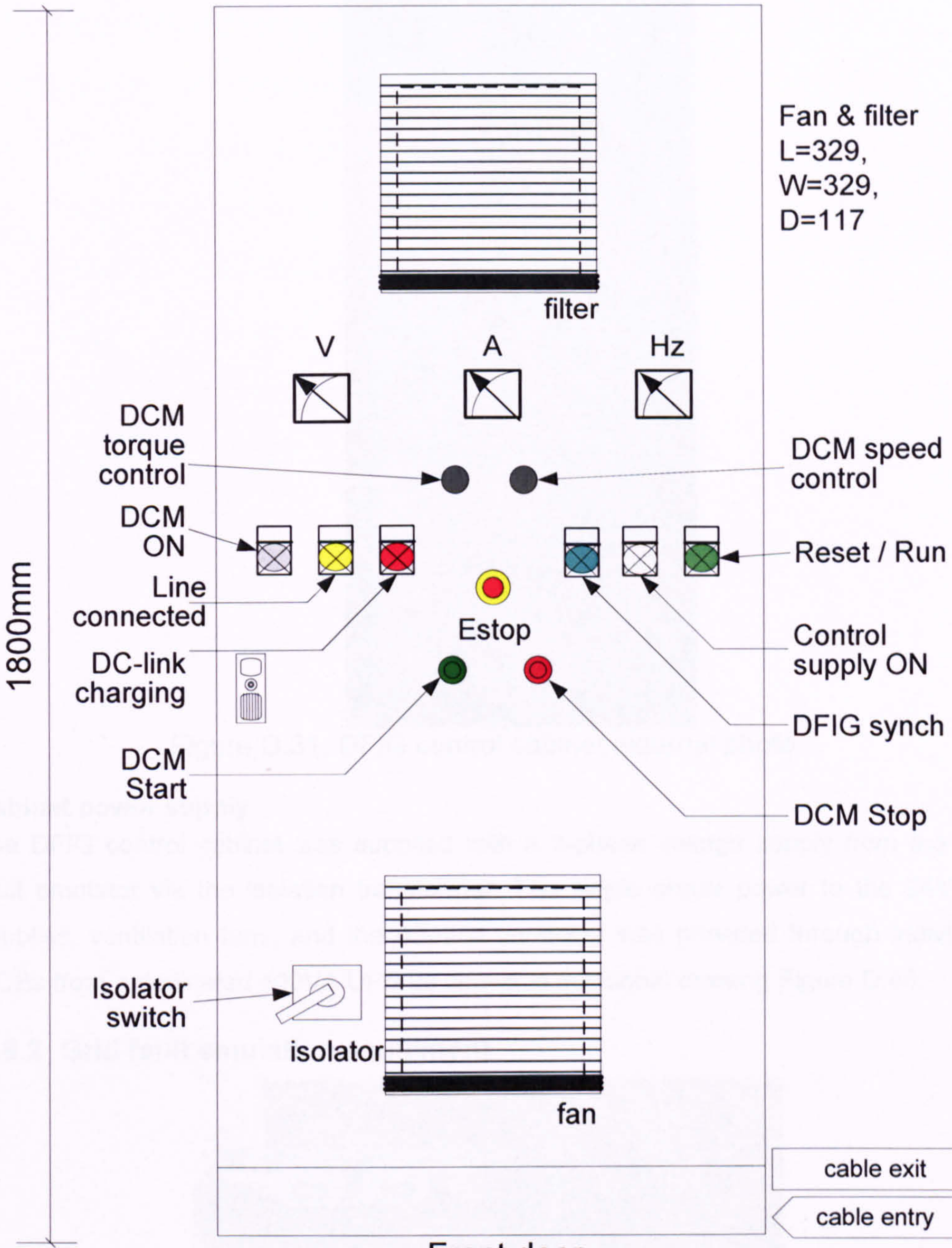

Note: all dimensions in mm

Figure D.30. Control cabinet door layout.

Figure D.31. DFIG control cabinet external photo.

Cabinet power supply

The DFIG control cabinet was supplied with a 3-phase voltage supply from the grid fault emulator via the isolation transformer. The single phase power to the 24V DC supplies, ventilation fans, and the dSpace controller was provided through individual MCBs from a dedicated 400VA UPS as shown in additional drawing Figure D.40.

D.8.2 Grid fault emulation equipment

Figure D.32. Grid fault emulator: contactors, reactors and electronics.

Except for the stand-alone three-phase variacs, the grid fault emulation equipment was divided between two enclosures. The contactors, inductors and overload detection were housed in a large caged enclosure, which was screened on top and earthed onto the motor housing. The IGBT transfer switching equipment was housed in a small flat enclosure which was screened and earthed via the neighbouring cage. These enclosures were mounted side-by-side on a bench above the DFIG. Note that both screens were clear to allow visual checks of the equipment. A picture of the two enclosures is shown in Figure D.32.

D.9 Additional drawings

Additional technical drawings follow, their titles listed below:

- Figure D.33. Test rig design electrical layout.
- Figure D.34. Electronics boards layout.
- Figure D.35. Control signal interconnection diagram.
- Figure D.36. Trip logic.
- Figure D.37. Trip clearance circuitry.
- Figure D.38. Crowbar operation.
- Figure D.39. Contactors, interlocks and emergency stop
- Figure D.40. 240V supply interconnections.
- Figure D.41. Over-speed protection sensor.

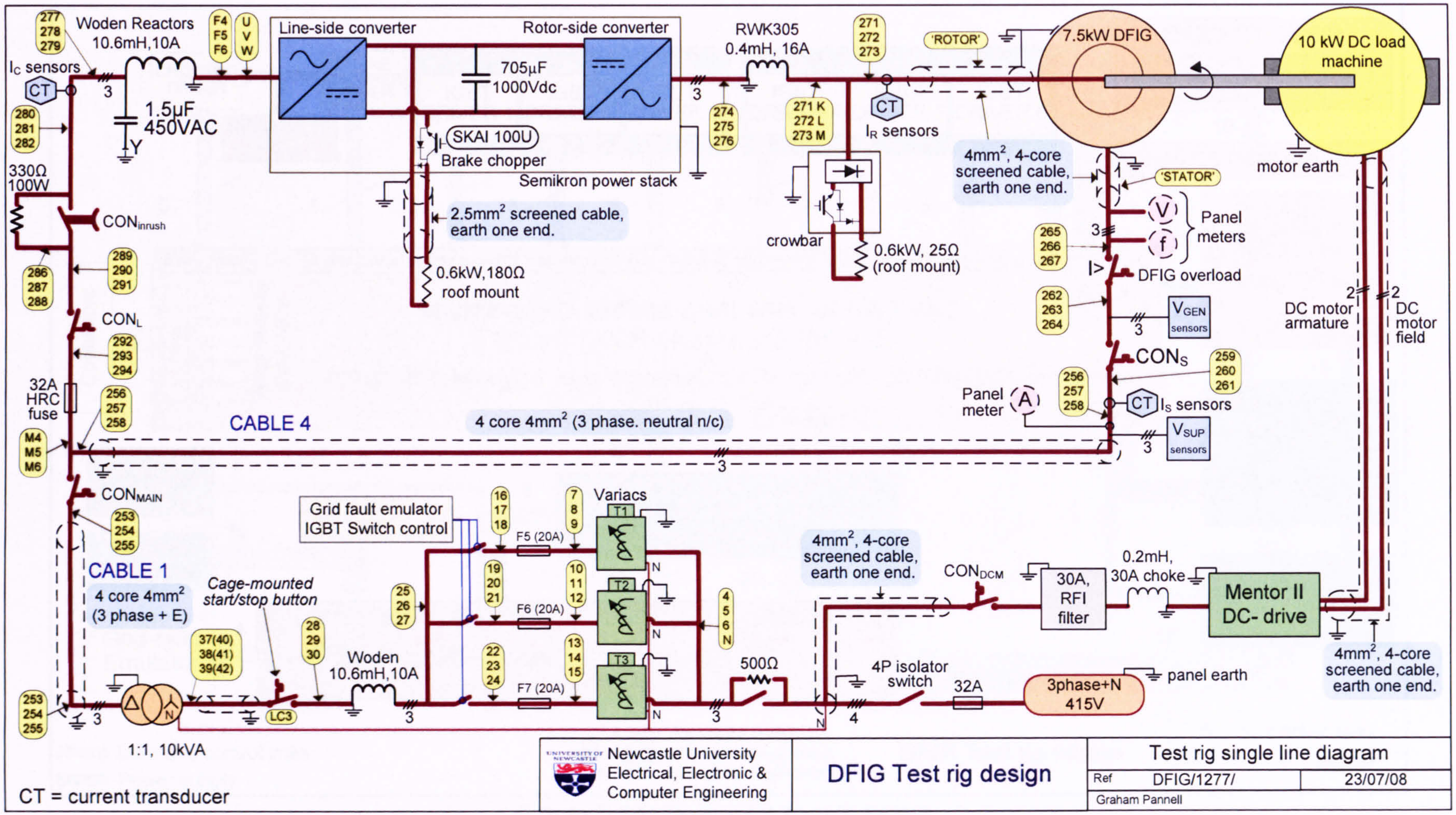

Figure D.33. Test rig design electrical layout.

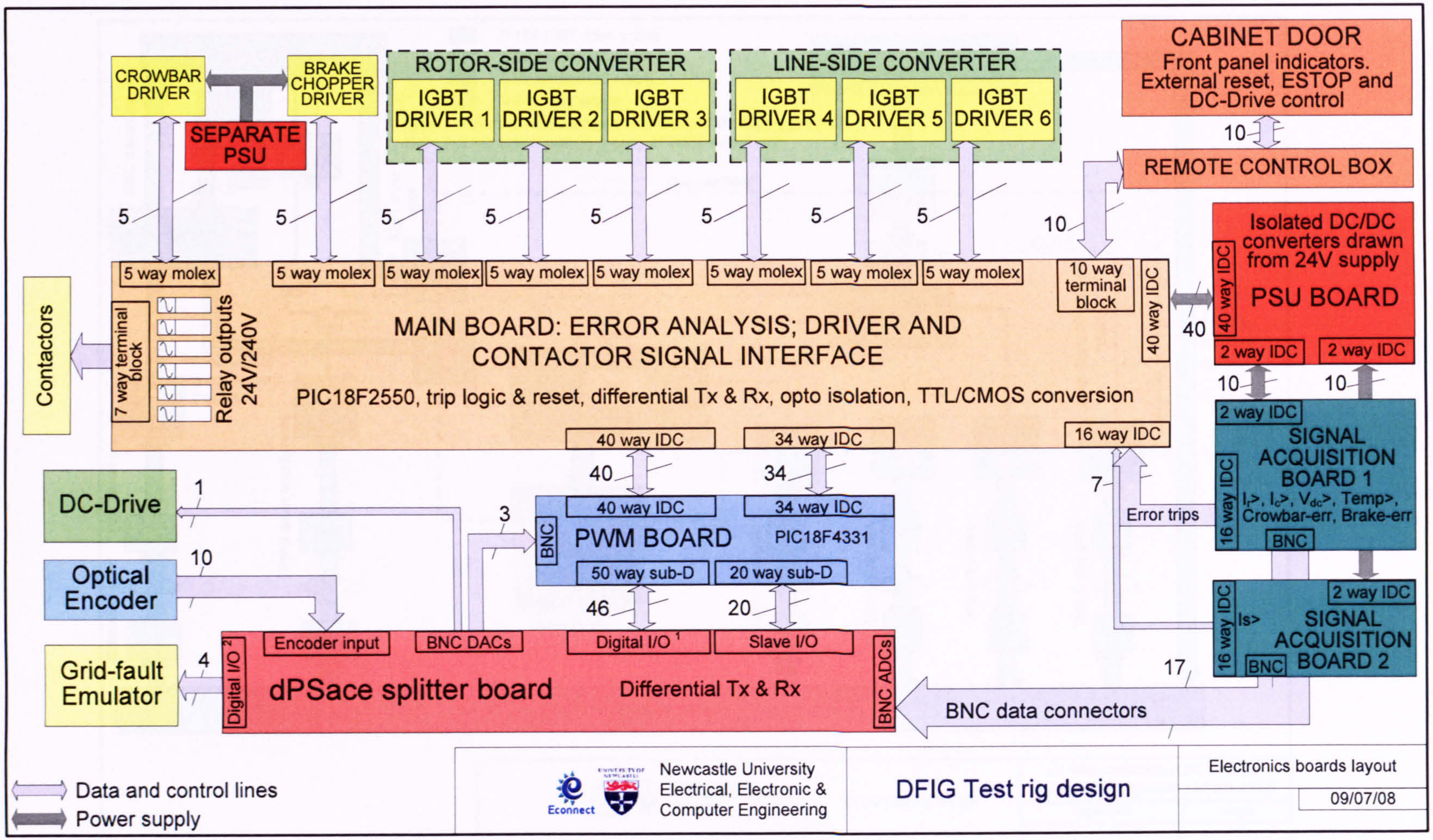

Figure D.34. Electronics boards layout.

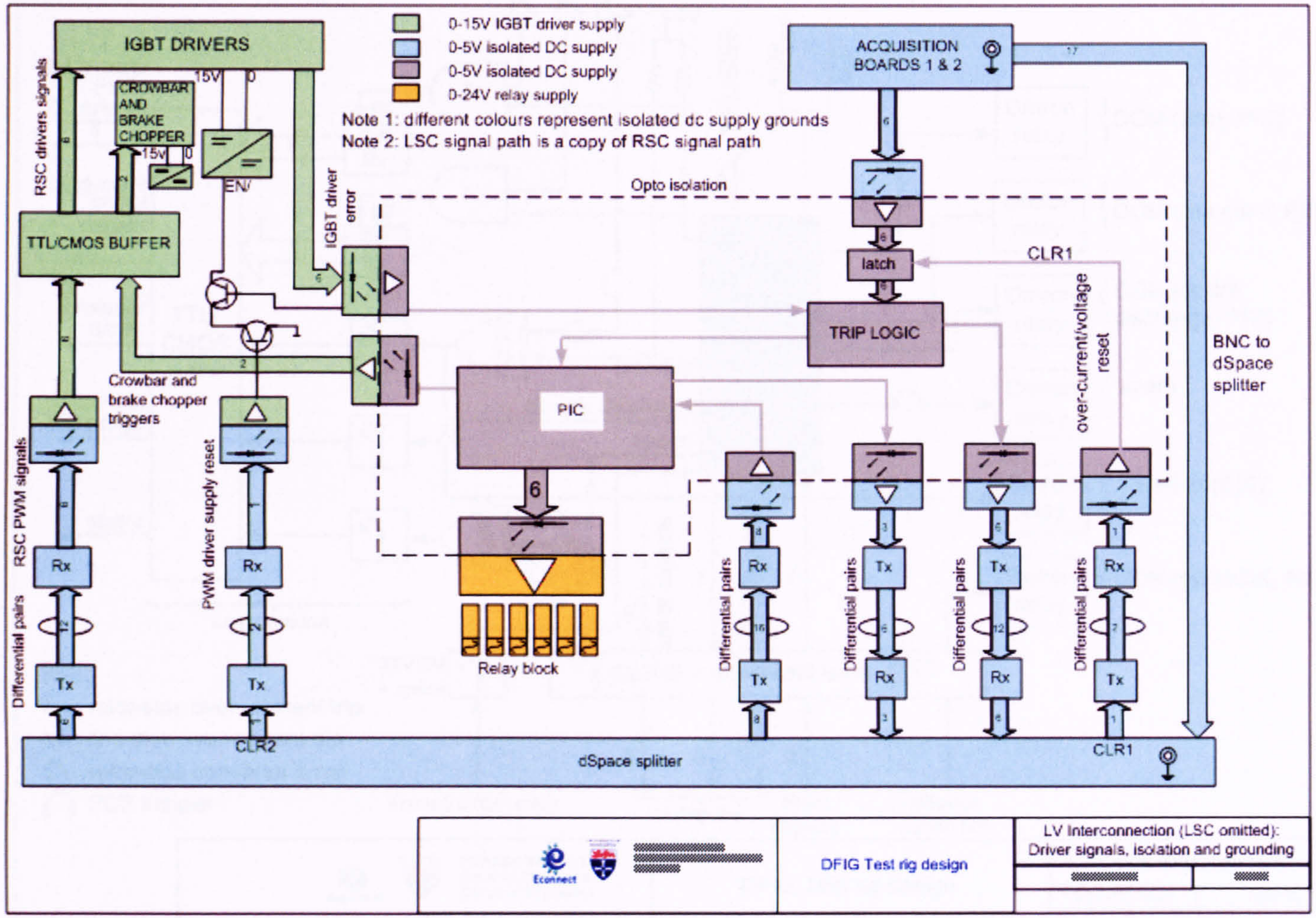

Figure D.35. Control signal interconnection diagram.

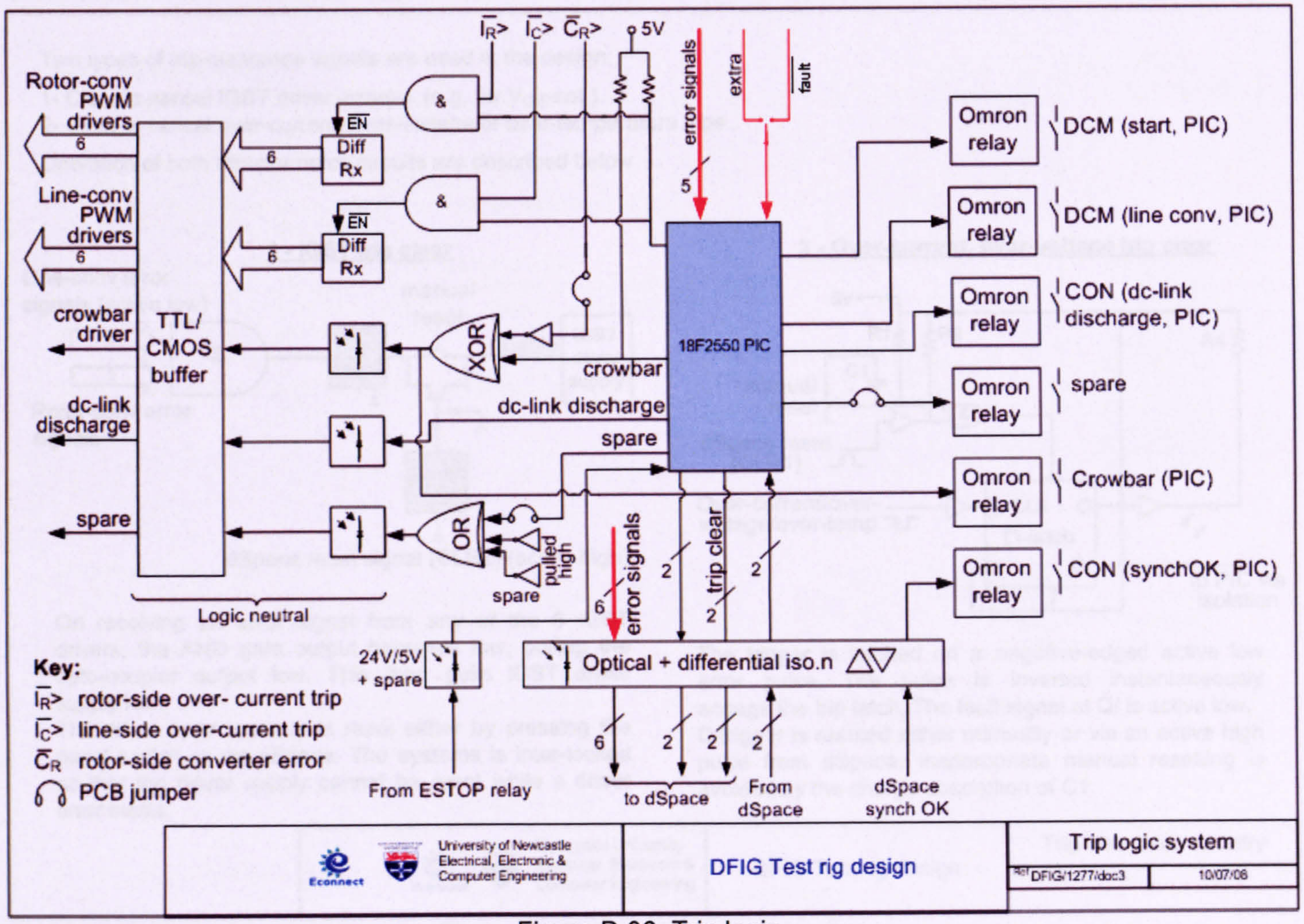

Figure D.36. Trip logic.

Two types of trip-clearance signals are used in the design:

1- Clear to cancel IGBT driver error(s) (e.g. for $V_{C\text{-}E}$-sat)
2- Clear to cancel over-current, over-voltage or over-temperature trips

Operation of both trip-clearance circuits are described below.

1 - IGBT trip clear

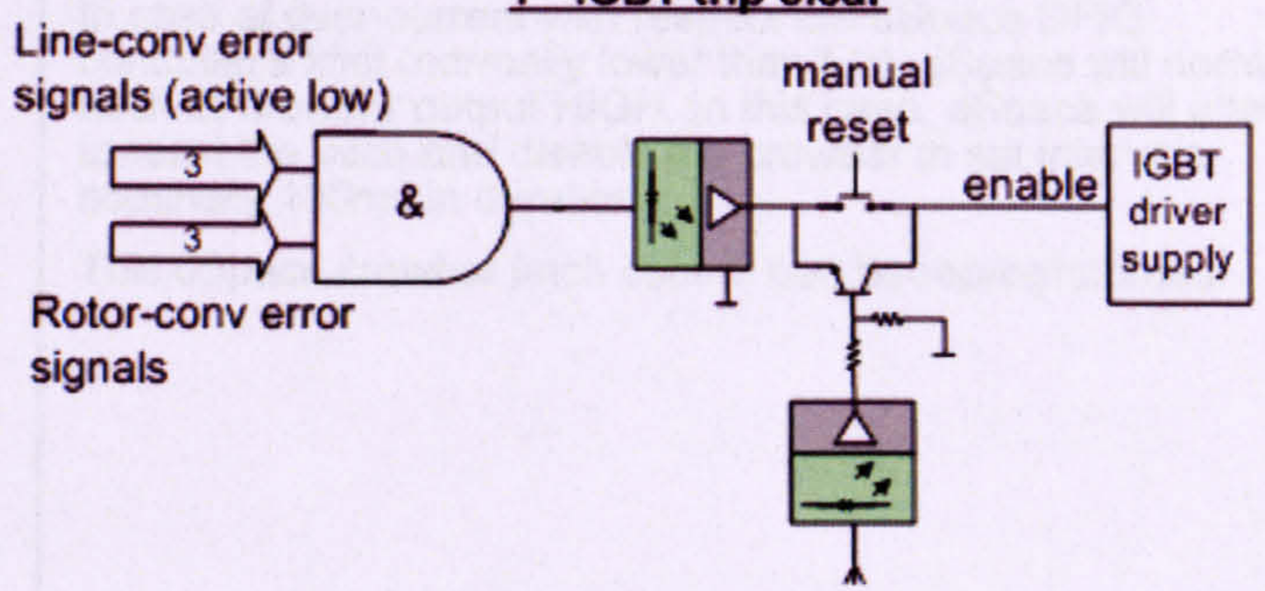

On receiving an error signal from any of the 6 IGBT drivers, the AND gate output becomes low, pulling the opto-coupler output low. This then pulls IGBT driver supply low.
The driver error memory is reset either by pressing the panel switch or via dSpace. The systems is inter-locked so that the driver supply cannot be reset while a driver error exists.

2 - Over-current, over-voltage trip clear

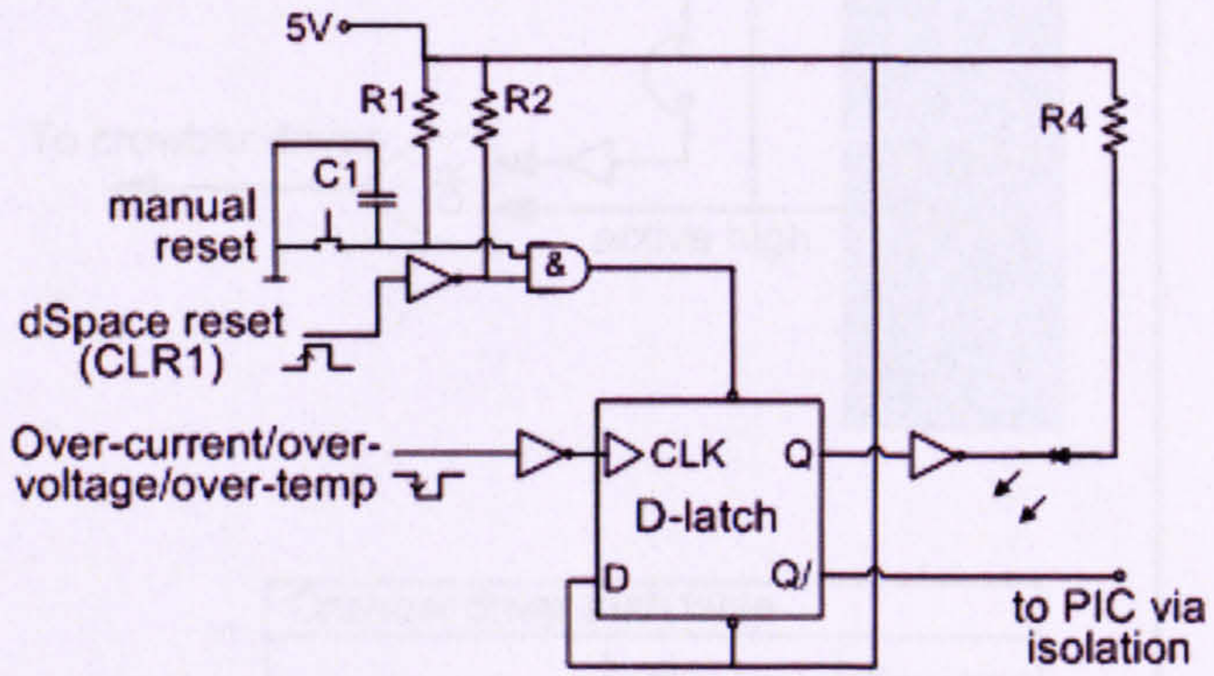

The trigger is latched on a negative-edged active low error pulse. The pulse is inverted instantaneously engage the trip latch. The fault signal at Q/ is active low. D-trigger is reseted either manually or via an active high pulse from dSpace. Inappropriate manual resetting is avoided by the charge absorption of C1.

Econnect · Newcastle University Electrical, Electronic & Computer Engineering	DFIG Test rig design	Trip-clearance circuitry
	Ref DFIG/1277/doc5	15/08/05

Figure D.37. Trip clearance circuitry.

Operational details

Crowbar is normally activated on either rotor-side converter error signal, $\overline{C_R}$> (active-low), or by a PIC command (active-high).

The PIC_{main} crowbar command is normally triggered high by a dSpace input command (active-high), unless PIC_{main} has otherwise disabled its crowbar output, in which case the PIC_{main} crowbar command is held LOW

In case of over-current with respect the dSpace DFIG controller's limit (normally lower than I_R>), dSpace will normally latch its crowbar output HIGH. In this case, dSpace will attempt to reset the latch and disable the crowbar in set intervals, nominally 100ms in duration.

This dSpace crowbar latch control can be reprogrammed.

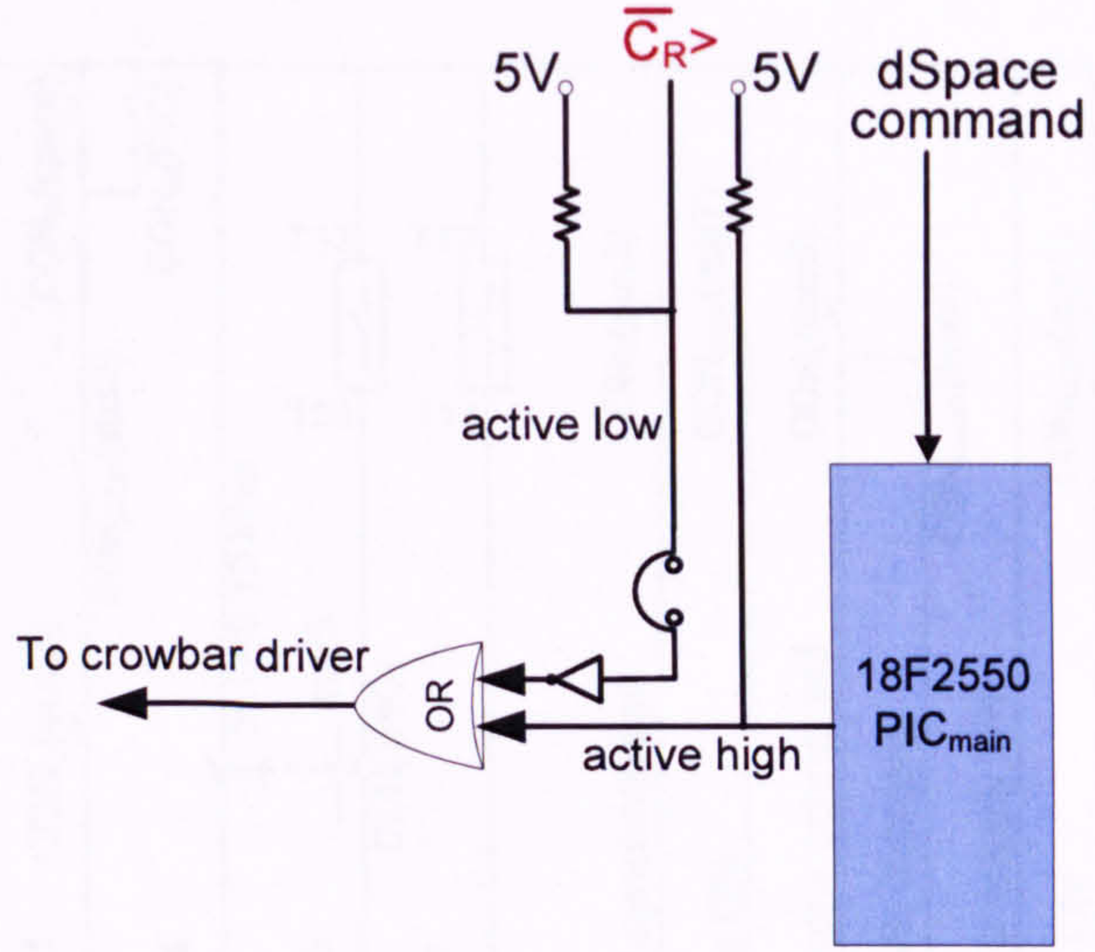

Referring to the truth table:

- The default state: PIC_{main} crowbar command is pulled low, RSC error is pulled high, the crowbar is OFF.
- If the PIC_{main} command is pulled HIGH the crowbar is turned ON regardless of RSC error
- If the RSC error is pulled LOW then the crowbar is turned ON regardless of PIC_{main} command.

Crowbar driver truth table

C_R>	not C_R>	PIC_{main} command	Crowbar driver
1	0	0	0
1	0	1	1
0	1	0	1
0	1	1	1

Econnect | Newcastle University Electrical, Electronic & Computer Engineering | DFIG Test rig design | Crowbar operation details | Ref DFIG/1277/doc4 | 10/07/08

Figure D.38. Crowbar operation.

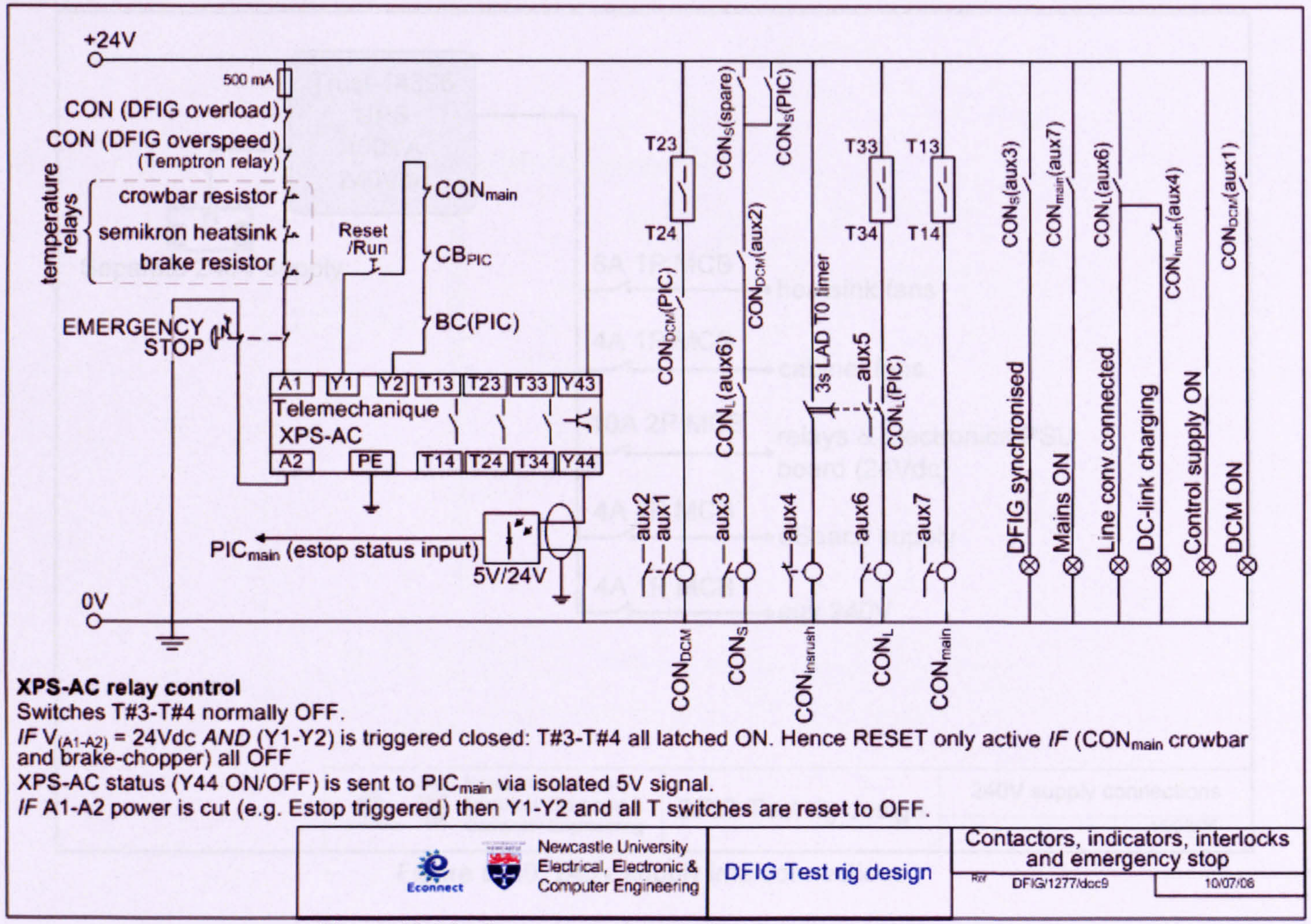

XPS-AC relay control
Switches T#3-T#4 normally OFF.
IF $V_{(A1\text{-}A2)}$ = 24Vdc *AND* (Y1-Y2) is triggered closed: T#3-T#4 all latched ON. Hence RESET only active *IF* (CON_{main} crowbar and brake-chopper) all OFF
XPS-AC status (Y44 ON/OFF) is sent to PIC_{main} via isolated 5V signal.
IF A1-A2 power is cut (e.g. Estop triggered) then Y1-Y2 and all T switches are reset to OFF.

Econnect	Newcastle University Electrical, Electronic & Computer Engineering	DFIG Test rig design	Contactors, indicators, interlocks and emergency stop
		RW DFIG/1277/doc9	10/07/06

Figure D.39. Contactors, interlocks and emergency stop

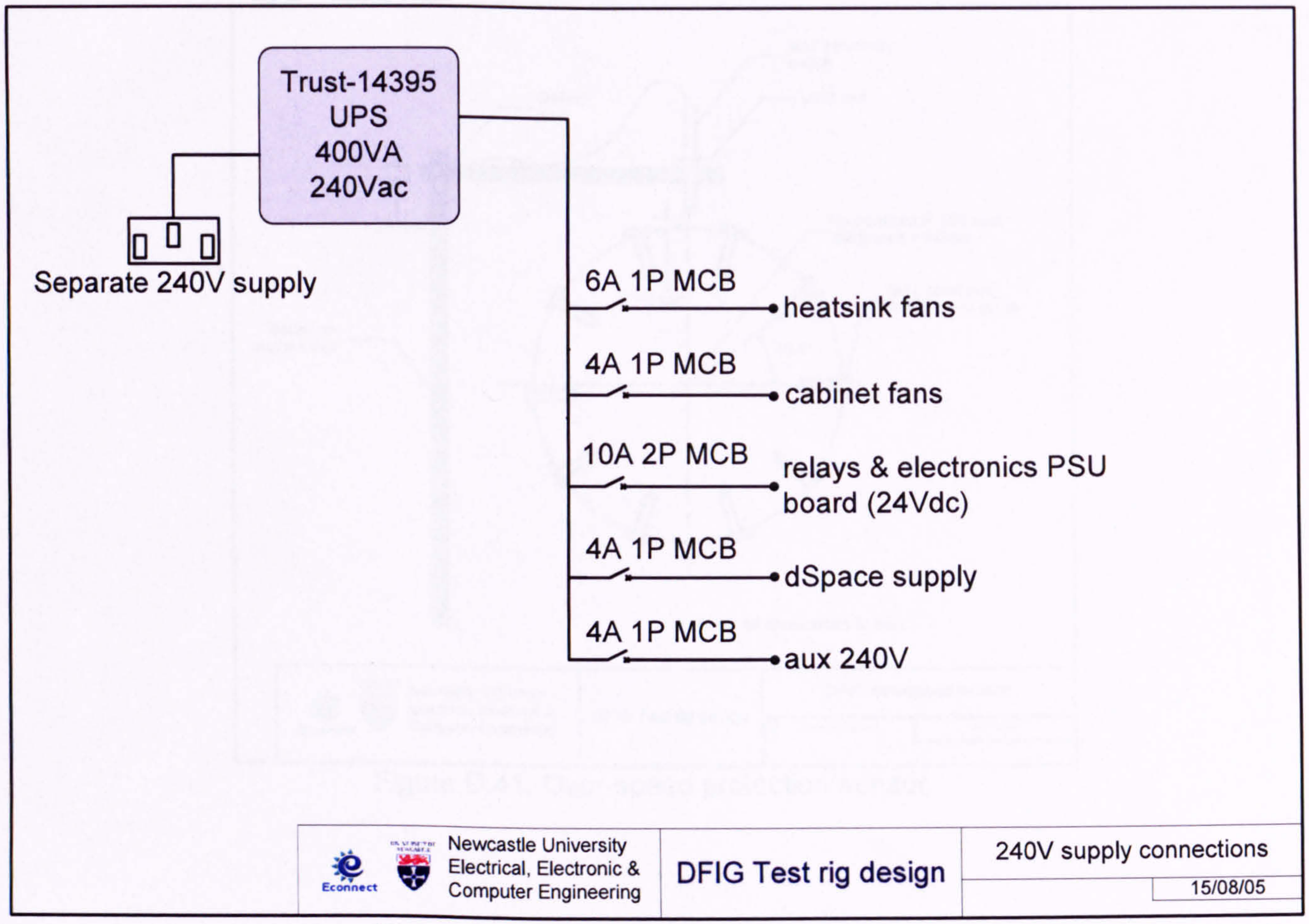

Figure D.40. 240V supply interconnections.

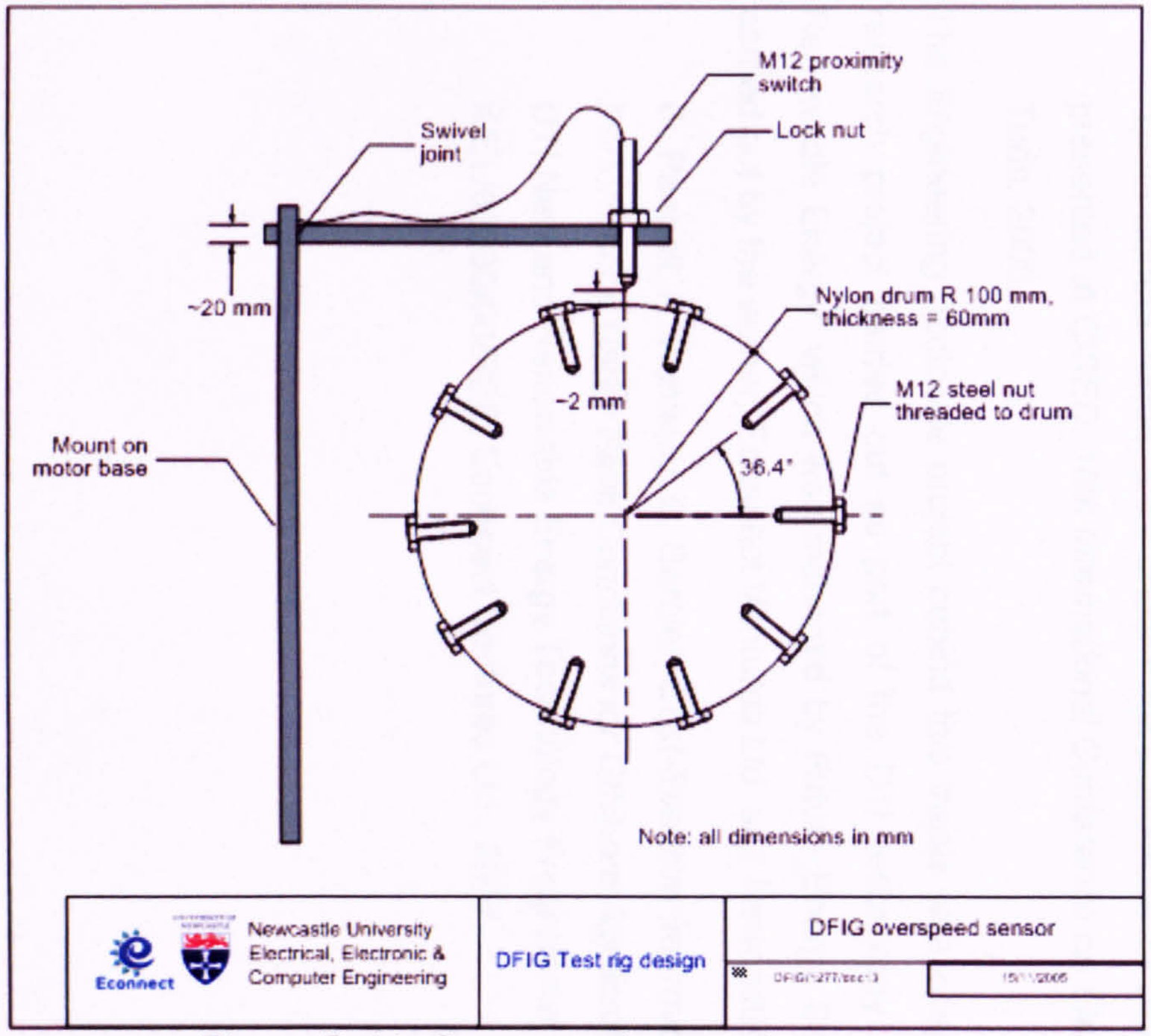

Figure D.41. Over-speed protection sensor.

ASSOCIATED PUBLICATIONS E

To date, the following peer-reviewed proceedings stemmed from this research [3]:

> G. Pannell, D. J. Atkinson, R. Kemsley, L. Holdsworth, P. Taylor, and O. Moja, "DFIG Control Performance under Fault Conditions for Offshore Wind Farms", presented at *CIRED: 18th International Conference on Electricity Distribution,* Turin, 2005.

The Engineering doctorate project behind this thesis was operated in parallel with a research project carried out as part of the DTI technology programme "New and Renewable Energy" which was managed by Future Energy Solutions. The work was carried out by the author, Econnect Ventures Ltd. and Newcastle University [2]:

> G. Pannell, R. Kemsley, C. Barbier, *Cost-Effective Improvements in DFIG Performance Under Fault Conditions for Offshore Applications,* prepared for the DTI New and Renewable Energy Technology Programme, Contract no. K/EL/00335/00/REP, Econnect Ventures Ltd., 2007.